LARGE-SCALE DYNAMICS OF THE UPPER MESOSPHERE AND LOWER THERMOSPHERE

By

Trevor Harris, B.Sc. (Hons)

Thesis

submitted for the degree of

DOCTOR OF PHILOSOPHY

at the

UNIVERSITY OF ADELAIDE

(Department of Physics and Mathematical Physics)

September 1993

Contents

List of Tables

List of Figures

Abstract

Observations in the upper mesosphere and lower thermosphere of a planetary scale wave known as the quasi-two-day wave (or simply the 2-day wave) have been made over several years at a mid-latitude site near Adelaide (34.5° S, 138.5° E), and over two years at a low-latitude site on Christmas Island (2° N, 157° W). These results, their interpretations and the consequences for current theory are presented in this thesis. In addition, an attempt is made to define and determine a response time for the solar tides. A number of data analysis techniques were also considered during the course of this thesis. An understanding of the usefulness and shortcomings of these different techniques is invaluable in any research. It is hoped that this thesis also contributes to this end.

The opening chapter gives the background in which contributions of this thesis are set. The atmosphere in general, and its remote sensing in particular, are discussed, with emphasis on the role of the tides and other planetary waves. The theory of atmospheric normal modes is also considered at this stage.

This is followed by some theory and discussion on various analytical techniques relevant to the research work. These include discussions on Doppler and Spaced-Antennae radars; full correlation analysis; Fourier techniques; the handling of missing data; the separation of wind components from a heterogenous wind field; sensitive measures for determining the period of a wave oscillation; moving power spectra; and higher-order spectral estimates. As all the wind data used in this thesis was derived by use of a full correlation analysis some time is spent in explaining this technique. The effects of varying some critical parameters in a general full correlation analysis algorithm are then investigated in Chapter 3 and comparisons made between three different algorithms.

Chapter 4 covers the main research work performed in this thesis — the investigation of the quasi-two-day wave. This is a large amplitude planetary scale wave whose wind perturbations maximise each year at mid-latitudes in the summer hemisphere. The term "quasi-" refers to previous observations that this wave has a period slightly longer than two days in the northern

hemisphere during the July solstice. As the period appears to be very close to two days in the southern hemisphere during the December solstice, the "quasi-" prefix is often dropped. The observed properties of the 2-day wave are investigated in some depth in this chapter.

Firstly, using 12 years of data from Adelaide, typical properties at mid-latitudes in the southern hemisphere were considered. These included the average vertical wavelength and mean and decile amplitudes. The concept that the wave is locked in phase to local time was also investigated.

Due to the amplitude structure of the wave, sites near the equator can observe the 2-day wave during both solstices. Therefore differences in the wave properties of the 2-day wave during its period of maximum amplitude in each hemisphere were investigated using observations at the equatorial site of Christmas Island. Other wave components, possibly harmonics of the 2-day wave, were observed and their properties determined. The presence of these additional waves suggested some non-linearity in the 2-day wave during times of large wave amplitude. Therefore interactions between the 2-day wave and the mean flow, and with the diurnal tide were also investigated. Finally, its zonal wavenumber and the impact of the 2-day wave on the atmospheric angular momentum budget were estimated at the end of the Chapter 4.

Chapter 5 details a preliminary study of the variability of the solar diurnal and semi-diurnal tides. Some measure of the response time for these tides was sought and an analysis scheme developed. Experimental estimates of a "minimal response time" were obtained and critically compared to the latest theoretical estimates. Further investigations were then suggested.

In summary, this work supports the theory that the 2-day wave is a manifestation of the atmospheric $(3,0)$ normal mode and is present in some form throughout the year. It also shows that considerable hemispherical assymetry exists for this particular planetary wave. If this is the case for one normal mode then it may easily be the case for all, reinforcing the need for more southern hemisphere and equatorial observations. The non-linear behaviour of this large amplitude oscillation has also been shown and the need for more non-linear, non-stationary, non-Gaussian analytical tools is highlighted. Lastly, an important contribution is made to the question of tidal response times, and it is suggested that *in situ* tidal modes play an important role in the observed variability of the solar tides.

This work contains no material which has been accepted for the award of any other degree or diploma in any university or other tertiary institution and, to the best of my knowledge and belief, contains no material previously published or written by another person, except where due reference has been made in the text.

I give consent to this copy of my thesis, when deposited in the University Library, being available for loan and photocopying.

Signed: _____ _____ dated: 5/10/93

Trevor Harris, B.Sc. (Hons)

Acknowledgements

A body of work such as this thesis, involving many years of study, results from the efforts and assistance of many people, not only the author. I would like to take this opportunity to thank some them.

Firstly, I would like to thank my supervisors: Dr Wayne Hocking, who took me on as a post-graduate student, and remained my supervisor until he left the University late in 1991; Dr Bob Vincent, who became my supervisor in 1991, and whose guidance during both the earlier and later years of my PhD was much needed and appreciated; and Dr Basil Briggs, who introduced me to the 2-day wave and continued to encourage and guide me throughout my candicature.

"No man is an Island.." and no course can be completed without the willing assistance of your colleagues and peers. Thus I would like to thank the "mob" at The Atmospheric Physics Group (some of whom have now moved on). Thanks go to Dr Laurence Campbell, Dr Pene Greet[1], Dr Damian Murphy, Dr Stephen Eckermann, Dr Drazen Lesicar (surely you will be a Doctor by the time this is completed), Brenton Vandepeer, David Low, David Holdsworth, Manuel Cervera, Simon Allen, Deepak Rajopadhyaya and those linch pins of the Department, Lynn Birchby and Dallas Kirby. Special thanks must go to Dr Iain Reid, for many helpful suggestions, for advancing the Departmental computing system into the 90's, and for bringing IDL to the University. Technical support from Bob Hurn, Alex Didenko, Shane Dillon, Lesley Rutherford, and Brian Fuller was much appreciated. Other members of the Group that I may have forgotten to mention, I apologize, but thanks to you too.

I would also like to thank the following visitors to the group for helpful conversations: Prof. Mike Kelley; Prof. Michael McIntyre; Dr Dan Senft; Dr Kevin Kwon and Dr Takuji Nakamura.

When I look at the notebook for the write-up of my PhD thesis I find that the first entry is on 16^{th} October, 1991. This was when I first sat down to seriously start my write-up. So what happened between then and now ? The 10^{th} AIP Congress in Melbourne, where I gave two oral and one poster presentation, and produced two extended abstracts for the published proceedings;

[1] who was actually with The Mawson Institute for Antarctic Studies

three publication papers in refereed journals; a change in work location (at the expiry of my cadetship) and consequent work habits; a shift in residential location on the completion of our newly built house in a new suburb; no car, just bicycles and public transport (for oh so many years); a son starting on the long road of education, first at Kindy, then to Junior Primary,.....

Throughout this particularly trying time, and throughout the previous years of my thesis I have been blessed by the continued support and encouragement of my employers and friends at HFRD within DSTO, Salisbury. Not only was I encouraged to pursue a PhD while I was a junior worker there, I was also financially supported by the organisation for the full extent of the cadetship, and extreme leniency and understanding was shown when it became obvious that my thesis was going to take a little more time to complete. This was much appreciated. Although an organisation such as DSTO, and the Division, HFRD, in particular, rely on a wide range of individuals to accomplish specific tasks — many of whom have helped towards the completion of this thesis is some way — special thanks must go to Dr Bruce Ward, my superviser when I first started at DSTO; Wayne Hough, who organised many administrative items for me, always with a genuine smile and extreme efficiency; Liz Ashforth and Geoff Ford for their always prompt and cheerful assistance with diagrams, documentation and the like; the members of IE Group, past and present; and especially my cadetship mentor, Dr Malcolm Golley, whose advice, generosity and foresight allowed the completion of this work. I would also like to thank my friend and colleague, Mike Wilson[2], for many helpful discussions.

Some of the work contained here, and some work that never reached final analysis stage, was assisted or stemmed from collaborations and/or correspondence with various other colleagues who I wish to thank. They are Dr D.M. Schlapp[3], Dr L.M.G. Poole[4], Dr T. Nakamura[5], Dr R.J. Stening[6], Dr P.A. Greet[7], Dr C.S. Gardner[8], Dr S.J. Anderson and Mr A.O. Zollo[9].

As many "PhD Widows" know, completing a thesis not only takes a toll on the author, but also on their loved ones. I am fortunate that my partner, Helen Windus, and our son, Daniel, are so understanding. They have put up with my working many late nights, both at home, at the University, and at the field site. They have put up with the stress and pressure of my PhD. They have put up with what seemed like an endless writing-up process. Throughout this time

[2]also of HFRD and completing his PhD

[3]Physics Department, University of Exeter, Exeter EX4 4QL,U.K.

[4]Department of Physics and Electronics, Rhodes University, Grahamstown, South Africa

[5]Radio Atmospheric Science Center, Kyoto University, Uji, Kyoto 611, Japan

[6]School of Physics, The University of New South Wales, Kensington 2033, Australia

[7]Australian Antarctic Division, Kingston, Tasmania 7050, Australia

[8]Department of Electrical and Computer Engineering, University of Illinois at Urbana-Champaign, Urbana IL 61801, U.S.A.

[9]both of High Frequency Radar Division, Defence Science and Technology Organisation, P.O. Box 1500, Salisbury, SA 5108, Australia

they have both encouraged and supported me. For this and many other things, I wish to thank both Helen and Daniel. The completion of my PhD is as much a joyous event for them as it is for me.

Finally, I would like to thank the rest of my family. Thanks to my brother, Glenon and sister Sharon. Thanks to Grandpop, Uncle Bill, Aunty Margaret, Liz, Pam and Rose. A big thankyou goes to my parents for their direct and continued support throughout my 19 years in the education system until the end of my Honours year at James Cook University, North Qld. Then their continued, but regrettably distant, support through my further 5 years in the education system at Adelaide. Thanks Mum and Dad.

Dedicated to my son, Daniel, who, for the first five years of his life thought that Dad ("the computer head") being a student was quite normal, and at the age of 5 was also delighted to become a student too.

Chapter 1

Introduction

1.1 Theme

In recent years it has become more widely recognised that the Earth's biosphere is a highly coupled system. Changes in the state of one component can have broad implications to the whole; recent concerns about "global warming" have emphasised this. The atmosphere is but a part of this chain; due to its nature though, it is a key factor in the dissemination of global changes. The uneven heating of the Earth causes circulation within the atmosphere in an attempt to transfer the heat from warmer to cooler regions. The circulation in turn transports minor constituents (and pollutants) around the globe. Sometimes the nature of the global circulation can cause the accumulation of minor constituents, which in term can cause changes in the local chemistry. This is evidenced by the formation of ozone depleted regions at the poles each spring.

As well as horizontal circulation, energy and momentum are also transported vertically through the atmosphere. This is mainly due to the action of buoyancy waves[1] whose restoring force arises from the vertical density gradient of the atmosphere. Various other wave motions can also be supported, each with a differing restoring force. As the horizontal scale of any of these waves become large (of the order of the Earth's diameter) the spherical nature of the atmosphere becomes increasingly important. As different latitudes are at different distances from the Earth's axis of rotation, gradients in the Coriolis force arise. This is the restoring mechanism for large-scale motions called Rossby waves. Waves of planetary scale are the central area of concern in this thesis. Some theory regarding these waves will be presented in Section 1.4.

Due to the complexity of studying an extended fluid such as the atmosphere, a variety of remote sensing tools is required. These are discussed later in this chapter. The particular means

[1] more commonly known as (internal) gravity waves, which should not be confused with gravitational radiation

used to probe the atmosphere for this work necessarily limited the study to the upper mesosphere ($\sim$ 80–100 km). This is an interesting region of the atmosphere, and will be discussed at the end of the next section.

1.2 The Atmosphere

Although the atmosphere is in reality a single fluid body, with a fixed lower boundary at the surface of the Earth, and a somewhat tenuous upper boundary extending into solar-terrestrial space, it is often segmented into altitude regions for the purposes of closer study. The segmentation or classification of the regions varies with the physical process under consideration. Due to the gravitational attraction of the Earth, the bulk of the atmosphere (by mass) remains at lower altitudes; the atmospheric density decreasing in an exponential fashion from the surface. This, combined with the fact that solar radiation enters from the "top" of the atmosphere, means that the recombination rate for ionised species decreases with altitude, while the dissociation rate increases. Thus the outer regions of the atmosphere are substantially ionised (although the number density of the neutral species is higher than that of the charged particles out to altitudes of the order of 1000 km). The atmosphere can therefore be classified *via* the properties of the neutral gases or *via* the ionisation (see Figure 1.1).

1.2.1 The Ionosphere

The regions where ionisation is important have been called the ionosphere since their discovery by Appleton in 1924. The term ionosphere was introduced by R. A. Watson-Watt in a letter to the United Kingdom Radio Research Board, in 1926 [*Rishbeth & Garriott*, 1969]. The vertical electron density profile causes three regions to be distinguished.

In the D-region ($\sim$ 60–90 km) the electron density increases with altitude during the day. Ionisation is essentially absent at night due to the removal of incoming radiation from the sun, the neutral density being sufficiently high so that recombination occurs in a very short time. Ionisation is insufficient to cause any significant distortions to the dynamics of the D-region, the ions (hence electrons) being advected with the neutral air. This is an important property of the region which is exploited in the remote probing by radar for the determination of neutral air motions.

Daytime electron densities tend to peak at $\sim$ 100 km (the E-layer) which marks the beginning of the E-region ($\sim$ 90–150 km). This region is "weakly" ionised. Ionisation in this region tends to remain during the night, increasing with altitude but decreasing throughout the night. Above

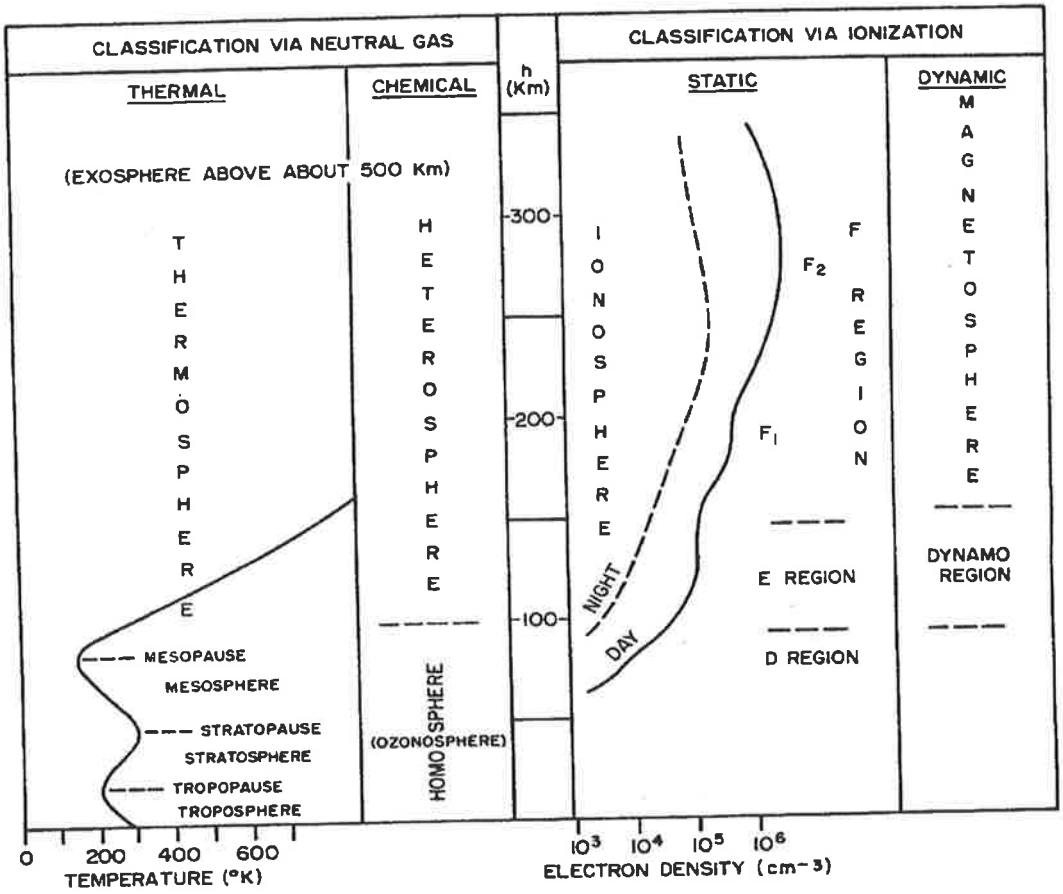

Figure 1.1: Various schemes for the classification of the atmosphere (Figure 1.1 of *Hines et al.* [1965])

the E-region the daytime electron densities begin to increase again; this is the F-region ($\sim$150–1000 km). Sometimes a minor peak or plateau in the electron density is observed near 200 km, which is referred to as the F1-layer. A broader but more consistent peak around 300 km is referred to as the F2-layer. The F-region is "partially" ionised with much of its structure being determined by the differential diffusion of the electrons and ions. Transport is therefore an important mechanism. The boundaries between all these regions are not well defined.

The E-region is associated with the dynamo currents. These are large currents in the ionosphere which are driven by the interaction of the coupled ion-neutrals and the Earth's magnetic field. In the E-region the ion-neutral collision frequency is high enough so that the neutral winds can drive the charged particles, which are forced to follow the Earth's magnetic filed lines. This gives rise to an electric field, $\mathbf{V} \times \mathbf{B}$, causing currents to flow (see, for example, Chapter 5 of *Kato* [1980] for more detail). Once into the F-region the ion-neutral coupling is not sufficient to cause as intense a dynamo action. The F-region is associated with the magnetosphere, which extends out into space. Above $\sim$1000 km the "atmosphere" is dominated by free protons so

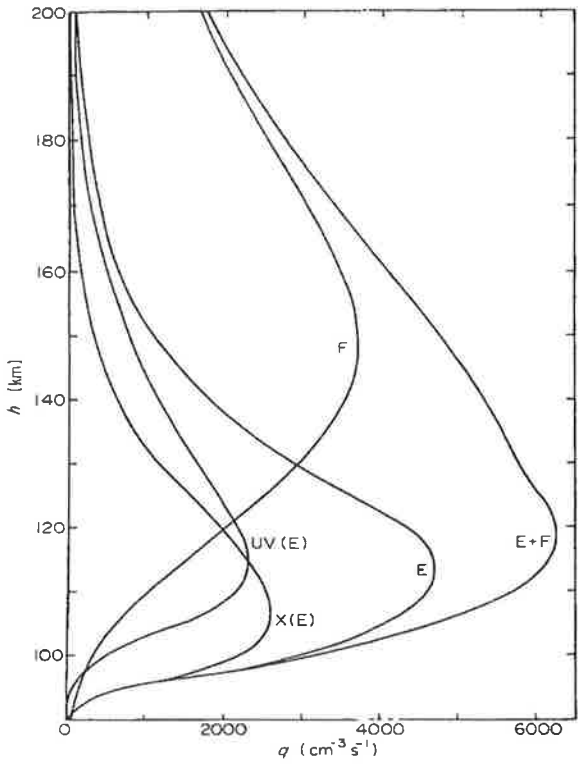

Figure 1.2: The height profiles for electron production due to the absorption of vertically incident solar radiation at sunspot number R $\approx$ 60 (Figure 24 of *Rishbeth & Garriott* [1969]). The curves refer to the following wavelength bands: X(E), 0.8–14 nm; UV(E), 79.6–102.7 nm; E = UV(E) + X(E); F, 14–79.6 nm; E + F, total 0.8–102.7 nm

is often termed the protonosphere (although it is still part of the magnetosphere). It is fully ionised at these altitudes.

Ionisation is mainly produced by the incoming solar UV and EUV radiation[2] and soft X-rays. The EUV ($\sim$ 17–80 nm) radiation is generally absorbed by the F-region and is largely responsible for the F1 layer. Hard UV ($\sim$ 80–100 nm) penetrates to the E-region where it too is absorbed. Soft X-rays ($\sim$ 0.8–14 nm) are absorbed in the D- and E-regions. The absorption of X-rays from $\sim$ 0.1–1.6 nm and UV from $\sim$ 100–180 nm help maintain the D-region. The height profiles for electron production due to the absorption of solar radiation are shown in Figures 1.2 and 1.3. Note that in these figures units of Angstroms, Å, are used (1Å= 0.1 nm). Figure 1.3 has the altitudes for peak absorption of the D-region X-ray bands marked. These profiles, when combined with the electron losses, should match the measured electron density profiles shown earlier. These figures show that the actual absorption profiles are a fairly broad function of altitude. The height at which most of the solar radiation has been absorbed is shown in Figure 1.4.

[2] Ultra-Violet, $\sim$ 100–400 nm ; Extreme-Ultra-Violet, $\sim$ 20–100 nm

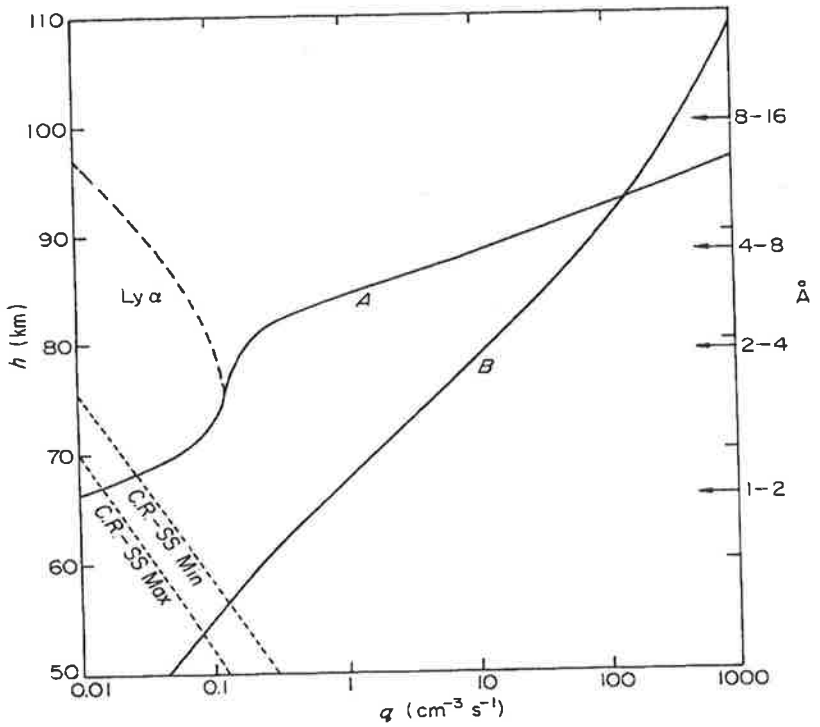

Figure 1.3: The height profiles for electron production in the D- and E-regions due to the absorption of vertically incident solar radiation (Figure 25 of *Rishbeth & Garriott* [1969]). Curve A is for moderate solar activity (sunspot number R $\approx$ 60, with the contribution from the Lyman-α lines) while curve B shows the higher activity levels during solar flares

As a note of historical interest, the notation of D, E and F came about from the way the ionosphere was "discovered". It was found that the E-mode (*i.e.* left-hand circularly polarised) of a radio signal was reflected from a layer in the atmosphere, naturally named the "E-layer". When reflecting layers were discovered below and above this layer they were naturally named the D- and F-layers.

These distinct ionospheric regions exist due to :-

- the different absorption characteristics of the atmosphere at different altitudes, causing differing solar energy deposition.
- recombination physics depending on the atmospheric density; again a function of altitude.
- the atmospheric composition changing with altitude.

The electron density profile varies with (amongst other things) latitude, season, and solar cycle. The differing physics of these regions are the real bases for their differentiation.

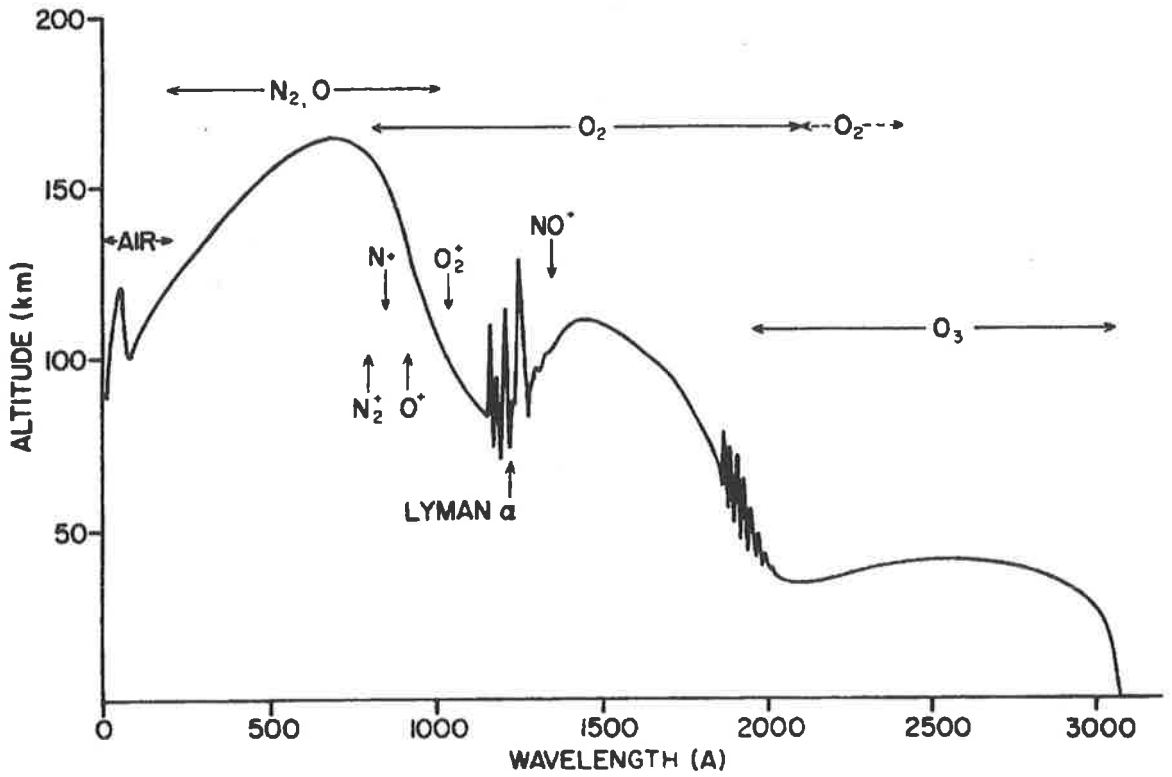

Figure 1.4: The height at which the intensity of solar radiation has dropped to 1/e of its value incident on the atmosphere (Figure 2.2 of *Hines et al.* [1965]). 1Å= 1 Angstrom = 0.1 nm.

1.2.2 The Neutral Atmosphere

The vertical temperature profile of the atmosphere also allows the distinction of a number of regions (again see Figure 1.1). These, like the ionospheric regions, are formed by the changing physics with increasing altitude.

The troposphere (0–$\sim$ 15 km) is the region of the atmosphere which most affects our day-to-day lives. Containing most of the atmospheric mass and energy, it is what is generally considered "the atmosphere" by non-specialists in the field. The temperature gradient in the troposphere is due to the emission of long-wave radiation from the Earth's surface — the temperature falling with distance from the source. If the atmosphere was transparent to this radiation then the temperature would fall at the *dry adiabatic lapse rate* of 9.8 K km^{-1}. "Greenhouse" gases such as water vapour and carbon dioxide absorb radiation at these wavelengths so that the actual lapse rate can be as low as 3 K km^{-1}, but is usually near 6.6 K km^{-1}. The spatial and temporal variability of the surface emission and thermal absorption causes turbulence and convection cells in the troposphere. Severe variations in the lapse rate are common and cause convective instabilities, making the troposphere a very turbulent, dynamic region. Troposphere literally means "turning-sphere".

At higher altitudes oxygen and ozone absorb incoming solar UV radiation in the ~200–300 nm range (see Figure 1.4), heating the atmosphere at the altitudes where they are most abundant. Between this altitude region and the surface there is a temperature minimum — the tropopause. Immediately above the tropopause the temperature gradient is near zero. This extends for several km before the temperature begins to increase, reaching a maximum at ~50 km. The small then positive temperature gradients make the atmosphere in this region highly stratified and very stable. Consequently this region is called the stratosphere. The altitude of zero temperature gradient is called the stratopause. Above this the temperature once again begins to decrease as the concentration of ozone decreases.

At higher altitudes the photo-ionisation of various molecular species causes the temperature to rise once again (at ~90 km). For consistency, the altitude of zero temperature gradient is called the mesopause — this can be the coldest place in the terrestrial environment. The region between the stratopause and mesopause is called the mesosphere (literally "middle-sphere"). This region corresponds to the ionospheric D-region. As has already been noted, the very weak ionisation allows electrons to be used as tracers for the neutral gases. This allows radar reflections to be used to determine neutral air motions. Figures 1.3 and 1.4 show that this region is responsible for the absorption of UV radiation (~100–180 nm, which includes the Lyman-α lines) and soft X-rays (~0.1–1.6 nm) from the sun (fortunate for life on Earth !). The stratosphere and mesosphere considered together are often termed the middle-atmosphere.

Above the mesopause the temperature rises sharply then plateaus. This extended region is referred to as the thermosphere (~90–400 km). The increased ionisation affects the dynamics through interactions with the Earth's magnetic field. Kinematic viscosity also has increased to a point where turbulent eddies are damped out so that the atmosphere can no longer be considered well mixed. Molecular diffusion therefore dominates, with the height distribution of the ion species reflecting their molecular or atomic weights. The altitude region above which turbulence can be ignored is called the turbopause. This is generally just above the mesopause.

The uppermost part of the atmosphere is called the exosphere (> 400 km), with reference to the neutral particles. Here neutral particles move along a ballistic trajectory with little probability of collision.

1.2.3 Dynamics of the Middle Atmosphere

The relative stability of the stratopause contrasts with the highly turbulent nature of the troposphere. It is in the stratosphere that significant global circulation occurs due to the stratified

nature of the region. The chemistry of the region — as in all of the middle atmosphere — is very sensitive to the temperature and concentration of the minor constituents. The change in the atmospheric stability causes tropospheric air to be "trapped" below the tropopause. Tropospheric air contains most of the pollutants introduced by human activity. Due to the well-mixed nature of the troposphere, the pollutants introduced near the Earth's surface can find their way up to the tropopause. At particular locations on the Earth — such as over the "maritime" continent near Indonesia, where there is a good mix of water and land near the equator — the topography is such that violent storms often erupt. These can and do cause convective mixing of tropospheric and stratospheric air. This is one means by which minor constituents can find their way into the middle atmosphere. These events also generate wave motions which then transport energy and momentum away into the upper reaches of the mesosphere. Once pollutants enter the stratosphere they can be more readily transported around the globe. This can have a disastrous effect on the chemistry. For example, the transport of chloroflurocarbons (CFCs) to the polar stratosphere causes a catalytic reaction with ozone during spring, when temperatures are at their lowest. This destroys large amounts of the atmosphere's UV-absorbing ozone. This is but one example of the importance of atmospheric coupling and transport.

As already mentioned, but worth repeating, while the ozone layer in the stratosphere absorbs most of the $\sim$200-300 nm UV, the upper mesosphere is responsible for the absorption of hard UV ($\sim$100-200 nm) and X-rays from the sun. These are more energetic than those absorbed by ozone, and would cause quick death to most life on Earth. Their absorption is important for high altitude aircraft. For this reason alone, study of this region is important.

The case of ozone in the middle atmosphere is a good example of the complex and often subtle interdependencies of atmospheric dynamics. Although the depletion of ozone mostly occurs during spring at the poles, the loss is redistributed around the globe during the remainder of the year (see, for example, *McIntyre* [1989], who discusses the dynamics of the Antarctic ozone hole). Thus the *dramatic* local depletion at the poles becomes a *small* global ozone depletion. UV levels at the ground depend on the total column ozone content, so increase slowly. The depletion of ozone, though, is not evenly distributed with height. This combined with circulation and the height distribution of ozone may mean that at certain altitudes large percentage losses may occur. As solar insolation by the upper ozone layer is the main driving mechanism for propagating modes of the solar semi-diurnal tide, variations in ozone concentration at these altitudes (not the total column abundance) would affect the strengths of these tides in the mesosphere [*Ross & Walterscheid*, 1991]. This would, in turn, affect mesospheric circulation

— the solar semi-diurnal tide being a major component in the dynamics of the mesosphere. Because of this and other factors, any signature of ozone loss (and also "global warming") would be expected to be first seen in the upper mesosphere. Thus, continued monitoring of this region is essential. Added to this, knowledge of the dynamics of the region is also required to enable accurate modelling and forecasting.

The importance of tidal dynamics in the coupling of the mesosphere and thermosphere prompted the recent cooperative global observational campaigns, termed the Lower Thermosphere Coupling Study (LTCS). Use of radar data collected in such coordinated campaigns have allowed the development of better empirical models for describing tidal behaviour. This has lead to more well defined lower boundary conditions for the large TGCMs[3] [*Forbes & Salah*, 1991; *Forbes & Vial*, 1991, for example].

Wave oscillations in the upper mesosphere, especially those of large scale or amplitude, drive the weak ionisation of the region (as it is strongly coupled to the neutrals). This, in turn, can force the ionisation of the thermosphere to also oscillate, the D- and E-regions being coupled through the electric field. Thus neutral density perturbations in the mesosphere can be transferred to electric field perturbations in the thermosphere. This can have implications on radiowave propagation for communications and OTHR[4].

1.3 Nomenclature

The nomenclature used throughout this thesis follows the standard aeronomy notation where possible. New quantities and symbols are defined when they are introduced.

1.3.1 Coordinates

- Eastward, westward, northward and southward mean travelling or directed toward the east, west, north or south respectively.

- When global mechanisms are being considered, such that the Earth's spherical geometry is important, spherical polar coordinates are used. These are (z, θ, ϕ). z can be defined either in log-pressure coordinates, $-ln(p/p_0)$, where p_0 is the ground pressure, or some predefined pressure level; in units of scale heights (which shall be defined in Section 1.4.2.2, but should be noted are a function of the temperature and geopotential and, in the middle-atmosphere, are to a good approximation linearly related to the "true" height, as shown

[3] Thermospheric Global Circulation Models
[4] Over-the-horizon Radar

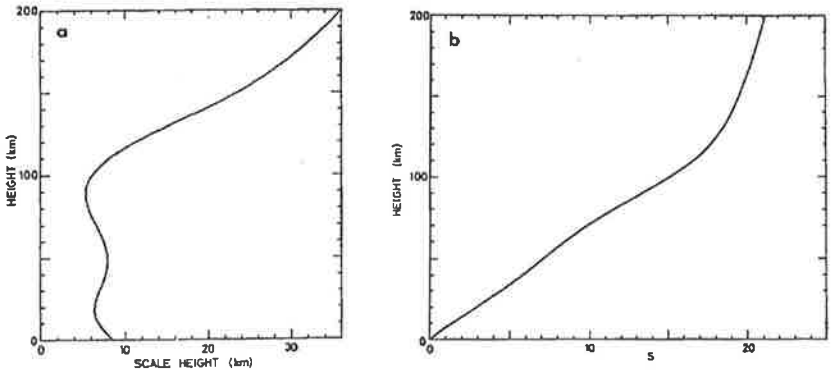

Figure 1.5: (a) Scale height, H, as function of altitude. (b) Altitude measured in units of scale height, $S = \int_0^z \frac{1}{H} dz$ (Figure A3 of *Kato* [1980])

in Figure 1.5.); or in linear units of km from a standard geopotential surface. θ is either the geographical latitude, ranging from +90° at the North Pole to -90° at the South Pole (0° is at the equator); or the geographical co-latitude, ranging from 0° at the North Pole to 180° at the South Pole. ϕ is the longitude, ranging from 0° at the prime meridian, through to +180° East and -180° West.

- For local, small scale considerations (and sometimes at global scales for convenience), a Cartesian coordinate system, (x, y, z), involving directions tangential to the sphere are used. The zonal direction, x, is tangent to the sphere in the east-west direction, eastward being positive. This is essentially the longitudinal direction. The meridional direction, y, is tangent to the sphere in the north-south direction, northward being positive. This is essentially the latitudinal direction. z has the same variation as in spherical polar coordinates. The rate of change of the zonal and meridional vectors are related to the spherical polar equivalents by,

$$\frac{\partial}{\partial x} = a \sin\theta \frac{\partial}{\partial \phi} \tag{1.1}$$

$$\frac{\partial}{\partial y} = -a \frac{\partial}{\partial \theta}, \tag{1.2}$$

where a is the mean radius of the Earth.

1.3.2 Variables

- Where possible vector notation has been used. Variables representing vectors and matrices are shown in **bold** type. Generally the same symbol is normal type is used to denote their magnitudes. Operators are shown as calligraphic characters. Where appropriate, tensor notation, using the Einstein convention of summing over like indices, has also been used.

- Overbars denote mean quantities, while $< >$ denote ensemble averages.
- d/dt has been used to represent the total or Lagrangian[5] time derivative,

$$\frac{d}{dt} = \frac{\partial}{\partial t} + \mathbf{U}.\nabla \tag{1.3}$$

1.3.3 The Phase

The term "phase" can have a number of meanings dependent on the context. The phase of a vector is its angle from a designated axis. This leads to the description of the phase of a sinusoidal motion being the angle that the generating vector has with (usually) the ordinate axis[6]. The phase velocity of a wave packet is therefore the velocity that points of constant phase[7] move at (as opposed to the group velocity which is the velocity of motion of the wave group or packet)[8].

Phase, when considered in the context of tidal waves, is defined as the time of day when the wave parameter has its maximum positive value. In the case of winds, where eastward and northward are positive, the "phase" of a solar tide is the time of day (generally given in local-time) when the tidal wind component has maximum eastward and northward velocities for the zonal and meridional components respectively. If, as theory predicts, the tidal winds are rotating anti-clockwise in the horizontal plane in a circular fashion then the phase of the zonal component should be 1/4 of a period earlier than that of the meridional. This is generally found to be the case. This definition of phase has also been applied to the planetary wave known as the quasi-two-day wave since its period has been found to be very close to 48 hr in the southern-hemisphere. Understanding of this use of the term "phase" will be assumed from now on.

1.4 Tides and Planetary Waves

1.4.1 Their Role in the Dynamics of the Middle Atmosphere

Planetary waves are known to carry a substantial portion of the dynamic energy of the troposphere [*Charney & Drazin*, 1961, for example]. *Charney & Drazin* [1961] found, though, that the wind structure of the middle atmosphere normally leads to a reflection of most of this energy

[5] The Lagrangian reference frame is one that is stationary with respect to the fluid flow, *i.e.* is moving with it, as opposed to the more common Eulerian reference frame that is external to the flow

[6] a sinusoid can be generated by tracing the projection onto the coordinate axis of a vector which is rotating at a constant angular velocity.

[7] or point on the sinusoid describing the wave

[8] The energy of the wave packet travels at the group velocity and in the same direction

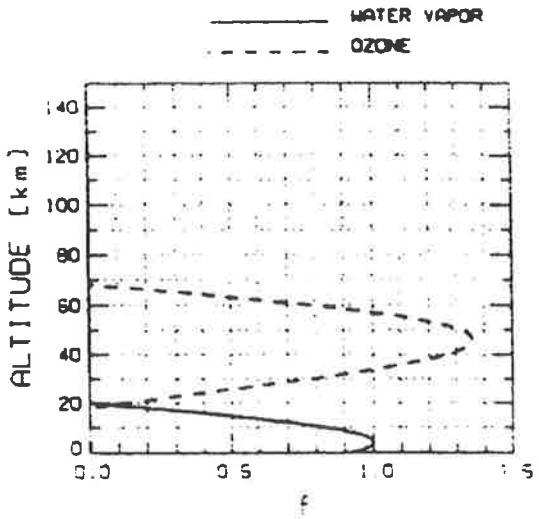

Figure 1.6: Thermal forcing functions assumed by *Aso* [1993] for the study of tidal transients (from Figure 2 of *Aso* [1993]). Note that the scale is only relative

in the stratosphere and lower mesosphere. They point out that were this not the case an extreme heating of the upper atmosphere would result. Further, their analysis revealed that the transmission of planetary waves through the middle atmosphere is severely inhibited in summer due to the prevalent westward winds, and to a lesser extent in winter. The smaller horizontal scales being reflected to a greater degree. Thus the presence during summer of the large amplitude, planetary scale, quasi-two-day wave at lower thermospheric heights poses a theoretical problem.

Miyahara et al. [1991] examined the possible origins of atmospheric heating and acceleration sources using a numerical circulation model with mean meridional motions based on monthly climatological winds from MF/HF radars. They concluded that "at low latitudes ($\leq 30°$) dissipation of atmospheric tides accounts for most of the derived heat and momentum sources; below 90 km at mid- to high-latitudes wave stress due to gravity waves appears to be the dominant source for mean zonal circulation." They went on to say that above 90 km between 40–70° latitude there exists significant regions of mean heating and acceleration not accounted for by these two mechanisms. They gave two possibilities:

1. oblique gravity wave propagation from the equatorial troposphere.

2. planetary waves which must propagate from the winter to the summer hemisphere — vertical propagation in the summer hemisphere being prohibited as already mentioned.

The theoretical framework for categorization and study of planetary scale waves stems from the same formalism as that of the ocean tides, originally formulated by Laplace. Ocean tides have been studied for many years, being first reported before 320 B.C. by Pytheas of Marseilles.

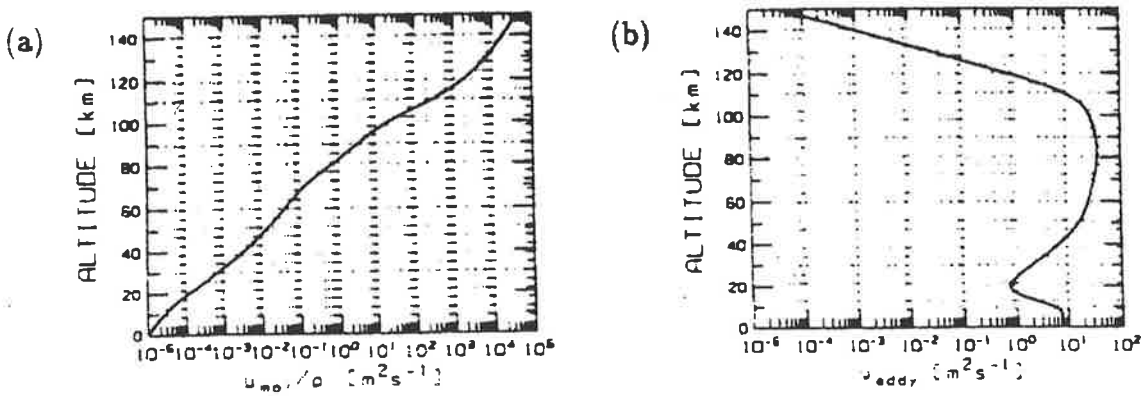

Figure 1.7: Altitude variations of (a) molecular and (b) eddy viscosity coefficients, μ and ν (from Figure 2 of *Aso* [1993]). Note that the scales are different

Tidal oscillations in the atmosphere were not recognised until the invention of the barometer by Torricelli (C. 1643). A good historical account of the development of the study of atmospheric tides can be found in *Lindzen* [1974]. One of the major differences between atmospheric tides and those of the oceans are that the latter are purely forced by the gravitational attraction of the sun and the moon — the lunar tide being stronger than the solar due to the moon's proximity. Atmospheric tides, although influenced by the same gravitational attraction, are mainly forced by thermal insolation over a specific range of altitudes. Thus the solar tides are more dominant than the lunar by orders of magnitude. Thermal forcing at set altitude ranges (see Figure 1.6 for example), and the unbounded nature of the atmosphere causes the study of these tidal mechanisms to be more complicated than for the oceans.

Although tidal oscillations can be treated as a special case of internal gravity waves, the traditional approach will be taken here. From the formalism for forced tidal oscillations come solutions for freely propagating wave modes — termed atmospheric normal modes. These, like the tides, are planetary scale waves, where the rotation and spherical nature of the Earth have significant effects.

1.4.2 Tidal Theory

The theory of tidal oscillations has been known for many years and can be found in numerous references [*Chapman & Bartels*, 1940; *Craig*, 1965; *Lindzen*, 1967; *Chapman & Lindzen*, 1970; *Lindzen*, 1974; *Kato*, 1980; *Forbes*, 1984]. A brief overview of the classical theory will be given here.

1.4.2.1 Assumptions

It is usual to first consider the conservation of momentum for a gas in local thermodynamic equilibrium — the Navier-Stokes equations [*Gossard & Hooke*, 1975; *Fleagle & Businger*, 1980; *Kelley*, 1989, for example].

$$\rho\frac{d\mathbf{U}}{dt} = \mathbf{F} + \eta\nabla^2\mathbf{U} - \nabla p - \nabla.\tau\,, \tag{1.4}$$

where $\mathbf{U}$ is the full wind vector, (U, V, W), whose components are in the zonal, x, meridional, y, and vertical, z, directions respectively. p is pressure and ρ the atmospheric density. $\mathbf{F}$ represents the external body forces such as $+\rho\mathbf{g}$ due to the *effective* gravity[9], $\mathbf{g}$; $-\rho\nu_{ni}(\mathbf{U}-\mathbf{V}_i)$ from ion drag due to the differential velocities of the neutral and charged particles, where ν_{ni} is the neutral-ion collision frequency and $\mathbf{V}_i$ the ion velocity; and $-2\rho(\boldsymbol{\Omega}\times\mathbf{U})$ from the Coriolis force due to the rotation of the Earth, our reference frame — $\boldsymbol{\Omega}$ being the angular velocity of the Earth. $\eta\nabla^2\mathbf{U}$ represents the frictional force per unit mass and arises from viscous drag. η is the dynamic viscosity coefficient which will be essentially equal to the eddy viscosity coefficient, ν, in the middle atmosphere (Figure 1.7 shows that *nu* is at least an order of magnitude larger than the molecular viscosity, *mu*, below $\sim 90\,$km. At this altitude the two are of equal importance, with *nu* becoming insignificant compared to *mu* above 100 km). τ represents the momentum flux density tensor due to wave motions, *i.e.* the Reynold's stress tensor. In cartesian coordinates, the (j,k) elements are

$$\tau_{jk} = \overline{\rho\mathbf{U}_j\mathbf{U}_k}\,. \tag{1.5}$$

For planetary scale motions the vertical velocity, W, is small compared to the horizontal velocity, (U, V). Typically W is of the order of $0.01\,\mathrm{ms}^{-1}$ while U and V are of the order of $10\,\mathrm{ms}^{-1}$. Also the vertical acceleration, $d\mathrm{W}/dt$, and the Coriolis term in the expansion for equation 1.4 are both small compared to that of gravity and the vertical pressure gradient force. These conditions are consistent with the motions being in hydrostatic equilibrium. Neglecting ion drag and momentum fluxes due to wave motions the Navier-Stokes equation can be simplified to

$$\frac{d\mathrm{U}}{dt} - \mathrm{fV} = -\frac{1}{\rho}\frac{\partial p}{\partial x} - \frac{\partial\Phi_x}{\partial x} + \frac{\eta}{\rho}\frac{\partial^2\mathrm{U}}{\partial z^2}\,, \tag{1.6}$$

$$\frac{d\mathrm{V}}{dt} + \mathrm{fU} = -\frac{1}{\rho}\frac{\partial p}{\partial y} - \frac{\partial\Phi_y}{\partial y} + \frac{\eta}{\rho}\frac{\partial^2\mathrm{V}}{\partial z^2}\,, \tag{1.7}$$

$$\frac{1}{\rho}\frac{\partial p}{\partial z} = \frac{\partial\Phi_z}{\partial z}\,, \tag{1.8}$$

where f is the Coriolis parameter, $2|\boldsymbol{\Omega}|\sin\phi$, and the *effective* gravity has been considered in terms of a gravitational potential, $\mathbf{g} = \nabla\boldsymbol{\Phi}$. Equation 1.8 is commonly termed the hydrostatic

[9] this takes into account the contribution of the Earth's angular momentum, $-\boldsymbol{\Omega}\times(\boldsymbol{\Omega}\times\mathbf{r}) = |\boldsymbol{\Omega}|^2\sin\phi$, which is directed towards the axis of rotation

equation. Other equations that are necessary are those for mass and heat continuity (equations 1.9 and 1.10) and the ideal-gas equation (equation 1.11):

$$\frac{d\rho}{dt} + \rho\nabla.\mathrm{U} = 0\,, \tag{1.9}$$

$$\rho c_v \frac{d\mathrm{T}}{dt} = \mathrm{RT}\frac{d\rho}{dt} + \mathrm{J} - \mathrm{C}\,, \tag{1.10}$$

$$p = \rho\mathrm{RT}\,. \tag{1.11}$$

where R is the gas constant for air (universal gas constant divided by a mean molecular mass for air), T the temperature, c_v heat capacity at constant volume, J the thermotidal heating and C the heat diffusion and radiative cooling.

Other assumptions are:-

- The gas constant, R, is assumed constant for air. This is nearly so up to 90 km but by 200 km a 10% error is introduced.
- The atmosphere is assumed to be thin compared to the radius of the Earth, a, so that terms of order z/a can be ignored.
- The Earth is assumed to be spherical — its ellipticity is ignored.
- The Earth's surface is assumed to be a smooth and rigid — the surface topography is ignored.
- The distribution of radiation absorbing gases is assumed independent of longitude.
- Frictional forces, $\eta\nabla^2\mathbf{U}$, are assumed negligible, as is the heat diffusion and radiative cooling, C. This essentially means that the atmosphere is assumed to be inviscid.
- Tidal oscillations are taken to be perturbations on a mean flow (*e.g.*$\mathrm{U} \Rightarrow \overline{\mathrm{U}} + \mathrm{U}'$). Furthermore, they are considered as linear perturbations. *i.e.* quadratic and higher-order terms in the perturbational quantities can be neglected. This implies that the perturbational amplitudes are *small.* Just what *small* means is usually determined *posteriori.*
- Lastly, but most importantly, some constraints must be placed on the basic state in order to reduce the possible solutions to the six equations of state above. These are that $\overline{\mathrm{V}} = 0$ and $\overline{p}$, $\overline{\rho}$, and $\overline{\mathrm{T}}$ are independent of latitude and longitude.

The perturbations on the gravitational potential are the means by which gravitational tidal forcing is introduced.

$$\Phi = \overline{\Phi}(z) + \Phi'(x, y, z, t)\,. \tag{1.12}$$

Thermal forcing already being embodied in the thermotidal heating term, J.

1.4.2.2 Solution to Laplace's Tidal Equation

The six equations, 1.6 – 1.11, can be reduced to a single equation which is a function of a single variable, G [*Lindzen*, 1974; *Kasahara*, 1976, for example]:

$$H\frac{\partial^2 \mathrm{G}}{\partial z^2} + \left(\frac{dH}{dz} - 1\right)\frac{\partial \mathrm{G}}{\partial z} - \frac{g}{4a^2\Omega^2}\mathcal{F}\left[\left(\frac{dH}{dz} + \kappa\right)\mathrm{G} - \frac{\kappa \mathrm{J}}{\gamma g H}\right] = 0\,, \tag{1.13}$$

where,

$$\mathrm{G} = \nabla.\mathbf{U} - \frac{\kappa \mathrm{J}}{gH} \tag{1.14}$$

$$= -\frac{1}{\gamma \bar{p}}\frac{dp}{dt} \tag{1.15}$$

$$H = \frac{\mathrm{RT}}{g} \tag{1.16}$$

$$\kappa = \frac{\gamma - 1}{\gamma}\,. \tag{1.17}$$

H is termed the "scale height" and γ is the ratio of specific heats. $\mathcal{F}$ is a differential operator given by

$$\mathcal{F} = \frac{1}{\sin\theta}\frac{\partial}{\partial\theta}\left(\frac{\sin\theta}{f^2 - \cos^2\theta}\frac{\partial}{\partial\theta}\right) - \frac{1}{f^2 - \cos^2\theta}\left(\frac{\mathrm{k}}{f}\frac{f^2 + \cos^2\theta}{f^2 - \cos^2\theta} + \frac{\mathrm{k}^2}{\sin^2\theta}\right)\,, \tag{1.18}$$

with k the zonal wavenumber, and $f = \omega/2\Omega$ a dimensionless frequency where ω is the radial frequency of the wave. θ is the co-latitude.

The solution of equation 1.13 is shown in various references [*Lindzen*, 1974; *Kasahara*, 1976; *Walterscheid*, 1980; *Salby*, 1984].

Since $\mathcal{F}$ is only operating on latitude while the remainder of equation 1.13 involves functions of altitude, equation 1.13 should be separable in its latitude and altitude dependence if G is. Hence it is assumed that G is indeed separable, expanding about a complete orthonormal set,

$$\mathrm{G} = \sum_n L_{s,n}(z)\Theta_{s,n}(\theta)e^{i(\omega t + s\phi)}\,, \tag{1.19}$$

and,

$$\mathrm{J} = \sum_n J_{s,n}(z)\Theta_{s,n}(\theta)e^{i(\omega t + s\phi)}\,. \tag{1.20}$$

The factor of $e^{i(\omega t + s\phi)}$ implies a zonal wave solution of frequency ω. This leads to the two sets of differential equations: the horizontal structure equation for $\Theta_{s,n}$,

$$\mathcal{F}(\Theta_{s,n}) + \frac{4a^2\Omega^2}{gh_{s,n}}\Theta_{s,n} = 0\,, \tag{1.21}$$

and the vertical structure equation for $L_{s,n}$,

$$\left\{H\frac{d^2}{dz^2} + \left(\frac{dH}{dz} - 1\right)\frac{d}{dz} + \frac{1}{h_{s,n}}\left(\frac{dH}{dz} + \kappa\right)\right\}L_{s,n} = \frac{\kappa}{\gamma g H h_{s,n}}J_{s,n}\,. \tag{1.22}$$

where $h_{s,n}$ is the separation constant.

The horizontal structure equation is essentially Laplace's tidal equation, originally developed for the study of ocean tides. In that case $h_{s,n} = h$, the depth of the ocean. Thus the $h_{s,n}$ are often referred to as the atmospheric equivalent depths (or height). The solutions to equation 1.21 are therefore formally the same as for Laplace's tidal equation. The eigenfunctions, $\Theta_{s,n}$, are called Hough functions and will be discussed in more detail in the next section. The full solutions corresponding to each Hough function are termed Hough or normal modes of the atmosphere.

It is at this point that the derivations for the forced tidal oscillations and that of the "free" planetary waves diverge. For tidal and other forced oscillations the response of the atmosphere due to external excitation at a given frequency is sought. Hence the wave frequency, ω, and zonal wavenumber, k, are specified. $h_{s,n}$ is then determined as an eigenvalue of equation 1.21. The vertical structure function, $L_{s,n}$, can then be obtained from equation 1.22 for a given forcing, $J_{s,n}$.

For "free" waves ($J_{s,n} = 0 \; \forall \; s, n$) the frequencies of oscillation for a given zonal wavenumber are sought. In this situation the frequencies[10], $f_{s,n}$, are obtained as eigenvalues of equation 1.21 for a given value of $h_{s,n}$, which are in turn eigenvalues of the homogeneous equation 1.22 (with $J_{s,n} = 0$). Truly free oscillations cannot exist in the real atmosphere, where there is always some form of dissipation, so there must always be some minor form of forcing. The "free" modes are preferred waves in that they can have large amplitudes without a related periodic forcing — the forcing may consist simply of thermal "noise" or random momentum deposition from many scales of gravity waves.

The vertical structure function for free oscillations can be put in the canonical form,

$$\frac{d^2}{dZ^2} y_{s,n} - m^2 y_{s,n} = 0 \,, \tag{1.23}$$

by a change of variable.

$$y_{s,n} = e^{-Z/2} L_{s,n} \tag{1.24}$$

$$Z = \int_0^z \frac{dz}{H} \,. \tag{1.25}$$

with

$$m^2 = \frac{1}{4} - \frac{1}{h_{s,n}} \left(\kappa H + \frac{dH}{dZ} \right) \,. \tag{1.26}$$

By analogy to electromagnetic wave theory, $-m^2$ may be interpreted as a refractive index squared. Thus if $m^2 > 0$ the wave is evanescent, and if $m^2 < 0$ the wave is propagating. The

[10] the subscripts denoting that there are now a number of possible normalised frequencies

solutions to the $y_{s,n}$ for the forced tidal oscillations have two branches once above the source regions. These are,

$$y_{s,n} \propto \begin{cases} e^{-i|m_{s,n}|Z} & m_{s,n}^2 < 0 \\ e^{-m_{s,n}Z} & m_{s,n}^2 > 0 \end{cases} . \tag{1.27}$$

The first solution corresponds to a vertically propagating internal wave, while the second is a "trapped" external wave. The latter cannot transfer energy vertically, but is confined to near the source region. It may be recognised as the Lamb mode for which $h_{s,n} = \gamma H \simeq 10\,\mathrm{km}$.

The conservation of flux of vertical energy density of the wave and the exponential decrease in atmospheric density causes the geopotential and velocity amplitudes to grow exponentially with altitude. *i.e.* $\rho \mathrm{V}^2 =$ constant while $\rho \propto e^{-z}$, thus $\mathrm{V} \propto e^{z/2}$.

The horizontal and vertical structure functions specify the respective variations in the state of the waves; the state variables being simple functions of these [*Lindzen*, 1967, for example].

When a full treatment of this derivation is performed [*Richmond*, 1971; *Forbes & Garrett*, 1976; *Forbes & Garrett*, 1978; *Forbes & Garrett*, 1979], retaining the viscid, non-linear terms for molecular viscosity, thermal conductivity, anisotropic drag, and the rotation on a sphere, the tidal equations become inseparable with respect to altitude and latitude. For some special cases the tidal equations still remain separable but the solutions for the $y_{s,n}$ are more complicated and are often found numerically. Thermal damping for example, has the effect of making the "refractive index", m, a complex quantity. *Forbes & Garrett* [1979] present a review of classical and full tidal theory. They treat the viscid case and find that the vertical tidal functions no longer have exponential growth (for propagating modes) or decay (for trapped modes) but asymptote to constant solutions in the upper atmosphere. They stress the importance of the inclusion of molecular viscosity and thermal conductivity for a full description of the solar tides; the exclusion of these can alter tidal amplitudes by an order of magnitude at thermospheric heights. These parameters and more extensive data are included in the model descriptions by *Forbes* [1982*a*] and *Forbes* [1982*b*]. The assumption of an inviscid atmosphere and the linearization of the tidal perturbations essentially distinguishes the classical tidal theory from more recent full tidal theory.

1.4.3 Atmospheric Normal Modes; The Hough Functions

Hough [1898] first obtained solutions of Laplace's tidal equations in terms of a series of spherical harmonics, $\Theta_{s,n}$, called Hough Functions — a linear combinations of the Associated Legendre Polynomials. They are a function of two indices, the degree, n, and the order, s. The order, s, corresponds to the zonal wavenumber, k, while the degree, n, is related to the number of nodes

in the meridional direction. The degree of the harmonic is always greater than or equal to the order, thus $n - s \geq 0$. For a given s, the series of $\Theta_{s,n}$ alternate from being symmetric to being anti-symmetric about the equator. The perturbational height and zonal velocity have the same symmetry as the Hough functions, while the meridional velocity has the opposite symmetry. The number of nodes along a line of longitude, but excluding at the poles, is given by $n - s$.

Often the normal modes are referred to by their zonal wavenumber, k, and meridional "mode" number, m, by the notation (k,m), where the k $= s$ and $|\mathrm{m}| = n - s$ with m positive for a vertically propagating mode, and negative for a "trapped" or evanescent mode. This notation will be used in this thesis. The notation (s, n) has been used by some authors, generally when reference is made to the basic Hough functions rather than the geopotential (or other state variable) corresponding to an atmospheric normal mode.

The normal modes are extensively investigated in *Longuet-Higgins* [1968] and *Kasahara* [1976] and are found to divide into two distinct branches. The first comprises high frequency irrotational gravity waves, where the main restoring force is the buoyancy of the medium. Because of this the particle motions are mainly in the vertical plane, orthogonal to the direction of propagation. These waves may propagate either eastward or westward, a solution existing for each direction for each $n - s$. The eastward propagating modes with $n - s = 0$ (no nodes in the meridional) are known as Kelvin waves, and have small meridional but large zonal velocity perturbations. They play an important role in the dynamics of the middle atmosphere at the equator [*Vincent*, 1993]. Buoyancy waves, more commonly known as gravity waves, are the focus of a large amount of atmospheric research [*Hines*, 1960; *Hines*, 1974; *Lindzen*, 1981; *Fritts*, 1984; *Reid*, 1986]. Although not always of planetary scale (where the normal gravity wave results are modified by the rotation of the Earth), the commonality and universality of gravity waves mean they have a large impact on the dynamics of the atmosphere. Although free solutions of the same general equation as the tidal waves, the planetary and smaller scale gravity waves will not be considered further in this thesis.

The second branch of wave solutions are low frequency non-divergent rotational waves, where the main restoring force is the latitudinal gradient of the Coriolis force. These waves are generally called Rossby or Rossby-Haurwitz waves.

1.4.4 Rossby Waves

Rossby waves are westward propagating *with respect to the medium*, which does not preclude eastward propagation with respect to ground-based observations. They are still transverse waves,

but due to the horizontal restoring force the particle motions are in the horizontal plane [*Gossard & Hooke*, 1975; *Holton*, 1979; *Fleagle & Businger*, 1980].

Rossby wave propagation can be qualitatively understood by examining the simple situation of eastward fluid flow at the equator. Since the Coriolis force tends to deflect motions to the left in the southern hemisphere and to the right in the northern hemisphere, if a parcel of this fluid is displaced away from the equator it will encounter a restoring force and will therefore undergo a wavelike oscillation. Although not as obvious, this same type of mechanism is responsible for Rossby waves at mid-latitudes.

By taking the curl of the Navier-Stokes equations (equations 1.6 and 1.7), and assuming a non-divergent, frictionless flow with no vertical motions, it is possible to show that

$$\frac{d}{dt}\left[\frac{\partial \mathrm{V}}{\partial x} - \frac{\partial \mathrm{U}}{\partial y}\right] + \mathrm{V}\frac{\partial \mathrm{f}}{\partial y} = 0\,. \tag{1.28}$$

Recognising the first term as the relative vorticity, ζ_r, and remembering that the Coriolis parameter, f, only varies with latitude, equation 1.28 can be reduced to,

$$\frac{d}{dt}[\zeta_r + \mathrm{f}] = 0\,, \tag{1.29}$$

which simply states that the absolute vorticity is conserved for Rossby type oscillations.

This allows a better description of the wave mechanism for mid-latitudes. For a fluid parcel at rest in a non-divergent rotating atmosphere (assume it is in the southern hemisphere at mid-latitudes) the pressure gradient force will cause a southward motion. As the Coriolis force increases with increasing latitude, the relative vorticity must decrease in order to conserve absolute vorticity. Thus the parcel motion will be deviated to the left. The further south the parcel goes the stronger the deflection. Eventually the parcel motion will be northward. Once past its initial latitude the relative strength of the Coriolis force decreases and the relative vorticity increases. The pressure gradient force can then return the fluid parcel to a southward motion. A wave oscillation is therefore set up. Consider the Lagrangian reference frame. During the oscillation process, as the relative vorticity decreases, the radius of curvature of the fluid motion increases. As the relative vorticity is smallest for the fluid motion while at higher latitudes, after one complete cycle the fluid parcel will be displaced to the west of its initial position. Thus in the absence of a zonal flow Rossby waves propagate westward.

Solving equation 1.29 is achieved by defining a perturbation streamfunction, ψ, and assuming that the latitudinal gradient of the Coriolis parameter is a constant, $\beta = df/dy$. Mean meridional velocities are considered zero. Wave solutions of the form $\psi = \mathrm{A}\cos(kx + ly - vt)$ are found. k and l are the zonal and meridional wavenumbers respectively. The zonal phase speed relative to

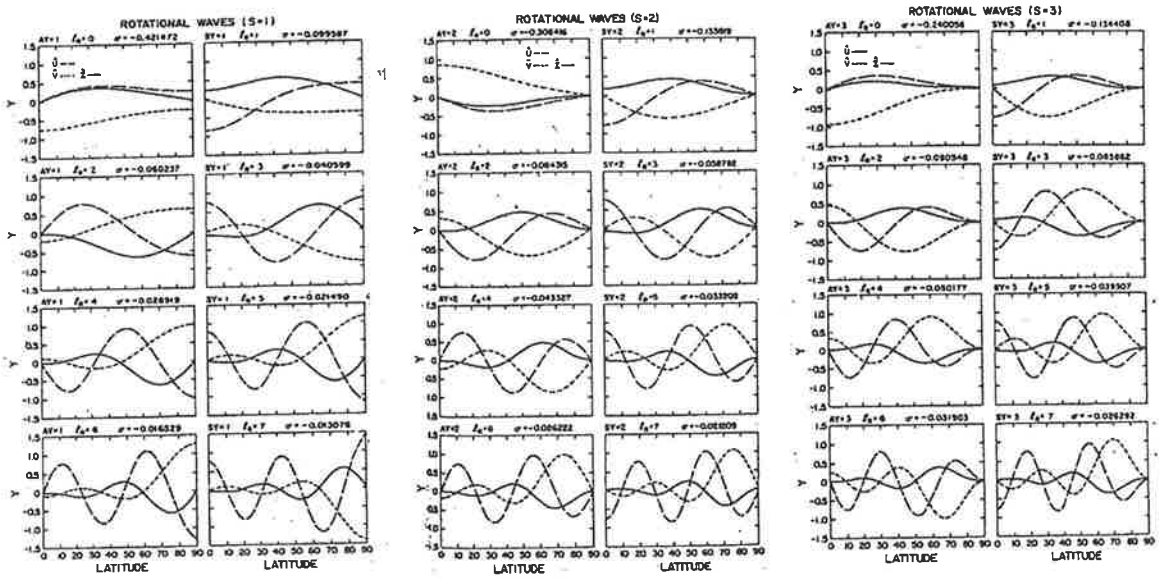

Figure 1.8: The Hough functions for the three gravest zonal wavenumber normal modes for the rotational wave solutions, for an equivalent height of 10 km (Figures 5,7 & 8 *Kasahara* [1976]). The labels at the top of each panel distinguish the different mode numbers, l_R, and normalised frequencies, $\sigma = \omega/\Omega$ (symbols defined in text). AY and SY stand for anti-symmetric and symmetric respectively

the mean wind is then found to be,

$$c_x - \overline{\mathrm{U}} = -\frac{\beta}{k^2 + l^2}\,, \tag{1.30}$$

which shows that the Rossby waves propagate westward relative to the mean zonal flow, as anticipated by the qualitative considerations. When some of the above assumptions are relaxed, the form of solution for the Rossby waves are modified so that restoration by buoyancy forces also play a role. Waves most affected are those of lowest (or gravest) meridional index. The modes corresponding to $n - s = 0$ (*i.e.* $m = 0$ above) are therefore called "mixed Rossby-gravity waves", to denote their mixed character.

The Hough functions for the three gravest zonal wavenumber normal modes are shown in figures 5–8 in *Kasahara* [1976] for both the rotational and irrotational branches, for an equivalent height of 10 km. Those for the rotational branches have been reproduced in Figure 1.8. The mixed Rossby-gravity wave modes are those with $l_R = 0$ (the top left-hand side plot for each zonal wavenumber)

1.4.5 Observational Evidence

Using recent (1985) heating rates and zonally averaged winds, temperature and pressure (from *CIRA86* [1990][11]) *Forbes & Vial* [1989] found that simulated solar semi-diurnal tides agree

[11] COSPAR International Reference Atmosphere

well with the average monthly observations in the mesosphere and lower thermosphere. Recent progress on gravity-wave – tidal interactions and non-linear tidal interactions was reported by *Vial & Forbes* [1989] in the context of recent modelling work. They concluded that the seasonal – latitudinal structure of the semi-diurnal tide could be accurately modelled, at least on a global basis. Therefore tidal theory, at least for the semi-diurnal case, appears to be well understood.

The theory of atmospheric normal modes has been supported by a growing body of observations [*Stening et al.*, 1978; *Walterscheid*, 1980; *Salby*, 1981a; *Salby*, 1984; *Prata*, 1989; *Harris*, 1993]. *Hamilton & Garcia* [1986] look at observations of some shorter period Kelvin and gravity wave normal modes. *Vincent* [1987] gives a review of planetary waves in the mesosphere and lower thermosphere. Although many of the model predictions regarding the wave properties of these modes refer to a windless, isothermal atmosphere, the effect of realistic background states can be estimated [*Salby*, 1981b; *Salby*, 1981c]. In general, "gradients in the mean wind and temperature fields have the collective effect of depressing, shifting and broadening the characteristic response" [*Salby*, 1981b][12] The various influences which degrade the resonant response increase with zonal wavenumber and higher-order meridional mode index. "Hence in realistic conditions, the response of the Rossby modes will necessarily be suppressed and diffused beyond identification" for sufficiently higher order modes [*Salby*, 1981b]. *Salby* [1981c] suggests that the lower-order modes for the first few zonal wavenumbers should be readily identifiable in typical atmospheric conditions. "'At least' the first three modes of wavenumber 1, the first two of wavenumber 2, and the first of wavenumber 3 should occur with periods ... within 12.5% of the median values"[*Salby*, 1981c]. The horizontal structures of these modes are expected to be robust under variations in the mean field, influences being only local. Enhanced amplitudes are expected in the summer mesosphere due to magnified vertical growth rates resulting from the weak eastward prevailing winds (relative to the waves) and equatorward temperature gradients (see Appendix E).

Notable wave oscillations that have been identified as corresponding to particular atmospheric normal modes are the "2-", "5-" and "16-day" waves. The names reflecting the approximate wave periods which have been observed to range from 1.9–2.2, 4–7 and 10–20 days respectively. The observational evidence appears to suggest that the 5-day wave is a manifestation of the (1,1) normal mode (the gravest symmetric mode). With satellite observations the zonal wavenumber of particular oscillations can be easily determined [*Rodgers & Prata*, 1981; *Prata*, 1989; *Rosenlof & Thomas*, 1990, for example]. The lack of atmospheric remote sensing with good latitudinal coverage for a given longitude makes the meridional structure

[12]The characteristic response in this case is a height integrated spectral energy density.

more difficult to determine. The 16-day wave appears to be a manifestation of the (1,3) normal mode (the next gravest symmetric mode). Considerable evidence suggests that the 2-day wave is a manifestation of the $(3,0)$ anti-symmetric Rossby-gravity wave normal mode [*Salby*, 1981a; *Phillips*, 1989; *Poole*, 1990; *Harris*, 1993; *Harris & Vincent*, 1993]. Investigation of the 2-day wave forms a significant part of this thesis (*c.f.* Chapter 4).

1.5 Remote Sensing of the Middle Atmosphere

Remote sensing of the atmosphere provides some form of spatially-averaged estimate of the measured parameters. This is often more representative of the region being probed than are point measurements. Observations also often cover all three space dimensions and may be continuous or over extended time periods. They may also be at a reasonably high resolution. These properties make remote sensing an extremely useful tool for atmospheric studies (amongst other disciplines).

In this section some of the techniques for extracting atmospheric parameters are discussed. Emphasis will then be placed on ground-based radar techniques. First, though, a brief discussion of *in situ* measurements and other forms of remote sensing will be given. Historical accounts of the development of some remote-sensing techniques can be found in *Rishbeth & Garriott* [1969] and *Chapman & Bartels* [1940].

1.5.1 Observational Techniques

It has already been described how the atmosphere is a complex fluid, whose physics changes with altitude. This is not to say that different fundamental physical laws are obeyed in different regions, rather, that the relative importance of various terms change as the state of the atmosphere changes. Due to this, no single technique can be used to define the atmosphere throughout its entire depth. Different techniques exploit different properties of the atmosphere, making them useful over certain altitude ranges.

Information can be gained about the atmosphere in three basic ways. The first, and most obvious way, is to place a probe in the medium and take measurements, hence these techniques are called *in situ*. A less intrusive technique is to measure some phenomenon whose source of variation is in the atmosphere, then infer atmospheric properties. These techniques are called passive remote sensing. In the last group of techniques, some property of the atmosphere is exploited by actively stimulating it. These techniques are called active remote sensing.

Much of the discussion that follows is derived from Volume 13 of the MAP[13] Handbook [*Vincent*, 1984b] and Volume 2 of the WITS[14] Handbook [*Liu*, 1989], and the interested reader is referred to these for more detailed information. Appendix A of *Kelley* [1989], Chapter 2 of *Rishbeth & Garriott* [1969], and Chapter 7 of *Fleagle & Businger* [1980] also contain more detailed information than will be provided here.

1.5.1.1 *In situ* Measurements

In order to perform a measurement *in situ* some form of probe needs to be placed in the medium. This can be achieved by attaching the probe to a rocket, aircraft, spacecraft (including satellites), balloon or even a kite, which is then allowed to ascend. A number of variations can be performed such as the launch vehicle releasing the probe, or releasing some contaminant material for tracking by ground-based radar or optical means. The latter, although possibly an *in situ* measurement, will be discussed later with other active remote sensing techniques. An important consideration with *in situ* measurements are the possible effects that the probe and launch vehicle could have on the quantities being measured. This generally presents a design problem rather than a measurement one.

In situ probes can take the form of :-

- electrostatic sensors (such as Langmuir probes) which have been used to give an understanding of the global electron density and temperature morphologies, particularly in the F-region.
- ion and neutral mass spectrometers. These have been used to determine the abundance of ion and neutral species along the paths of the launch vehicles.
- a retarding potential analyser, which can be used to measure the thermal energy of ion species, by estimating the ion densities and temperatures.
- an ion drift meter, which can measure the field aligned and perpendicular components of the ion drift velocities in the ionosphere. Variations on this form of probe can be used to measure the neutral wind.
- Omega navigation and telemetry equipment on free flying balloons give prevailing neutral wind information. Probes attached to such balloons can also directly measure wind perturbations, pressures and temperatures in the Lagrangian frame.

[13] Middle Atmosphere Program
[14] World Ionosphere Thermosphere Study

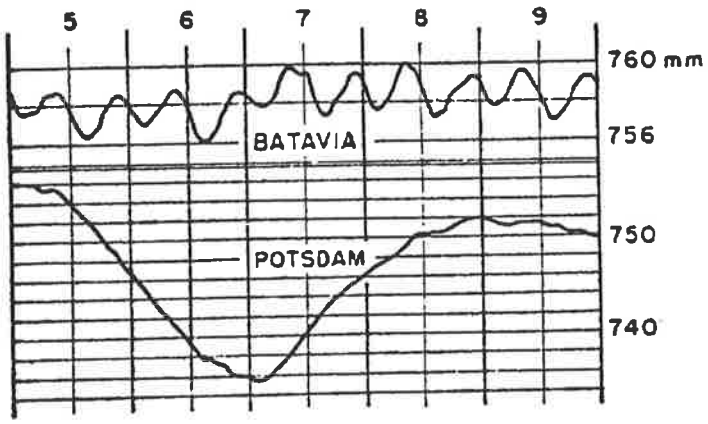

Figure 1.9: Barometric variations at Batavia (6° S) and Potsdam (52° N). the pressure tide is clear at Batavia (now known as Jakarta) whilst meteorological disturbances obscure the variations at Potsdam (Figure 3.17 of *Kato* [1980])

- rocket flights have been widely used to obtain vertical profiles of atmospheric parameters such as pressure and temperature and, to a lesser extent, density. These give a picture of the atmosphere at an instant in time.

In situ measurement techniques generally suffer from their lack of temporal or spatial coverage. Rocket and balloon launches are also prohibitively expensive for repeated observations. They do have the advantage of high vertical spatial resolution, but lack horizontal and temporal coverage. Satellite-borne probes can have ample temporal coverage but then lack high spatial resolution. *In situ* measurements can have high precision and accuracy, making them excellent calibration points for remote sensing techniques and high resolution atmospheric models.

An important feature of these techniques are the known responses of the instruments. Accurate laboratory simulations are possible so that the physics of the measurement process can be well understood. Thus a lot of confidence is often placed in their results.

1.5.1.2 Passive Remote Sensing

Much of the impetus for atmospheric research came from the observations of perturbations in ground level atmospheric parameters, such as pressure. Indeed, the observed regular variations in the surface pressure at the equator (*c.f.* Figure 1.9) lead to Laplace concluding in 1799 that the atmospheric tides were mainly thermally driven. This was surmised as the observed pressure oscillations were at a period that corresponded to the solar semi-diurnal tide. Since the lunar gravitational tidal potential is approximately twice that of the solar, if the atmospheric tides were mainly driven by gravitational forcing then oscillations at a lunar semi-diurnal period

should dominate.

Small temporal variations in the magnetic field measured at ground level also lead to the conclusion by Gauss in 1839 that an ionised layer existed in the atmosphere. The speculation of a conducting layer which was blown across the Earth's magnetic field, thus generating electric currents, led to the dynamo theory.

These are examples of passive observations. More recently, passive optical techniques have been developed. These mainly rely on "airglow", whereby the absorption of solar radiation energises atomic and molecular species into excited states (species such as Oxygen and the Hydroxyl ion). As the excited species return to their ground state they emit photons of specific frequencies related to the difference in energy. Tuned optical instruments such as a Fabry-Perot interferometer can measure the intensity of the airglow, which is related to the partial pressure of the parent species. Perturbations on the intensity give a measure of density fluctuations, while the ratio of intensities for molecular lines, and the spectral width for atomic species, are related to the atmospheric temperature. The Doppler shift of the spectral lines allows the estimation of neutral winds. Fortuitously, owing to the complex chemistry of the atmosphere, airglow from a specific species is usually confined to a small altitude range, so that a reasonable height resolution can be maintained.

If a number of horizontally separated regions of the sky are viewed simultaneously, the airglow intensity perturbations can be cross-correlated, allowing an estimate of gravity wave phase velocities.

By observation through the atmosphere of the fluctuations of radiation from stellar objects (stellar scintillation), either in radio or optical frequencies, refractive index variations with altitude can be estimated [*Campbell & Elford*, 1990; *Campbell*, 1992, for example]. In the observation of scintillation, the atmosphere is assumed to behave like a random diffraction screen which is moving at the wind speed. Thus, wind speeds can be estimated.

Although often ground based, passive optical remote sensing is ideally suited to deployment on satellites. When observing from "above" the atmosphere, thermal radiation is generally looked for. By choosing specific frequency bands, it is possible to observe selected altitude regions of the atmosphere. Thus temperature perturbations from medium to global scales can be observed. These correspond to wave activity. Radiance data of this type have been extensively collected over the last 20 years (*e.g.* the SCR and PMR instruments[15] on Nimbus 5 and 6, launched in December, 1972, and June, 1975 respectively). More recently, a special upper atmosphere research satellite (UARS) has been outfitted with new passive optical instruments

[15] Selective Chopper Radiometer, and Pressure Modulated Radiometer

(HRDI and WINDII[16]) designed to measure middle atmosphere temperature and winds. Many of these types of instruments measure relative values which then need to be calibrated. This usually means a parameter or set of parameters need to be specified at some initial altitude. New instruments such as HRDI and WINDII need to be validated by comparisons with ground-based observations.

1.5.1.3 Active Remote Sensing

As well as passive, there are also active optical devices called lidars[17]. These are the optical equivalent of a radar. Two important types can be distinguished, dependent on the mechanisms for backscatter of the transmitted laser pulses. The first relies on resonant scatter from neutral particles in the atmospheric. The mechanism is much like the airglow, except in this case the atoms are forced to resonate by bombardment with photons of the appropriate energy. Altitude information is also available as the laser pulses are timed and the received signal range gated as for any pulsed radar system. Species that form layers in the mesosphere and are susceptible to this form of forcing are sodium (80–105 km) and oxygen (90–100 km). Lasers of sufficient power have been made to suit the resonant frequencies of these constituents. The strength of the backscattered signal is proportional to the density of the neutral species. From the density, temperature estimates can be made (assuming thermal and hydrostatic equilibrium). The thermal wind equation then allows estimation of neutral winds. High time and height resolution also allow the observation of gravity wave motions. The second important form of backscatter mechanism is Rayleigh backscatter. In this case a more powerful laser is required. Rayleigh backscatter occurs from the interaction of the laser light and neutral air, and is proportional to the atmospheric density. As for resonant scatter, the temperature can be estimated. Rayleigh lidars are not restricted to the altitude region of a particle species, so are more versatile. Gravity wave motions can also be studied as for the resonant case.

In order to operate, optical instruments, either passive or active, require clear views up to the altitudes of interest. Thus clouds and rain cause a problem. Instruments operating at radio frequencies are not affected by these phenomena.

Ground-based radars can be used to track or monitor the effect of artificial atmospheric tracers, such as chaff or barium clouds released by rockets. The dispersion of these contaminants gives information about turbulence, while the motion of the centroid is a measure of the mean winds. The release of small spheres ("falling spheres" experiment) allows the estimation of

[16] High Resolution Doppler Imager, and Wind Imaging Interferometer
[17] Light Detection and Ranging, as opposed to RADAR which is an acronym for Radio Detection and Ranging

atmospheric density. These methods, like the *in situ* measurements, are difficult to do over an extended time period as payloads need to be launched and released. Nevertheless, they have provided a large database from which lower-atmospheric models have been derived.

Acoustic radars use sound waves to create atmospheric perturbations which are then monitored by an appropriate frequency radar[18] [*May et al.*, 1988]. These can be used to obtain estimates of atmospheric parameters in clear air and can run on a semi-continuous basis (noise pollution laws allowing).

Ground-based radars can also be used to remotely probe the atmosphere itself. Perhaps the first form of atmospheric radar was the ionosonde. This is basically a swept frequency vertical incidence radar. Usually the entire HF[19] spectrum is swept. Total reflection occurs for all frequencies less than a critical value ($\propto \sqrt{N}$) for a given electron density (N). The critical frequency is equal to the local plasma frequency, and for ionospheric electron densities lies within the HF region of the electro-magnetic spectrum[20]. Since the atmospheric electron density increases with altitude, an ionosonde obtains reflections from different altitudes as the frequency is changed. These vertical profiles, or ionograms, can be used to infer the vertical electron density profile, or at least the peaks in density, as "troughs" are hidden. Ionosondes placed on satellites can obtain ionograms from the "topside" of the ionosphere (topside sounding). When these are combined with ground-based ionograms a more complete picture of the ionosphere is obtained.

For sufficiently high frequencies (VHF[21] and above), the atmosphere is essentially transparent. Nevertheless, partial reflections from clear air turbulence in the troposphere and lower stratosphere can be seen using VHF radars. This allows the study of weather systems and gravity waves. These radars are called MST[22] radars (although sometimes it is just ST, dependent on the radar power). At altitudes above $\sim 80\,\mathrm{km}$ HF and VHF radars can obtain reflections from incoming meteors. When operating in this mode they are referred to as Meteor radars (in addition to the references mentioned above, a complete description of this technique can be found in *Muller* [1974]). Meteors create an ionised column as they pass through and ablate in the atmosphere. Observations of meteors allow estimation of atmospheric density by the expansion rate of the ionised column, and of neutral winds by their bulk motion.

Radars operating in the VHF and UHF[23] range can obtain partial reflections from the free

[18] this is known as a Radio Acoustic Sounding System or RASS

[19] High-Frequency, 3–30 MHz

[20] in fact, to a good approximation the critical frequency is $\approx 9000\sqrt{N}$ Hz, for N in cm^{-3}. Since the peak electron density in the ionosphere is of the order of $10^6\mathrm{cm}^{-3}$, the critical frequency $\leq 10\,\mathrm{MHz}$

[21] Very-High-Frequency, 30–300 MHz

[22] Mesosphere, Stratosphere, Troposphere

[23] Ultra-High-Frequency, 0.3–3 GHz

electrons in the ionosphere. Such radars are called Incoherent Scatter Radars (ISR) as the partial reflections are due to incoherent scatter from individual electrons (this process will be discussed in more detail in the next section). As the fraction of transmitted power backscattered in this fashion is exceedingly small, these radars must have large power-aperture products ($\sim 10^{11}\,\mathrm{Wm}^2$). The returned power is proportional to the electron number density in the radar volume. Information about the ionospheric dynamics is contained in the spectrum of the returned power, which is Doppler shifted and spread. Parameters such as ion and electron temperatures and the mean ion line-of-sight velocity can be obtained.

MF[24] and HF radars have been used to study the totally reflected signals from the E- and F-regions. In this situation the radio signals are reflected from isoionic contours perpendicular to the beam. Thus phase velocities and horizontal wavelengths of wave disturbances can be measured. More complex analyses can reveal the full horizontal wave field. Radars of this form can also be used to study partial reflections from the D-region. In this case the radio waves are coherently backscattered from refractive index variations caused by a mixture of turbulence and wave action. Since, as previously mentioned, the ionisation is strongly coupled to the neutral air, measurements of the scatterer motions can be associated with motions of the neutrals. Thus neutral winds can be estimated. Data for this thesis has been collected using such partial reflections.

1.5.2 Causes of Radar Backscatter

Radio waves are backscattered by variations in the radio refractive index, n, which, for the middle atmosphere, can be represented by,

$$n = 1 + \alpha_1 \frac{p_{H_2O}}{T^2} + \alpha_2 \frac{p}{T} - \alpha_3 \frac{\mathrm{N}_e}{f_0^2} \tag{1.31}$$

where the α_i are positive proportionality constants, p_{H_2O} is the partial pressure of water vapour (the humidity), p is the pressure, T the temperature, N_e the electron number density and f_0 is the radar operating frequency [*Gage & Balsley*, 1980]. The three variable terms are called the "wet term", the "dry term", and the "ionospheric term" respectively. For pressure in mb, everything else in SI units, the values of α_i at radio frequencies are generally $3.7 \times 10^{-1}, 7.76 \times 10^{-5}$ and 40.3 respectively. n is generally a function of time, latitude, longitude and altitude. The significance of each term varies with altitude. Below the E-layer the last three terms are small compared to unity (order of 0.001) but are sufficient to cause refraction and partial reflections. The "average" relative contributions from each of these terms as a function of altitude, assuming a constant

[24] Medium-Frequency, 0.3–3 MHz

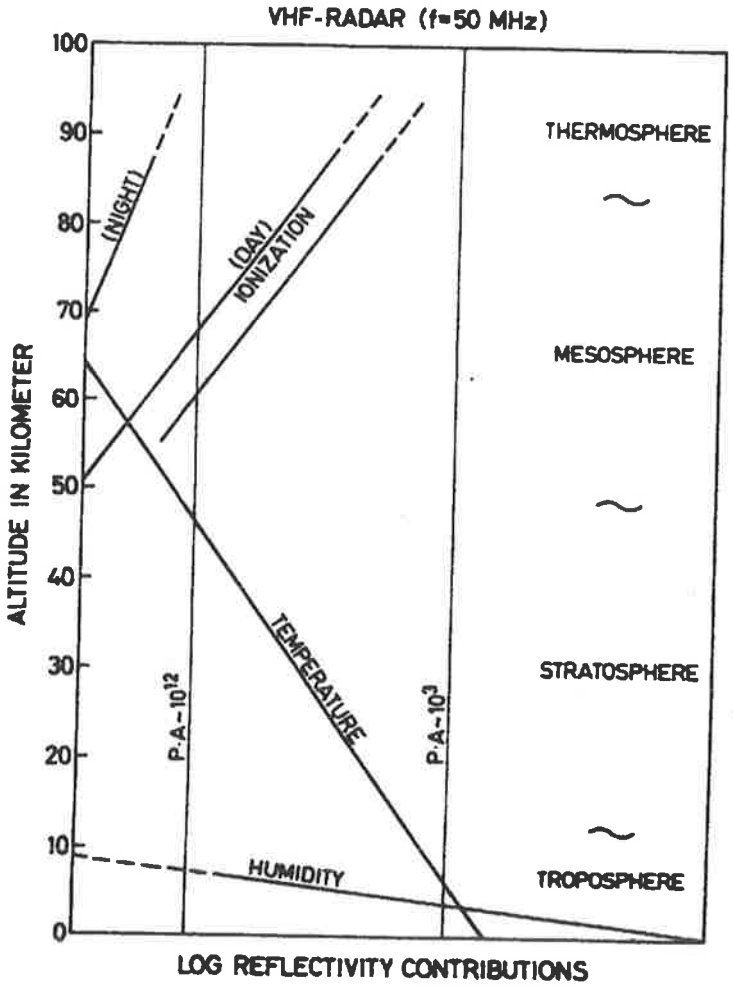

Figure 1.10: Altitude variation of relative reflectivity contributions for VHF radars (Figure 2 of *Vincent* [1984b])

level of refractive index fluctuations, are shown in Figure 1.10. The vertical lines show the relationship between radar power-aperture product and the expected altitudes for reflections at 50 MHz (VHF). Real vertical profiles for reflectivity change with turbulence intensity and the presence of horizontally aligned structures, giving preferred levels of reflection in addition to the variations shown (see Figure 1.11). The wet term is primarily responsible for the reflections noted on page 28 regarding VHF observations of clear air turbulence in the troposphere. The coefficient for the wet term is slightly frequency dependent as it is related to the dipole moment of water. At high frequencies there is not enough time for the dipole moment to align with the electric field before it is reversed, so that at optical wavelengths this term is nonexistent. Once above the troposphere the wet term is not applicable due to the lack of water vapour. Once into the E-region and beyond, the last term in equation 1.31, modified to allow for the effects of magnetic fields on charged particles, is the main contributor to the radar reflectivity. The

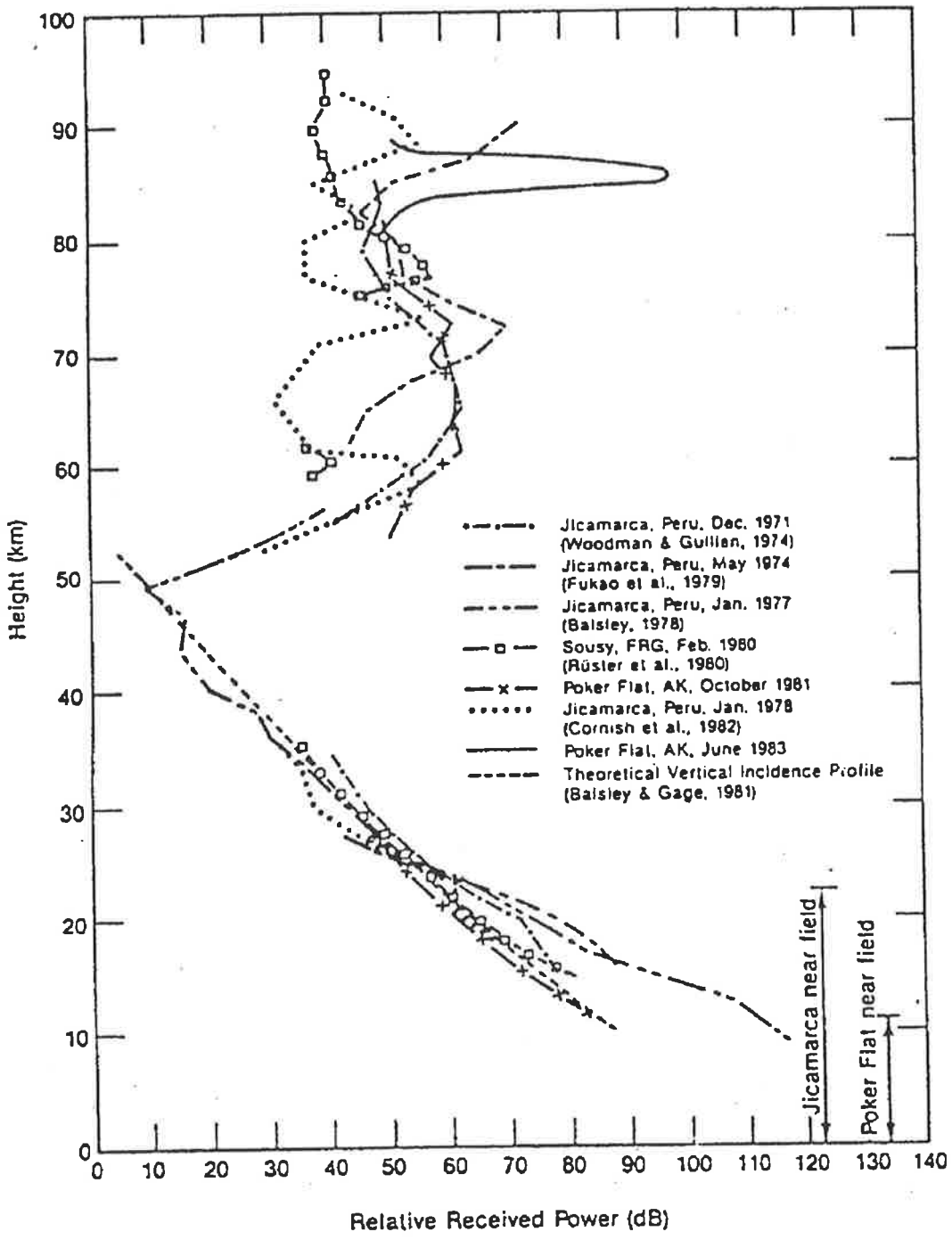

Figure 1.11: Relative echo power profiles for various MST radars (Figure 2.2 of *Nakamura* [1991])

relative importance of this term also varies with the radar frequency. This causes the "ionisation" curve in Figure 1.10 to move down to lower altitudes as the radar frequency decreases from the 50 MHz assumed in that diagram. This means that HF and MF radars do not require as much power (*c.f.* the indicated power-apperture products at VHF) in order to obtain reflections in the 60–100 km altitude range. For this reason frequencies of the order of 3 MHz are often used for studies of the middle atmosphere.

Refractive index variations embodied by equation 1.31 cause backscatter from scales at half the radar wavelength by the Bragg mechanism. Such scatter comes from all irregularities within the radar volume, each of which contain a large number of molecules which contribute to the scattered electric field in a phase coherent manner. Thus this form of scatter is called coherent scatter. The scattered power is proportional to the square of the number density of the scatterers. Another mechanism for radio backscatter comes from incoherent or Thomson scatter which has already been mentioned on page 29. This occurs when the electromagnetic field of the radio waves interact with that of the individual charged particles, causing forced oscillation. This causes re-radiation at or near the incident radio frequency. When the radio wavelength is small compared to the Debye or electron shielding length ($= \sqrt{\epsilon_0 k \mathrm{T}/\mathrm{N}e^2}$, introduced by Debye in the theory of electrolytes) the phases of the re-radiated signals are uncorrelated, thus the powers add and the scattered signal is incoherent. As the electrons and positive ions exhibit thermal and spatial variations, electrostatic fields are set up. This has the effect of enforcing some form of correlation on the charged particle motions so that the scattered radiation is not completely incoherent for scales larger than the Debye length. The Thomson scattering cross-section for an electron is $10^{-28}\,\mathrm{m}^2$, so for typical total electron contents of $\sim 10^{17}\,\mathrm{m}^{-2}$, maybe only 1 part in 10^{11} of the transmitted power is backscattered [*Rishbeth*, 1974]. Hence ISR require large power-aperture products. In contrast, usable coherent backscatter can be obtained using small power-aperture products. At HF/MF frequencies the backscattered power from the middle atmosphere due to coherent scatter is orders of magnitude greater than that due to incoherent scatter.

Equation 1.31 also implies that radio waves are refracted as they pass through the atmosphere. The refraction is insignificant below the thermosphere, since as has been mentioned, the refractive index is very close to unity. In the ionosphere though, refraction becomes significant as the plasma frequency approaches the radio frequency. This is near the point of total reflection of the radio wave. Thus radio waves are "bent" in the ionosphere rather than "rebounded". For accurate range calculations the retardation of the radar signal above the mesosphere should be

taken into account [*Brownlie et al.*, 1973, for example]. For D-region work the correction is insignificant, especially when compared to the usual radar pulse widths, hence height resolution. No such correction has been applied to the data in this thesis.

1.5.3 Intrinsic Frequencies and Critical Levels

The frequencies or periodicities that are commonly referred for waves found in the atmosphere are those that are observed from the ground. These are, naturally enough, ground-based frequencies (Ω), and are determined from an Eulerian frame of reference. The intrinsic frequency, ω, of a wave is its frequency in the Lagrangian frame. The intrinsic wave frequencies are essentially the observed ground-based frequencies which have been Doppler shifted by the mean fluid flow,

$$\Omega = \omega + \mathbf{k}.\overline{\mathbf{U}}\,, \tag{1.32}$$

where $\mathbf{k}$ is the vector wavenumber and $\overline{\mathbf{U}}$ the mean vector wind.

The intrinsic phase velocity, $\boldsymbol{v}'$, of a wave can be defined from the intrinsic frequency by

$$|\boldsymbol{v}'| = \frac{\omega}{|\mathbf{k}|} \tag{1.33}$$

Equation 1.32 can then be written in terms of the phase velocities of the waves as

$$|\boldsymbol{v}'| \approx |\boldsymbol{v} - \overline{\mathbf{U}}|\,. \tag{1.34}$$

Since $\overline{\mathbf{U}}$ is essentially confined to the horizontal plane, and is mainly in the zonal direction, this equation is more easily understood in terms of the zonal components,

$$|\boldsymbol{v}'_x| \approx |v_x - \overline{U}|\,. \tag{1.35}$$

As a wave propagates vertically in the atmosphere it encounters different mean flows. It is possible that in some regions the mean flow is of the order of the component of wave phase speed in that direction, *e.g.* the zonal component of the phase velocity equals the prevailing zonal wind speed. From equation 1.35 this implies that the intrinsic velocity, hence intrinsic frequency, of the wave will approach zero. In such regions the wave will begin to deposit much of its energy and momentum into the mean flow [*Hines & Reddy*, 1967; *Charney & Drazin*, 1961; *Reid & Vincent*, 1987, for example]. The phase and group velocities of gravity-wave type motions are orthogonal, hence if the horizontal intrinsic phase speed is zero, the vertical group velocity must also be zero. Thus these regions represent "critical levels" beyond which the wave will not propagate. Modulation of the mean flow, by such mechanisms as the solar tides, therefore modulate or filter the propagation of smaller scale waves (such as gravity waves)

[*Fritts & Vincent*, 1987]. This is an important filtering mechanism, causing the wave field in the mesosphere to have dominant frequency components, the distribution of which changes with season and the time of day.

These concepts will be drawn upon in some of the chapters that follow.

1.6 Scope of Thesis

As described in this chapter, and further emphasised in those that follow, the atmosphere has been increasingly recognised as a highly coupled system. Due to its complexity though, it is difficult to advance our knowledge without undertaking studies of a more specific nature.

It has already been mentioned that the central area of concern for this thesis regards planetary scale wave motions. More specifically, a planetary wave, known as the 2-Day Wave, is studied in depth utilising an extended mid-latitude dataset and a shorter equatorial dataset. The morphology of this wave is developed and the implications of its non-linear character are discussed in Chapter 4.

A quantitative study of the variability of the solar tides, followed by a short investigation of the lunar tides, is presented in Chapter 5, after which the contributions of this thesis are summarised.

Before embarking on the main research topics it is instructive, and to some extents vital, to consider some of the analytical techniques employed. These are discussed in the following chapter.

Chapter 2

General Data Analysis Techniques

2.1 Introduction

Throughout this thesis there has been the need to use a variety of data analysis techniques. In this chapter some of the theory behind them, and the reasons they were used, will be explained. Mention will also be made of alternative techniques which could produce similar results.

The basic data are wind estimates collected from a spaced-antenna configuration and processed by full correlation analysis. However, first the alternative and more familiar Doppler radar configuration will be briefly described. Some time will then be spent describing the full correlation analysis itself. After a brief description of Fourier techniques in Section 2.4, Section 2.5 describes the effects that missing data can have on spectral estimates using standard fast-Fourier-transforms (FFT). Alternate transforms are then discussed. Section 2.6 describes some methods for extracting spectral components from a composite wind field, and the technique used in this thesis. Complex-demodulation, and time-varying power spectra are also discussed in the sections that follow.

2.2 Doppler and Spaced-Antenna Methods

There are a number of remote sensing techniques for probing the middle atmosphere (*c.f.* Section 1.5), but few can directly measure the neutral winds on a continuous basis. For ground-based radars there are two basic techniques; the Doppler and spaced-antenna methods [*Röttger*, 1984]. Both must assume that the reflectors responsible for the returned power are carried along with the neutral wind. This seems a valid assumption given the good agreement between these methods and *in situ* measurements [*Hocking et al.*, 1989; *Manson & Meek*, 1987; *Röttger & Vincent*, 1978; *Vincent*, 1987; *Vincent & Röttger*, 1980].

The Doppler techniques are conceptually the easiest to understand, so they will be dealt with first. In these methods narrow beam systems and single point "reflectors" are often considered. In order to estimate the vertical motions, a beam is pointed to the zenith and the line-of-sight Doppler velocity (from equation 2.1) can be associated directly with the vertical wind motions.

$$v_r = c\frac{(f - f_0)}{2f_0} \tag{2.1}$$

where v_r is the line-of-sight velocity, c the phase velocity of the radio wave (which can be taken as the velocity of light in free space at the altitudes of concern in this thesis), f_0 the transmitted radio frequency, and f the frequency of the returned signal which has been Doppler shifted by the motion of the reflector. The Doppler shift, $f - f_0$, can be measured by the shift in the peak of the power spectrum from that of the transmitter, or by the slope of the phase of the complex auto-correlation function of the received time series [*Woodman & Guillen*, 1974, see Appendix C for a summary of the relevant information]. The accuracy of the alignment of the beam is critical in this measurement due to the much larger horizontal velocities in the middle atmosphere. Problems also arise if the scattering irregularities are not horizontally aligned, so that a component of their horizontal motion will be measured as a vertical velocity even if the radar beam is perfectly vertically aligned.

To determine the horizontal wind motions a more elaborate setup is required. Line-of-sight Doppler velocities for the same reflector need to be measured from at least 3 different ground locations in order to obtain the full three-dimensional wind vector. Unfortunately, multi-static MF radar systems are more expensive in every respect compared to their mono-static counterparts. If it is assumed that the atmospheric motions are statistically homogeneous on large horizontal scales, then a mono-static system can be used to estimate the horizontal wind. If at least three distinct off-vertical narrow beams are formed, then the combination of their line-of-sight Doppler velocities, appropriately range gated, gives the full wind vector (see Figure 2.1). An alternate procedure is to use a single beam that is steered to different spatial locations within the time constant of the horizontal wind variations [*Röttger*, 1984]. The beam can be scanned over all azimuths, α, for a given zenith angle, δ. This is called a velocity-azimuth display (VAD). Scans can also be made through all zenith angles for a given azimuth, and perhaps repeated for a number of azimuths. This is called a velocity-elevation display (VED). Both the VAD and VED methods are used in MST radars.

Doppler methods rely on converting the line-of-sight Doppler velocities, v_r, to zonal, U, meridional, V, and vertical, W, wind velocities by an equation like

$$v_r(\alpha, \delta) = \mathrm{U} \sin\alpha \sin\delta + \mathrm{V} \cos\alpha \sin\delta + \mathrm{W} \cos\delta \tag{2.2}$$

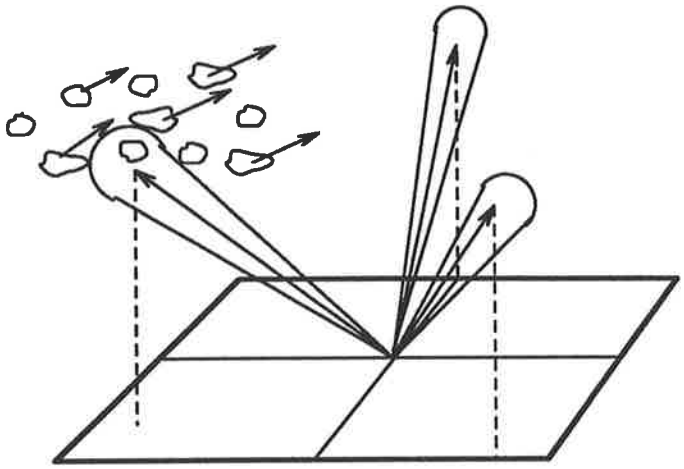

Figure 2.1: Simplest Doppler radar for determining atmospheric wind velocities

where the azimuthal angle , α, has been measured clockwise from north. For a constant zenith angle,

$$v_r(\alpha) = \mathcal{A}\sin\alpha + \mathcal{B}\cos\alpha + \mathcal{C} \ . \tag{2.3}$$

Fourier analysis of $v_r(\alpha)$ using equation 2.3 gives the coefficients $\mathcal{A},\mathcal{B},\mathcal{C}$, hence the wind velocities, U,V,W. It should be noted that the effective beam pointing angle may be closer to the zenith than the radar's polar diagram would indicate. This is due to the aspect sensitivity of the scatterers in the middle atmosphere [*Murphy*, 1990; *Reid*, 1988; *Röttger*, 1981; *Whitehead et al.*, 1983]. The assumption of spatial homogeneity is better for beams set at smaller zenith angles, but the anisotropy and aspect sensitivity of the scatterers become more important.

An alternate approach for determining the horizontal wind vector is to look at the correlation between the fluctuations in returned signal strength on at least three receivers. For this class of analyses, broad beams and multiple or volume "scatterers" are often considered since this is the more general case in terms of the scatterers, and the cheapest in terms of the antenna design and construction. More volume averaging is implied by the use of broad beams than for the narrower Doppler beams. Consider the arrangement in Figure 2.2, where the amplitude of the signal at each of the three receivers is also shown (sometimes called "fading records"), then the combination of time lags, τ_{ij}, between each pair of receivers, and the receiver separations, d_{ij}, give an indication of the apparent horizontal motion along the line joining the receivers by

$$V_{ij} = \frac{d_{ij}}{\tau_{ij}} \ . \tag{2.4}$$

This is a measure of the velocity of the diffraction pattern on the ground. The geometry of the receivers has to be taken into account when reconstructing the full vector velocity, as the V_{ij} are not simple components of the full velocity vector. There are a number of ways of

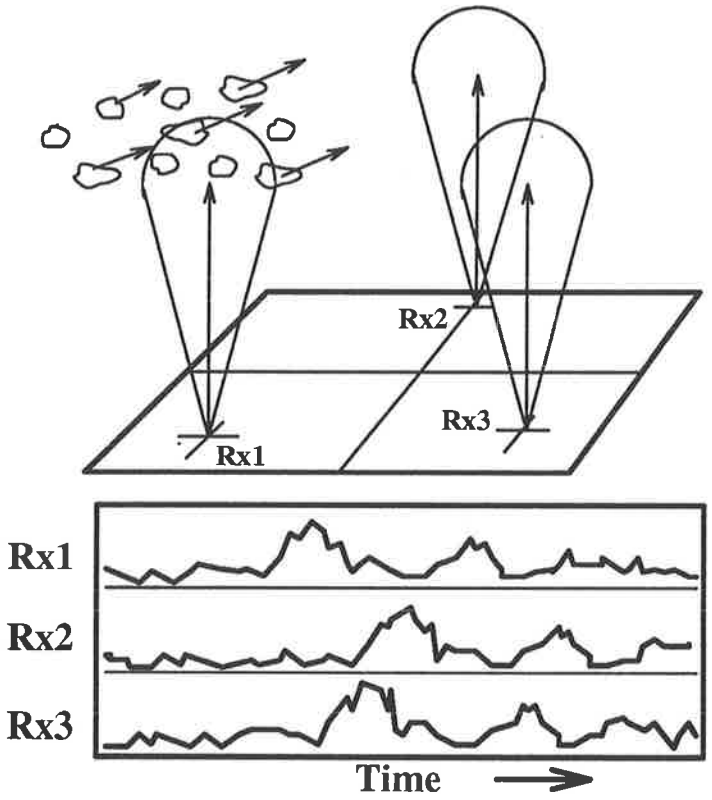

Figure 2.2: Simplest configuration for a spaced-antenna radar

finding an average value for each V_{ij}, which amounts to different ways of finding an average τ_{ij}. In the early work in this field the time series were aligned to give the "best" fit, and the time shift required was τ_{ij}. Another approach was to measure individual time shifts between similar peaks and form an average τ_{ij} from these. With advances in computing power it became feasible to form the cross-correlation between each time series pair, the peak of which is a direct measure of the average time shift required for a "best" fit τ_{ij}. At least three values of V_{ij} are required to give the full horizontal wind vector. The velocities determined in this manner are termed "apparent" velocities because they do not separate the random fluctuations of the wind field due to turbulence from the bulk motion of the scatterers (the neutral wind). Using a few assumptions, the "apparent" velocity can be corrected for random motions.

Note that although the Doppler and correlation techniques appear very different, they are basically the same [*Briggs*, 1980; *Whitehead et al.*, 1983], deriving information from the same properties of the radio scatterers, that is, the dependence of the Doppler shift on the angle of arrival. Practical considerations will determine which technique is best suited for the observations required and the budget allowed.

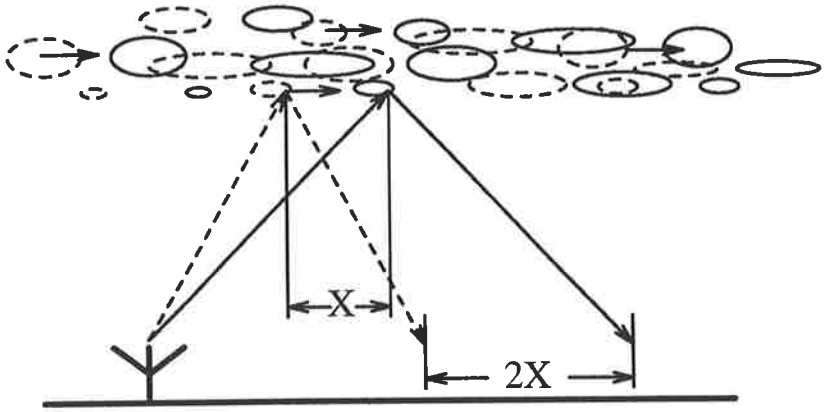

Figure 2.3: Illustration of the "point-source effect". A movement of the reflector by a distance X moves the reflection point on the ground by $2X$. Thus the velocity of the pattern on the ground will be twice that of the reflectors in the atmosphere

2.3 Full Correlation Analysis

Determining atmospheric winds by the comparison of "fading records" from a set of spaced receivers developed from the pioneering work of J.L. Pawsey, at the Cavendish Laboratory, Cambridge, in the 1930s. *Pawsey* [1935] interpreted similar amplitude fading of signals recorded on two receivers spaced 140 m apart as evidence for a wind at the level of reflection. Using diffraction theory he showed that if the reflectors behaved as a random diffraction screen, then the diffraction pattern formed on the ground by reflection of a point source transmission would move at twice the speed of the screen. This is now known as the "point-source effect" (see Figure 2.3).

Studies in the early 1950s [*Briggs & Spencer*, 1954, for example] showed that the variability of the recorded time lags could not be explained by a constant velocity drift of an irregular amplitude diffraction pattern, but could by assuming that the pattern changed as it moved (and was sometimes anisotropic). This meant that the reflecting layers were generally distorted by turbulent motions as well as a mean wind. Using the original method of Pawsey — which determines the "apparent" velocity (mentioned at the end of the last section) — in the presence of turbulence over-estimates the wind. This is easily seen by considering a pattern moving at a constant velocity. Two separated receivers aligned along the direction of motion of the pattern would record similar amplitude fluctuations and the time displacement for maximum correlation (in other words, the time lag of the maximum of the cross-correlation between the amplitudes of the two receivers) would give a true indication of the velocity of the pattern. Now, if some dynamic process like turbulence is introduced, so that the pattern now also evolves with time, the signal would decorrelate faster. Thus, the time lag of the maximum of the cross-correlation

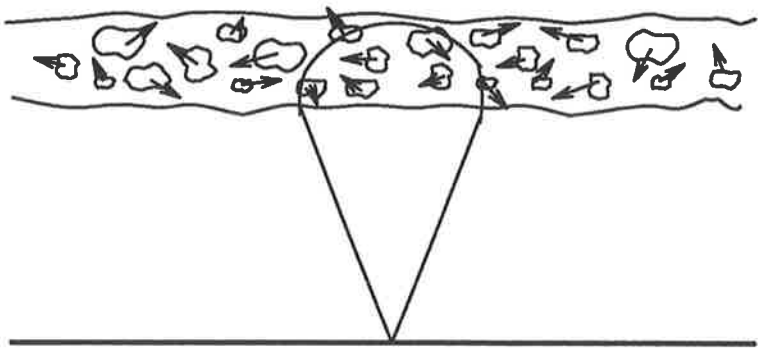

Figure 2.4: Radio waves are backscattered from numerous atmospheric irregularities within the radar volume. This causes a diffraction pattern on the ground

would be shifted towards zero lag. This would give rise to a larger velocity estimate. In the general three-dimensional case, the estimated direction of the wind will also be affected.

In order to correct for this the "method of similar fades" was initially pursued. In this technique the apparent velocities, V_{ij}, are calculated from individual time displacements — not from correlation functions or average τ_{ij} — and the mean velocity computed. This is then corrected using probability distributions. An alternate approach is to use auto- and cross-correlation functions. This method, known as "full correlation Analysis", was developed in the early 1950s by workers at the Cavendish Laboratory [*Briggs et al.*, 1950; *Phillips & Spencer*, 1955]. With the advances in computing power, this method has gained more popularity and is the subject of the rest of this section, which closely follows *Briggs* [1984]. Note that the theory presented here is developed in the time domain. This could alternatively be done in the frequency domain, which might provide some advantages. The analysis in the frequency domain is developed and discussed by *Briggs & Vincent* [1992] and will not be dealt with here.

2.3.1 Theory

Consider the backscatter arrangement shown in Figure 2.4. The returned signals from the various scatterers in the radar volume (often considered as irregularities in the refractive index[1]) add to form a diffraction pattern on the ground. If there is no wind, then the pattern will change in a random manner due to the random fluctuations associated with turbulence, but will remain statistically stationary. Thus the peaks of the various cross-correlation functions would all be at zero lag. With a horizontal wind, the randomly changing pattern, by the "point-source effect", is advected across the ground at twice the speed of the wind (as shown in Figure 2.3). This has been verified by workers such as *Felgate* [1970].

[1]see *Lesicar* [1993] for further discussions on the form of the scatterers in the middle-atmosphere

Firstly, consider a stationary, non-changing, random pattern. That is, an atmosphere without motion of any kind, but consisting of randomly arranged scatterers. The two-dimensional spatial correlation function can be expressed as

$$\rho(\xi,\eta) = \frac{< f(x,y)f^*(x+\xi,y+\eta) >}{< [f(x,y)]^2 >}, \tag{2.5}$$

where ξ and η are the displacements in the x and y directions respectively, and $f(x,y)$ is a complex function with zero mean. The averaging process denoted by <> would most naturally be a spatial one. That is, a large number of sensors at various positions (x,y) are used to measure the function, $f(x,y)$, and the product, $f(x,y)f^*(x+\xi,y+\eta)$, found for each pair (where (ξ,η) are the various vector separations). The product would then be averaged over all the positions for each possible separation (ξ,η). *Golley & Rossiter* [1970] used this method, employing the full array (89 receivers) at Buckland Park. This is not a practical method in most instances due to the large number of sensors required to give an accurate estimate of $\rho(\xi,\eta)$. When bulk and random motions are introduced, a spatio-temporal correlation function can be defined, hence the averaging can be performed in time rather than space. This allows a more practical means of measuring $\rho(\xi,\eta)$. A few sensors can be placed at fixed positions with separations (ξ,η), and $< f(x,y)f^*(x+\xi,y+\eta) >$ obtained as a time average. By the ergodic principle [*Bloomfield*, 1976, for example] this should tend to the same value as the spatial average provided that in both cases an unbiased set of random values are obatined. *Golley & Rossiter* [1970], and *Rossiter* [1970] compared the spatial correlation method with the standard three spaced receivers and found that the value of the "true" velocity depended on the triangle spacing, being larger for larger spacings (later known as the "triangle size effect"), and converging towards the spatial value. The "apparent" velocity did not change. However, as *Briggs* [1984] says "even with time averaging the determination of $\rho(\xi,\eta)$ would still be laborious if all values of (ξ,η) had to be sampled. If nothing is known about the form of $\rho(\xi,\eta)$ this cannot be avoided". To simplify the observational requirements and the following analysis, some assumptions have to be made.

An isometric diffraction pattern (Figure 2.5a) would give a spatial correlation function that only depended on the magnitude of the displacement and not the direction, hence would have concentric circular contours in the ξ,η plane (Figure 2.5b). Extending this to the more general model of an anisometric diffraction pattern — which allows for a preferred orientation of the scatterers — (see Figure 2.6a) and assuming that the anisotropy mainly results in an elongation of the ground pattern, an elliptical spatial correlation function (Figure 2.6b) is obtained

The correlation ellipse which has the value of half the maximum correlation is termed the "characteristic ellipse" and is a measure of the scale of the irregularities. For $\rho(\xi,\eta)$ to be an

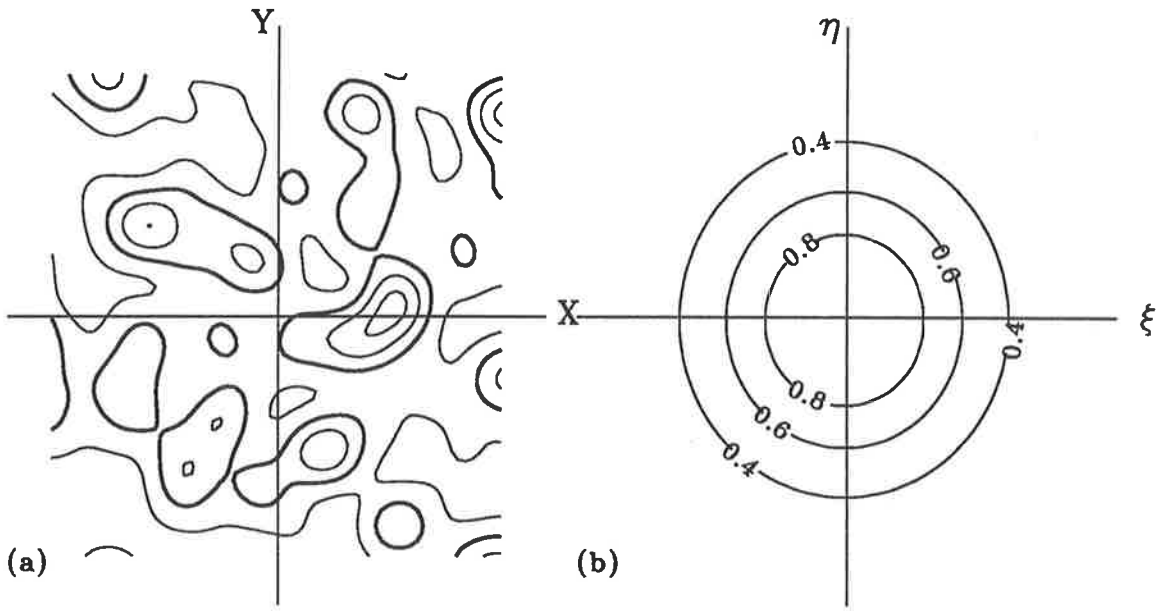

Figure 2.5: An isometric diffraction pattern on the ground (a), produces a radially symmetric spatial correlation function (b) [figures 8 & 9 from *Briggs* [1984]]

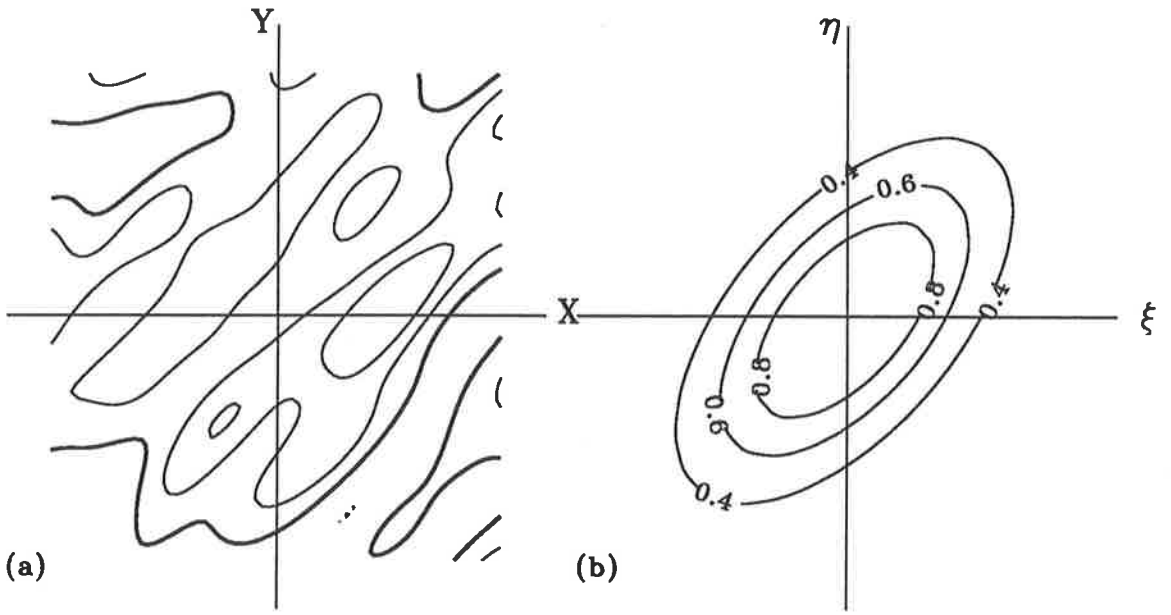

Figure 2.6: An anisometric diffraction pattern on the ground (a), produces a elliptical spatial correlation function (b) [figures 11 & 12 from *Briggs* [1984]]

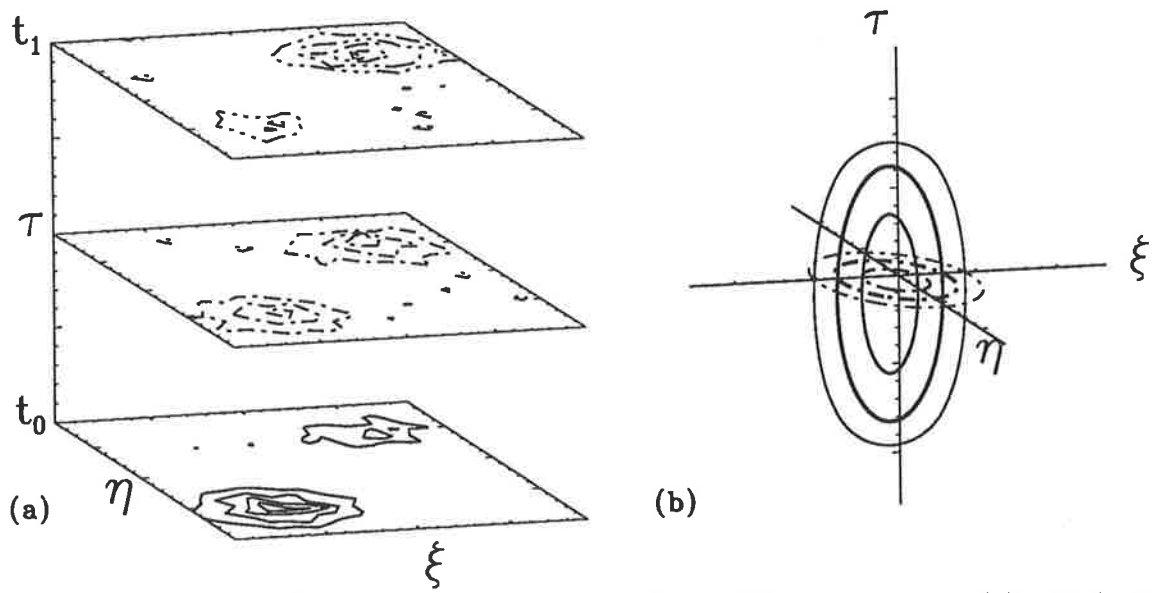

Figure 2.7: Surfaces of constant value for an evolving diffraction pattern (a), which produce ellipsoidal surfaces of equal correlation (b) [figures 13 & 14 from *Briggs* [1984]]

elliptical function of (ξ, η),

$$\rho(\xi, \eta) = \rho(A\xi^2 + B\eta^2 + 2H\xi\eta) \; . \tag{2.6}$$

"Note that the form of the function ρ is still arbitrary; the only assumption concerns the particular combination in which the variable ξ, η occur." [*Briggs*, 1984].

By allowing turbulence in the model atmosphere the diffraction pattern on the ground will change randomly with time but still remain statistically stationary. The spatial correlation function of equation 2.5 can then be extended to a spatio-temporal correlation function as in equation 2.7:

$$\rho(\xi, \eta, \tau) = \frac{< f(x, y, t) f^*(x + \xi, y + \eta, t + \tau) >}{< [f(x, y, t)]^2 >} \; . \tag{2.7}$$

Constant values of the evolving diffraction pattern, $f(x, y, t)$, can be represented by surfaces in x, y, t space (Figure 2.7a), with the actual ground patterns (as in Figure 2.6a) being the intersection with the x, y plane at some time, t. The pattern can be seen to evolve from time t_0 to time t_1. Since the spatial patterns can have no mean motion, the surfaces of Figure 2.7a must be aligned, on the average, in the direction of the t axis. Combining this with the previous determination of the spatial correlation function leads to a picture of the spatio-temporal correlation surfaces as in Figure 2.7b, where the value of the correlation decreases as ξ, η or τ increases. These surfaces may be represented as concentric ellipsoids having one axis in the τ direction. The assumption that the contours of equal correlation in the time domain are elliptical is perhaps the most tenuous of the FCA[2] assumptions and can be avoided if a spatial

[2]full correlation analysis

correlation technique is used [*Briggs*, 1968]. Even so, it still allows for a general description of the temporal behaviour of the correlation functions. $\rho(\xi, \eta, \tau)$ can therefore be defined as

$$\rho(\xi, \eta, \tau) = \rho(A\xi^2 + B\eta^2 + K\tau^2 + 2H\xi\eta) \; . \tag{2.8}$$

Note that there cannot be terms in $\xi\tau$ or $\eta\tau$ since these would lead to a tilt of the ellipsoidal correlation surfaces with respect to the τ axis.

If the turbulent irregularities now move at a constant speed, $\frac{1}{2}V$, in a direction, ϕ, clockwise from the positive y axis, then the diffraction pattern would move in the same direction but at a speed of V due to the "point-source effect". Consider an observer moving with the pattern. To this observer the situation is as has been described previously. To be consistent with *Briggs* [1984], primed coordinates have been used to denote the frame of reference of the moving observer. Thus

$$\rho(\xi', \eta', \tau') = \rho(A\xi'^2 + B\eta'^2 + K\tau'^2 + 2H\xi'\eta') \; . \tag{2.9}$$

A stationary observer's x, y, t reference frame is related to the moving observer's reference frame by the standard Galilean transformations

$$x = x' + V_x t \qquad y = y' + V_y t \; , \tag{2.10}$$

where $V_x = V sin\phi$ and $V_y = V cos\phi$ are the components of the velocity in the x and y directions respectively. It follows that

$$\xi = \xi' + V_x \tau \qquad \eta = \eta' + V_y \tau \; . \tag{2.11}$$

Substituting equation 2.11 into equation 2.9 gives a spatio-temporal correlation function of the form

$$\rho(\xi, \eta, \tau) = \rho(A\xi^2 + B\eta^2 + C\tau^2 + 2F\xi\tau + 2G\eta\tau + 2H\xi\eta) \; . \tag{2.12}$$

Thus the effect of the bulk motion of the scatterers is to cause the correlation surfaces to tilt away from the t axis, as would be expected on physical grounds.

Having considered the theory of full correlation analysis, it now remains to find the parameters, A, B, C, F, G, H, which define the ellipsoidal correlation surfaces, and hence derive some of the physical quantities which describe the scatterers.

2.3.2 Determining the Correlation Parameters

Firstly, as in the "method of similar fades", the lag times[3], τ_{ij}^M, corresponding to maxima in the cross-correlation functions, $\rho(\xi_{ij}, \eta_{ij}, \tau_{ij})$, need to be found. For better clarity, the constants

[3] where the subscripts denote the pair of receivers being compared

used are redefined such that,

$$a = \frac{A}{C}\,, \qquad b = \frac{B}{C}\,, \qquad f = \frac{F}{C}\,, \qquad g = \frac{G}{C}\,, \qquad h = \frac{H}{C}\,. \tag{2.13}$$

Setting $\partial\rho/\partial\tau_{ij} = 0$ and solving for τ in equation 2.12 gives the matrix equation

$$\tau^M = -(\xi, \eta) \begin{pmatrix} f \\ g \end{pmatrix}\,. \tag{2.14}$$

τ^M and (ξ,η) are measured quantities, so equation 2.14 can be solved for f and g. These parameters are over-determined so in general this may involve some least squares technique.

In order to find a, b and h use can be made of the auto-correlation function. In theory, the auto-correlation function for each receiver should be the same. In practice though, this will not be the case owing to the effects of noise and statistical errors. An average auto-correlation function can be computed which should minimise these errors. Finding the time lag, τ_{ij}, at which the average auto-correlation function has the same value as each cross-correlation function at zero lag, the equality

$$\rho(\tau_{ij}^2) = \rho(a\xi_{ij}^2 + b\eta_{ij}^2 + 2h\xi_{ij}\eta_{ij})\,. \tag{2.15}$$

is obtained. This then gives the matrix equation,

$$\tau^2 = (\xi^2, \eta^2, 2\xi\eta) \begin{pmatrix} a \\ b \\ h \end{pmatrix}\,. \tag{2.16}$$

Again, this can be solved (in general using a least squares technique), for the parameters, a, b and h. These parameters will be over-determined if more than three receivers are used.

It is shown by *Briggs et al.* [1950] that

$$\tau_{ij}^2 = (\tau_{ij}^M)^2 + t_{ij}^2\,, \tag{2.17}$$

where the t_{ij} are the lags at which the value of the auto-correlation function equals the maximum value of each of the cross-correlation functions. The relationship between the different lags and the correlation functions are shown in Figure 2.8. Both t_{ij} and τ_{ij}^M are estimated from regions with larger correlation values than a direct estimate of τ_{ij} so are therefore less susceptible to statistical variation. Hence equation 2.17 may give a better estimate of the τ_{ij} to be used in equation 2.16. This is the method recommended by *Fooks* [1965]. For most of the analysis used in this thesis, τ_{ij} is found directly from the correlation functions as described in *Briggs* [1984].

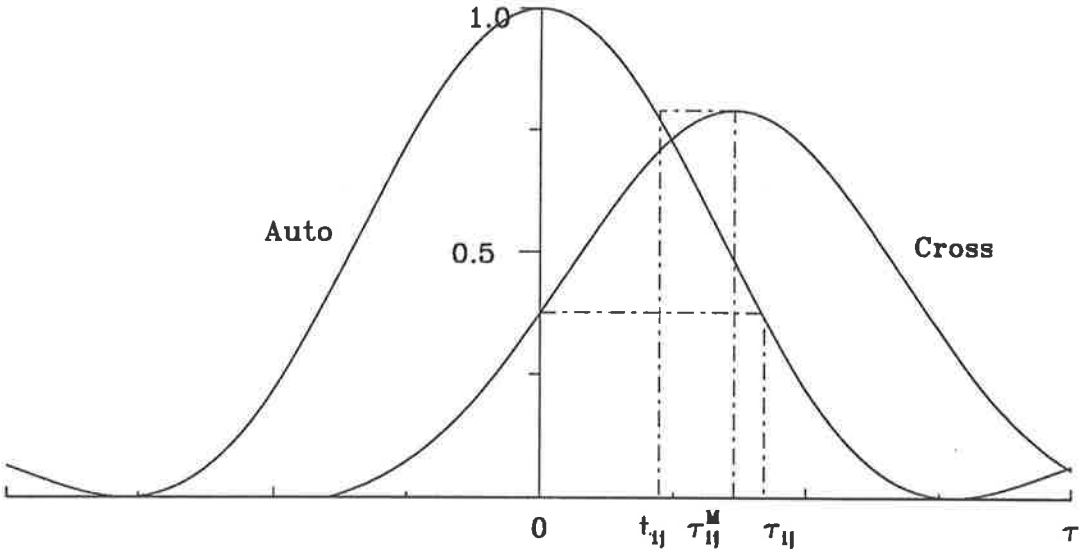

Figure 2.8: Relationship between the lag times used in the FCA. Shown are the average auto-correlation and a typical cross-correlation function. The lag times τ_{ij}^M, t_{ij} and τ_{ij} are defined in the text.

2.3.3 The Physical Parameters

Having obtained the parameters describing the correlation function, by the above means or any other, some physical quantities can now be derived.

In order to find the pattern velocity, $\boldsymbol{V}$, it is only necessary to find the rotation in x, y, t space required to re-align the ellipsoid with the t axis; that is, to remove the terms in $\xi\tau$ and $\eta\tau$. From analytical geometry, this is,

$$\begin{pmatrix} f \\ g \end{pmatrix} = - \begin{pmatrix} a & h \\ h & b \end{pmatrix} \begin{pmatrix} V_x \\ V_y \end{pmatrix} . \tag{2.18}$$

Inverting the matrix gives,

$$\boldsymbol{V} = \begin{pmatrix} V_x \\ V_y \end{pmatrix} = \frac{-1}{(ab - h^2)} \begin{pmatrix} b & -h \\ -h & a \end{pmatrix} \begin{pmatrix} f \\ g \end{pmatrix} . \tag{2.19}$$

Thus, the bulk motion of the scatterers can be found. Note that the velocity of the scatterers will be a factor of 2 less than the velocity of the pattern determined above, due to the "point source effect". The quantity, $\frac{1}{2}\boldsymbol{V}$, is termed the "true" velocity to distinguish it from the "apparent" velocity. Although called "true", the velocity found in this manner may not always truly represent the neutral wind, and rejection criteria must be applied to the data (this is discussed in more detail in Section 2.3.4.3)

The spatial correlation (equation 2.12 with $\tau = 0$) shows that contours of equal correlation are given by,

$$A\xi^2 + B\eta^2 + 2H\xi\eta = constant . \tag{2.20}$$

The "characteristic ellipse" is usually defined as that particular ellipse for which $\rho = \frac{1}{2}$. Setting $\xi = \eta = 0$ and $\tau = \tau_{\frac{1}{2}}$ in equation 2.12 gives,

$$\rho(0,0,\tau_{\frac{1}{2}}) = \rho(C\tau_{\frac{1}{2}}^2) = \frac{1}{2} \ . \tag{2.21}$$

It follows that the "characteristic ellipse" is the one satisfying

$$A\xi^2 + B\eta^2 + 2H\xi\eta = C\tau_{\frac{1}{2}}^2 \ , \tag{2.22}$$

or in terms of the coefficients a, b, f, g, h equation 2.22 becomes,

$$a\xi^2 + b\eta^2 + 2h\xi\eta = \tau_{\frac{1}{2}}^2 \ . \tag{2.23}$$

Since all the coefficients are known, the "characteristic ellipse" is fully defined. The major axis, axial ratio and orientation of the minor axis are sufficient to uniquely define the ellipse, and are usually used. These parameters can be found from equation 2.23 following standard analytical geometry techniques. They are given by,

$$\mathrm{A}^2 = \frac{2\tau_{\frac{1}{2}}^2}{(a+b-\mathrm{R})} \ , \tag{2.24}$$

$$\mathrm{B}^2 = \frac{2\tau_{\frac{1}{2}}^2}{(a+b+\mathrm{R})} \ , \tag{2.25}$$

$$\mathrm{R}^2 = (a-b)^2 + 4h^2 \ , \tag{2.26}$$

$$\tag{2.27}$$

where A, B are the lengths of the semi-major and semi-minor axes respectively. The direction of the major axis is given by, Θ, where

$$\tan(2\Theta) = \frac{2h}{(b-a)} \ . \tag{2.28}$$

Also of interest is a measure of the time-scale of the random fluctuations. To an observer moving with the pattern, the only time changes observed would be due to the random changes. The "mean lifetime" can be defined as the time lag, $T_{\frac{1}{2}}$, for which the auto-correlation function for the observer moving with the pattern falls to $\frac{1}{2}$. Setting $\xi' = \eta' = 0$ and $\tau' = T_{\frac{1}{2}}$ in equation 2.9 gives,

$$\rho(0,0,T_{\frac{1}{2}}) = \rho(KT_{\frac{1}{2}}^2) = \frac{1}{2} \ . \tag{2.29}$$

Comparing equations 2.21 and 2.29 it can be seen that

$$T_{\frac{1}{2}} = \frac{\tau_{\frac{1}{2}}}{\sqrt{k}} \ , \tag{2.30}$$

where, once again, $k = \frac{K}{C}$. Using equations 2.9, 2.11, and 2.12 the coefficients of τ^2 can be equated to give

$$k = (1 - aV_x^2 - bV_y^2 - 2hV_xV_y) \; ; \tag{2.31}$$

thus $T_{\frac{1}{2}}$ can be found.

Historically, another description of the random changes has been used. A velocity term, V_c, can be defined as the irregularity size divided by its mean lifetime. Since the pattern may in general be anisometric, V_c will have difference values in different directions, since the pattern scale will be different in different directions. The value of V_c in the direction of bulk motion of the pattern has special significance, and is written as $(V_c)_v$. Letting $d_{\frac{1}{2}}$ be the separation, in the direction of motion, where the spatial correlation function falls to $\frac{1}{2}$,

$$(V_c)_v = \frac{d_{\frac{1}{2}}}{T_{\frac{1}{2}}} \; . \tag{2.32}$$

From simple geometry it is known that

$$\frac{\xi}{V_x} = \frac{\eta}{V_y} = \frac{d}{V} \; . \tag{2.33}$$

Using equation 2.33 in equation 2.12 with $\tau = 0$ (since a spatial correlation function is required) gives

$$\rho(d) = \rho\{(AV_x^2 + BV_y^2 + 2HV_xV_y)\frac{d^2}{V^2}\} \; . \tag{2.34}$$

$d_{\frac{1}{2}}$ is the value of d when $\rho(d) = \frac{1}{2}$. Combining this with equation 2.29 then produces

$$(AV_x^2 + BV_y^2 + 2HV_xV_y)\frac{d_{\frac{1}{2}}^2}{V^2} = KT_{\frac{1}{2}}^2 \; . \tag{2.35}$$

Using $V^2 = V_x^2 + V_y^2$ and equation 2.35, equation 2.32 then becomes

$$(V_c)_v^2 = \frac{d_{\frac{1}{2}}^2}{T_{\frac{1}{2}}^2} = \frac{(V_x^2 + V_y^2)k}{(aV_x^2 + bV_y^2 + 2hV_xV_y)} \; . \tag{2.36}$$

Random fluctuations alone would produce a correlation function $\rho(0, 0, \tau) = \rho(K\tau^2)$. This is the same as the temporal auto-correlation function seen by the moving observer. The stationary observer sees a temporal auto-correlation function as shown in equation 2.21. Using this and equations 2.9, 2.11, and 2.12 it can be found that

$$\rho(0, 0, \tau) = \rho(C\tau^2) = \rho(AV_x^2 + BV_y^2 + 2HV_xV_y + K\tau^2) \; . \tag{2.37}$$

The last term has already found to represent the contribution from random fluctuations. The first three terms arise from the bulk motion of the pattern. Hence the ratio,

$$\frac{(V_c)_v^2}{V^2} = \frac{k}{(aV_x^2 + bV_y^2 + 2hV_xV_y)} \tag{2.38}$$

is a measure of the relative importance of random changes in the pattern compared with bulk motion.

The vertical velocity can be found from the slope of the phase of the average auto-correlation function [*Woodman & Guillen*, 1974]. Allowance should be made for the possibility that the scatter may be centred off-zenith [*Briggs & Vincent*, 1992].

2.3.4 Practical Considerations

2.3.4.1 Effects of Filtering

Since the FCA attempts to correct the "apparent" velocity for the effects of random motion, prior filtering of the fading records can introduce errors. This is discussed by *Chandra & Briggs* [1978], who show that the larger V_c is (implying more random motion in the atmosphere) the greater the effect filtering has on the "true" velocity. This is because the "apparent" velocity needs a greater correction for larger V_c. They concluded that it is essential to retain in the fading records frequencies of the order of $V_c/d_{\frac{1}{2}}$, which is the same as the reciprocal of the irregularity lifetime, $1/T_{\frac{1}{2}}$.

2.3.4.2 Interpolations

Other practical points to consider are the removal of the noise spikes at zero lag, due to high frequency noise, from both auto- and cross-correlation functions. The values at zero lag then need to be interpolated. The noise spike removal needs to be done at the auto- and cross-covariance stage prior to normalisation (and averaging in the case of the auto-correlation). The interpolated value of the autocovariance function at zero lag is a measure of the mean square signal variance, while the original value is a measure of the mean square variance due to both the signal and noise. From these two measurements an estimate of the signal-to-noise ratio can be made. In general, the maximum cross-correlation value, the lag at which the auto-correlation is the same as the interpolated cross-correlation value at zero lag, and the lag at which the auto-correlation reaches a value of 0.5 will all need to be interpolated.

2.3.4.3 Rejection Criteria

The assumptions that have been made in order to simplify the analysis will not always be valid. The data would have to be rejected in these cases. If any of the interpolation routines fail, or the signal is too weak then again the data would have to be rejected. The following tests allow an objective means of determining whether data should be rejected or not. Note that the

actual numerical values will depend on the nature of the data. Those stated are the ones used at Adelaide during the course of this thesis. The data and/or results should be rejected if :-

1. the receivers are saturated more than 50% of the time.
2. the standard deviation of the received signal is less than 1% of the mean (small fading).
3. the signal-to-noise ratio, $\frac{S}{N}$, is less than -6dB.
4. the mean auto-correlation function has not fallen to at least 0.5 by the maximum number of lags calculated (slow fading)
5. any cross-correlation functions have no maxima within the number of lags calculated
6. any of the cross-correlation functions are oscillatory
7. the sum of the time displacements, τ_{ij}^M, of the receivers is too large. The normalised time discrepancy, defined by
$$\frac{|\Sigma\tau_{ij}^M|}{\Sigma|\tau_{ij}^M|} \tag{2.39}$$
allows a more quantitative test. The data should be rejected if the normalised time discrepancy is greater than 0.5
8. V_c^2 is too large a negative number. A *small* negative value may mean that the true value is zero and there are no random fluctuations. In practice the "apparent" velocity is used in this case.
9. hyperbolic, rather than elliptical, contours are indicated, *i.e.* $h^2 < ab$.
10. the corrections due to the FCA are very large, *i.e.*
$$V_{apparent} \geq 4V_{true} \tag{2.40}$$
$$V_{apparent} \leq \frac{2}{3}V_{true} \tag{2.41}$$
$$(\phi_{apparent} - \phi_{true}) \geq 40^\circ \tag{2.42}$$
$$\tag{2.43}$$
11. the apparent velocity is very large, $V_{apparent} \geq 250\,\mathrm{ms}^{-1}$. This value must be changed if the analysis was to be used for higher altitude work where larger velocities are expected (*e.g.* F region).

2.4 Fourier Techniques

Much of the remainder of this chapter relies on an understanding of Fourier analysis. This analysis technique finds a spectral representation for a given time series, hence is a powerful tool in data analysis. The basis of the analysis is the Fourier transform.

Any arbitrary continuous function, $f(t)$, can be expanded about the basis set of sine and cosine functions as a Fourier series,

$$f(t) = \sum_{j=1}^{n} [\mathcal{A}_j \cos \omega_j t \ + \ \mathcal{B}_j \sin \omega_j t] \ . \tag{2.44}$$

For $f(t)$ a complex function, the expansion can be expressed as a continuous complex series so that

$$f(t) \propto \int \mathcal{F}(\omega) \ e^{i\omega t} \ d\omega \ . \tag{2.45}$$

Multiplying by $e^{-i\omega_0 t}$ and integrating over t, the inverse transform is obtained;

$$\mathcal{F}(\omega) \propto \int f(t) e^{-i\omega t} \ dt \ , \tag{2.46}$$

(having dropped the subscript on ω). $f(t)$ and $\mathcal{F}(\omega)$ form a Fourier transform pair, linked through equations 2.45 and 2.46. The constants of proportionality come from conservation of energy, which implies that the variance remains constant through the transform, thus

$$\int |\mathcal{F}(\omega)|^2 \ d\omega = \int |f(t)|^2 \ dt \ . \tag{2.47}$$

$\mathcal{F}(\omega)$ expresses the distribution of energy (or more precisely, the variance) through frequency space. So far $f(t)$ has been considered to be continuous and of infinite extent. This leads to $\mathcal{F}(\omega)$ being a continuous function of infinite resolution. In practice, $f(t)$ is finite and discrete. The Fourier transform of equation 2.46 can be approximated by a discrete Fourier transform, or DFT.

$$\mathcal{F}(\omega) \propto \sum_{j=1}^{n} f(t_j) e^{-i\omega t_j} \ . \tag{2.48}$$

This differs from the theoretical in two important ways. Firstly, aliasing occurs due to the finite data length, which causes an effective replication of the frequency spectrum at intervals of $2\omega_{max}$ (starting at ω_{max}), thus folding energy from higher frequencies back into the range of $\pm\omega_{max}$. ω_{max}, the highest frequency estimate before aliasing occurs, is termed the Nyquist Frequency. This depends on the time sample interval, δt (assumed constant), by the relation

$$\omega_{max} = 2\pi / 2\delta t \ . \tag{2.49}$$

Secondly, the spectral peaks are artificially broadened. This can be seen by considering the finite length time series as the product of an infinite time series and a "window" which is zero everywhere except over the finite interval, then the Fourier transform of the finite time series is the convolution of the Fourier transforms of the infinite time series and the window function. The latter causes the former to broaden. In principle, the DFT can be used to calculate the energy density at any arbitrary frequency below the Nyquist. In practice the window function may determine an optimal frequency sampling.

Calculating a DFT can be a slow process. For a normal N-point DFT, N^2 operations — a complex multiplication and a complex addition — are required per transform. *Cooley & Tukey* [1965] developed an algorithm which significantly improved the speed of a Fourier transform. Rather than considering the N-point time series as a one-dimensional sequence, they first considered a two-dimensional representation. Reforming the N data points into a $N_1 \times N_2$ array and performing a Fourier transform on each row and column the work-load is $N_1 \times N_2^2$ operations for the rows, plus $N_1 \times N_2$ phase shifts to realign the time origins, then $N_1^2 \times N_2$ operations for the column transforms. This is a total of $N_1 N_2 (N_1 + N_2)$ operations compared to the usual $N_1 N_2 (N_1 \times N_2)$ for a one-dimensional DFT. They then extended this to an M-dimensional analysis whereby the N-point time series is broken into M factors,

$$N = r^m s^n t^p \ldots, \tag{2.50}$$

giving $N(mr+ns+pt+\cdots)$ operations per transform. If $N = r^m$ then the number of operations is $rN \log_r N$, where r is the radix of the transform. This algorithm gave a significant improvement in speed for any reasonable N, so that it became known as a fast Fourier transform, or FFT. Due to the binary representation of data in computers, a radix of 2 is most often used, reducing the number of operations required to perform a DFT from N^2 down to $2N \log_2 N$. If N is a power of 4 then the algorithm can be improved since the Fourier transform of 4 values needs only 3 operations, rather than the 4 that would be used in a Radix 2 scheme. In a Radix 4 FFT there are 25% fewer operations and 50% fewer memory fetches, making a large improvement in performance — on current machines (1990 vintage) memory accesses account for 80% of an FFT execution time. Highly optimised code has been developed for higher radixes such as 8 and 16, and also for the smaller value prime numbers. A mixed radix FFT, such as *Singleton* [1969], reduces the N data points to a small set of prime factors (as in equation 2.50) before transformation. Various other FFT schemes have been developed, some, like the Good-Thomas (or Prime-Factor) algorithm obtain speeds of the order of 2N.

The final point that can be made about an FFT is with regard to the frequencies derived. The

Cooley-Tukey algorithm and its derivatives force the frequency resolution, $\delta\omega$, to be dependent on the total length of the time series,

$$\delta\omega = \frac{2\pi}{T} , \tag{2.51}$$

and the frequency range to be $\pm\omega_{max}$ (*c.f.* equation 2.49). The negative frequencies represent waves travelling in the opposite direction, and have the same values as the positive frequencies for real time series data. For complex time series data the negative and positive frequencies may have different energy densities. The frequency samples are evenly spaced at $\delta\omega$ increments, which is just the amount required to allow consecutive estimates to lie at the nulls of the transform of a square window function. Thus, spectral estimates from a FFT are independent of each other, and as they are complex valued, each estimate has 2 degrees of freedom.

Other important considerations of the FFT are that it

- performs a coherent average over time, which assumes stationarity of the data over the length of the time series.
- assumes evenly spaced data.

Missing data and non-stationarity are problems that are discussed in the sections that follow.

2.5 Handling Missing Data

When dealing with geophysical phenomena it is inevitable that not every sample yields a usable data value. Some data are lost due to the poor signal-to-noise for that particular sample or set of samples. The analyses may also reject the data sample for a number of other reasons. The rejection criteria used for FCA, which provides the bulk of the data for this thesis, have been discussed in Section 2.3.4.3. Equipment failures of one form or another can also result in often extended periods of patchy or no data. These factors all contribute to the existence of gaps where data are missing. This presents a problem for the standard spectral analyses, where regularly spaced data are assumed. When some data are missing the sinusoidal functions generally used as the orthogonal basis set for the Fourier expansion become non-orthogonal — they are no longer independent so cannot accurately represent the data without the use of cross-terms. Unequally spaced data present the same problem as for missing data and various schemes exist to handle both. These can be broken into two classes. The first use standard Fourier techniques to find the spectra after somehow "filling-in" the gaps in the time series, therefore allowing the use of a variety of FFTs. The second class actually reformulate the Fourier transform to take the uneven

data spacing into account. This normally means the use of a discrete slow Fourier transform. The two approaches are discussed in the next two subsections.

2.5.1 The Fast Fourier Transform

Gaps that are a shorter in duration than the periods of concern do not pose a problem as any reasonable interpolation method can be used to "fill them in" prior to applying a transform. As the data gaps become larger though, more care must be taken in the interpolation. Consider the simplest case where missing data values (from a regularly spaced data set) are replace by a zero value, or by the mean value of the time series. The power spectral density of the time series will be affected by the frequency distribution of the data gaps, leading to spurious power estimates. Also, since high frequency components will be seen not to exist within the data gaps (the local Nyquist frequency will be smaller), relatively more energy will appear to exist at lower frequencies than otherwise would be the case. Since the data gaps are given as much weight as any similar length section of the time series, relatively long gaps will cause drastic inaccuracies in the power spectral estimates. The top panels in Figure 2.9 show an artificial time series and its power spectrum (using a standard mixed-radix FFT). Missing data have been simulated by flagging random data points, and assigning a random width for the data gap, resulting in 25% of the data being "missing". The data "gaps" can be filled with the mean of the full time series, and the resulting power spectrum is shown in the middle panels of Figure 2.9. The gaps could have been filled with some sum of sinusoids, but this is introducing power directly into the frequency terms that are being measured. A cubic-spline interpolant was also used to fill the gaps (bottom of Figure 2.9) and the resulting power spectrum is also shown. Comparing the lower two spectra it can be seen that slight differences can occur in the power spectrum by choice of interpolant. Both "missing data" spectra differ from the real spectrum by having a different relative power distribution, and less total power in the real spectral peaks. Power has leaked into lower frequencies, as evidenced by the new peaks between 0–15 cycles/unit. On the whole, the gap filling spectra reproduce the standard spectrum quite well, identifying all the same peaks at the same positions. The relative powers for the mean-filled spectrum are not too different from the spectrum of the full time series

Another approach is to make use of the fact that the power spectrum is the Fourier transform of the auto-correlation function. Since the auto-correlation function is a normalised sum of the products of time sample values, it can be corrected for the actual number of data points that are used. That is, each lag value of the auto-covariance function is "normalised" by the actual

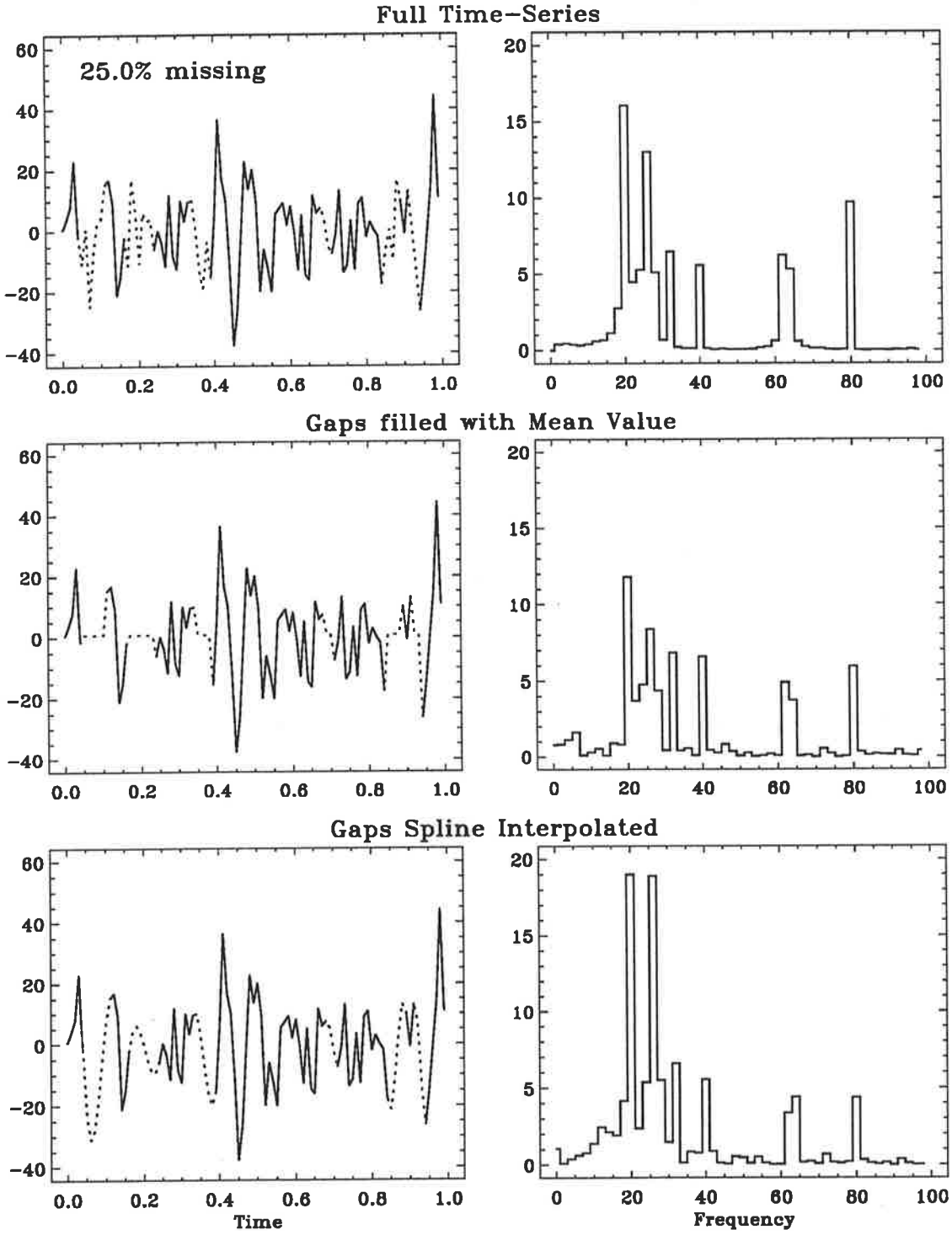

Figure 2.9: **TOP:** The original time series and its power spectrum (by a standard mixed-radix FFT). The time series was generated using a sum of sinusoids of random relative phases, and frequency components at 21, 25, 28, 32, 40, 63, and 80% of the Nyquist frequency, with relative strengths of 10, 10, 5, 5, 4, 7, and 6, and a random noise value with Gaussian distribution between $\pm$ 1. Regions where the data will be treated as missing are dotted. These have been chosen at random positions and duration, covering 25% of the time series;
MIDDLE: This time series has had the "missing" data replaced by its mean value. The resulting power spectrum is shown on the right;
BOTTOM: Here the missing data have been replaced by a cubic-spline interpolant.

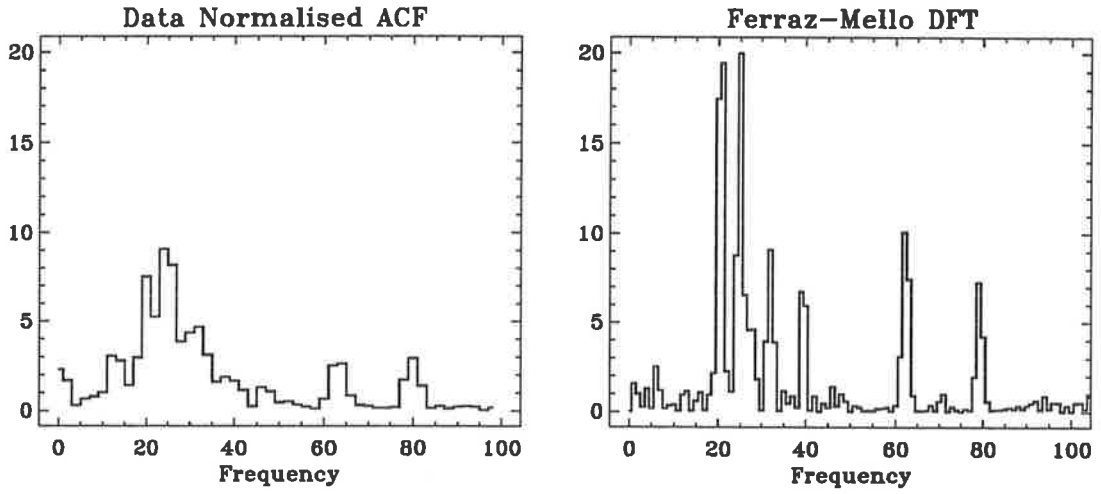

Figure 2.10: The power spectrum from **LEFT:** a pointwise normalised auto-correlation function; **RIGHT:** a data compensated Fourier transform [*Ferraz-Mello*, 1981, *c.f.* Appendix D]

number of points that went into its sum. A power spectrum calculated in this manner is shown on the left-hand side of Figure 2.10 using the time series data shown at the top of Figure 2.9. It can be seen that in this case a lot of spectral energy has been lost to the mean. This result is very sensitive to the amount and relative positioning of the missing data, making it unreliable for real data where the "real" spectrum is unknown.

The first two approaches — really variations of the same approach — allow the time series to be filled, transformed, bandpassed, then re-transformed to give a time series containing only the frequency components selected. The third approach, the data-normalised auto-correlation function loses the phase information required to reform a bandpassed time series. *Moore et al.* [1988] shows further examples of how the use of equally-spaced data techniques can give poor results when applied to unequally-spaced data.

2.5.2 Alternative Fourier Transforms

Scargle [1982] outlines a procedure whereby the standard periodogram (or power spectral density estimator),

$$P_x(\omega) = \frac{1}{n}\left|\left(\sum_{j=1}^{n} X(t_j)\cos(\omega t_j)\right)^2 + \left(\sum_{j=1}^{n} X(t_j)\sin(\omega t_j)\right)^2\right| \tag{2.52}$$

is redefined to take into account possible uneven spacing of the time samples, $X(t_j)$. The redefined periodogram is,

$$P_x(\omega) = \frac{1}{2}\left\{\frac{\left[\sum_{j=1}^{n} X(t_j)\cos\omega(t_j-\tau)\right]^2}{\sum_{j=1}^{n}\cos^2\omega(t_j-\tau)} + \frac{\left[\sum_{j=1}^{n} X(t_j)\sin\omega(t_j-\tau)\right]^2}{\sum_{j=1}^{n}\sin^2\omega(t_j-\tau)}\right\} \tag{2.53}$$

where τ is defined by,

$$\tau = \frac{\sum_{j=1}^{n} \sin(2\omega t_j)}{\sum_{j=1}^{n} \cos(2\omega t_j)} \,. \tag{2.54}$$

The advantages of the new definition are that:

- the error associated with each spectral estimate in the periodogram maintains its exponential distribution, for normally distributed $X(t_j)$, even when the data spacing in non-uniform,
- time-translation invariance is maintained for unevenly-spaced data by the τ term,
- the periodogram becomes exactly equivalent to a least-squares fitting of sinusoids,
- and it reduces to the standard form when the time sampling is regular.

The false alarm rate, detection efficiency and other statistical properties of this periodogram are then developed. *Horne & Baliunas* [1986] clarify this method, showing that the normalisation must be performed using the total variance of the data.

This method, known as the "Lomb-Scargle" method, weights the data on a per point basis rather than a per time basis as in a normal Fourier transform. Since it is closely akin to the standard periodogram, techniques have been developed that can evaluate this periodogram in a very efficient manner using standard FFTs [*Press & Rybicki*, 1989; *Press & Teukolsky*, 1988]. A disadvantage of this technique is that, like the renormalised auto-correlation method mentioned above, it does not allow for a bandpassed time series to be formed, although a better estimate of the power spectrum has been attained.

Rather than redefining the standard periodogram to maintain its statistical properties when the data sampling is non-uniform, *Ferraz-Mello* [1981] redefines the basis set the time series is expanded upon in frequency space such that it is orthogonal for the current data set. This is achieved using the Gram-Schmidt orthogonalisation process on the sinusoid functions using the actual data sampling times (*c.f.* Appendix D). This allows the evaluation of the amplitude spectrum, hence bandpassing and re-transformation are possible. The Ferraz-Mello DFT was investigated for use in forming bandpassed time series and power spectral estimates. The power spectrum shown on the right-hand side of Figure 2.10 results when the Ferraz-Mello DFT is applied to the time series shown at the top of Figure 2.9. The spectrum has been calculated at twice the resolution of a standard FFT. Notice how the spectral line at 63% is now resolved, and little energy has been shifted to lower frequencies. The overall noise level has increased from that of the FFT of the full time series but the relative strengths of the peaks are in good agreement with the input time series.

2.6 Separating Components in a Heterogeneous Wind Field

However the winds in the atmosphere are determined, there will be a need to extract a range of different periodic components in order to study such phenomena as the solar tides and planetary waves. A number of techniques can be used. In this section a few of these will be briefly discussed, then it will be explained why spectral filtering was used in the analysis of data in this thesis.

2.6.1 Time-Domain Filtering

Filtering in the time domain can be accomplished by using running means with various weighting windows, which is the same as convolving the time series with the weighting function (a simple function giving equal weighting to all the data is often used). This convolution is exactly equivalent to applying a spectral window (or filter) in the frequency domain, so practical considerations will normally determine which domain is used. The auto-covariance of a time series can be formed, giving information about the time dependency and repetition periods. This is equivalent to using the power spectrum in the frequency domain, and again practical considerations will normally determine which domain is appropriate.

Block averaging the data is a related time-domain technique. This is the same as applying an equally weighted n point running mean, then only keeping every n^{th} data point. The advantage of block averaging is that the number of data points are reduced yet statistical independence is maintained. Both block averaging and running means remove the high-frequency components which presumably contain most of the instrumental noise, leaving the longer periods more evident in the raw data. Although this improves the reliability and accuracy of the data it does not separate the different period components.

The use of a running mean necessitates that the data be rejected for half the width of the weighting window at either end of the data set. If the data length is not a multiple of the block size when performing block averaging then the excess data must be handled differently. The most natural way is to simply take the average of the remaining data points.

An alternative technique is to break the time series into consecutive segments of the period to be investigated, then overlayed on each other and averaged. This method is sometimes called superposed epochs. The superposition causes frequencies not multiples of the one of concern to cancel out. Longer periods need to have been previously removed from the time series. Of course, the exact frequency of the component of interest needs to be known *a priori*. The length of time used for the superposition can be varied and the effects observed. When the superposition time length coincides with a dominant frequency in the data, enhancement of this component and its

harmonics will occur. Thus periodicities in the data can be found.

2.6.2 Parametric Methods

In order to by-pass problems associated with standard Fourier techniques for non-stationary variables or unevenly spaced data points, and to obtain higher resolution for spectral estimates, parametric techniques have been developed to estimate spectral power [*Bath*, 1974; *Brillinger & Krishnaiah*, 1983; *Lacoss*, 1971]. Non-stationarity of the data becomes less of a problem as the parametric methods rely on adapting the data window to suit the data, maximising some parameter; thus short data segments can still yield good spectra. Adapting the data window also allows unevenly spaced data points to be handled. Parametric methods tend to take the form of either a "maximum entropy method" (MEM) or a "maximum likelihood estimator" (MLE). The former will be considered first.

The auto-covariance function, $\gamma(\tau)$, for a time series and the power spectrum, $P(\omega)$, are a Fourier transform pair. That is

$$P(\omega) \propto \int_{-m}^{+m} \gamma(\tau) e^{-i\omega\tau}\, d\tau \tag{2.55}$$

$$\gamma(\tau) \propto \int_{-\pi}^{\pi} P(\omega) e^{i\omega\tau}\, d\omega \; . \tag{2.56}$$

The auto-covariance can be found from the time series, $x(t)$, by shifting and summing with itself:

$$\gamma(\tau) = \sum_{-n}^{+n} x(t)\, x(t-\tau) \; . \tag{2.57}$$

Rather than performing a Fourier transform to obtain an estimate of the spectrum, one can be found that satisfies equation 2.56 while maximising the entropy

$$\int_{-\pi}^{\pi} \log P(\omega)\, d\omega \; . \tag{2.58}$$

Not surprisingly, this is called a "maximum entropy" spectrum. *Press et al.* [1986] gives an alternate view of power estimation by MEM. Transforming the complex frequency plane (in which the traditional spectral frequency values lie along the real axis) to the $\mathcal{Z}$-plane by applying a $\mathcal{Z}$-transform,

$$\mathcal{Z} = e^{i\omega\,\delta t} \; , \tag{2.59}$$

where δt is the time sampling interval and $\omega = 2\pi f$. Note that the normal Fourier-transform frequency samples (or Nyquist interval), $1/\mathrm{N}\delta t$, map one-to-one from the real frequency axis onto the unit circle in the $\mathcal{Z}$-plane. The power density function from a FFT can then be written

as

$$P(\omega) \propto \left| \sum_{k=-\frac{N}{2}}^{\frac{N}{2}-1} c_k \mathcal{Z}^k \right|^2 , \tag{2.60}$$

which is an approximation to the "true" power density,

$$P(\omega) \propto \left| \sum_{-\infty}^{\infty} c_k \mathcal{Z}^k \right|^2 . \tag{2.61}$$

The approximation made in the FFT implies that the model spectrum can have zeroes in the $\mathcal{Z}$-plane, but not poles. Thus, the spectrum can not have discontinuities and specular peaks are approximated by polynomial fits. If, on the otherhand, equation 2.61 is approximated by

$$P(\omega) \propto \frac{a_0}{\left|1 + \sum_{k=1}^{M} a_k \mathcal{Z}^k\right|^2} \tag{2.62}$$

then poles can exist on the unit circle. This corresponds to allowing sharp spectral peaks (actually infinite power spectral densities) in the model spectrum. The MEM problem is then to find the coefficients a_k. Equation 2.62 is a continuous function of frequency as in a DFT, and M is the maximum number of specular peaks considered.

A MEM spectrum can also be considered as an "auto-regressive" spectrum. An "auto-regressive" process, $x(t)$, can be parameterised by its values at earlier times, so that

$$x(t) = \theta_1 \, x(t-1) + \cdots + \theta_n \, x(t-n) + \phi(t) , \tag{2.63}$$

where $\phi(t)$ is a random white-noise process with variance θ_0. The spectrum, $f(\omega; \theta_0, \ldots, \theta_n)$, is given by

$$P(\omega; \theta_0, \ldots, \theta_n) = \frac{\theta_0}{2\pi \left|1 - \theta_1 e^{i\omega} - \cdots - \theta_n e^{in\omega}\right|^2} , \tag{2.64}$$

where the $\theta_0, \ldots, \theta_n$ are unknown parameters which will be estimated from the data. This is the same as equation 2.62 but approached from the viewpoint of auto-regressive processes.

To introduce maximum-likelihood spectral estimators, first consider a convolutional filtering process (after *Lacoss* [1971]) as may happen to a raw time series during the process of sampling from some continuous geophysical process. X is the sampled time series — the output of the filter — while Y is the physical "input" time series and a_n the filter weights.

$$X(k\,\delta t) = \sum_{i=1}^{n} a_n Y((k+1-n)\,\delta t) . \tag{2.65}$$

Now, consider the physical mechanism to be composed of a single complex sinusoid with some additive random noise, so that

$$Y(k\,\delta t) = A e^{i\omega\,\delta t\,k} + \mathcal{N} , \tag{2.66}$$

then for the sampled values, X, to be an unbiased estimator of $Ae^{i\omega\,\delta t\,k}$, the coefficients, a_n, need to be chosen to satisfy

$$Ae^{i\omega\,\delta t\,k} = \sum_{i=1}^{n} a_n Y((k+1-n)\,\delta t)\ . \tag{2.67}$$

Following *Lacoss* [1971], $\boldsymbol{R}$ can be defined to be an N×N correlation matrix such that $R_{ij} = \rho_{j-i}$, with ρ being the correlation function for the Y. $\boldsymbol{\mathcal{E}}$ can likewise be defined to be the column vector such that $\mathcal{E}_j = e^{j\omega\,\delta t}$ with $j \in$ [0,N-1]. Therefore equation 2.67 can be expressed in matrix form as

$$\boldsymbol{\mathcal{E}}^{*T}\boldsymbol{a} = 1\ , \tag{2.68}$$

where $\boldsymbol{a}$ is the column vector of the a_n, and the * and ^{T} denote conjugation and transposition respectively. The variance of the X, σ^2, is given by

$$\sigma^2 = \boldsymbol{a}^{*T}\boldsymbol{R}\boldsymbol{a}\ . \tag{2.69}$$

Minimising the variance with the constraint of equation 2.68 leads to

$$P(\omega) = \frac{1}{\boldsymbol{\mathcal{E}}^T\boldsymbol{R}^{-1}\boldsymbol{\mathcal{E}}^*}\ , \tag{2.70}$$

which is a maximum likelihood spectral estimator.

Lacoss [1971] performs a comparison between a standard Fourier power spectral technique [*Bartlett*, 1956; *Blackman & Tukey*, 1959], a MEM (following the approach described in *Parzen* [1969]) and a MLE technique (based on that used by *Capon* [1969] and described above). An example is shown in Figure 2.11 which is taken from *Lacoss* [1971], figure 4a. Note that a least-squares fit is a MLE, as the above treatment would suggest.

These parametric methods can be used to give high resolution spectra, but it can be difficult to interpret the spectral estimates. Moreover, they do not allow a convenient means of separating different frequency components for individual analysis.

2.6.3 Harmonic Analysis

This has been the most favoured technique for extracting tidal and mean wind information from the composite wind field. Usually a function containing a constant term plus a number of sinusoidal periodic terms at the frequencies where the main variance is thought to be contained, is fitted to the data using some least-squares criterion [*Bloomfield*, 1976; *Brillinger*, 1975]. The periodic terms are usually the solar tidal terms with periods of 24, 12 and 8 hours, which gives

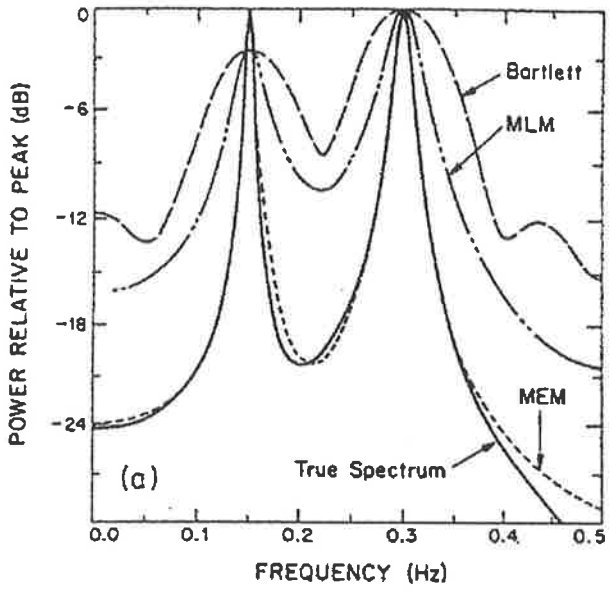

Figure 2.11: Comparison of parametric methods and standard spectral technique. The spectra are obtained from the artificial correlation function $\rho(t) = [e^{-\alpha_1 t}(\cos\beta_1 t + \alpha_1/\beta_1 \sin\beta_1 t)] + [2e^{-\alpha_2 t}(\cos\beta_2 t + \alpha_2/\beta_2 \sin\beta_2 t)]$, with $\alpha_1 = 0.02$, $\alpha_2 = 0.04$, $\beta_1 = 2\pi(0.15)$ and $\beta_1 = 2\pi(0.30)$ [figure 4a from *Lacoss* [1971]].

a function,

$$\begin{aligned} f(t) &= \mathcal{A} + \mathcal{B}_1 \sin(\omega t) + \mathcal{B}_2 \sin(2\omega t) + \mathcal{B}_3 \sin(3\omega t) \\ &\quad + \mathcal{C}_1 \cos(\omega t) + \mathcal{C}_2 \cos(2\omega t) + \mathcal{C}_3 \cos(3\omega t) \ , \end{aligned} \tag{2.71}$$

with $\omega = 2\pi f$ where $f = 1\,\mathrm{cpd}$. The amplitudes and phase of each component can be found from the values of the regression coefficients, *e.g.* the diurnal tidal amplitude would be given by $\sqrt{\hat{\mathcal{B}}_1^2 + \hat{\mathcal{C}}_1^2}$ and the phase by $\arctan(\hat{\mathcal{C}}_1/\hat{\mathcal{B}}_1)$, where the $\hat{}$ denotes the estimator. As will be seen in Chapter 4, but already generally recognised, a 48-hour term should also be fitted if the data are from equatorial latitudes, or it is during local summer at higher latitudes. This term corresponds to the quasi-two-day wave. High frequency terms can be removed by some time-domain filtering as discussed above, but should not affect the harmonic analysis. Low frequency terms[4] on the otherhand need to be removed[5].

Usually the covariance of the harmonic terms and their significance is not considered. This method also suffers from the necessity of *a priori* knowledge of the frequencies of the major variance terms. It also must assume that these terms are at discrete fixed frequencies; not Doppler shifted as a function of time or broadened in any manner[6], nor non-stationary or

[4] such as seasonal variations, dependent on the temporal extent of the data

[5] This is known as detrending

[6] such as by the effects of the mean winds at lower altitudes, variations in the driving force, non-linear interactions, mixed modes, or amplitude and phase variations

impulsive. This may be a lot to ask for many planetary waves, and even the solar tides. As discussed in Section 1.4.5, atmospheric normal modes can have a broad frequency distribution under normal atmospheric conditions.

Advantages of this method are its ease of implementation (hence its popularity, especially in earlier work when computing power was in its infancy), the direct interpretations that can be made about the amplitude and phase of each component (and associated errors), and the ability to use all the data present — no rejection need be applied. Variance terms relating to high frequency activity can be found by subtracting the time series determined from the harmonic terms from the original.

2.6.4 Spectral Filtering

Since it is the different frequency components that are of interest in the present study, it seems natural to filter the data in the spectral domain. The time series can be Fourier transformed and weights applied to individual frequencies prior to performing a reverse transform. In this way low-, band-, or high-pass filtering can be achieved. The advantages are that no assumption needs to be made about the stability of the frequency component; if the energy is spread over a broad frequency band then an appropriate bandpass can be used. With the advances in computing this method of filtering has become more common.

Some caution needs to be taken when using such a filter [*Forbes*, 1988, for example]. A major cause for concern is the possibility of "ringing" in the re-transformed time series. This is caused by the "Gibbs" phenomenon [*Bath*, 1974; *Bloomfield*, 1976; *Bracewell*, 1978] where sharp boundaries of the spectral window cannot be properly represented by a finite sum of sinusoids giving rise to an "overshoot" and following "ripples" when passed through the Fourier transform. This causes an over-emphasis of the extreme frequencies of the bandpass of the order 10%, producing results as shown in Figure 2.12. Ringing in this case not only occurs as the filter window has sharp boundaries (a rectangular window was used), but also as the spectral line is not at an integer multiple of the frequency sampling interval, which is usually the real situation. This leads to spectral spillage into a few frequency bins, hence ineffective bandstopping (or bandpassing) when a narrow frequency window is used. As the window size increases, the spectral line is fully covered by the filter, but ringing still occurs (bottom of Figure 2.12) due to the sharp window boundaries.

For a bandpass between frequencies f_1 and f_2, the fastest variation that can be observed in the re-transformed time series is one with a frequency of $f_2 - f_1$, imposing a minimum

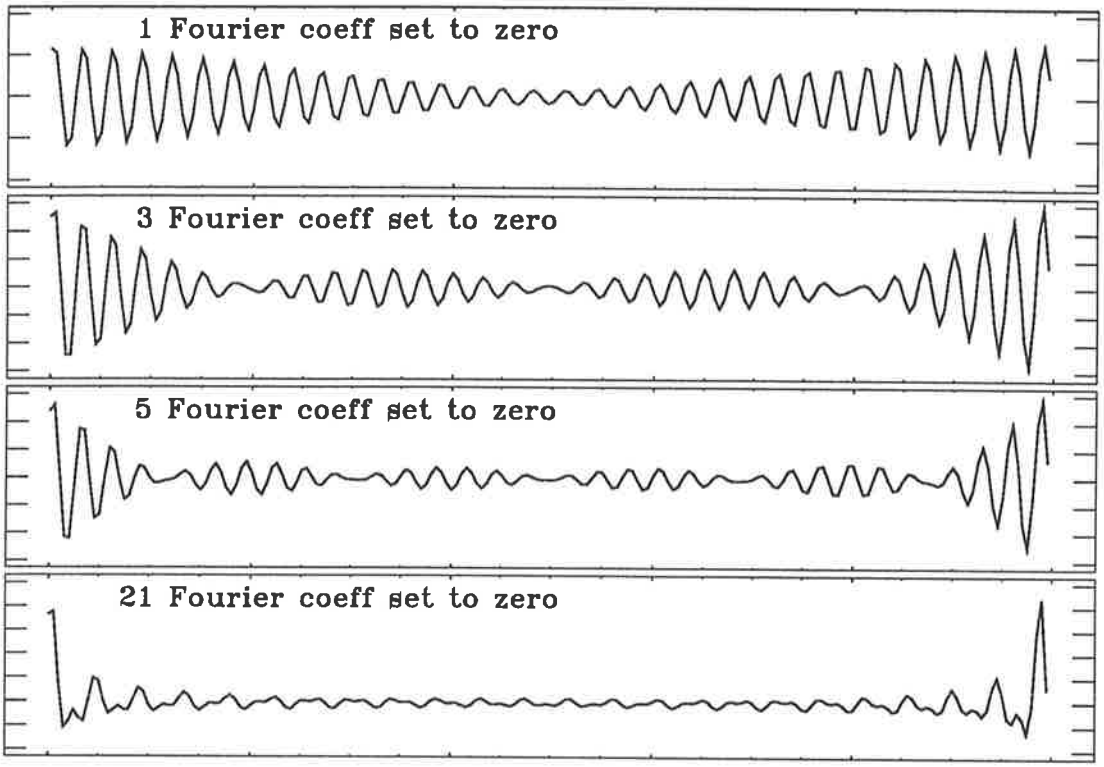

Figure 2.12: Filtered results from bandstopping an artificial time series. The number of Fourier coefficients used in the bandstop are shown in the figures [figure 5. from *Forbes* [1988]].

coherence time on the data. This is caused by the beating of the components at the edges of the bandpass and implies that the width of the bandpass must be tuned to the maximum time-scale variation that is to be observed in the time series. Further, if a white-noise spectrum is bandpassed, then this beat frequency will tend to dominate the resultant time series causing a discernible amplitude modulation. Both the "Gibbs" phenomenon, and amplitude modulation can be minimised by using a smooth-edged pass window in the frequency domain.

2.6.5 Choice of Technique

Spectral shift and broadening (discussed in Section 1.4.5 with regard to atmospheric normal modes) may mean that the wind component that is being sought may not always exist at a prespecified frequency. Moreover, it will have a frequency distribution about a known value. As it was intended to isolate this component then a band of frequencies had to be separated from the wind time series. With the ease of computing Fourier transforms, spectral filtering seemed the most appropriate means. This allowed the ability to specify a frequency of concern and a frequency width that best suited the final use of the filtered time series. Whenever filtered or bandpassed data are referred to in this thesis, they have been spectrally filtered using a spectral window of equal weighting except for the end values, which have only half the weighting (if they

were not also one of the positive or negative limits of the spectral estimates). This gave enough tapering to reduce the effects described earlier. For handling missing data (see Section 2.5) a spectral filter using a Ferraz-Mello DFT (see Appendix D for the details of this algorithm) as the forward transform, and a Singleton mixed radix FFT [*Singleton*, 1969] as the inverse transform was investigated. It was eventually decided that the Singleton FFT could be used for both transforms, producing adequate results. Missing data were replaced by the mean of the time series — this has already been discussed in more detail in Section 2.5. The filtering was applied simultaneously to both the positive and negative frequency halves. A number of tests were performed on the filtering routines so that a high degree of confidence could be placed in them.

2.7 Complex-Demodulation

For the work on the quasi-two-day wave, a method was required that could distinguish between periods of 48 and 50 hours, when the time sampling was only of the order of an hour, and few cycles were involved. This method therefore needed to be very sensitive to the frequency variations within the time series. For this purpose a complex demodulation method [*Bloomfield*, 1976; *Brillinger & Krishnaiah*, 1983] was used. This method, as applied here, is a combination of time- and frequency-domain filtering, but could be implemented as a purely time-domain technique. Consider a real time series comprised of a single frequency sinusoidal variation, $\mathcal{A}\cos\omega t$. If this is multiplied by a complex sinusoid, $e^{-i\omega_0 t}$, where ω_0 is an arbitrary frequency near ω, the resultant complex waveform will consist of the sum of terms of frequency $|\omega+\omega_0|$ and $|\omega-\omega_0|$, namely

$$\mathcal{A}\cos\omega t\; e^{-i\omega_0 t} = \frac{\mathcal{A}}{2}\left[e^{i(\omega-\omega_0)t} + e^{-i(\omega+\omega_0)t}\right]. \tag{2.72}$$

By low-pass filtering (or a symmetric bandpass around zero frequency if negative frequencies are used as well), the summation terms can be removed leaving only the frequency difference terms. The filtering stage can be performed in the frequency domain (as was done in this thesis), or a time-domain filtering technique could be used. Extending this to the more realistic case where the raw time series can be considered to consist of a possibly infinite sum of sinusoids of different strengths and frequencies, multiplication by $e^{-i\omega_0 t}$ gives a resultant complex waveform consisting of the sum of terms as on the right-hand-side of equation 2.72 for various ω. That is, all existing frequency components in the raw time series now exist in the complex-demodulated complex time series as two terms, one shifted down in frequency by ω_0, the other shifted up

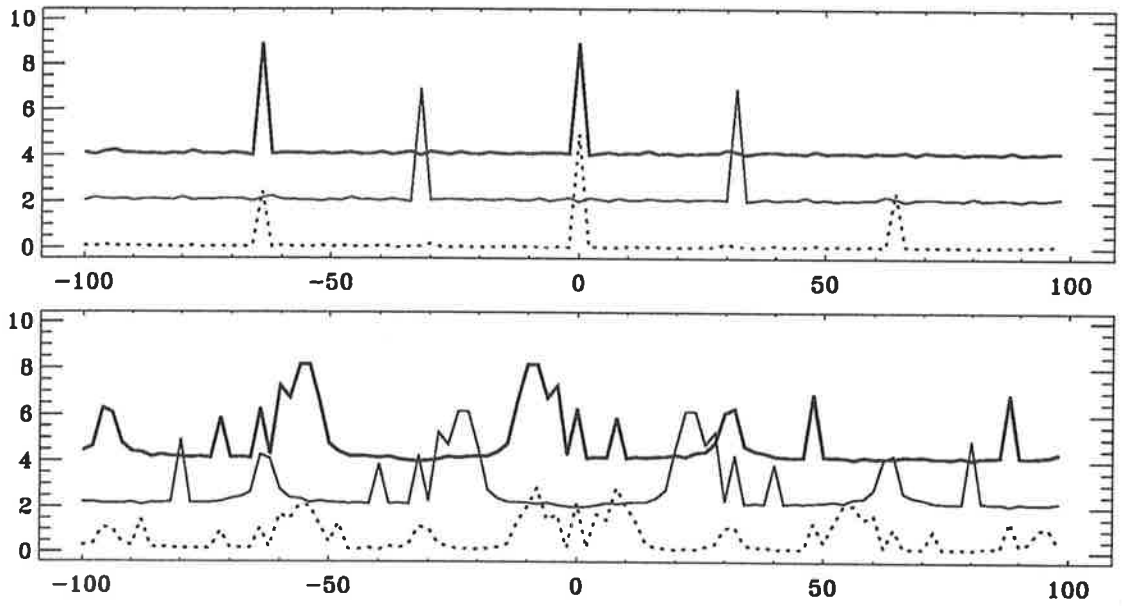

Figure 2.13: Amplitude spectra showing the shift in frequency caused by complex-demodulation. The amplitude and frequency units are only relative. The three separate spectra shown in each diagram have been successively shifted by 2 amplitude units. Shown are the amplitude spectrum of the real component of the complex-demodulated time series, the original time series, and the complex-demodulated complex time series as dotted, solid, and bold lines respectively. A demodulation frequency of 32 units was used. The top diagram shows the effect on a pure sinusoid at 32 frequency units, whereas the bottom diagram combines a full spectrum (which includes a signal at 32 units).

by ω_0. This is shown by the spectral representation in Figure 2.13. Three separate spectra are shown in both the top and bottom diagrams, successively shifted upwards by 2 amplitude units to aid in viewing their features. The top diagram shows the effect of the complex-demodulation on a single frequency component. The amplitude spectrum of the original sinusoidal signal, at a relative frequency of 32, is shown as a narrow solid line. Below this is the spectrum of the real component of the complex-demodulated time series (dotted line), showing energy peaks at the sum and difference frequencies. A demodulation frequency of 32 was used. Above these two spectra is the amplitude spectrum of the complex-demodulated complex time series. The additional phase information in the complex time series causes the two summation terms to merge, giving an effective shift in the whole amplitude spectrum with respect to that of the original time series. Similarly the bottom diagram shows the effect when a more continuous spectrum of frequencies is present in the time series. Only the frequency components near zero, *i.e.* where $\omega \approx \omega_0$, are not contaminated by mixing of the sum and difference terms in the spectrum of the real component of the complex-demodulated time series. Again, the amplitude spectrum of the complex-demodulated complex time series is just a shifted version of the original

time series spectrum. It can be seen that a narrow bandpass is required to obtain the energy peak near zero while rejecting the neighbouring peaks. From this example it can be seen that an idea of the power spectral density function in the neighbourhood of the demodulation frequency is essential in order to choose an appropriate low frequency cutoff.

As the complex multiplication is a point-by-point operation in time, missing or unevenly spaced data do not present a problem at this stage. Stationarity of the data is also not an important consideration. More importantly, if the time samples start off as independent estimates they remain so after the complex multiplication. The same cannot be said for the filtering process. If a spectral filtering technique is used, the width of the pass-band will determine the minimum coherence time imposed on the data (as covered in the previous section). The spectral estimates will also be affected by any data gaps (*c.f.* Section 2.5). A time domain low-pass filtering process, such as the application of a running mean, will also limit the independence of the data points.

The magnitude of the complex-demodulated time series is a measure of the amplitude of the dominant frequency within the band-pass around the demodulation frequency. This is fairly robust under variations in the demodulation frequency since it mainly depends on the amplitude of the dominant frequency component. The rate of change of the phase of the complex-demodulated time series, on the other-hand, is very sensitive to the difference between the demodulation frequency and the frequency of the dominant component within the band-pass (*c.f.* equation 2.72), and therefore provides a good means of estimating the latter, since the former is known. As long as the same strong signal remains within the bandpass, the frequency (or period) of the signal determined in this manner should be independent of the demodulation frequency. As the demodulation frequency moves closer to the dominant frequency the slope of the phase of the complex demodulation approaches zero. This provides a consistency check on the results of the complex-demodulation technique. If the period estimate remains the same as the demodulation frequency is varied then it is highly likely that a dominant signal is present within the bandpass. Otherwise the determined periods may be simply random noise.

One of the advantages of the complex-demodulation technique is that it allows an estimate of the frequency of the dominant component at every time sample within the time series. Thus variations of the period with time can be studied, and statistics formed. This is precisely what was done for the two-day wave analysis in Chapter 4.

2.8 Moving Power Spectra

A power spectrum is a convenient way to summarise the variability in the wind field, but it assumes stationarity over the time interval of the time series. In order to study non-stationary phenomena short time segments can be used to produce individual power spectral estimates, which can then be grouped together to reveal the time evolution of spectral features. The segments ideally should be shorter than the coherence time of the phenomena so that stationarity can be assumed. In practice, this needs to be balanced by the loss of frequency resolution as the time series length decreases. Moving power spectra have been used in this thesis to study the frequency and temporal behaviour of the quasi-two-day wave (Chapter 4). Time segments typically of 14 and 40 days have been used, with steps of 7 and 20 days respectively between each segment. These data lengths are a compromise between frequency and time resolution. The life-time of a two-day wave event is typically 20 days, so that the assumption of stationarity becomes quite tenuous, even for short segments such as 14 days. Nevertheless, useful — in fact, vital — information can still be gained from the moving power spectra.

The Ferraz-Mello DFT was used for the moving power spectra in this thesis, although a standard FFT could have been used for the Christmas Island data due to the completeness of that data set. Use of the DFT allowed spectral estimates to be calculated at a higher resolution than the normal FFT. Often this was smoothed back to the standard 1/T frequency resolution. Comparison with power spectra derived from a standard FFT using mean-filled data showed that aliasing was not a problem for the Ferraz-Mello spectra within the frequency range used.

2.9 Higher-Order Spectra

In Chapter 4 use is made of higher order spectral estimates to investigate possible non-linear effects of the quasi-two-day wave. *Tukey* [1965] gives a good account of how and why these form of spectra are useful. Higher-order spectra are a natural extension to the more familiar set of amplitude and power spectrum. *Bath* [1974] describes the relationship between time series, n^{th} dimensional correlation functions ($(n+1)^{th}$ order moments), n^{th} order spectra and n^{th} order cepstra. This is shown diagrammatically in Figure 2.14 which is taken from *Bath* [1974]. An n^{th} dimensional correlation functions can be represented as

$$< f(t)\, f(t+\tau_1)\, f(t+\tau_2) \cdots f(t+\tau_n) > , \tag{2.73}$$

with the n^{th} order spectrum its Fourier transform. The n^{th} order cepstrum is then the Fourier transform of this.

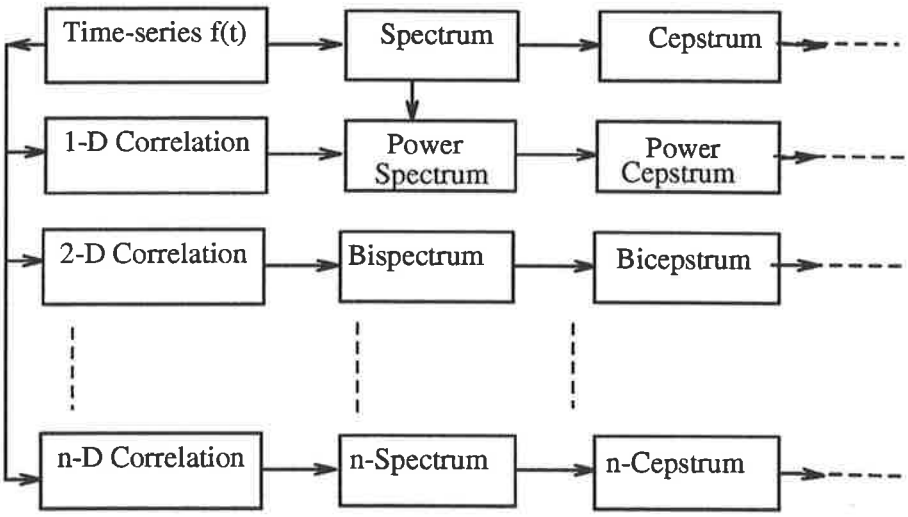

Figure 2.14: A pedigree of various spectral functions [figure 29 from *Bath* [1974], page 112]. Each step across to the right represents the operation of a Fourier transform while motions downward introduce higher-order interactions.

Mendel [1991] describes higher-order spectra from a different viewpoint, using cumulants (also see *Brillinger* [1975] or *Brillinger & Krishnaiah* [1983]). The k^{th} order cumulant is the k^{th} coefficient of the Taylor series expansion of the cumulant generating function,

$$K(v) = \ln E[e^{ivx}] \tag{2.74}$$

and is analogous to a k^{th} order correlation function. $E[\,]$ denotes an expectation value. Cumulants have properties which allow them to easily extend into higher-order spectra in the same way that ordinary correlation functions Fourier transform to a power spectrum. In fact, the ordinary correlation function is a 2^{nd} order cumulant. An important feature of cumulants is that, once greater than the 2^{nd} order, they are "blind" to any Gaussian process. The higher-order cumulant of a Gaussian process is zero. Thus Gaussian noise is automatically eliminated. *Mendel* [1991] says that "higher-order statistics are applicable when we are dealing with non-Gaussian (or, possibly nonlinear) processes, and many real world applications are truly non-Gaussian."

The 2^{nd} order, or bi-spectrum as described by *Kim & Powers* [1979], has been used to some extent in this thesis. The analysis was performed by Mr Tony Zollo[7] as part of a collaboration with DSTO [*Anderson et al.*, 1992, describes the technique and some other investigations].

The significance of the bispectral estimates can be seen when a quadratic nonlinear interaction is considered between two waves, X_k and X_l [*Kim & Powers*, 1979], to produce a third component, X_M,

$$X_m = \sum_{k+l=m} A_{k,l} X_k X_l \tag{2.75}$$

[7]HFRD, DSTO, P.O. Box 1500, Salisbury, SA 5108, Australia

Two primary waves at frequencies ω_k and ω_l interact to produce a third at the sum or difference frequency, $\omega_m = \omega_k \pm \omega_l$, with a coupling coefficient, $A_{k,l}$.

It can be shown [*Kim & Powers*, 1979] that,

$$A_{k,l} = \frac{B^*(k,l)}{E[|X_k X_l|^2]} \tag{2.76}$$

where, once again, $E[\,]$ denotes an expectation value, and $B^*(k,l)$ the conjugate of the bispectral estimator. Thus the bispectrum can be used to estimate the quadratic coupling coefficient for non-Gaussian processes. The bicoherence, $b(k.l)$, can be defined where,

$$b^2(k,l) = \frac{|B(k,l)|^2}{E[|X_k X_l|^2]E[|X_m|^2]} \tag{2.77}$$

This is a measure of the fraction of power at ω_m due to quadratic coupling from waves at ω_k and ω_l.

2.10 Total Linear Least Squares Regression

In Chapter 3 two estimates of the same quantity are compared in scatter diagrams as in Figure 2.15. To quantify the relationship between the two variables, $\mathcal{X}$ and $\mathcal{Y}$, some form of regression can be applied. The most common is one which minimises the square of the residuals.

Consider the set of M linear equations with N unknowns,

$$\mathbf{A}\boldsymbol{x} = \boldsymbol{b}, \tag{2.78}$$

defining the linear model that is to be fitted, where $\mathbf{A}$ is a M×N matrix called the "Design Matrix" containing the functions of $\mathcal{X}$, $\boldsymbol{x}$ is the N element vector of coefficients and $\boldsymbol{b}$ the M element vector of the $\mathcal{Y}$. If the variance is solely in one variable, say $\mathcal{Y}$, and is the same for all the $\mathcal{Y}$, then a model fit to the data can be found that minimises the square of the residuals

$$\boldsymbol{r}^2 = \|\mathbf{A}\boldsymbol{x} - \boldsymbol{b}\|^2 \tag{2.79}$$

This is a standard linear least squares fit whose solution is given by,

$$\boldsymbol{x} = (\mathbf{A}^T\mathbf{A})^{-1}\mathbf{A}^T\boldsymbol{b}. \tag{2.80}$$

The results of applying this form of regression to the sample data in Figure 2.15 are shown in that figure using the $\mathcal{X}$ (a $\mathcal{X}$ on $\mathcal{Y}$ regression) and then the $\mathcal{Y}$ (a $\mathcal{Y}$ on $\mathcal{X}$ regression) as the independent variable.

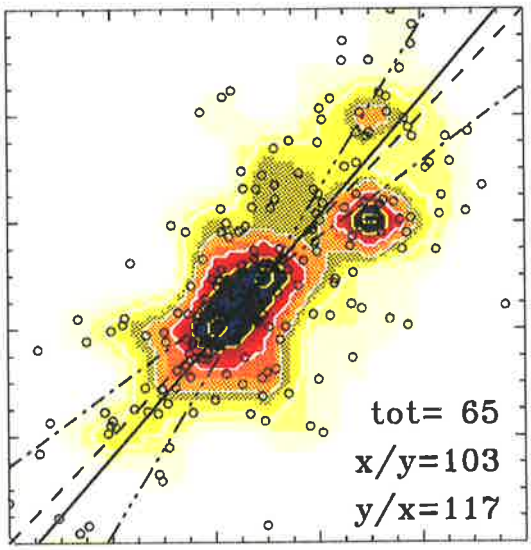

Figure 2.15: An example scatter plot showing the spread and regression fits. The dashed line shows the expected 1:1 relationship; the dot-dashed and dot-dot-dot-dashed lines are standard linear least-squares fits with X and with Y as ordinates respectively (*i.e.* Y on X and X on Y). The thick solid line is a total regression fit. The slopes give an indication of the trend and the intercepts the bias between the two variables. The contours and shading indicate the distribution of the scattered points (shown as small symbols overlayed on the shading). The appropriate χ^2 values are also shown.

Note that if the variance in the $\mathcal{Y}$ is taken into account in the residual formula of equation 2.79 so that

$$r^2 = \| \frac{\mathbf{A}\boldsymbol{x} - \boldsymbol{b}}{\sigma} \|^2 \tag{2.81}$$

then the residual has a χ^2 distribution. Therefore a least-squares estimator also minimises the χ^2 when all of its assumptions are met.

This form of regression seems fine until it is realised that in this case both quantities have some unknown uncertainty associated with them. How does this change the least-squares fit? Now not only must the deviations in the $\mathcal{Y}$ direction be taken into account, but also those in the $\mathcal{X}$. It is therefore desirable to minimise the distance between the data and the regression fit *normal* to the fitted curve. This form of regression is called a "total least squares" regression. With this in mind the residuals to be minimised become

$$r^2 = \frac{\|\mathbf{A}\boldsymbol{x} - \boldsymbol{b}\|^2}{1 - \boldsymbol{x}^T\boldsymbol{x}}, \tag{2.82}$$

leading to a solution [*Golub & Van Loan*, 1983; *Golub & Van Loan*, 1980],

$$\boldsymbol{x} = (\mathbf{A}^T\mathbf{A} - \hat{s}_{n+1}\mathbf{I})^{-1}\mathbf{A}^T\boldsymbol{b}, \tag{2.83}$$

where $\hat{s}_{n+1}$ is the minimum singular value (the reciprocal of the maximum eigenvalue) for the augmented matrix $\mathbf{A}{:}\boldsymbol{b}$ — the matrix $\mathbf{A}$ with the vector $\boldsymbol{b}$ included as an additional column —

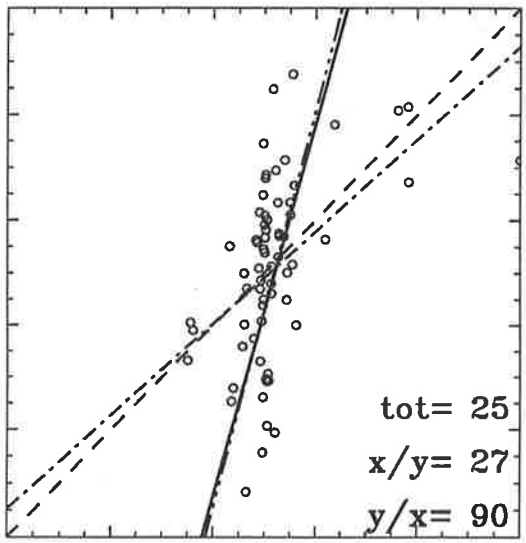

Figure 2.16: With the X (horizontal axis) and Y (vertical axis) values having different distributions, particularly the X being sharply peaked while the Y is more even, a minimisation of the deviations in the Y direction does not lead to an adequate line-of-best-fit. In such a case, either the deviations in the X direction, or a combination of the X and Y deviations, need to be minimised. The lines have the same meanings as in Figure 2.15 and, again, the appropriate χ^2 values are also shown.

and **I** is the identity matrix. The result of this form of regression is also shown in Figure 2.15.

The difference in the standard least-squares fit when using the $\mathcal{X}$ instead of the $\mathcal{Y}$ as the co-ordinate is more marked the greater the slope of the line. This can easily be seen if for example $\mathcal{X}$ are heavily grouped around a constant value, with a few points at the extremes, whereas the $\mathcal{Y}$ values have a more constant distribution (as shown in Figure 2.16).

Minimising the squares of the deviations along the $\mathcal{Y}$ co-ordinate heavily favours the points at the extreme $\mathcal{X}$. The dot-dashed line is such a regression. By minimising the deviations normal to the curve (solid line), or those along the $\mathcal{X}$ co-ordinate (dot-dot-dot-dashed line), a near vertical regression line results, in better agreement with the line-of-best-fit by eye.

Total linear least-squares regression is more sensitive to the relative variances of the $\mathcal{X}$ and $\mathcal{Y}$ than a normal least-squares regression. Therefore care must be taken when determining the weights that should be applied to each data point. A scheme whereby the $\mathcal{X}$ and $\mathcal{Y}$ were scaled to lie within the range of ± 1 was used in the implementation of the total regression for this thesis. This also had the desirable effect of keeping the range and size of all eigenvalues small, thus reducing the arithmetic errors.

Chapter 3

Full Correlation Analysis Comparisons

3.1 Introduction

This chapter describes a set of comparisons performed on different FCA algorithms. The goal was to estimate the spread which could be expected for a given parameter by use of different algorithms. This spread in values could take the form of a constant error independent of the magnitude of the parameter, or some constant fraction of the value, or a combination. In the following tests and discussions constant actual errors, and constant percentage errors are considered.

At the time of commencement of this author's PhD candidature, in July, 1988, there was only one FCA algorithm in general use within the Atmospheric Physics Group. This algorithm was written to run in real-time on a 1970 style computer. Another algorithm was in the developmental stages, and was also intended to be run in real-time. As it was intended to obtain an improved height coverage and data acceptance rate, and there was only a need to run on a campaign basis, it was decided to pursue a separate FCA algorithm which used the full power of the main-frame computers and the advantages of off-line analysis.

The following sections describe the three different algorithms in existence within the Atmospheric Physics Group during 1990; the tests that were applied to them; and the results and inferences. The general theory and practical considerations for the analysis have already been discussed in detail in Chapter 2 and will not be further discussed here. Rather, emphasis will be placed on the differences amongst the three algorithms in their implementation of the general theory.

3.2 Alternate Algorithms

3.2.1 Real-time Analysis Prior to 1989

The algorithm used to deduce "true" wind velocities at Adelaide prior to 1989 was written in an early version of Fortran in the early 1970s. It was designed to run on the main-frame computer of the day — a Cyber 6600, and later a Cyber 173. This was run as an off-line algorithm. When the Adelaide facility at Buckland Park was upgraded in the late 70's to have a mini-computer (NOVA-II), this algorithm was used to perform on-line analysis. The NOVA-II was later upgraded to a NOVA-IV Eclipse. A few years later, around 1984, the algorithm on the Cyber was modified to run on the University of Adelaide's newly installed VAX 785 computers. It was transferred in 1989 to the Physics Department's SUN-4 computer with essentially no changes in the algorithm. It is this last version of the algorithm (henceforth called FCA1) that has been used in these comparisons.

FCA1 finds full matrix solutions to equations 2.14 and 2.16 using a linear least-squares procedure. The values of the auto- and cross-correlations at zero lag are interpolated using Aitken's scheme of Lagrange interpolation using values from lags $-6, -4, -2, +2, +4, +6$ and $-2, -1, 0, +1, +2$ respectively. The maxima of the cross-correlations are found by fitting a quartic to the five points around the maximum value (*i.e.* the maximum data point and two points either side). The lag for the maxima of the quartic lying between ± 1 lag of the lag for the maximum data point is then found. The τ_{ij} are then found by fitting a second-order polynomial to the auto-correlation function and finding the lag at which the value is the same as determined for the cross-correlation at zero lag. The value of $\tau_{\frac{1}{2}}$ is found in a similar way.

3.2.2 Real-time Analysis Post 1989

During 1989, Dr Vincent, head of the Atmospheric Physics Group, was developing a real-time FCA routine (henceforth called FCA2), written in C, to estimate wind velocities for the new generation of solid-state MF transmitters and receivers developed by the group. This algorithm was used for the field sites of Blanchetown (34° S, 139° E), and Christmas Island (2° N, 157° W) but FCA1 continued to be used as the on-line algorithm at the Adelaide site of Buckland Park (35° S, 138° E) due to the computing system there.

In FCA2 Gaussian functions are fitted to the auto-correlation functions using all lags with values greater than 1/3 of the first lag. The value at zero lag is not used. The fitted Gaussians are then used to interpolate the zero lag value of the auto-correlation functions and a mean

function calculated. The value for $\tau_{\frac{1}{2}}$ is also found by fitting a Gaussian function to the mean auto-correlation function using all lags with values greater than 0.4. This fitted Gaussian is also used to give the τ_{ij} — the lags where the value of the auto-correlation is the same as the zero lag value of the cross-correlations. The zero lag values of the cross-correlation functions are linearly interpolated from the points either side. Another Gaussian function is fitted to the cross-correlations using the point of maximum value and 3 points either side. This is used to find the lags for maximum cross-correlation, τ_{ij}^M. Note that later in the development of this algorithm, the recommendations of *Fooks* [1965] are used (see Section 2.3.2), whereby equation 2.17 is used rather than a direct estimate of the τ_{ij}. The amended algorithm is compared to the earlier version in the next section.

Three receivers are assumed in the solution to equations 2.14 and 2.16. Thus equation 2.14 can be solved exactly. For speed and simplicity a particular solution to the over-determined equation 2.14 is used. Varying the particular solution used forms part of the tests described in the next section.

3.2.3 Off-line Analysis Post 1989

Also during 1989 an off-line FCA routine (henceforth called FCA3) was developed by this author. This was to allow the ability to post-process data in the form of raw signal time-series, using different averaging techniques to try to improve the data acceptance rate, and test the dependence of the FCA on the interpolation procedures.

Full matrix solutions to equations 2.14 and 2.16 are implemented using an IMSL linear least-squares procedure. The interpolations used for the zero lag value of the correlation functions, the τ_{ij}, and for $\tau_{\frac{1}{2}}$, were varied and form a part of the tests described in the next section. A quadratic fit to the cross-correlations was used to determine the lags of the maxima, τ_{ij}^M, for all the tests presented here.

3.3 The Test Data

Two forms of data have been used for the comparisons that follow. One is a short data set comprising a 1 hour time-series of complex receiver output collected on spaced antenna at the Atmospheric Physics Group's field site at Buckland Park near Adelaide at 1400 LT on the 15^{th} of January, 1989. The complex receiver output consisted of 256 in-phase and 256 phase-quadrature 8-bit unsigned integers. Coherently averaged data were obtained every 2 minutes but 10 altitudes were simultaneously collected, so that in the space of an hour 300 independent sets

of complex signals were obtained. This data set was used for the majority of the tests described in the sections that follow.

The second form of data used was simulated from a computer model. This was written in the same form as the real data, *i.e.* 256 pairs of 8-bit unsigned integers, but in this case there were 360 independent sets. This data was generated by Mr Drazen Lesicar using the radar scatter model (described later in Section 3.5.4 on page 90) of the Atmospheric Group [*Lesicar*, 1993]. Simulated data has the advantage that the "real" values of the FCA output parameters are the inputs to the model, hence are known. For this data set the "true" velocity was varied while the diffraction pattern size was held constant.

3.4 The Tests

Four forms of comparisons were undertaken.

1. Various interpolation routines were used in the FCA3 algorithm. With each change, the processed winds were rederived from the same 1 hour time-series of "real" complex receiver output discussed in Section 3.3. Of the possible 300 data points (for 100% data acceptance) only ~ 170 were accepted, although these were not always the same 170 for each version of the algorithm. Of the 44 different variations of the FCA3 algorithm, the 5 with the most significant interpolation changes are compared to the last (and most satisfactory) one. Comparisons could only be made using data which had been accepted by both the algorithms in question, and this significantly reduced the number of comparison points for the earlier trials. Finally, two variations using the same simulated data (described in Section 3.3), but a minor change in the number of points used in the interpolations, are compared.

2. Three particular solutions to equation 2.14 can be found when there are three receivers. Two different particular solutions are used in different versions of the FCA2 algorithm. The results from these are compared with the latest version (as at May 1990) of FCA2. Also, a modification of the standard FCA that reduces the number of interpolations required — hence improving the speed and reliability — is tested. Two versions of the FCA2 algorithm using the modified analysis are compared to the latest version. The data used were the same 1 hour time-series of "real" complex receiver output discussed in Section 3.3 and used for the FCA3 interpolation tests

3. The best versions of all three algorithms (FCA1, FCA2, FCA3) are compared in a number of different tests, all using the 1 hour time-series of "real" complex receiver output as before.

4. Since there is no independent validation of the *real* wind parameters when real data is used, the FCA3 algorithm was run on a simulated data set described in Section 3.3. The results were compared to the model input parameters.

Details of the definitions and interpretations of the actual, percentage and vector differences used in this chapter can be found in Appendix A.

3.5 Results and Inferences

The results for each set of tests are presented in Appendix B as a selection of scatter and distribution plots to aid in visualising the spread, and summarised in this chapter in table form for ease of critical comparison. Some of the figures referenced in this section appear in Appendix B.

The results are divided into subsections equating to each form of comparison mentioned in Section 3.4. The interpretation of the results and inferences that can be drawn are discussed within each subsection. Emphasis will be placed on the major parameters of the FCA, namely the magnitude and direction of the "true" velocity, and the size and orientation of the ellipse defining the scatterers diffraction pattern on the ground. On almost all occasions for these parameters (with the exception of the velocity direction) the total regression linear fits produce χ^2 values which are significant at the 99% level. That is, there is a high degree of confidence that a linear fit is valid. Thus the parameters from the various algorithms have a 1:1 correspondence in a statistical sense. The χ^2 values for the velocity direction are more than 4 standard deviations above the expected mean, implying that a linear fit is not valid for these data. Thus the trends and rms errors derived from the regressions for the wind directions should be ignored. The final results are summarised and discussed as a whole in the next section.

Note that although the standard deviation is tabulated for each distribution, it is the mean and percentile values which best describe the spread of the differences. The standard deviation in these comparisons is only of value when the distribution is approximately symmetrical around a near zero mean difference, which is not generally the case. The quoted percentile values have been calculated from the absolute values of the differences (described in Appendix A).

Test	$\rho(0,0,0)$	$\rho(\xi,\eta,0)$	$\tau_{\frac{1}{2}}, \tau_{ij}$	τ_{ij}^M
t16	CSCON	none	3 pt linear least-square	analytic 3 pt quadratic
t22	CSCON	4 pt CSCON	4 pt CSCON	analytic 3 pt quadratic
t23	CSCON	4 pt CSAKM	4 pt CSAKM	analytic 3 pt quadratic
t26	CSCON	4 pt CSAKM	4 pt CSAKM	analytic 3 pt quadratic
t42	CSCON	4 pt CSAKM	4 pt CSAKM	analytic 3 pt quadratic
t44	CSCON	4 pt CSAKM	4 pt CSAKM	analytic 3 pt quadratic
t3	CSCON	4 pt CSAKM	9 pt CSAKM	analytic 3 pt quadratic
t4	CSCON	4 pt CSAKM	6 pt CSAKM	analytic 3 pt quadratic

Table 3.1: Summary of the differences in the test runs for the FCA3 algorithm. See text for more details

3.5.1 The Dependence of the FCA on the Interpolations

Of the 44 variations of the FCA3 algorithm tested up to May, 1990, the 5 most distinctly different, termed test versions t16, t22, t23, t26 and t42 were compared to the latest version, t44. Versions prior to t14 suffered from errors in the coding. These versions did show that it was sufficient to use a quadratic fit to the cross-correlations to determine the τ_{ij}^M (the lags of the maxima). An analytical function is required to be fit in this case as the position of the maxima is required, rather than its value.

Test algorithms t16 to t23 used different interpolations for the $\rho(\xi,\eta,0)$, the $\tau_{\frac{1}{2}}$, and the τ_{ij} (see Figure 2.8). From t26 to t44 only the oscillatory rejection algorithm was modified. This only changed the amount of data kept, but did not alter the data values. The differences are summarised in Table 3.1 where CSCON and CSAKM are the "convex/concavity preserving" and the Akima IMSL cubic spline routines respectively. Both routines are non-linear piecewise cubic interpolants, and are described in the IMSL manual [*IMSL Inc*, 1987]. CSCON is based on the method described by *Micchelli et al.* [1985] and *Irvine et al.* [1986] to preserve the convexity and the concavity of the original data, while CSAKM is based on the method of *Akima* [1970] which was developed to prevent the "wiggles" that so often occur in the interpolants. Where no interpolant was used, the word "none" is placed in the table. All algorithms used a least-squares estimator for the over-determined parameters. Test runs t3 and t4 used the same version algorithm as t44 but with minor changes in the number of points used for the interpolation of the τ_{ij}. Simulated data was also used for these runs.

Figures B.1, B.2, and B.3 show the scatter plots for the comparisons, t16-t44, t22-t44, and t42-t44 respectively. Comparisons of t26, t43 and t44 showed that the common data for these runs were the same, only differing in the amount of accepted data. The value-range distributions

	|Vt|	/Vt	N-S	E-W	|Va|	/Va	Vc/Vt	tau1/2	T1/2	A	A/B	/A
Regression Parameters												
Y/X Regression												
Trend	0.712	0.605	0.399	0.751	0.686	0.652	0.344	0.737	0.278	0.328	0.251	0.254
(error)	0.005	0.003	0.007	0.004	0.005	0.003	0.150	0.125	0.084	0.002	0.331	0.003
Bias	17.8	105.9	-2.0	-17.4	21.0	94.2	0.2	0.4	3.1	166.8	1.2	64.4
(error)	0.3	0.6	0.1	0.2	0.4	0.6	0.3	0.3	0.4	0.5	0.5	0.3
RMS error	17.1	13.8	11.9	16.5	11.4	17.5	0.3	0.6	1.6	55.3	0.5	30.1
Chi-sq	20.9	8.1	37.6	14.5	16.5	10.4	29.0	19.3	40.4	44.9	50.8	47.2
% Signif.	100.0	100.0	93.3	100.0	100.0	100.0	99.6	100.0	58.6	74.7	52.0	66.5
X/Y Regression												
Trend	0.849	1.400	0.727	0.968	1.004	1.232	1.316	0.863	0.297	0.466	0.164	0.435
(error)	0.005	0.004	0.010	0.004	0.007	0.003	0.294	0.135	0.087	0.002	0.268	0.004
Bias	5.4	-110.7	-0.1	4.9	1.3	-67.2	0.6	0.5	2.8	141.3	1.2	46.3
(error)	0.3	1.0	0.1	0.3	0.5	0.9	0.2	0.3	0.4	0.6	0.5	0.4
RMS error	18.6	20.9	16.1	18.8	13.8	24.0	0.7	0.7	1.7	65.9	0.4	39.4
Chi-sq	20.9	8.1	37.6	14.5	16.5	10.4	29.0	19.3	40.4	44.9	50.8	47.2
% Signif.	100.0	100.0	93.3	100.0	100.0	100.0	99.6	100.0	58.6	74.7	52.0	66.5
Total Regression												
Trend	0.889	0.619	0.583	0.858	0.788	0.683	0.392	0.905	0.806	0.473	5.439	0.309
(error)	0.005	0.003	0.009	0.004	0.006	0.003	0.163	0.141	0.183	0.003	2.497	0.005
Bias	8.7	102.5	-1.7	-12.8	13.7	86.6	0.1	0.1	1.0	130.9	-6.5	61.4
(error)	0.3	0.7	0.1	0.2	0.5	0.7	0.3	0.4	0.8	0.8	3.7	0.4
RMS error	13.3	11.7	10.7	12.9	9.2	14.5	0.3	0.5	1.5	50.9	0.4	28.9
Chi-sq	11.7	3.9	22.6	7.8	8.8	5.2	13.1	10.7	31.4	31.9	39.8	33.2
% Signif.	100.0	100.0	100.0	100.0	100.0	100.0	100.0	100.0	90.6	98.7	89.2	98.0
Data Distribution Statistics												
Raw Value Differences												
Mean	-2.89	-8.93	0.73	6.55	1.54	-7.85	0.82	0.16	-0.16	6.89	-0.14	-2.07
sd	19.3	25.5	16.7	19.0	13.9	25.9	0.7	0.7	2.1	73.9	0.6	43.7
90%ile	24.0	50.0	26.2	24.4	19.0	46.0	1.8	1.0	3.9	100.0	0.9	62.0
% Mean	-3.67	-3.31	50.63	4.88	0.31	-2.63	37.28	3.23	-2.05	1.03	-4.05	-4.86
% sd	14.7	10.7	921.3	93.7	8.8	7.9	39.3	11.2	20.7	13.4	14.8	30.2
% 90%ile	24.4	12.2	287.3	79.3	11.1	10.6	102.2	18.2	37.2	23.1	24.3	44.7
Value Range Normalised Differences												
Mean	-5.83	-32.00	2.26	7.75	3.50	-18.00	0.78	0.05	0.00	22.00	-0.09	-3.50
sd	16.0	8.5	12.8	15.4	10.0	21.0	0.5	0.5	1.7	61.5	0.4	43.0
90%ile	24.0	50.0	17.0	21.3	16.0	36.0	1.1	0.7	3.2	94.0	1.0	46.0
% Mean	-4.57	-6.74	24.49	-4.92	2.22	-5.36	38.08	1.46	-0.11	5.64	-3.24	-1.43
% sd	14.9	2.3	62.6	28.5	6.7	4.3	25.1	10.2	20.3	10.8	10.4	17.6
% 90%ile	24.4	15.5	78.0	33.9	10.1	13.1	61.8	15.0	31.4	16.6	25.0	26.4
Vector Differences												
10%ile	1.8	1.0										
67%ile	15.4	9.0										
90%ile	25.8	23.4										
Rho	0.87	0.95	0.73	0.92	0.90	0.94	0.81	0.89	0.53	0.62	0.45	0.57
num. pts	54	54	54	54	54	54	54	54	45	54	54	54

Table 3.2: Statistics for FCA3 test 16 vs 44. Vt denotes the "true" velocity and Va the "apparent". A and B are the major and minor axes of the diffraction ellipse, with the last column denoting the direction of the major axis.

	|Vt|	/Vt	N-S	E-W	|Va|	/Va	Vc/Vt	tau1/2	T1/2	A	A/B	/A
Regression Parameters												
Y/X Regression												
Trend	0.750	1.167	0.625	0.871	0.775	1.111	0.257	0.777	0.302	0.414	0.356	0.176
(error)	0.004	0.003	0.005	0.003	0.004	0.003	0.128	0.105	0.052	0.001	0.239	0.002
Bias	11.2	-50.2	0.0	-2.2	15.9	-35.2	0.4	0.6	2.9	165.3	0.9	70.0
(error)	0.2	0.7	0.1	0.2	0.3	0.7	0.2	0.2	0.2	0.3	0.4	0.2
RMS error	17.3	20.1	13.8	18.9	19.0	22.3	0.4	0.8	1.6	89.2	0.4	43.3
Chi-sq	47.3	18.5	62.0	36.8	48.8	22.1	79.2	55.4	79.7	84.6	91.8	101.0
% Signif.	100.0	100.0	100.0	100.0	100.0	100.0	96.1	100.0	77.2	90.7	77.7	53.9
X/Y Regression												
Trend	0.728	0.705	0.646	0.742	0.685	0.709	0.925	0.601	0.410	0.451	0.329	0.166
(error)	0.004	0.002	0.005	0.003	0.004	0.002	0.243	0.093	0.061	0.001	0.230	0.002
Bias	17.0	81.8	0.9	-16.1	25.2	80.9	0.7	0.8	2.4	154.6	1.0	71.4
(error)	0.2	0.5	0.1	0.2	0.3	0.5	0.2	0.2	0.3	0.3	0.3	0.2
RMS error	17.1	15.6	14.1	17.4	17.9	17.8	0.7	0.7	1.9	93.2	0.4	42.2
Chi-sq	47.3	18.5	62.0	36.8	48.8	22.1	79.2	55.4	79.7	84.6	91.8	101.0
% Signif.	100.0	100.0	100.0	100.0	100.0	100.0	96.1	100.0	77.2	90.7	77.7	53.9
Total Regression												
Trend	1.023	1.342	0.974	1.110	1.095	1.313	0.311	1.219	0.621	0.876	1.207	-4.030
(error)	0.005	0.003	0.007	0.004	0.005	0.003	0.145	0.137	0.079	0.002	0.553	0.037
Bias	-4.0	-96.0	-0.5	9.8	-8.8	-88.7	0.3	-0.3	1.6	35.4	-0.3	450.6
(error)	0.3	0.8	0.1	0.2	0.4	0.8	0.2	0.3	0.3	0.5	0.8	3.3
RMS error	13.0	12.6	10.9	13.5	14.0	14.3	0.3	0.6	1.5	76.2	0.3	44.9
Chi-sq	27.2	9.4	37.9	20.3	28.2	11.4	38.6	32.5	57.2	59.0	68.3	111.2
% Signif.	100.0	100.0	100.0	100.0	100.0	100.0	100.0	100.0	99.7	100.0	99.7	27.3
Data Distribution Statistics												
Raw Value Differences												
Mean	2.70	6.62	0.55	-4.26	1.41	6.10	0.64	-0.14	-0.01	-0.03	0.02	0.50
sd	18.5	21.1	15.5	19.3	20.0	22.8	0.7	0.8	2.1	108.4	0.5	56.2
90%ile	26.0	36.0	21.2	26.8	26.0	39.0	1.7	1.3	2.7	185.0	0.7	95.0
% Mean	3.16	2.11	-2.42	-7.80	1.26	1.80	24.83	-2.23	-0.74	-0.15	0.74	0.76
% sd	15.0	8.1	170.3	96.7	11.7	6.4	38.2	14.3	19.4	16.3	13.3	34.8
% 90%ile	26.7	7.5	245.9	59.4	19.4	9.3	69.5	26.0	32.3	27.1	23.5	63.8
Value Range Normalised Differences												
Mean	4.53	10.80	3.55	-7.76	2.81	15.00	0.83	-0.03	-0.15	14.50	0.01	4.47
sd	12.1	17.1	16.0	14.1	15.5	18.5	0.5	0.8	1.9	58.3	0.4	49.3
90%ile	28.0	49.0	19.5	24.8	26.0	39.0	1.3	1.3	3.9	181.0	0.9	85.0
% Mean	3.65	3.17	4.54	2.23	3.26	3.18	27.73	-0.69	-1.14	1.77	0.53	3.11
% sd	14.0	2.9	45.5	21.0	13.7	3.4	25.2	14.4	17.7	11.7	13.1	32.5
% 90%ile	26.0	15.5	55.2	27.0	19.4	14.3	51.7	26.5	39.1	19.3	24.1	62.2
Vector Differences												
10%ile	1.7	1.0										
67%ile	13.7	7.0										
90%ile	27.7	16.1										
Rho	0.86	0.95	0.79	0.89	0.85	0.94	0.70	0.82	0.59	0.65	0.58	0.41
num. pts	105	105	105	105	105	105	105	105	92	105	105	105

Table 3.3: Statistics for FCA3 test 22 vs 44.

	|Vt|	/Vt	N-S	E-W	|Va|	/Va	Vc/Vt	tau1/2	T1/2	A	A/B	/A
Regression Parameters												
Y/X Regression												
Trend	0.706	1.256	0.762	0.843	0.712	1.155	0.544	0.763	0.258	0.334	0.321	0.388
(error)	0.004	0.003	0.006	0.004	0.004	0.003	0.129	0.111	0.053	0.001	0.242	0.003
Bias	11.8	-74.6	-0.4	-1.7	18.5	-48.5	0.8	0.7	3.0	187.0	0.9	55.3
(error)	0.2	0.8	0.1	0.2	0.3	0.7	0.2	0.3	0.2	0.3	0.4	0.2
RMS error	17.1	18.5	11.6	18.4	13.7	20.7	0.7	0.8	1.6	85.8	0.4	40.4
Chi-sq	46.3	14.8	42.3	35.5	34.8	18.2	67.4	54.7	76.0	82.7	84.8	83.7
% Signif.	100.0	100.0	100.0	100.0	100.0	100.0	98.6	100.0	69.5	81.1	76.5	79.0
X/Y Regression												
Trend	0.734	0.674	0.733	0.748	0.896	0.702	0.547	0.564	0.371	0.414	0.364	0.330
(error)	0.004	0.002	0.006	0.003	0.004	0.002	0.129	0.095	0.064	0.001	0.258	0.002
Bias	17.8	90.6	1.0	-17.3	11.3	84.2	0.6	0.8	2.6	168.8	0.9	53.8
(error)	0.2	0.6	0.1	0.2	0.3	0.6	0.2	0.2	0.3	0.3	0.4	0.2
RMS error	17.4	13.5	11.4	17.4	15.4	16.1	0.7	0.7	1.9	95.6	0.4	37.3
Chi-sq	46.3	14.8	42.3	35.5	34.8	18.2	67.4	54.7	76.0	82.7	84.8	83.7
% Signif.	100.0	100.0	100.0	100.0	100.0	100.0	98.6	100.0	69.5	81.1	76.5	79.0
Total Regression												
Trend	0.976	1.425	1.026	1.083	0.861	1.344	0.978	1.276	0.527	0.667	0.765	1.413
(error)	0.005	0.003	0.007	0.004	0.004	0.003	0.186	0.151	0.082	0.002	0.469	0.006
Bias	-3.0	-119.1	-0.8	10.5	7.0	-98.6	0.2	-0.4	1.9	93.2	0.3	-30.5
(error)	0.3	0.8	0.1	0.2	0.4	0.8	0.3	0.3	0.4	0.5	0.7	0.6
RMS error	13.1	11.1	8.7	13.4	10.8	13.1	0.5	0.6	1.5	76.9	0.3	33.2
Chi-sq	26.9	7.3	24.2	19.7	19.2	9.3	43.6	32.5	55.3	59.6	62.9	61.3
% Signif.	100.0	100.0	100.0	100.0	100.0	100.0	100.0	100.0	99.2	99.8	99.5	99.7
Data Distribution Statistics												
Raw Value Differences												
Mean	4.30	7.33	0.78	-6.25	3.65	7.55	-0.14	-0.20	0.03	3.32	0.05	-4.73
sd	18.7	20.6	12.4	19.1	15.7	21.6	0.8	0.8	2.2	110.4	0.5	47.5
90%ile	21.0	31.0	18.9	24.7	24.0	32.0	1.3	1.4	3.0	180.0	0.7	83.0
% Mean	4.57	2.33	-69.96	-2.10	2.13	2.11	-9.02	-3.38	-0.42	0.29	1.65	-1.97
% sd	15.0	8.3	460.6	95.4	10.0	6.3	39.4	14.1	19.5	16.6	13.0	31.6
% 90%ile	26.4	6.6	216.5	55.0	15.2	7.5	100.5	26.0	33.3	24.9	20.0	49.7
Value Range Normalised Differences												
Mean	4.93	21.50	1.39	-8.47	6.08	31.00	-0.22	-0.01	0.07	13.83	0.02	-4.17
sd	12.1	12.6	10.9	13.0	10.1	18.5	0.8	0.8	2.0	62.1	0.4	40.0
90%ile	21.0	50.0	17.3	23.3	19.0	36.0	1.1	1.2	3.9	123.0	0.7	66.0
% Mean	4.45	6.94	4.76	4.78	3.51	6.93	-4.60	-0.19	0.84	1.73	0.63	-3.48
% sd	10.4	2.7	33.7	13.6	8.0	3.3	28.4	13.2	17.9	11.6	12.5	27.7
% 90%ile	24.5	15.7	61.8	32.8	11.9	14.3	45.9	25.6	40.0	18.1	23.5	42.9
Vector Differences												
10%ile	1.9	1.0										
67%ile	14.3	7.2										
90%ile	27.0	15.3										
Rho	0.84	0.95	0.86	0.89	0.89	0.94	0.74	0.81	0.55	0.61	0.58	0.60
num. pts	97	97	97	97	97	97	97	97	85	97	97	97

Table 3.4: Statistics for FCA3 test 42 vs 44.

$\|V_t\|$ (ms^{-1})			$\angle V_t$ (°)			A (m)			A/B			$\angle$A (°)		
$\overline{x}$	s.d.	90%	$\overline{x}$	s.d.	90%	$\overline{x}$	s.d.	90%	$\overline{x}$	s.d.	90%	$\overline{x}$	s.d.	90%
-0.5	2.3	2.0	0.3	3.2	2.9	6.5	30	51	0.0	0.06	0.1	1.3	15	2.9

Table 3.5: Statistics for FCA3 test 4 vs 3.

for each comparison are shown in Figures B.4, B.5, and B.6. It is apparent from these that the estimated parameters are generally clustered around preferred values. This is due to a combination of the physical setup of the radar, the prevailing wind conditions, and the FCA rejection criteria. It is generally considered that prevailing wind conditions are the major source of these value-range distributions.

In order to construct a distribution of the differences combining data from all value ranges, the differences should be independent of the value range. If this were not the case then the statistics derived would not be truly indicative of the data. Figures B.7, B.8, and B.9 show the mean and spread of the actual differences as a function of the value range, while Figures B.10, B.11, and B.12 show the percentage differences. These plots can be used to decide whether an actual or a percentage error best describes the difference in the estimates by finding which is most independent of the value range. *i.e.* which is the most constant with the abscissa. Note that for a constant percentage difference the actual differences should be an increasing function of value range, while for a constant actual difference the percentage difference should be a decreasing function of value range. A good example of this behaviour is the V_c/V_t parameter, which generally has an increasing actual difference as a function of value range and a constant percentage difference. The other parameters are more difficult to interpret. Looking at the percentage differences (Figures B.10, B.11, and B.12) it can be seen that in general the "true" velocity parameters show a decrease with value range. Except for the zonal winds the actual differences are not constant. This indicates that the differences are not purely independent of the value ranges nor are they simply fractionally related. For the velocity estimates a vector difference will be applied and used to indicate the expected errors. The differences in the major axis and axial ratio of the diffraction ellipse are an increasing function of value range both in actual and percentage form. In this case a percentage error should be more representative than the actual. The error in the orientation of the ellipse on the otherhand appears to be better represented by the spread of the actual differences.

The statistics for the differences that can be expected by varying the FCA interpolation routines are tabulated in Tables 3.2–3.5. The main sections of interest in these tables (and those that follow) are the total regression trends, bias and rms errors, the vector differences and the value-range normalised percentage differences. It is these values that will be specifically referred to in the remainder of this section.

Consider the "true" velocity, V_T. The trends for the magnitude were consistently near unity, with rms deviations of the order of $13\,\mathrm{ms}^{-1}$. The vector differences indicate that variations in

the interpolation routines could cause the velocity estimates to differ by more than 25 % of the magnitude and $> 15°$ for 10 % of the time, and to be > 13 % of the magnitude and $> 7°$ for at least one-third of the time. Mean errors in the magnitude over the entire data set were more of the order of 4 % (or $5\,\mathrm{ms}^{-1}$).

The derived ground diffraction pattern showed considerable variation with interpolation routines. The trends ranged from near a 1:1 relation to near 2:1, with rms errors of ~ 70 m, and $30°$, and consequently poor correlation coefficients. The high degree of clustering of the major axis values (*c.f.* Figures B.1–B.3, and B.4–B.6) can account for the variable trends. The ellipse major axis and orientation estimates differed by > 16 % and $> 60°$ respectively for 10 % of the time. Mean errors in the magnitude of the major axis over the entire data set were of the order of 2 % (or 14 m).

From this series of comparisons it is evident that the correlation parameters are fairly sensitive to the exact values of the cross-correlation functions at zero lag, and the exact (fractional) lags where the auto-correlation function has the same value, and where it has fallen to a value of one-half. Hence they are sensitive to the exact form of interpolation used. This is most evident in the comparison t4-t3, where the algorithms only differ in the number of data points used to compute the interpolation. A discrepancy greater than $2\,\mathrm{ms}^{-1}$, and $3°$ was found 10 % of the time for the wind estimates. The ellipse parameters, major axis, axial ratio and orientation of the major axis, had discrepancies of 50 m, 0.1 and $3°$, respectively. This would be indicative of the minimum error that could be expected from choosing a particular size section of the correlation functions to interpolate with.

To put these errors in context, it must be remembered that the radio wavelength employed was 150 m, so the mean errors in the major axis are ~ 10 % of the wavelength, but the upper decile ranges up to ~ 50 %. The effective minimum antenna spacing was ~ 90 m, and the total time series was 102.4 seconds in length. Therefore the slowest ground pattern speed that could be detected, if the cross-correlation functions are calculated out to a maximum lag of half the length of the time series, would be $\sim 90/102.4/0.5 \equiv 1.8\,\mathrm{ms}^{-1}$. As it is more usual to only calculate the lags out to ~ 10 % of the time series length, the effective slowest detectable ground pattern speed increases to $\sim 8.8\,\mathrm{ms}^{-1}$. This corresponds to a wind speed of $\sim 4.4\,\mathrm{ms}^{-1}$ (from the "point-source-effect"). As the time samples are spaced at 0.4 seconds and the effective maximum antenna spacing was ~ 180 m, the fastest pattern speed detectable would be $\sim 180/0.4 \equiv 450\,\mathrm{ms}^{-1}$, corresponding to a wind speed of $225\,\mathrm{ms}^{-1}$. From the 67-percentile value of the wind magnitude, or the rms error in the total regression fit of the wind estimates (*c.f.* Tables 3.2,

3.3, 3.4, and 3.5) the maximum wind speed error due to the interpolations is approximately twice the minimum detectable velocity while the minimum error was only one quarter.

3.5.2 Effects of Changes in Particular Solutions and Fooks' Recommendations

Five versions, r1, r2, r5, r6 and r9, of the FCA2 algorithm are compared. Runs r1 and r2 use the standard analysis with different choices of a particular solution to equation 2.14. Runs r5, r6 and r9 use an alternative scheme, recommended by *Fooks* [1965], to reduce the number of interpolations required. These runs also differ in their choice of particular solutions to equation 2.14 and some rejection criteria, notably the detection of oscillatory correlation functions.

Similarly to the FCA3 comparisons, Figures B.13–B.16 show the scatter plots for the comparisons, r1-r9, r2-r9, r5-r9, and r6-r9 respectively. Again, the value-range distributions for each comparison are shown in Figures B.17–B.20 while Figures B.21–B.24 show the mean and spread of the actual differences as a function of the value range, and Figures B.25–B.28 show the percentage differences.

From the scatter plots it is obvious that some erroneous $T_{\frac{1}{2}}$ data points have not been removed causing severely skewed distributions. Thus the values derived for the $T_{\frac{1}{2}}$ parameter should be ignored. Tables 3.6–3.9 summarize the statistics for the differences that can be expected by varying particular solutions and reducing the number of interpolations. These show that the correlation coefficients and rms error estimates for the FCA2 comparisons are similar to those found in the FCA3 comparisons.

Comparing the behaviour of the actual and percentage differences (*c.f.* Figures B.21–B.24 and Figures B.25–B.28) it can be seen that the best indicators for the errors in this case are not the same as for the FCA3 comparisons. While the V_c/V_t parameter still shows a constant percentage error, both the wind magnitudes and the ellipse major axis appear to have more of a constant *actual* error. Nevertheless, the velocity differences still need to be expressed as percentage vector differences.

The trends for the magnitude of the "true" velocity were again close to unity, with rms deviations of the order of $13\,\mathrm{ms}^{-1}$ (the same as for FCA3). The vector differences indicate that variations in the particular solutions and number of interpolations could cause the velocity estimates to differ by more than 40 % of the magnitude and $> 30°$ for 10 % of the time, and to be > 20 % of the magnitude and $> 9°$ for at least one-third of the time. Mean errors in the

magnitude over the entire data set were more of the order of 0.5 % (or 1 ms^{-1}).

The derived ground diffraction pattern ellipse for the FCA2 comparisons also showed a large deviation from the expected 1:1 relation, being more 3:1 for all trials. Again, the high degree of clustering of the major axis values is the cause of this. The ellipse major axis and orientation estimates differed by > 120 m (22 %) and $> 70°$ respectively for 10% of the time. Mean errors in the magnitude of the major axis over the entire data set were of the order of 7 % (or ~ 40 m).

From these comparisons it can be seen that the original formulation of the FCA by *Briggs* [1984] and the modification suggested by *Fooks* [1965] give similar variations in the FCA parameters. This does not vary significantly by different choices of particular solutions for the τ_{ij}. Individual errors can be quite large but appear to be of a random nature. Thus the mean differences in each parameter are quite small.

3.5.3 Real Data and the Three Algorithms

Now to compare the three different algorithms. The best[1] versions of FCA1 , FCA2 and FCA3 are compared with the other two. The version of FCA2 used was the same as denoted by "r9" in the previous section . The version of FCA3 used was denoted as "t44" in Section 3.5.1

As in the previous comparisons, Figures B.29–B.31 show the scatter plots for the FCA1-FCA2, FCA1-FCA3, and FCA2-FCA3 comparisons respectively. The value-range distributions, and the mean and spread of the actual and percentage differences for each comparison are shown in Figures B.32–B.40.

Like the FCA2 comparisons, the $T_{\frac{1}{2}}$ scatter plots involving the FCA1 algorithm have an obvious erroneous data point causing an extended tail for those distributions, and a poor regression fit. Thus the values derived for the $T_{\frac{1}{2}}$ parameter should again be ignored. It is also apparent that there is a smaller degree of scatter than in the previous comparisons. This is confirmed by the high correlation coefficients shown in Tables 3.10–3.12. The rms error estimates for the regression fits are also only half those of the FCA3 and FCA2 comparisons. These tables summarize the statistics for the differences that can be expected by using different implementations of the FCA. The better correlations between these three algorithms as compared to the previous comparisons can be attributed to the fact that in this case final versions of the algorithms are compared rather than developmental versions.

Comparing the behaviour of the actual and percentage differences it can be seen that the best indicators for the errors in this case are the same as for the FCA3 comparisons.

[1] Best in the sense that they gave the highest data acceptance rates

	|Vt|	/Vt	N-S	E-W	|Va|	/Va	Vc/Vt	tau1/2	T1/2	A	A/B	/A
Regression Parameters												
Y/X Regression												
Trend	0.524	0.397	0.296	0.580	0.643	0.320	0.043	0.493	3.310	0.503	-0.129	0.126
(error)	0.004	0.002	0.007	0.003	0.004	0.002	0.114	0.093	0.070	0.002	0.318	0.002
Bias	23.7	157.2	0.5	-20.3	31.9	178.9	0.0	1.2	-5.2	159.3	1.6	77.0
(error)	0.2	0.5	0.1	0.2	0.3	0.4	0.2	0.2	0.3	0.4	0.4	0.2
RMS error	15.9	36.5	12.1	17.9	21.4	38.6	0.2	0.9	18.1	90.7	0.4	39.3
Chi-sq	61.4	74.9	86.9	52.8	63.5	80.1	93.4	72.9	92.7	87.2	97.7	97.1
% Signif.	99.9	96.0	78.2	100.0	99.7	90.6	61.4	97.3	63.4	77.4	49.0	50.7
X/Y Regression												
Trend	0.725	0.613	0.413	0.804	0.558	0.596	1.335	0.535	0.019	0.236	-0.102	0.153
(error)	0.005	0.002	0.008	0.004	0.004	0.002	0.637	0.097	0.005	0.001	0.282	0.003
Bias	13.5	96.6	1.6	-7.2	27.7	98.1	1.4	1.0	3.8	189.3	1.5	72.7
(error)	0.3	0.6	0.1	0.2	0.3	0.6	0.1	0.2	0.1	0.3	0.4	0.2
RMS error	18.7	45.3	14.3	21.1	20.0	52.7	0.9	0.9	1.4	62.2	0.3	43.3
Chi-sq	61.4	74.9	86.9	52.8	63.5	80.1	93.4	72.9	92.7	87.2	97.7	97.1
% Signif.	99.9	96.0	78.2	100.0	99.7	90.6	61.4	97.3	63.4	77.4	49.0	50.7
Total Regression												
Trend	0.737	0.463	0.630	0.767	1.132	0.270	0.044	0.903	51.371	3.451	-1.735	-0.178
(error)	0.005	0.003	0.010	0.004	0.006	0.002	0.116	0.136	0.276	0.005	0.885	0.005
Bias	13.4	141.5	-0.2	-12.3	-2.8	193.5	0.0	0.3	-193.5	-605.8	3.8	107.4
(error)	0.3	0.7	0.1	0.2	0.4	0.6	0.2	0.3	1.1	1.2	1.2	0.5
RMS error	13.4	33.2	11.1	14.9	16.3	37.4	0.2	0.7	1.4	60.0	0.3	41.0
Chi-sq	37.2	50.1	62.0	30.8	39.5	55.1	16.7	48.1	7.1	55.6	84.1	96.2
% Signif.	100.0	100.0	99.8	100.0	100.0	100.0	100.0	100.0	100.0	100.0	84.1	53.3
Data Distribution Statistics												
Raw Value Differences												
Mean	-0.14	-3.57	0.94	1.79	-6.55	-6.77	1.49	-0.10	-3.83	-31.24	-0.04	-1.70
sd	19.6	48.3	16.3	21.8	23.3	55.7	0.9	1.0	18.5	97.0	0.5	55.1
90%ile	31.0	62.0	27.7	31.3	40.0	85.0	2.7	1.7	2.8	177.0	0.6	88.0
% Mean	-2.65	-1.60	-198.02	-17.19	-4.33	-2.55	87.55	-2.72	-3.64	-4.62	-1.41	-1.47
% sd	21.4	15.6	2050.3	76.7	16.0	16.9	14.7	18.2	27.1	16.0	14.3	38.2
% 90%ile	34.5	13.1	351.2	60.4	26.4	17.8	98.8	29.8	38.1	27.7	21.4	71.4
Value Range Normalised Differences												
Mean	1.10	-3.04	2.16	10.44	-3.50	-4.56	2.31	-0.20	-2.40	-51.85	-0.01	3.84
sd	19.2	43.0	16.4	18.3	18.0	24.8	0.3	1.0	2.9	62.5	0.3	43.5
90%ile	31.0	83.0	30.7	29.2	35.0	102.0	2.8	1.6	5.4	133.0	0.9	77.0
% Mean	0.93	-0.67	4.97	2.51	-3.60	-0.73	86.71	-5.00	-15.71	-8.29	-0.40	1.90
% sd	19.7	11.2	55.6	39.2	19.9	4.7	14.9	20.0	19.8	15.3	9.9	20.9
% 90%ile	31.6	14.4	111.6	56.5	26.2	51.1	98.7	25.6	35.5	22.7	29.0	56.5
Vector Differences												
10%ile	3.4	1.5										
67%ile	22.4	9.5										
90%ile	39.9	28.2										
Rho	0.78	0.70	0.59	0.82	0.77	0.66	0.49	0.71	0.50	0.58	0.34	0.37
num. pts	100	100	100	100	100	100	100	100	100	100	100	100

Table 3.6: Statistics for FCA2 test 1 vs 9.

	|Vt|	/Vt	N-S	E-W	|Va|	/Va	Vc/Vt	tau1/2	T1/2	A	A/B	/A
Regression Parameters												
Y/X Regression												
Trend	0.645	0.375	0.294	0.652	0.643	0.320	0.083	0.493	1.003	0.503	-0.129	0.126
(error)	0.004	0.002	0.007	0.003	0.004	0.002	0.114	0.093	0.070	0.002	0.318	0.002
Bias	18.6	162.5	0.0	-18.0	31.9	178.9	0.0	1.2	1.0	159.3	1.6	77.0
(error)	0.2	0.5	0.1	0.2	0.3	0.4	0.2	0.2	0.3	0.4	0.4	0.2
RMS error	14.9	35.8	12.8	17.0	21.4	38.6	0.2	0.9	9.5	90.7	0.4	39.3
Chi-sq	48.2	76.3	88.1	44.5	63.5	80.1	88.3	72.9	96.8	87.2	97.7	97.1
% Signif.	100.0	94.9	75.3	100.0	99.7	90.6	74.8	97.3	51.6	77.4	49.0	50.7
X/Y Regression												
Trend	0.796	0.611	0.374	0.845	0.558	0.596	1.301	0.535	0.022	0.236	-0.102	0.153
(error)	0.005	0.002	0.007	0.004	0.004	0.002	0.451	0.097	0.010	0.001	0.282	0.003
Bias	9.3	97.3	1.8	-4.6	27.7	98.1	1.4	1.0	3.8	189.3	1.5	72.7
(error)	0.3	0.6	0.1	0.2	0.3	0.6	0.1	0.2	0.1	0.3	0.4	0.2
RMS error	16.5	45.7	14.4	19.4	20.0	52.7	0.8	0.9	1.4	62.2	0.3	43.3
Chi-sq	48.2	76.3	88.1	44.5	63.5	80.1	88.3	72.9	96.8	87.2	97.7	97.1
% Signif.	100.0	94.9	75.3	100.0	99.7	90.6	74.8	97.3	51.6	77.4	49.0	50.7
Total Regression												
Trend	0.846	0.413	0.701	0.821	1.132	0.270	0.088	0.903	43.853	3.451	-1.735	-0.178
(error)	0.005	0.003	0.010	0.004	0.006	0.002	0.118	0.136	0.463	0.005	0.885	0.005
Bias	8.8	154.2	-0.9	-10.8	-2.8	193.5	0.0	0.3	-166.9	-605.8	3.8	107.4
(error)	0.3	0.7	0.1	0.2	0.4	0.6	0.2	0.3	1.8	1.2	1.2	0.5
RMS error	11.9	33.2	11.7	13.7	16.3	37.4	0.2	0.7	1.4	60.0	0.3	41.0
Chi-sq	27.9	51.3	64.8	25.3	39.5	55.1	22.1	48.1	14.4	55.6	84.1	96.2
% Signif.	100.0	100.0	99.6	100.0	100.0	100.0	100.0	100.0	100.0	100.0	84.1	53.3
Data Distribution Statistics												
Raw Value Differences												
Mean	-1.04	-3.25	1.44	2.67	-6.55	-6.77	1.47	-0.10	-1.01	-31.24	-0.04	-1.70
sd	17.2	48.6	16.8	19.9	23.3	55.7	0.8	1.0	9.5	97.0	0.5	55.1
90%ile	26.0	64.0	31.0	26.3	40.0	85.0	2.6	1.7	2.9	177.0	0.6	88.0
% Mean	-2.86	-1.58	33.87	-20.56	-4.33	-2.55	87.49	-2.72	-1.34	-4.62	-1.41	-1.47
% sd	19.0	15.6	641.6	121.3	16.0	16.9	16.9	18.2	23.7	16.0	14.3	38.2
% 90%ile	33.3	13.4	476.0	72.3	26.4	17.8	98.2	29.8	35.8	27.7	21.4	71.4
Value Range Normalised Differences												
Mean	1.18	-5.00	3.09	2.41	-3.50	-4.56	2.26	-0.20	-0.08	-51.85	-0.01	3.84
sd	18.4	24.6	12.8	17.7	18.0	24.8	0.3	1.0	2.1	62.5	0.3	43.5
90%ile	25.0	84.0	31.0	26.3	35.0	102.0	2.6	1.6	92.9	133.0	0.9	77.0
% Mean	0.64	-1.06	31.51	-1.32	-3.60	-0.73	87.44	-5.00	-0.46	-8.29	-0.40	1.90
% sd	18.6	6.2	72.5	39.9	19.9	4.7	15.8	20.0	22.1	15.3	9.9	20.9
% 90%ile	32.4	17.8	115.5	45.7	26.2	51.1	96.8	25.6	88.4	22.7	29.0	56.5
Vector Differences												
10%ile	3.1	1.0										
67%ile	19.7	9.3										
90%ile	39.1	30.8										
Rho	0.84	0.69	0.57	0.86	0.77	0.66	0.57	0.71	0.39	0.58	0.34	0.37
num. pts	100	100	100	100	100	100	100	100	100	100	100	100

Table 3.7: Statistics for FCA2 test 2 vs 9.

	|Vt|	/Vt	N-S	E-W	|Va|	/Va	Vc/Vt	tau1/2	T1/2	A	A/B	/A
Regression Parameters												
Y/X Regression												
Trend	0.657	0.379	0.299	0.680	0.653	0.326	0.090	0.445	0.435	0.439	-0.105	0.090
(error)	0.004	0.002	0.006	0.003	0.004	0.002	0.110	0.093	0.070	0.002	0.322	0.002
Bias	18.2	161.2	-0.2	-17.2	30.8	176.1	0.0	1.3	2.6	164.8	1.5	80.8
(error)	0.2	0.5	0.1	0.2	0.3	0.4	0.2	0.2	0.3	0.4	0.5	0.2
RMS error	15.0	36.9	11.7	17.0	20.8	40.6	0.2	0.8	4.5	84.7	0.3	38.6
Chi-sq	47.3	76.7	85.6	42.1	63.0	81.0	83.8	75.0	97.1	88.6	97.8	97.9
% Signif.	100.0	94.5	81.1	100.0	99.8	89.3	84.5	95.9	50.6	74.1	48.6	48.3
X/Y Regression												
Trend	0.795	0.594	0.455	0.846	0.557	0.557	1.702	0.545	0.043	0.240	-0.112	0.121
(error)	0.005	0.002	0.008	0.004	0.004	0.002	0.480	0.103	0.022	0.001	0.333	0.003
Bias	8.6	100.8	1.2	-3.6	27.3	107.9	1.4	1.0	3.7	190.0	1.5	75.5
(error)	0.3	0.6	0.1	0.2	0.3	0.6	0.1	0.3	0.1	0.3	0.5	0.2
RMS error	16.5	46.1	14.4	18.9	19.2	53.0	0.8	0.9	1.4	62.6	0.3	44.8
Chi-sq	47.3	76.7	85.6	42.1	63.0	81.0	83.8	75.0	97.1	88.6	97.8	97.9
% Signif.	100.0	94.5	81.1	100.0	99.8	89.3	84.5	95.9	50.6	74.1	48.6	48.3
Total Regression												
Trend	0.860	0.426	0.579	0.849	1.150	0.274	0.094	0.782	21.221	3.208	-0.858	-0.202
(error)	0.005	0.003	0.009	0.004	0.006	0.003	0.113	0.134	0.492	0.005	0.628	0.004
Bias	8.5	150.4	-0.6	-10.2	-4.0	191.1	0.0	0.5	-79.0	-550.8	2.6	110.0
(error)	0.3	0.7	0.1	0.2	0.4	0.6	0.2	0.3	1.9	1.3	0.9	0.4
RMS error	12.0	34.0	10.8	13.5	15.8	39.3	0.2	0.7	1.4	60.1	0.3	40.2
Chi-sq	27.3	52.2	59.1	23.8	39.1	58.1	19.1	49.8	30.6	60.3	88.1	91.4
% Signif.	100.0	100.0	99.9	100.0	100.0	100.0	100.0	100.0	100.0	99.9	75.4	66.7
Data Distribution Statistics												
Raw Value Differences												
Mean	-1.61	-3.73	1.12	3.48	-6.57	-6.49	1.50	-0.04	-0.36	-20.97	-0.02	-2.31
sd	17.2	49.4	16.0	19.4	22.5	56.9	0.9	1.0	4.6	92.9	0.5	56.6
90%ile	27.0	63.0	28.2	29.3	39.0	85.0	2.7	1.7	3.0	159.0	0.6	94.0
% Mean	-3.58	-1.66	-73.43	-11.74	-4.41	-2.43	87.48	-1.77	-0.41	-3.06	-0.68	-2.83
% sd	18.9	15.6	1356.7	136.9	15.8	17.2	16.1	18.1	23.1	15.8	13.9	38.7
% 90%ile	32.4	13.8	294.9	92.8	26.4	17.8	98.2	30.2	33.3	26.9	21.4	73.2
Value Range Normalised Differences												
Mean	-1.00	-6.77	2.49	4.11	-4.07	1.00	2.28	-0.16	0.03	-38.47	-0.01	5.50
sd	18.5	22.5	12.9	18.0	15.5	26.8	0.5	0.8	1.5	70.0	0.4	46.5
90%ile	25.0	83.0	27.6	23.6	35.0	124.0	2.6	1.3	4.9	122.0	0.7	78.0
% Mean	-0.47	-1.39	4.37	-1.22	-4.49	-0.36	86.83	-5.23	-1.45	-6.57	-0.22	1.77
% sd	17.6	4.5	53.9	21.7	19.9	4.5	15.6	19.6	20.2	14.3	13.6	21.8
% 90%ile	29.9	14.6	100.0	39.9	26.2	51.1	96.8	27.3	49.5	22.5	22.6	41.1
Vector Differences												
10%ile	3.1	1.0										
67%ile	19.9	10.0										
90%ile	37.4	30.1										
Rho	0.85	0.69	0.60	0.87	0.77	0.65	0.62	0.70	0.37	0.57	0.33	0.32
num. pts	100	100	100	100	100	100	100	100	100	100	100	100

Table 3.8: Statistics for FCA2 test 5 vs 9.

	|Vt|	/Vt	N-S	E-W	|Va|	/Va	Vc/Vt	tau1/2	T1/2	A	A/B	/A
Regression Parameters												
Y/X Regression												
Trend	0.657	0.379	0.299	0.680	0.653	0.326	0.416	0.445	0.435	0.439	-0.105	0.090
(error)	0.004	0.002	0.006	0.003	0.004	0.002	0.110	0.093	0.070	0.002	0.322	0.002
Bias	18.2	161.2	-0.2	-17.2	30.8	176.1	1.0	1.3	2.6	164.8	1.5	80.8
(error)	0.2	0.5	0.1	0.2	0.3	0.4	0.2	0.2	0.3	0.4	0.5	0.2
RMS error	15.0	36.9	11.7	17.0	20.8	40.6	0.7	0.8	4.5	84.7	0.3	38.6
Chi-sq	47.3	76.7	85.6	42.1	63.0	81.0	77.2	75.0	97.1	88.6	97.8	97.9
% Signif.	100.0	94.5	81.1	100.0	99.8	89.3	94.1	95.9	50.6	74.1	48.6	48.3
X/Y Regression												
Trend	0.795	0.594	0.455	0.846	0.557	0.557	0.531	0.545	0.043	0.240	-0.112	0.121
(error)	0.005	0.002	0.008	0.004	0.004	0.002	0.125	0.103	0.022	0.001	0.333	0.003
Bias	8.6	100.8	1.2	-3.6	27.3	107.9	0.8	1.0	3.7	190.0	1.5	75.5
(error)	0.3	0.6	0.1	0.2	0.3	0.6	0.2	0.3	0.1	0.3	0.5	0.2
RMS error	16.5	46.1	14.4	18.9	19.2	53.0	0.8	0.9	1.4	62.6	0.3	44.8
Chi-sq	47.3	76.7	85.6	42.1	63.0	81.0	77.2	75.0	97.1	88.6	97.8	97.9
% Signif.	100.0	94.5	81.1	100.0	99.8	89.3	94.1	95.9	50.6	74.1	48.6	48.3
Total Regression												
Trend	0.860	0.426	0.579	0.849	1.150	0.274	0.741	0.782	21.221	3.208	-0.858	-0.202
(error)	0.005	0.003	0.009	0.004	0.006	0.003	0.159	0.134	0.492	0.005	0.628	0.004
Bias	8.5	150.4	-0.6	-10.2	-4.0	191.1	0.4	0.5	-79.0	-550.8	2.6	110.0
(error)	0.3	0.7	0.1	0.2	0.4	0.6	0.3	0.3	1.9	1.3	0.9	0.4
RMS error	12.0	34.0	10.8	13.5	15.8	39.3	0.6	0.7	1.4	60.1	0.3	40.2
Chi-sq	27.3	52.2	59.1	23.8	39.1	58.1	51.7	49.8	30.6	60.3	88.1	91.4
% Signif.	100.0	100.0	99.9	100.0	100.0	100.0	100.0	100.0	100.0	99.9	75.4	66.7
Data Distribution Statistics												
Raw Value Differences												
Mean	-1.61	-3.73	1.12	3.48	-6.57	-6.49	-0.01	-0.04	-0.36	-20.97	-0.02	-2.31
sd	17.2	49.4	16.0	19.4	22.5	56.9	0.9	1.0	4.6	92.9	0.5	56.6
90%ile	27.0	63.0	28.2	29.3	39.0	85.0	1.3	1.7	3.0	159.0	0.6	94.0
% Mean	-3.58	-1.66	-73.43	-11.74	-4.41	-2.43	-1.01	-1.77	-0.41	-3.06	-0.68	-2.83
% sd	18.9	15.6	1356.7	136.9	15.8	17.2	26.3	18.1	23.1	15.8	13.9	38.7
% 90%ile	32.4	13.8	294.9	92.8	26.4	17.8	38.7	30.2	33.3	26.9	21.4	73.2
Value Range Normalised Differences												
Mean	-1.00	-6.77	2.49	4.11	-4.07	1.00	-0.05	-0.16	0.03	-38.47	-0.01	5.50
sd	18.5	22.5	12.9	18.0	15.5	26.8	1.1	0.8	1.5	70.0	0.4	46.5
90%ile	25.0	83.0	27.6	23.6	35.0	124.0	1.3	1.3	4.9	122.0	0.7	78.0
% Mean	-0.47	-1.39	4.37	-1.22	-4.49	-0.36	-0.85	-5.23	-1.45	-6.57	-0.22	1.77
% sd	17.6	4.5	53.9	21.7	19.9	4.5	26.0	19.6	20.2	14.3	13.6	21.8
% 90%ile	29.9	14.6	100.0	39.9	26.2	51.1	37.4	27.3	49.5	22.5	22.6	41.1
Vector Differences												
10%ile	3.1	1.0										
67%ile	19.9	10.0										
90%ile	37.4	30.1										
Rho	0.85	0.69	0.60	0.87	0.77	0.65	0.68	0.70	0.37	0.57	0.33	0.32
num. pts	100	100	100	100	100	100	100	100	100	100	100	100

Table 3.9: Statistics for FCA2 test 6 vs 9.

The trends for the magnitude of the "true" velocity (and most other parameters) were very close to unity, with rms deviations of the order of $5\,\mathrm{ms}^{-1}$. The vector differences indicate that variations in the implementation of the FCA could cause the velocity estimates to differ by more than 20 % of the magnitude and $> 7°$ for 10 % of the time, but are less than 9 % of the magnitude and 3° for at least two-thirds of the time. Mean errors in the magnitude over the entire data set were as large as 5 % (or $3\,\mathrm{ms}^{-1}$). The FCA2 algorithm gave the largest differences, with the FCA1-FCA3 comparison giving errors in the wind velocity less than 8 % of the magnitude and 4° for 90 % of the time. The rms error in the regression fit for the FCA1-FCA3 comparison were also only half that of the FCA1-FCA2 and FCA2-FCA3 comparisons.

Unlike the FCA3 and FCA2 comparisons, the derived ground diffraction pattern ellipse for the current comparisons show the expected 1:1 relation, even though there is still a high degree of clustering of the major axis values. The 1:1 relation stems from the few outlier points in the major axis value-range distribution. In the previous comparisons these outliers were well scattered causing the poor regression fits. The ellipse major axis and orientation estimates differed up to 16 % (150 m) and 20° respectively for 90% of the time. This is reduced to < 4 % (40 m) and $< 10°$ for the FCA1-FCA3 comparisons. Mean errors in the magnitude of the major axis over the entire data set were as large as 9 % (or ~ 50 m) and down to ~ 1 % (or ~ 9 m).

The major difference between the FCA2 and the other algorithms is that the former solves a particular solution for the τ_{ij} (equation 2.14) while both the FCA1 and FCA3 algorithms use some form of optimisation for these over-determined parameters. This may be the reason FCA1 and FCA3 compare better than any combination involving the FCA2. Even so, the discrepancies in the estimation of the FCA parameters are still larger than one would like — at least of the order of 10% in the wind velocity.

3.5.4 Simulated Data and the FCA3 Algorithm

Simulated spaced-antennae receiver data was produced by Mr Drazen Lesicar using a radar scatter model. This model will be briefly described here, a more thorough description can be found in Chapter 2 of *Lesicar* [1993].

The radar scatter model used to produce the simulated data for the following comparisons consisted of a sampling area (where the radar is considered to be situated) of limited "horizontal" extent, at what can be thought of as ground level. Above this, at a scaled distance equivalent to 90 km, an extensive horizontal layer of point scatterers was positioned. The point scatterers were first placed uniformly over a 2-dimensional grid then their positions were randomly perturbed in

	|Vt|	/Vt	N-S	E-W	|Va|	/Va	Vc/Vt	tau1/2	T1/2	A	A/B	/A
Regression Parameters												
Y/X Regression												
Trend	0.796	0.950	0.751	0.822	0.890	0.902	1.489	0.874	0.064	0.595	0.566	0.660
(error)	0.003	0.002	0.005	0.003	0.004	0.002	0.197	0.073	0.018	0.001	0.277	0.002
Bias	6.2	13.9	0.3	-4.7	7.3	22.9	0.6	0.2	3.6	90.6	0.6	29.1
(error)	0.2	0.4	0.1	0.1	0.3	0.4	0.2	0.2	0.1	0.2	0.4	0.2
RMS error	9.4	11.2	8.0	9.6	8.5	31.3	0.5	0.1	1.5	33.8	0.2	31.7
Chi-sq	24.4	6.0	38.9	16.1	18.6	39.2	52.4	2.1	130.5	26.6	84.0	76.0
% Signif.	100.0	100.0	100.0	100.0	100.0	100.0	100.0	100.0	59.3	100.0	100.0	100.0
X/Y Regression												
Trend	1.031	1.005	0.950	1.072	0.969	0.789	0.413	1.127	0.628	1.352	0.676	0.668
(error)	0.004	0.002	0.006	0.003	0.004	0.001	0.104	0.083	0.056	0.001	0.303	0.002
Bias	2.7	-2.9	-0.3	-0.1	2.2	54.4	0.0	-0.2	2.5	-68.0	0.5	28.8
(error)	0.2	0.4	0.1	0.2	0.3	0.4	0.2	0.2	0.2	0.3	0.4	0.2
RMS error	10.7	11.5	9.0	11.0	8.9	29.2	0.3	0.1	4.7	51.0	0.2	31.9
Chi-sq	24.4	6.0	38.9	16.1	18.6	39.2	52.4	2.1	130.5	26.6	84.0	76.0
% Signif.	100.0	100.0	100.0	100.0	100.0	100.0	100.0	100.0	59.3	100.0	100.0	100.0
Total Regression												
Trend	0.866	0.971	0.870	0.867	0.955	1.092	2.204	0.880	0.071	0.631	0.855	0.991
(error)	0.004	0.002	0.005	0.003	0.004	0.002	0.241	0.073	0.019	0.001	0.361	0.003
Bias	2.6	8.7	0.3	-2.8	2.9	-24.9	0.1	0.2	3.6	80.7	0.1	0.6
(error)	0.2	0.4	0.1	0.1	0.3	0.5	0.2	0.2	0.1	0.2	0.5	0.2
RMS error	7.2	8.1	6.2	7.3	6.3	22.2	0.2	0.1	1.5	28.8	0.2	24.6
Chi-sq	12.7	3.1	20.9	8.2	9.6	21.2	23.2	1.0	41.6	12.8	51.6	45.7
% Signif.	100.0	100.0	100.0	100.0	100.0	100.0	100.0	100.0	100.0	100.0	100.0	100.0
Data Distribution Statistics												
Raw Value Differences												
Mean	4.19	-1.53	-0.35	-3.03	0.11	1.72	-0.92	0.11	0.99	22.32	0.06	0.24
sd	10.7	11.5	9.0	11.2	9.0	31.8	0.6	0.2	4.7	57.9	0.3	35.0
90%ile	17.0	18.0	11.8	16.4	11.0	13.0	1.6	0.3	3.7	75.0	0.4	45.0
% Mean	4.14	-0.95	9.54	-3.18	-0.06	0.53	-41.59	1.71	5.78	2.60	1.91	-0.39
% sd	10.1	5.7	141.6	61.9	5.5	8.7	24.1	3.1	18.3	7.7	7.9	24.7
% 90%ile	17.3	5.0	100.0	22.6	8.3	2.8	72.8	5.0	32.4	12.4	12.5	35.0
Value Range Normalised Differences												
Mean	2.93	-1.33	-0.54	-0.96	0.00	0.82	-1.07	0.25	2.12	66.00	0.05	-0.96
sd	10.4	16.0	6.1	9.3	5.3	5.2	0.3	0.2	0.9	48.7	0.3	27.4
90%ile	17.0	24.0	10.8	14.5	15.0	7.0	1.7	0.4	7.1	146.0	0.4	23.0
% Mean	4.97	-0.30	4.47	2.60	0.09	0.24	-38.37	3.58	13.81	8.80	1.80	-1.25
% sd	9.5	4.4	19.8	9.5	5.0	1.3	13.0	2.0	12.4	5.8	8.0	20.5
% 90%ile	21.3	5.3	36.5	21.7	10.0	2.2	50.4	5.7	45.3	15.8	11.8	19.3
Vector Differences												
10%ile	1.3	0.5										
67%ile	8.5	4.0										
90%ile	18.2	8.8										
Rho	0.95	0.99	0.92	0.97	0.96	0.92	0.88	0.99	0.45	0.94	0.78	0.81
num. pts	137	137	137	137	137	137	137	137	137	137	137	137

Table 3.10: Statistics for FCA1 vs FCA2.

	|Vt|	/Vt	N-S	E-W	|Va|	/Va	Vc/Vt	tau1/2	T1/2	A	A/B	/A
Regression Parameters												
Y/X Regression												
Trend	0.920	0.910	0.934	0.948	0.975	0.877	1.683	0.926	0.156	0.933	0.888	0.849
(error)	0.004	0.002	0.005	0.003	0.004	0.002	0.206	0.078	0.018	0.001	0.267	0.002
Bias	3.3	20.9	0.2	-1.3	6.2	32.4	0.3	0.1	3.4	19.1	0.1	11.3
(error)	0.2	0.4	0.1	0.2	0.3	0.4	0.2	0.2	0.1	0.2	0.4	0.2
RMS error	4.8	30.8	7.2	4.4	5.1	32.2	0.3	0.1	1.5	21.1	0.1	27.9
Chi-sq	5.5	37.4	22.8	3.1	6.4	41.4	14.6	0.6	97.2	5.7	15.3	49.7
% Signif.	100.0	100.0	100.0	100.0	100.0	100.0	100.0	100.0	95.2	100.0	100.0	100.0
X/Y Regression												
Trend	1.041	0.781	0.882	1.030	0.975	0.774	0.527	1.075	1.342	1.025	0.993	0.724
(error)	0.004	0.002	0.005	0.003	0.004	0.002	0.115	0.085	0.052	0.001	0.282	0.002
Bias	-1.3	57.1	-0.1	0.3	-2.7	56.4	-0.1	-0.1	-0.6	-7.4	0.0	24.7
(error)	0.2	0.4	0.1	0.2	0.3	0.4	0.2	0.2	0.2	0.3	0.4	0.2
RMS error	5.1	28.6	7.0	4.6	5.1	30.3	0.1	0.1	4.5	22.1	0.1	25.8
Chi-sq	5.5	37.4	22.8	3.1	6.4	41.4	14.6	0.6	97.2	5.7	15.3	49.7
% Signif.	100.0	100.0	100.0	100.0	100.0	100.0	100.0	100.0	95.2	100.0	100.0	100.0
Total Regression												
Trend	0.938	1.106	1.033	0.959	1.000	1.087	1.844	0.928	0.171	0.953	0.942	1.116
(error)	0.004	0.002	0.006	0.003	0.004	0.002	0.216	0.079	0.019	0.001	0.276	0.002
Bias	2.4	-29.0	0.2	-0.8	4.5	-21.1	0.2	0.1	3.3	13.5	0.1	-11.6
(error)	0.2	0.5	0.1	0.2	0.3	0.5	0.2	0.2	0.1	0.2	0.4	0.2
RMS error	3.5	21.8	5.2	3.2	3.6	23.1	0.1	0.1	1.5	15.4	0.1	20.1
Chi-sq	2.8	20.2	11.9	1.5	3.2	22.7	6.4	0.3	32.3	2.9	7.9	27.7
% Signif.	100.0	100.0	100.0	100.0	100.0	100.0	100.0	100.0	100.0	100.0	100.0	100.0
Data Distribution Statistics												
Raw Value Differences												
Mean	0.69	1.95	-0.18	-0.98	-4.53	-1.12	-0.80	0.06	0.81	-0.59	0.02	1.55
sd	5.2	31.3	7.3	4.7	5.1	33.0	0.4	0.1	4.6	22.3	0.1	28.7
90%ile	8.0	8.0	8.4	7.9	10.0	15.0	1.3	0.2	1.8	28.0	0.1	23.0
% Mean	0.06	0.39	-42.14	1.76	-3.77	-0.02	-37.41	0.78	3.65	-0.35	0.75	2.87
% sd	5.2	9.1	321.9	18.2	4.3	9.0	23.4	1.4	15.1	3.4	3.9	18.8
% 90%ile	8.3	1.9	60.7	14.5	7.6	2.8	53.2	2.2	15.8	4.2	4.8	16.6
Value Range Normalised Differences												
Mean	1.33	-0.93	0.84	-0.45	-4.24	-0.33	-0.80	0.14	3.65	9.29	0.04	3.43
sd	4.3	6.0	4.4	4.9	4.6	7.1	0.2	0.1	0.6	14.0	0.1	19.6
90%ile	10.0	8.0	6.4	6.9	10.0	13.0	1.3	0.2	9.1	37.0	0.1	10.0
% Mean	1.15	-0.17	-0.80	0.49	-3.14	-0.06	-34.27	1.91	21.56	1.24	1.06	4.93
% sd	3.8	1.7	9.4	4.3	4.2	1.7	7.6	1.1	7.1	2.6	3.1	16.1
% 90%ile	8.1	2.2	17.7	8.2	6.8	2.4	42.3	3.0	44.8	4.2	3.4	12.5
Vector Differences												
10%ile	0.0	0.0										
67%ile	3.7	1.5										
90%ile	8.3	4.0										
Rho	0.99	0.92	0.95	0.99	0.98	0.90	0.97	1.00	0.67	0.99	0.97	0.88
num. pts	130	130	130	130	130	130	130	130	124	130	130	130

Table 3.11: Statistics for FCA1 vs FCA3.

	|Vt|	/Vt	N-S	E-W	|Va|	/Va	Vc/Vt	tau1/2	T1/2	A	A/B	/A
Regression Parameters												
Y/X Regression												
Trend	0.944	1.010	1.000	1.001	0.911	0.968	0.709	1.049	0.681	1.249	0.709	0.887
(error)	0.004	0.002	0.006	0.003	0.003	0.001	0.113	0.087	0.057	0.001	0.259	0.002
Bias	6.9	-2.3	0.7	-3.0	10.4	10.7	0.3	-0.1	1.5	-43.3	0.5	5.8
(error)	0.2	0.4	0.1	0.2	0.2	0.4	0.2	0.2	0.2	0.3	0.4	0.2
RMS error	13.2	10.3	9.7	13.1	9.1	10.0	0.6	0.1	1.7	43.3	0.3	25.6
Chi-sq	41.6	5.4	44.5	27.2	19.8	4.7	79.7	1.0	98.4	24.2	88.2	46.5
% Signif.	100.0	100.0	100.0	100.0	100.0	100.0	100.0	100.0	98.7	100.0	100.0	100.0
X/Y Regression												
Trend	0.751	0.953	0.689	0.809	0.946	0.999	0.624	0.947	0.382	0.665	0.540	0.761
(error)	0.003	0.002	0.005	0.003	0.003	0.002	0.106	0.083	0.043	0.001	0.226	0.002
Bias	8.7	11.7	-0.3	-5.6	-0.2	-2.5	0.7	0.1	2.3	72.0	0.6	24.9
(error)	0.2	0.4	0.1	0.2	0.3	0.4	0.2	0.2	0.2	0.2	0.3	0.2
RMS error	11.8	10.0	8.1	11.8	9.3	10.2	0.5	0.1	1.3	31.6	0.3	23.7
Chi-sq	41.6	5.4	44.5	27.2	19.8	4.7	79.7	1.0	98.4	24.2	88.2	46.5
% Signif.	100.0	100.0	100.0	100.0	100.0	100.0	100.0	100.0	98.7	100.0	100.0	100.0
Total Regression												
Trend	1.146	1.030	1.250	1.126	0.979	0.984	1.119	1.052	1.770	1.417	1.271	1.106
(error)	0.004	0.002	0.006	0.003	0.003	0.001	0.148	0.087	0.095	0.001	0.366	0.002
Bias	-2.8	-7.4	0.5	2.3	5.7	6.8	-0.4	-0.1	-2.7	-86.4	-0.3	-14.1
(error)	0.2	0.4	0.1	0.2	0.3	0.4	0.3	0.2	0.4	0.3	0.5	0.2
RMS error	9.2	7.2	6.5	9.0	6.6	7.2	0.4	0.1	1.2	26.0	0.2	18.2
Chi-sq	22.4	2.7	23.8	14.2	10.2	2.3	47.8	0.5	60.4	12.0	53.7	25.4
% Signif.	100.0	100.0	100.0	100.0	100.0	100.0	100.0	100.0	100.0	100.0	100.0	100.0
Data Distribution Statistics												
Raw Value Differences												
Mean	-4.19	-0.17	-0.69	3.08	-4.26	-2.73	0.16	-0.04	-0.24	-20.43	-0.06	4.41
sd	13.3	10.4	9.8	13.1	9.4	10.2	0.6	0.1	1.8	47.5	0.3	26.1
90%ile	20.0	14.0	10.8	20.2	16.0	18.0	1.1	0.2	2.1	68.0	0.5	33.0
% Mean	-4.45	0.37	38.83	-2.48	-3.46	-0.56	8.89	-0.73	-1.59	-2.71	-1.71	4.76
% sd	11.1	4.0	405.5	27.1	6.2	2.2	31.6	2.0	14.9	6.7	8.7	21.3
% 90%ile	18.6	3.7	100.0	27.3	12.8	4.1	42.2	3.7	25.6	10.7	15.2	27.0
Value Range Normalised Differences												
Mean	-3.46	-0.10	0.01	3.17	-3.69	1.83	0.22	-0.07	-0.60	-47.33	-0.10	2.95
sd	9.9	12.0	8.4	10.2	7.8	5.0	0.6	0.1	1.3	44.0	0.2	21.0
90%ile	20.0	17.0	10.8	19.2	15.0	13.0	1.0	0.2	2.4	84.0	0.5	31.0
% Mean	-3.62	-0.04	-8.78	-3.82	-2.53	0.34	5.94	-1.01	-5.66	-5.14	-3.08	3.66
% sd	8.6	3.0	19.5	12.9	7.1	1.6	18.0	1.9	12.8	4.5	8.3	22.9
% 90%ile	16.9	3.5	28.9	21.1	11.3	4.3	27.4	3.2	25.6	10.7	13.5	20.3
Vector Differences												
10%ile	1.5	0.5										
67%ile	9.5	3.0										
90%ile	18.9	7.0										
Rho	0.91	0.99	0.91	0.95	0.96	0.99	0.81	1.00	0.71	0.95	0.78	0.90
num. pts	144	144	144	144	144	144	144	144	134	144	144	144

Table 3.12: Statistics for FCA2 vs FCA3.

3-dimensions, leaving a quasi-uniform 2-dimensional distribution with a small finite "thickness". A uniform wind is then simulated by moving the grid, containing the point scatterers, across the field of view of the sampling area. From the geometry of the transmitter and receiving antennae, and a given point scatterer, the amplitude and phase of the reflected radio wave could be determined. This was found for each of the scatterers present. Aspect sensitivity of the scatterers and the radar two-way polar diagram was taken into account by applying an azimuthally symmetric but zenith dependent weighting function to the amplitude of the returned signals. The weighted signals were then vectorially summed for each receiving antenna. This "raw signal" was then processed using the FCA3 algorithm — the results of which should accurately match those input into the model.

This comparison therefore differs from the preceding ones in that *all* the error can be attributed to the FCA3 algorithm. The scatter plots and distributions are shown in Figures B.41–B.44. Some parameters have no values, in which case an empty box has been plotted in order to be consistent with the previous sets of comparisons. Note that no turbulence was introduced into the model winds for the comparisons presented here.

The wind direction, and major axis, axial ratio and orientation of the diffraction pattern ellipse were not varied in the model and had values of 90° , 484 m, 1.19 and 90° respectively. For these parameters the best measure of the error in the FCA3 values are from the distribution of the raw actual differences; change with value-range not being an issue. Percentage differences may be more representative for other value ranges though. Thus both will be quoted.

The wind magnitude was stepped from 30 to 200 ms^{-1} in 10 ms^{-1} increments with 20 points for each value; a total of 360 data points. The "apparent" velocity and life-time parameters were not recorded for these trials hence the zero values in Table 3.13. The distribution of the data values on the scatter plots also caused some poor regression fits as indicated by the significance levels. This mainly affected the Y on X regression as would be expected from the discussion in Section 2.10. The values of the normal 2-dimensional correlation coefficient used here are meaningless for these forms of scatter.

The trend from the total regression and, more accurately, visual inspection of Figure B.41 shows that FCA3 systematically underestimates the wind magnitude at larger velocities ($> 130\,ms^{-1}$), with rms errors of $\sim 4\,ms^{-1}$. For 90% of the time the vector differences are less than 6% of the magnitude and 1.5° . Considering the spread in wind direction on its own (without regard to the wind magnitude), the error is $\sim \pm 3°$ to one standard deviation. Comparing this to the vector difference indicates that the error in the direction determination must decrease as the

	|Vt|	/Vt	N-S	E-W	|Va|	/Va	Vc/Vt	tau1/2	T1/2	A	A/B	/A
Regression Parameters												
Y/X Regression												
Trend	0.852	#####	#####	0.853	0.000	0.000	0.929	0.000	0.000	#####	1.000	#####
(error)	0.001	#####	#####	0.001	0.000	0.000	0.009	0.000	0.000	91.163	0.065	#####
Bias	11.4	#####	-0.4	11.2	0.0	0.0	0.9	0.0	0.0	#####	0.0	#####
(error)	0.1	#####	0.1	0.1	0.0	0.0	0.1	0.0	0.0	#####	0.1	9217.5
RMS error	5.0	2.8	4.0	5.1	99.9	99.9	0.7	99.9	99.9	70.2	0.0	60.1
Chi-sq	4.6	323.2	320.2	4.6	999.9	999.9	5.0	999.9	999.9	323.7	0.0	324.9
% Signif.	100.0	47.1	51.8	100.0	0.0	0.0	100.0	0.0	0.0	46.2	100.0	44.4
X/Y Regression												
Trend	1.157	0.000	0.000	1.155	0.000	0.000	1.060	0.000	0.000	0.000	1.000	0.000
(error)	0.001	0.020	0.014	0.001	0.000	0.000	0.009	0.000	0.000	0.001	0.065	0.001
Bias	-11.6	90.0	0.0	-11.3	0.0	0.0	-0.8	0.0	0.0	484.0	0.0	91.0
(error)	0.2	1.8	0.1	0.2	0.0	0.0	0.1	0.0	0.0	0.4	0.1	0.1
RMS error	5.9	0.0	0.0	5.9	99.9	99.9	0.8	99.9	99.9	0.0	0.0	0.0
Chi-sq	4.6	0.0	320.2	4.6	999.9	999.9	5.0	999.9	999.9	0.0	0.0	0.0
% Signif.	100.0	100.0	51.8	100.0	0.0	0.0	100.0	0.0	0.0	100.0	100.0	100.0
Total Regression												
Trend	0.857	0.901	#####	0.858	0.000	0.000	0.935	0.000	0.000	1.072	1.000	9.365
(error)	0.001	0.350	#####	0.001	0.000	0.000	0.009	0.000	0.000	0.000	0.065	1.210
Bias	10.8	8.7	-147.9	10.6	0.0	0.0	0.8	0.0	0.0	-35.4	0.0	-761.4
(error)	0.1	31.5	1.7	0.1	0.0	0.0	0.1	0.0	0.0	0.0	0.1	110.1
RMS error	3.8	2.1	0.0	3.8	99.9	99.9	0.5	99.9	99.9	47.8	0.0	6.4
Chi-sq	2.3	0.0	0.0	2.3	999.9	999.9	2.5	999.9	999.9	0.0	0.0	0.0
% Signif.	100.0	100.0	100.0	100.0	0.0	0.0	100.0	0.0	0.0	100.0	100.0	100.0
Data Distribution Statistics												
Raw Value Differences												
Mean	5.65	0.18	-0.51	5.74	0.00	0.00	-0.10	0.00	0.00	0.34	0.00	0.23
sd	8.8	2.8	4.0	8.8	0.0	0.0	0.9	0.0	0.0	70.3	0.0	60.0
90%ile	20.0	3.0	5.5	20.0	0.0	0.0	1.0	0.0	0.0	107.0	0.0	85.0
% Mean	1.55	0.12	-54.94	1.61	0.00	0.00	-1.53	0.00	0.00	0.53	0.00	13.33
% sd	3.3	1.5	49.8	3.2	0.0	0.0	3.3	0.0	0.0	6.9	0.0	41.4
% 90%ile	6.1	1.7	100.0	6.2	0.0	0.0	6.1	0.0	0.0	11.5	0.0	78.4
Value Range Normalised Differences												
Mean	4.42	-0.42	6.01	4.82	0.00	0.00	0.17	0.00	0.00	-17.60	0.00	10.00
sd	5.0	0.5	1.0	5.0	0.0	0.0	0.5	0.0	0.0	11.9	0.0	5.4
90%ile	12.0	8.0	12.8	12.0	0.0	0.0	1.3	0.0	0.0	110.0	0.0	54.0
% Mean	1.84	-0.23	#####	2.01	0.00	0.00	0.62	0.00	0.00	-1.77	0.00	5.89
% sd	2.1	0.3	0.0	2.0	0.0	0.0	2.1	0.0	0.0	1.1	0.0	3.0
% 90%ile	6.1	4.7	100.0	6.1	0.0	0.0	4.0	0.0	0.0	12.7	0.0	27.5
Vector Differences												
10%ile	0.4	0.0										
67%ile	3.6	1.0										
90%ile	6.1	1.5										
Rho	1.00	0.00	0.31	1.00	0.00	0.00	1.00	0.00	0.00	0.00	1.00	0.00
num. pts	324	324	324	324	0	0	327	0	0	324	327	324

Table 3.13: Statistics for simulated data vs FCA3. No values could be compared for the apparent velocity parameters, V_a and $\angle V_a$, and the half-lives, $T_{\frac{1}{2}}$ and $\tau_{\frac{1}{2}}$, hence these columns only contain zeroes.

wind magnitude increases, as would be expected on purely statistical grounds.

The difference in the estimate of the major axis of the diffraction ellipse has a spread of $\pm 70\,\mathrm{m}$, with 10% of the differences having magnitudes greater than 107 m. This rather large spread is of the order of $\pm 7\%$ and 11% of the actual value respectively. It can be seen that the X on Y regression is the better fit for this data, giving a bias or intercept value which is exactly the actual major axis and close to the orientation. Errors in the ellipse axial ratio are minimal. Estimates of the orientation give differences with a standard deviation of $\pm 60°$, which is very large. The small axial ratio would make the determination of the orientation of the ellipse difficult and prone to large errors, the ellipse being basically a circle.

3.6 Discussion

Comparison	Description	$\lvert V_t \rvert$ (%)		$\angle V_t$ (°)		A (%)		$\angle$A (°)	
		$\overline{x}$	90%	$\overline{x}$	90%	$\overline{x}$	90%	$\overline{x}$	90%
FCA3	Vary Interpolations	4.0	25		15	2.0	16	4.0	60
FCA2	Vary Particular Sol^n	0.5	40	6.0	30	7.0	22	5.0	70
FCA1,2,3	Vary Algorithm	5.0	20	1.0	7.0	9.0	16	3.0	20
	...(FCA1 vs FCA3)		(8)		(4.0)	(1.0)	(4)		(10)
FCA3	Model Winds	1.5	6	0.2	1.5	0.5	11	0.2	85

Table 3.14: Summary of possible spread in FCA values

The results of this chapter are summarised in Table 3.14.

In Section 3.5.1 it was shown that the FCA technique is very sensitive to the exact values of the cross-correlation functions at zero lag, and the exact (fractional) lags where the auto-correlation function has the same value, and where it has fallen to a value of one-half. Hence they are sensitive to the exact form of interpolation used. This criteria may lessen as the signal-to-noise ratio improves and the form of the correlation functions become more Gaussian.

It was also found that the maximum error in the wind estimates that was introduced by variation of the interpolation routines[2] was of the order of twice the minimum detectable wind speed, or less than 25 % of the wind speed. Minor variations in the interpolations caused differences of the order of only $2\,\mathrm{ms}^{-1}$.

The FCA2 comparisons in Section 3.5.2 show that the choice of particular solution is important if execution speed is required, although the results of the three algorithm comparison in Section 3.5.3 show that it is better to find an optimal solution in order to obtain more consistent results. The comparisons in Section 3.5.2 also showed that the original formulation of the FCA

[2] where only *reasonable* interpolation routines were considered

by *Briggs* [1984] and the modification suggested by *Fooks* [1965] give similar variations in the FCA parameters, which do not vary significantly more by different choices of particular solutions for the τ_{ij}.

The comparison of the various algorithms (see Section 3.5.3 and the third row in Table 3.14) perhaps gives a more typical error that could be expected between competing FCA algorithms. Note that these three sets of comparisons were performed using only a single hour of real data. Individual errors were sometimes quite large but in general appeared to be of a random nature. Thus the mean differences in each parameter were quite small. This can be seen in Table 3.14 where the mean differences are significantly smaller than the 90 percentile values. This suggests that the accuracy of the FCA improves with averaging.

The last row of Table 3.14 shows the differences between the FCA3 algorithm and the "real" values — the model inputs. These errors therefore represent the expected accuracy of the FCA as implemented in FCA3. Assuming that $50\,\mathrm{ms}^{-1}$ is a representative wind speed, then an error of less than $\pm 3\,\mathrm{ms}^{-1}$ could be expected in its estimate using FCA3. This is of the order of the effective minimum detectable wind speed for most applications. The FCA1–FCA3 comparison suggests that a similar error could be expected from other implementations of the FCA as long as an optimal solution is found for the over-determined equations. Use of particular solutions may increase this expected error by a factor of 3–4.

As the model winds contained no turbulence, the additional errors found in the other comparisons, which used real wind data, may be attributed to the complicating effects of random motions in the wind field.

May [1988] discusses the statistical errors associated with the FCA technique, and, more importantly for the current work, he performs a comparison of the wind estimates from co-located spaced antenna at Buckland Park using the FCA1 algorithm. The measurements were taken over a 4 hr period, using reflections from altitudes ranging from 70 to 90 km. The wind speeds ranged from 70 to over $100\,\mathrm{ms}^{-1}$. *May* [1988] found that the distribution of the differences in the estimate of the wind speed peaked around $10\text{–}20\,\mathrm{ms}^{-1}$. This is a measure of the statistical uncertainty in the wind speed estimates using the FCA. Taking $80\,\mathrm{ms}^{-1}$ as a typical wind speed, this error is of the order of 20 %, which is comparable with the upper decile error expected by varying the FCA algorithm.

In conclusion it was found that variations in the form of interpolation used in the FCA could cause large variations in the instantaneous wind field parameter estimates. These were significantly reduced by averaging over the order of one hour. The same was found for variations

in the choice of particular solutions to some of the over-determined equations, although using some form of optimal solution provided significantly smaller average and instantaneous errors. Local interpolations, using tightly constrained cubic splines, gave the best results in these trials (which were by no means extensive). This is equivalent to use of a polynomial least-squares regression but does not rely on *apriori* knowledge of its order. This method does not rely on any assumptions about the shape of the correlation function so is robust in poor signal-to-noise environments. In good signal-to-noise environments further assumptions about the shape of the correlation functions (*e.g.* they are Gaussian) could give better (and/or more efficient) interpolation results.

The errors or uncertainty in the estimated wind speed, associated with the use of different implementations of FCA, were found to be of the same order as the statistical uncertainty due to the sampling over a small area of a temporal and spatially varying (large scale) diffraction pattern. Finally, in the absence of turbulence it was shown that the FCA correctly reproduces the winds in the middle atmosphere.

Chapter 4

The Quasi-Two-Day Wave

4.1 Introduction

Long-period wave activity has been observed in the atmosphere for many years. Some waves were readily explained as being of tidal origin (*c.f.* Section 1.4). These have an obvious lunar or solar forcing. Others appear to be resonant modes of the atmosphere [*Salby*, 1984; *Prata*, 1989] — the theory for atmospheric normal modes has been covered in Section 1.4.2. The quasi-two-day wave (hereafter referred to as the 2-day wave) is a large amplitude planetary wave with a period near 48 hr. Its existence has been known for many years, but the generating mechanisms and its role in the middle atmosphere are still undetermined. *Salby* [1981a] proposed that it is a manifestation of the $(3,0)$ atmospheric normal mode driven by "noise" at lower levels. The $(3,0)$ mode has a period of about 50 hr (depending on what equivalent depth is used) in an atmosphere at rest. *Salby* [1981b] and *Salby* [1981c] discuss how the mode structure changes in an atmosphere with realistic background winds and temperatures. In particular, he shows that the wave becomes locally propagating in the summer mesosphere where the prevailing wind is slightly eastward relative to the wave, and where there is an equatorward temperature gradient. In this region wave energy has exponential growth with height. An alternative generating mechanism was proposed by *Plumb* [1983] and *Pfister* [1985] who suggested that the wave could be due to baroclinic instability of the westward jet in the summer stratosphere and lower mesosphere. Stability analyses show peaks of unstable wave growth at zonal wavenumbers 2–4 with periods of 1.5–3 days.

It is known that the 2-day wave has its peak amplitudes at mid-latitudes in the summer hemisphere. Amplitudes then decrease towards higher and lower latitudes. The effect crosses the equator but amplitudes continue to diminish so that very little evidence of the 2-day wave

is found at mid-latitudes in the winter hemisphere. The effects of the 2-day wave can be seen during both solstices at the equator. Its importance for the meridional mixing in the upper middle atmosphere at mid-latitudes is shown by *Plumb et al.* [1987] who calculate that with a typical maximum amplitude of $55\,\mathrm{ms}^{-1}$ in the southern hemisphere, the 2-day wave could transport a parcel of air $\sim 3000\,\mathrm{km}$ in the course of a day. This is approximately half the distance from the equator to the Antarctic circle. Due to the large amplitudes, this wave can directly affect the mean flow by non-linear interaction [*Plumb et al.*, 1987]. There are also suggestions that this long period wave directly affects the equatorial ionisation anomaly [*Chen*, 1992].

The 2-day wave was first noticed in Adelaide data in 1967 by a research student studying meteor winds [*Doyle*, 1968, whose observations are shown in Figure 4.1]. Later, concerted efforts were made to isolate and characterise the phenomenon in both the southern and northern hemispheres using meteor radars [*Coy*, 1979; *Craig & Elford*, 1981; *Craig et al.*, 1983; *Muller & Nelson*, 1978; *Vincent*, 1984a]. More recently MF and meteor radars from varied geographical locations have been used [*Clark*, 1989; *Manson & Meek*, 1990; *Tsuda et al.*, 1988; *Poole*, 1990]. Satellite observations of the 2-day wave [*Rodgers & Prata*, 1981] have also been made. These depend on the temperature perturbations observed from radiance measurements.

From these studies it is known that the 2-day wave at mid- to high-latitudes is small in amplitude for most of the year and reaches its peak amplitude approximately one month after the solstice in each hemisphere. It invariably has a very long vertical wavelength at mid-latitudes — $\sim 100\,\mathrm{km}$ at Adelaide [*Craig et al.*, 1980; *Craig & Elford*, 1981] — while shorter wavelengths are found at low latitudes [*Craig et al.*, 1980; *Reddi & Lekshmi*, 1988; *Harris & Vincent*, 1993]. The altitude of maximum amplitude appears to be between 85 to 95 km. The satellite observations and longitudinally spaced radar comparisons suggest that the wave is westward propagating, and has a zonal wavenumber of three [*Rodgers & Prata*, 1981; *Vincent*, 1984a]. This is in agreement with the proposal of *Salby* [1981a] that the wave is a manifestation of the free-mode mixed Rossby-gravity wave, the (3,0) normal-mode of the atmosphere (*c.f.* Section 1.4.4). Hemispheric differences are also apparent. Amplitudes are up to a factor of two larger in the southern hemisphere than those found in the northern hemisphere. In the southern hemisphere there are also suggestions of a locking of the phase with local time [*Craig & Elford*, 1981; *Poole*, 1990; *Harris*, 1993]. That is, during the time interval of maximum wave amplitude there is a tendency for the 2-day wave to have maximum wind speeds at the same local time from summer to summer. It has also been noticed that there is a tendency for the wave period to be greater

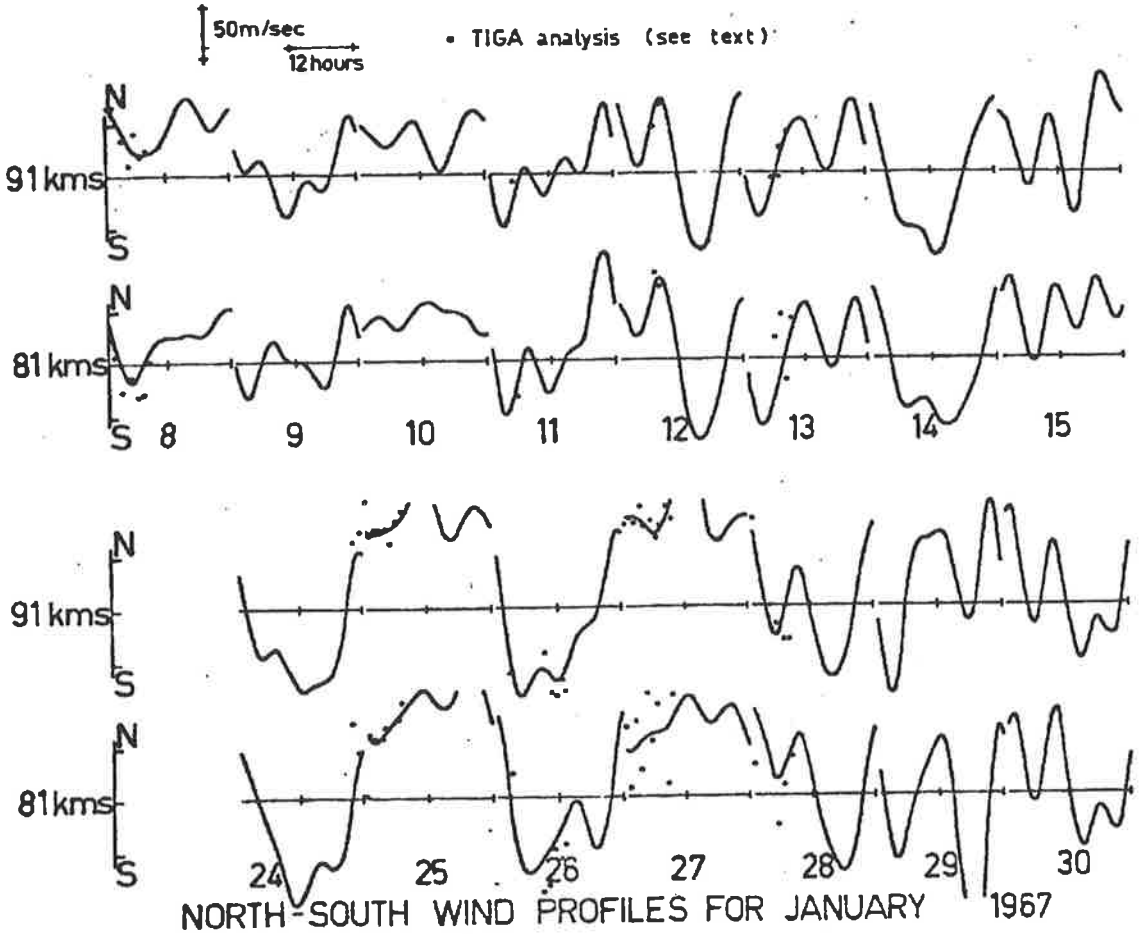

Figure 4.1: Hourly values of meridional wind velocity for January, 1967, determined from a Groves analysis (which fits tidal harmonics on a daily basis) of meteor echoes (figure 5.12 of *Doyle* [1968]). The 2-day wave can clearly be seen during the period from 24^{th} –28^{th} of January.

than 50 hr in the northern hemisphere, but often indistinguishable from 48 hr in the southern hemisphere [*Muller & Nelson*, 1978; *Craig & Elford*, 1981; *Tsuda et al.*, 1988; *Poole*, 1990; *Harris & Vincent*, 1993]. These last two points are the focus of Sections 4.3 and 4.4 respectively.

The following section discusses the equipment and sites used to obtain the wind estimates from which parameters for the 2-day wave are derived in the later sections of this chapter. The general morphology of the 2-day wave in the southern hemisphere middle atmosphere over Adelaide (34.5° S, 138.5° E) is developed and discussed in Section 4.3 using data accumulated over 12 years — of which only the last three years were collected by this author ! The first morphology of the 2-day wave over the equator is presented and discussed in Section 4.4. With the advantages of equatorial observations for the first time the effects at both solstices have been observed in detail from the same site. These results and possible non-linear interactions are also presented and discussed in Section 4.4. The transfer of horizontal momentum by the

2-day wave is investigated in Section 4.5. By comparing data from latitudinally similar but longitudinally separated observation sites estimates of the 2-day wave zonal wave number are made in Section 4.6. Lastly, in Section 4.7 the variations in the solar tides are compared to the 2-day wave amplitudes at mid- and low-latitudes. Sections 4.3 and 4.4 form the bases for the two papers *Harris* [1993] and *Harris & Vincent* [1993], hereafter referred to as paper-1 and paper-2, which can be found in Appendices H and I respectively.

4.2 Data Collection

4.2.1 Introduction

The raw data used for the work in this chapter are mainly wind estimates derived using full correlation analysis (see Section 2.3) of partial reflection backscattered radio waves (see Section 1.5) sampled on three spaced antennae. This form of wind data is often termed Spaced-Antenna Partial-Reflection (SAPR) winds, or simply Spaced-Antenna winds. Data from two University of Adelaide field sites have been used, each being briefly described in the next subsection. Samples of the raw winds obtained from these sites can be found in Appendices F and G. Data from South Africa has also been used for comparisons. The geographical locations of all the radar sites are shown in Figure 4.2. The data from Grahamstown (33.3° S, 26.5° E), South Africa, formed part of a collaboration with Dr Graham Poole[1], and consisted of wind estimates from a meteor radar for the summers of 1984 to 1992.

4.2.2 Field Sites

4.2.2.1 Buckland Park (34.5° S, 138.5° E)

The MF radar situated at the University of Adelaide field site at Buckland Park (34.5° S,138.5° E), $\sim$ 40 km north of Adelaide, South Australia, is a pulsed radar operating at 1.98 MHz. Full details of the site and radar installation can be found in *Briggs et al.* [1969] or *Felgate & Golley* [1971]; a brief description follows.

The transmitting array (see Figure 4.3) consists of four half-wave dipoles which are suspended from steel towers at a height of 30m; this is approximately 1/4 of a wavelength. The towers are arranged in a square, each separated by $\sim$ 75m. The half-power-half-width of the polar diagram is $\sim 40°$. Linear, right-hand[2] (Ordinary or O-mode) or left-hand[3] (Extra-ordinary or E-mode)

[1] Rhodes University, South Africa
[2] clockwise rotation when viewed in the direction of propagation
[3] anti-clockwise rotation when viewed in the direction of propagation

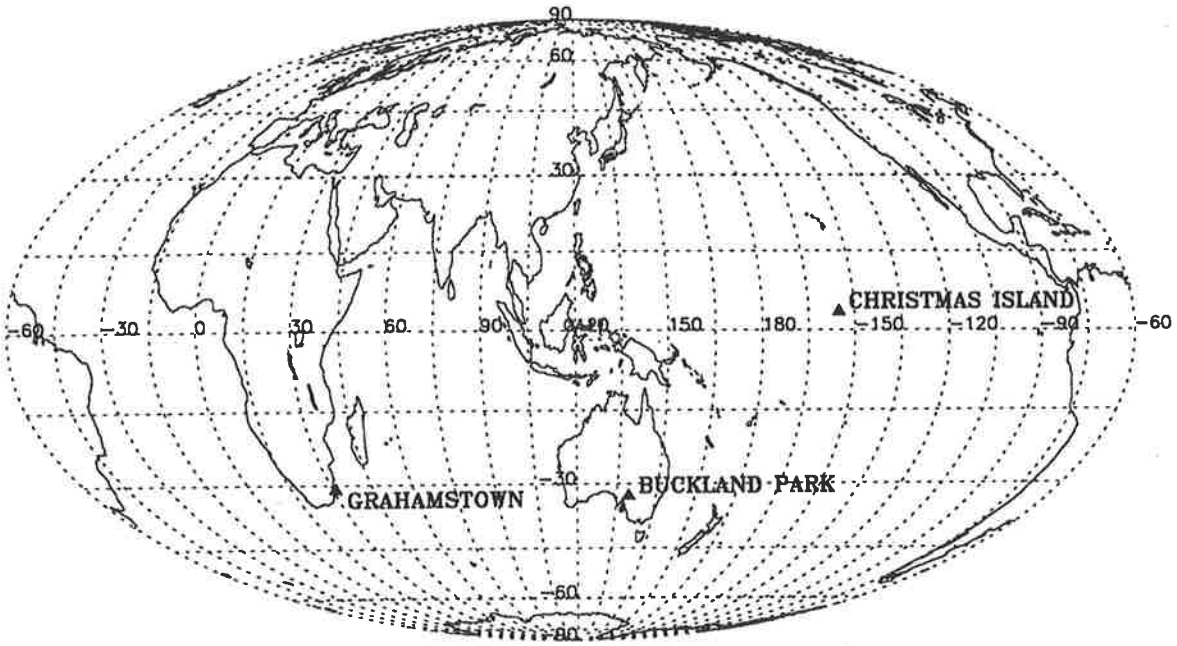

Figure 4.2: Schematic of the radar locations from which data were obtained.

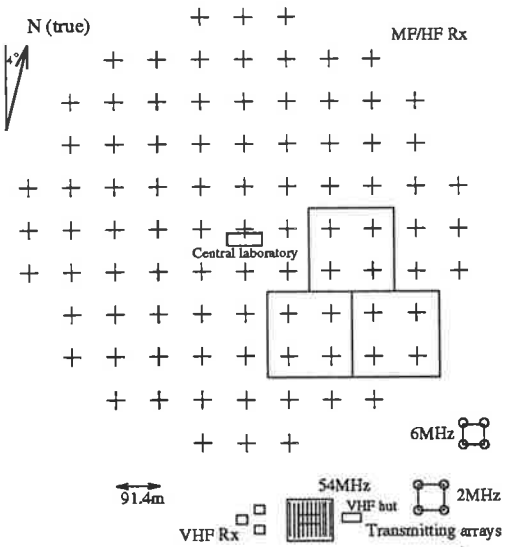

Figure 4.3: Schematic of the radars at Buckland Park. A scale is shown on the lower left-hand side of this figure. The large MF/HF receiving array dominates this diagram, covering nearly 1 km^2, with the main laboratory shown in the centre. The three enclosed sets of 4 elements are those used for the spaced antenna experiment for most of the observations described in this thesis. The transmitting array for the 2 MHz system can be seen in the lower right-hand corner (south-east). The transmitting array for the 6 MHz system is the smaller square immediately above and to the right. South of the MF receiving array (below) are the transmitting and receiving arrays for the 54 MHz VHF radar.

circular polarisation modes can be transmitted. Normally O-mode transmission is used during the day as the E-mode is more strongly absorbed in the D-region. During the night E-mode is used as this should provide stronger reflections. Up until late 1992 a valve transmitter was used, generating 25 kW peak-peak power (dependent on the state of the valves) for Gaussian-shaped pulses with a half-width of $\sim 25\,\mu$s. This gives a raw height resolution of 4 km (see *Röttger* [1984] for a proof of this). The pulse repetition frequency (PRF) was fixed at 20 Hz up until the beginning of 1991, when a new receiving system was installed. This allowed the PRF to be chosen from a number of preset steps ranging from 8 to 120 Hz.

The receiving array (see Figure 4.3) consists of 89 crossed dipoles, giving 178 independent elements (89 aligned near north-south, and 89 aligned near east-west). Each crossed dipole is supported 11 m above the ground by a wooden pole. The entire array occupies an area of $\sim 1\,\mathrm{km}^2$, with the elements 91.4 m apart. The array is aligned 4° west of true north, so that the north-south aligned dipoles actually line up at a bearing of 356°. The signals from each of the 178 elements are independently carried to a central control room via coaxial cable an integral number of half-wavelengths long. A polar diagram with half-power-half-width of 4.5° can be achieved when all 89 north-south or east-west elements are appropriately combined. The first nulls appear at 11.6° off-zenith. This relatively narrow beam (for an MF radar) can be used for Doppler work. Beam swinging is achieved by varying the phasing of separate elements, normally grouped as rows. To improve the signal-to-noise ratio four elements were clustered to form a single antenna for use in spaced-antennae work (as shown in Figure 4.3). This also served to improve the reliability of the signal as not all four elements are required to obtain an adequate return. Thus broken dipoles were not such an issue as they could have been.

Prior to 1991 the data from Buckland Park were recorded on magnetic tape as the digitised receiver outputs (in the form of in-phase and quadrature components) or as the processed winds from a FCA (*c.f.* Section 2.3) produced online through a Nova IV Eclipse. The in-phase and quadrature components of the signal can be considered as a single complex value, therefore each receiver can be thought of as producing a "complex" signal as output. During 1991 the Atmospheric Physics Group was developing and testing state-of-the-art 2 MHz receivers. The outputs from these new receivers are controlled by a IBM/AT type PC[4]. This allows a higher PRF and a shorter duty cycle. The raw signal returns are analysed in real time using a FCA program. Wind estimates have been collected on these systems at Buckland Park since the later part of 1991. During the summer of 1991 a 5-channel receiving system was also installed at Buckland Park. This was the forerunner of the new equipment upgrade planned for the site

[4]personal computer

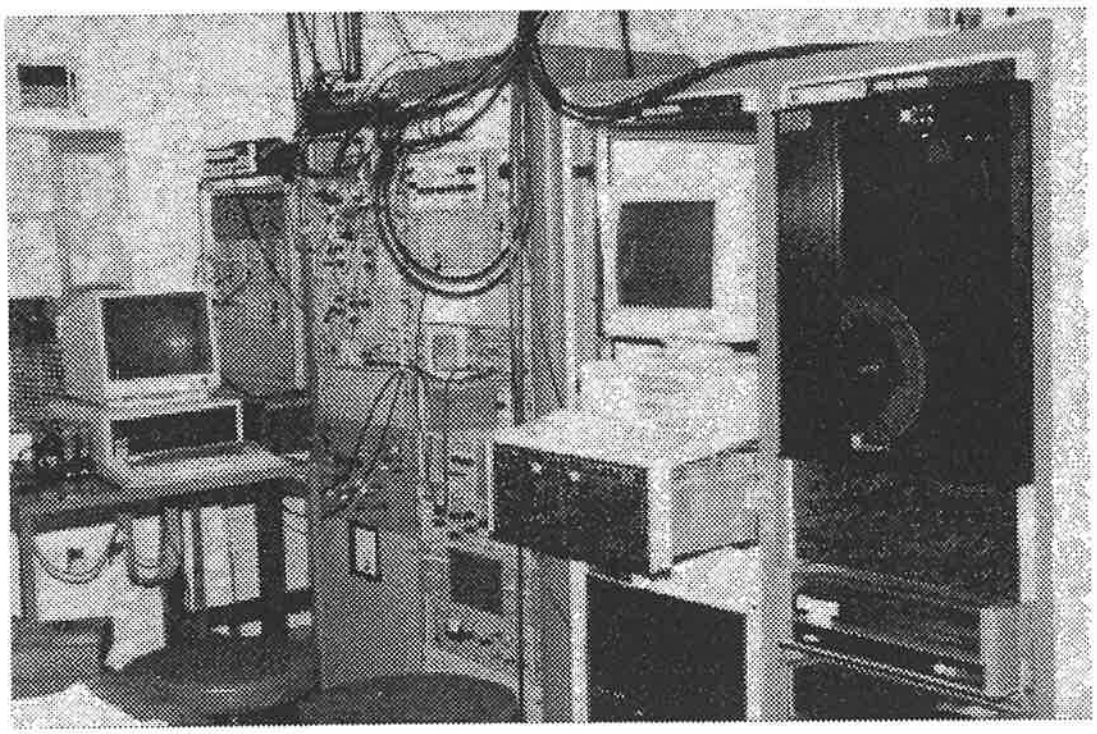

Figure 4.4: The receiving equipment at Buckland Park during the summer of 1991. Three systems are pictured. In the foreground is the 1600bpi tape drive unit controlled by a Nova IV, with the hard-disk drives below. The next rack holds the Nova itself (lower section), now inoperative, and a Compaq 286 PC (above) which controlled the 5-channel system. The rack behind these holds the receivers and digitisers being used for the 5-channel system. The coaxial cables coming down from the roof carry the signal from the patch-board which goes to the actual dipoles. The last large rack holds the 6 MHz receivers, digitisers and power supply, currently not in use. The PC at the back of the picture is an Olivetti M24 running a spaced-antennae FCA program using the data from the solid-state receiver system in the small rack at the very back — the three receivers and digitisers can be seen, with a coaxial connection between them. Both the 5-channel and the spaced-antennae systems are operating, with the spaced-antennae system controlling the transmitter.

during 1992-95. The 5-channel system allowed five complex digitised receiver outputs to be stored for post-processing. All three sytems mentioned can be seen in Figure 4.4.

Over-sampling of the returned signal on all these systems was used, giving a height sampling interval of 2 km for each complex valued data point. Coherent averaging of the raw signals by the hardware usually provided data at a time resolution of one complex data value for each height every 0.4 seconds. Normally a time series of 256 data points was collected for each height before processing or storage, then the cycle would start again. Thus one wind estimate for each height was attempted every 2 minutes. This was sometimes reduced to one estimate every 4 or 6 minutes in order to reduce the data storage requirements and extend the observational period. This was accomplished by simply waiting a set time before reinitiating the data collection. Generally, two-hourly averages were then made of the wind estimates as only long-period wave

activity was of concern. The averaging also had the effect of reducing the number of data gaps, both in time and in altitude. To further reduce the number and extent of the data gaps in the Adelaide data, values from adjacent range bins were also averaged together. This reduced the height sampling interval back to 4 km, equal to the actual height resolution of the transmitted pulse.

4.2.2.2 Christmas Island (2° N, 157° W)

Full details of the radar installation on Christmas Island, in the mid-pacific, operated by the Atmospheric Physics Group of the University of Adelaide, can be found in *Vincent & Lesicar* [1991]. Only a brief description will be given here.

Christmas Island is a small, flat, coral atoll situated near the equator in the middle of the Pacific Ocean well away from any large land mass; hence atmospheric dynamics should exhibit little or no effects arising from orographic forcing. Like the radar at Buckland Park, the MF radar at Christmas Island operates at 1.98 MHz, producing SAPR wind estimates every 2 minutes at 2 km height intervals. The height range from 60 to 98 km is covered during the day, and 70 to 98 at night. The lack of ionisation at night restricts the useful data to above ~ 78 km. The radar system is one of the new generation systems developed in Adelaide and whose receivers were field tested at Buckland Park. The raw signal returns are analysed in real time by a dedicated PC.

As in the analysis for the previous section, two-hourly averages were made of the wind estimates, as only long-period wave activity was of concern. Unlike in the previous section though, as the data quality was very good (*c.f.* Appendices F and G), with a high data retention rate for the FCA, averaging of values from adjacent range bins was not required.

4.3 Long-Term Trends at Mid-Latitudes

4.3.1 The Raw Data

Wind data over Adelaide for each summer from 1980 to 1991 have been used in the study of the long-term trends in the 2-day wave in the southern hemisphere. The data for each summer normally covered the three months of December, January and February. This time period was sometimes reduced to only January for the earlier years due to the campaign nature of the data collection at that time. Since 1984 near continuous wind observations have been made at Buckland Park. Therefore when continuous data coverage throughout the year was required only

the years 1984 to 1991 have been used. Within this section, and throughout this thesis, the year associated with a particular summer is the year containing the January of that summer, so that the summer of 1980 refers to the time period from December, 1979, to February, 1980. In some figures November and March are referred to. In these cases the data starts at the very end of November or ends at the very beginning of March. The complete set of raw data used is shown in Figure 4.5 for a single height range of 86 to 90 km, with the region of high 2-day wave activity in late January expanded in Figure 4.6. This is similar to figure 1 of paper-1. The 2-day wave can clearly be seen in the raw meridional winds for most years. It is not so obvious in the zonal winds. Inter-annual variations in the strength of the wave are evident and will be investigated in the subsections that follow. Data quality also varies from year to year. The many gaps are where data are missing, either failing the FCA acceptance criteria (*c.f.* Section 2.3.4.3), falling outside a campaign period (in the earlier years), or could not be collected due to equipment failure. This last cause of data gaps was probably the most frequent for this data set due to the harsh environment in which the radar operates during the hot Adelaide summers.

4.3.2 Wave Amplitude and Phase Information from Wind Data

In order to compare the amplitudes and phases of the 2-day wave over a number of different years a single technique was desirable. This technique had to separate the near 48 hour wind oscillations from the raw wind data to give a time domain representation of the 2-day wave — so that the times of maximum wind amplitudes (*i.e.* the phases) could be found — yet be able to handle unevenly spaced data gaps of various sizes, making few assumptions about the period of the wave and its continuity from year to year; allow at least a cycle to cycle variation in the wind amplitudes; be relatively fast and automated to handle the large amount of data; be robust enough to handle small amplitudes for the wave amongst larger amplitude waves with periods that are harmonics of 48 hours, such as the diurnal and semi-diurnal tides; and lastly, be able to handle a non-linear, non-stationary process such as the 2-day wave.

A complex demodulation technique (*c.f.* Section 2.7) can be used to give an estimate of the amplitude of the 2-day wave as a function of time. It has the advantage of producing a time series with a data point for every data point in the original series. However, this technique does not produce a real-valued time series from which perturbational wind velocities can be obtained, hence does not allow an estimate of the phase of the wave. Therefore a complex demodulation technique is not suited for the present study.

Preliminary studies using a 10 km averaged data set from 87 to 97 km for the 10 summers of

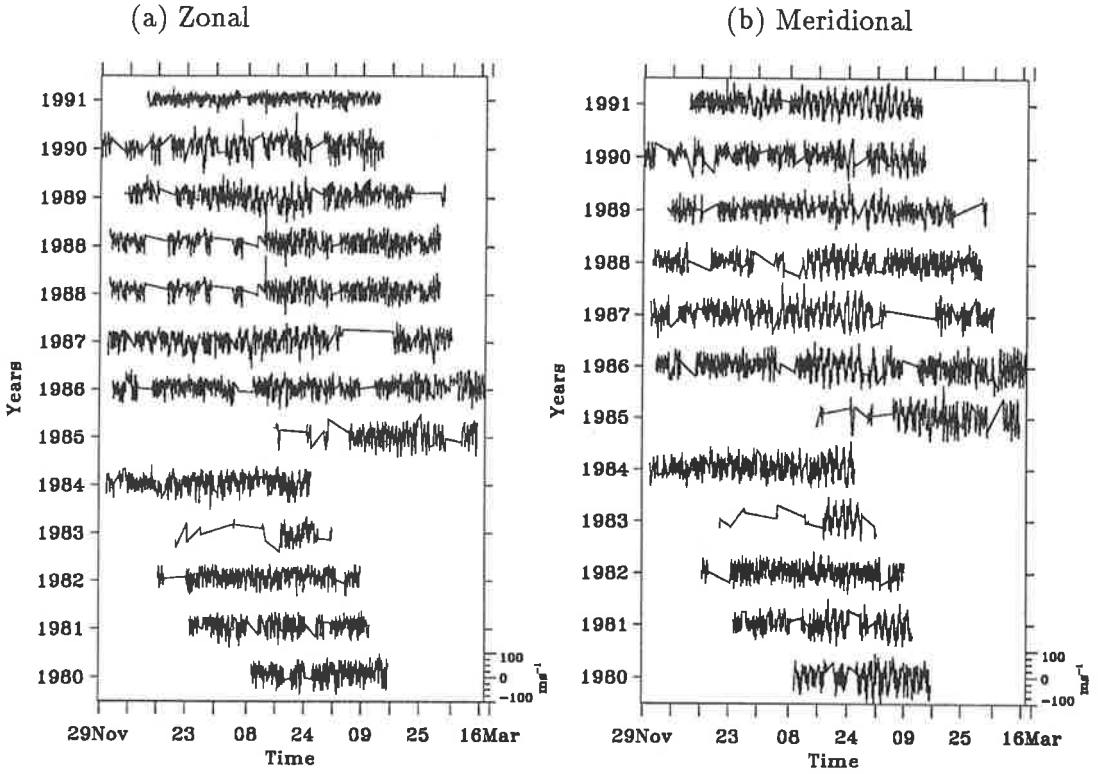

Figure 4.5: Two-hourly winds from 86 to 90 km, for the summers of 1980 to 1991 (years shown at left). (a) Zonal (b) Meridional component. The 2-day wave is evident in all years during the later half of January. The extended near horizontal lines are where the points either side of a data gap have been connected.

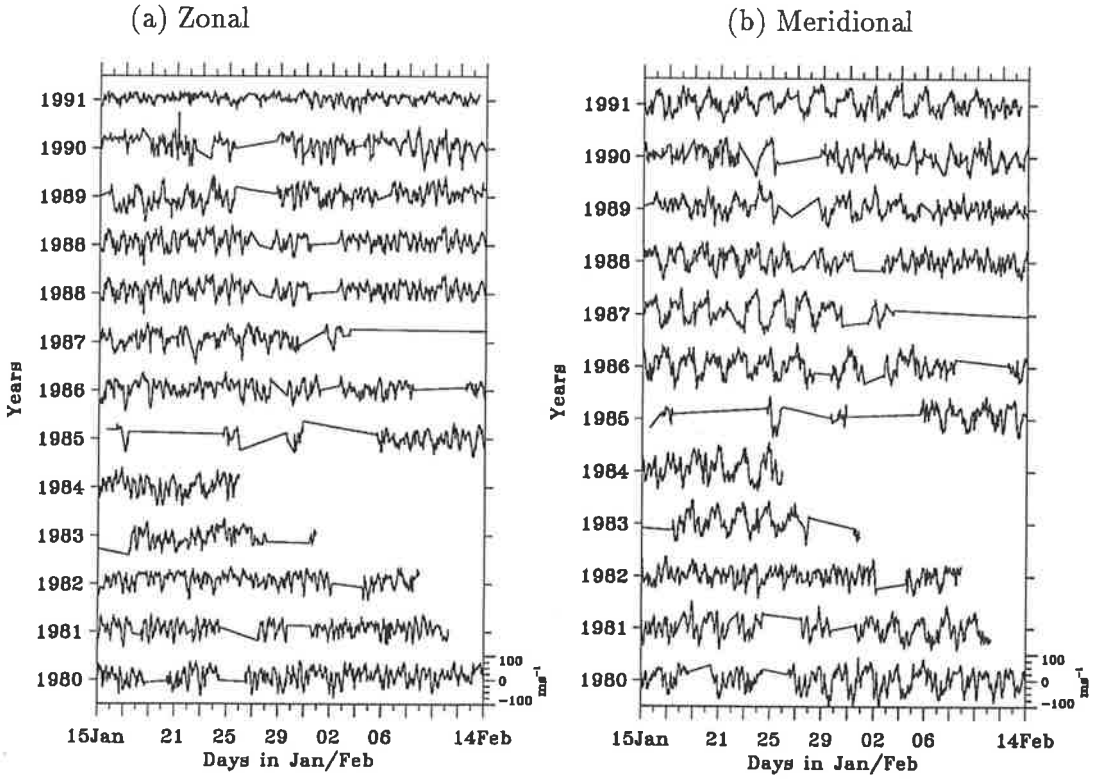

Figure 4.6: Two-hourly winds from 86 to 90 km, during January, for the 12 year period from 1980 to 1991 (years shown at left). (a) Zonal (b) Meridional component. Again, the extended horizontal lines are where data gaps exist.

1980 to 1989 indicated that most of the variability in the period and phase of the wave would come from yearly differences. This is in accord with the phase results of *Craig & Elford* [1981] using 10 years of meteor wind data collected at Buckland Park in the 70's. It was therefore decided to ignore the non-stationarity of the data and treat it as a secondary effect for the current analysis. This assumption allows the use of Fourier transform techniques.

A spectral filter with a broad pass-band centred on 48 hours was used to extract the 2-day wave from the raw time series. This has the advantage of producing a real-valued time series of wind velocities. To decide on an appropriate bandpass a moving power spectrum (see Chapter 2.8) was formed for the Adelaide data from an altitude range of 86 to 90 km over the time interval from January 1984 to January 1991 (Figures 4.7 and 4.8). The white bands over all frequencies are where data are missing. The maximum power spectral densities have been "clipped" to be less than $2.4 \times 10^7 \, m^2 s^{-2} Hz^{-1}$. The spectral values were then folded back into a single calendar year to give an average or superposed moving power spectrum (Figure 4.9) for both the zonal and meridional winds, as in figure 2 of paper-1. From this diagram it can be seen that the 2-day wave power (the strong peak during January-February) is spread over a wide frequency band but is fully contained within the bandpass of 32 to 96 hours (0.25 to 0.75 cpd[5]). This was the bandpass used to form a time series of 2-day wave data, allowing variations on time scales as small as 48 hours to be seen (*c.f.* Section 2.6). Some activity near a period of 48 hours can be seen during July in Figure 4.9. This can be tentatively identified as the occurrence of the 2-day wave in the northern hemisphere weakly extending down to 35° S. The amplitude of the solar diurnal tide appears to be a minimum near the time of the 2-day wave event. This behaviour is discussed further in Section 4.4. The raw wind data shown in Figures 4.5 and 4.6 were bandpass filtered to give the 2-day wave data shown in Figures 4.10 and 4.11 respectively. Figure 4.11 is the same as figure 3 of paper-1. The maximum wind speeds were obtained as a function of time from the perturbation wind velocities. The phase of the 2-day wave was obtained by determining the local time of the maximum northward and southward winds. This necessarily gave the phase information in the range from 0 to 24 hr. Using some arbitrary starting time, the number of wave cycles could be calculated to the start of the day for which the phase is to be estimated. This number, when added to the local time estimate, would give the phase as a fraction of a cycle relative to this start time. Shifting the start time by a fraction of a cycle would change the phase estimates by the same amount. Having the phase in fractions of a cycle allows comparisons of the phases of the zonal and meridional components. However, the phases found in this manner are not directly comparable from year to year as

[5] cycles per day

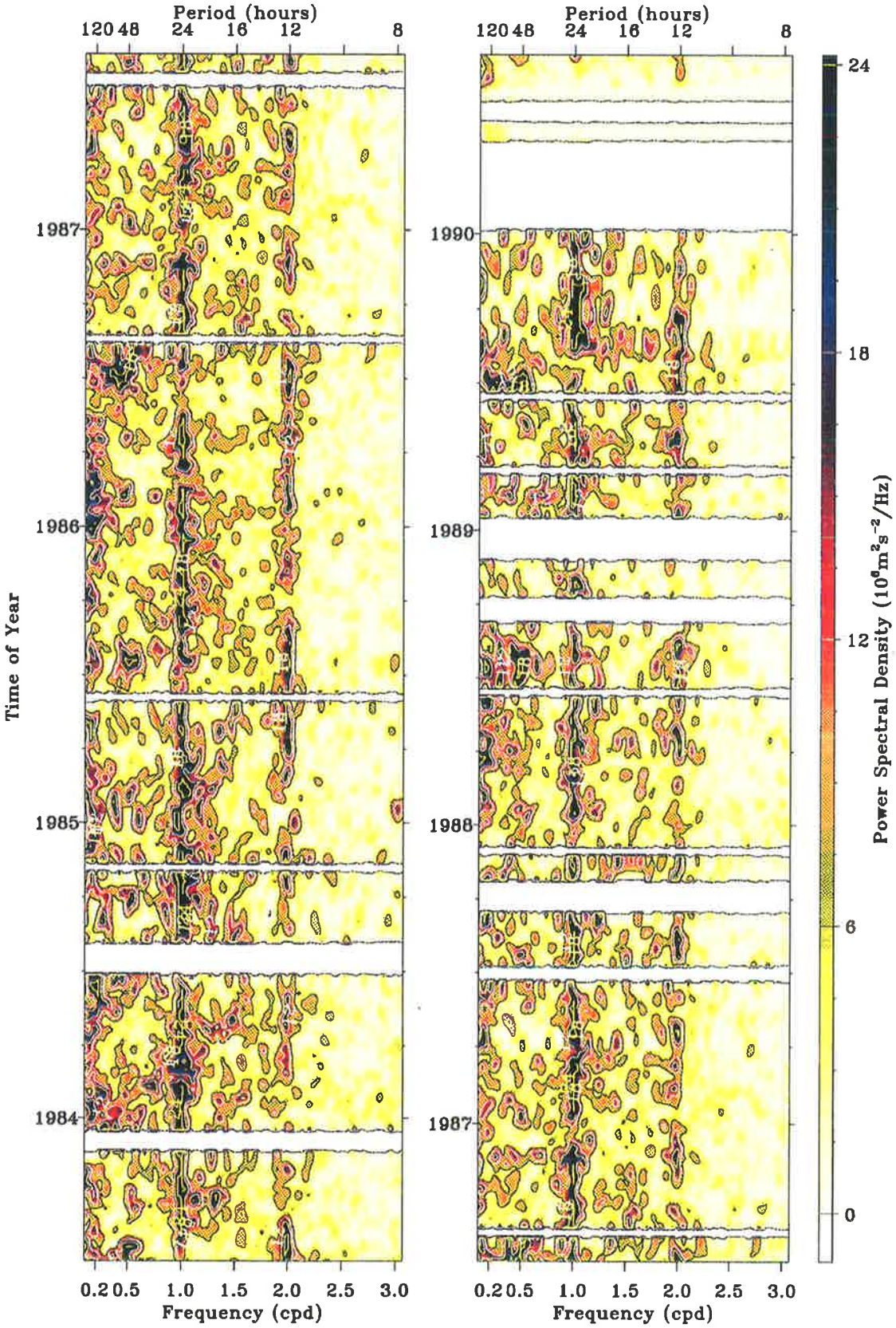

Figure 4.7: Moving power spectra for 1984 to 1991 for the zonal winds for an altitude range of 86-90 km over Adelaide (34.5° S, 138.5° E). A 14 day sliding window has been used, with a step of 7 days. Over-sampling in frequency space gives an effective resolution of 0.036 cycles per day. The tick marks on the time axis are at the beginning and end of every three months. The year labels are at the beginning of each July (mid-year).

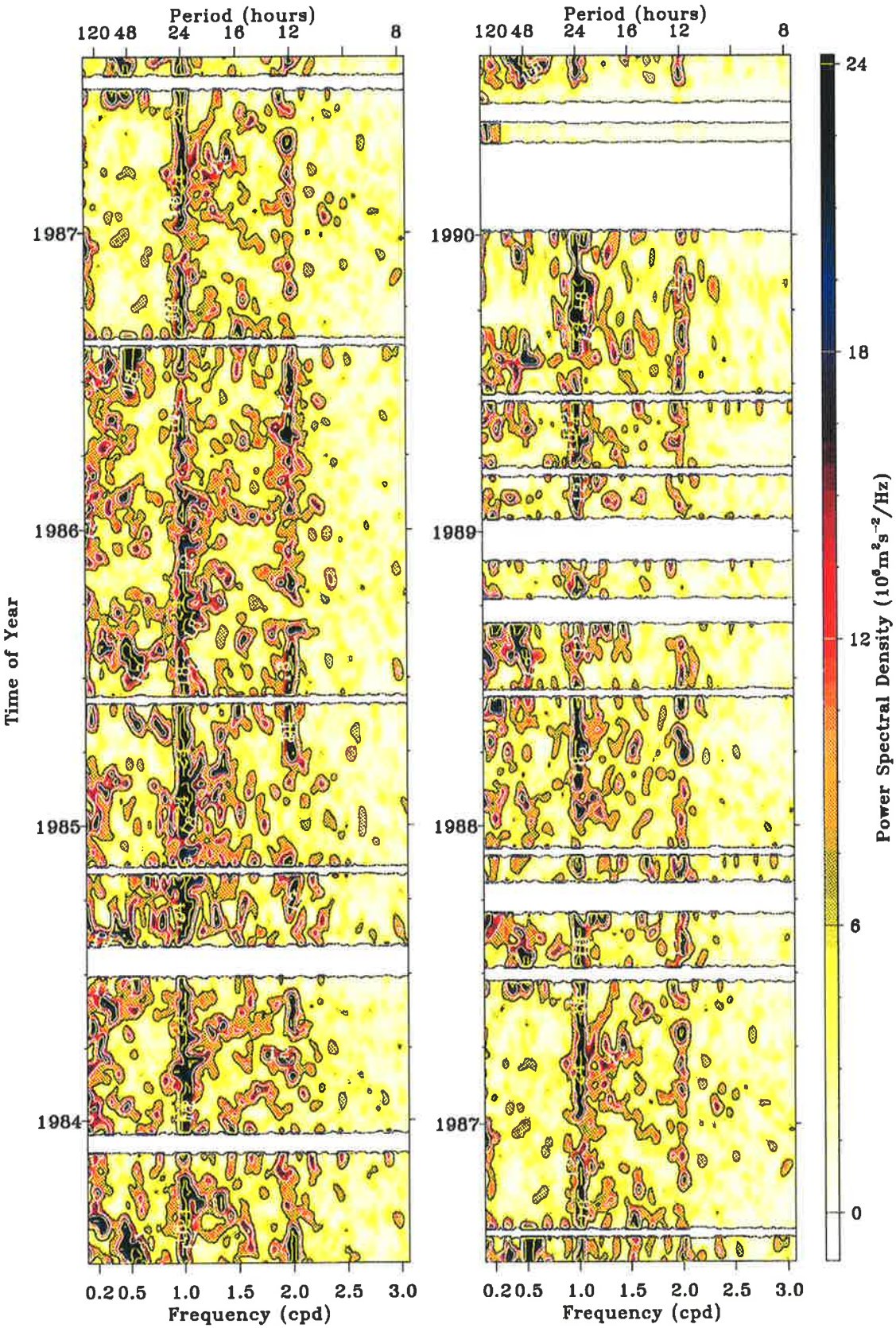

Figure 4.8: As for Figure 4.7 but for the meridional winds.

(a) Zonal

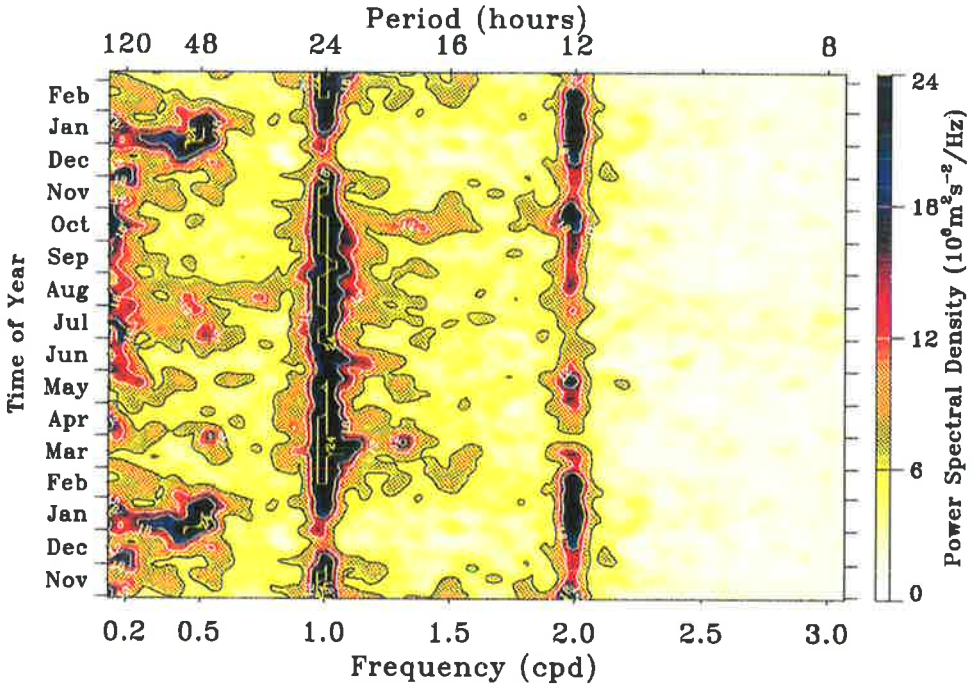

(b) Meridional

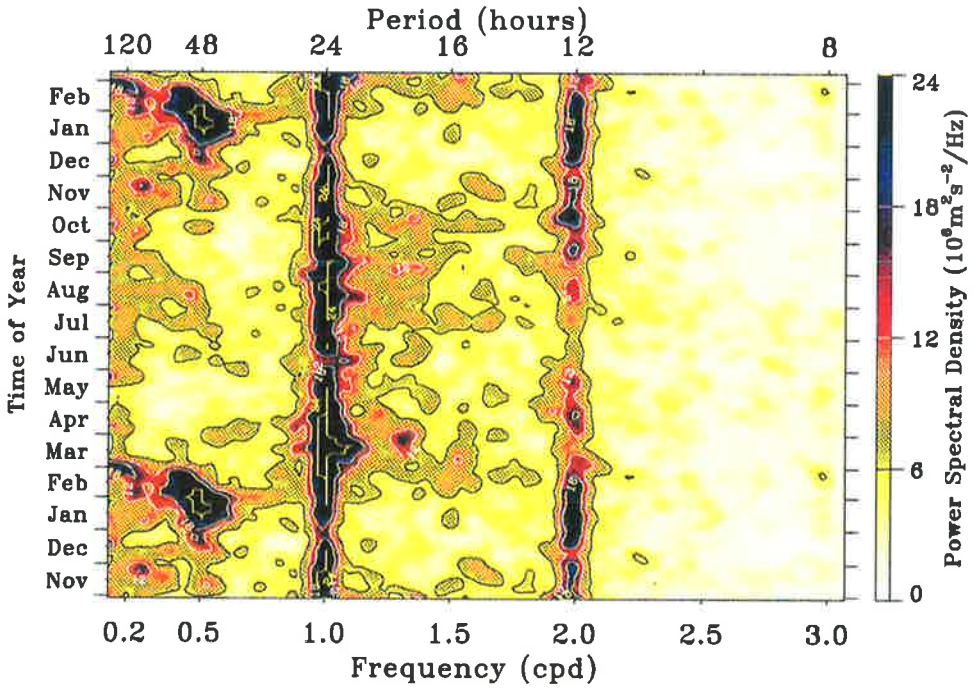

Figure 4.9: Yearly average moving power spectra for the (a) zonal and (b) meridional winds. The spectra in Figures 4.7 and 4.8 have been averaged into a "typical" year. The tick marks on the time axis are at the beginning and end of the months.

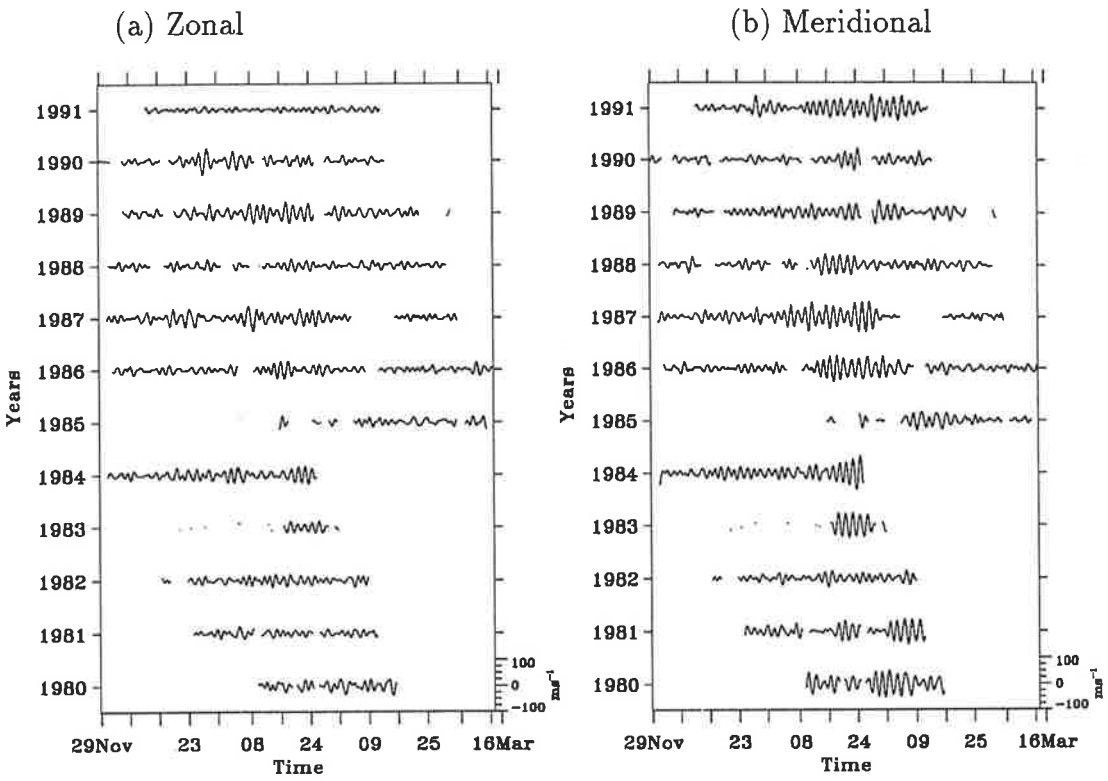

Figure 4.10: Broad-band filtered quasi-two-day wave at 86 km for the summers of 1980 to 1991. Bandpass of 32 to 96 hours. (a) Zonal (b) Meridional component.

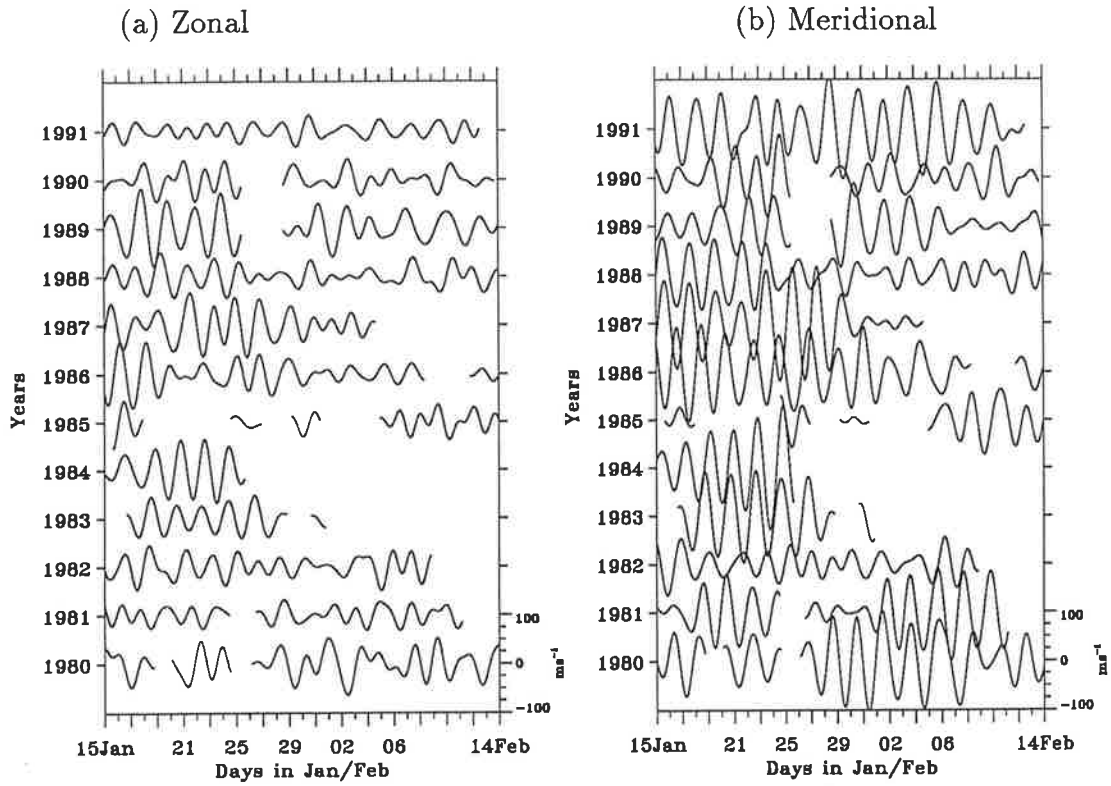

Figure 4.11: Expanded view of January for the broad-band filtered data in Figure 4.10. (a) Zonal (b) Meridional component.

the use of a single relative start time does not allow for phase variations throughout the year. In fact it assumes the phase is locked with local time — an assumption that is to be tested. Any variation in wave period will also cause a phase drift which will confuse the comparisons of phases from year to year. It also assumes that the wave is a continuous entity throughout the year rather than a phenomenon that may arise in summer from a fortuitous combination of events. This is another assumption that will be tested so cannot be implicitly assumed here !

As the wave period is expected to be close to 48 hr during the summer at Adelaide, the phase estimates could be left in local time and be expected to cluster about a particular value for any given summer. As well, leaving the phases in local time means that a phase locking can be investigated by comparing many summers without the concern about whether the correct day has been used as the relative start date. Average phases over many summers also becomes a meaningful quantity. Further, since the phase values range over only half a cycle, phase estimates can be made from both the maximum positive and maximum negative wind speeds, thus doubling the number of phase samples. It must be born in mind that a 24 hr ambiguity will exist in all the phase estimates when done this way. Also, this form is only valid if the wave period is indeed close to 48 hr. This assumption is tested in Section 4.3.8.

4.3.3 Amplitude and Phase Distributions

The maximum wind speeds were collected to form a distribution of the amplitude of the 2-day wave for each altitude and each summer and are shown in Figures 4.12 and 4.13. Zonal amplitudes are small (Figure 4.12), exhibiting little variation with altitude and over each summer. In contrast, the meridional amplitude distributions with altitude for each summer (Figure 4.13) show a strong inter-annual variation, the 2-day wave being stronger in some years than in others. In all cases the amplitude maximises near 86 to 90 km. To obtain a picture of the average behaviour of the amplitude of the 2-day wave as a function of altitude, all the 12 summers have been used in Figure 4.14 for both the zonal and meridional components. The amplitudes maximise near 86 km in both cases, with a sharp drop off in the maximum wind speeds below, and more slowly above.

The phases can be collected as a function of altitude and year in a similar fashion to the amplitudes. As the phase is a cyclic parameter, with 0 hr LT[6] being the same as 24 hr LT, a decile approach to the distribution cannot be used. If the amplitudes of the 2-day wave are ignored for the moment then the phase values can be formed into a histogram to visually determine the

[6]Local Time, which in this case is Australian Central Standard Time, or CST (UT + $9\frac{1}{2}$ hr)

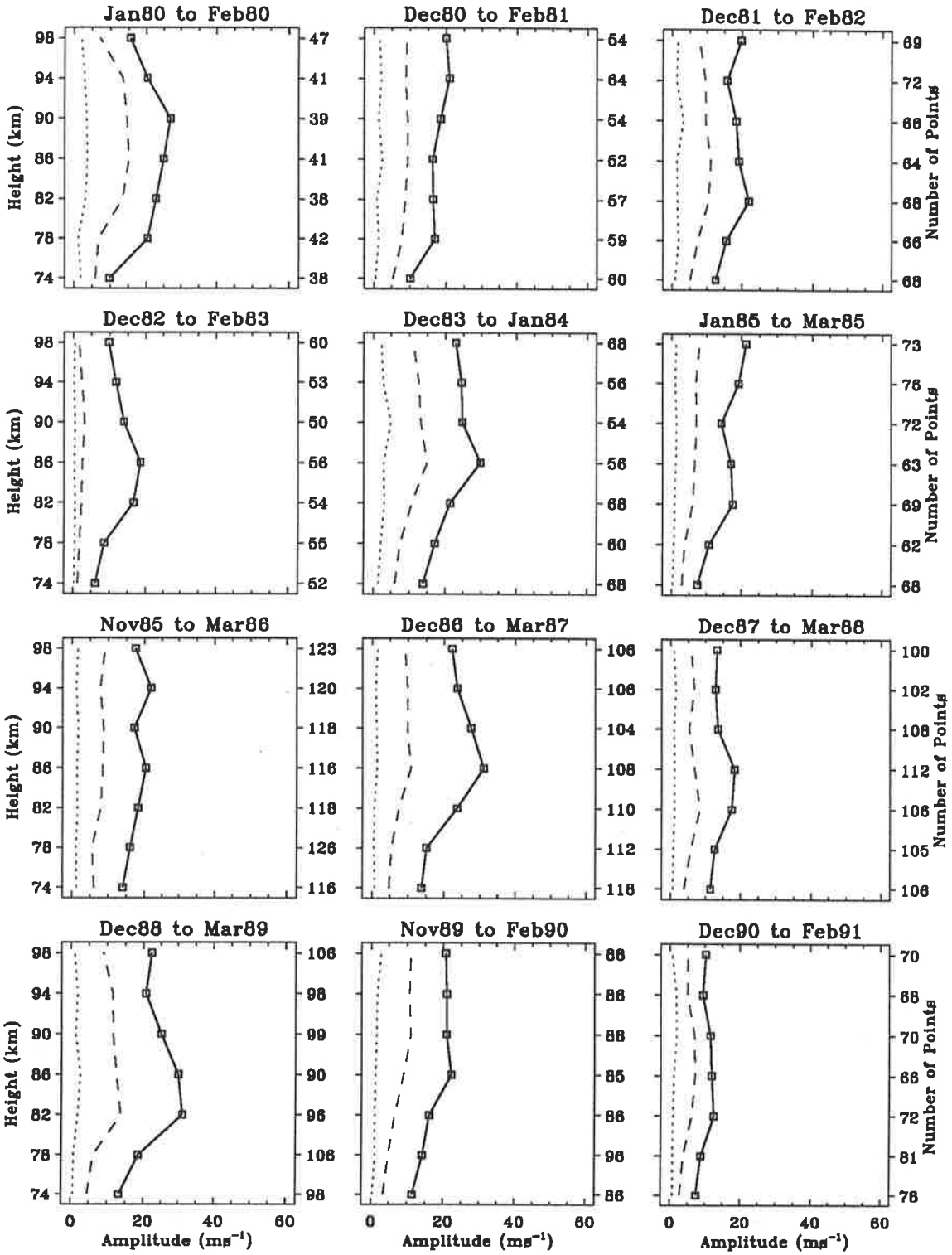

Figure 4.12: Zonal amplitude distribution with altitude for each summer at Adelaide. The thick solid line shows the upper decile values, which correspond with the time interval of maximum wave amplitude. The dashed and dotted lines are the median and lower decile ampliutdes.

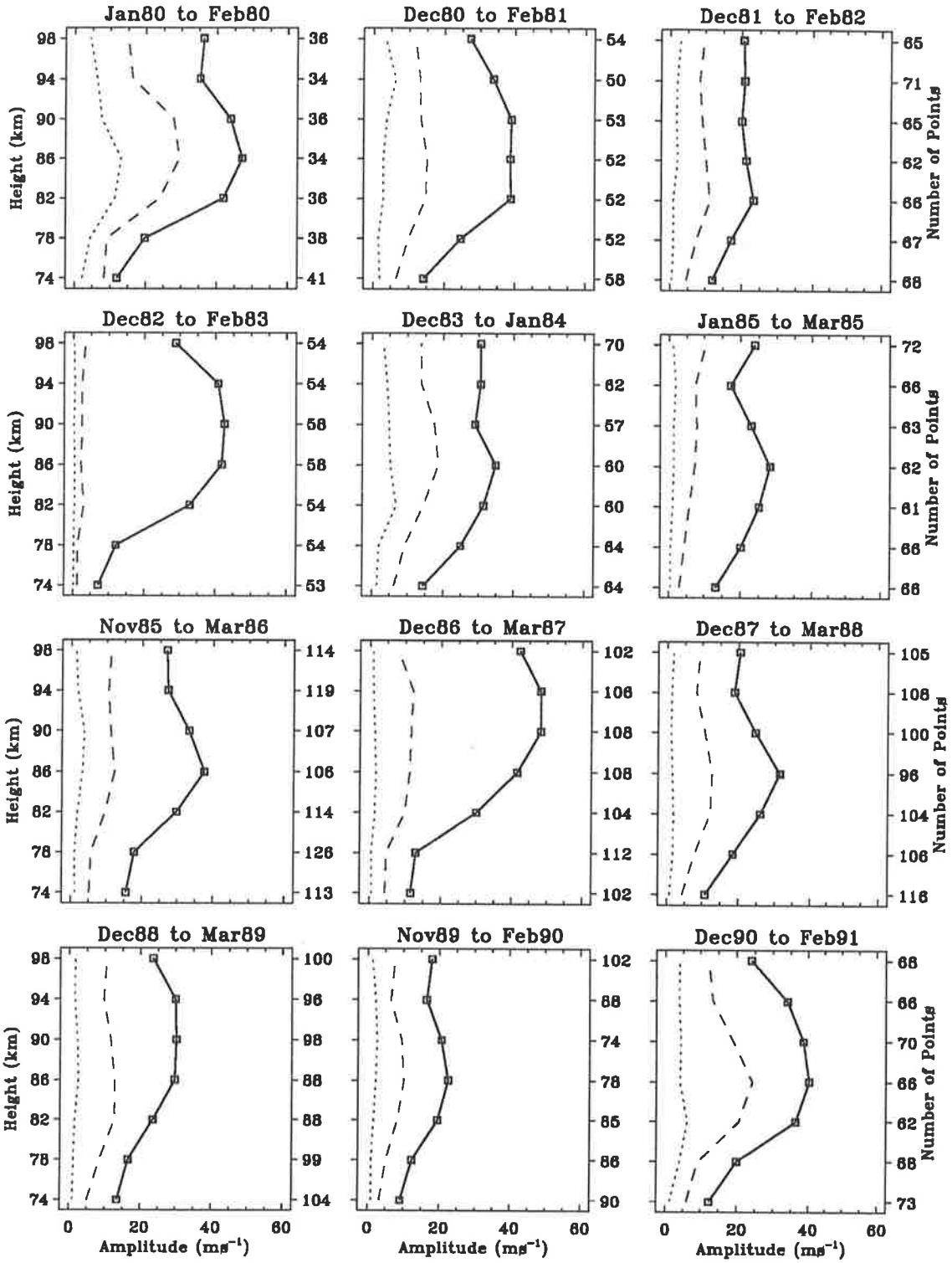

Figure 4.13: Meridional amplitude distribution with altitude for each summer at Adelaide, otherwise the same as Figure 4.12.

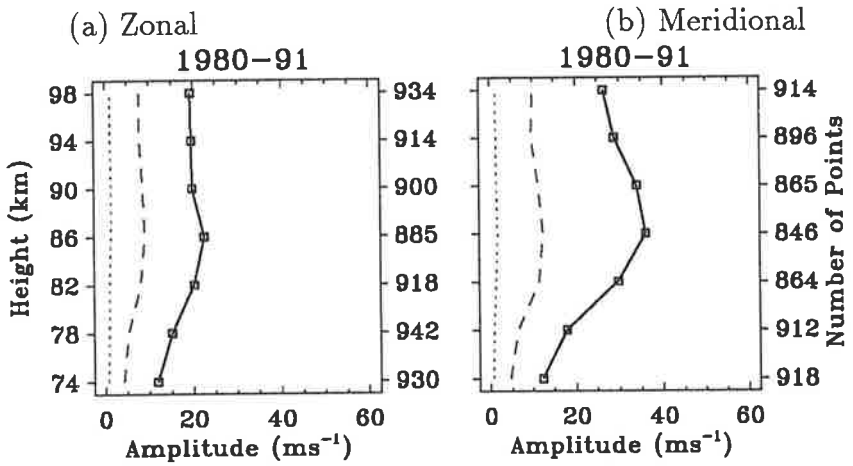

Figure 4.14: Average amplitude distribution with altitude over summer. (a) Zonal, (b) Meridional.

range of most likely phases. If, as the literature suggests, the 2-day wave has a large vertical wavelength at Adelaide then the data from all altitudes can be used in order to increase the statistical reliability of the results. Histograms of the phases for the meridional wind component are shown in Figure 4.15 for each individual summer, and Figure 4.16 for all the summers combined, both using all the data from 74 to 98 km. Zonal amplitudes are small (as shown in Figure 4.12) so that the phase determinations are of dubious quality, reflecting more the random phase due to bandpassing a white noise spectrum rather than some systematic phase due to a wave phenomenon. Random phases would be expected to have a uniform distribution; thus they increase the floor level of the histograms. Phases determined from small amplitude intervals of the meridional component also affect the histograms in Figures 4.15 and 4.16. The reliability of the phase histograms can be improved if the phase estimates associated with intervals when the wave amplitudes are small are ignored. Figures 4.17, 4.18 and 4.19 show how the phase histograms change with increasing cutoff levels for each summer, using the same data as in Figure 4.15 — it can be seen that the first row of Figures 4.17, 4.18 and 4.19 are the same as the histograms in Figure 4.15. Considerable inter-annual variability of the phases are revealed as the cutoff amplitudes are increased. During 1980, 1985, 1986 and 1987 the phases at times of larger wave amplitudes are concentrated around 1200 hr LT while in 1981 and 1983 they are near 1600 hr LT. Some years, such as 1988 and 1991, show a bi-modal phase distribution, with significant[7] peaks at both 1200 and 1600 hr LT. In most cases the phase distribution is largely isotropic until the data for amplitudes $< 20\,\mathrm{ms}^{-1}$ are removed. During some years the phase does not appear to concentrate on any value even when only the larger amplitudes are

[7]The number of counts in each phase bin may be considered a Poisson process. Hence, for a bin with n counts, a sample standard deviation of around $\sqrt{n}$ can be assumed

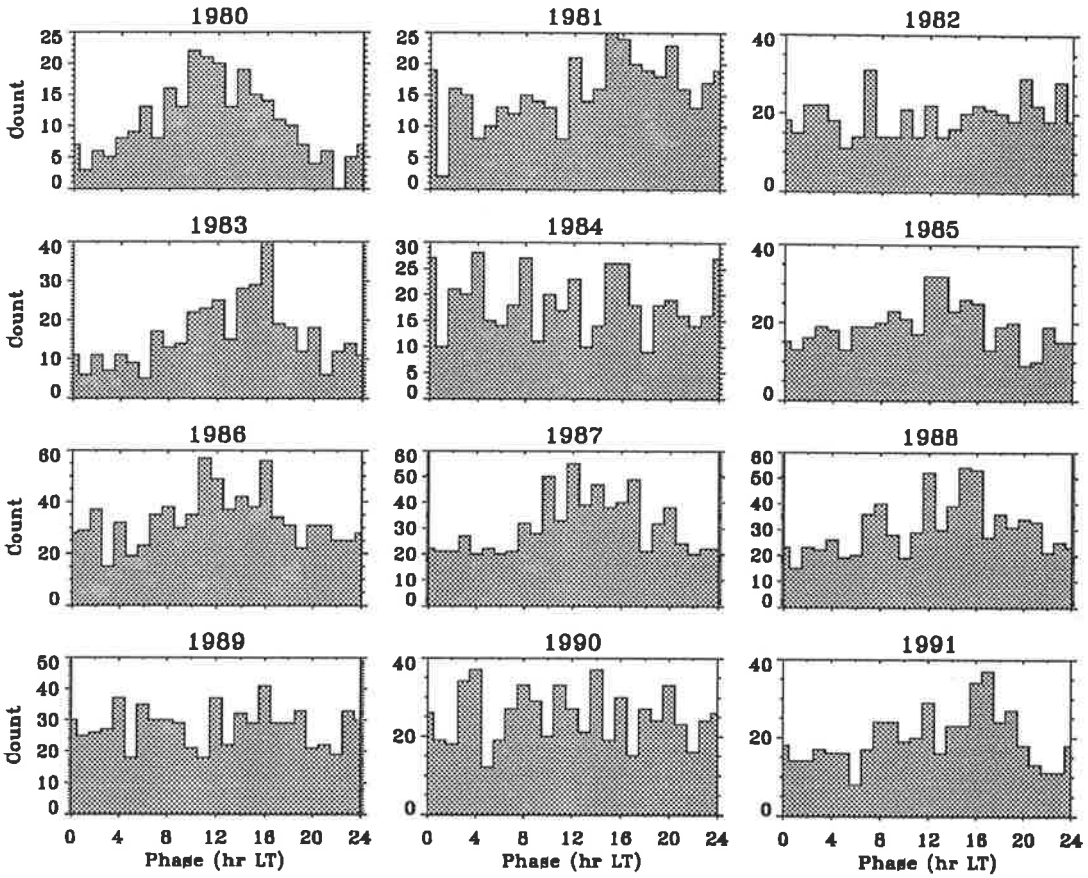

Figure 4.15: Histogram of all the meridional phases for each summer.

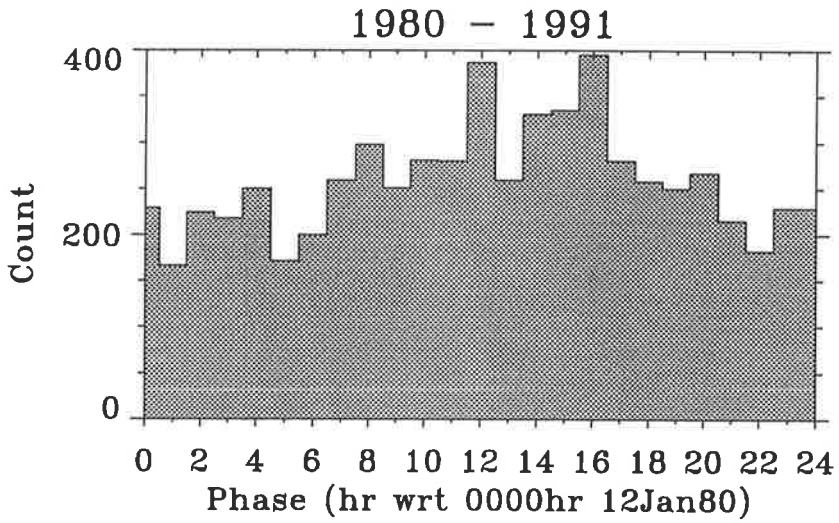

Figure 4.16: Histogram of all the meridional phases.

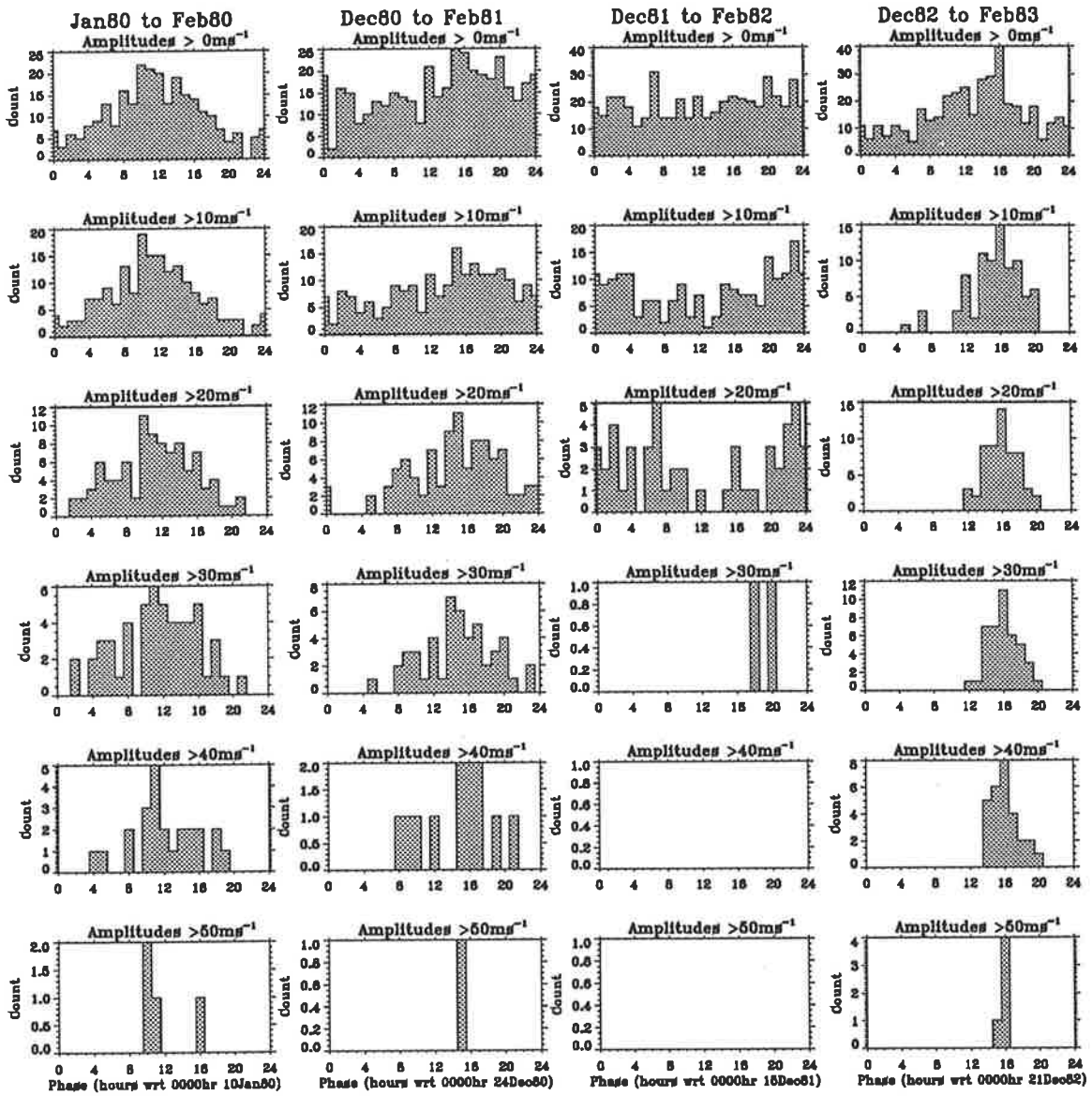

Figure 4.17: Variation in phase histogram with cutoff value for the summers of different years. The time period is shown at the top of each column, with the results of different cutoff levels shown in each row.

considered (*e.g.* 1982, 1984 and 1990) suggesting that the wave period is not 48 hours at these times. A period of 50 hours will give an isotropic phase distribution when measured over at least 12 cycles, which is approximately a month — remembering that the phase in LT ranges from 0 to 24 hours.

Figures 4.21 (individual summers) and 4.22 (all summers combined) show the histograms of the phases, ignoring those values where the wind speed was $< 20\,\mathrm{ms}^{-1}$. The plots in Figure 4.21 are the same as the third row of Figures 4.17, 4.18, and 4.19, and show the features mentioned earlier. In general the most frequent phases are spread from 1000 to 1800 hr, centred on 1400 hr LT.

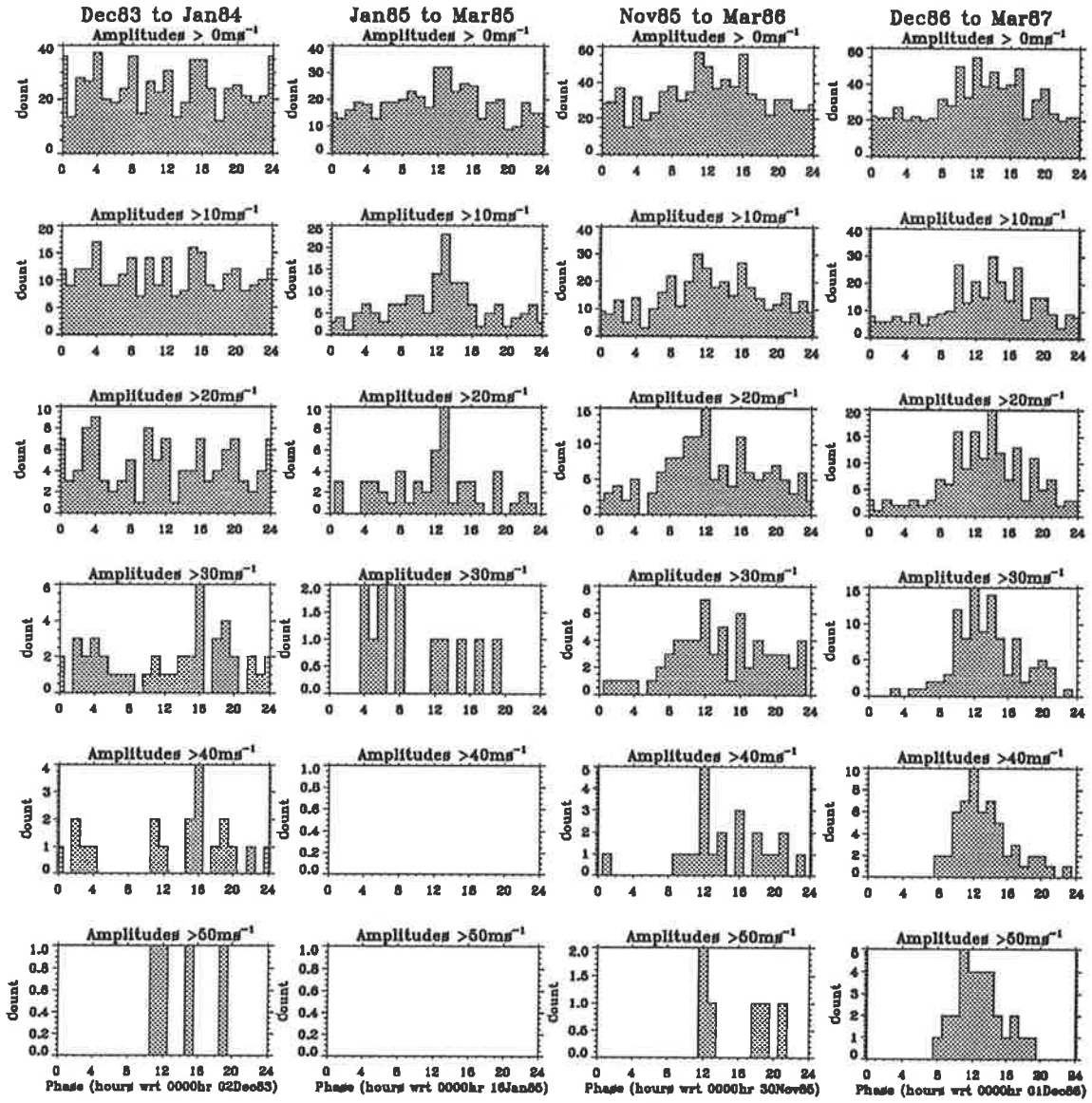

Figure 4.18: Variation in phase histogram with cutoff value for the summers of different years. The time period is shown at the top of each column, with the results of different cutoff levels shown in each row.

Figure 4.20 shows how the histogram of the phase changes with increasing cutoff levels for each season, using data from all altitudes for the 7 years from December, 1983 to February, 1991. All amplitudes are small for the non-summer months so that the phase estimates have a large uncertainty. An isotropic phase distribution is evident, being maintained as the cutoff amplitude is increased. From these results it is doubtful whether a coherent wave is present throughout these months. During the summer months the phases for amplitudes $< 20\,\mathrm{ms}^{-1}$ also have a near isotropic distribution. For amplitudes $< 10\,\mathrm{ms}^{-1}$ this may be due to poor estimation of the phase of the 2-day wave, components at the edge of the bandpass contributing as much to the time series as components near 48 hours. For amplitudes $> 10\,\mathrm{ms}^{-1}$ this should not be the case.

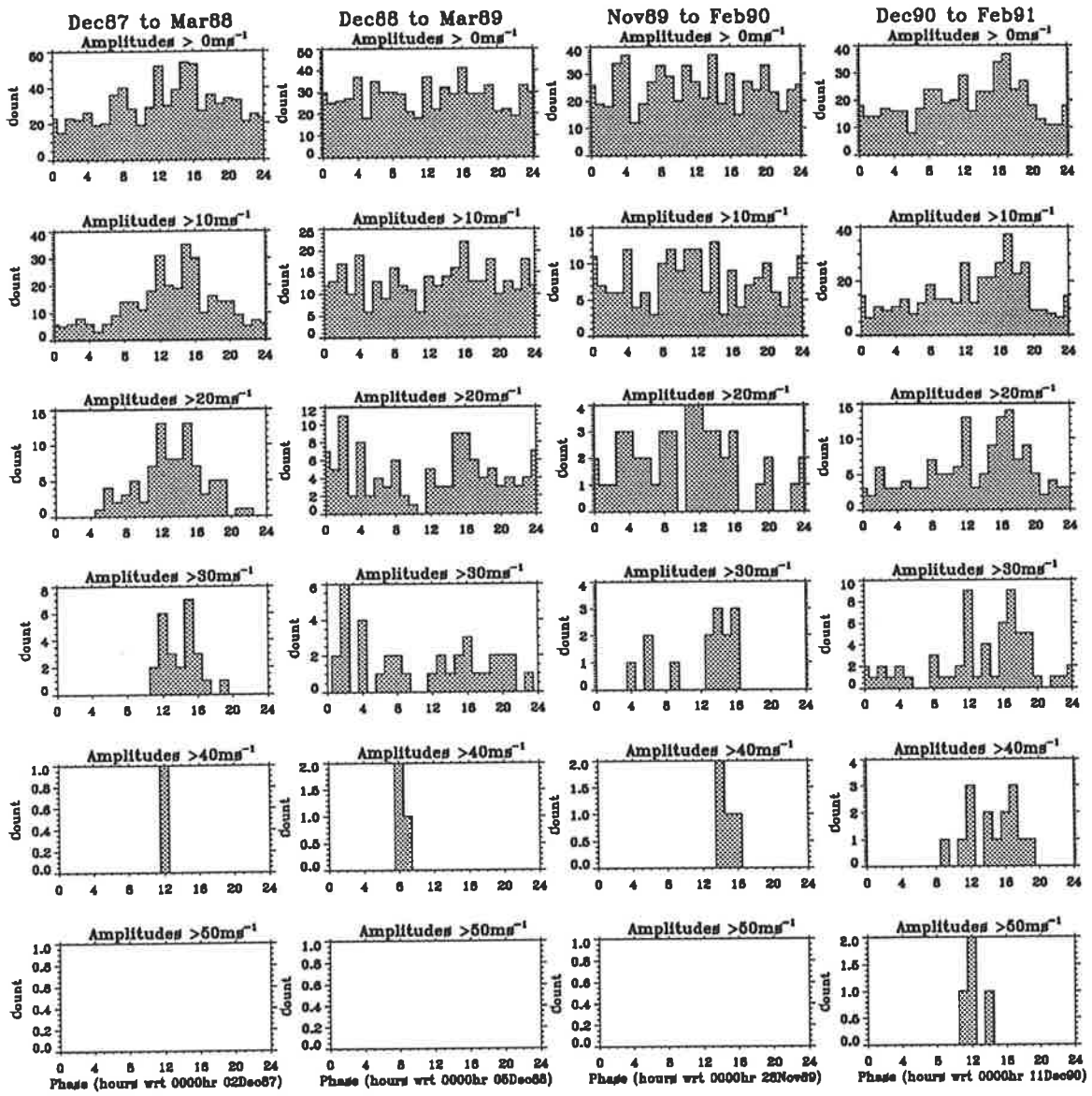

Figure 4.19: Variation in phase histogram with cutoff value for the summers of different years. The time period is shown at the top of each column, with the results of different cutoff levels shown in each row.

Therefore it would appear that during intervals of low amplitude the phase of the 2-day wave is not constant with time, implying either the period is not 48 hours and/or the vertical wavelength is shorter than ~ 40 km (as all the available heights have been used). When the amplitudes are large, so that the wave is more likely to be non-linear, the phase is more constant, implying that the wave period is closer to 48 hours and there is a long vertical wavelength. The summer phases appear to lock 1200 hr LT, becoming more discernable as the amplitude cutoff is increased. This indicates that the 2-day wave has the same preferential phase, during intervals of large wave amplitude, from year to year: a phase locking as first suggested by *Craig & Elford* [1981].

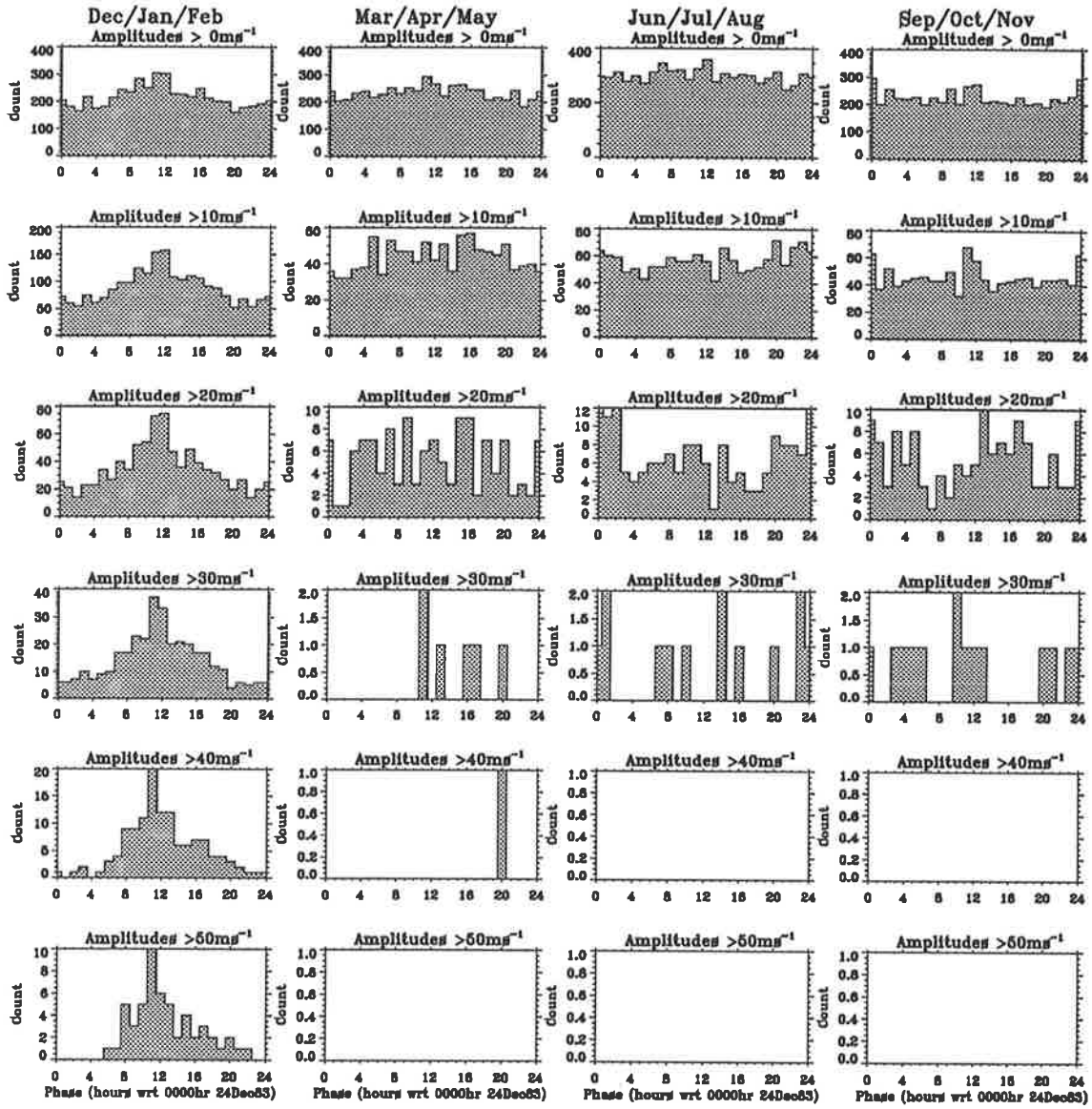

Figure 4.20: Variation in phase histogram with cutoff value for each season. Data from December, 1983, to February, 1991, have been used. The seasons are indicated at the top of each column, with the results of different cutoff levels shown in each row.

4.3.4 The Mean Phase

From the above results it is apparent that the wave amplitude must be considered when determining an average phase for the 2-day wave. An alternative approach to using histograms of the phases is to form a "vector phase", or phasor. The wave amplitude associated with each phase estimate can be used as the magnitude of a vector with the phase giving the angle clockwise from the "12 O'clock" position. The phasors thus formed can be positioned on a phasor diagram (sometimes called a harmonic dial) as in Figure 4.23, with the phase range from 0 to 24 hr being represented by the angles 0 to 360 degrees. A vector mean phasor can then be found.

Figure 4.24 shows the vector mean phase, using data from all altitudes and all summers, as

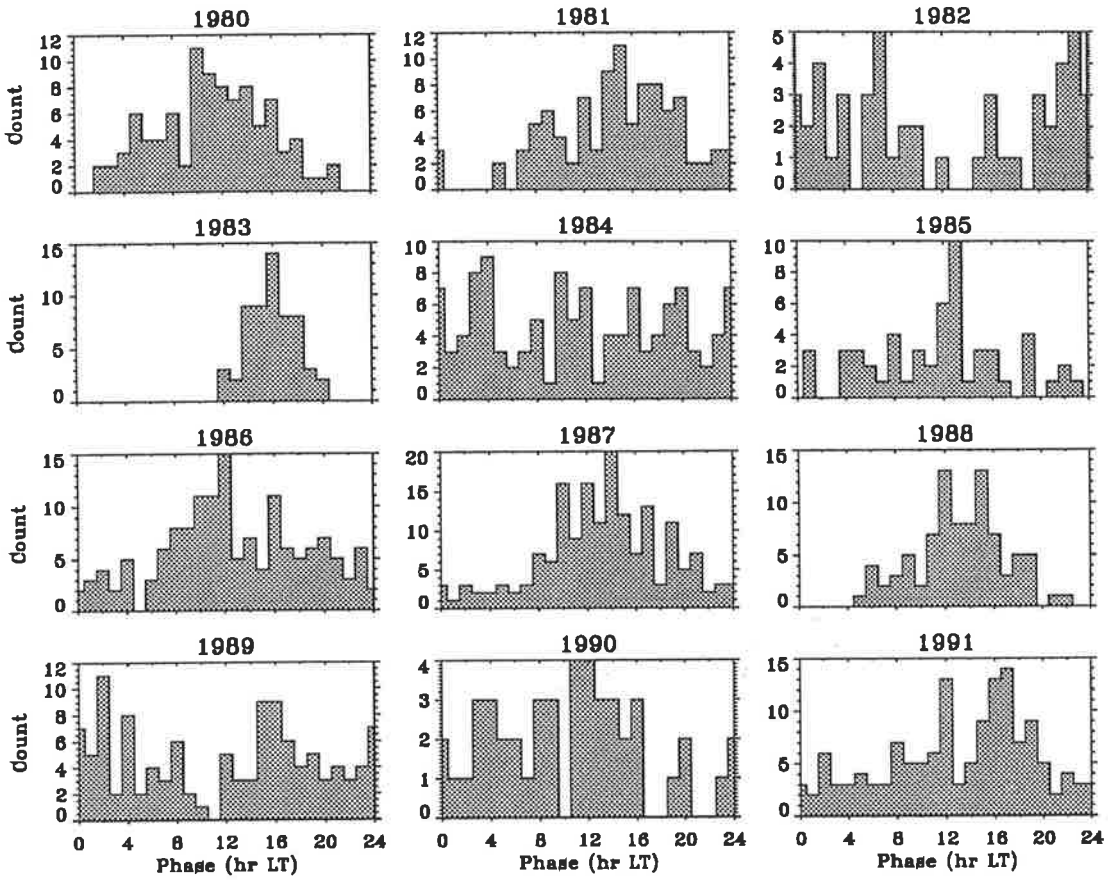

Figure 4.21: Histogram of meridional phases for each summer where the amplitudes exceed $20\,\mathrm{ms}^{-1}$.

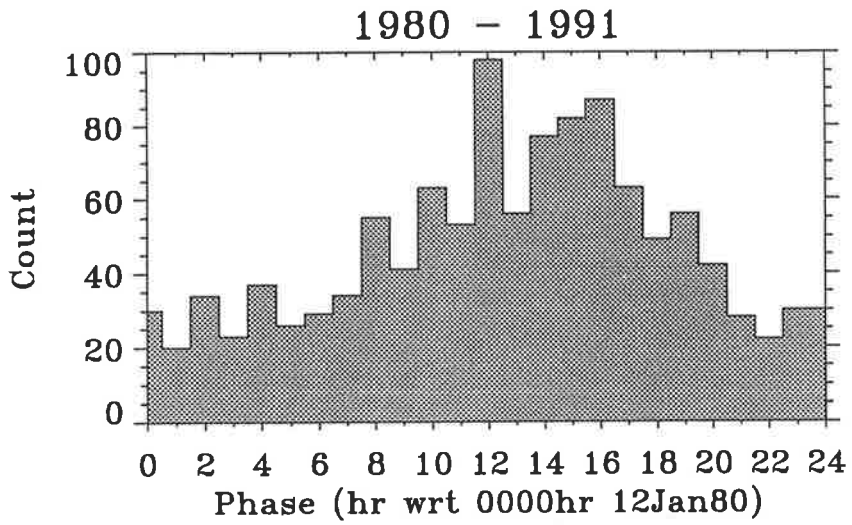

Figure 4.22: Histogram of all the meridional phases where the amplitudes exceed $20\,\mathrm{ms}^{-1}$.

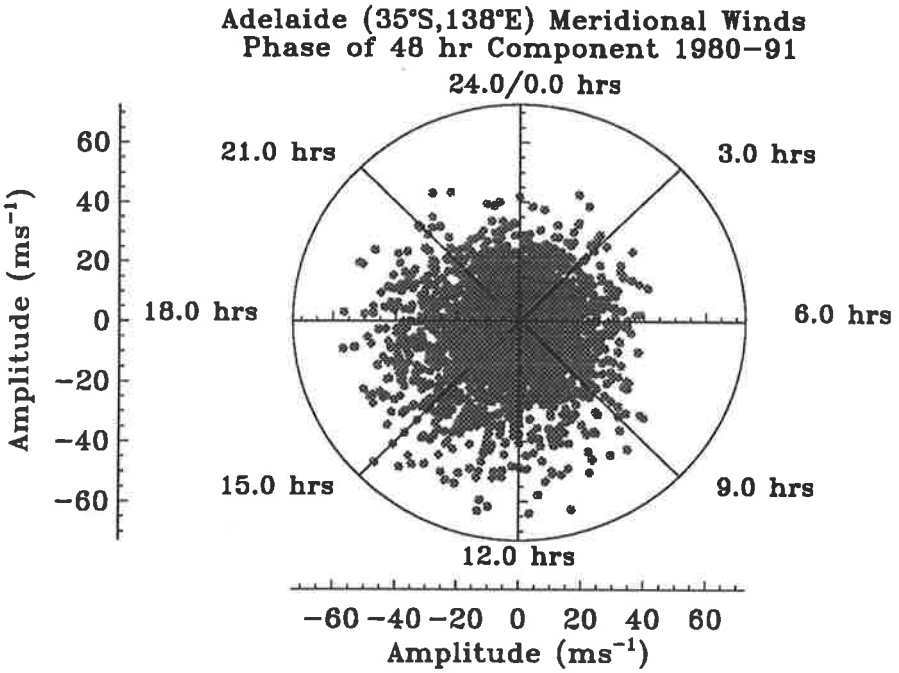

Figure 4.23: Instantaneous phasors scattered on a harmonic dial.

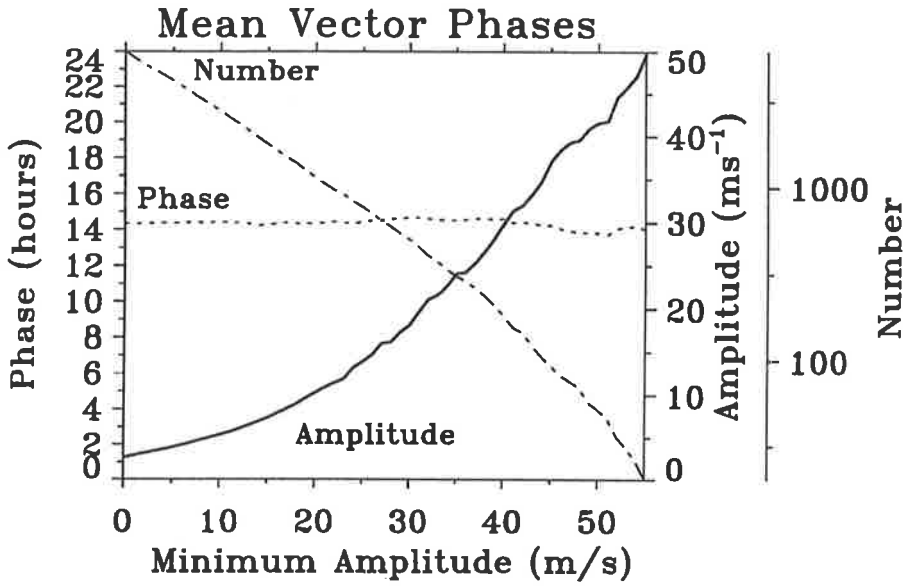

Figure 4.24: Mean amplitude and phase as a function of cutoff amplitude. The number of points in the mean is also shown on a log scale.

a function of the cutoff wind speed. The number of data values used is also shown on the same diagram. The mean phase estimate remains constant with change in cutoff amplitude. This is most likely due to the isotropic nature of the phase estimates when the wave ampltiude is small, which tend to cancel and therefore not contribute to the mean vector phase. The mean amplitude on the otherhand increases with increasing cutoff as expected. This shows that the vector mean phase is robust with respect to "noisy" estimates and is therefore the preferred

choice for further study.

The vector phase representation in Figure 4.23 can be clarified if the data is reformed into a polar histogram. The harmonic dial can be divided into equal angular segments and the data values binned into a range of radii for each. The counts for each bin can then be represented as colours. This is essentially a density plot of the vector phases, necessarily coarse due to the data sparcity in the 2-D plane. Figure 4.25 shows the meridional phases in this form, using data for all heights for each year. The colour scaling is shown on the right-hand side, with the maximum value scale including regions with counts equal to or greater than that value. The contours labelled "90" approximately enclose 90% of the data. Similarly the "50" contour line approximately encloses 50% of the data for each plot. As shown by the previous histogram analysis, here too it can be seen that the phase during intervals of large amplitudes varies from year to year. Some of this variation is due to the period of the wave not being precisely a multiple of 24 hours, as with the smaller amplitudes mentioned on page 121. This causes a spreading of the phase when wrapped as modulo 24, the effect being different for different years and different altitudes. Again, the smaller amplitudes tend to have a uniform distribution of phases as would be expected for a random signal. This is consistent with the previous histogram analysis. Figure 4.26 combines all the data in the one polar histogram for both the zonal and meridional components. This differs from figure 6 of paper-1 in that data from all the altitudes from 74 to 98 km have been used here, whereas only those from 84 to 96 km — where the ampltitude of the 2-day wave is largest — were used in that figure. As the 2-day wave is weak in the zonal, the phases are dominated by noise resulting in a largely uniform distribution. From Figure 4.26 it can be seen that waves with larger amplitudes tend to have phases in the afternoon quadrant from 1000 to 1600 hours LT, although the number of occurrences of larger amplitudes are fewer in the zonal component.

The vector mean phase as a function of altitude for each summer is shown in Figure 4.27. It differs from figure 7 of paper-1 in that the zonal phases in that figure had some good data erroneously removed prior to the mean vector calculation. This has been corrected in Figure 4.27. The differences introduced are small, the correct phases tending to emphasis the departures from 1200 hr LT. Figure 4.28 shows the results for all the summers. A preference for a mean phase between 1200 and 1600 hours LT is indicated, the mean phases over all altitudes and summers being 13 ± 3 hr and 14.4 ± 0.8 hr for the zonal and meridional components respectively. The consistency of the mean phase with altitude for the meridional component suggests that the individual errors have been over-estimated. During 1982, 1984, and 1990, the change in

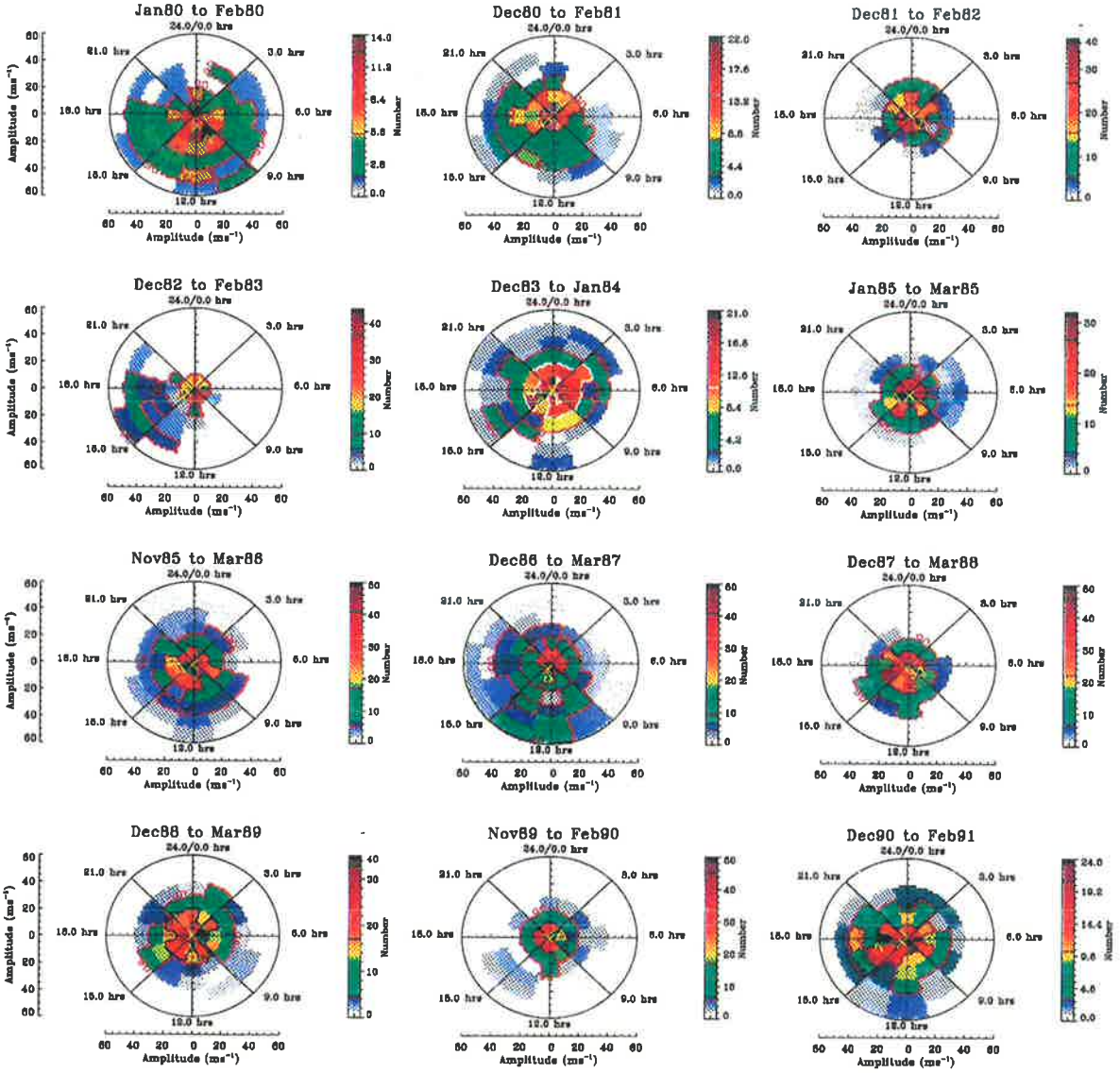

Figure 4.25: Polar histograms showing the strength (ms^{-1}) and phase (0-24 hours LT) of the meridional component of the 2-day wave using broad-band filtered wind data for each summer from 1980 to 1991. The bandpass used was 32 to 96 hours. The bin size is 2 hours by $10\,ms^{-1}$, with all the data from 74 to 102 km included. The number of occurrences in each bin is colour coded and shown on the right-hand side of each plot.

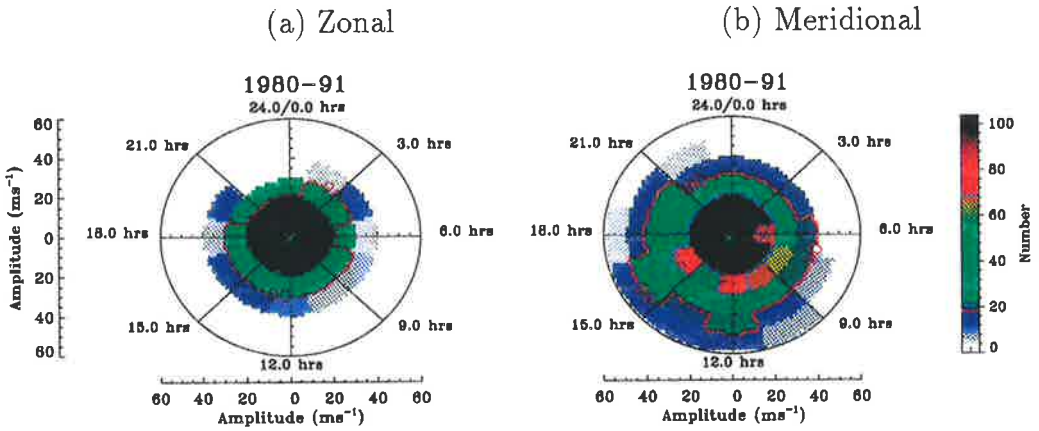

Figure 4.26: A polar histogram as for Figure 4.25 but combining all the wind data shown in that figure. The bin size is the same (2 hours by $10\,\mathrm{ms}^{-1}$). Again, the number of occurrences in each bin is colour coded, where the darkest shade represents 100 or more counts. (a) Zonal (b) Meridional component.

phase with altitude suggests vertical wavelengths $\leq 80\,\mathrm{km}$, whereas a much larger wavelength ($\geq 150\,\mathrm{km}$) is indicated for the other years. The actual values are tabulated in Table 4.1 in Section 4.3.7. The variation of the mean phase with altitude for all the summers suggests an average vertical wavelength $\geq 150\,\mathrm{km}$. From Figure 4.13 and Figures 4.17, 4.18 and 4.19 it is clear that the amplitude of the 2-day wave is small during 1982 and 1990. This possibly means that the 2-day wave structure is significantly different when the amplitudes are large or *vice-versa*. The short vertical wavelength is most likely responsible for a large portion of the spread seen for these years in Figures 4.17, 4.18 and 4.19.

If there is some form of phase-locking of the 2-day wave, this raises the question of whether the actual days of maximum northward winds are related from one year to the next. Notice from Figure 4.11 that the 2-day wave appears to be in anti-phase, in general, from one year to the next. This is deceptive since the data have been plotted in calendar days, but the actual relationship between cycles in one summer compared to the next depends on the number of days (hence cycles) separating the two. A non-leap year has an odd number of days whereas a leap year has an even number. If the wave existed as a single structure throughout the year then it would be expected that on the same *day of the year* (*e.g.* 17, meaning 17^{th} January) for consecutive years the wave would be in-phase, if the first year was a leap year, or otherwise in anti-phase. On the whole, this appears to be the case. A notable exception is the phase relationship between the summers of 1987, 88 and 89. From the foregoing it would be expected that 1987 and 1988 would appear to be in anti-phase (as 1987 is a non-leap year) while 1988 and 1989 would be in-phase (since 1988 is a leap year). In fact 1987 and 1988 are in-phase while

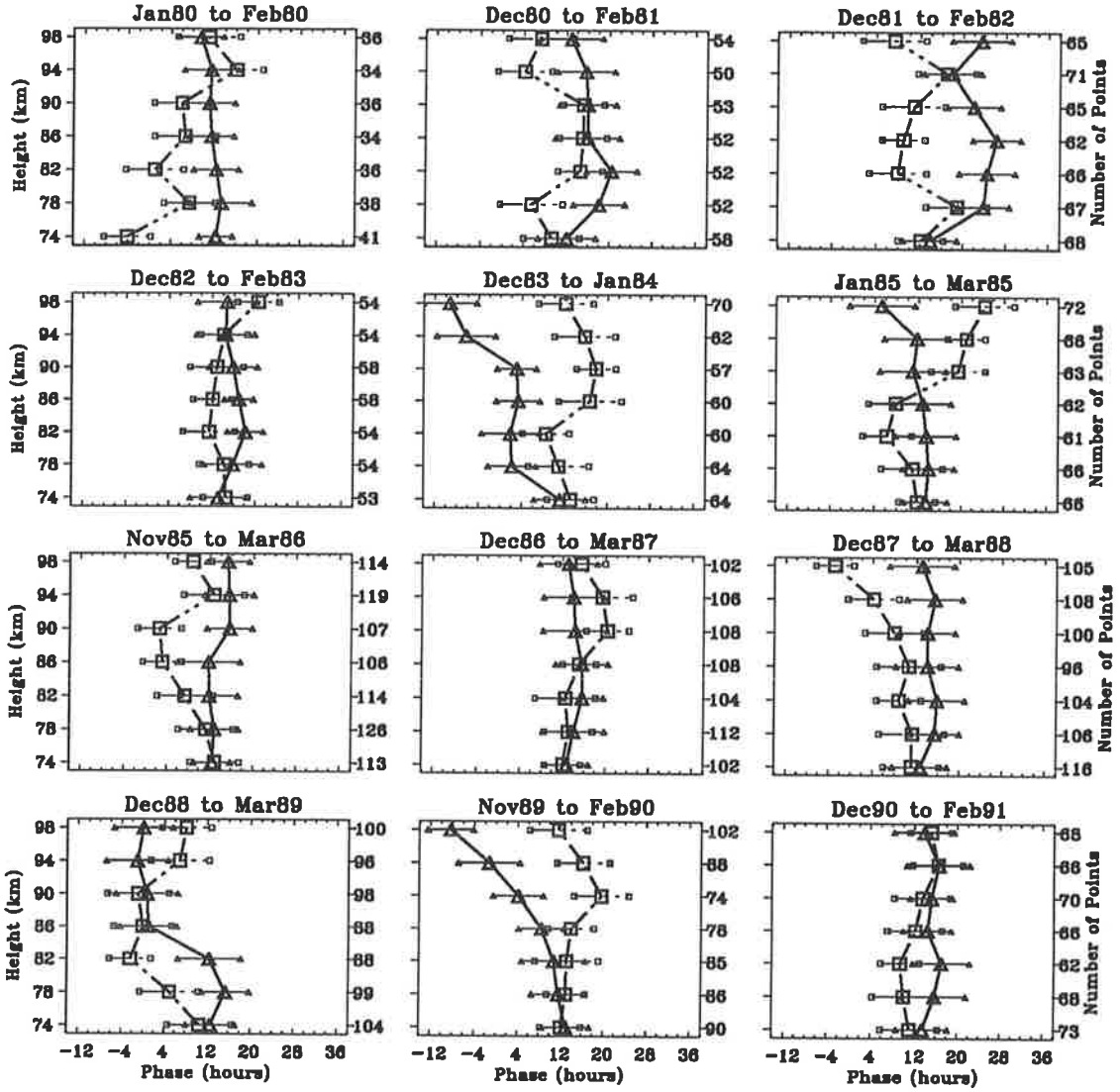

Figure 4.27: The vector mean phase (in local time), with one sample standard deviation error bars, of the 2-day wave for each summer from 1980 to 1991. The zonal component is shown as dash-dotted line with square symbols, the meridional as a solid line with triangles. The number of data points used in each mean is shown on the right-hand side of each plot.

1988 and 1989 are in anti-phase.

In their figure 7, *Craig & Elford* [1981] show the scatter of the mean vector phases of the meridional component of the 2-day wave for 1961, and 1966 to 1975, derived from approximately 10 days of meteor observations during each January from St. Kilda near Buckland Park. In order to compare the phases for 1980 to 1991 with the earlier years the mean vector phase of the meridional component was found in as similar a fashion as used for the meteor data. The average was computed over all heights using data only from the time intervals when the 2-day wave was at its largest amplitude for each summer. The resulting values differ slightly from those in Figure 4.28, where data for all of each summer were used. The vector mean phases for 1980 to

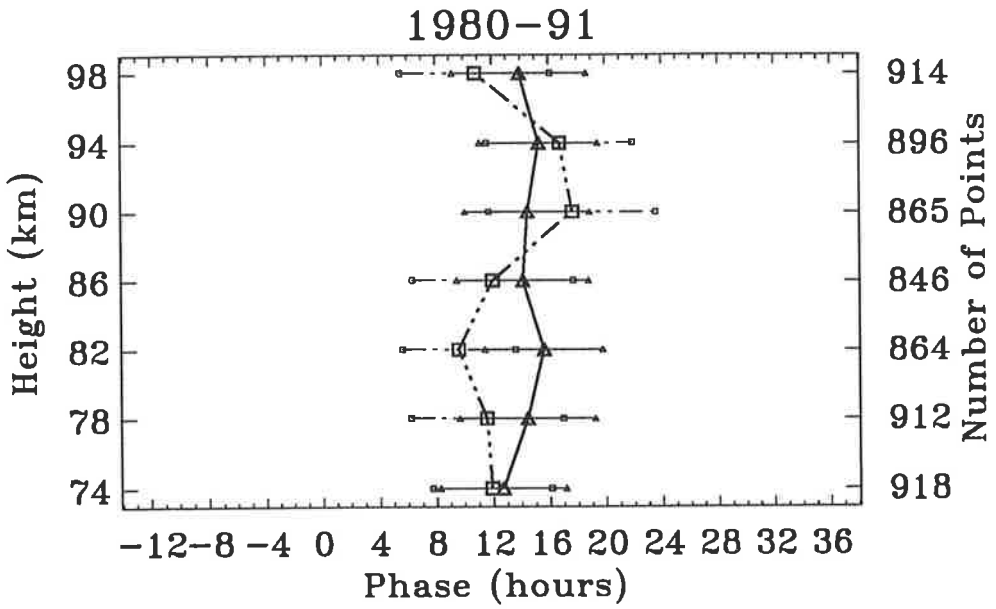

Figure 4.28: The vector mean phase (in local time), with one sample standard deviation error bars, of the 2-day wave using all the summers from 1980 to 1991. The zonal component is shown as dash-dotted line with square symbols, the meridional as a solid line with triangles. The number of data points used in each mean is shown on the right-hand side of each plot.

1991 have been plotted in Figure 4.29 (solid circles) along with those for 1961, and 1966 to 1975, taken from *Craig & Elford* [1981], figure 7 (open circles). The vector mean of the combined data set has a phase of 1342hr LT. A most probable error ellipse [*Chapman & Bartels*, 1940] has been plotted to assist with determining the significance of this. There is a 50% probability that any data point will lie within this error ellipse. The extra data in Figure 4.29 have reduced the size of the error ellipse from that in *Craig & Elford* [1981], but have not changed the orientation nor the mean phase significantly. These results are in good agreement with the phases found earlier.

4.3.5 Phase Relationships

From the polar histograms in Figure 4.26 it would appear that the zonal phase distribution is very similar to the meridional. Moreover, the mean phase plots (Figures 4.27 and 4.28) perhaps suggest that the zonal and meridional 2-day wave components are nearly in-phase.

The bandpass filtered winds are not purely sinusoidal, often having multiple peaks within a cycle due to the interaction of different frequency components within the broad 2-day wave spectral peak. In the previous analysis these form statistical fluctuations in the phase estimates. As the fluctuations are not the same for both the zonal and meridional components the bandpassed data is not suited for calculating instantaneous phase differences. An alternative approach for

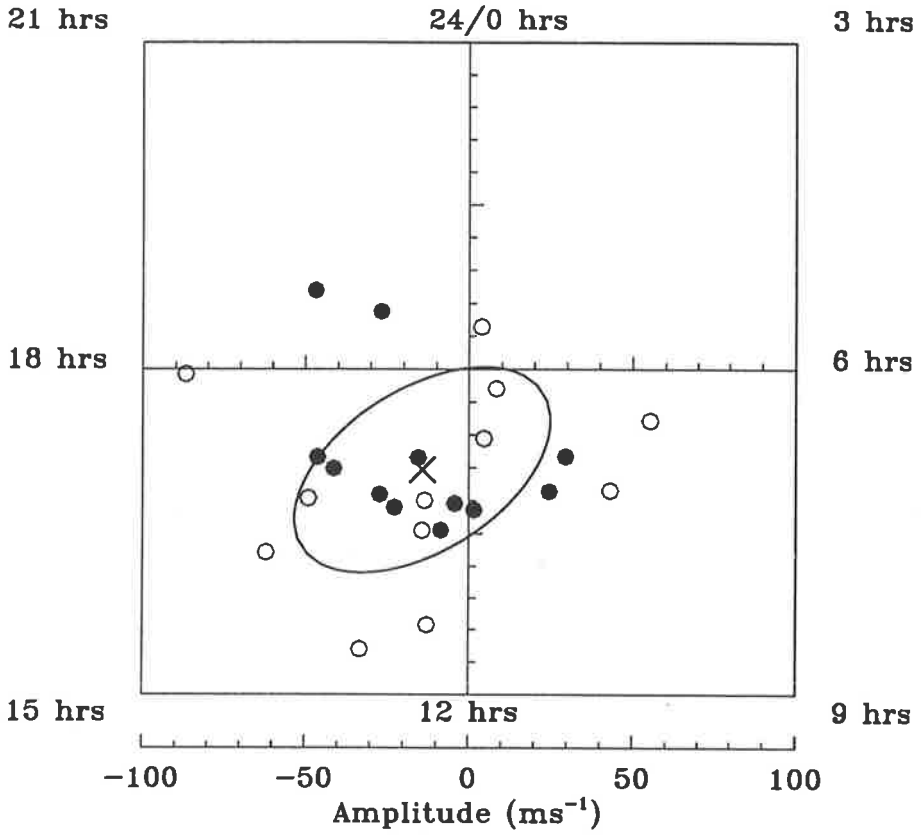

Figure 4.29: Polar plot of the amplitude and phases of the quasi-two-day wave meridional oscillations. The vector mean phases for the summers of 1980 to 1991 are shown as solid circles, while those for 1961, and 1966 to 1975, taken from *Craig & Elford* [1981], figure 7, are open circles. The mean and the error ellipse have also been plotted.

determining the phase of the 2-day wave was therefore developed. This involved least-squares fitting a sinusoid to each 48 hour cycle of the bandpassed data for each component and noting the phase. That is, a cosine function, $A\cos(2\pi f\tau + \phi)$, with $f = 0.5$ cpd, was fitted to the data for each day using a least-squares method, and the amplitude, A, and phase, ϕ, determined. This gave equivalent results to simply choosing the local time of maximum positive amplitude of the bandpassed time series. Inspection of Figure 4.30 — which shows the sinusoidal fits overlayed on the bandpassed data for a typical selection of cycles in 1991 — indicates that the phase of the sinusoids were a very good approximation to the phase of the 2-day wave for more than 90% of the time. The phases for the summer of 1991 are shown in Figure 4.31. Note that the phases are expressed in LT so are cyclic around a 24 hr period rather than the 48 hr period that might be expected. The phases in Figure 4.31 have been "unravelled" so that there are no discontinuities. It can be seen that the zonal and meridional phases are indeed quite different, apparently being as often in-phase as in anti-phase. Forming the instantaneous differences of the phases (meridional minus zonal), taking care to use phases from the same cycle of the

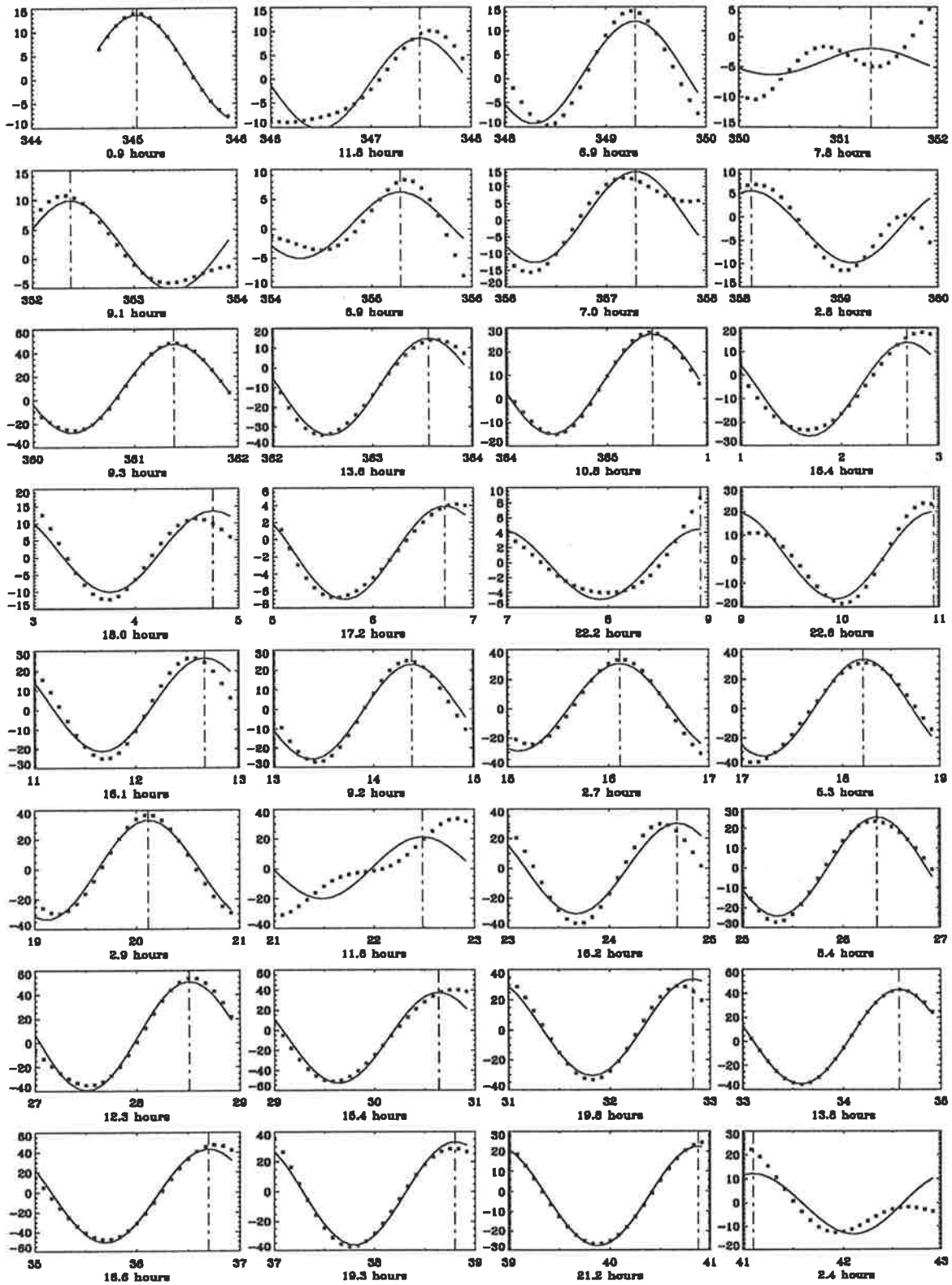

Figure 4.30: Sinusoidal fits overlayed on the bandpassed data for the meridional component of the 2-day wave during the summer of 1991. All cycles for that summer are shown. The numbers along the x-axis indicate the day-of-year, starting on day 344 of 1990, and ending on day 43 of 1991. The phase determined from the sinusoidal fit is plotted as a vertical line on each plot, the actual value being shown below.

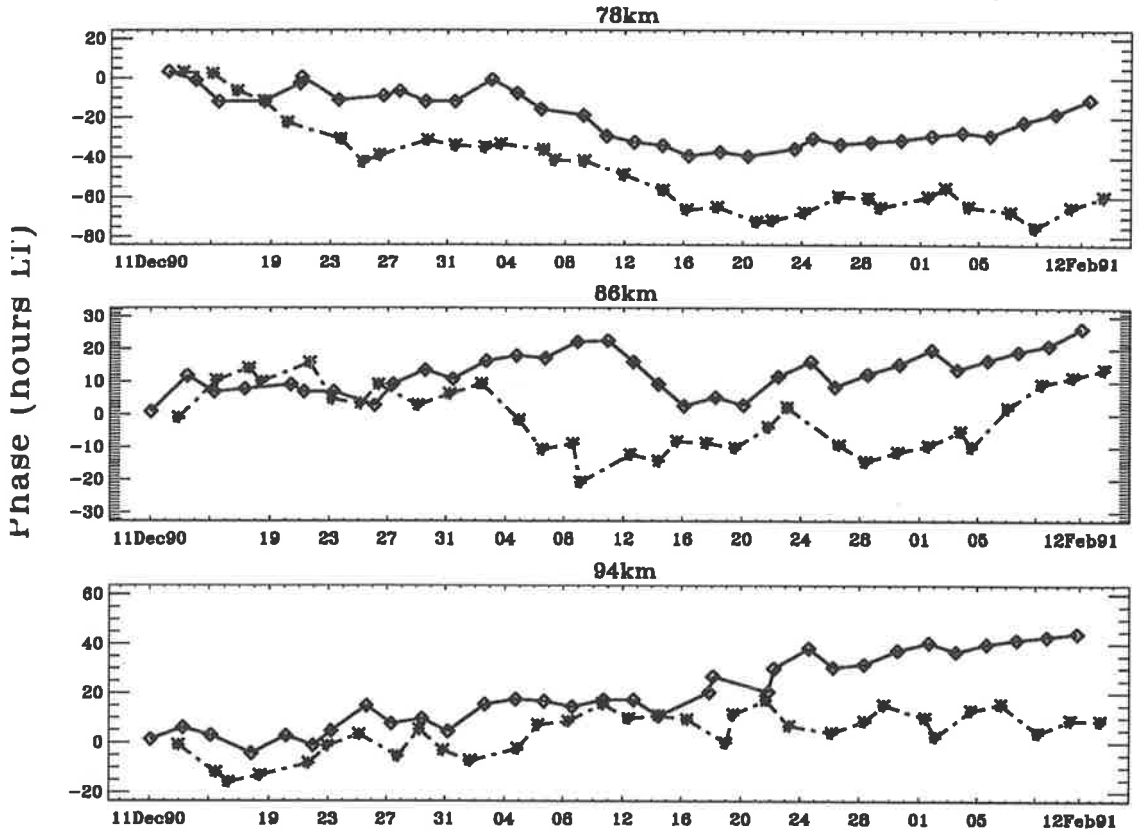

Figure 4.31: The relative phases of the zonal (dot-dashed line with crosses) and meridional (solid line with diamonds) components of the 2-day wave for 78 (top), 86 (middle) and 94 km (bottom), during the summer of 1991.

wave, the histograms in Figure 4.32 were obtained for each year. A combined histogram of the phase differences for all years is shown in Figure 4.33. In all cases the zonal wind component appears to lead the meridional by anywhere from 0 to 15 hr most of the time. *Plumb et al.* [1987] determined that the components of the 2-day wave during the summer of 1984 were roughly in phase-quadrature. Here it is found that the phase relationship is time dependent, generally being between in-phase and phase-quadrature.

The zonal component of the 2-day wave usually maximises several days earlier than the meridional (*c.f.* Figure 4.9) so that the mean vector phase over the summer can be the same for both yet the instantaneous phases may differ. It is interesting in itself that the distribution of the phases are similar, and that the instantaneous phase difference is small. This has implications to the horizontal transport of horizontal momentum investigated in Section 4.5.3.

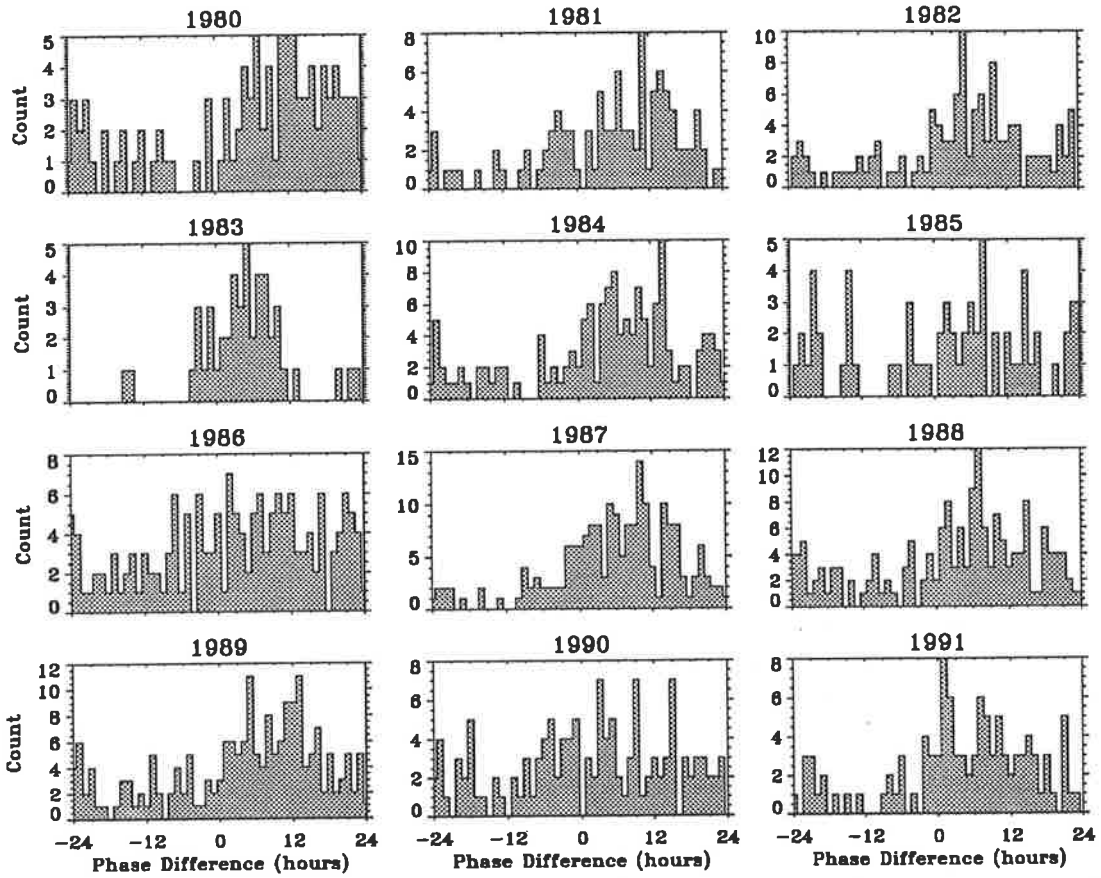

Figure 4.32: Histogram of the instantaneous phase differences between the zonal and meridional components for each summer from 1980 to 1991, for all altitudes from 74 to 98 km.

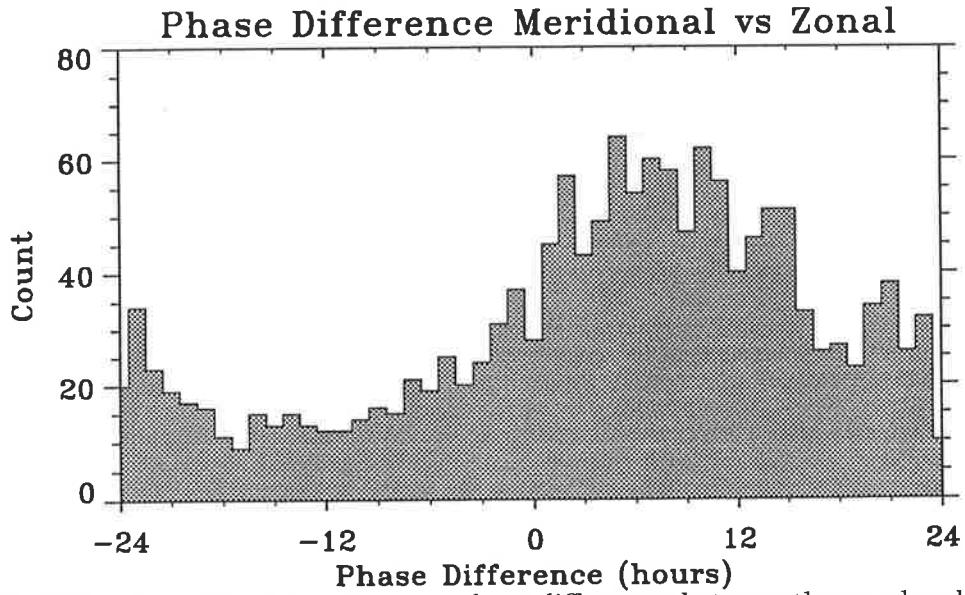

Figure 4.33: Histogram of the instantaneous phase differences between the zonal and meridional components for all the summers of 1980 to 1991, for all altitudes from 74 to 98 km.

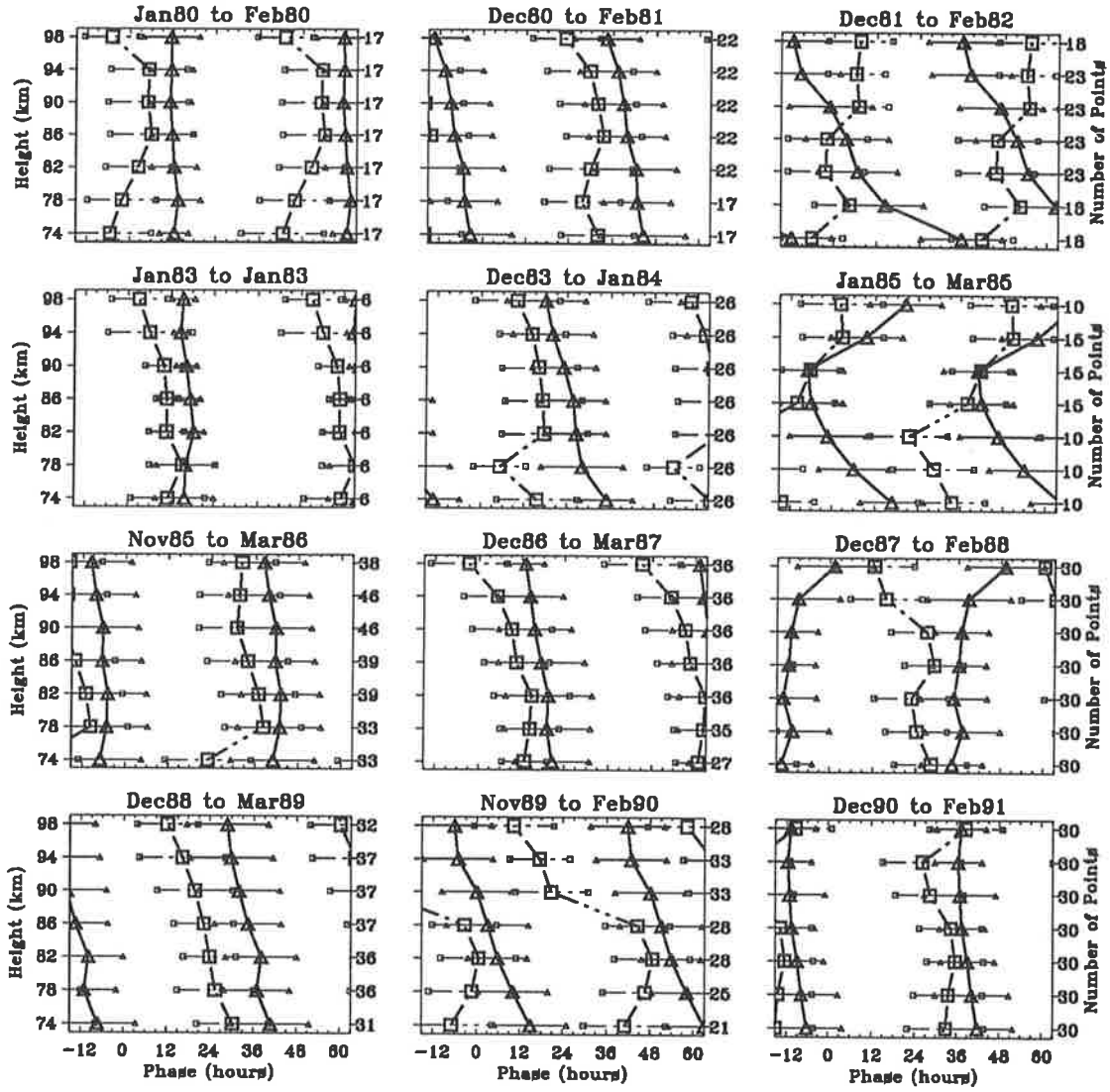

Figure 4.34: The vector mean phase (in wave periods), otherwise as for Figure 4.27.

4.3.6 The Mean Phase Revisited

In Section 4.3.2 the 24 hr (or half a cycle) ambiguity of the phase estimates, and the reason for estimating the phase in this way, were discussed. Section 4.3.5 has removed this ambiguity, concluding that the wave components are more in-phase than anti-phase. It would be reassuring to confirm that expressing the phases in LT has not biased the estimates of the mean. This can be done if the phases are expressed as fractions of cycles and the means found. The phases from the bandpassed data could be used to do this as outlined in Section 4.3.2. As the required values have already been calculated in Section 4.3.5 using the sinusoidal fits to the bandpassed data, it is more convenient to use those. Finding the mean vector phase for each summer as before, where the phases now range from 0 to 48 hr, or one cycle, Figure 4.34 is obtained. This can be compared directly with Figure 4.27. Notice that the number of data points used for the

mean phases in the current figure are $\sim 1/3$ of those used in Figure 4.27 (see the discussion at the end of Section 4.3.2, page 109). The time labels also differ for some summers (*e.g.*1983). This is due to the different data rejection criteria applied to the sinusoidal fits as opposed to the previous phase determination method. In interpretting Figure 4.34 it must be remembered that each point can be ± 24 hr from the corresponding point in Figure 4.27. With this in mind the mean zonal and meridional phases for the summers all compare favourably, the major differences being the association of the phase to the cycle. That is, for two adjacent heights, whether to join the mean phases for points separated by ~ 24 hr in the positive or the negative sense; does the next phase point correspond to the cycle before or the cycle after? This is most marked for the summer of 1982 where a slight displacement of the phase value for 78 km has caused the phase continuity algorithm to decide that that phase must correspond to an earlier cycle than the phase for 74 km. Two cases show marked differences: the meridional mean phases above 90 km for the summer of 1985; and the zonal phases above 82 km for the summer of 1987.

The favourable comparison between Figures 4.27 and 4.34 gives confidence in the measure of the phases in the previous sections.

There is no point in comparing the mean vector phases for the combined summers for the reasons mentioned in Section 4.3.2.

4.3.7 Vertical Wavelengths

Using the rate of change of the mean phase with altitude in Figures 4.27 and 4.34 the vertical wavelength can be estimated. These have been tabulated in Table 4.1 along with the maximum upper decile wave amplitude. The phases in Figure 4.34 appear to have more continuity with altitude giving more reliable vertical wavelength estimates. As already mentioned, their form is consistent with the phases of Figure 4.27. Even so, the error in the wavelength estimates may be as large as 50 % using the error bars for each phase point. It can be seen from Table 4.1 that during the summers of small maximum wave amplitude (1982, 1985 and 1990) the wavelengths derived from Figure 4.34 are also small, being ~ 40 km. This is consistent with the discussion on page 121 regarding the phase distributions. As mentioned in the discussion on page 125, the variation of the mean phase with altitude for all the summers (see Figure 4.28, in Section 4.3.4) suggests an average vertical wavelength ≥ 150 km.

Summer	Vertical Wavelength (km)		Max 90%ile	
of	from fig. 4.27	from fig. 4.34	Ampl. (ms^{-1})	Height (km)
1980	> 150	> 150	47	86
1981	> 150	96	40	86
1982	82	43	23	82
1983	> 150	> 150	42	90
1984	64	64	42	82
1985	> 150	24	27	86
1986	> 150	> 150	35	86
1987	> 150	> 150	48	90
1988	> 150	96	31	86
1989	> 150	96	30	90
1990	50	55	22	86
1991	> 150	> 150	38	90

Table 4.1: Vertical wavelengths and maximum upper decile amplitudes for the 2-day wave for the 12 summers from December, 1979 – February, 1980 to December, 1990 – February, 1991. The last two columns show the value and altitude of the maximum upper decile wave amplitude.

4.3.8 The Mean Period

A complex demodulation technique was used to find the period for the 2-day wave as a function of time by the method described in Section 2.7. No period estimates were made for the intervals where data was missing. The amplitudes of the 48 hr complex demodulated time series for both the zonal and meridional wind components from January, 1984, to January, 1991, for the altitudes from 78 to 98 km, are shown in Figures 4.35 and 4.36 respectively. Note that the amplitude scales are different in the two figures. Due to the finite resolution required for the plot, the fine structure of the temporal variations in the amplitude have been lost. This has a similar effect as applying a smoothing to the displayed amplitudes. Thus the maximum values are not a true reflection of the real maxima, having values no larger than 50 ms^{-1} in the meridional component. The true demodulated meridional maxima are more of the order of 70 ms^{-1}, but may only last a few cycles, less than 0.2 mm in this figure. These amplitudes are also smaller than those observed in the bandpassed winds. Much of this can be accounted for by the difference in the effective bandpasses; the demodulated amplitudes coming from a much smaller bandwidth. Therefore Figures 4.35 and 4.36 are best interpreted as relative amplitudes. Nevertheless, the recurrence of the 2-day wave can be seen quite clearly in the meridional amplitudes. Figures 4.37 and 4.38 show the demodulated phase over the summer of 1991 for a 48 and 51 hr demodulation period respectively. The effective bandpasses used were 43.9 to 53.0 hr for the "48" hr demodulation (156 degrees of freedom), and 46.6 to 56.9 hr for

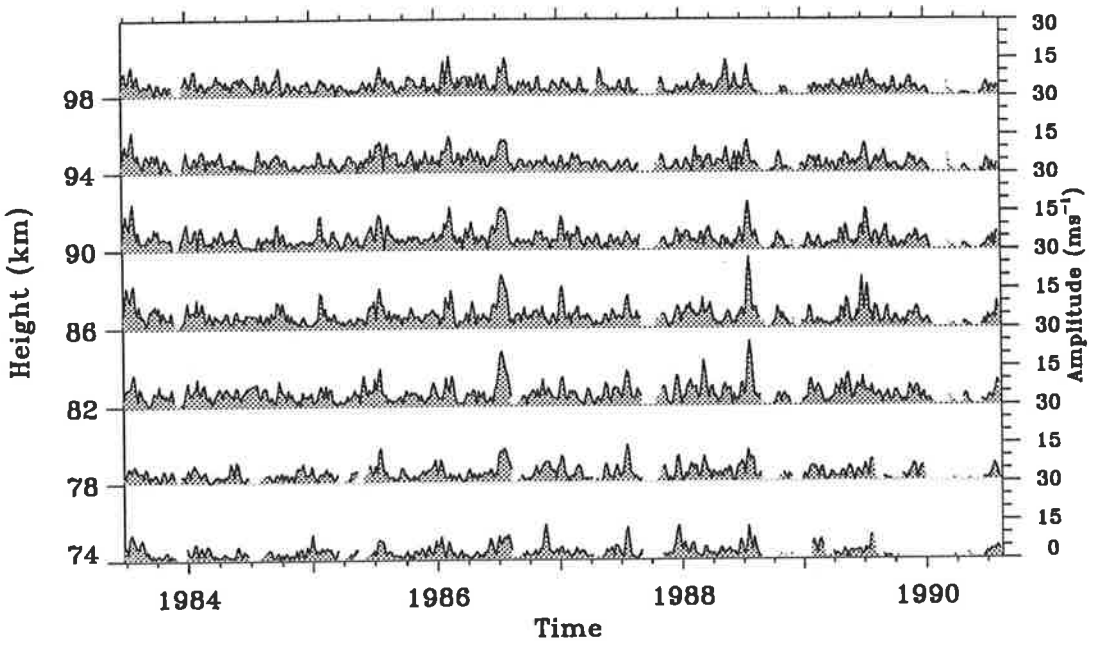

Figure 4.35: The amplitude of the zonal component of the 2-day wave from a complex demodulation procedure for the altitudes indicated on the left-hand side. The amplitude scale is indicated on the right-hand side. An effective bandpass from 43.9 to 53.0 hr was used, giving 156 degrees of freedom. The major ticks mark the middle of each year, so that the time period shown extends from the beginning of January, 1984, to the end of January, 1991.

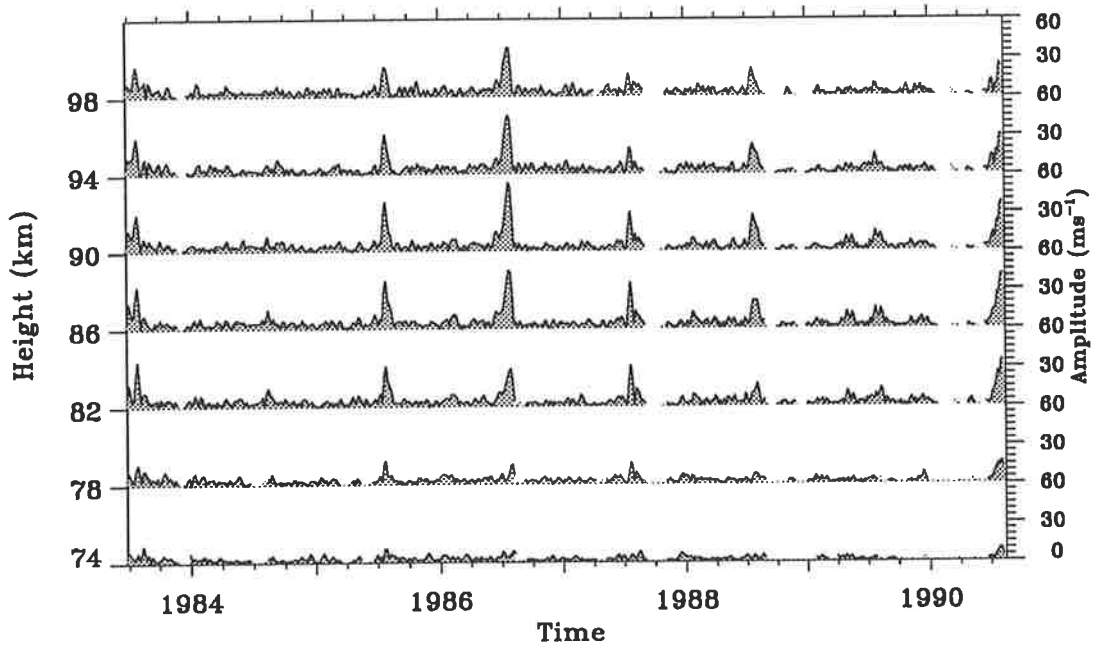

Figure 4.36: The amplitude of the meridional component of the 2-day wave from a complex demodulation procedure for the altitudes indicated on the left-hand side. Otherwise as for Figure 4.35.

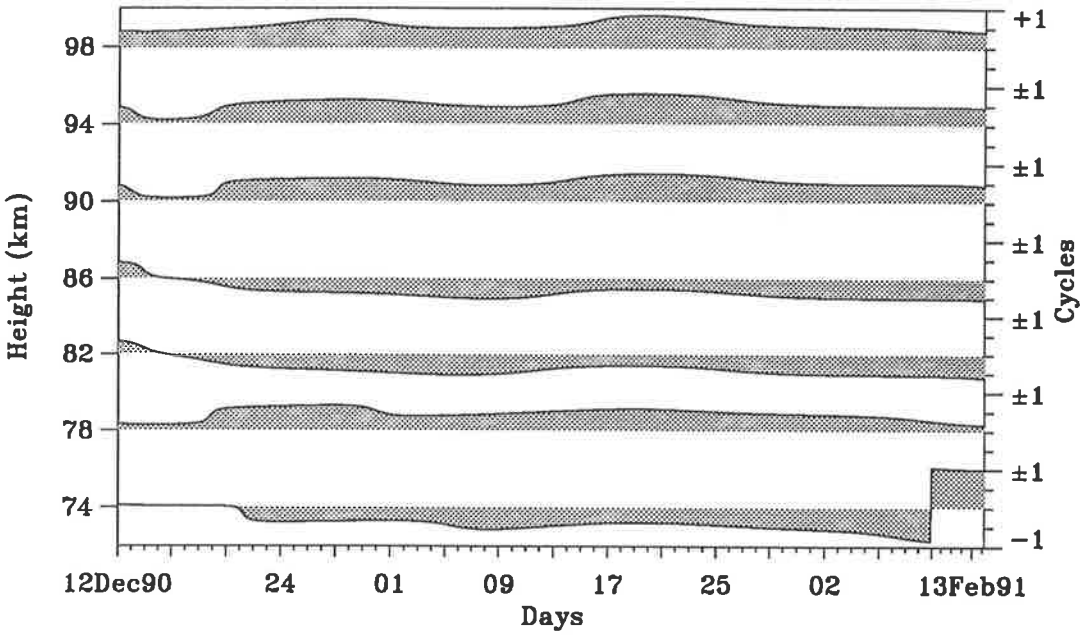

Figure 4.37: The phase of the complex demodulated meridional component of the 2-day wave using a demodulation period of 48 hr for the summer of 1991. The altitudes are indicated along the y-axis on the left-hand side, with the phase values on the right-hand side.

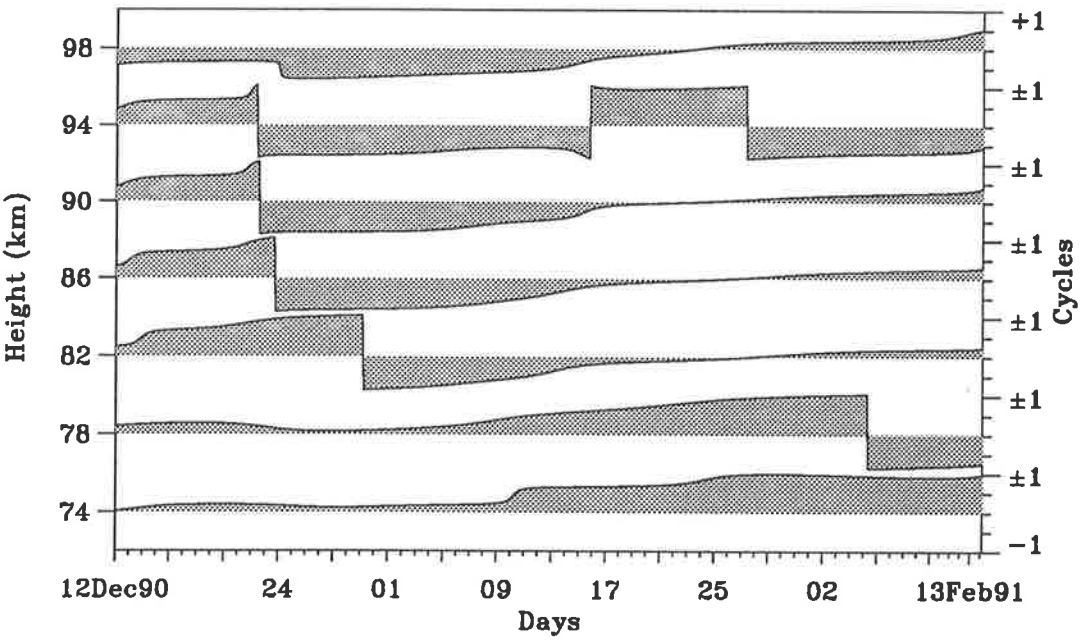

Figure 4.38: The phase of the complex demodulated meridional component of the 2-day wave using a demodulation period of 51 hr for the summer of 1991. Otherwise as for Figure 4.37.

the "51" hr demodulation (162 degrees of freedom). The phase is constant for most heights during January for the 48 hr demodulation, but has a positive rate of change with time for the 51 hr demodulation. Since the rate of change of the demodulated phase is proportional to the difference between the demodulation frequency and the frequency of the dominant signal within the bandpass (see Section 2.7 for further details), then these results suggest a period near 48 hr. Only the data from each December, January and February have been used to determine the period statistics.

In order to reduce the effects of noise, the period of the 2-day wave was only calculated for time intervals where the wave had a demodulated amplitude $> 10\,\mathrm{ms}^{-1}$. It can be seen from Figure 4.20 and Figures 4.17, 4.18 and 4.19 that this cutoff value is large enough to reduce the effects of noise, yet small enough to allow data to be accepted for all years. Figure 4.13 shows that the wind speed maximises in the region of 86 to 90 km every year. Using a $10\,\mathrm{ms}^{-1}$ cutoff value for the minimum demodulated amplitude of the 2-day wave restricts the height range of the data, removing all the data from the lower altitudes for some summers.

To confirm that the periods determined from the complex demodulation are independent of the demodulation period (as anticipated in the discussion on page 2.7 in Section 2.7) the periods were calculated using both a 48 and a 51 hr demodulation period and are shown as histograms for each altitude and in total in Figure 4.39. This shows that the period determination is only mildly dependent on the demodulation period. The statistics of the period distribution are even less dependent, the median and deciles being very similar regardless of demodulation period – as long as the bandpass still encompasses the main variances. From now on only a 48 hr demodulation period is considered. Figure 4.40 shows the median and decile periods as a function of altitude for each summer using a 48 hr demodulation. The number of points used in each distribution are shown on the right-hand side for each altitude. It can be seen that the 2-day wave occurs most frequently near a period of 48 to 50 hr, with some years showing a tendency for shorter periods. In order to determine some form of mean period consideration must be made of the averaging process. As shown in Figure 4.13 each summer would contribute a different amount of data for each altitude if a simple mean value is used. This may be a good thing as the years when the 2-day wave had larger amplitudes would contribute the most data, weighting the average towards these years. To comply with the sense of the term, a yearly average period should weight each year the same. Therefore the average of the median periods for each summer was found for each altitude. In this way each year contributes the same amount of data. The altitude variations of the mean of the summer median periods is shown in Figure 4.41. The

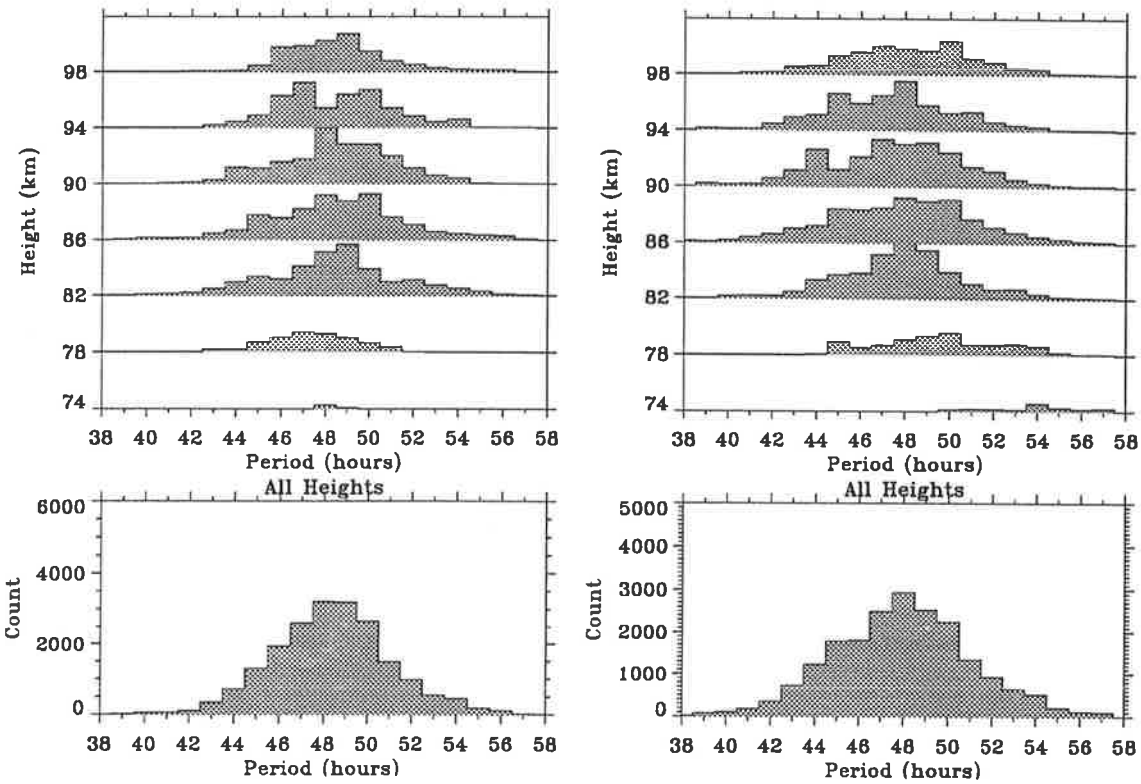

Figure 4.39: Period histograms for each altitude over all summers using a (a) 48 hr, and (b) a 51 hr, demodulation period. The bottom plots are the combined histograms using all the altitudes.

mean period over all altitudes is 48.7 ± 0.5 hr for the meridional and 48.0 ± 0.4 hr for the zonal component. The yearly variations (as shown by the standard errors for each altitude) are of the order of 30 min from the mean, although variations of the mean period with altitude are twice this value. Similar results are obtained using different demodulation frequencies.

As the wave period is close to 48 hr the assumptions made in Section 4.3.2 appear to be valid.

4.3.9 Summary

In Section 4.3.3 it was found that the zonal amplitudes of the 2-day wave at Adelaide are less than $20-30\,\mathrm{ms}^{-1}$ for 90 % of the time during summer, the amplitude exhibiting little variation with altitude or from year to year. The meridional amplitudes are larger, maximising between 86 – 90 km with speeds larger than $40-50\,\mathrm{ms}^{-1}$ for 10 % of the summer. Strong inter-annual variation was found for the meridional component, with some years having speeds less than $20\,\mathrm{ms}^{-1}$ for 90 % of the summer.

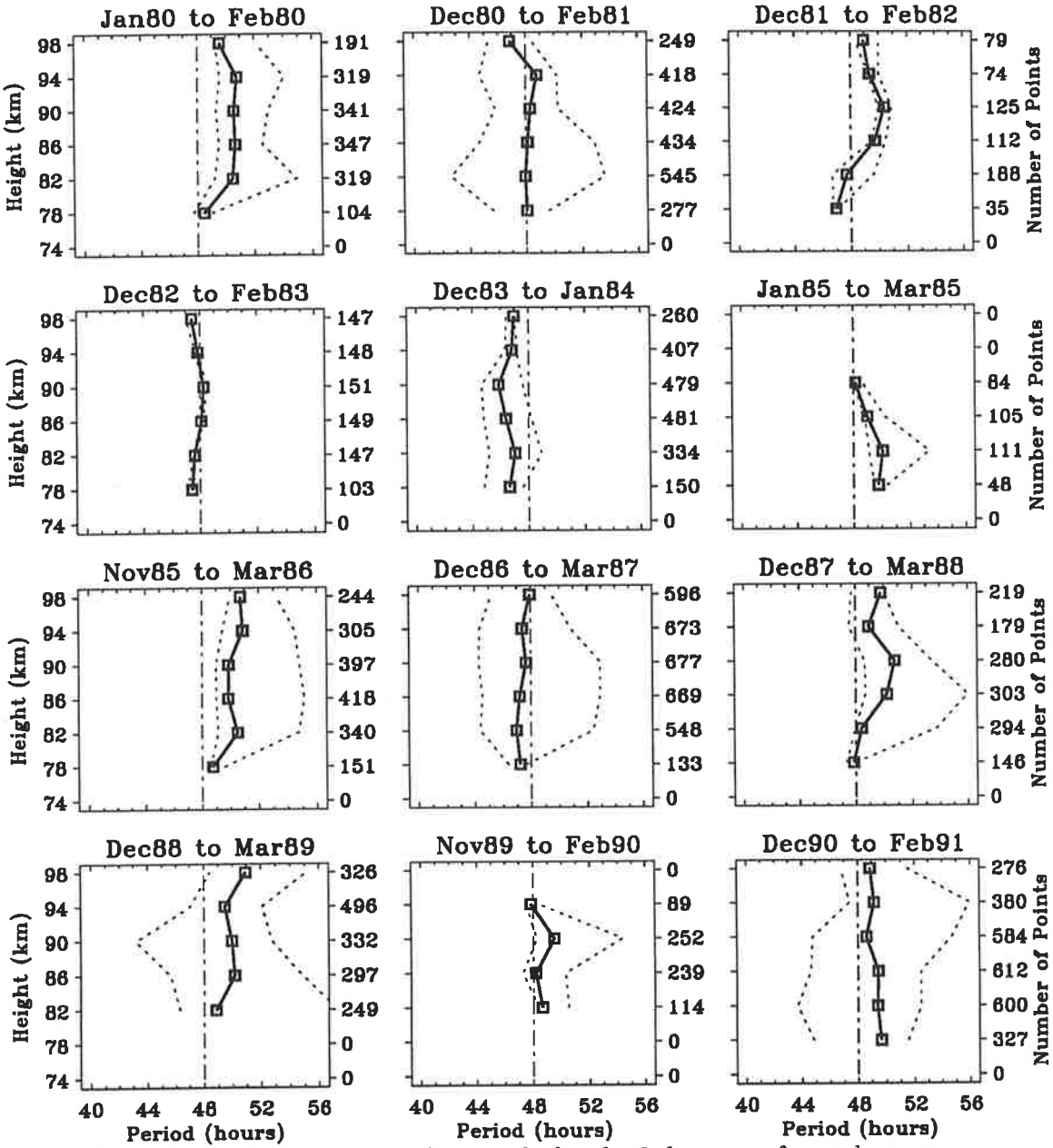

Figure 4.40: Median and decile periods for the 2-day wave for each summer.

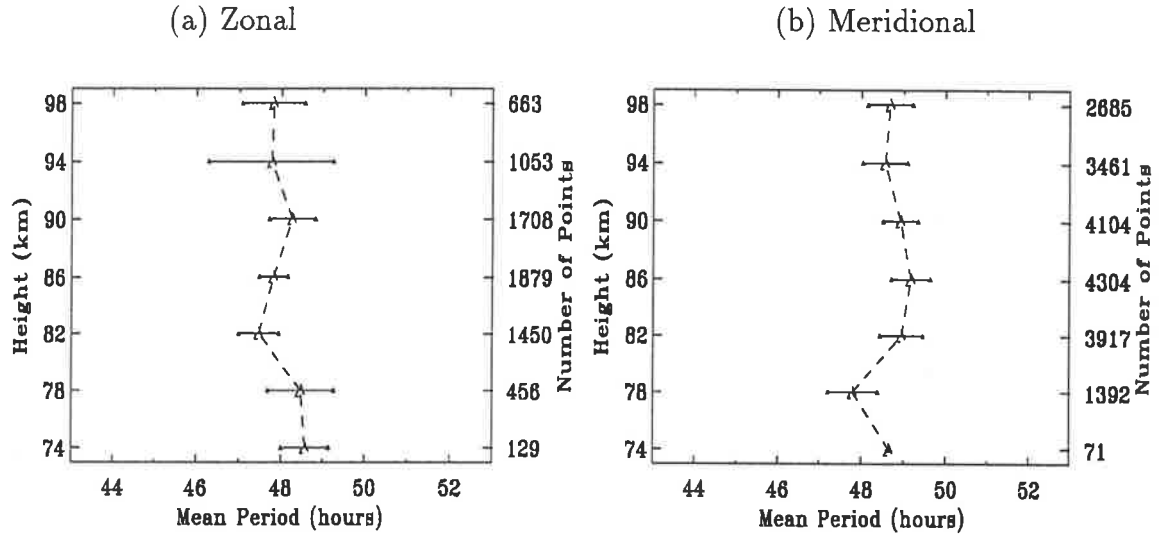

Figure 4.41: Mean period of the 2-day wave over the 12 summers from 1980 to 1991. Shown are the means (and standard errors) of the individual summer median periods. (a) Zonal, (b) Meridional.

It was found that some form of phase locking of the 2-day wave occurs when the wave amplitudes are large, which may be a result of some non-linear interaction during those times. The raw meridional phases are spread from 1000 – 1800 hr LT. Considerable inter-annual variation in the meridional phase was found, with clustering around 1200 and 1600 hr LT during different summers.

In general, during intervals of low wave amplitude ($\leq 20\,\mathrm{ms}^{-1}$) in summer and during all non-summer months the phase of the 2-day wave is not constant with time, implying that the period is not close to 48 hr and/or the vertical wavelength is ≤ 40 km (as all the available heights were combined to obtain a significant number of phase estimates). The opposite is true for time intervals when the wave amplitude was large. In this case the phase is more constant implying a stable period near 48 hr and a long vertical wavelength (> 80 km).

In Section 4.3.4 it was shown that the vector phases during intervals of larger amplitudes cluster between 1000 – 1600 hr LT for both the zonal and meridional components. Again, large inter-annual variations were evident. The individual summer mean vector phases lie between 1200 – 1600 hr LT over the altitude range of 74–98 km. The mean phases over all altitudes and summers were found to be 13 ± 3 hr and 14.4 ± 0.8 hr for the zonal and meridional components respectively. As the errors indicate, more variation with altitude was found for the zonal than for the meridional phases. This can be explained by the smaller average wave amplitude in the zonal component. No phase locking was apparent for small wave amplitudes in both components.

The mean vector phase over all altitudes for time intervals of large wave amplitude, combining

data from 1961, 1966–75, and 1980–91, was found to be 1340 hr LT. The error ellipse lies mostly in the afternoon quadrant. This agrees with the previous results for individual altitudes.

In Section 4.3.5 it was found that the zonal leads the meridional by 0–15 hr for the 2-day wave. This is from 0–0.3 cycles, so that the 2-day wave components generally vary between being in-phase to phase-quadrature.

It was also noted in Section 4.3.4 that the 2-day wave appears to have a phase from year to year consistent with a coherent wave structure persisting throughout the 12 year time interval, although for some summers there appears to have been a phase flip causing the 2-day wave to be in anti-phase with respect to the previous summer. Therefore counting the number of cycles from some arbitrary start time would not give a meaningful average phase over the full 12 year time interval. Using different start times for each year, assuming that the period is close to 48 hr, should give similar phase results to those already found using a 24 hr LT scheme. This was found to be the case in Section 4.3.6.

In Section 4.3.7 the estimated vertical wavelengths for each summer were tabulated. They show that the 2-day usually has a vertical wavelength > 90 km, being smaller (≈ 40 km) when the maximum wave amplitude is small ($\approx 20\,\mathrm{ms}^{-1}$). The vertical wavelength derived from the 12 year mean phase was > 150 km.

In Section 4.3.8 the mean period over the 12 summers and all altitudes was found to be 48.7 ± 0.5 hr for the meridional and 48.0 ± 0.4 hr for the zonal component. Altitude variations were of the order of ± 1 hr. Yearly median periods ranged from 46 up to 51 hr but gave a one standard deviation spread of the order of only ± 0.5 hr from their mean. A mean period close to 48 hr justifies the use of the phase in the range of 0–24 hr LT.

4.4 Equatorial Observations

4.4.1 Introduction

In order to resolve questions regarding the generating mechanism of the 2-day wave, and to better understand its role in the middle atmosphere, reviews of the phenomenon [*Walterscheid*, 1980; *Salby*, 1984; *Vincent*, 1984a] have pointed to the need for further observations at equatorial latitudes. The small number of previous equatorial observations have found evidence of a strong 2-day oscillation in the mesospheric winds [*Coy*, 1979; *Kalchenko*, 1987; *Vincent & Lesicar*, 1991; *Fritts & Isler*, 1992]. In this section, data from the equatorial site at Christmas Island (2° N, 157° W) have been used to obtain information about the 2-day wave at the times when

it maximises in each hemisphere.

Hemispheric differences have been noted in the structure of the 2-day wave. Amplitudes are up to a factor of two larger in the southern hemisphere than those found in the northern hemisphere. It has also been noted that the wave period is near 50 hr in the northern hemisphere, but often indistinguishable from 48 hr in the southern hemisphere [*Muller & Nelson*, 1978; *Craig & Elford*, 1981; *Tsuda et al.*, 1988; *Poole*, 1990; *Harris & Vincent*, 1993]. By observing at an equatorial site where the effects of the 2-day wave can be seen during both solstices – one when the wave amplitude maximises in the southern hemisphere (December solstice), the other when it has maximum amplitudes in the northern hemisphere (June solstice) – hemispherical differences can be directly compared.

The main results of this section have already been reported in *Harris & Vincent* [1993], which has been included in Appendix I, hereafter referred to as "paper-2". This section will expand on the analysis used in paper-2, and present some additional results.

4.4.2 The Data

Data from the beginning of January, 1990, to mid April, 1992, has been analysed. During this interval the system ran continuously, although some data were lost due to disk storage overflow. The periods where data are missing are the two 14 day intervals from 28^{th} October to 12^{th} November, 1990, and from 24^{th} December, 1990, to 8^{th} January, 1991. As data are only obtained for the full 24 hour period for heights from 80 to 98 km, it is this altitude region which has been focussed on in this section.

The temporal variations in the wind variance as a function of frequency for a representative height are shown in Figure 4.42. Periods from 120 hr down to 8 hr are shown although higher frequency components were calculated. Like Figure 4.7, a 14 day window with a step of 7 days was used. The maximum power spectral densities have been "clipped" to be less than $2.4\text{x}10^{7}\text{m}^{2}\text{s}^{-2}\text{Hz}^{-1}$ in order to reduce the dynamic range for plotting purposes. The white bands across all frequencies during October and December, 1990, indicate missing data. Figure 4.42 is the same as figure 1 in paper-2, the major features being discussed there (see section 2.1 of Appendix I).

From previous observations [*Clark*, 1989; *Craig & Elford*, 1981; *Craig et al.*, 1983; *Muller & Nelson*, 1978; *Tsuda et al.*, 1988; *Vincent*, 1984a] large enhancements in wave amplitude might be expected at low-latitudes during the northern and southern hemisphere summers, as well as possible frequency shifts. To investigate these possibilities the spectral analysis was repeated

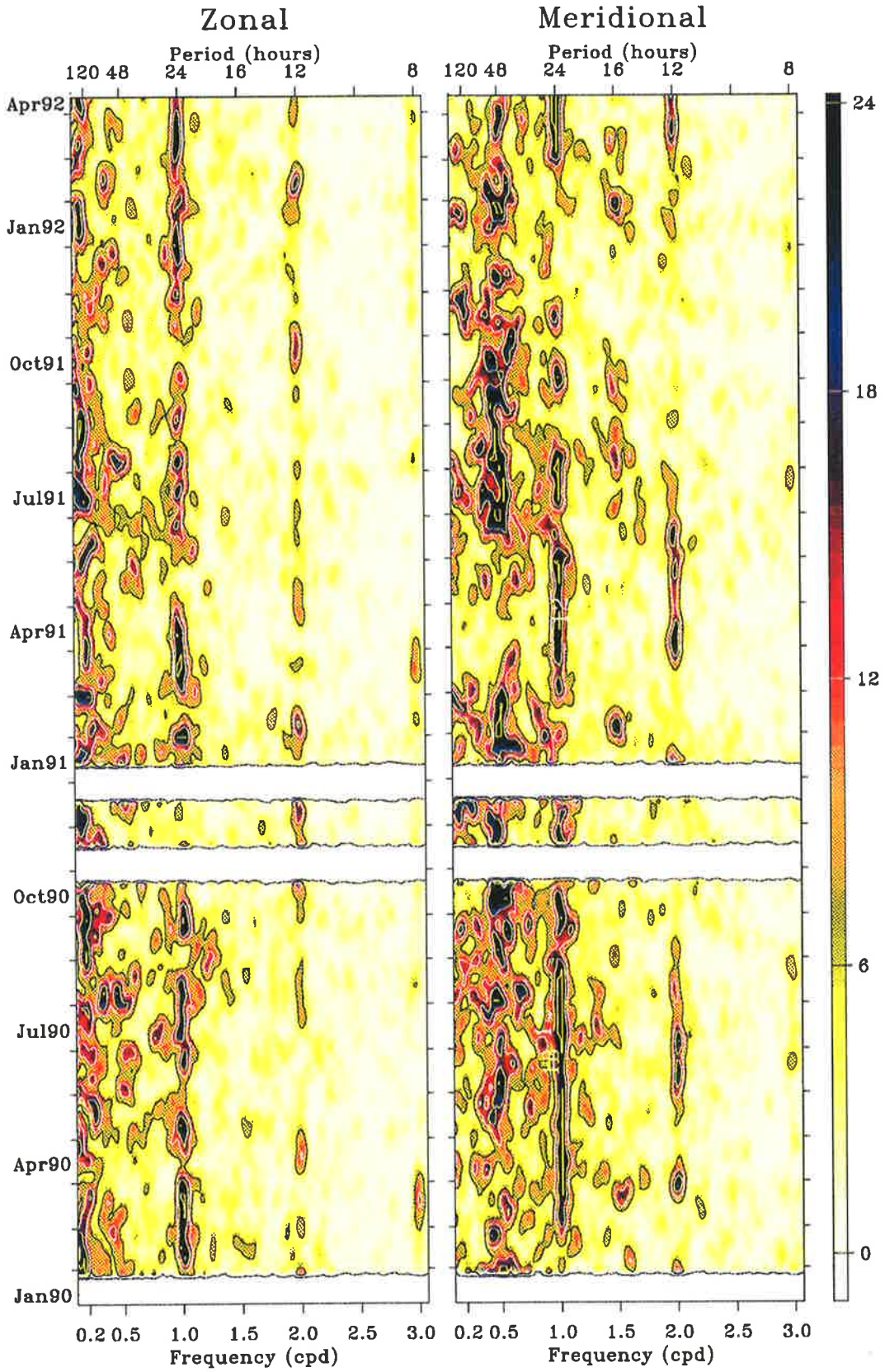

Figure 4.42: Moving power spectra for the zonal (left) and meridional (right) winds measured at an altitude of 86 km over Christmas Island (2° N, 157° W). A discrete Fourier transform and a 14-day sliding window have been used. The tick marks on the time axis (vertical) mark the start of each month. The colour scale indicated on the extreme right-hand-side shows the power spectral density in units of $10^6 m^2 s^{-2} Hz^{-1}$.

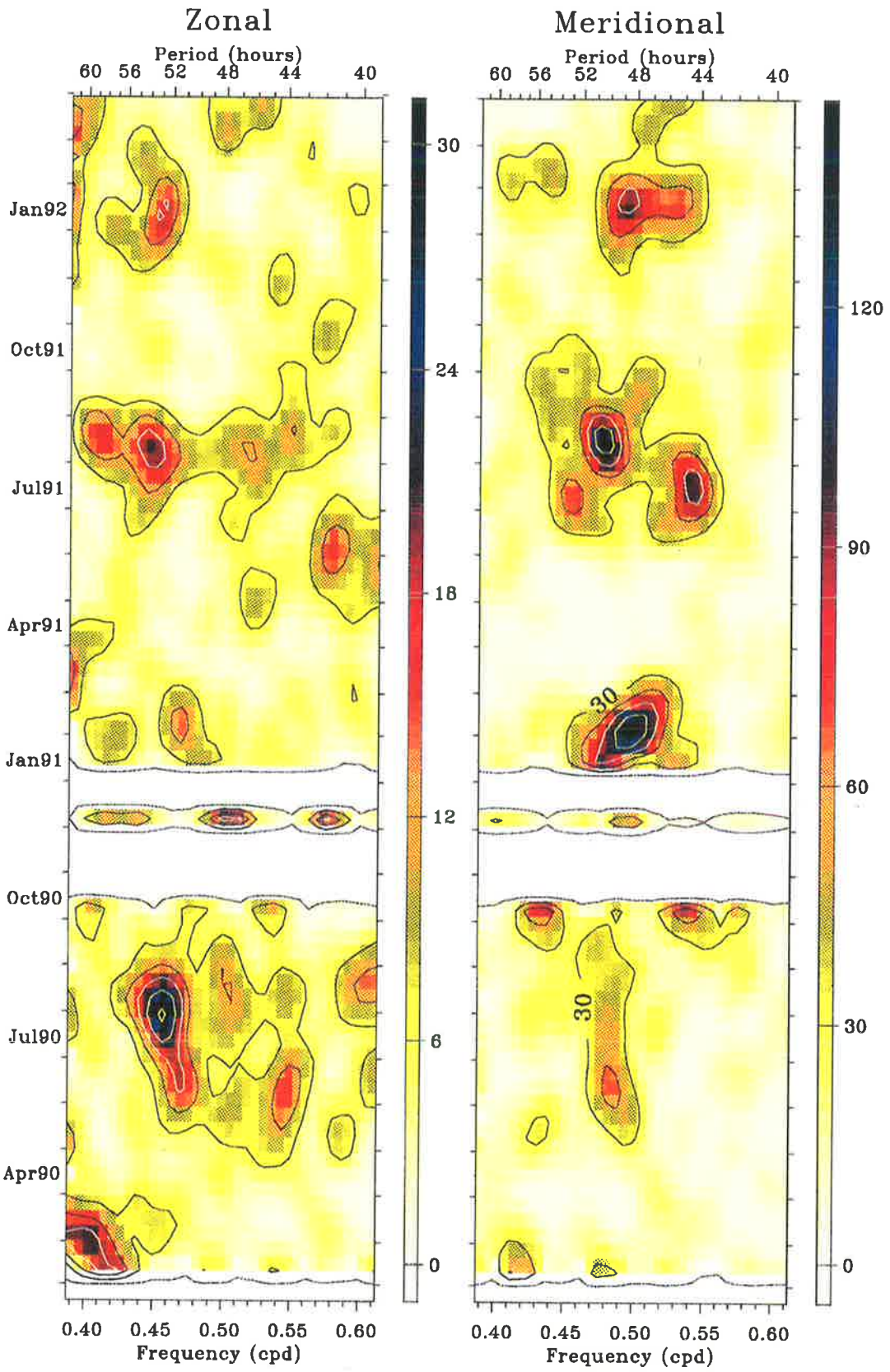

Figure 4.43: Moving power spectra as in Figure 4.42 but using a 40 day sliding window giving an effective resolution of 0.012 cycles per day. Zonal winds are shown on the left and the meridional on the right, with the the colour scale indicating the power spectral density in units of $10^6 m^2 s^{-2} Hz^{-1}$. Note that the scale is different for the zonal and meridional winds.

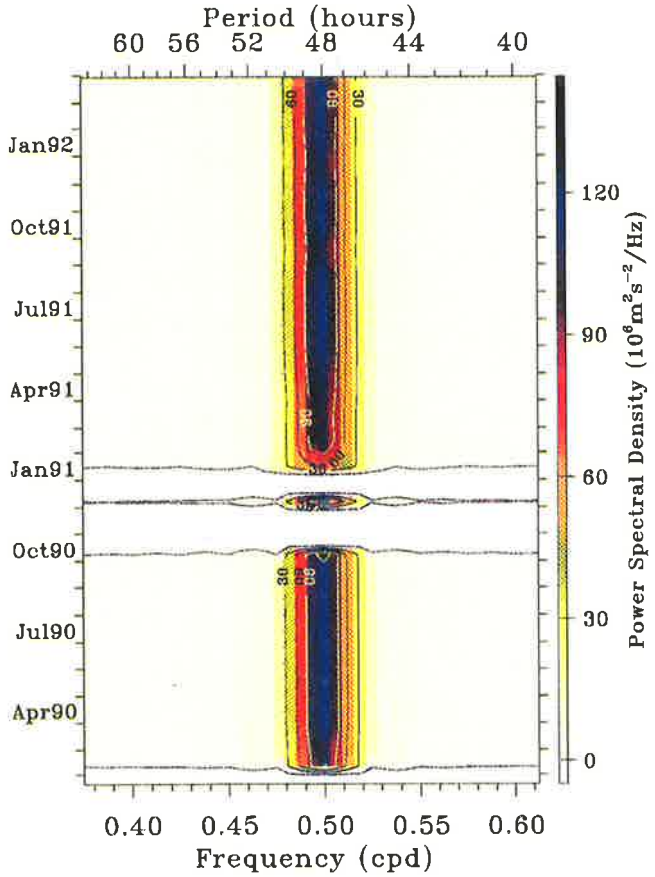

Figure 4.44: Moving power spectra as in Figure 4.42 using the same 40 day sliding window but applied to simulated sinusoidal data. The colour scale indicates the power spectral density in units of $10^6 m^2 s^{-2} Hz^{-1}$.

with a finer frequency resolution, as shown in Figure 4.43 using the same moving power spectrum as in Figure 4.42, but with the window width increased to 40 days, to give an effective frequency resolution of 0.025 cpd. A step size of 20 days was used. The frequency band of concern has also been focussed on . It should be noted that in Figure 4.43 the power spectral amplitudes are not truncated and that the scales are different. Hence, these plots give not only a more accurate measure of the relative strength of the oscillation in each wind component, but also a better representation of seasonal changes in wave energy. It is apparent that the power spectral amplitudes of the meridional wind are usually up to ten times those of the corresponding values for the zonal component. Figure 4.43 is the same as figure 2 in paper-2. Once again the major features are discussed there (see section 2.1 of Appendix I). Simulated data were used to test the analysis procedure in order to ensure that sidelobe effects due to the windowing are negligible. A plot of the response to simulated data using the same spectral techniques as in Figure 4.43 is shown in Figure 4.44. The data was a pure sinusoid at 0.5 cpd which was subjected to the same processing as for the real data, using exactly the same data gaps. The half-power-half-width

is of the order of 0.01 cpd. The power is -12dB down at ±0.02 cpd, decreasing to nearly -20dB at ±0.025 cpd. As the frequency resolution is 0.025 cpd this means that each spectral point leaks <10% of its maximum power to its neighbour. No large sidelobes appear so that the two peaks observed during July, 1991, in the meridional power spectrum, are distinctly separate phenomena.

4.4.3 Period as a Function of Season

As in Section 4.3.8, a complex demodulation technique was used to determine the period of the 2-day wave as a function of time (see Section 2.7 for the details of the technique). The complex demodulated amplitudes for both the zonal and meridional components are shown as a function of altitude and time in Figures 4.45 and 4.46 for a 48 hr demodulation period. Note that these two figures have different scales. The rate of change of the phase with time of the complex demodulation is a measure of the period of the dominant wave within the bandpass. The phases for a 48 and 51 hr demodulation are shown in Figures 4.47 and 4.48. As in Section 4.3.8, it can be seen that the phase is relatively constant during January and February for the 48 hr demodulation, whereas it has a positive slope with time in the 51 hr demodulation, which can be interpreted as the 2-day having a period close to 48 hr during this interval. The phase during July and August for both the 48 and 51 hr demodulations show a more oscillatory change with time. A positive slope can be seen during early August using the 51 hr demodulation, while a smaller negative slope is suggested for the 48 hr. Converting the rate of change of the phase of the complex demodulation to a period measurement (again, see Section 2.7) Figure 4.49 is obtained. This shows the period as a function of altitude and time. These results, like the phase, have little meaning unless they are coupled with the amplitudes. The phase of a signal with small signal-to-noise ratio has little significance. Collecting this information into seasons and finding the median and decile values Figure 4.50 is obtained. The same procedure has been performed for the zonal wind component and these deciles are also shown in Figure 4.50. In order to use the same bandpass for both the zonal and meridional components a 50 hr demodulation period and a bandpass from 46.0 to 54.8 hr (*c.f.* Figure 4.43) was used in determining the period statistics. Only data for times when the amplitudes were greater than 5 ms^{-1} have been used in the compilation of the period distributions in order to ensure the values are meaningful. The number of points used for each altitude is shown on the right-hand side of each plot. The thick lines with the symbols show the median period as a function of altitude, with the upper and lower deciles shown as narrow lines.

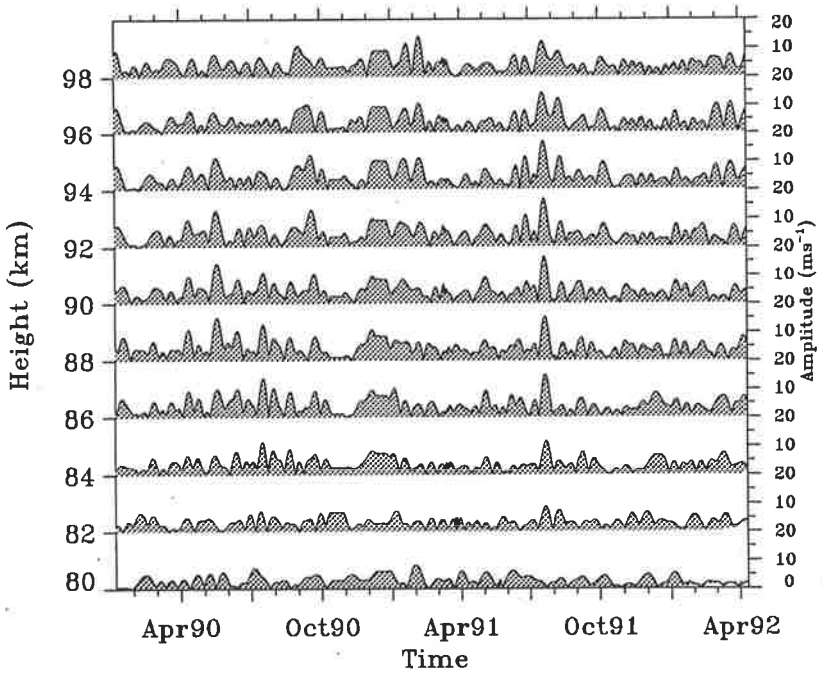

Figure 4.45: The amplitude of the zonal component of the 2-day wave from a complex demodulation procedure. As for Figure 4.35 but for data from Christmas Island.

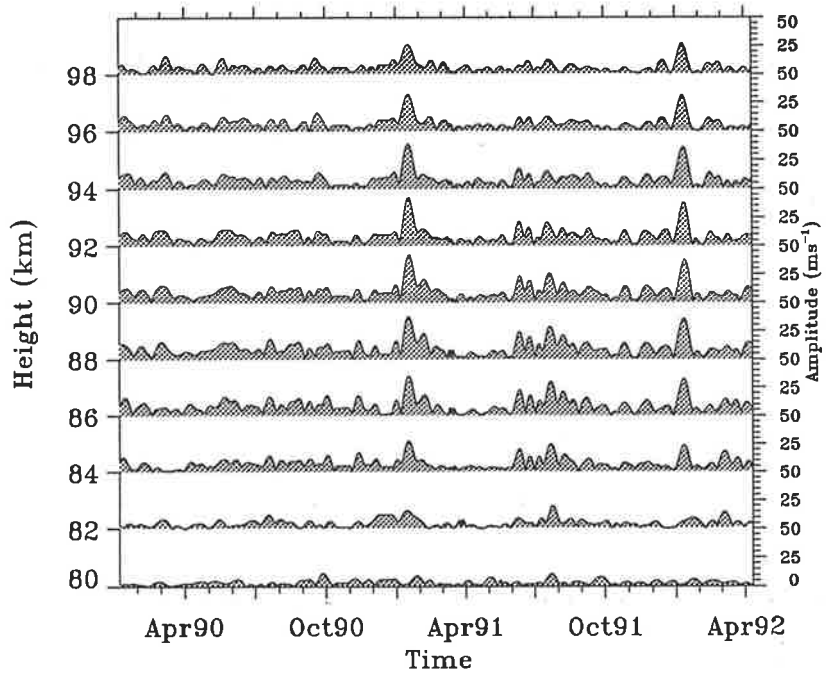

Figure 4.46: The amplitude of the meridional component of the 2-day wave from a complex demodulation procedure. As for Figure 4.36 but for data from Christmas Island.

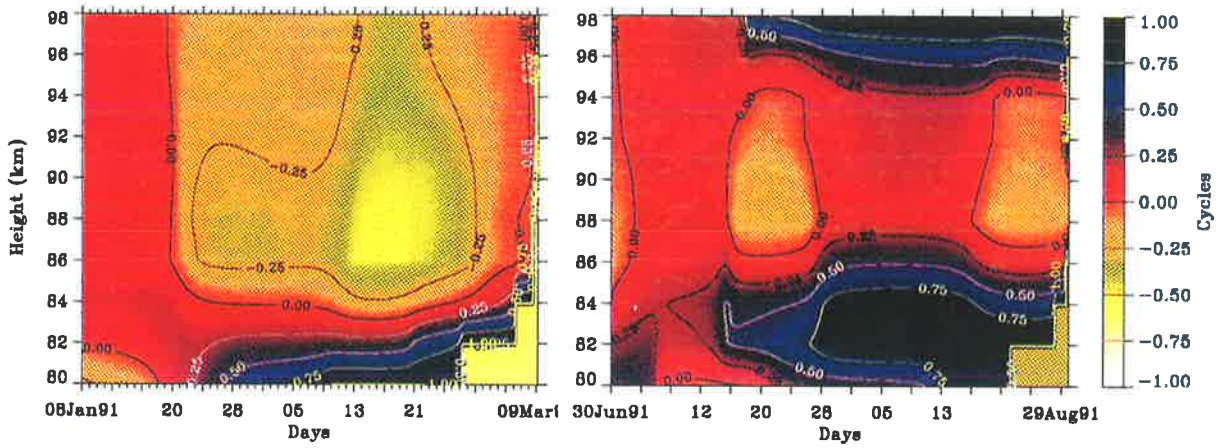

Figure 4.47: The phase of the complex demodulated meridional component of the 2-day wave using a demodulation period of 48 hr for two segments of the equatorial data. A bandpass of 43.5 to 53.5 hr has been used, allowing 14 degrees of freedom. The altitudes are indicated along the y-axis on the left-hand side, with the phase values on the extreme right-hand side.

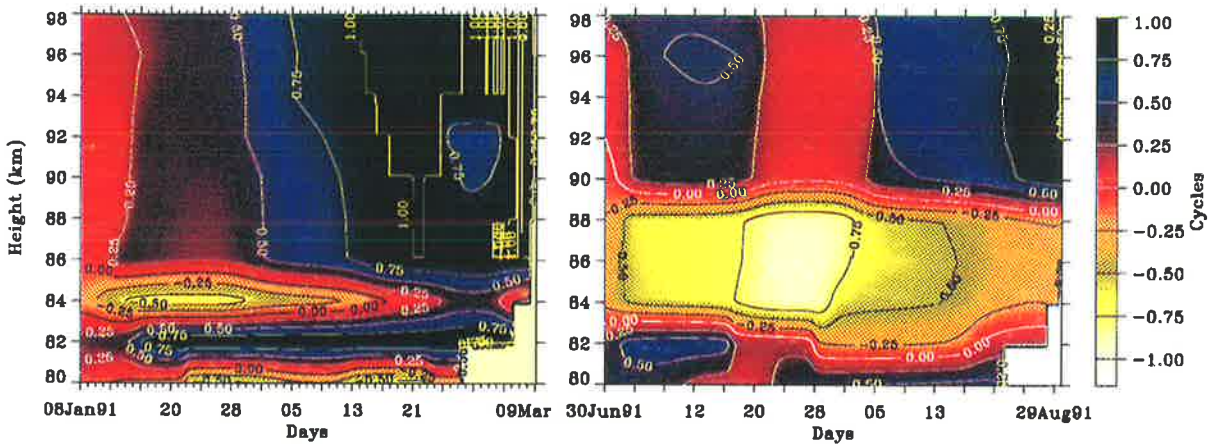

Figure 4.48: As for Figure 4.47 but using a demodulation period of 51 hr. A bandpass of 46.4 to 57.9 hr (14 d.f.) has been used.

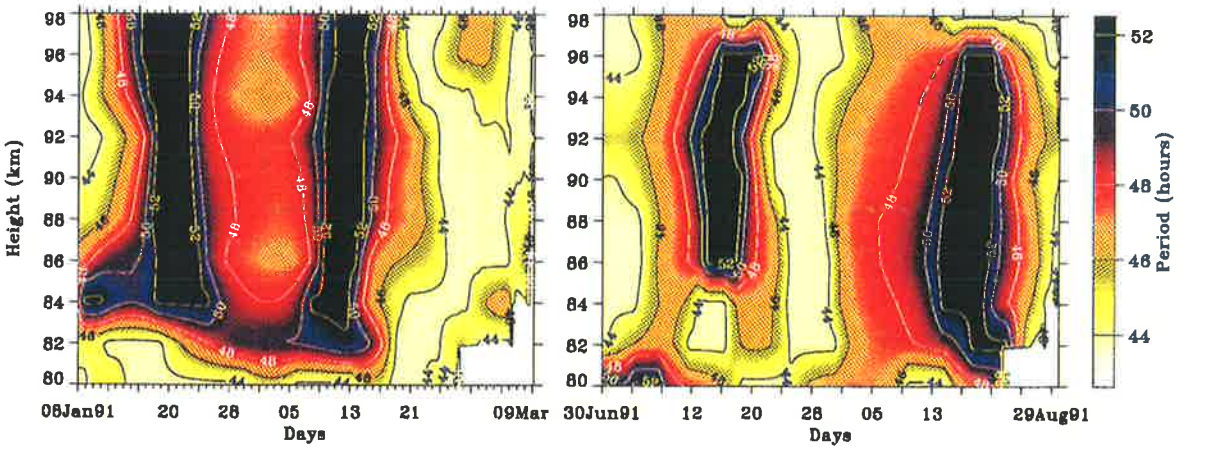

Figure 4.49: The period of the 2-day wave near the equator. Otherwise as for Figure 4.47.

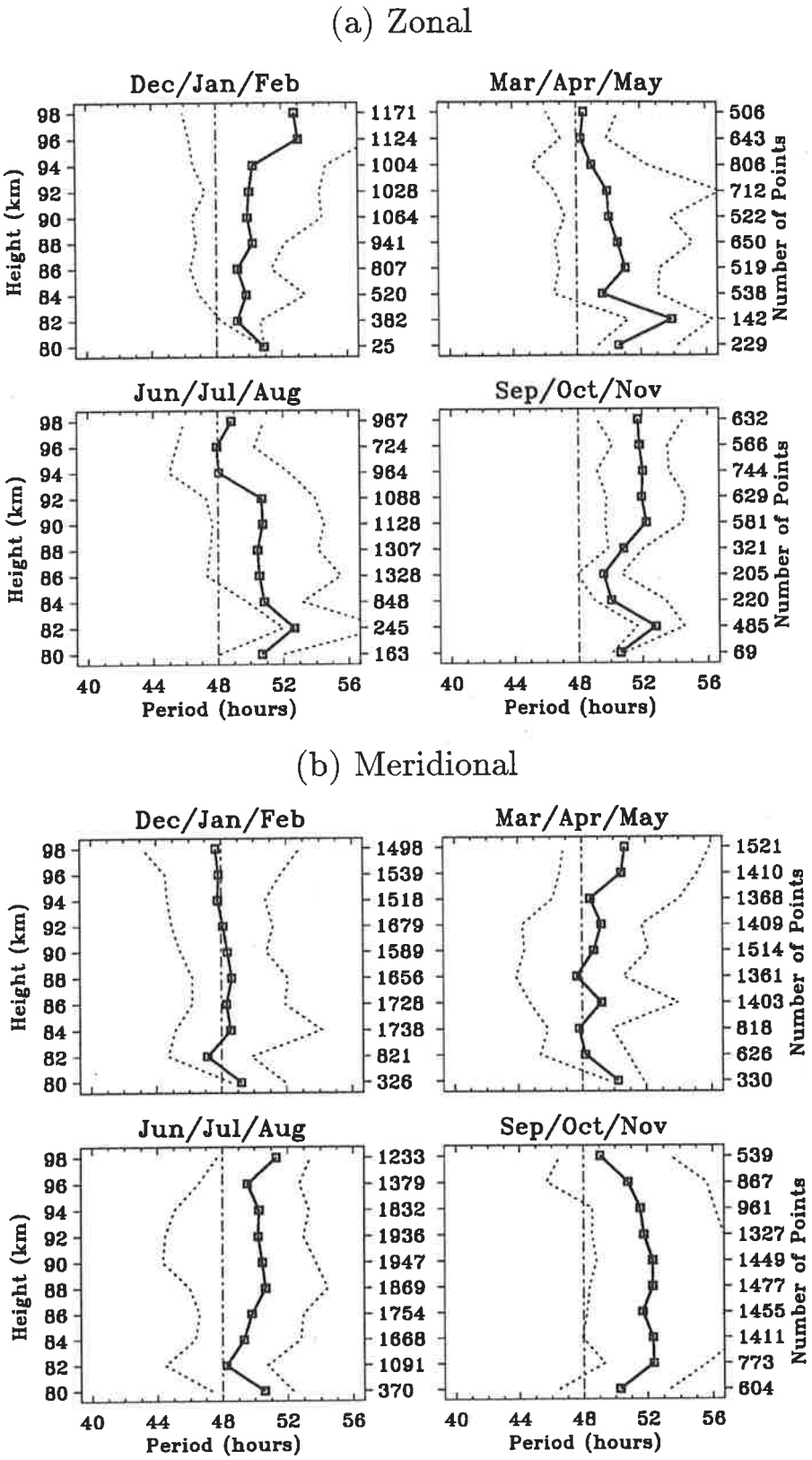

Figure 4.50: Median and decile periods of the 2-day wave as a function of season. (a) Zonal, (b) Meridional.

For the meridional component it can be seen that during December to February the median period is 48 hr (for 84 km and above) with deciles spreading from 45 to near 51 hr. This is in agreement with the sliding spectral results presented earlier. From June to August the median period is just as firmly placed at 50 hr (for 86 km and above). The deciles range from 44 to 53 hr. For the zonal component, the median period is close to 50 hr during both solstice periods. For both the zonal and meridional winds the amplitudes of the near 48 hr period components are small during the equinoctial months, so that the period determination has a larger uncertainty. Nevertheless, the March equinox shows a strong tendency to have a median period near 48 hr (for both the zonal and meridional winds) whereas the September equinox shows a tendency towards a 52 hr period.

4.4.4 Phase as a Function of Season

The same sinusoidal fitting technique used in the previous section was applied to the Christmas Island data in order to determine the phase of the 2-day wave as a function of time. The error in the daily phase estimate from fitting a sinusoid with a period of 48 hr to 2 days of data with a dominant period of 52 hr is less than 1 hr. This reduces to 30 min for data with a dominant period of 50 hr. In both cases this error is less than the natural variation of the phase observed in the raw bandpassed time series.

Figure 4.51 shows the median and deciles of the zonal and meridional wind speed estimates as a function of altitude. The upper decile values mostly come from time intervals around the maximum 2-day wave amplitudes. For the two solstice conditions the meridional amplitudes increase to a maximum in the region of 86 to 90 km and then slowly decrease with further increase of altitude. Amplitudes during each solstice season exceed 30 ms^{-1} for 10% of the time at these altitudes. Median values are around 15 ms^{-1} from 86 to 90 km and just over 5 ms^{-1} at 80 km for both solstices. There is good coherence with height. For equinoctial conditions the amplitudes show a more constant variation with altitude. The median increases from 5 ms^{-1} at 80 km to 10 ms^{-1} at 98 km for the March equinox, whereas during the September equinox the median amplitude increases from 7 ms^{-1} at 80 km to 15 ms^{-1} at 86 km, and then decreases down to 10 ms^{-1} at 98 km. There is a large amplitude burst at 86 km in the September equinox which raises the upper decile to 25 ms^{-1}, otherwise this value would be between 7 and 10 ms^{-1} greater than the median for both equinoxes. Figure 4.52 shows the mean vector phase for the meridional (solid line and triangles) and zonal (dotted line with squares) components of the 2-day wave. The bars shown indicate one standard deviation. The phase has been calculated assuming a

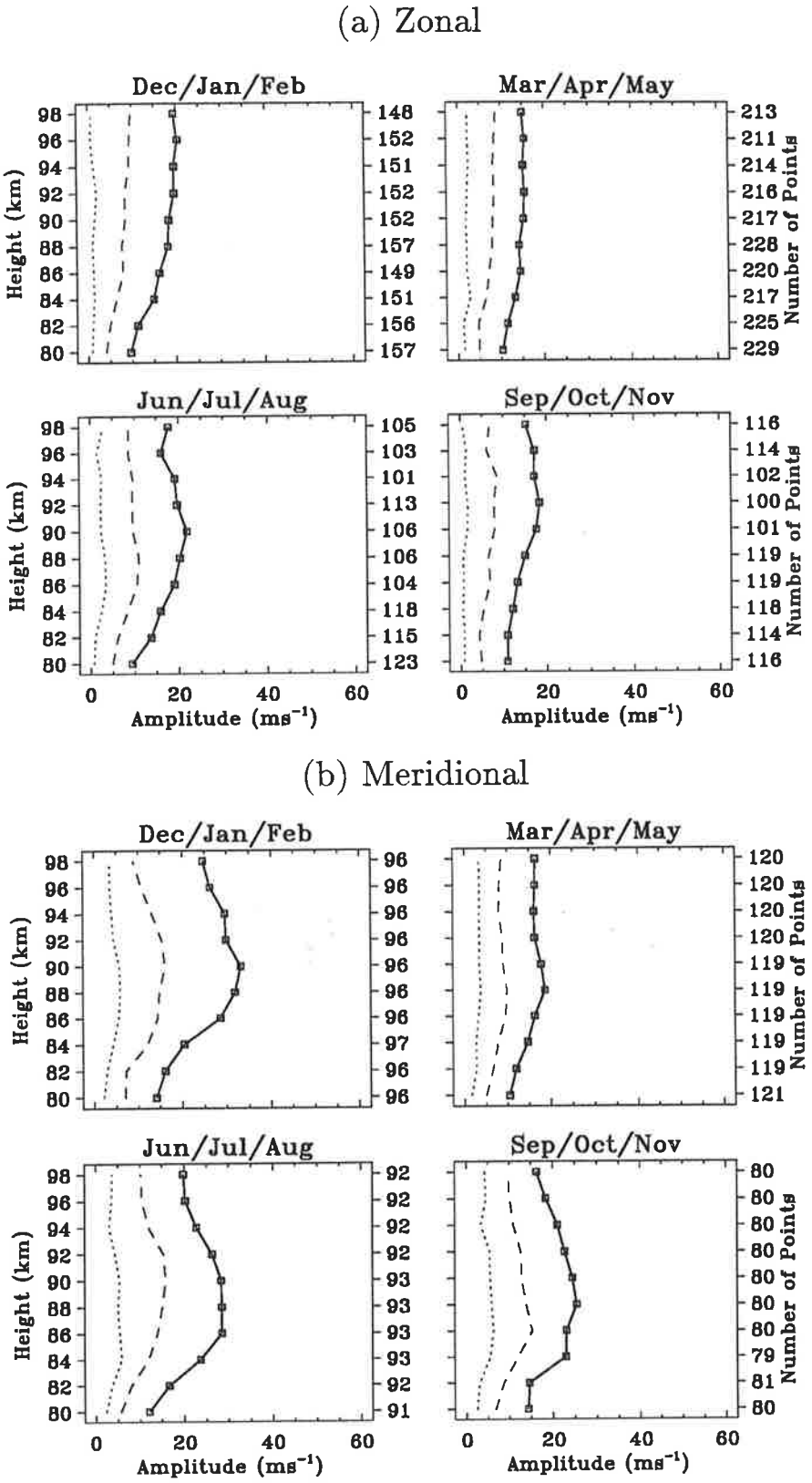

Figure 4.51: Amplitude statistics for (a) the zonal and (b) the meridional components of the 2-day wave at the equator as a function of season.

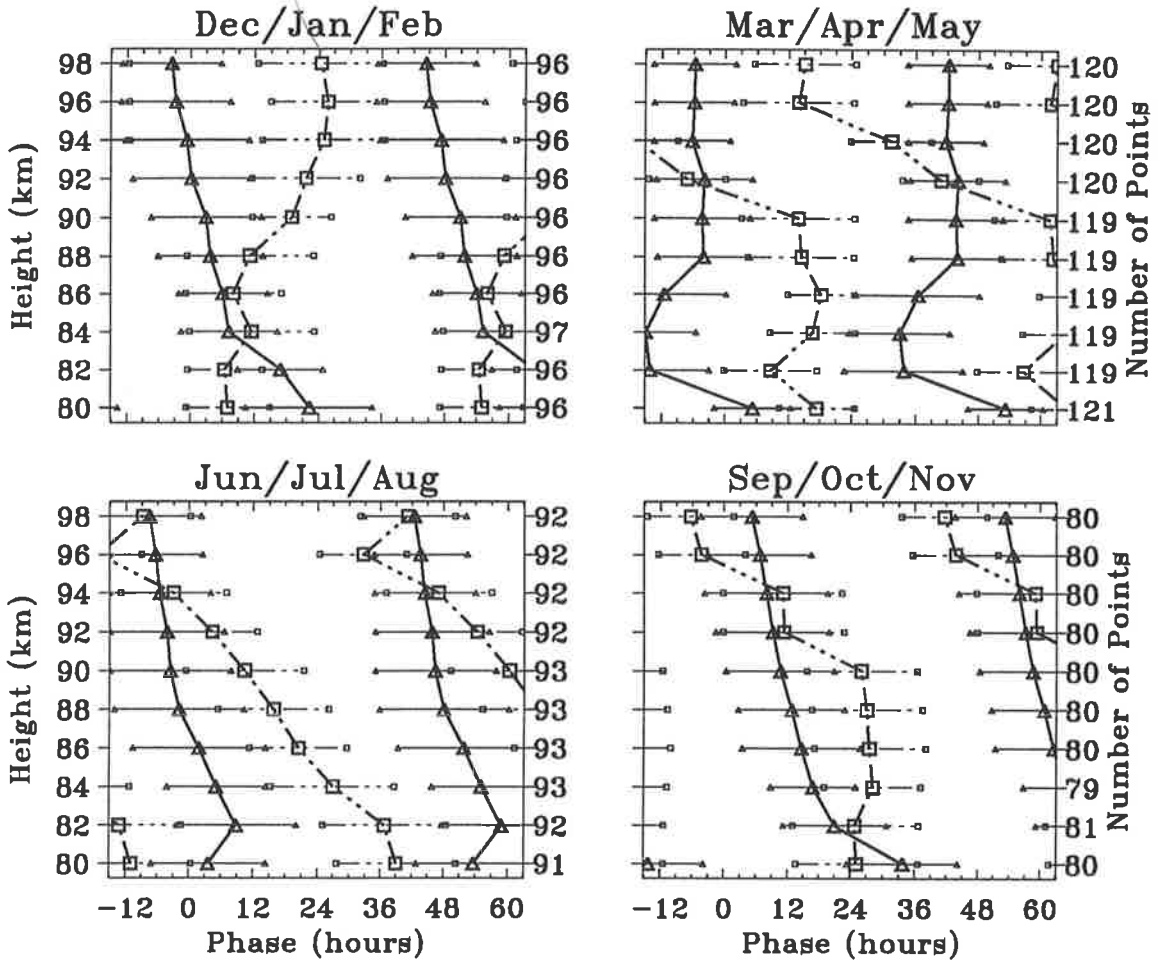

Figure 4.52: The mean vector phase (hr LT) for the meridional (solid line and triangles) and zonal (dotted line with squares) components of the 2-day wave for each season as function of altitude. The bars indicate one vector standard deviation.

wave period of 48 hr for all seasons except the June solstice where a 50 hr period has been used. Thus the values for the phase in Figure 4.52 can be taken as hours LT except for the June solstice where the phase is simply a relative measure with altitude. This figure is the same as figure 5 of paper-2 but has had the zonal phases corrected – the same problem mentioned on page 125 that affected figure 7 of paper-1 also affected figures 5 and 7 of paper-2. The main effect of the corrections to the zonal phases shown in figure 5 of paper-2 are: the phase estimate at 90 km for the season starting in December has shifted by 24 hr causing the zonal phases to be more continuous with altitude; phase estimates for 92 and 94 km for the season beginning in March have shifted by between 12 – 24 hr causing the altitude variation of the phase to have a large slope in this region; the zonal phases for the season beginning in June now have a rapid retardation with altitude rather than being near constant, changing the phase relationship interpretations; the phases for 80, 82, 96 and 98 km have been retarded by 24 hr for the season beginning in September, causing the zonal and meridional components to be in-phase at the lower and upper

heights.

From Figure 4.52 it can be seen that the meridional phase tends to advance towards earlier times with increasing altitude, indicating descending phase and upward energy propagation. The main exception to this is during the period from March to May at altitudes of 82 to 88 km, where the phase is retarded with height. During this period the zonal and the meridional components are in anti-phase - the phase values for 92 and 94 km perhaps being out by 24 hr. This is in contrast to the September equinox where the meridional component leads the zonal by about 12 hr from 86 to 90 km, decreasing to 0 hr at 92–94 km, then lagging by 12 hr above 94 km. The change in the meridional phase with altitude suggests an average vertical wavelength greater than 150 km during the March equinox (above 86 km), and of the order of 60 km for the September equinox. The amplitude of the near 48 hr wind component (as previously mentioned) is small during the equinoctial months, so that the uncertainty in the phase is greater than for the solstices. However, the consistency with altitude and the consistent phase difference between the zonal and meridional components gives some confidence in these results. Note that the values for 80 and 82 km have the least confidence as the wave amplitudes are smallest at these altitudes.

During the December solstice the average zonal and meridional 2-day wave wind components are in-phase from 82 to 88 km, where the zonal winds start increasing in phase relative to the meridional. Above 90 km the zonal and meridional winds are in anti-phase. The vertical wavelength, obtained from the change in the meridional phase with altitude, is of the order of 70 km. During the June solstice the average zonal phase rapidly decreases with altitude suggesting a vertical wavelength as small as 15 km. The zonal and meridional wind components change from being in anti-phase at 82 km to in-phase at 94 km. The average vertical wavelength was estimated from the meridional phases to be 80 km above an altitude of 86 km, and 40 km below.

4.4.5 Case Studies

Since the 2-day wave can be quite intermittent, the seasonal averages may not describe the full behaviour of the wave. To address this possibility the temporal behaviour of the 2-day wave was examined during three short time intervals. Each interval, consisting of two weeks of data, represent each solstice and an interval in April 1990, when wave activity was small. Figure 4.53 shows the bandpassed meridional winds for these intervals. High temporal and spatial coherence is evident for those intervals of large amplitude. The coherence with altitude is apparent for all three intervals with a downward phase progression at both solstices, indicating upward energy

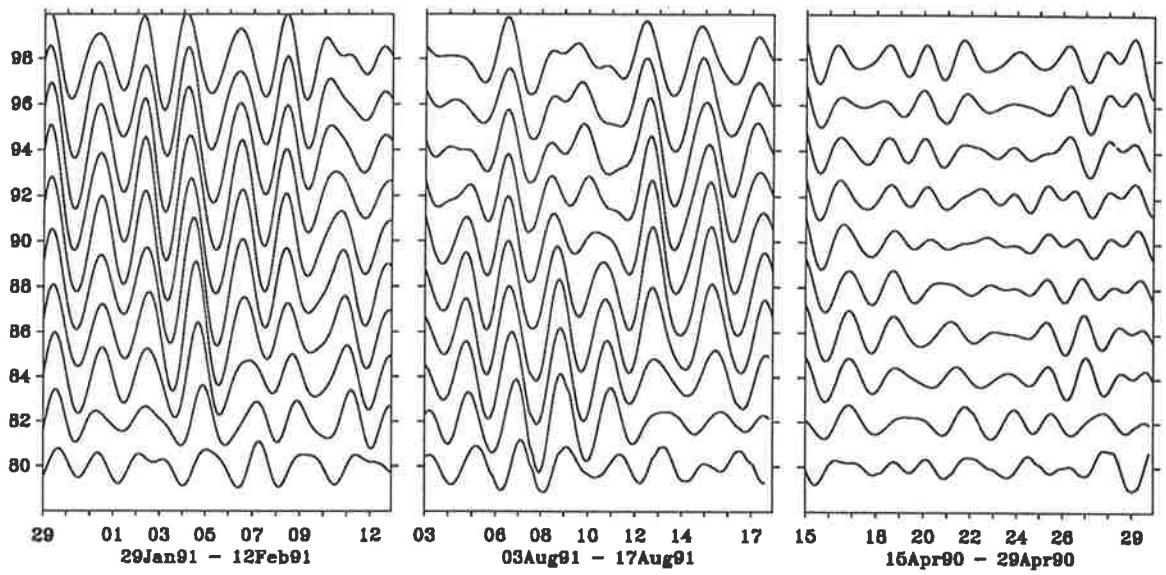

Figure 4.53: Bandpass filtered meridional winds for the near 48 hr component during February 1991 (left), August 1991 (centre), and April 1990 (right). A pass-band of 30 to 80 hr was used. The time axis tick marks indicate 1200 LT. The plots are displaced vertically by 30 ms^{-1}.

Height	Meridional						Zonal					
(km)	February		April		August		February		April		August	
98	*25*	**32**	*9*	**12**	*16*	**27**	*18*	**23**	*8*	**11**	*5*	**11**
96	*29*	**32**	*7*	**15**	*25*	**32**	*17*	**20**	*10*	**19**	*7*	**12**
94	*30*	**38**	*7*	**13**	*25*	**37**	*16*	**29**	*13*	**18**	*9*	**13**
92	*34*	**40**	*7*	**8**	*26*	**38**	*15*	**22**	*13*	**19**	*10*	**13**
90	*33*	**39**	*5*	**6**	*28*	**38**	*14*	**20**	*13*	**15**	*15*	**15**
88	*28*	**43**	*5*	**11**	*30*	**35**	*9*	**17**	*11*	**18**	*18*	**19**
86	*23*	**40**	*7*	**12**	*27*	**32**	*10*	**11**	*8*	**13**	*19*	**23**
84	*19*	**30**	*6*	**14**	*22*	**31**	*10*	**13**	*6*	**8**	*16*	**24**
82	*12*	**20**	*7*	**10**	*21*	**30**	*5*	**12**	*5*	**9**	*12*	**19**
80	*10*	**15**	*5*	**8**	*12*	**17**	*7*	**11**	*8*	**12**	*7*	**11**

Table 4.2: Amplitudes (ms^{-1}) of the 2-day wave as a function of altitude for the zonal and meridional wind components for two-week intervals in February 1991, April 1990 and August 1991. Median values are in *italics* and upper decile values in **bold**. There are 15 to 20 points in each estimate.

transport. The change in phase with altitude for both the two-week solstice intervals appears to indicate a similar wavelength to that estimated from the seasonal averages.

Table 4.2 summarizes the median and decile amplitudes as a function of altitude for the zonal and meridional 48 hr period wind components for the selected time intervals. The amplitudes were calculated in a similar manner as for the seasonal data. It can be seen that the April period is indeed a time of low amplitude, with median values around $8-13\,ms^{-1}$ for all heights in both components. The deciles are also fairly constant with altitude. The largest amplitudes

are found in the meridional component during the February interval which coincides with the southern-hemisphere summer 2-day wave event.

The impulsive nature of the 2-day wave can be seen in the meridional 2-day wave amplitudes for the February interval in Figure 4.54. The colour scale and contours represent the wind speeds in ms^{-1}. At 86 km on the 1^{st} of February, 1991, peak wave amplitudes are around $20\,ms^{-1}$. These increase to over $45\,ms^{-1}$ on the 4^{th}, then diminishes to near $15\,ms^{-1}$ by the 9^{th}. This is only four cycles. Figure 4.55 shows the period as a function of altitude and time which can be compared with the amplitudes in Figure 4.54. The periods have been estimated from the rate of change of the phase using the complex demodulation technique for the full time series from January, 1990, to April, 1992, not from the short time interval shown, in order to allow a large enough bandwidth and number of degrees of freedom. It can be seen that during the times and at the heights of large wave amplitude the period is just under 48 hr. The colour scale indicates that the period may vary by ± 0.5 hr. The same procedure has been performed for the August interval, with the 2-day wave amplitudes shown in Figure 4.56 and the periods in Figure 4.57. Again the period has been estimated from the demodulation of the full time series. Here it can be seen that during the times and at the heights of large wave amplitude the period is very close to 50 hr. In this case the colour scale indicates that the period may vary by ± 1 hr.

Figures 4.58 shows the mean vector phase as a function of altitude for the selected solstice periods. The phases have been calculated in a similar manner as for the seasonal data with a cyclic period of 48 hr used for the January/February time interval and 50 hr for the interval in August. For the February time interval, the variation of the phase with altitude indicates a vertical wavelength of around 70 km, with the zonal and meridional winds in anti-phase, the corrections to the bad data flagging for the zonal phases having little effect (*c.f.* figure 7 of paper-2). Prior to correcting the bad data flagging for the zonal component the August phases indicated that the meridional led by between 8 – 12 hr. This is what has been reported in paper-2. After correction the mean zonal phases have moved closer to the meridional so that the zonal and meridional winds are less in phase-quadrature, with the meridional leading by only 3 – 9 hr for most altitudes. The indicated vertical wavelength is also of the order of 70 km for the August interval. This is in agreement with the seasonal estimates. The error bars for the zonal phases are larger than for the meridional during both time intervals reflecting the lower reliability in the determination of the phases due to the smaller zonal amplitudes of the 2-day wave.

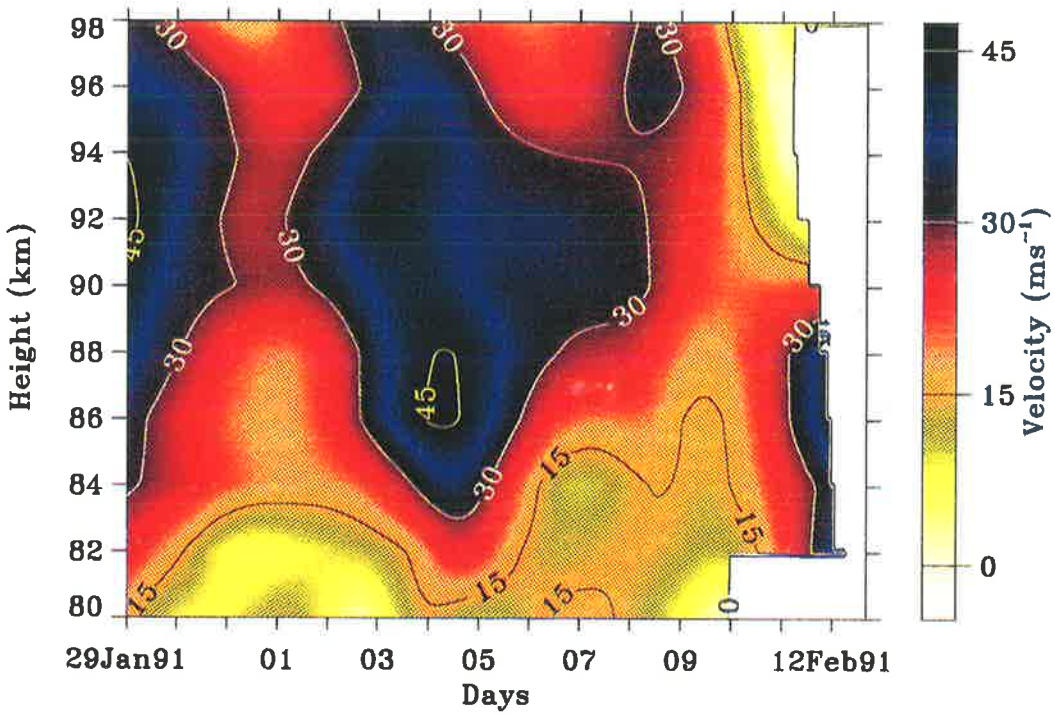

Figure 4.54: Wind speeds for the 2-day wave meridional wind component during February, 1991. The colour and contours (scales shown on the right-hand side) represent the wind speeds in ms^{-1}.

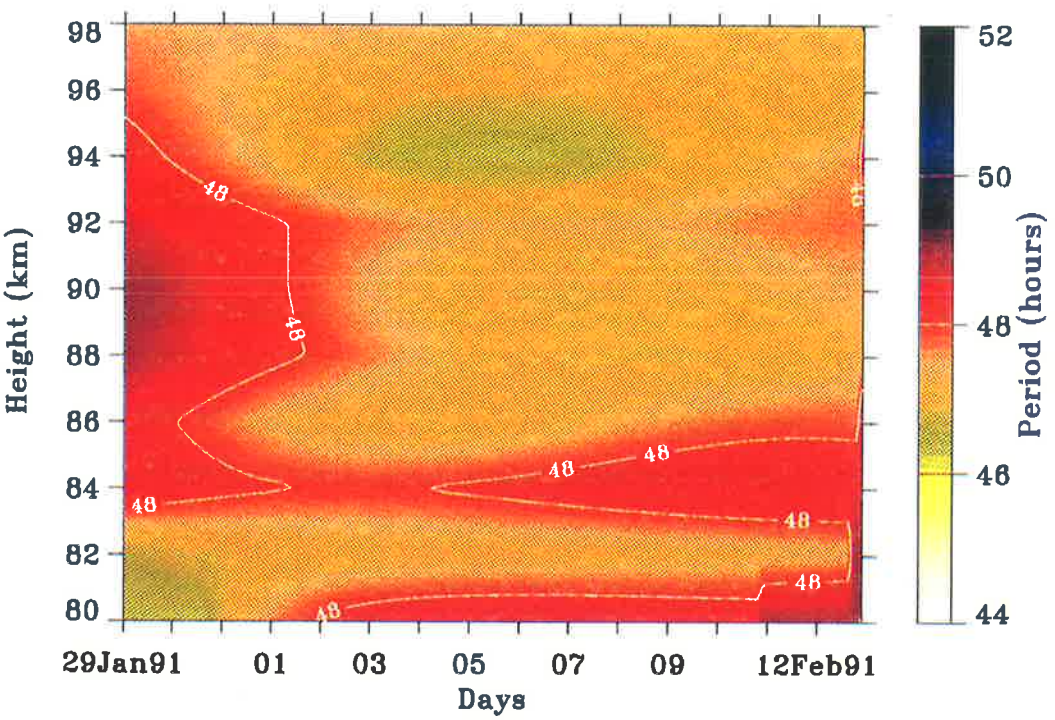

Figure 4.55: Period for the 2-day wave during February, 1991. The colour and contours (scales shown on the right-hand side) represent the wave period in hours. The time axis is identical to that in Figure 4.54.

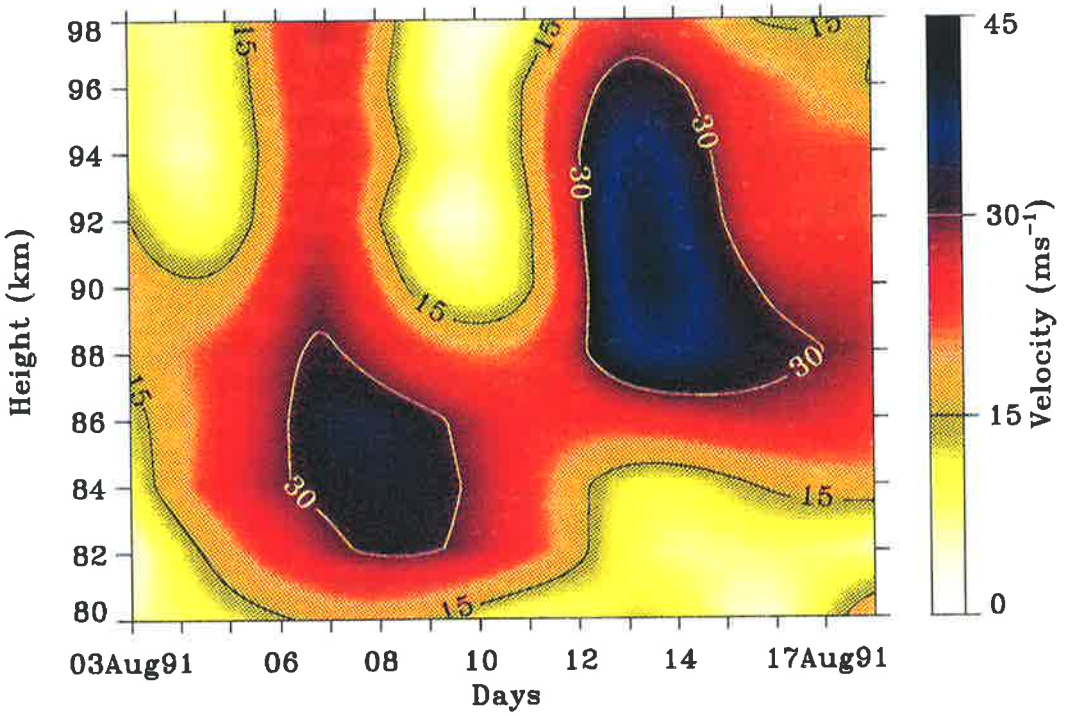

Figure 4.56: Wind speeds for the 2-day wave meridional wind component during August, 1991. The colour and contours (scales shown on the right-hand side) represent the wind speeds in ms^{-1} as for Figure 4.54.

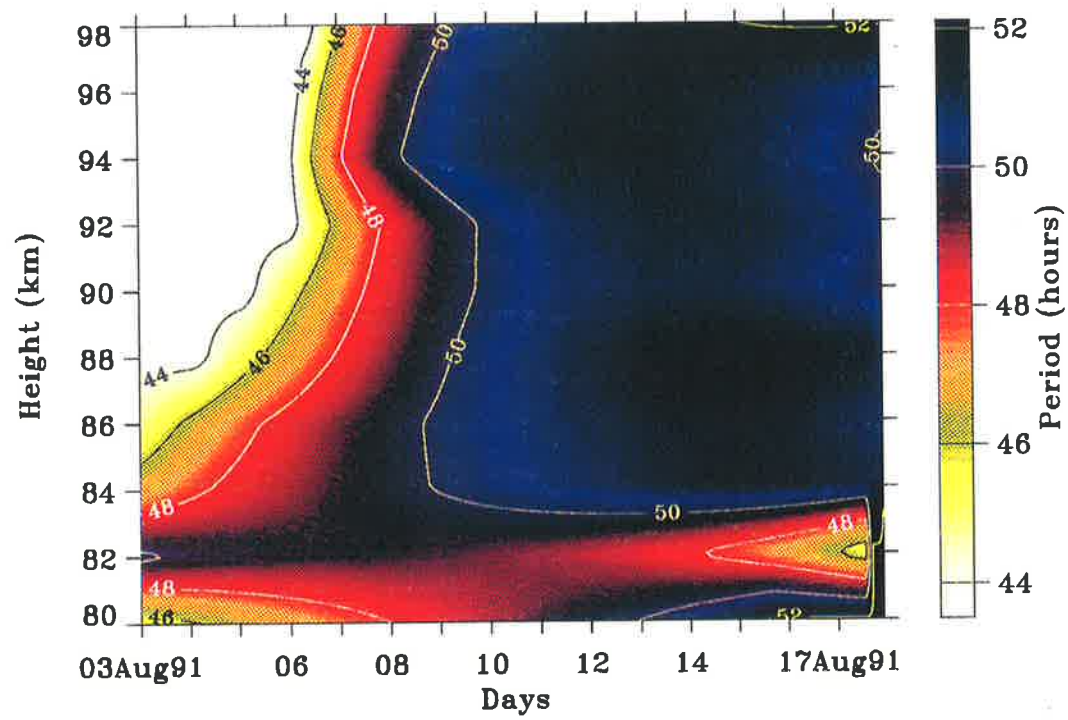

Figure 4.57: Period for the 2-day wave during August, 1991. The colour and contours (scales shown on the right-hand side) represent the wave period in hours as for Figure 4.55. The time axis is identical to that in Figure 4.56.

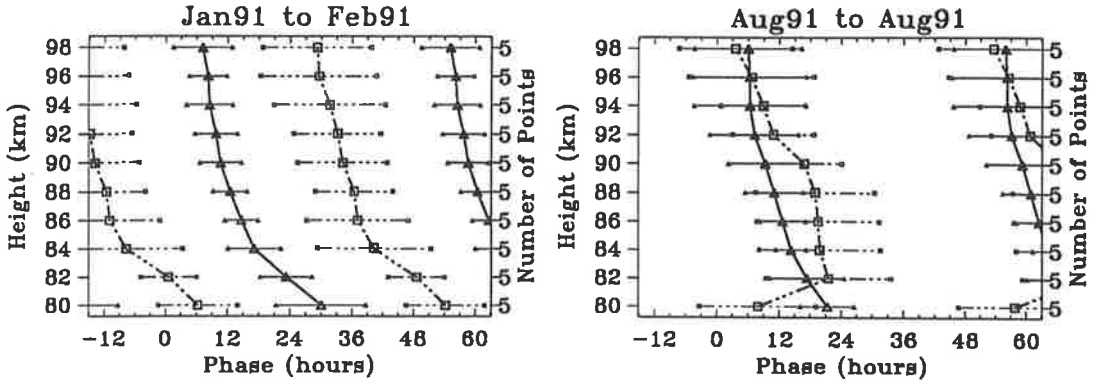

Figure 4.58: The mean vector phase (hr LT) for the meridional and zonal components (as for Figure 4.52) for time intervals in February (left) and August (right) 1991, as a function of altitude.

4.4.6 Evidence for Non-linear Interactions

Figure 4.42 shows that during both December solstices there is a strong peak at a period of 16 hr. Peaks are also present during both the June solstices but have considerably less power. The presence of a 16 hr oscillation at the time of large 2-day wave amplitudes has been noted before [*Manson & Meek*, 1990, for example]. Since a 16 hr component is the third harmonic of 48 hr this may be evidence of non-linearity in the 2-day wave oscillation. Alternatively, a non-linear interaction between the 2-day wave and one of the solar tides could produce a sum or difference term at a period of 16 hr [*Manson & Meek*, 1990; *Teitelbaum & Vial*, 1991]. These arise from the product of two sinusoids:

$$A\sin(\omega_1 t)\sin(\omega_2 t) = \frac{1}{2}A\{\cos[(\omega_1-\omega_2)t] + \cos[(\omega_1+\omega_2)t]\}\,. \tag{4.1}$$

It can be seen that $1/12 - 1/48 = 1/16$ and $1/24 + 1/48 = 1/16$.

The structure of the 16 hr component was studied by bandpass filtering the raw wind data in a similar manner to that used for the 2-day wave, but with a bandpass extending from 15.0 to 17.1 hr. This bandpass allows amplitude variations with time scales larger than 5 days to be discerned, compared with 10 days for the 48 hr component. The same time interval in January/February 1991 as for the 2-day wave was selected. The 16 hr meridional wind component was found to have amplitudes exceeding 25 ms^{-1} for 10% of this time interval at altitudes near 90 km (Figure 4.59). The median amplitude is near 12.5 ms^{-1} for altitudes from 86 to 98 km. The phase fronts are highly coherent with altitude and time and have a downward progression. The estimated vertical wavelength is in excess of 150 km. Comparison of the temporal and vertical structure of the 16 hr component, as shown in Figure 4.60, with that of the 2-day wave (*c.f.* Figure 4.54) shows that the times and heights of peak amplitudes agree well.

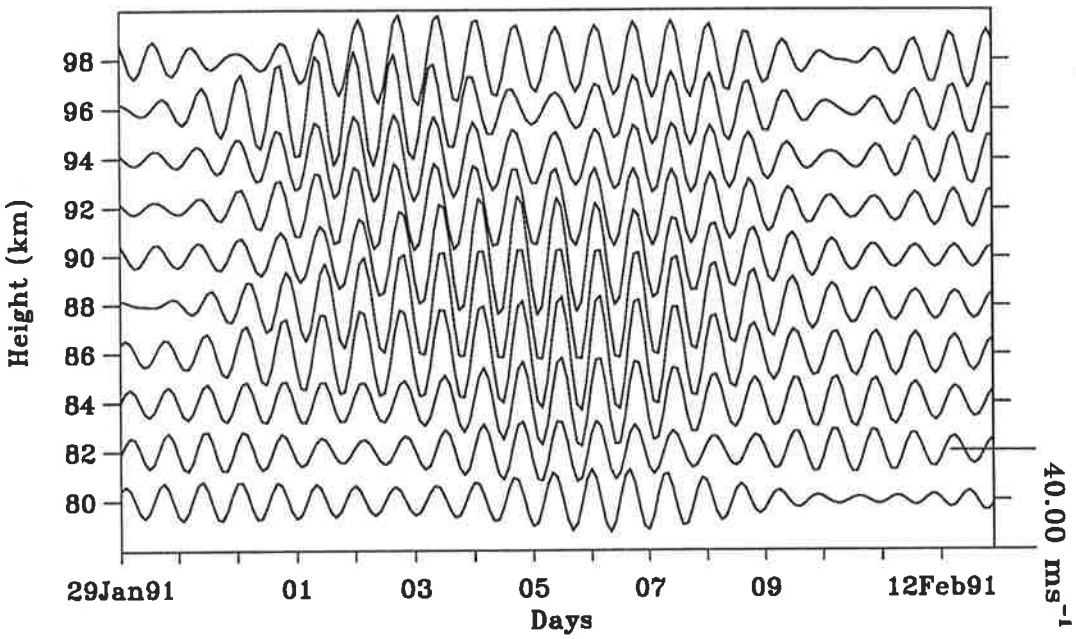

Figure 4.59: Bandpass filtered meridional winds for the near 16 hr component during February 1991. A pass-band of 15.0 to 17.1 hr was used. Axes are the same as in Figure 4.53.

The period of the near 16 hr component was determined at each height by a complex demodulation technique using data taken in the February time interval, when the 48 hr component was largest. The effective bandpass used was 15.0 to 17.1 hr (as for the filtered time series). The period as a function of altitude and time is shown in Figure 4.61 in the same fashion as the amplitudes in Figure 4.60. In the altitude region from 84 to 92 km during the interval from the 2^{nd} to the 7^{th} of February 1991, when the amplitude of the 16 hr component is large (*c.f.* Figure 4.60), the period is 16 $\pm$ 0.5 hr. This result is independent of the demodulation period and exact bandpass, indicating that there is a dominant 16 hr period wave present. Closer inspection shows that the amplitude peak in the 16 hr component during February 1991 occurs just after the peak in the 48 hr component. The sharp rise in the amplitude of the 16 hr component starts near the time of the maximum in the 48 hr component for all altitudes from 84 to 98 km.

A 16 hr wind component could arise as a harmonic of the non-linear 2-day wave. In this case a weaker 9.6 hr wave should also be observed. Figure 4.62 shows a section of the time series formed using a bandpass from 9.2 to 10.0 hr which has been designed to capture any 9.6 hr wave component while allowing as many degrees of freedom as for the 16 hr bandpass. A fair degree of coherence with altitude can be seen although the amplitudes are small and peak at a different time and altitude range to the 16 hr component. Figure 4.63 shows a section of a bandpassed time series of a quiet portion of the spectrum around a central period of 14 hr. The bandpass is from 13.2 to 14.8 hr, giving an equivalent width to the other frequency intervals. The amplitude

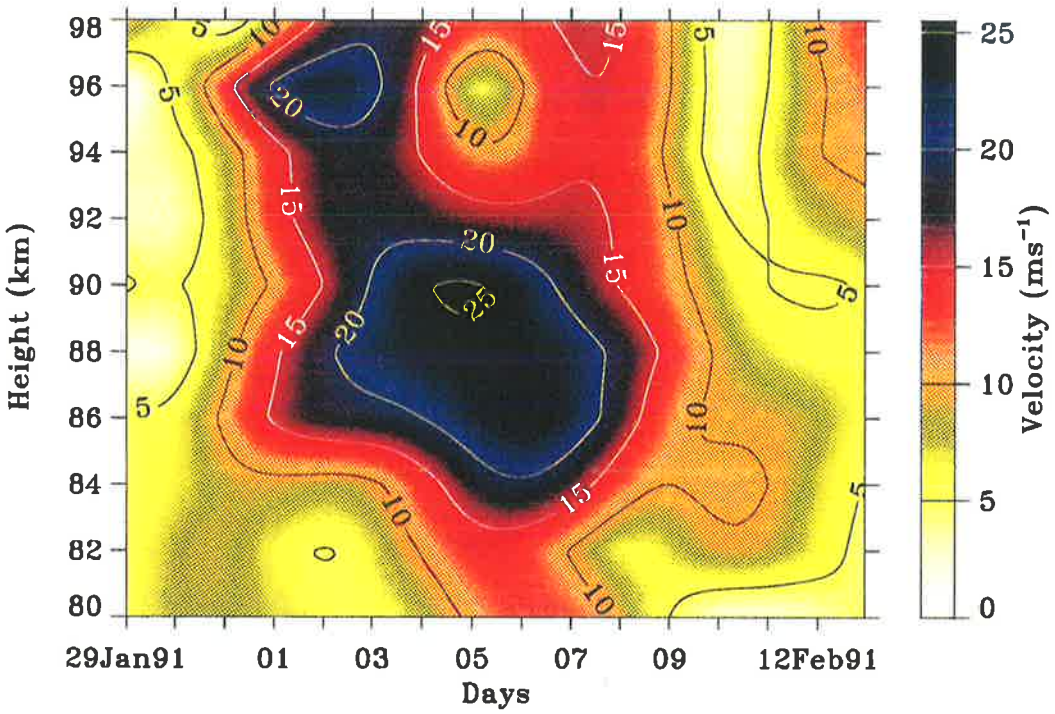

Figure 4.60: Wind speeds for the 16-hour meridional wind component during February, 1991. The colour and contours (scales shown on the right-hand side) represent the wind speeds in ms^{-1} as in Figure 4.54. The time axis is identical to that in Figure 4.54.

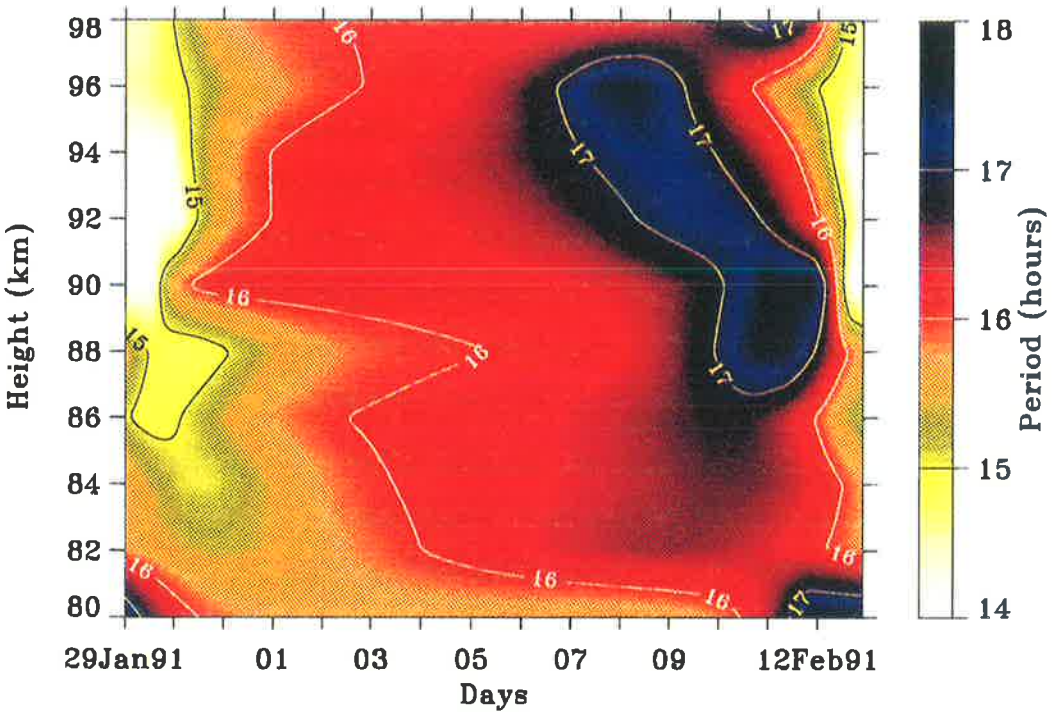

Figure 4.61: Period for the 16-hour wind component during February, 1991. The colour and contours (scales shown on the right-hand side) represent the wave period in hours. The time axis is identical to that in Figure 4.54.

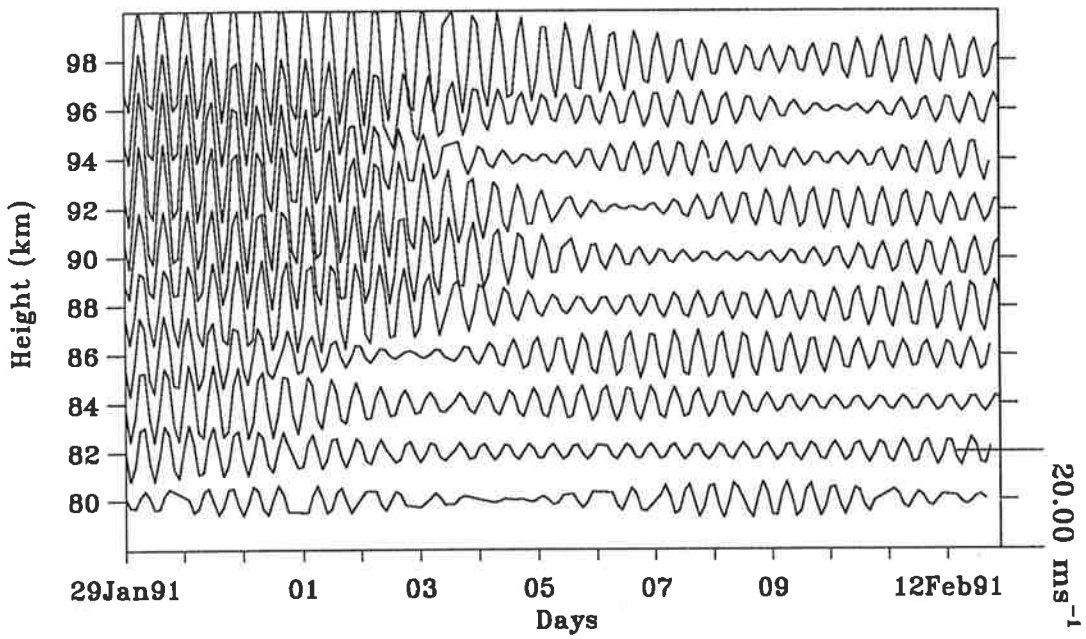

Figure 4.62: Bandpass filtered meridional winds for the near 9.6 hr component during February 1991. A pass-band of 9.2 to 10.0 hr was used. Axes are the same as in Figure 4.53.

in this period range rarely exceeds $10\,\mathrm{ms}^{-1}$ at all altitudes at any time of year, only slightly smaller than the maximum of the 9.6 hr bandpassed winds. The moderate phase coherence with altitude exhibited by the 14 hr component could either reflect the nature of the bandpass or be a property of the winds in this spectral range. To decide between these two options – which has a bearing on the confidence of the 16 and 9.6 hr winds but not on the 2-day bandpasses due to their much wider bandwidth – a randomised wind field was generated. This was made by using the values of the raw winds for the full dataset and assigning them to random time intervals. In this way the overall statistical properties of the wind field remained unchanged but any short or medium term periodicity was removed. Extracting a 14 hr component from this wind field as before gave a wind as shown in Figure 4.64. A phase coherence with altitude is not so evident here as in Figure 4.63, suggesting that it is a real phenomenon in the latter. This gives more confidence that the coherent height and time structures apparent for the 48-, 16- and 9.6 hr components are real rather than manifestations of the processing.

Figure 4.65 places the temporal behaviour of the 2-day wave and the 16 hr and 9.6 hr components in context with the variations of the prevailing zonal wind and the solar tides at an altitude of 92 km. Each plot is displaced vertically by a distance equivalent to $30\,\mathrm{ms}^{-1}$, except for the the mean zonal wind which extends through $\pm 50\,\mathrm{ms}^{-1}$ (eastward shown positive), and the 2-day wave, which extends from 0 to $45\,\mathrm{ms}^{-1}$. The low levels near October and December 1990 indicate missing data. As a reference against which the amplitudes of the various wave

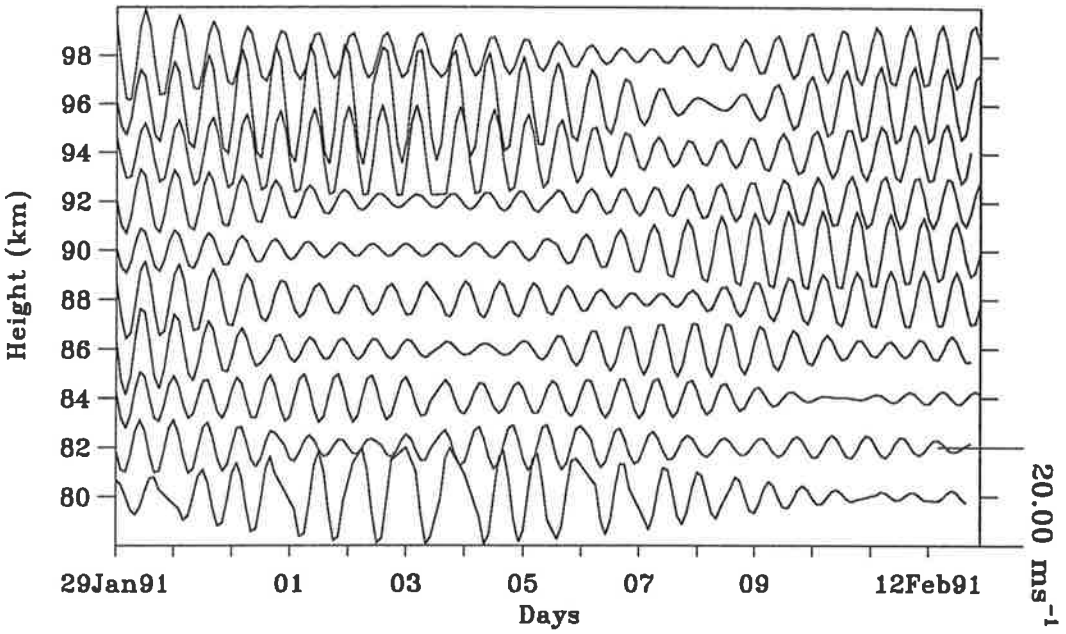

Figure 4.63: Bandpass filtered meridional winds for the near 14 hr component during February 1991. A pass-band of 13.2 to 14.8 hr was used. Axes are the same as in Figure 4.53.

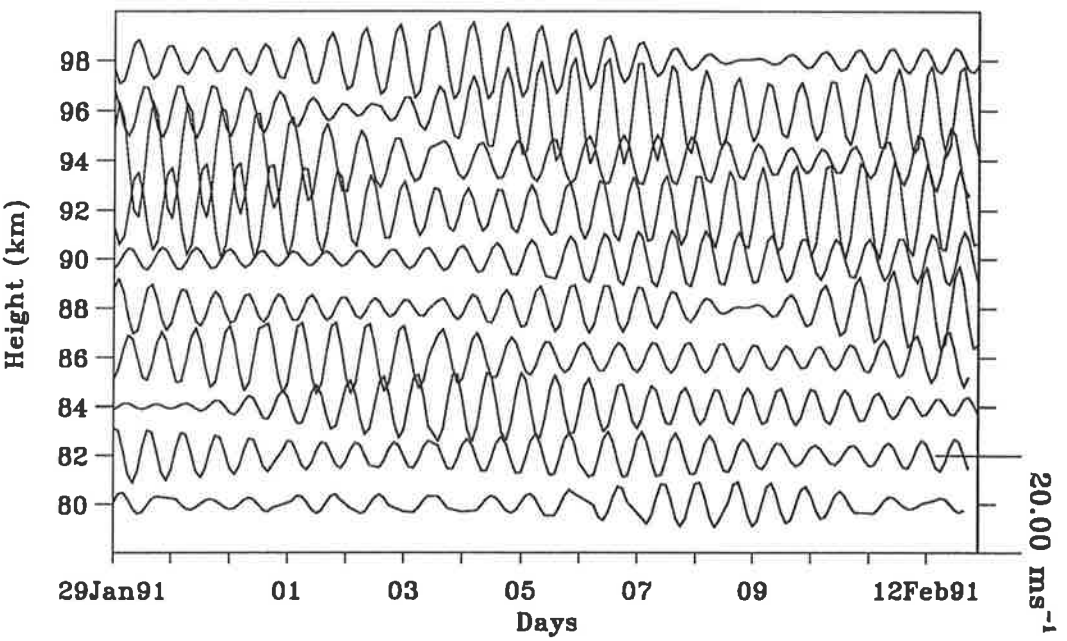

Figure 4.64: Bandpass filtered winds for the near 14 hr component from a randomised wind field. Otherwise as for Figure 4.63.

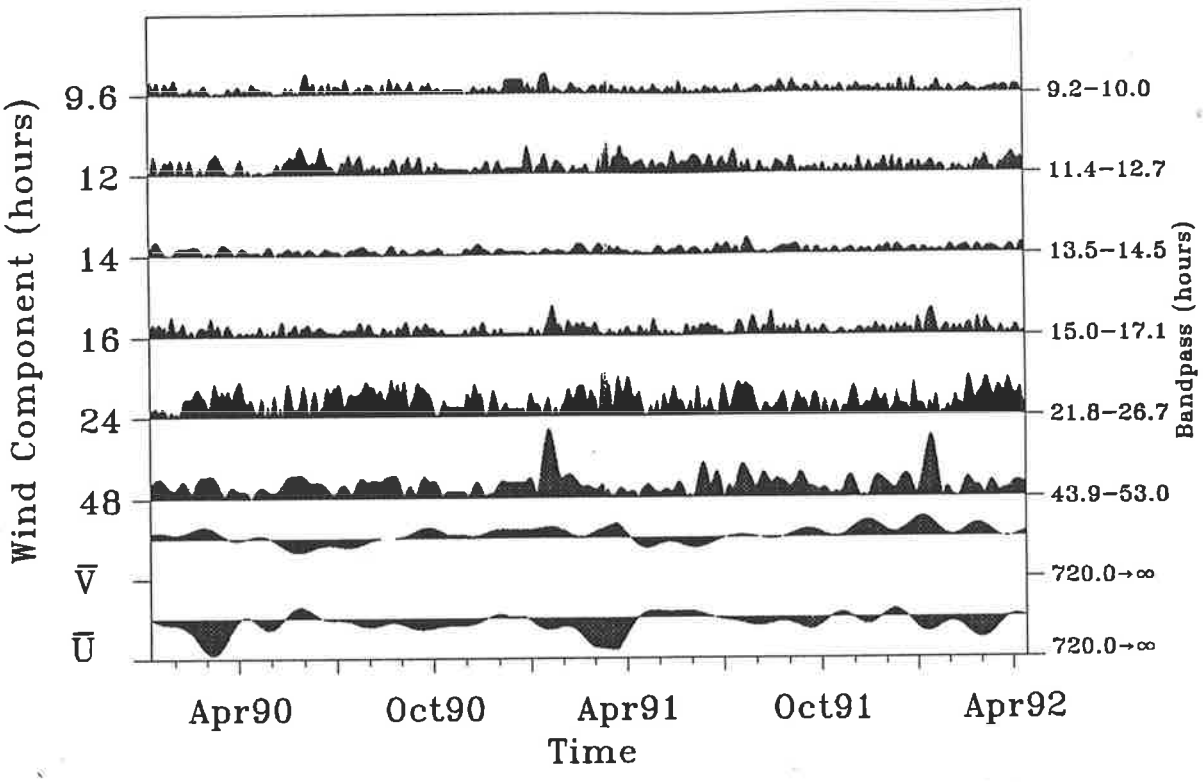

Figure 4.65: Amplitudes of the meridional wind components at 92 km from late January, 1990, to the end April, 1992. The major tick marks along the horizontal axis are for the middle of January, April, July and October. The scale of the mean zonal wind (U) is from $\pm 50\,\mathrm{ms}^{-1}$ (eastward positive). The range of the 48 hr component is $45\,\mathrm{ms}^{-1}$. Each subsequent plot is separated by a distance equivalent to $30\,\mathrm{ms}^{-1}$. The bandpasses used are shown on the right-hand side.

components can be compared, the demodulated amplitude of the 14 hr bandpass is also shown.

Figure 4.42 as well as Figure 4.65 show that the amplitude of the diurnal solar tide is reduced during the time of greatest amplitude of the 2-day wave in February 1991 and 1992. This effect is not obvious at the time of the other period of enhanced 2-day wave activity in July. In contrast, the semi-diurnal solar tidal amplitude does not appear to change significantly during these intervals compared with its behaviour during the rest of the year.

4.4.6.1 Bispectral Analysis

One way to test whether the 16 hr component is a product of non-linear interaction of the 2-day wave and one of the solar tides is to perform a higher-order spectral analysis. Section 2.9 gives a brief description of the hierarchy of the linear spectral estimates. There are some subtle problems with these forms of analyses, the most important for the present study are their lower tolerance of non-stationarity than for a power spectral analysis, and the often ambiguous

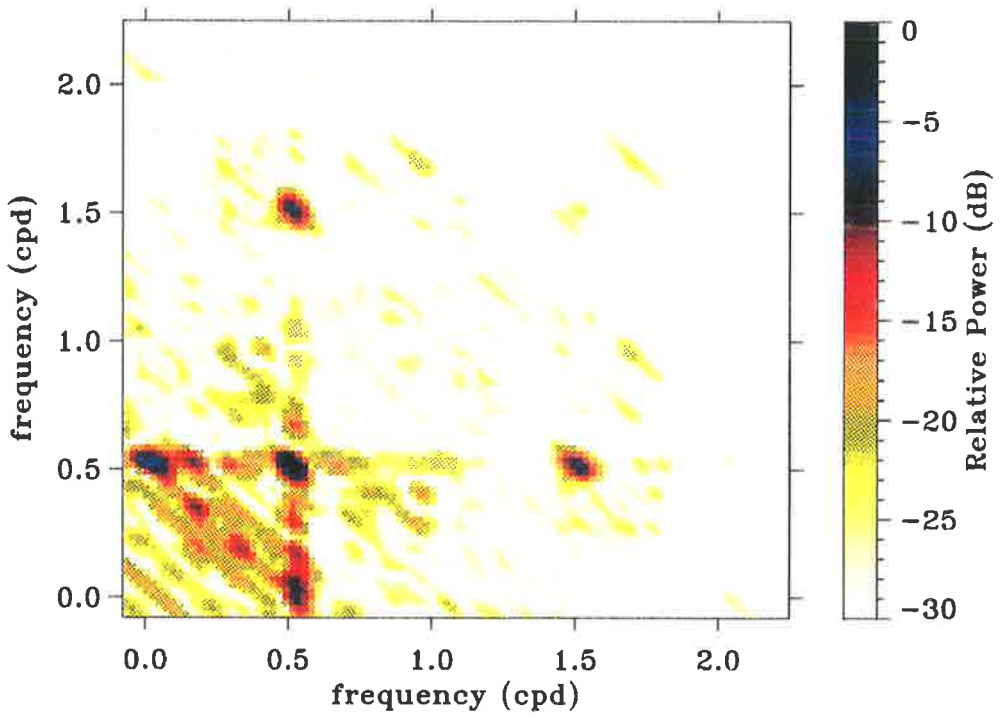

Figure 4.66: Bispectrum of the meridional winds near the equator during February, 1991. The colour scale indicated on the extreme right-hand-side shows the relative power in dB.

interpretations. Nevertheless, a bispectral analysis of the February 1991 data was performed with the collaboration of Dr S. Anderson and Mr A.O. Zollo of the High Frequency Radar Division of the Defence Science and Technology Organisation[8]. Higher-order spectra require a larger volume of data in order to obtain the same resolution as a power spectrum. In order to increase the amount of data available and yet maintain the short time interval necessary to not mask the 2-day wave signal, the data collected simultaneously from several altitude regions were used as though they were separate estimates of the same signal. Due to the wind data being real the bispectrum has an 8-fold symmetry (see Chapter 2). A plot of the bispectrum for the positive quadrant is shown in Figure 4.66. Strong peaks indicate that the two frequency components labelled on the axes interact in some non-linear way. Thus a non-linear correlation between the 16 hr component and the 48 hr 2-day wave appears to exist. Perhaps more significantly, no such correlation is found between the 16 hour component and any of the solar tides. This, coupled with the similarity of the amplitude height-time structure between the 16 and 48 hr components, would suggest that the observed 16 hr spectral peaks are due to the non-linearity of the 2-day wave when its amplitude is very large. Peaks indicating an interaction between the 9.6 and 48 hr waves are also evident (not shown in Figure 4.66 due to the frequency scale). These contain little

[8]HFRD, DSTO, P.O. Box 1500, Salisbury, SA 5108, Australia

energy, which is not unexpected if the 9.6 hr component is the 4^{th} harmonic of the 48 hr wave as it would therefore carry a relatively smaller fraction of the available energy. The bispectral analysis also indicates non-linear interactions between the 48 hr component and the mean wind, and to some extent with the 24 hr solar tide. A self interaction is also evident.

4.4.7 Summary

In Section 4.4.3 it was found that for the December season the 2-day wave at Christmas Island had a median period of 48 hr, with decile ranges from 45 – 51 hr. For the season beginning in June the median period was 50 hr with a similar decile range. For the March and September equinoctial months the periods were found to be 48 and 52 hr respectively.

It was found in Section 4.4.4 that the mean meridional phases advanced towards earlier times with increasing altitudes. This indicates a descending phase and therefore upward energy propagation. Average vertical wavelengths of ~ 70 and ~ 80 km were found for the December and June solstices respectively, and >150 and ~ 60 km for the March and September equinoxes.

In Section 4.4.5 two time intervals were chosen for a closer inspection. These were intervals where the 2-day wave amplitude was at its maximum in each solstice - one in February, 1991, and the other in August, 1991. The upper decile wave amplitudes for each of these intervals were $\sim 40\,\mathrm{ms}^{-1}$. For the February interval, corresponding to when the 2-day wave maximises in the southern-hemisphere, it was found that the period was 48 ± 0.5 hr and the vertical wavelength was 70 km. The zonal and meridional components were in anti-phase. For the August interval, corresponding to when the 2-day wave maximises in the northern-hemisphere, it was found that the period was 50 ± 1 hr and the vertical wavelength was also 70 km. The meridional component was found to lead the zonal by 3 – 9 hr, which is between being in-phase and phase-quadrature.

It was noted in Section 4.4.6 that a peak in variance was observed at a period near 16 hr at the time when the 2-day wave had its maximum amplitude. The properties of this 16 hr component were examined. Upper decile amplitudes during February, 1991, were of the order of $25\,\mathrm{ms}^{-1}$, with median values of $12.5\,\mathrm{ms}^{-1}$. Phase fronts appeared to be highly coherent with altitude and time, exhibiting a downward progression. The vertical wavelength was found to be >150 km and the period was 16 ± 0.5 hr.

A weak 9.6 hr component was also observed but had different temporal variations of the amplitude than for the 16 hr component. The ampltiude of the diurnal solar tide was observed to be reduced during times of large 2-day wave amplitude for the December but not for the June solstice. The semi-diurnal solar tidal amplitudes appeared unchanged.

Bispectral analysis of the meridional winds during February, 1991, indicated that the 16 and 48 hr components had a phase correlation. No such correlation was found between the 16 hr component and any of the solar tides. This implies that the observed 16 hr peaks are due to the non-linear behaviour of the 2-day wave rather than an interaction with the solar tides.

Correlations between the 48 and each of the 9.6, 24 and mean wind components were also found.

4.5 Horizontal Flux of Horizontal Momentum

4.5.1 The Angular Momentum Budget

Average global surface winds are found to be westward at low latitudes but eastward at high latitudes. Due to surface friction the earth therefore exerts an eastward torque on the atmosphere near the equator. This is equivalent to an eastward flux of angular momentum from the earth to the atmosphere. At high latitudes the torque is in the opposite sense, which is equivalent to an eastward flux of angular momentum from the atmosphere to the earth [*Palmen & Newton*, 1969]. For angular momentum to be conserved it must be transferred polewards from the equator, the upward flux at low latitudes being balanced by the downward flux at high latitudes. Global circulations such as the Hadley cells at low latitudes can directly transfer meridional momentum. Other processes such as eddy and wave fluxes appear to be the main agents for the poleward momentum transfer.

Besides the momentum transfer required by latitudinal differences in mean wind motion, seasonal variations also exist which must be accompanied by adequate momentum fluxes. For example, at mid-latitudes the direction of the zonal winds in the middle atmosphere reverse at the beginning and end of summer (see Appendix E), requiring a massive reduction in angular momentum.

Using meteor wind data at Adelaide, *Elford* [1979] estimated a horizontal flux of horizontal momentum, $<U'V'>$[9], due to the diurnal tide of the order of $-100\,m^2s^{-2}$ during summer, with maximum values of $\sim -200\,m^2s^{-2}$. Using a few approximations a maximum drag on the zonal mean flow is calculated at $\sim 7\,ms^{-1}d^{-1}$, which is sufficient to account for the annual changes in the zonal flow at those altitudes. The semi-diurnal tide contributes minimal flux, hence drag, at these times. *Hines* [1972] estimates – from theoretical graphs of the dominant propagating diurnal tide presented by *Lindzen* [1967] – that the upward flux density of eastward momentum,

[9] where U',V', W' are the perturbational wind velocities in the zonal, meridional and vertical directions respectively

$< \rho U'W' >$, could possibly cause an acceleration of the zonal mean flow of $\sim 20\,\mathrm{ms^{-1}d^{-1}}$ at 85 km, increasing to $\sim 200\,\mathrm{ms^{-1}d^{-1}}$ at 100 km. These values show that the tides can deposit large amounts of momentum into the atmosphere. For momentum to be conserved it is found that even larger amounts of deposition are required. *Ebel* [1974] estimated from Groves' atmospheric wind model [*Groves*, 1969; *Groves*, 1971] that the zonal acceleration at 90 km due to the mean meridional and vertical motions would be $\sim 180\,\mathrm{ms^{-1}d^{-1}}$ in summer and $\sim 90\,\mathrm{ms^{-1}d^{-1}}$ in winter. The measured zonal acceleration in mid-winter at these altitudes is no greater than $2\,\mathrm{ms^{-1}d^{-1}}$ [*Elford*, 1979]. Thus the flux of angular momentum of the tides alone is not enough to balance that of the mean motions.

It is now recognised that short-period gravity wave activity can account for most of this discrepancy. *Reid & Vincent* [1987], for example, found that the upward flux of horizontal momentum for gravity waves of periods < 8 hr accelerated the mean flow by between $50-80\,\mathrm{ms^{-1}d^{-1}}$ in the local summer at Adelaide. Peak values of $190\,\mathrm{ms^{-1}d^{-1}}$ were found. 70% of the total momentum flux was attributed to gravity waves with periods < 1 hr.

The 2-day wave is a large amplitude wave event and the results of previous sections indicate that its components are mostly in-phase or in anti-phase, thus it could transport large amounts of momentum and possibly have a large effect on the zonal acceleration. As only the zonal and meridional components of the 2-day wave are available from this work, only the horizontal flux of horizontal momentum, $< U'V' >$, can be directly estimated here.

4.5.2 The Zonal Momentum Equation

The time evolution of the mean zonal flow, $\partial\overline{U}/\partial t$ for a latitudinal belt bounded by the latitudes ϕ to $\phi + d\phi$ and altitudes z to $z + dz$, can be derived from the general momentum equation for the atmosphere. This is found by considering the total momentum flux through a volume of fluid (see for example *Gossard & Hooke* [1975] or *Kelley* [1989]).

$$\rho\frac{d\mathbf{U}}{dt} = \mathbf{F} + \eta\nabla^2\mathbf{U} - \nabla p - \nabla.\boldsymbol{\tau}\,, \tag{4.2}$$

which is simply the Navier-Stokes equation (equation 1.4) described on page 14.

Considering only the zonal (longitudinal) component, and a zonal and temporal average, gradients in the zonal direction vanish, as do gradients of the mean zonal wind. As only the regions below 100 km are of concern, ion drag is negligible. Equation 4.2 then reduces to,

$$\begin{aligned}\rho\frac{d\overline{U}}{dt} &= 2\Omega\sin\phi\,\rho\overline{V} \\ &\quad -\frac{\rho}{a\cos^2\phi}\frac{\partial}{\partial\phi}(\overline{U'V'}\cos^2\phi)\end{aligned}$$

$$-\frac{\partial}{\partial z}(\rho\overline{U'W'}), \tag{4.3}$$

when expressed in spherical coordinates. $\overline{U}$, $\overline{V}$ and $\overline{W}$ are the mean zonal, meridional and vertical velocities respectively, with U′, V′ and W′ being the perturbations as before. The atmospheric density, ρ, is considered constant for a given altitude. a is the radius of the Earth ($\approx 6.37 \times 10^6$ m). As the total derivative,

$$\frac{d\overline{U}}{dt} = \frac{\partial\overline{U}}{\partial t} + \frac{\overline{V}}{a\cos\phi}\frac{\partial}{\partial\phi}(\overline{U}\cos\phi) + \overline{W}\frac{\partial\overline{U}}{\partial z}, \tag{4.4}$$

equation 4.3 gives

$$\begin{aligned}\frac{\partial\overline{U}}{\partial t} &= \overline{V}\left[2\Omega\sin\phi - \frac{1}{a\cos\phi}\frac{\partial}{\partial\phi}(\overline{U}\cos\phi)\right] \\ &\quad -\overline{W}\frac{\partial\overline{U}}{\partial z} \\ &\quad -\frac{1}{a\cos^2\phi}\frac{\partial}{\partial\phi}(\overline{U'V'}\cos^2\phi) \\ &\quad -\frac{1}{\rho}\frac{\partial}{\partial z}(\overline{U'W'}\rho),\end{aligned} \tag{4.5}$$

The first term in equation 4.5 reflects the conservation of angular momentum with variation in latitude. The second term reflects how $\overline{U}$ for an air parcel resists change as the parcel is displaced vertically. The third and fourth terms arise from the divergence of horizontal and vertical momentum fluxes respectively. The third term can be further broken down into two terms,

$$-\frac{1}{a\cos^2\phi}\frac{\partial}{\partial\phi}(\overline{U'V'}\cos^2\phi) = \left\{\frac{2\tan\phi}{a} - \frac{1}{a}\frac{\partial}{\partial\phi}\right\} < U'V' >, \tag{4.6}$$

where the mean values have been replaced by an ensemble average denoted by $< \ldots >$. Equation 4.6 shows that $< U'V' >$ combined with its gradient in the meridional direction is a direct measure of the acceleration on the zonal flow applied by whatever has caused the perturbation velocities.

4.5.3 Momentum Fluxes at Mid- and Low-Latitudes

Since the data has been bandpassed, the zonal and meridional components of the 2-day wave can be considered as perturbation velocities, U′ and V′. Weekly averages of the product U′V′ have been taken for the data from Adelaide (35° S) and Christmas Island (2° N) . These are shown in Figure 4.67 for the seven-year interval from 1984 to 1991 for the Adelaide data, and in Figure 4.68 for the full equatorial data set. The large fluxes coinciding with the peaks in the 2-day wave amplitudes during the solsticial months (*c.f.* Figures 4.36 and 4.46) dominate

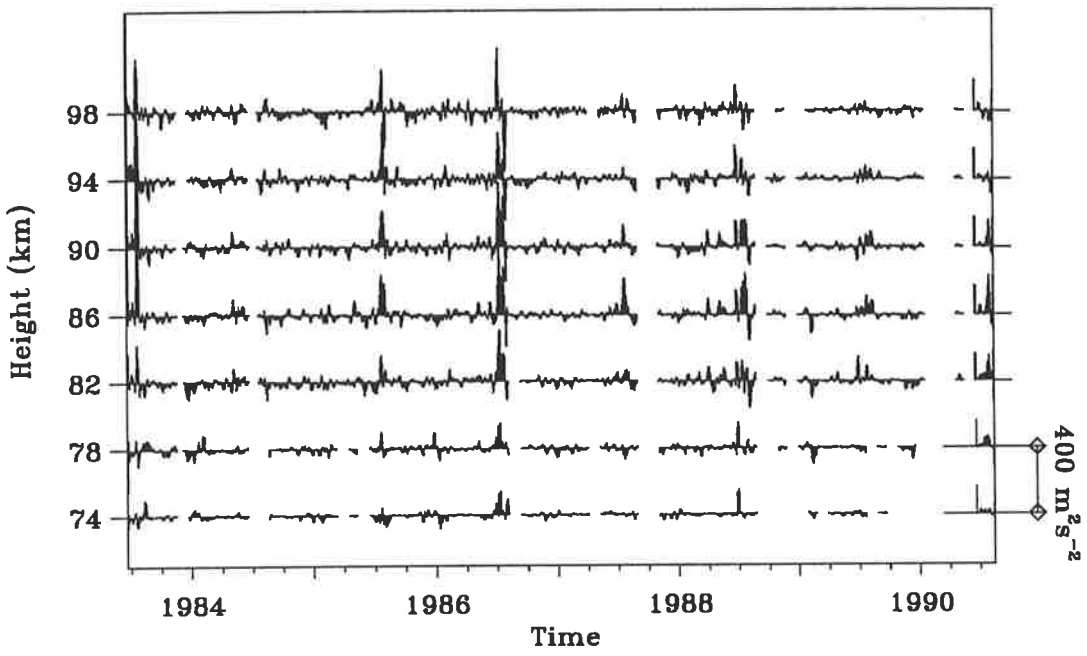

Figure 4.67: Horizontal transport of horizontal momentum flux associated with the 2-day wave throughout the 7 year period for all altitudes. Each altitude has been displaced vertically as indicated by the scale on the right-hand side. The major ticks mark the 1^{st} of July of each year, with minor ticks at three monthly intervals

Figures 4.67 and 4.68 respectively. It should be noted that at the equatorial site the sense of the momentum flux is mostly negative during the southern hemisphere summer and positive during the northern hemisphere summer. The sense of the flux at Adelaide on the otherhand is positive during the local (southern hemisphere) summer.

Firstly, consider the mid-latitude results. Collecting the momentum fluxes into separate seasons (Figure 4.69) it is immediately clear that a different process is occurring during summer. The horizontal transport of horizontal momentum flux is greater than $+150\,m^2s^{-2}$ for about 10% of the time during summer at 86 km. A small positive median momentum flux is obtained, with larger mean fluxes ($+30\,m^2s^{-2}$ at 86 km). The horizontal momentum flux is between -40 and $+20\,m^2s^{-2}$ 80% of the time for all other seasons, with median and mean values near zero for the equinoxes and small negative values during winter. The fluxes for each individual summer from 1980 to 1991 are shown in Figure 4.70. More inter-annual variation is shown than Figure 4.69 indicates. Upper decile fluxes reach values of $+250\,m^2s^{-2}$, although median and mean values rarely exceed $+40\,m^2s^{-2}$. The summer[10] of 1983 is an exception. On this occasion the mean flux was near $+160\,m^2s^{-2}$ at 86 km. Mean fluxes are also large during the summer of 1983

[10] December, 1982 – February, 1983

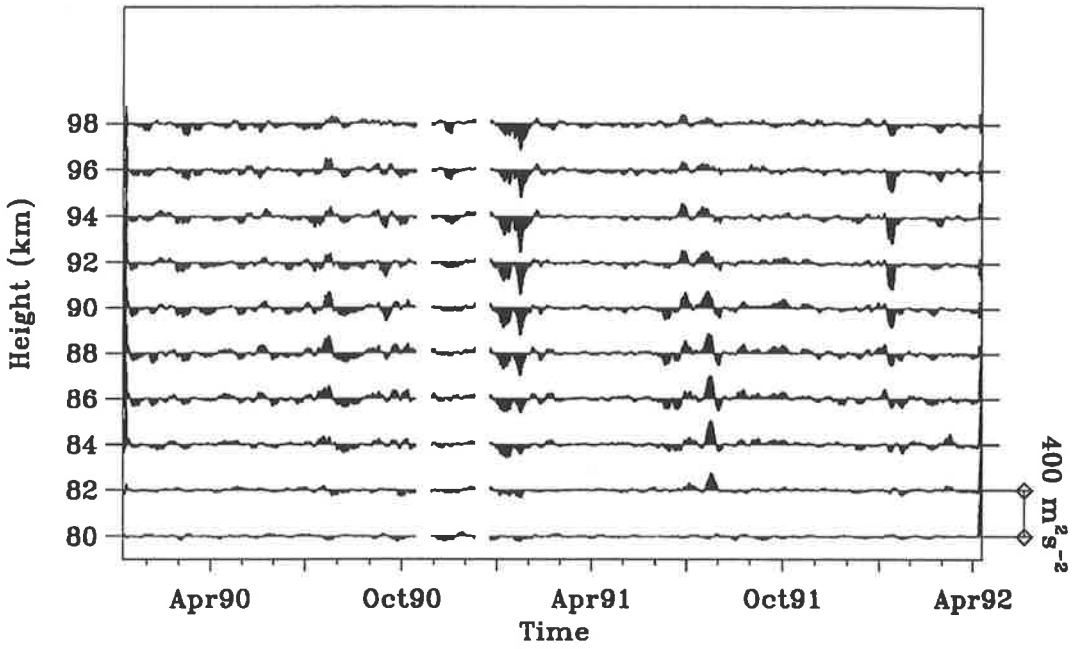

Figure 4.68: Horizontal transport of horizontal momentum flux per unit mass associated with the 2-day wave for all altitudes over the equatorial data set. Major ticks along the x-axis mark the middle of April, July and October (*i.e.* each season), with minor ticks marking the middle of the remaining months. Otherwise as for Figure 4.67.

($+100\,\mathrm{m^2s^{-2}}$). Peak fluxes attain values of over $+400\,\mathrm{m^2s^{-2}}$ but are as short lived as the peaks in the 2-day wave.

Like at mid-latitudes, collecting the momentum fluxes for Christmas Island into separate seasons (Figure 4.71) shows that a different process is occurring during the solsticial and the equinoctial months. Peak fluxes are of the order of $\mp 400\,\mathrm{m^2s^{-2}}$.

The peak values for $< \mathrm{U'V'} >$ give an *acceleration* due to the first term in equation 4.6 of $\sim -7.6\,\mathrm{ms^{-1}d^{-1}}$ during the December solstice at Adelaide and $\sim -0.4\,\mathrm{ms^{-1}d^{-1}}$ during the December solstice and $\sim +0.4\,\mathrm{ms^{-1}d^{-1}}$ during the June solstice at Christmas Island. Upper decile values for these occasions are ~ -2.8, ~ -0.1, and $\sim +0.1\,\mathrm{ms^{-1}d^{-1}}$ respectively.

The gradient of $< \mathrm{U'V'} >$ with latitude cannot be determined from a single site. In the absence of observations from nearby sites, some approximations to the second term in equation 4.6 have to be made.

In Table 2 of *Phillips* [1989] the phase difference between the zonal and meridional components of the 2-day wave during the December solstice at Mawson (66.5° S, 63.0° E) are given, with the average being 11 hr. This means that the components are in near phase-quadrature so that $< \mathrm{U'V'} >$ must approach zero at this latitude.

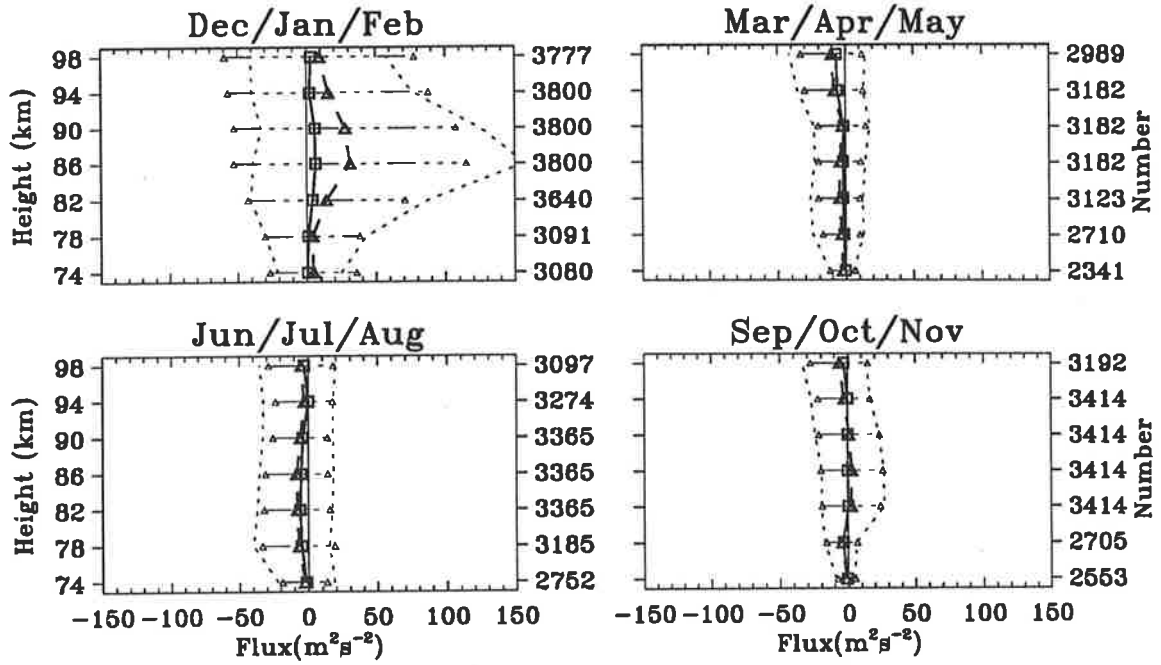

Figure 4.69: Distribution of the horizontal momentum fluxes in Figure 4.67 for each season as a function of altitude. The solid line with the square symbols shows the median value with the upper and lower deciles shown as dotted lines. Means are shown as triangle symbols – with 1 standard deviation error bars – connected by dashed lines.

Tsuda et al. [1988] found amplitudes for the components of the 2-day wave at Kyoto (35° N, 136° E) of ~ 10 and $\sim 20\,\mathrm{ms}^{-1}$ during June, 1983. A phase difference of 120° was also found, giving an estimate for $< \mathrm{U'V'} >$ of $-100\,\mathrm{m}^2\mathrm{s}^{-2}$. The amplitudes and phase difference during January, 1984, were estimated as ~ 5 and $\sim 10\,\mathrm{ms}^{-1}$ and 150°, giving an estimate for $< \mathrm{U'V'} >$ of $-43\,\mathrm{m}^2\mathrm{s}^{-2}$.

Using these values and those obtained in this section it is possible to estimate the change in flux with latitude for both the mid- and low-latitude sites. Four points can be used for the December solstice for both Adelaide and Christmas Island, while only two points are available to determine $-\frac{1}{a}\frac{\partial}{\partial\phi} < \mathrm{U'V'} >$ for the June solstice. The relationship between the latitudes and estimates of the horizontal flux of horizontal momentum are shown in Figure 4.72.

The rate of change of the horizontal momentum flux with latitude at 35° S and 2° N, for the December solstice, was first found by fitting a cubic (using a method of least-squares) to the four horizontal momentum flux estimates (*c.f.* Figure 4.72). This allowed estimates for the second term in equation 4.6 to be made. Using the maximum horizontal momentum flux of $400\,\mathrm{m}^2\mathrm{s}^{-2}$, zonal accelerations were estimated as $\sim +11.0$ and $\sim +12.5\,\mathrm{ms}^{-1}\mathrm{d}^{-1}$ at Adelaide and Christmas Island respectively. Upper decile horizontal momentum flux values of $\sim +150$ and $\sim -120\,\mathrm{m}^2\mathrm{s}^{-2}$ gave zonal accelerations of $\sim +3.4$ and $\sim +4.6\,\mathrm{ms}^{-1}\mathrm{d}^{-1}$ at these sites. The

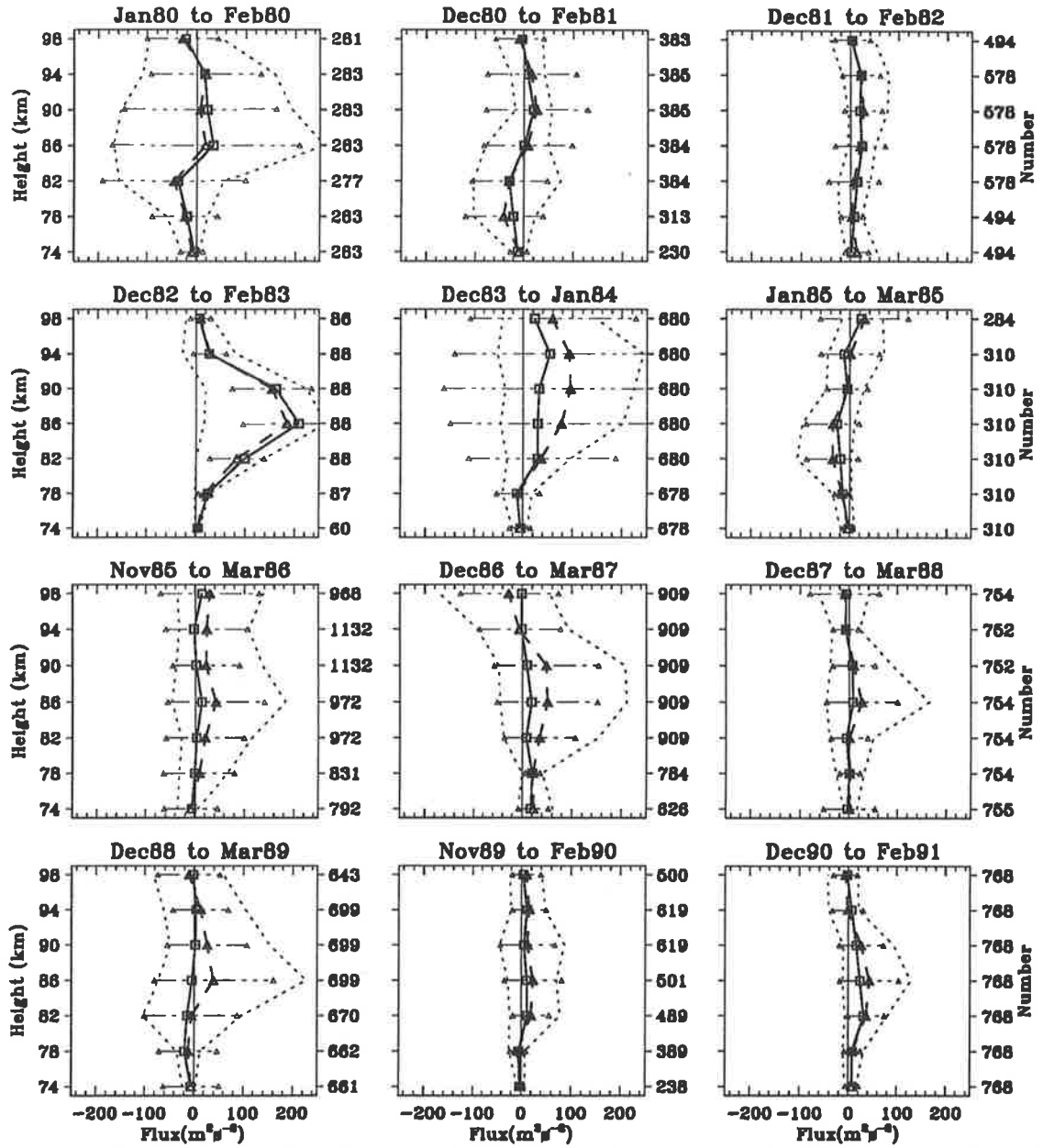

Figure 4.70: Distribution of the horizontal momentum fluxes for each of the summers from 1980 to 1991 as a function of altitude. Mean, median and deciles as for Figure 4.69.

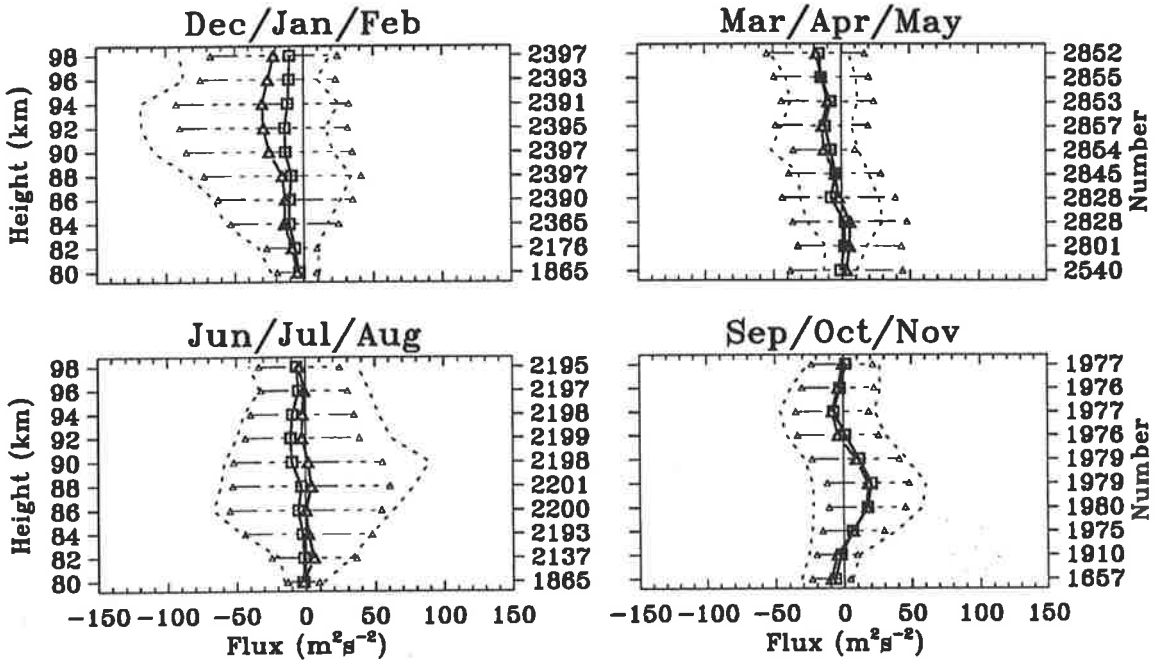

Figure 4.71: Distribution of the horizontal momentum fluxes in Figure 4.68 for each season as a function of altitude. Otherwise as for Figure 4.69.

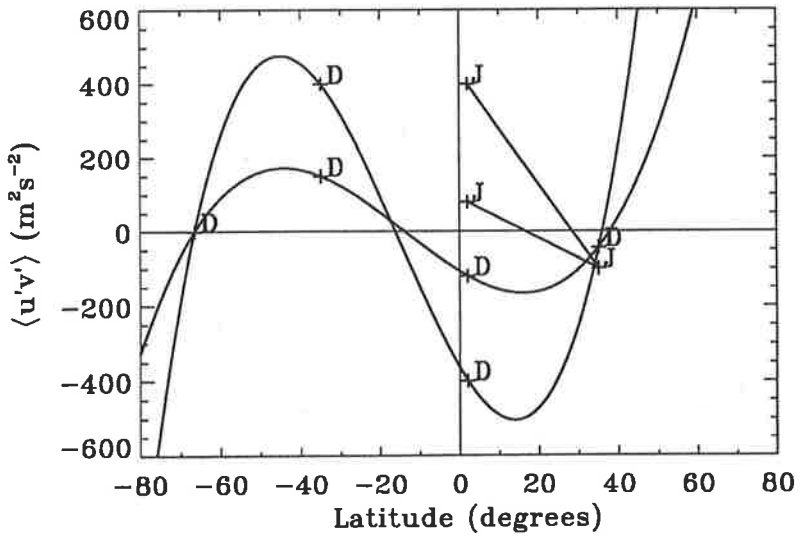

Figure 4.72: Horizontal flux of horizontal momentum estimated for various latitudes. The values for the December solstice are marked with a D while those for the June solstice with a J. Both the maximum and upper decile values are marked. The December solstice values have had a cubic fitted in order to estimate the rate of change with latitude. Linear variations are assumed for the June solstice.

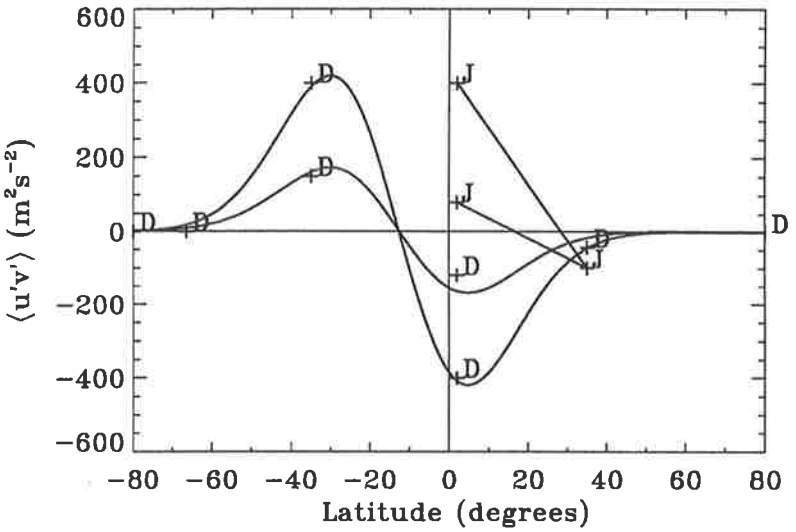

Figure 4.73: Horizontal flux of horizontal momentum estimated for various latitudes as in Figure 4.72 but fitting $\phi \exp(-\phi^2)$ to the December solstice values. The notation and axes are the same as in Figure 4.72.

flux values at both Mawson and Kyoto were assumed to represent both the upper decile and peak values.

Assuming a linear variation of the momentum flux with latitude for the June solstice (which most likely overestimates the slope), the maximum value of the gradient term is estimated as $-11.8\,\mathrm{ms^{-1}d^{-1}}$. Using the upper decile momentum flux value of $\sim 80\,\mathrm{m^2s^{-2}}$ gives a zonal acceleration of $-4.2\,\mathrm{ms^{-1}d^{-1}}$.

Care must be taken when interpretting the zonal accelerations derived from the latitudinal gradients in the momentum flux since values are known at only a few latitudes. Looking at Figure 4.72 it can be seen that a small shift of latitude of the peaks of the cubic fits could cause the gradients at -35° S and +2° N to change sign, dramatically changing the interpretations that can be made. The choice of a cubic fit may also be questionable since it gives unrealistic horizontal momentum flux values at high latitudes. To illustrate this point a different function was fit to the December solstice data and the slopes at -35° S and +2° N found. The function chosen was of the form $\phi \exp(-\phi^2)$, which has the property of being small at high latitudes. This was fit using a non-linear χ^2 minimisation regression. The resulting fit is shown in Figure 4.73

From inspection of this figure it is immediately clear that the estimated latitudinal gradients at -35° S and +2° N have changed markedly. Using this functional fit gives estimates of the maximum zonal acceleration of ~ -8.6 and $\sim +6.3\,\mathrm{ms^{-1}d^{-1}}$ at Adelaide and Christmas Island respectively. The upper decile zonal accelerations were estimated as ~ -3.5 and

Site	Lat.	$<U'V'>$ (m^2s^{-2})	$\frac{2\tan\phi}{a}<U'V'>$ $(ms^{-1}d^{-1})$	$-\frac{1}{a}\frac{\partial}{\partial\phi}<U'V'>$ ϕ^3 fit	$\phi\exp(-\phi^2)$	Total $(ms^{-1}d^{-1})$ ϕ^3 fit	$\phi\exp(-\phi^2)$
Adl	$-35°$ S	$+400$	-7.6	$+11.0$	-8.6	$+3.4$	-16.2
C.I.	$+2°$ N	-400	-0.4	$+12.5$	$+6.3$	$+12.1$	$+5.9$
Adl	$-35°$ S	$+150$	-2.8	$+3.4$	-3.5	$+0.6$	-6.3
C.I.	$+2°$ N	-120	-0.1	$+4.6$	$+2.6$	$+4.5$	$+2.5$

Table 4.3: Zonal accelerations induced by the horizontal flux of horizontal momentum due to the 2-day wave during the December solstice. Estimates for both the maximum (top two rows) and upper decile values (lower two rows), using two techniques to estimate the latitudinal gradient, are shown.

$\sim +2.6\,ms^{-1}d^{-1}$ respectively.

4.5.4 Summary

It has been found that the 2-day wave at mid-latitudes can contribute as much as twice the amount of horizontal momentum to the middle atmosphere as the solar tides during local summer.

Table 4.3 summarises the zonal accelerations induced by the horizontal flux of horizontal momentum due to the 2-day wave during the December solstice. As already mentioned, the estimate of the gradient contribution can vary considerably, especially at the latitude of Adelaide. As this term is at least of the order of the purely latitudinally dependent term, the estimate of the total contribution to the zonal acceleration can also vary considerably.

Taking the second model (the $\phi\exp(-\phi^2)$ fit) as being more physically correct, it can be tentatively concluded that over its lifetime the 2-day wave at southern mid-latitudes can cause a drag on the zonal flow which is of the same order as that associated with the diurnal tide. During times of peak amplitude though, the 2-day wave decelerates the mean flow by as much as twice this amount. Even at these maximum values, the combined efforts of the 2-day wave and the solar tides are not enough to counter-balance the strong Coriolis contribution, $2\Omega\sin\phi\,\overline{V}$, at mid-latitudes. This is in agreement with *Plumb et al.* [1987] who found maximum horizontal flux values of $\sim 800\,m^2s^{-2}$ at 90 km for the 2-day wave at Adelaide during the summer of 1984. They too concluded that the eddy momentum flux contribution of the 2-day wave was not enough to counter-balance the Coriolis contribution.

At near Equatorial latitudes the Coriolis contribution is small. Thus the zonal accelerations associated with the 2-day wave become more significant. Both forms of estimation of the gradient term at $2°$ N indicated that the zonal flow was accelerated by the action of the 2-day horizontal

momentum flux. The total acceleration of the zonal flow was determined as being in the region from $+5.9$–$12.1\,\mathrm{ms^{-1}d^{-1}}$. There are very few other studies of the zonal acceleration in general, and the horizontal flux of horizontal momentum in particular, at equatorial latitudes so no comparisons can be made at this stage.

As has been shown, the gradient with latitude of the momentum flux is a significant term, but is currently not well defined. Observations of the 2-day wave at spaced latitudes are required to determine this parameter more accurately. Judging from the plots of the momentum flux values (Figures 4.72 and 4.73), observations at latitudes near 20° S could give valuable information about the gradients with latitude.

4.6 Estimation of the Zonal Wavenumber

4.6.1 Introduction

As mentioned in Section 4.1, satellite observations and longitudinally spaced radar comparisons suggest that the 2-day wave is westward propagating, and has a zonal wavenumber of three[11]. This is in agreement with the proposal of *Salby* [1981a] that the wave is a manifestation of the free-mode mixed Rossby-gravity wave, the $(3,0)$ normal-mode of the atmosphere.

The zonal wavenumber can be estimated using two sites situated at similar latitudes but separated in longitude. A zonal wavenumber of three means that a wave will have three cycles circling the globe. Due to the vagaries of atmospheric motion it is desirable to have the two sites as close as possible in longitude, as the shorter the path difference the less chance the wave disturbance has of changing its characteristics. As the wave structure may be different for each cycle as they circle the globe, it is also desirable for the two sites to simultaneously sample the same cycle, *i.e.* to be within 120° of longitude of each other. Opposed to these considerations is the need for a large longitudinal separation in order to obtain an accurate estimate of the phase difference of the wave. The closer the sites the smaller the phase difference hence the larger the relative error in its estimate. For an error of 1% of a cycle in each phase estimate, the difference will have an error of 2% of a cycle. For a zonal wavenumber 3 wave this is $\sim 2.5°$ of longitude. In order for this to contribute less than a 10% error in an estimate of the zonal wavelength, the sites should be separated by at least 25° in longitude. There may also be latitudinal variations in the phase which makes the determination of the zonal wavenumber difficult to perform unless the latitudes of the two sites are very similar.

Poole [1990] obtained estimates of the zonal wavenumber, k, by comparing wave phase and

[11] termed the k-value for the remainder of this section

period data from the summer of 1987 for the three southern hemisphere sites of Grahamstown, Adelaide and Mawson. The latter two being derived from graphs published in *Phillips* [1989]. Poole estimated k to be 2.7 ± 0.1 for Adelaide-Grahamstown, with similar results for the other two combinations. This is less than expected. Using several years of data it should be possible to obtain more definitive results

4.6.2 The Data and Analysis

Comparisons are made between data from Grahamstown (33.3° S, 26.5° E) and Adelaide (34.5° S, 138.5° E). The relative geographic positions of these two sites are shown in Figure 4.2. As these two sites are essentially at the same latitude, variations of phase with latitude will not affect these results.

The data from Grahamstown consists of meteor wind data for the summers of 1987 to 1992 and forms part of a collaboration with Dr L.M.G. (Graham) Poole[12]. The data is nominally from a 20 km height region centred at an altitude of 95 km. Mean zonal and meridional winds over 45 min intervals have been used. Details of the radar installation at Grahamstown are given in *Poole* [1988].

The radar site at Buckland Park, near Adelaide has already been described in Section 4.2.2 and the data in Section 4.3.1. For these comparisons the wind data was further averaged into 45 min intervals. Initially a 20 km average from 86 to 106 km was performed in order to obtain the same form of resolution as the Grahamstown data. Later, to test whether possible local height variations of the 2-day wave structure were affecting the k-values, 8 km averages starting at 78, 86 and 94 km were performed and the analysis repeated.

The zonal wavenumber can be estimated if the phases of the 2-day wave are known for the two sites simultaneously. The phase difference along with the known longitudinal separation of the observation sites gives an estimate of the zonal wavelength, hence wavenumber. A more statistical approach is to use the phase of the cross-spectrum of the two wind time series. This is a measure of the average phase difference of the time series.

In order to compare the time series from spacially separated sites, first the data was converted to a common time frame, Universal Time or UT. A 14 day time interval was used for the data from each year, starting just after 0000 hr UT on the 15^{th} of January and ending just before 2359 hr UT on the 28^{th}. A FFT was used to obtain the cross-spectral phases and the k-values

[12] Department of Physics and Electronics, Rhodes University, Grahamstown, South Africa

Zonal wavenumbers from Meridional Winds
Adelaide (86–106 km) — Grahamstown (~85–105 km)

Years	1987	1988	1989	1990	1991	1992	mean
Ampl	438	44	117	44	74	77	–
Raw	2.83	2.75	2.27	3.43	2.89	3.02	2.9±0.3
Smooth	2.82	2.94	2.23	3.51	2.78	2.96	2.9±0.4

Table 4.4: K-values for the 2-day wave using meridional wind data averaged from 86–106 km for Adelaide and meteor heights for Grahamstown for the interval from 15^{th}–28^{th} January of each year. The peak cross-spectral amplitudes near 0.5 cpd are shown along with the k-values determined from the phases of the raw cross-spectrum and from a 5-point smoothed cross-spectrum. The last column shows the mean k-values along with a single standard deviation error estimate.

were computed as,

$$\mathrm{k} = \frac{360^\circ}{\Delta\theta}\left(\frac{\delta\varphi + 2\mathrm{n}\pi}{2\pi}\right), \tag{4.7}$$

where $\Delta\theta$ is the longitudinal difference between the observational sites in degrees and $\delta\varphi$ is the wave phase difference in radians as measured by the phase of the cross-spectrum at a frequency of 0.5 cpd. The $2n\pi$ is to account for the 2π ambiguity in the cross-spectrum phase. Equation 4.7 can be rewritten as

$$\mathrm{k} = \frac{360^\circ}{\Delta\theta}\frac{\delta\varphi}{2\pi} + \mathrm{n}\frac{360^\circ}{\Delta\theta}. \tag{4.8}$$

$\Delta\theta$ is 112° for Adelaide to Grahamstown, therefore the last term in this equation comes to a value of 3.21. In the calculation of the k-values that follow, if adding 3.21 to the derived k-value brought it closer to 3 then this became the new k-value estimate.

A k-value was also calculated from a smoothed cross-spectrum in order to increase the number of degrees of freedom of the estimator. This was achieved by applying a five point boxcar smoothing to the separate complex amplitude spectra prior to computing the cross-spectrum.

4.6.3 K-Values

Table 4.4 summarizes the zonal wavenumber estimates for the six summers from 1987 to 1992. The Adelaide data was averaged over a 20 km height interval to simulate the meteor height ranges from which the Grahamstown data was derived. There is little difference between the results from the raw and the smoothed cross-spectra.

Both give a mean value which are within the experimental error of the expected value of three. The standard deviations are of the order of 10 % of the mean. These results indicate that the zonal wavenumber of the 2-day wave is three assuming that there are no major local influences.

Zonal wavenumbers from Meridional Winds
Adelaide (94–102 km) — Grahamstown (~ 85–105 km)

Years	1987	1988	1989	1990	1991	1992	mean
Ampl	415	29	110	44	48	61	–
Raw	2.93	2.72	2.35	3.55	3.09	3.09	2.9±0.4
Smooth	2.94	3.09	2.30	3.53	2.93	2.93	3.0±0.4

Adelaide (86–94 km) — Grahamstown (~ 85–105 km)

Years	1987	1988	1989	1990	1991	1992	mean
Ampl	458	47	130	53	90	84	–
Raw	2.80	2.72	2.20	3.45	2.86	2.98	2.8±0.4
Smooth	2.79	2.93	2.27	3.49	2.77	2.93	2.9±0.4

Adelaide (78–86 km) — Grahamstown (~ 85–105 km)

Years	1987	1988	1989	1990	1991	1992	mean
Ampl	235	38	100	56	67	80	–
Raw	2.55	2.69	2.03	3.14	2.73	2.73	2.6±0.3
Smooth	2.59	2.70	2.11	3.37	2.56	2.68	2.7±0.4

Table 4.5: K-values for the 2-day wave using meridional wind data averaged over 8 km for 94, 86 and 78 km for Adelaide and meteor heights for Grahamstown for the interval from 15^{th} – 28^{th} January of each year. The format is the same as for Table 4.4.

The computed k-values can be affected by possible differences in the vertical wavelength of the 2-day wave at the two sites. From the previous results of this chapter it is known that the vertical wavelength at Adelaide during the summers of 1987–92 are most often >90 km. This long vertical wavelength would suggest that it is valid to perform these comparisons using height averaged data.

To remove any doubt about local height variations, at least from the Adelaide data, comparisons using 8 km averages were made. The results are tabulated in Table 4.5.

It can be seen that the estimated k-values increase with altitude, but on average are still within error of the expected value of three. Combining all the different altitude and summer data, which appears to be a legitimate thing to do as all the errors in the means overlap, an overall mean k-value of 2.81 ± 0.09 is obtained from the raw estimates (a total of 36 degrees of freedom) and 2.83 ± 0.04 from the 5-pt smoothed estimates (a total of $5 \times 36 = 180$ degrees of freedom). The standard error has been quoted in both cases as interest is now in the possible deviations that a separate mean may have.

4.6.4 Conclusion

The mean zonal wavenumber for the 2-day wave was found to be 2.81±0.09 using a 14 day interval and 8 km averaged wind data from Adelaide for three altitudes, compared to the meteor winds from Grahamstown by a cross-spectral technique. The theoretically expected value of three is two standard errors away from this mean. Using the student-t distribution[13], the 90% confidence interval for this k-value estimate is between 2.66–2.96. That is, there is a 90% probability that the "true" mean value lies within this range. This interval is significantly reduced for the smoothed estimate (2.76–2.90 at 90%, and 2.73–2.93 at 99/suggest that the zonal wavelength of the 2-day wave is slightly smaller than the theortical value of 3.00. This does not invalidate the normal-mode interpretation for the 2-day wave. It is possible that some interference by a wave with a period near 48 hr has occurred, rendering a composite k-value estimate. Such a candidate is a 44 hr peak seen during July, 1991, in the Christmas Island moving power spectra of Figure 4.43. It is unknown whether this spectral peak is due to a wave motion, and whether it exists at all at mid-latitudes during January/February.

As the two sites are separated by $\sim 112°$ in longitude, there may be a problem that different cycles of the 2-day wave are being sampled. This concern has been mentioned in the introduction to this section on page 178. As the temperature contour of *Rodgers & Prata* [1981], figure 3, clearly shows, each of the three cycles of the wavenumber-3 pattern differ. If this is an observation purely of the 2-day wave and the phase is being sampled from different cycles then it is conceivable that the computed zonal wavenumber will differ from 3.00.

4.7 Comparisons with the Solar Tides

4.7.1 Introduction

Further to the observations in Section 4.4.6, the temporal relationship between the solar tides and the 2-day wave and its harmonics can be qualitatively examined by looking at the respective wave amplitudes as a function of time. These could be obtained by forming bandpassed winds as in Figure 4.10, although it would be better to use a narrower pass-band in order to reduce the energy contributions due to noise. This would have the deleterious effect of increasing the coherence time of the filtered winds, reducing the effective time resolution. The amplitudes of a complex demodulation as shown in Figure 4.36 could be used. The effective bandpasses employed are sufficiently narrow to remove most of the energy not directly related to the wave

[13] which gives an estimate of the difference that can be expected between a sample and a population mean, given that the population variance is estimated by a sample variance

of concern (the 2-day wave for example), yet still allow ~ 10 day variations to be discerned. This is sufficient for the comparisons in this section. For convenience an alternative method, using the the moving power spectra shown in Figures 4.7, 4.8 and 4.42 (also see Chapter 2.8), was employed for the following comparisons. This has the advantage that a broad visual image of the power distribution has already been presented in these figures. Averaging of the power spectral estimates also maintains the energy content of the wave so that the resultant wind amplitudes will reflect the mean power.

4.7.2 Analysis and Results

A power spectrum measures the variance associated with each frequency interval, the width of which is determined by the length of the time series. Provided the frequency resolution is fine enough, the variance associated with a wave of a given frequency can be directly determined. Therefore a moving power spectra, as shown in Figure 4.8 for example, provides a convenient way to obtain the relative strengths of the 2-day wave, its harmonics and the solar tides, as a function of time.

A short temporal window of 14 days was used as before. This provides a reasonable temporal resolution. The resulting poor frequency resolution is not detrimental to the analysis as it is desired to gather all the energy which can be associated with each wave component hence the power will be summed from a range of frequency bins centred around the main wave frequency.

Looking at a higher resolution view of the running power spectra of Figures 4.7, 4.8 and 4.42 it was found that the 2-day wave and tidal energies were completely contained within ± 3 frequency bins from the central frequency when using the 14 day window. Summing the power contained within the seven frequency bins and knowing the frequency interval the total variance associated with each wave was found. The square-root of this is a measure of the rms[14] wind speed. This operation was performed for the meridional wind component for each time step in the moving power spectra, producing a time evolution of the rms wind speeds for each bandpass component. The results are shown in Figures 4.74 and 4.75 for the meridional winds at 86 km at Adelaide and Christmas Island respectively. The bandpasses used were 58.5–38.4, 26.4–21.3, 17.0–14.8, 12.6–11.3, 10.0–9.1, and 8.2–7.7 hr for the central periods of 48, 24, 16, 12, 9.6, and 8 hr respectively.

The first thing to notice in Figure 4.74 is the lack of any obvious quasi-biennial variation of the amplitude of the 2-day wave component. A suggestion of a five year cycle can be seen, but

[14] the square-root of the mean of the squares of a quantity, or root-mean-square

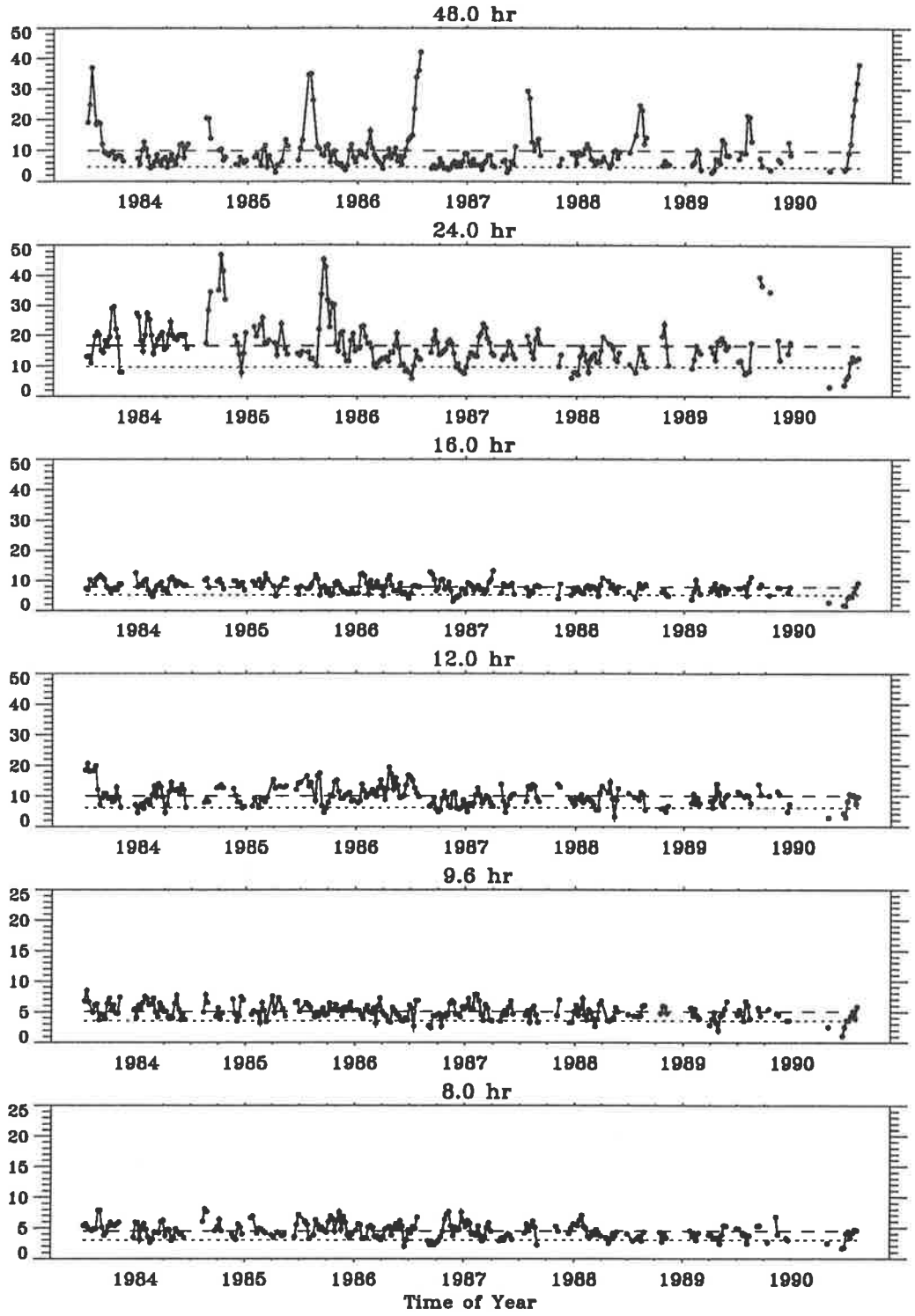

Figure 4.74: Rms meridional wind speeds as a function of time for various wind components at Adelaide (34.5° S, 138.5° E). The central periods are shown above each panel. The x-axis major ticks mark the middle (1^{st} July) of each year. The y-axis is labelled in ms^{-1}. The dashed lines indicate the mean amplitude while the dotted line the lower decile. Note that the amplitude scale has been doubled for the 9.6 and 8 hr wind components.

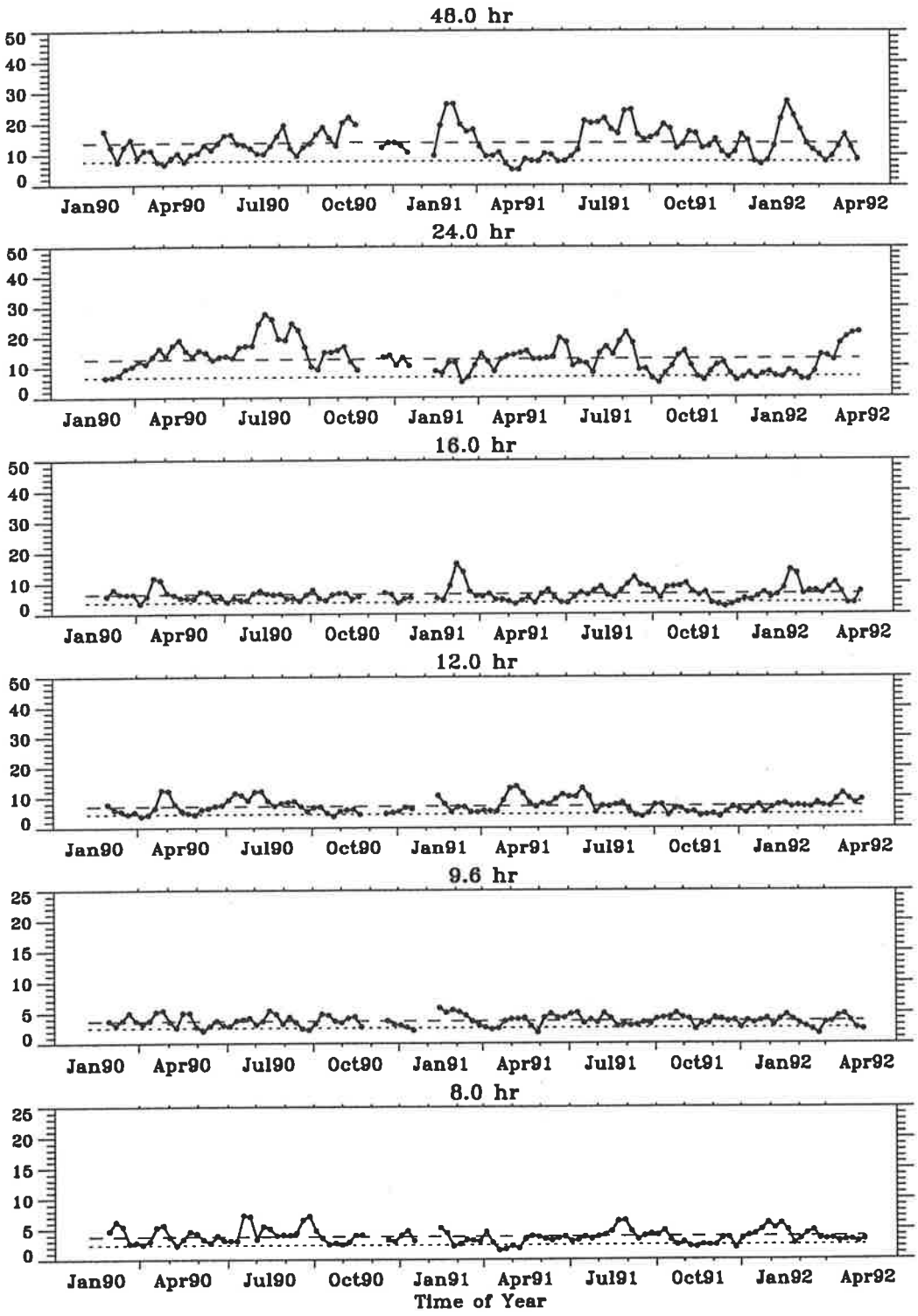

Figure 4.75: Rms meridional wind speeds as a function of time for various wind components at Christmas Island (2° N, 157° W). The x-axis major ticks mark the beginning of each season, with the minor ticks marking the beginning of each month. The labels refer to the middle month of each season. Otherwise as for Figure 4.74.

since there is only seven summers of data this is only speculative. The 2-day wave amplitudes compare well with those for 86 km in Figure 4.36, as do those of Figure 4.75 with Figure 4.46. No obvious correspondence can be seen at Adelaide (Figure 4.74) between the peaks in the 2-day wave amplitudes and peaks or troughs in the diurnal or semi-diurnal tides. It is hard to discern any peaks in the 16 hr wind component making any visual comparison impossible. The terdiurnal tide and the 9.6 hr wind component both show little seasonal or interannual activity.

In contrast, the equatorial data from Christmas Island (Figure 4.75) shows a definite tendency for the amplitude of the diurnal tide to be diminished and for peaks to occur in the 16 hr wind component when the 2-day wave amplitude maximises during Januray/February as already noted in Section 4.4.6. Peaks in the semi-diurnal tide may also appear after the Januray/February peak in the 2-day wave amplitudes. The activity shown in the terdiurnal tide does not correspond well with that of the 2-day wave.

An interesting feature shown in this figure is the similar behaviour of the 16 hr wind component and the 2-day wave – not only for the December solstice maxima, but also during the enhanced activity from June to October, 1991. Also of note is the smaller peak amplitudes of the 2-day wave and diurnal tide at the low-latitude site compared with that of the mid-latitude site of Adelaide.

A better picture of the average behaviour of the wind components can be obtained if a superposed moving power spectra is formed (as was done in Section 4.3.2 for Figure 4.9). The averaged spectra should reduce the random variations in the rms wind amplitudes and give a clearer picture of the relationship between the 2-day wave and the tidal components. This should be especially beneficial for the Adelaide data where many years of data have been used. The rms winds derived in this way are shown in Figures 4.76 and 4.77. This is essentially an incoherent average as the mean power has been calculated rather than the mean wave amplitude.

Unlike the raw rms winds, the rms average yearly values clearly show that the amplitude of the diurnal tide is diminished at mid-latitudes as well as at low-latitudes during the time of large 2-day wave amplitude near the December solstice. As expected from the raw winds, the average winds for the 2-day wave and the diurnal tide are less at low- than at mid-latitudes, assuming that Adelaide and Christmas Island are typical for their latitudes.

In Figure 4.76 it can be seen that the diurnal tide increases in strength after the 2-day wave has diminished, reaching a maximum amplitude during March. It then decreases to its mean level before beginning to decrease in strength in December as the 2-day wave again begins to increase. At low latitudes a similar relationship is found. The diurnal tide there does not decrease

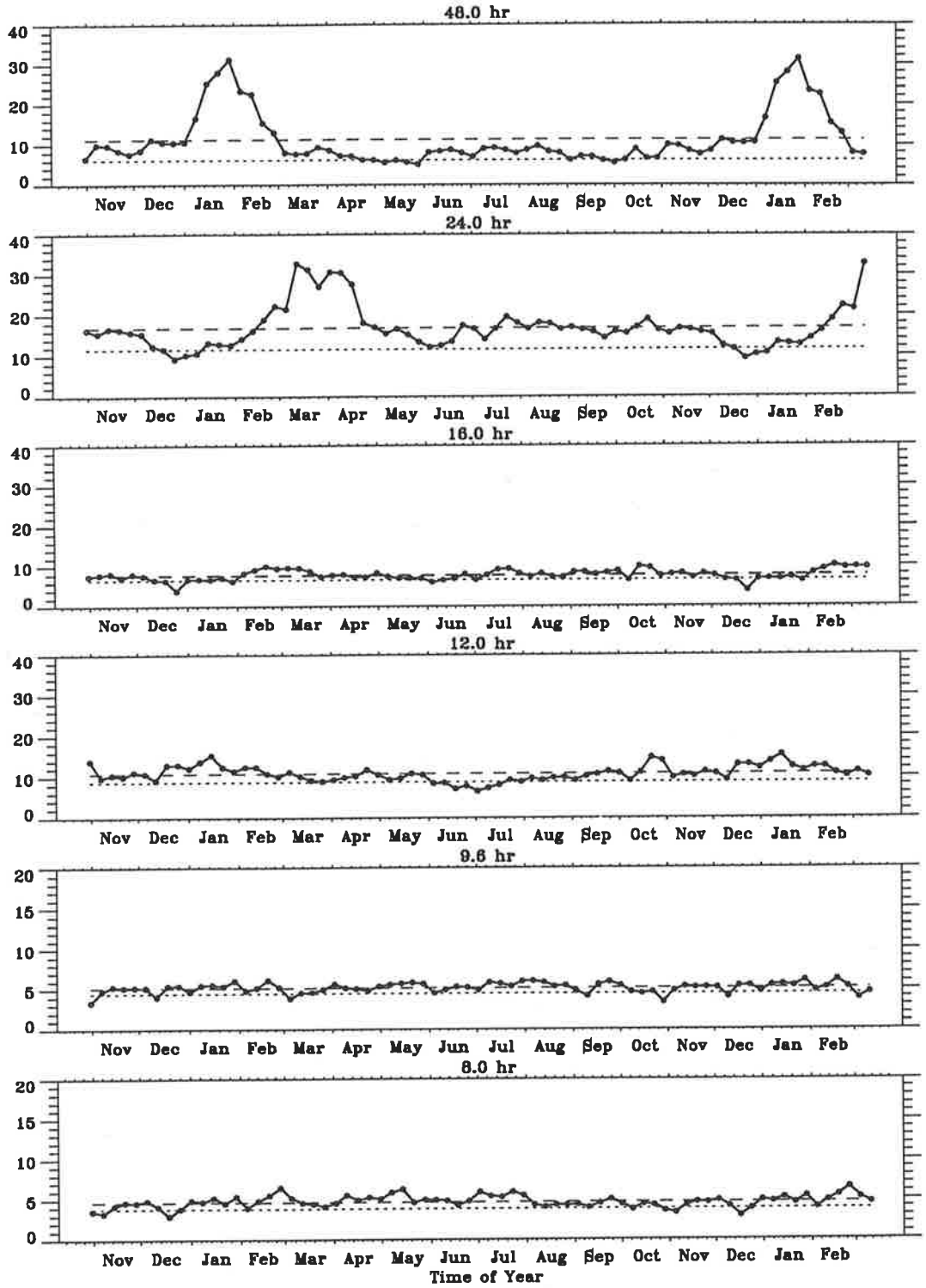

Figure 4.76: Rms meridional wind speeds for an average year for various wind components at Adelaide (34.5° S, 138.5° E). The central periods are shown above each panel. The x-axis major ticks mark the separation between each month. The dashed lines indicate the mean amplitude while the dotted line the lower decile. Note that the amplitude scale has been doubled for the 9.6 and 8 hr wind. Otherwise as for Figure 4.74.

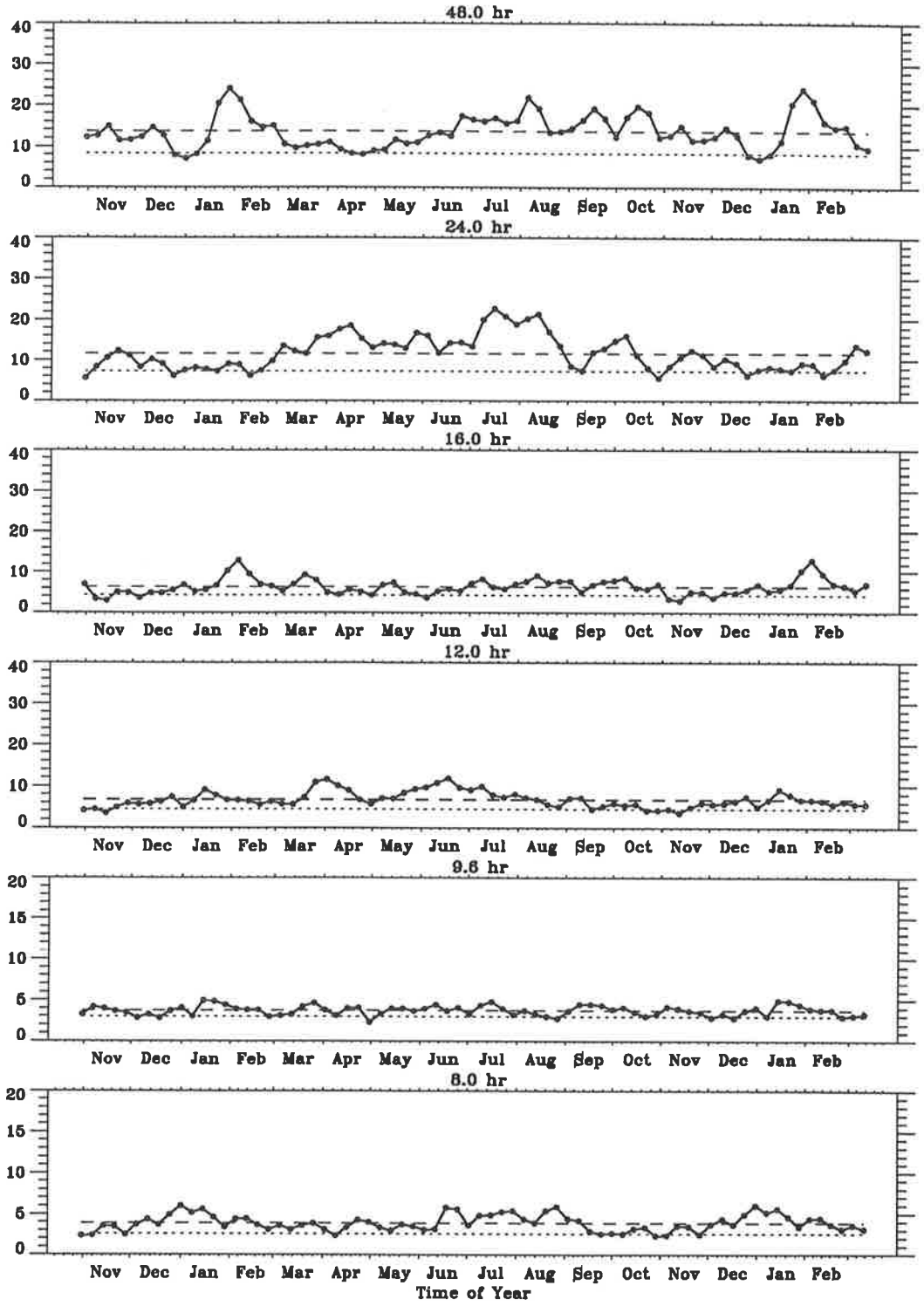

Figure 4.77: Rms meridional wind speeds for an average year for various wind components at Christmas Island (2° N, 157° W). Otherwise as for Figure 4.74.

in amplitude in April as at mid-latitudes though. Rather the amplitude remains relatively large until October when they begin to decrease again with the onset of the 2-day wave in the southern-hemisphere.

The semi-diurnal tide has maximum amplitude near June at Christmas Island but is a minimum at Adelaide. A seasonal variation can be seen at both sites. No obvious relationship is seen between this and the 2-day wave.

As noted in the raw rms winds, the 16 hr wind component appears to map the amplitude variations of the 2-day wave near the equator, but not at mid-latitudes. This is also consistent with the findings of Sections 4.3 and 4.4.

Little variation is seen in the 9.6 hr wind component and the terdiurnal tide at Adelaide. The 9.6 hr component also shows little variation at Christmas Island. The terdiurnal tide on the otherhand shows a clear seasonal variation, having minimum amplitudes during the equinoctial months.

4.8 Discussion

In this Chapter some average as well as specific features of the planetary wave, known as the 2-day wave, have been presented – both for the southern-hemisphere mid-latitude site of Adelaide (34.5° S, 138.5° E) and for equatorial site of Christmas Island (2° N, 157° W).

The results from Christmas Island, discussed in Section 4.4, show that the 2-day wave is a prominent feature of the dynamics of the equatorial middle atmosphere, especially in the meridional wind component. These observations support the findings of *Kalchenko & Bulgakov* [1973], *Kascheev* [1987] and *Kalchenko* [1987], who discussed mesospheric wind observations made with a meteor radar located at Mogadishu (2° N, 45° E) from 1968 to 1970. Most of the Mogadishu measurements were made at a single height near 94 km. The current measurements, however, provide important new information on both the temporal variability and the vertical structure of the wave. Further discussion of these observations can be found in *Harris & Vincent* [1993].

The wave is found to be present most of the time in the equatorial mesosphere, although its amplitude varies with season. Largest amplitudes are attained about one month after the solstices, and the smallest amplitudes observed in April. The period of the wave is also found to change. For much of the year the period is near 50 hr, but at the time of the largest amplitudes, in January/February, the period is close to 48 hr. It is a propagating mode in the equatorial mesosphere during the solstices, with a vertical wavelength of the order of 70 km. This compares

with values of ~ 50 km found at Townsville (19° S, 147° E) [*Craig et al.*, 1980] and 20 km at Trivandrum (8.5° N, 76.9° E) [*Reddi & Lekshmi*, 1988]. An average vertical wavelength >150 km was found at Adelaide.

The fact that the wave is present for most of the time in the meridional wind component at Christmas Island supports the proposal of *Salby* [1981a] that it is a manifestation of the (3,0) Rossby-gravity normal mode, randomly forced in the lower atmosphere. The (3,0) mode is an asymmetric mode, and would therefore produce oscillations only in the meridional wind component at the equator. The nearly year-round presence of the wave may not preclude the baroclinic instability hypothesis, which could occur only for limited times of the year when the summer stratospheric jet has its greatest curvature. Recently *Randel* [1993], using potential vorticity arguments, concluded that the baroclinic instability mechanism could indeed be a main forcing mechanism for the 2-day wave, the energy being channelled into the (3,0) normal mode due to the close frequency and wavenumber characteristics. It is the suggestion here that the possible half-yearly impulsive forcing caused by this mechanism[15] may be sufficient to maintain the 2-day wave throughout the year, given that it is a resonant mode of the atmosphere.

The current measurements of the 2-day wave are in accord with previous findings for mid- and high-latitude observations, in that the amplitudes are greatest at the solstices with the amplitude coinciding with the southern-hemisphere summer larger than for the northern summer. The changes in period from 48 ± 0.5 hr during the December solstice to 50 ± 1 hr during the June solstice are also in basic accord with previous observations [*Vincent*, 1984a]. Another feature, reported in *Harris & Vincent* [1993], is that two frequency components seem to be present during the June solstice, one with a period near 50 hr and the other with a period near 44 hr (see Figure 4.43). The component near 50 hr period is dominant and is the one that has been focussed on as it seems to have all the characteristics of what is usually referred to as the 2-day wave. The 44 hr component is tentatively identified as a manifestation of the (2,0) Rossby-gravity normal mode [*Harris & Vincent*, 1993]. This is an anti-symmetric westward propagating zonal wavenumber 2 wave with a period of 1.6 days (38 hr) in an atmosphere at rest [*Kasahara*, 1976], but a peak near 1.8 days (43 hr) and an enhanced response in the range 1.6 to 1.9 days (38–46 hr) in an atmosphere with realistic wind and temperature [*Salby*, 1981b; *Salby*, 1981c]. The larger amplitudes in the meridional component compared with the zonal (again, see Figure 4.43) are consistent with an anti-symmetric mode. This mode has been tentatively noted in surface pressure data by *Hamilton & Garcia* [1986].

[15] during summer in each hemisphere

The results from Adelaide, discussed in Section 4.3, show that the 2-day wave is also a dominant feature of the dynamics of the mid-latitude middle atmosphere, especially in the meridional wind component. It shows a strong inter-annual variation in amplitude, with suggestions of a five year cycle. The dynamical properties of the wave are observed to be a strong function of the wave amplitude. For example, smaller vertical wavelengths ($\approx$40 km) are found for summers when the 2-day wave has small amplitudes ($\approx$20 ms^{-1}). The wave period for a given summer is also further from 48 hr for time intervals when the amplitude is small. A mean period over 12 summers and 7 altitudes was found to be 48.7 ± 0.5 hr for the meridional winds. During times of large wave amplitude the phase of the 2-day wave was found to align such that the times of maximum northward winds were generally between 1000–1600 hr LT during any summer. A mean vector phase over 12 summers and 7 altitudes was found to be 14.4 ± 0.8 hr LT.

This phase locking at mid-latitudes implies some strong solar interaction at a preferred location on the globe, causing something similar to a forced oscillation. Close inspection of the meridional component in Figure 4.43 shows that at the beginning of January 1991 the 2-day wave at low-latitudes has a period near 50 hr. As time progresses the peak shifts to 48 hr and the amplitude increases, as if the 50 hr wave has been "pulled" into some resonance condition whose natural period is 48 hr. This could be mediated by a non-linear interaction between the 2-day wave and the diurnal tide. In Section 4.7 it was seen that the solar diurnal tide has a low amplitude at the same time that the amplitude of the 2-day wave is beginning to increase during the December solstice. This was found at both Adelaide and Christmas Island. In order for this to be a simple triad mechanism the sum of the zonal wavenumbers for two of the triad must be equal to that of the third. The same must also be true for the frequencies, with the members appearing in the same order. The observation of a 16 hr wind component in the equatorial data initially gave hope to a resolution of the non-linear interaction as the 48, 24 and 16 hr components satisfy the frequency summation criteria for a wave-wave interaction triad. For the zonal wavenumbers to also satisfy the summation criteria, and for the diurnal tide to still be one of the gravest modes (which contain most of the tidal energy) the 16 hr component would have to be a large-scale planetary wave as is the 2-day wave. Unfortunately the only normal mode that has a period of 16 hr is a Kelvin wave [*Kasahara*, 1976; *Hamilton & Garcia*, 1986, for example] which would produce oscillations in only the zonal wind component. Furthermore the bispectral analysis carried out in Section 4.4.6 suggests that the 16 hr component is simply a harmonic of the 2-day wave. Large meridional velocities would produce large north-south parcel displacements. In a detailed analysis of one two-day wave event at Adelaide (where peak meridional velocities

of greater than $50\,\mathrm{ms}^{-1}$ are not uncommon) *Plumb et al.* [1987] estimated horizontal parcel displacements of at least 3000 km, that is peak-to-peak latitudinal displacements of 60°. They concluded that wave overturning in the horizontal plane was possible. In such circumstances the presence of high-order harmonic components would be observed in the wind field. The 16 hr amplitude variations are observed to map those of the 2-day wave throughout the year at Christmas Island (*c.f.* Section 4.7) and both were found to have large vertical wavelengths. No phase relation between the 16 hr component and any of the solar tides were revealed by the bispectral analysis, although the 2-day wave and the diurnal tide were found to have a phase relationship. This of course could arise from the interaction of the 2-day wave with its harmonic at 24 hr, which would be indistinguishable from the solar diurnal tide. This harmonic could also be responsible for the observed decrease in the amplitude of the 24 hr tide during times of large 2-day wave activity by destructive interference with the actual diurnal tide.

The results of this Chapter suggest that the $(3,0)$ normal mode is always present in the atmosphere, but at levels which are not detectable at mid-latitudes except in the summer middle atmosphere where the wave encounters a critical level (*c.f.* Section 1.5.3). *Salby* [1981c] showed that the $(3,0)$ mode becomes locally propagating, with wave growth, in regions where the background zonal flow is westward and the wave is Doppler shifted down to frequencies closer to zero. That is, regions where the intrinsic frequency is less than 0.5 cpd. The growth is more pronounced the smaller the intrinsic frequency until wave breaking occurs when the critical level (of zero intrinsic frequency) is reached. This is a similar mechanism to the filtering of gravity waves discussed in Section 1.5.3.

Referring to equation 1.32 in Section 1.5.3, for planetary scale waves the relevant average for $\mathbf{U}$ is a total global one. Over this scale the average vertical and meridional velocities vanish so that,

$$\overline{\mathbf{U}} = (\overline{U}(z), 0, 0)\,. \tag{4.9}$$

Therefore equation 1.32 reduces to

$$\Omega = \omega + \mathrm{k}\overline{U}\,, \tag{4.10}$$

or,

$$f_{intrinsic} = \frac{\overline{U}}{\lambda_x} - f_{observed}\,. \tag{4.11}$$

As the $(3,0)$ normal mode has, by definition, three cycles zonally around the globe, the zonal wavelength, λ_x, at a latitude of ϕ, is given (in metres) by

$$\lambda_x = \frac{1}{3} 2\pi a \cos\phi\,. \tag{4.12}$$

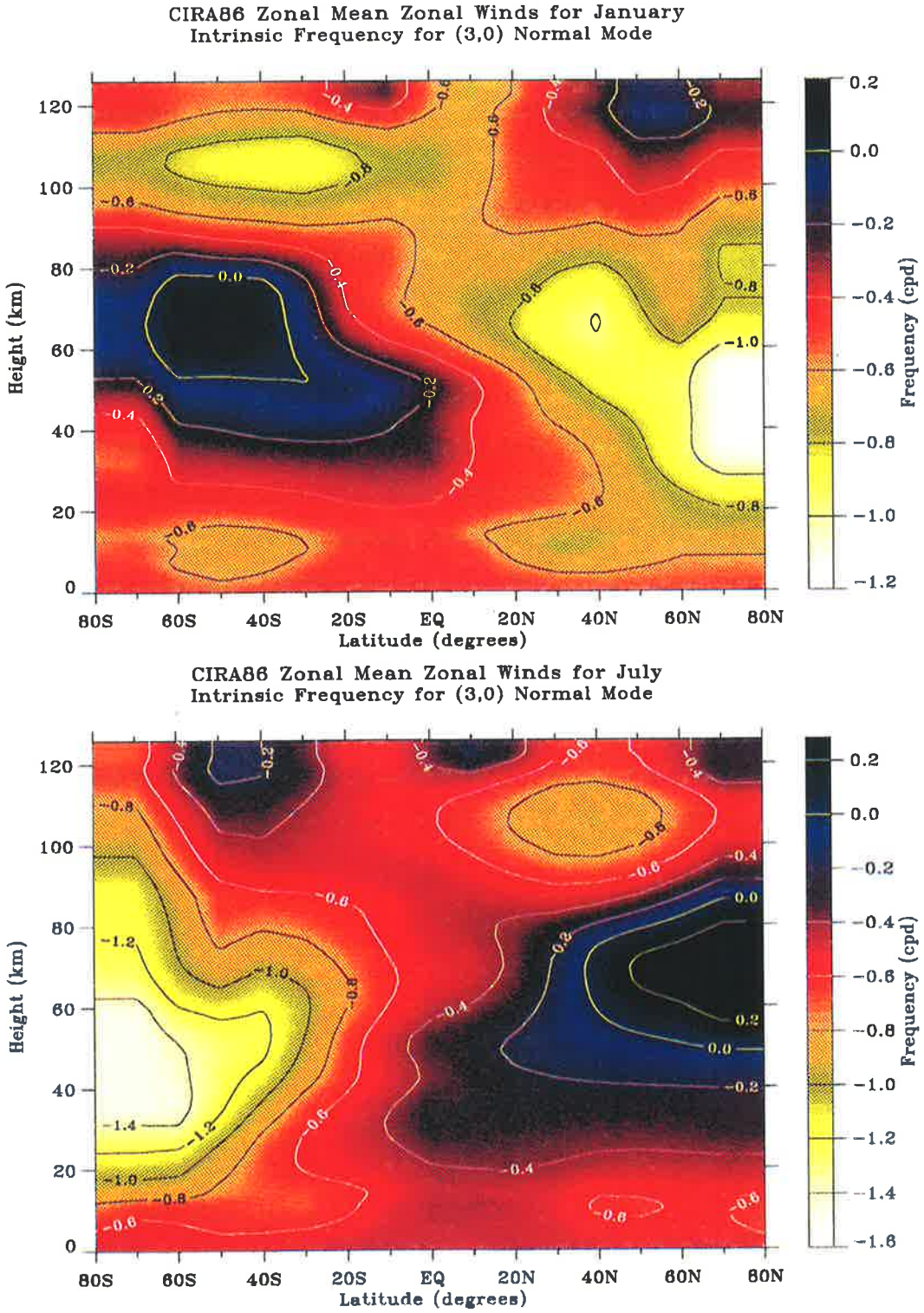

Figure 4.78: Intrinsic frequency for the $(3,0)$ atmospheric normal mode from CIRA86 zonal mean zonal winds (which are shown in Appendix E).

The observed frequency ($f_{observed}$) is -0.5 cpd (negative as it is a westward propagating wave), so that, using the zonally averaged zonal winds from CIRA86, the expected intrinsic frequency for this mode can be calculated. These are shown in Figure 4.78 for both solstices. Critical levels can be seen around 55 km in the summer hemisphere at mid-latitudes (the zero level contours). These are surrounded by regions of small intrinsic frequency (~ -0.2 cpd). Differences are apparent between the two solstices, when the 2-day wave maximises in different hemispheres. The regions of small intrinsic frequency during January extend to lower latitudes than during July. Critical levels are also at a higher altitude during January than during July. These factors may have a bearing on the observed differences in the 2-day wave during each solstice. It should be noted that the CIRA86 winds do not reflect the equatorial mesosphere very well [*Vincent*, 1993] hence the calculated intrinsic frequencies are not reliable in this region.

A westward flow prevails for much of the year in the equatorial mesosphere [*Vincent*, 1993]. This could account for the relatively large year round amplitudes observed within that region . It also appears that the $(2,0)$ mode is also present, but with smaller amplitudes than the $(3,0)$ mode. One reason could be that it has a phase speed of $\sim 130\,\mathrm{ms}^{-1}$ compared with $\sim 75\,\mathrm{ms}^{-1}$ for the $(3,0)$ mode at the equator, and hence will suffer less Doppler shifting. According to *Salby* [1981c] the $(2,0)$ mode too should encounter a critical level in the summer middle atmosphere, but at a higher latitude than the $(3,0)$ wave and so will also show enhanced amplitudes in this season. The presence of a 44 hr mode could be one reason that the calculated zonal wavenumber for the 2-day wave was often less than three (the 6 year mean being 2.80 ± 0.09).

Chapter 5

The Variability of the Solar Tides

5.1 Introduction

The strength of the solar tides can be quite variable on a number of time scales. Consider the raw two-hourly averaged winds shown in Appendix F. Periods where diurnal and semi-diurnal oscillations dominate are clearly evident in both the zonal and meridional winds. A diurnal oscillation is seen more often than a semi-diurnal at this latitude. The strength of these oscillations can be seen to vary over time scales of a few days to weeks. This variation is only a qualitative indicator of tidal variability as it is the full wind vector that has been plotted, so constructive and destructive interference, especially between the diurnal and semi-diurnal tides, can cause rapid amplitude fluctuations. This is evidenced by the non-sinusoidal shape of the diurnal oscillation for example in the zonal wind component during August, 1985, and in the meridional wind component during November, 1987. The apparent modulation of the diurnal tide from $20–30^{th}$ March, 1986, is evidence for other forms of interactions.

One of the goals of the ATMAP[1] community [*Forbes*, 1985; *Forbes*, 1986a; *Forbes*, 1986b] has been to define a minimum time period for which data could be analysed for tides. Based on current experimental and theoretical experience the consensus was that the determination of tidal parameters must be made with observations of at least 10 days duration. Part of the reasoning for this value stemmed from the work of *Bernard* [1981] who argued "that if the intrinsic time ... to set up stationarity around the Earth for a particular tidal mode is greater than a characteristic time scale associated with its variability, then the horizontal and vertical structure of the oscillation will not exactly correspond to a particular eigenfunction or eigenvalue of Laplace's tidal equations. " [*Vial et al.*, 1991] (see Section 1.4.2 for the theory of

[1] Atmospheric Tides Middle Atmosphere Program

tidal oscillations).

The solar diurnal tide in the middle atmosphere is mainly generated by absorption of solar radiation by water vapour in the troposphere and then propagates upwards to the middle atmosphere (see for example *Chapman & Lindzen* [1970]). To a lesser extent, ozone in the stratosphere and mesosphere also contribute to this tide. The solar semi-diurnal tide is generally considered to be primarily due to insolation by ozone in the upper stratosphere and lower mesosphere (see for example *Butler & Small* [1963]). This too then propagates upwards to the middle atmosphere. Variations in the abundance and height profile of these important thermal absorption species will cause changes in the tidal forcing (Figure 1.6 shows an example of typical forcing profiles). It is known that water vapour concentrations can vary by the order of 5% at low-latitudes and by up to 20% at mid-latitudes over the course of several days. Variations in cloud cover can also change the water vapour insolation, thus causing variability in the tidal forcing.

Variability in the amplitude and phase of the solar tides observed in the upper mesosphere can arise from a number of mechanisms; changes in the tidal forcing, background propagation, additional energy near the tidal frequencies by local or synoptic scale disturbances to name a few (a review of recent progress in determining these mechanisms is given in *Vial et al.* [1991]). Non-linear interactions between the diurnal and semi-diurnal tides, or between the tides and planetary waves can generate secondary waves at tidal frequencies (see for example *Aso* [1993] and Section 4.4.6). Further, if mean winds are modulated at tidal periods by the presence of the tides then their interaction with gravity waves will also induce oscillations at the tidal periods, which are referred to as "pseudo tides" by *Walterscheid et al.* [1986]. Both of these features can be quite variable from day to day. The interaction between higher-order tidal modes (which have shorter vertical wavelengths) and the more prevalent lower order tidal modes can also cause observed variability in tidal parameters. Such mechanisms may account for the short term variability observed by workers such as *Vincent & Ball* [1977] and *Phillips & Briggs* [1990]. Longer term variations are also observed [*Fraser et al.*, 1989, for example].

Considerations of this kind led *Vial & Forbes* [1989] to ask, "Are observed diurnal and semi-diurnal harmonics of time series of radar measured winds global tidal oscillations, in the sense of classical tidal theory, or does significant local energy exist at or near tidal frequencies ?". This is a difficult question to answer. In order to help clarify this, the variability of the solar tides needs to be quantified. *Phillips & Briggs* [1990] looked at the daily tidal amplitudes at Adelaide (35° S, 138° E) and concluded that the fluctuations of the semi-diurnal tide were uncorrelated

from one day to the next. In contrast, *Kaydalov & Portnyagin* [1981] found that fluctuations in the semi-diurnal tidal winds at high latitudes in the northern hemisphere were correlated over several days. Transient tidal response times can be measured or defined in a number of ways [*Bernard*, 1981; *Vial et al.*, 1991; *Aso*, 1993, for example]. Using different atmospheric models, these authors find that variations in tidal forcing can give relaxation times in the upper mesosphere which range from 2.5 days up to 40 days for the $(2,2)$ mode and from 6 to 20 days for the $(1,1)$ mode.

The way that the tides are calculated and the duration of the data used are important factors when considering relaxation or response times. It is of importance to establish some characteristic time scale for the variability of the solar tides and how this may change with the data length.

5.2 The Data and Analysis Technique

In this preliminary study, spectral techniques have been used to try to quantify the response time of both the diurnal and semi-diurnal solar tides. A variable-size window, sliding Fourier transform (see Section 2.8 of Chapter 2 for more details) has been applied to experimental wind data from Adelaide for 1984 to 1991 averaged in three altitude ranges, 78–82, 86–90, and 94–98 km. Only the meridional component of the wind field at 86 km will be considered in depth. Comparison of the raw winds in Appendix F shows that the tidal amplitude and variability are similar for the zonal and meridional wind components. The radar site near Adelaide has already been discussed in Section 4.2.2 of Chapter 4 and a spectral representation of the data is shown in Figures 4.7 and 4.8 on pages 110 and 111. An idea of the variable nature of the solar tides can be gained from these figures, remembering that the absolute power spectral amplitudes have been "clipped" in order to reduce the dynamic range for plotting purposes. Figure 4.74 on page 184 (in Section 4.7 of Chapter 4) also gives an indication of the tidal variability, the yearly averaged response being shown in Figure 4.76 on page 187. Figure 5.1 shows a high resolution view of the average spectral response for a calendar year near the solar tidal frequencies of 1 and 2 cpd. This superposed spectrum has been derived as explained on page 109 for Figure 4.9. For the current figure a 30 day data window has been stepped by 30 days, over the span of 8 years from January, 1984 to January, 1992, then folded back into a single calendar year. The power spectral densities have been "clipped" to be less than 80 and $40 \times 10^6\,\mathrm{m^2 s^{-2} Hz^{-1}}$ for the diurnal and semi-diurnal tides respectively. The actual maximum values were $420 \times 10^6\,\mathrm{m^2 s^{-2} Hz^{-1}}$, during March, for the diurnal tide, and $100 \times 10^6\,\mathrm{m^2 s^{-2} Hz^{-1}}$, during January, for the semi-diurnal tide. The times

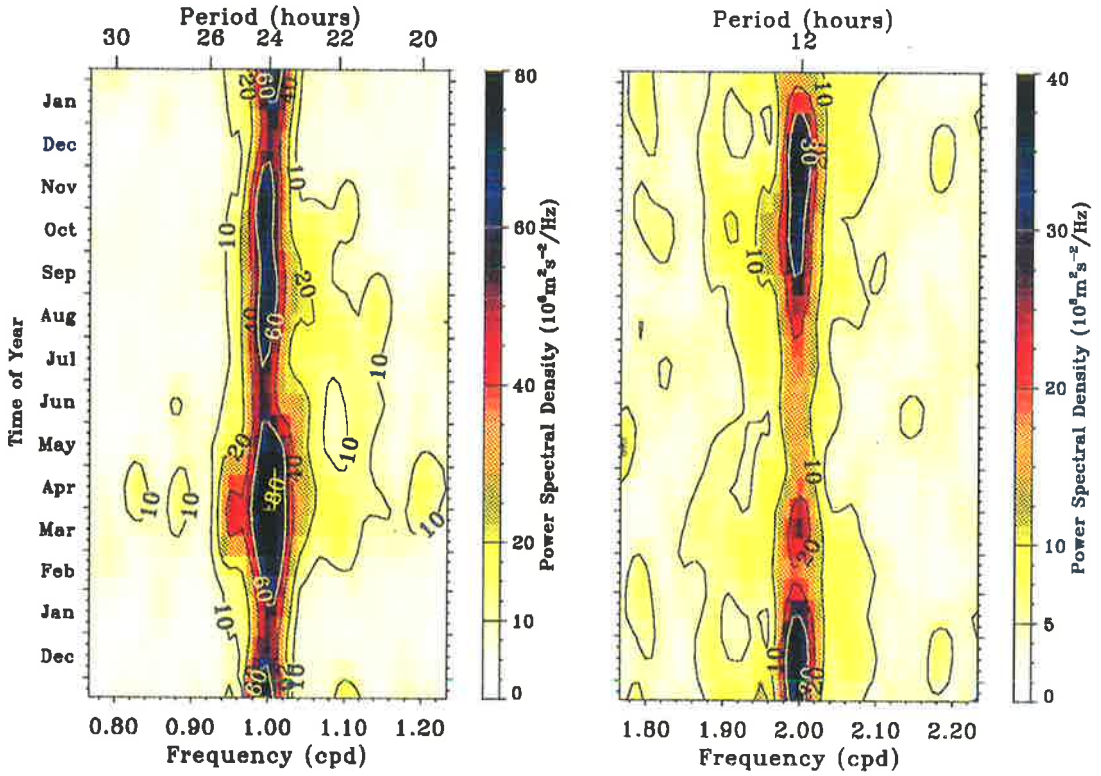

Figure 5.1: Average spectral responses for the years 1984 to 1991, for the meridional components of the diurnal and semi-diurnal solar tides at 86 km. Variations in the width of the tidal spectral "lines" can be seen. The power spectral densities have been "clipped" in both cases to reduce the dynamic range for plotting purposes. A 30 day data window length has been used to provide a high frequency resolution while still maintaining a reasonable time resolution. The data windows have been stepped by 30 days, covering the span of 8 years from January, 1984 to January, 1992 (complete data set shown in Figure 4.74 using a 14 day moving window).

of the maxima have been determined from a 14 day superposed moving power spectrum for better time resolution. It is the variations in the width of the tidal spectral lines which are of most concern here, therefore a 30 day window has been used in Figure 5.1, allowing a better frequency resolution. Both the diurnal and semi-diurnal tides show a clear seasonal variation in amplitude but not so clear a variation in spectral spread. The diurnal tide shows a strong, spread response during the equinoxes, with minima in amplitude and spectral width during the solstices. The semi-diurnal tide shows a strong response with a large spectral width in early summer with continued spread activity during the remainder of the year. A minimum spectral power and width is evident during winter.

Preliminary inspection of the spectral shape of the tidal lines suggested that they could be assumed to consist of three portions (see Figure 5.2). Firstly, a narrow spike at the tidal frequency due to components which add in a near coherent manner over the time interval of the data window. This can be due to a steady-state tidal response combined with variations whose

(a)

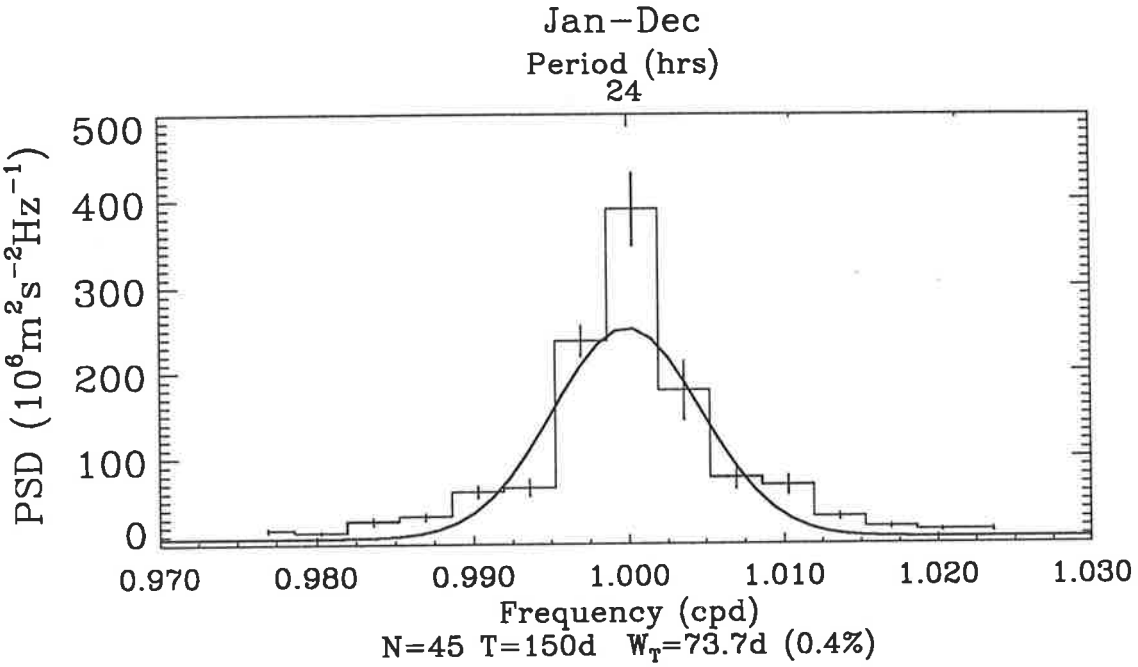

(b)

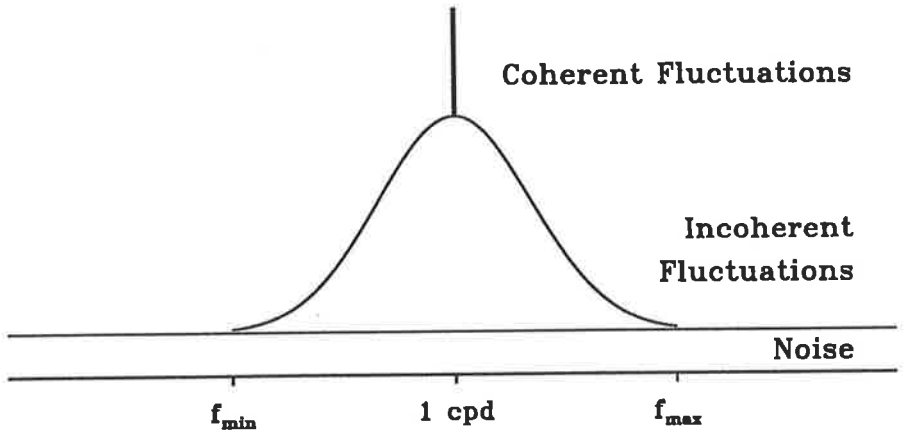

Figure 5.2:
(a) Spectrum of the frequency band immediately around the solar diurnal tide showing the tidal spectral shape. This is the average spectrum from 45 non-independent raw spectra using 150 day data windows, stepped by 30 days, over the span of 8 years from January, 1984 to January, 1992. Note the broad "skirt" and narrow "spike".
(b) An idealised tidal spectral shape showing the portions due to coherent and incoherent fluctuations and "noise". In practice the spike would have a small finite width.

time scales are longer than the data length. This main tidal line is modulated, sometimes up to 50%, by shorter term variations which add in an incoherent fashion leading to a spread about the tidal frequency. The width of the spread is a measure of the characteristic time scale of the variability, or response time, of the tide. The spread region or "skirt" has been assumed to be Gaussian for the current analysis, hence the amount of spread can be quantified by the half-width. A Gaussian skirt is a reasonable assumption for a single broadening process, but as shall be seen later it may not be valid here. All of this is superimposed on some constant noise level.

Using this model of the spectral shape the width of each spread region was found by fitting a χ^2 minimised Gaussian. Prior to this operation the noise contribution and the coherent spike had to be removed. The determination and removal of these components are non-trivial processes when automation of the technique is required and will be covered in the sections that follow. The width of the Gaussian "skirt" was found for each spectrum as a data window of given length was moved over the full data set, *i.e.* for each time step of the moving power spectrum. The data window length was then changed and the process repeated. In this way a number of width estimates were obtained for each data window length. In order to determine the effects of the processing the analysis was also applied to simulated data, which consisted of pure sinusoids at frequencies of precisely 1 and 2 cpd but with the same data gaps as in the experimental data (such as shown in Figure 4.44 on page 147). The two sets of results are used to give an estimate of the response time for the tides.

5.2.1 Determining Components of the Tidal Spectral Peaks

Consider the spectral shape shown in Figure 5.2. The width of the spread region of the signal peak is to be determined. The most obvious technique to use would be to remove the noise floor then fit a Gaussian function to the remainder, ignoring the central spike.

This procedure is easy to implement when done in a manual fashion as it is relatively easy for an experimenter to judge the level of the noise floor and then to fit a Gaussian function by perhaps some least-squares technique. A problem arises when this procedure has to be repeated the order of 1000 times, as in the current work, and then perhaps repeat that a few more times with differing parameters or data. Clearly an automated technique is required. Unfortunately it is not as easy for a computer routine to simply "judge" where the noise level is, especially when there are a large number of variations of the spectral shape and the signal-to-noise ratio. A region of the spectrum close to the region of concern but devoid of any signal peaks could be

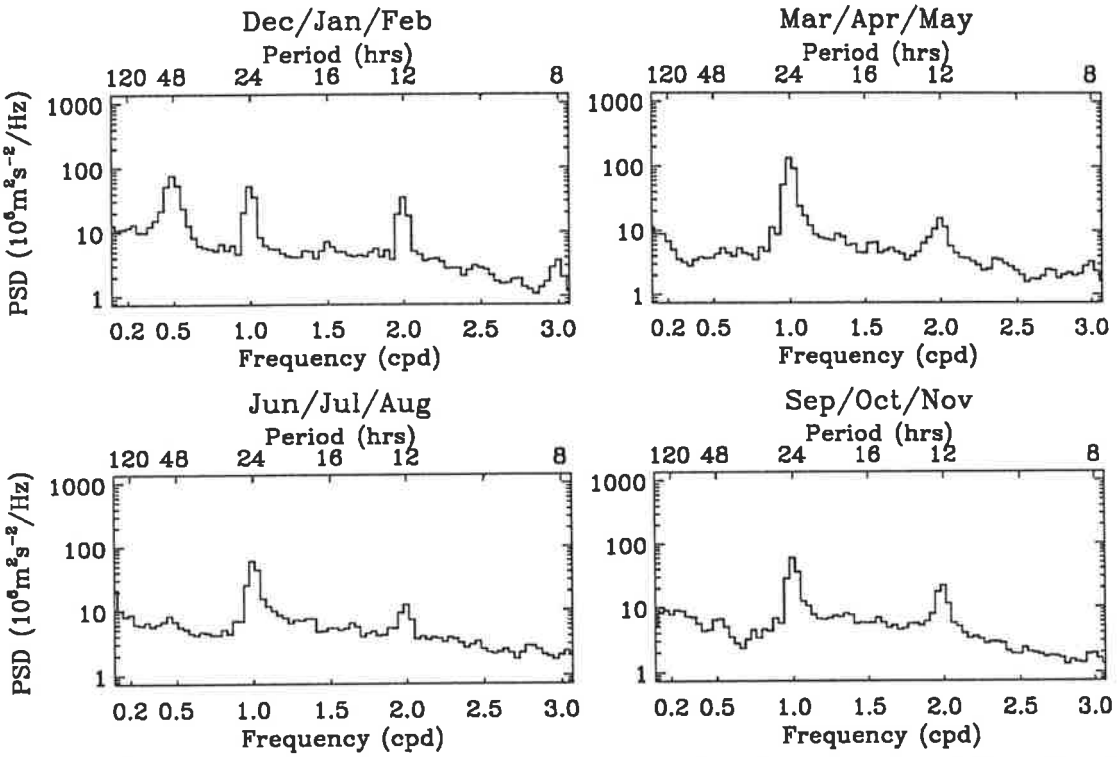

Figure 5.3: Seasonal average power spectra of the meridional winds at Adelaide. The diurnal and semi-diurnal solar tides can clearly be seen. The 2-day wave peak is also evident in summer. Of note is the "red-noise" spectrum and asymmetry of the "skirts" about the solar tidal peaks. A 14 day data window has been used.

chosen and the mean spectral power found. This could then be taken as the noise level for the region containing the signal. As can be seen in Figure 5.3, the power spectrum of the mesospheric winds exhibit an underlying "red-noise" spectrum. A log scale for the power spectral density has been used to emphasize this. Also of note is the asymmetry of the "skirts" about the solar tidal peaks (note that the frequency has been plotted in a linear scale so as not to artificially create any asymmetry in the spectral shapes). As the noise varies with frequency, the simple method for determining the noise power spectral density mentioned above is not valid for this work. The noise has to be estimated from regions as close to the signal peak as possible. The problem reduces to how to determine the critical frequencies, f_{min} and f_{max}, in Figure 5.2, which define the extent of the spread of the signal peak. One, perhaps overly complicated, method developed and initially used for this work is described below.

The power contained within a region of width W centred on the frequency of the spectral "spike" is the sum of the noise and signal components. As W is increased the total power, $P(W)$, will increase, generally in some complicated fashion, until a critical width, $W_T = f_{max} - f_{min}$ is reached after which the contribution from the signal remains constant. At this stage it would

be expected, at least to first order, that the total power would become a linear function of the bandwidth, W. Therefore, for P_S the total power in the signal (both coherent and incoherent components), and β the noise power spectral density (assumed constant over the small range of frequencies that are being dealt with), the total power as a function of the bandwidth W is given by

$$P(W) = \begin{cases} \alpha P_S + \beta W & W < W_T \quad \alpha \epsilon [0,1] \\ P_S + \beta W & W > W_T \quad (\alpha = 1) \end{cases} , \tag{5.1}$$

where α is a function of $(\frac{W}{W_T})$. Taking the second derivative of $P(W)$ with respect to W gives,

$$P''(W) = \begin{cases} \alpha'' P_S & W < W_T \quad \alpha \epsilon [0,1] \\ 0 & W > W_T \quad (\alpha = 1) \end{cases} . \tag{5.2}$$

Determining the minimum bandwidth where $P''(W)$ remains near zero gives a good estimate of the effective frequency limits of the signal peak.

The approach described so far has implied a folding of the power spectra about a central frequency by having the bandwidth centred on this value, giving a one-sided cumulative power, $P(W)$. In order to take into account any possible asymmetries in the signal peak (as observed in Figure 5.3) the total power can be computed for increasing bandwidths starting at some minimum frequency, f_0, to a maximum frequency, f_1, such that $f_0 \ll f_{min} < f_{max} \ll f_1$. Once f_{min} and f_{max} are found, a least squares fit of a straight line from f_0 to f_{min} and from f_{max} to f_1 gives an estimate (by the slope) of the noise level near the signal peak (see equation 5.1). This process is shown for an idealised case in Figure 5.4. Having estimated the noise floor, a noise-corrected $P(W)$ can be found which should be constant (and zero) from f_0 to f_{min}, then increase in some manner dependent on the signal spectral shape, then stay at a constant maximum value, which is equal to the total signal power, from f_{max} to f_1 (Figure 5.4d). Examples of how this process works using real data are shown in Figures 5.5, and 5.6 for two data window lengths for both the diurnal and semi-diurnal tides. The jump near 0.5 cpd is due to the 2-day wave signal peak.

The derivative of the corrected cumulative power spectrum could be used to give the signal peak free from "noise". Otherwise the noise level so determined could then be subtracted from the raw power spectra prior to fitting some optimal Gaussian function to the skirt.

Estimating the noise floor using a cumulative power spectrum perhaps has the advantage that the random fluctuations in the spectral estimates have a reduced effect as their sum tends to zero. Thus the regions between f_0 to f_{min} and f_{max} to f_1 are smoother in the cumulative than in the raw spectrum, making the change to the region containing the signal peak more

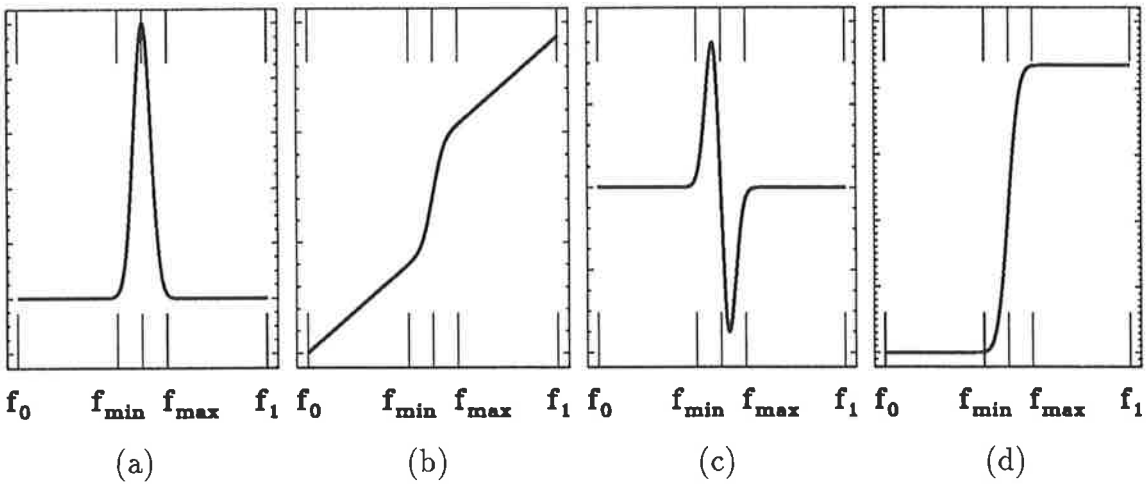

Figure 5.4: Idealised cumulative spectra for determining the spectral noise floor in the vicinity of a broad signal peak, and the total signal power. (a) The raw power spectrum. (b) The cumulative power spectrum. (c) The second derivative of (b). (d) Noise-corrected cumulative power spectrum. The maximum value is the total signal power.

marked. This makes it easier to determine the critical frequencies, f_{min} and f_{max}.

Another, more intuitive method — one which is closer to the semi-manual procedure described earlier — is to simultaneously fit a Gaussian and a constant to a narrow region of the spectrum around the tidal frequencies. As this is a non-linear function of frequency an iterative procedure, as opposed to a straight-forward linear least-squares one, has to be used. The iterative procedure used minimised the χ^2. In order to ensure a meaningful convergence for highly variable data, such as tidal spectra, the initial parameters need to be moderately close to their final values.

The three methods for obtaining a fit to the noise level and signal skirt described above — the folded cumulative spectrum; the straight-forward cumulative spectrum; and the minimal χ^2 simultaneous Gaussian and constant fit — have each been used in the development of the results of this chapter. Little difference was found between the noise estimates from each method, but the reliability of the Gaussian fit varied. Overall, the last method was favoured for the determination of the spectral widths as it proved to be the most simple yet robust and reliable. The straight-forward cumulative spectrum was still used to estimate the critical frequencies. This gave a good initial estimate for the width of the Gaussian skirt for the iterative fitting procedure. The noise-corrected version of the cumulative spectrum also provided an accurate measure of the total signal power.

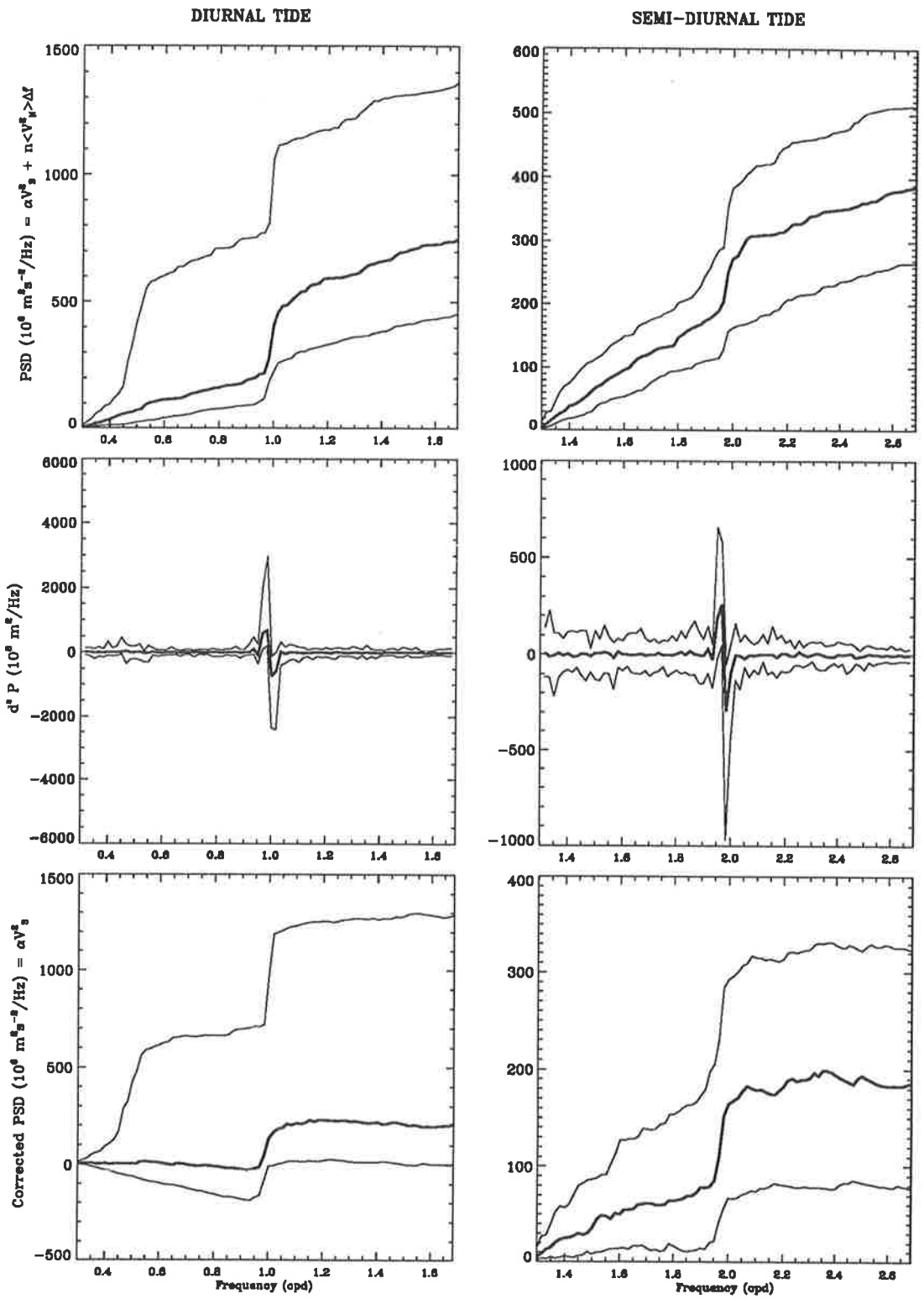

Figure 5.5: Cumulative spectra for a data window length of 30 days used for determining the spectral noise floor in the vicinity of the diurnal and semi-diurnal solar tides. The median and upper and lower deciles are shown for the collection of cumulative power spectra (top), the second derivatives (middle), and the noise-corrected cumulative power spectra (bottom).

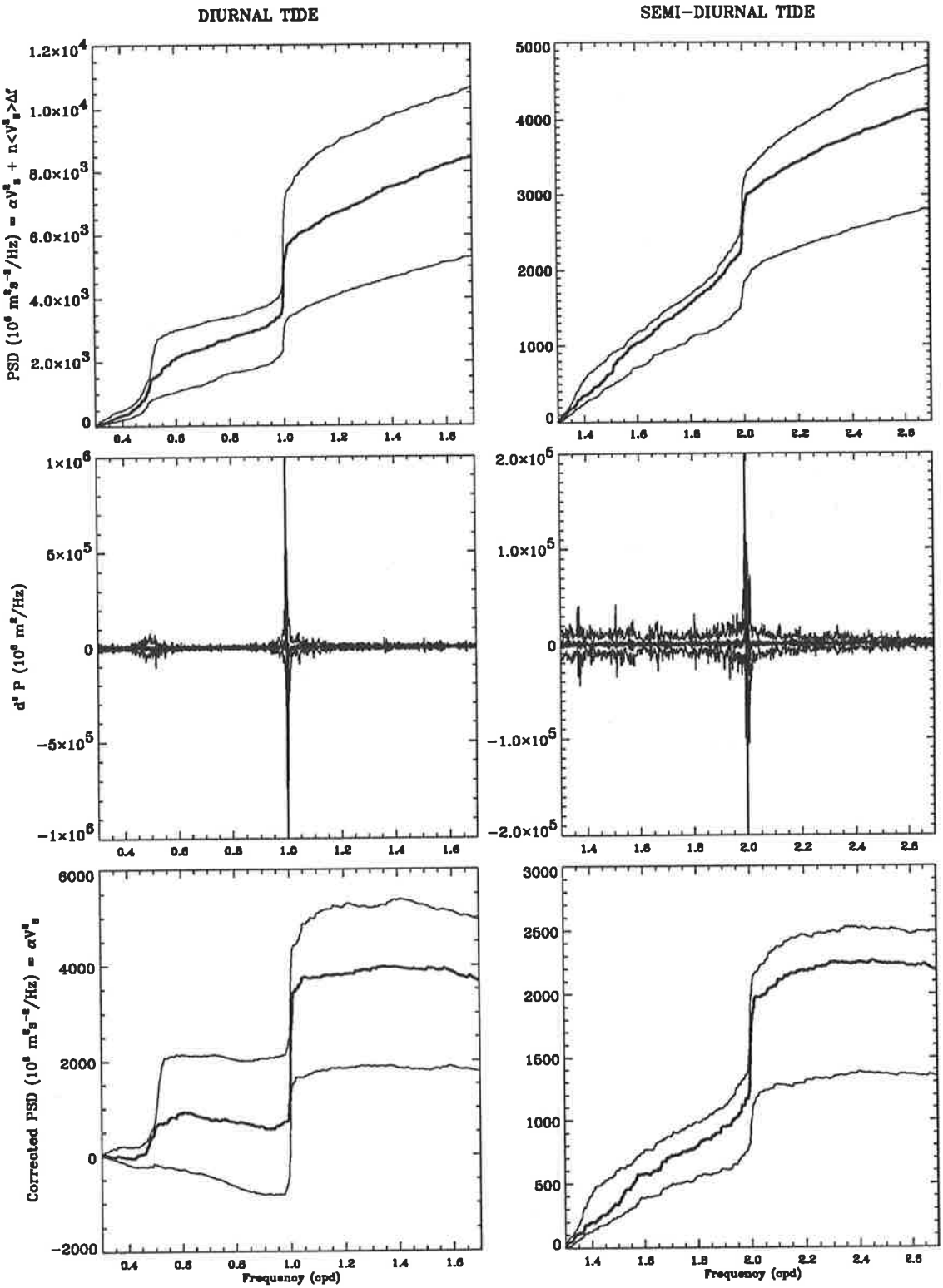

Figure 5.6: Cumulative spectra for a data window length of 300 days. Otherwise as for Figure 5.5.

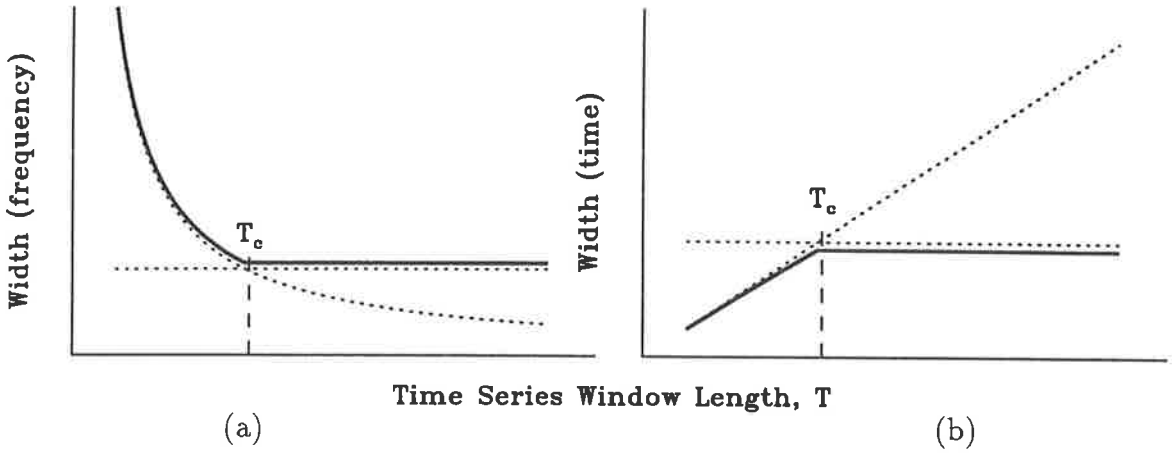

Figure 5.7: Response of spectral-width to data window length for a single incoherent process. The left-hand panel shows the width in frequency units, levelling off at some "natural" width once T is larger than some critical time, T_c. The right-hand panel is simply the reciprocal, showing the width response in time units.

5.2.2 A Minimal Tidal Response Time

It was expected that the skirt of the signal peak would have a finite "natural" width determined by atmospheric processes. As the data window length, T, increases, the resolution of the spectra becomes finer. At some stage, T_c, the resolution becomes finer than the "natural" width of the skirt. As T is increased further the width of the skirt remains constant at this value, although more structure becomes apparent, much of which is from statistical fluctuations. This is shown in Figure 5.7 for an idealised case, assuming that there is only one broadening mechanism. In practice there may be many processes on different time scales, so that this is a simplistic picture. As the data window length increases it capture more broadening processes, creating an ever increasing set. The determined width of the skirt is then more a measure of the dominant process over the time period T.

Even for a single spectral broadening mechanism, the change in spectral behaviour near T_c would be more gradual than that shown Figure 5.7. Three regions can be distinguished dependent on the data window length, T.

1. $T \ll T_c$. In this region the spectral width is dominated by the frequency resolution imposed by the analysis.

2. $T \approx T_c$. This is a transitional region where the analysis broadening is of the order of that due to natural variations.

3. $T \gg T_c$. Here the spectral width should be constant at a level set by the natural processes — the natural width.

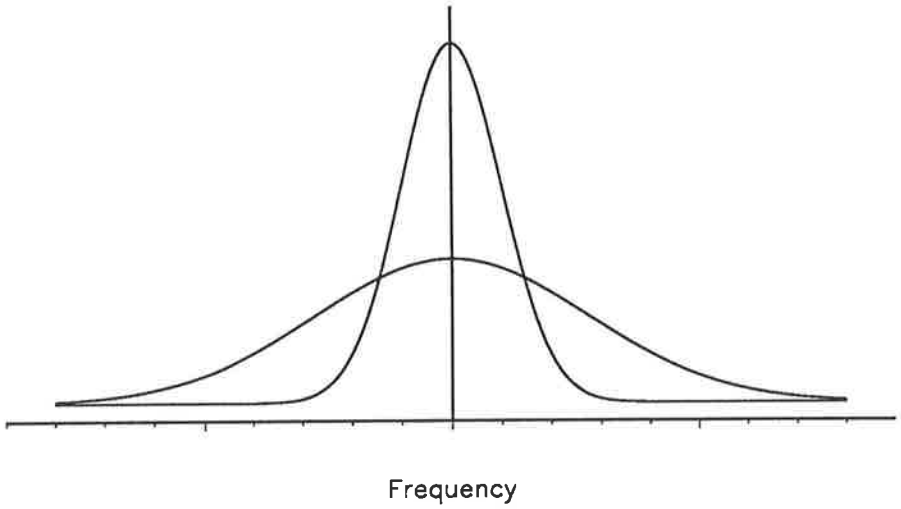

Figure 5.8: Case of two mechanisms causing tidal amplitude or phase variations, one at a shorter time scale than the other, resulting in the tidal power spectral peak having two skirts.

For multiple broadening processes (the number possibly increasing with increasing data length) Region-3 may not have a constant spectral width. For example, consider the case of two mechanisms causing tidal amplitude or phase variations, one at a shorter time scale than the other. This would cause the tidal power spectral peak to have two skirts, as shown in Figure 5.8. Notice the similarity with the power spectrum shown in Figure 5.2a for real data.

At a coarse resolution the longer period variation, causing the narrow skirt, would not be distinguished from the central peak, and in the current analysis would be ignored; a Gaussian being fit to the broader skirt. At a finer frequency resolution (which corresponds to a longer data window length) both skirts would be resolved so that when a single Gaussian is fitted only an average spectral width results (*c.f.* the fit in Figure 5.2a). Extending this to multiple broadening mechanisms on different time scales it can be seen that the fitted Gaussian will have a smaller and smaller width as more and more skirts are resolved. Thus in a realistic situation it could be expected that the estimated spectral width would decrease exponentially in Region-1 then slowly decrease with increasing data lengths once in Region-3. This is shown schematically in Figure 5.9. As for Figure 5.7, the change in the behaviour of the spectral width in going from Region-1 to Region-3 is better shown by plotting the reciprocal of the spectral width, which shall be interpretted as a response time, against the data window length.

A "minimal" response time, T_m, for the tides can be defined by fitting a straight line in Region-3 of Figure 5.9b and finding where this intersects the resolution defined curve. T_m is an estimate of the spectral width at the stage when the spectral resolution is just fine enough to resolve the broadest natural skirt, hence is an estimate of the minimum tidal response time.

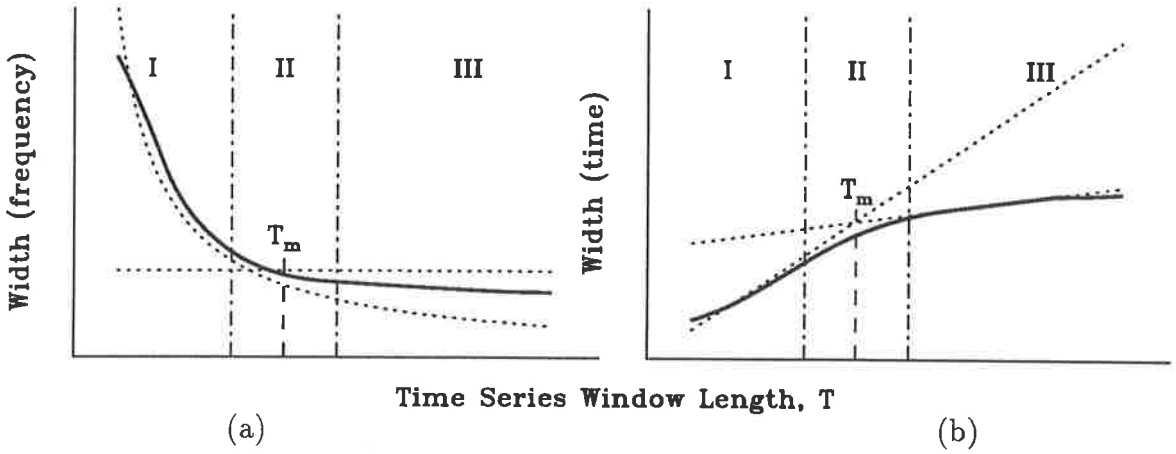

Figure 5.9: Response of the mean spectral-width to data window length for multiple incoherent processes. The three regions discussed in the text are marked. The left-hand panel shows the width in frequency units. The right-hand panel is simply the reciprocal, showing the width response in time units (as for Figure 5.7). A "minimal" response time, T_m, is shown.

This corresponds to the critical time, T_c, shown in Figure 5.7, and can be interpretted as the time after which tidal variations due to transient behaviour become averaged out. That is, the steady state tidal behaviour then dominates.

5.3 Results

5.3.1 The Diurnal Tide

An example of the fits to the raw data are shown in Figures 5.10 and 5.11 for a short and a long data window respectively. The "spike" in the tidal spectrum is first removed prior to fitting a Gaussian to the "skirt"(*c.f.* Figure 5.2). As the frequency sampling is not always optimal — being dependent on the exact data length, which is dependent on the amount and relative times of any missing data — often the tidal spike may influence two adjacent frequency bins. In this case both are removed and a Gaussian is fitted to the remainder. In most cases the width of the fitted Gaussian is in good agreement with the data, although the peak amplitudes are often larger than that of the skirt and even the spectral peak. It is the widths that are of concern for this study.

An alternative to finding the width of the skirt for each spectrum and then averaging to give a mean width is to first average the spectra and then fit a single Gaussian. In order to investigate seasonal variations, the spectra for each season were averaged and the skirt width found. This only has meaning for data windows smaller than 90 days. The seasonal spectra using a 14 day window for both the zonal and meridional diurnal tide components are shown

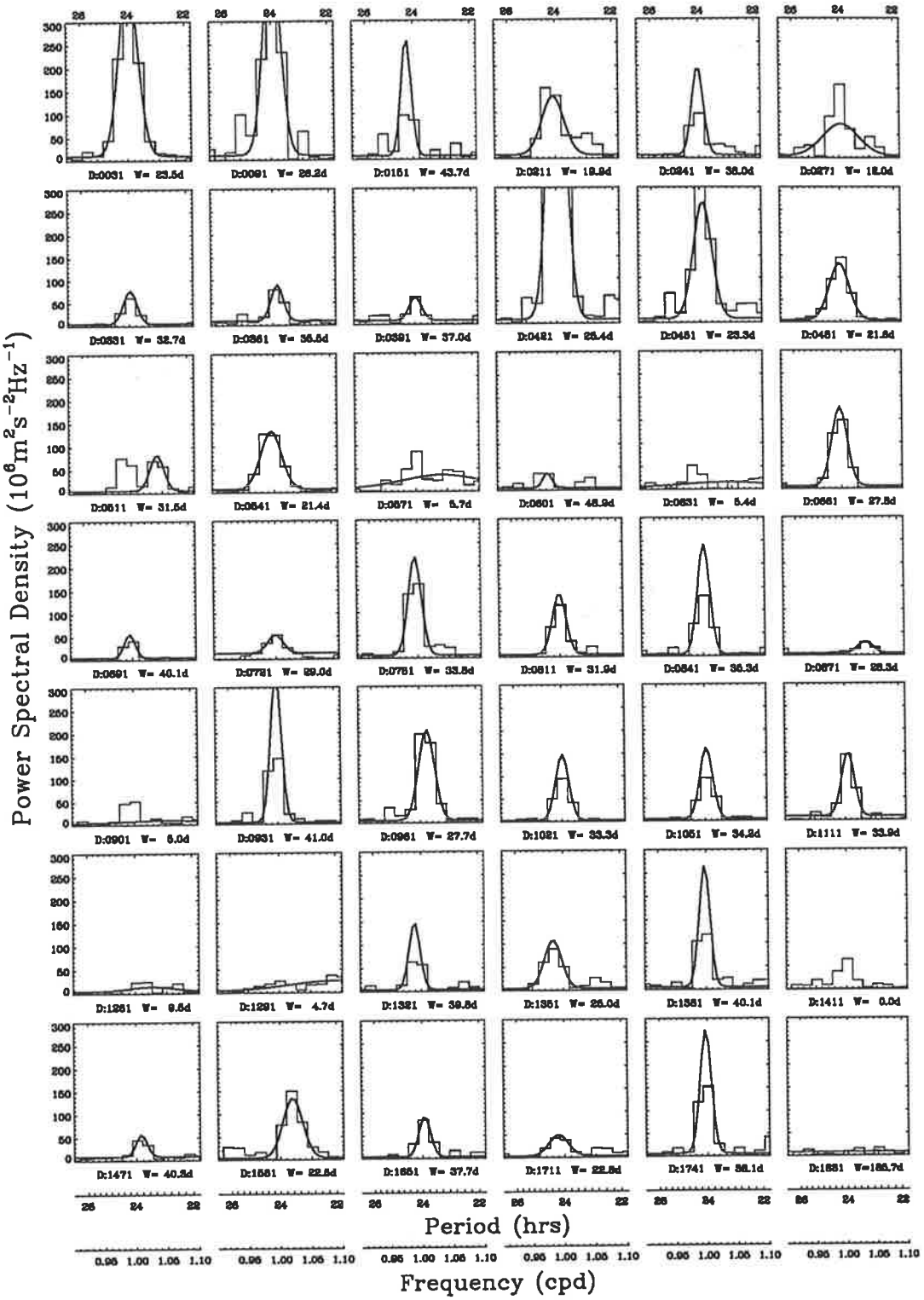

Figure 5.10: Power spectra for the meridional component of the solar diurnal tide at 86 km using a 30 day window, with a 30 day step. The Gaussian fits to the "skirt" are shown. The starting day for the data window is shown below each plot, and is expressed in days from 1st January, 1984. The 1/e full-width, expressed in days, is also shown below each plot. Spectra where a tidal peak could not be discerned, or a Gaussian curve could not be fitted, have not been shown.

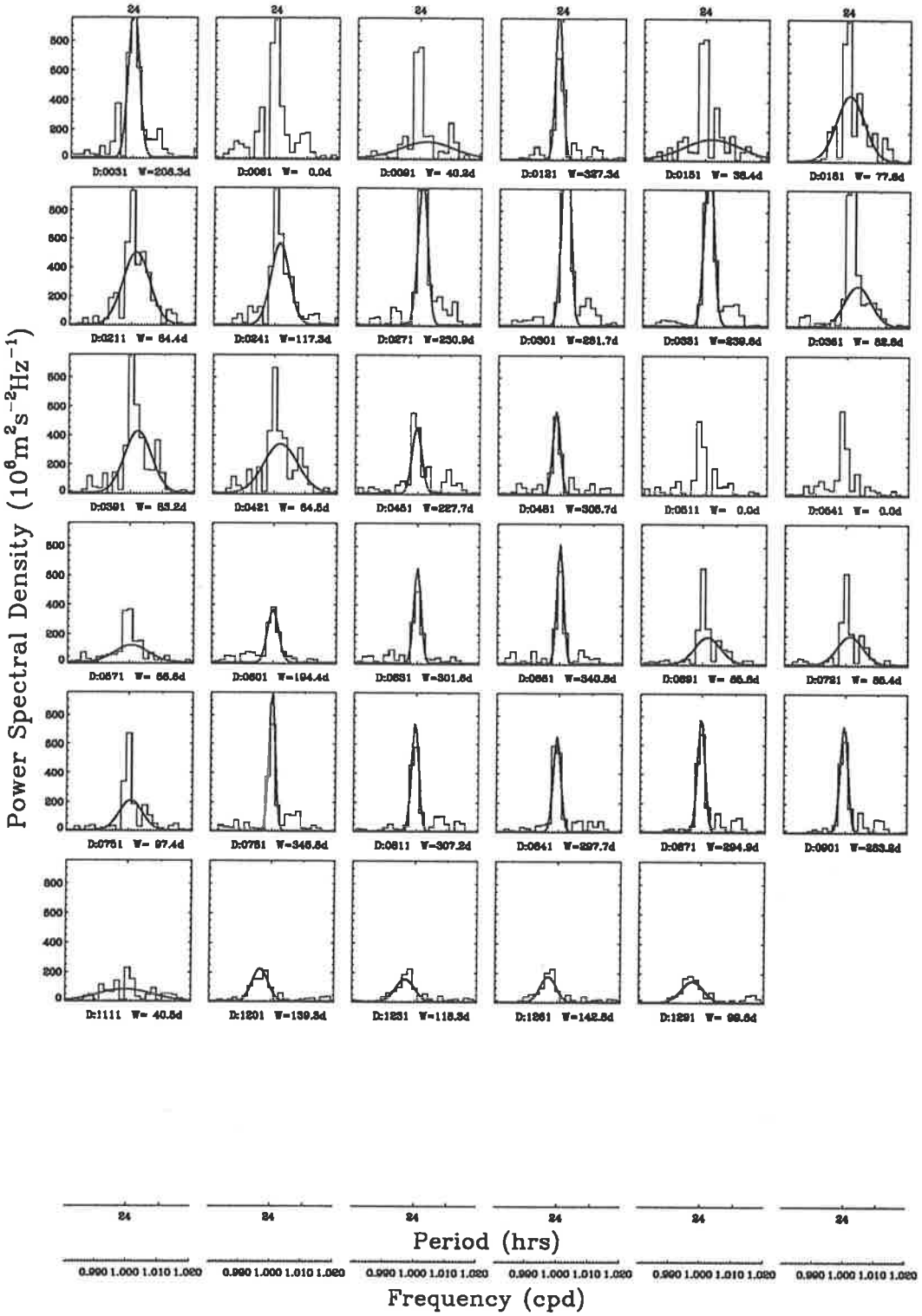

Figure 5.11: Power spectra for the meridional component of the solar diurnal tide at 86 km using a 300 day window, showing the Gaussian fits to the "skirt". Otherwise as for Figure 5.10.

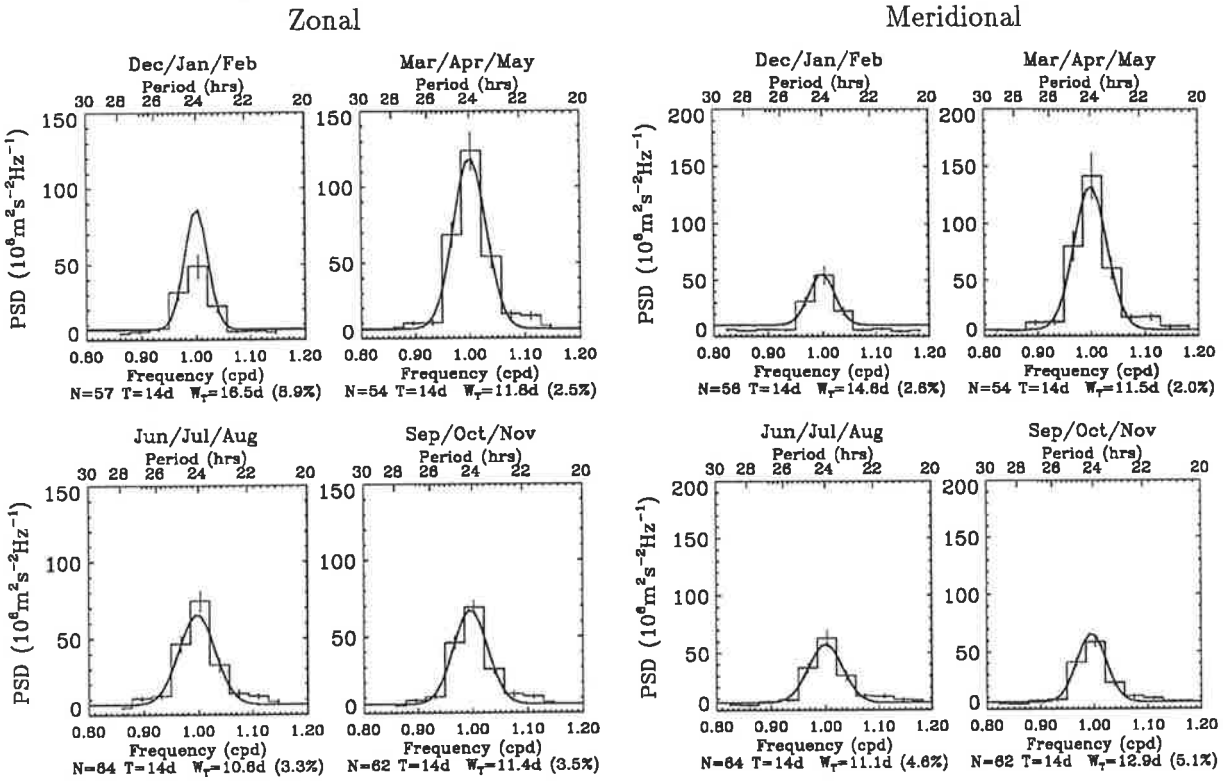

Figure 5.12: Seasonal average power spectra for the zonal and meridional components of the solar diurnal tide at 86 km. A 14 day data window was used. The Gaussian fits to the "skirt" and the errors for the spectral estimates are also shown. The number of points used, the data window size (in days), and the 1/e full-width (in days), with percentage error, are shown below the plot for each season.

in Figure 5.12. Note the similarity between the seasonal behaviour of both components. Again, it is the width, not the height, of the Gaussian fit which is important. At this resolution the "spike" expected in the tidal spectrum due to the coherent fluctuations cannot be distinguished from the "skirt". At higher resolutions (*e.g.* Figures 5.2a, 5.11 and 5.13) the distinction is more pronounced. Ignoring any seasonal variations in the short time-scale fluctuations, all the spectra for a given data window length can be averaged and a single Gaussian fitted. The averaged spectra show the general form of signal peaks in a clearer fashion than the individual spectra, as would be expected since the random variations have been averaged out. This in turn should give more reliable measures of the width of the spectral skirts. The averaged spectra and the fitted Gaussians for some of the data window lengths are shown in Figure 5.13 for the meridional wind component. Figure 5.13c possibly shows the multiple "skirts" discussed in the previous section.

The estimated spectral skirt widths were converted to a response time, which is defined here as the time it would take for an auto-correlation to fall to 0.5. By comparing the coefficients of

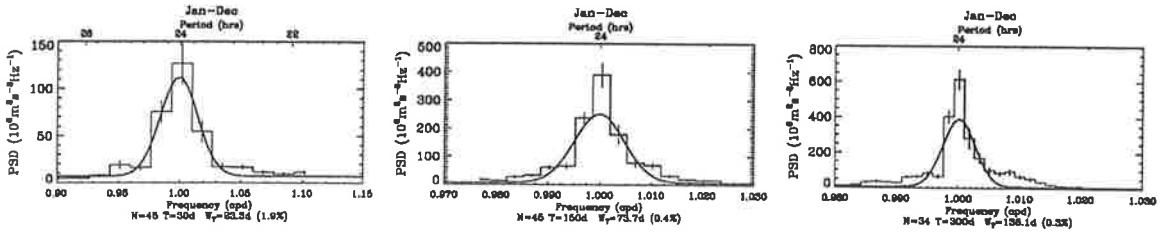

Figure 5.13: Average power spectra for the meridional component of the solar diurnal tide at 86 km. Data window lengths of (a) 30, (b) 150 and (c) 300 days have been used. The Gaussian fits to the "skirt" and the error bars for the spectral estimates are also shown.

a Gaussian function and its Fourier transform it is easily shown that the response time, $\tau_{\frac{1}{2}}$, is related to the half-width-half-maximum of the Gaussian spectral skirt, $W_{1/2}$, by the relation,

$$\tau_{\frac{1}{2}} = \frac{1}{\pi W_{1/2}}, \tag{5.3}$$

and to the 1/e half-width, $W_{1/e}$, by the relation,

$$\tau_{\frac{1}{2}} = \frac{\sqrt{\ln 2}}{\pi W_{1/e}}. \tag{5.4}$$

Figure 5.14 shows the various estimates of the spectral width, converted to a response time, for the diurnal tide out to a data window length of 120 days. The widths of the fits to the seasonal average spectra are shown as dotted lines connecting different symbols. This estimate becomes meaningless for data lengths > 100 days as more than one season of data is averaged into each spectrum. The dotted line with the larger triangles at each data point is from the widths determined from the simulated data mentioned earlier. This shows the broadening due to the finite window size, the data gaps and any other artificial processes due to the analysis. The mean of the individual width estimates are shown as unconnected crosses, with an associated error. The width of the fit to the overall average spectra are shown as solid lines connecting square symbols — the error bars are also shown but are generally smaller than the symbols themselves. The two measures of the mean spectral widths give similar results for data lengths up to 100 days. The response time estimates differ by ~ 7 days once the data length is greater than 60 days, which is far more than their combined error estimates, although maybe not much more than any realistic total error estimate for this form of analysis. The difference is greater as the data length increases, with the mean spectra giving shorter response times.

The response times for autumn, winter and spring are little different from those for the overall mean. The response times for winter are consistently less than those for autumn, which are less than for spring. During summer the response times appear to follow a different pattern.

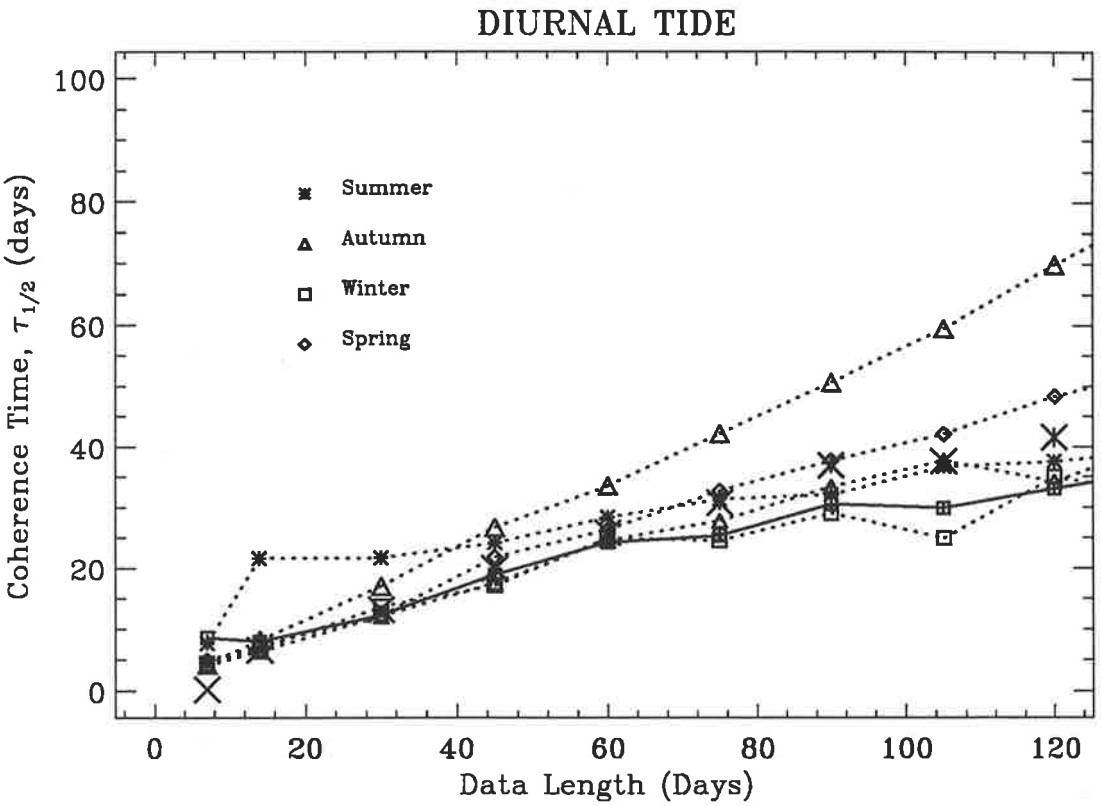

Figure 5.14: The seasonal response times for the diurnal solar tide at 86 km. The dotted line with triangles at each data point is from the widths determined from the simulated data. This shows the broadening due to the finite window size, the data gaps and any other artificial processes due to the analysis. The solid line with squares at each data point is from the width of the average spectrum for each data window length T. The large X with the y error bar show the weighted means. The seasonal means are shown as dotted lines connecting various symbols shown on the plot.

For the shortest data lengths, reflecting shorter term variations, the response time is apparently of the order of 20 days. This value does not increase with the increased data lengths. In fact, it is already larger than for the simulated data, meaning the fitted spectral skirt is on the average narrower than the spectral resolution! The reliability of this form of interpolation is probably dubious, so that those values which give response times greater than the simulated data should be truncated back to that of the simulated data. Ignoring the two high response times for the summer means leaves values which are not too different from the overall mean. Unlike the other seasons though, the summer values are not consistently in the same relative position, sometimes having longer response times than for spring and other times having values shorter than for autumn. The conclusion from this diagram is that on the average there is little seasonal difference in the response times of the broadening process for the diurnal tide. If anything, the diurnal tide appears to have shorter response times during the winter and longer times during

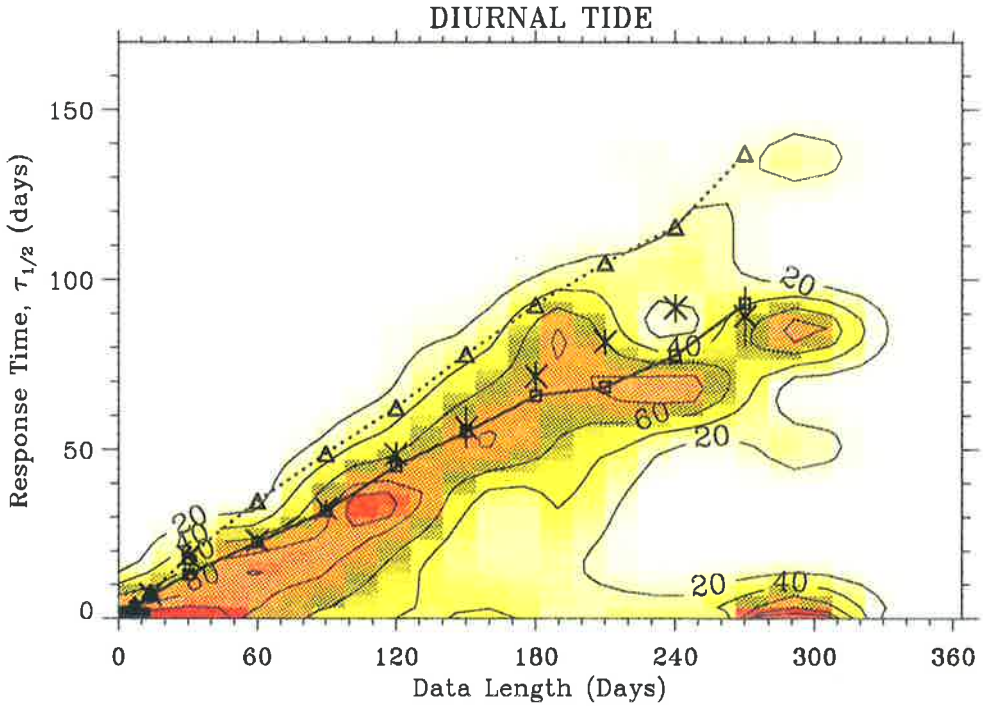

Figure 5.15: The distribution of response times for the diurnal solar tide at 78 km. The simulated data, values from the average spectrum and the weighted means of the individual spectral width estimates are shown as for Figure 5.14. The shading shows the distribution of the individual width estimates for each data length, T, of which the large X with the y error bar show the weighted means. The contours are the relative numbers, with the distribution for each T being normalised to 100. Note that there is no data for T greater than 270 days.

spring. This roughly follows the spread seen in Figure 5.1.

Displaying the response times as a histogram for each data window length out to 360 days, individually normalised and with a moderate degree of smoothing, (Figures 5.15, 5.16, and 5.17) it can be seen that the unusual distribution of the spectral-width estimates causes the average of the spectral-widths to be unreliable. The values which follow the simulated data curve are where the artificial broadening has been the dominant process for that particular run; where the model spectral shape is invalid; or the coherent and incoherent contributions were not separated successfully. These values bias the average. The width of the mean spectra on the otherhand should not be biased by these values as they represent highly peaked spectral lines whose skirt would be swamped in the averaging process by the more numerous broader spectra. Thus the width of the mean spectra should represent a good estimate of the average skirt width.

Concentrating on the response times derived from the average spectra it can be seen that the behaviour predicted in Section 5.2.2 and shown schematically in Figure 5.9 is validated by the data. The three regions described in that section can be identified in Figures 5.15, 5.16, and 5.17. Finding a minimal response time as described at the end of Section 5.2.2 gives the

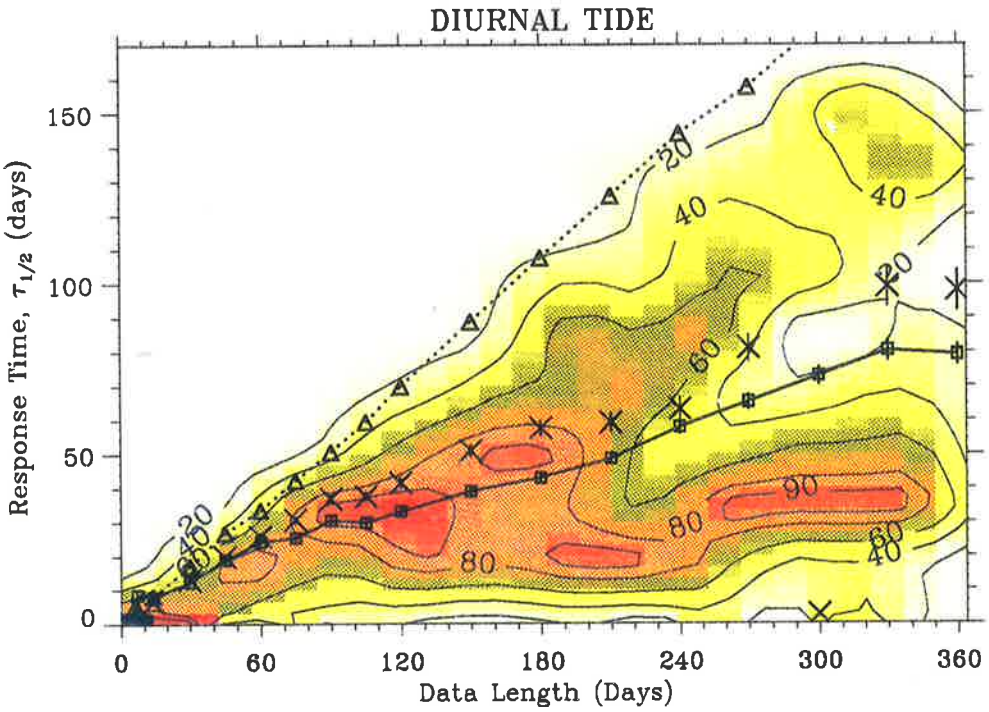

Figure 5.16: The distribution of response times for the diurnal solar tide at 86 km. Otherwise as for Figure 5.15. In this case the data extends out to 360 days.

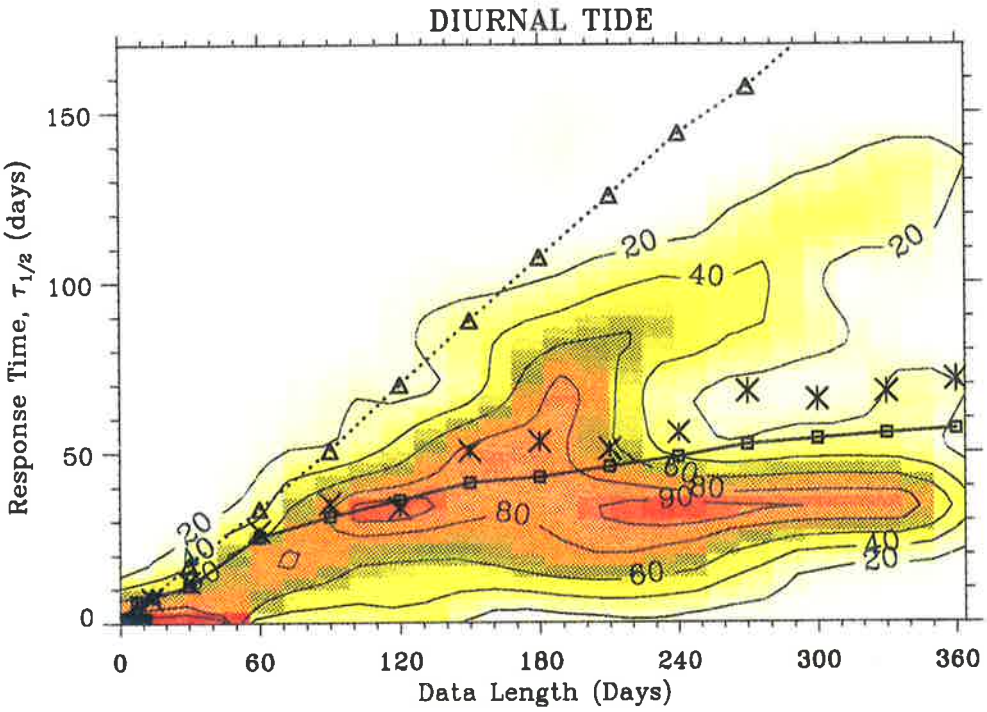

Figure 5.17: The distribution of response times for the diurnal solar tide at 94 km. Otherwise as for Figure 5.16.

			78 km	86 km	94 km
$\tau_{\frac{1}{2}}$	(all modes)		15 ± 5	20 ± 3	27 ± 5
τ_b	(1,1)	[*Bernard*, 1981]	12	12	12
τ_b	(1,3)	[*Bernard*, 1981]	27	27	27
τ_e	(1,1)	[*Vial et al.*, 1991]	6		
τ_c	(1,1)	[*Vial et al.*, 1991]	8.5		
$\tau_s(1)$	(1,1)	[*Vial et al.*, 1991]	20		
$\tau_s(2)$	(1,1)	[*Vial et al.*, 1991]	15		

Table 5.1: Response times (in days) for the various modes of the diurnal tide. The definition of the different estimates is explained in the text.

values shown in Table 5.1. Since these values are derived from the intersection of two lines with similar slopes, the errors are accordingly large. The errors quoted arise from the minimum and maximum slopes. Also tabulated are some estimates for tidal relaxation times from equivalent gravity wave considerations by *Bernard* [1981] and time-dependent modelling work by *Vial et al.* [1991]. The definitions for the various relaxation times can be found in Section 4.2 of *Vial et al.* [1991]. *Bernard* [1981] estimates a setup time, τ_b, for stationarity of the tides by using the horizontal group velocities of equivalent gravity waves to calculate the time needed for a perturbation to circle the globe for a number of tidal modes. *Vial et al.* [1991] defines three different response times. The first, the "critical forcing time", τ_c, relates to how fast the tidal thermal forcing can change yet still maintain thermal equilibrium with the tidal oscillations. The second, τ_e, is the e-folding time of the tidal transients. Lastly, they define a settling time, τ_s, which measures how long it takes for a tidal mode to reach 10% of its steady state value. τ_s is dependent on the time it takes the forcing to reach its maximum value, thus two estimates for τ_s are given in Table 5.1; one for a thermal forcing rise time of 50 hours, the other for 100 hours. The response time, $\tau_{\frac{1}{2}}$, defined in this section is approximately related to the e-folding time, τ_e, by

$$\tau_{\frac{1}{2}} \approx \sqrt{\ln 2}\,\tau_e \approx 0.8\,\tau_e\,. \tag{5.5}$$

This can easily be seen by considering $\tau_{\frac{1}{2}}$ as equivalent to the time taken for an exponential decay to halve in value (an exponential decay being its own auto-correlation), as opposed to τ_e which is the time for it to reduce by a factor of $1/e$.

5.3.2 The Semi-Diurnal Tide

An example of the fits to the raw data are shown in Figures 5.18 and 5.19 for a short and a long data window respectively. As for the diurnal tide, fits to the seasonal and total average

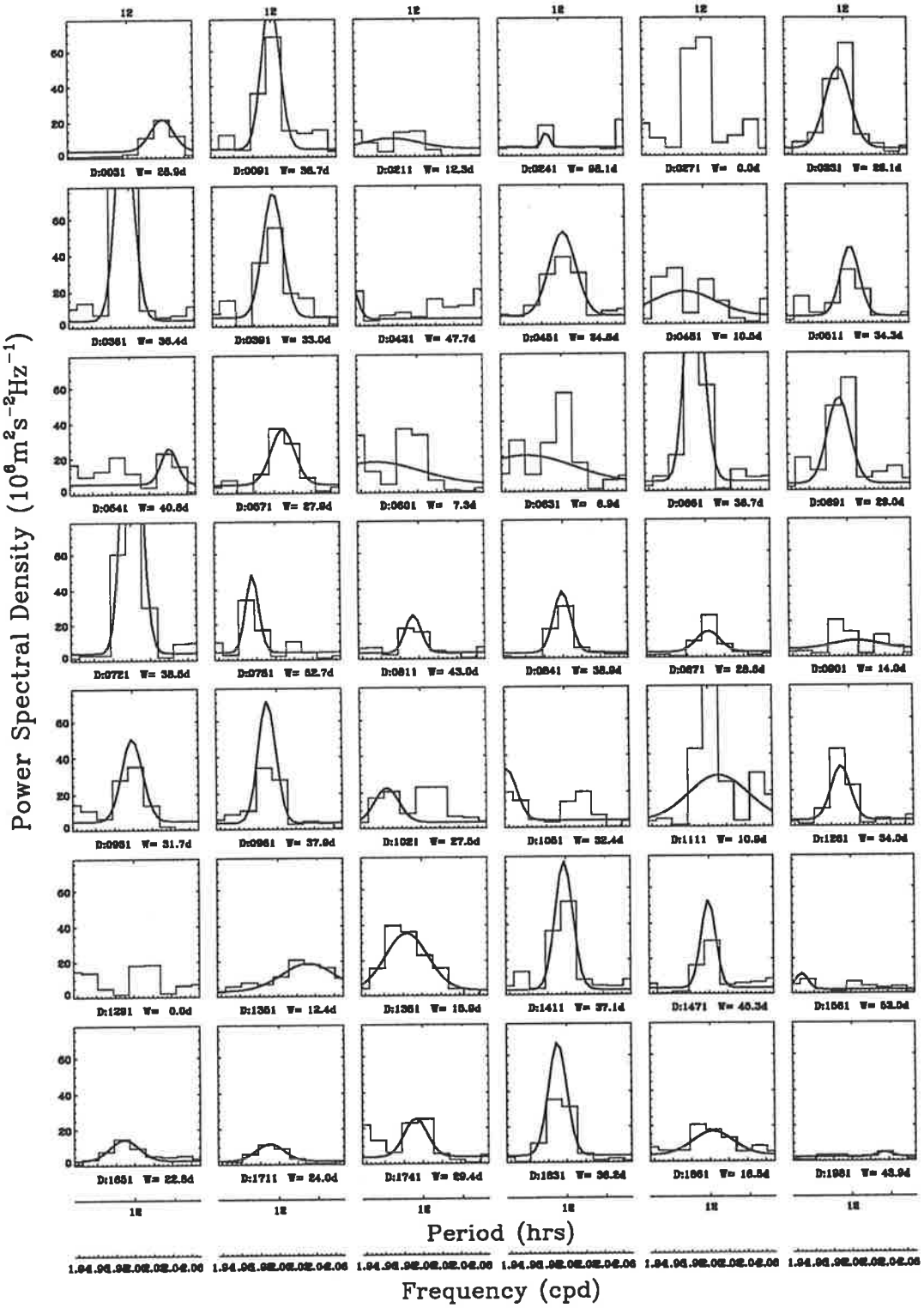

Figure 5.18: Power spectra for the meridional component of the solar semi-diurnal tide using a 30 day window. Otherwise as for Figure 5.10.

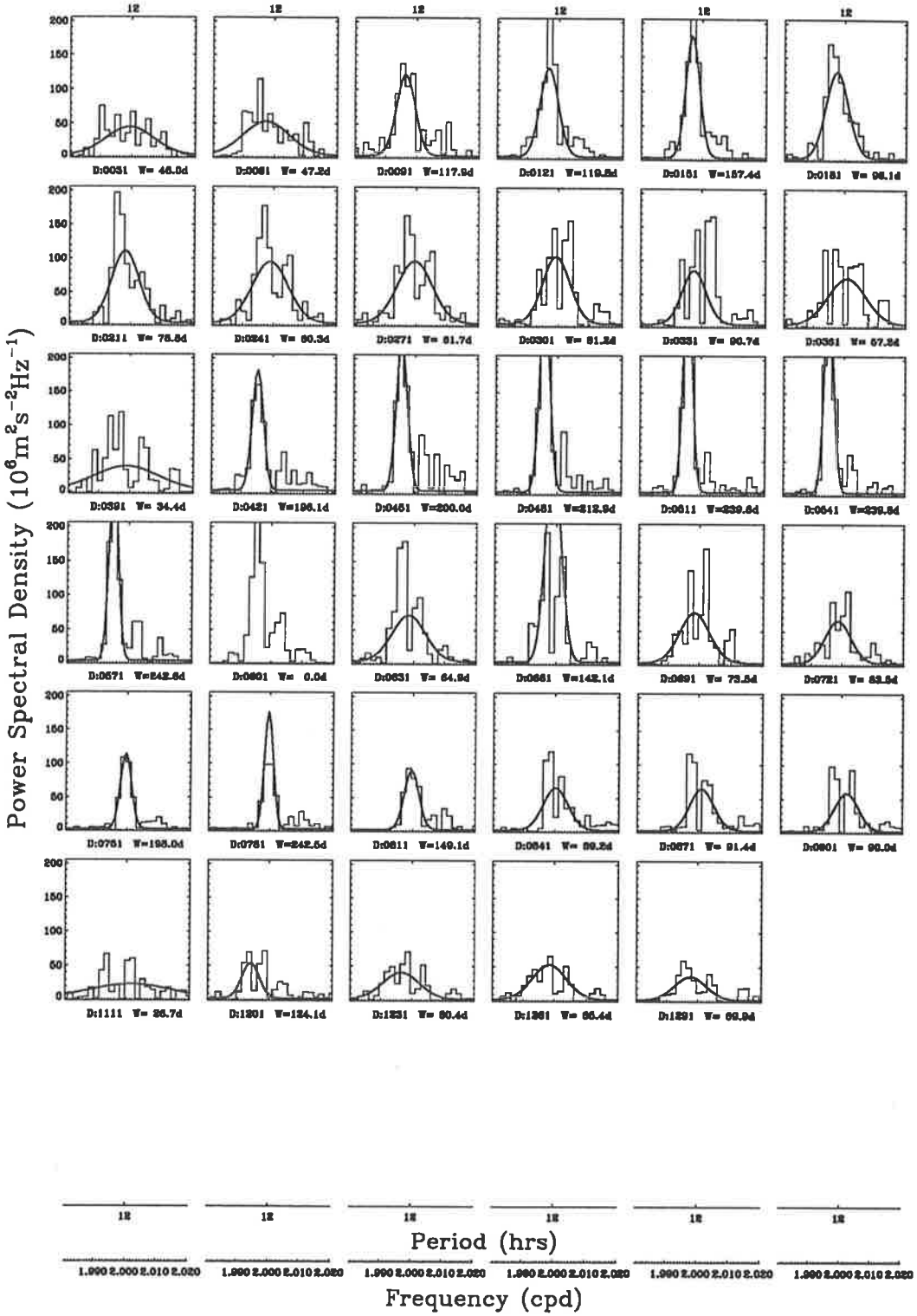

Figure 5.19: Power spectra for the meridional component of the solar semi-diurnal tide using a 300 day window. Otherwise as for Figure 5.18.

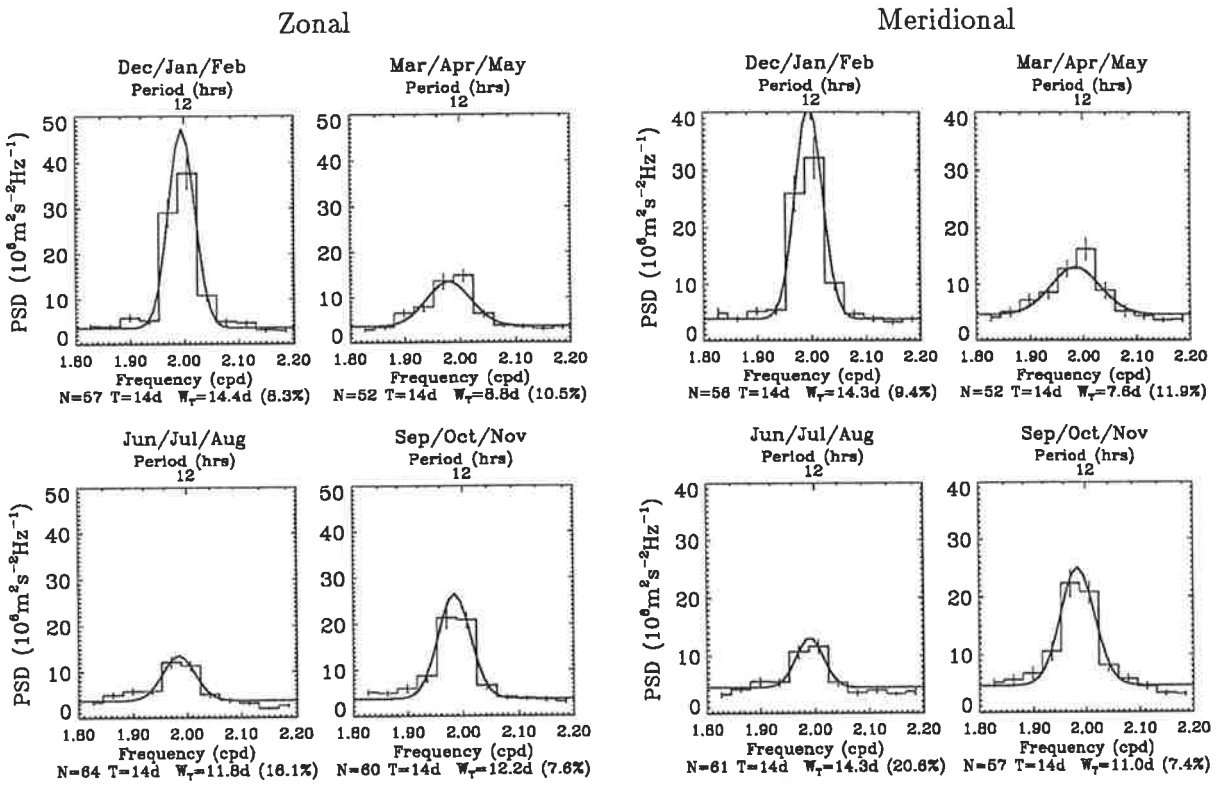

Figure 5.20: Seasonal average power spectra for the zonal and meridional components of the solar semi-diurnal tide at 86 km. Otherwise as for Figure 5.12.

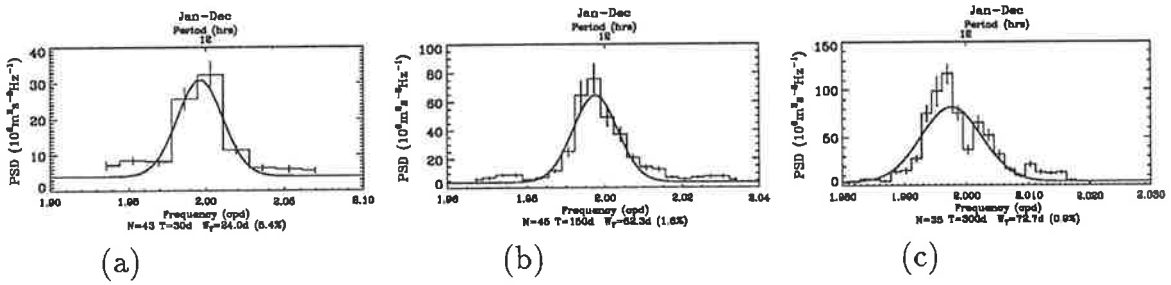

Figure 5.21: Average power spectra for the meridional component of the solar semi-diurnal tide. Data window lengths of (a) 30, (b) 150 and (c) 300 days have been used (as in Figure 5.13). The Gaussian fits to the "skirt" and the error bars for the spectral estimates are also shown.

spectra have also been made.The seasonal spectra, using a 30 day window, for both the zonal and meridional semi-diurnal tide components are shown in Figure 5.20. The averaged spectra and the fitted Gaussians as for Figure 5.13 are shown in Figure 5.21 for the meridional wind component.

Figure 5.22 shows the various estimates of the spectral width, converted to a response time, for the semi-diurnal tide at 86 km. The symbols are the same as used in Figure 5.14. The two measures of the mean spectral widths give similar results for data lengths up to 60 days, then differ by ~ 10 days.

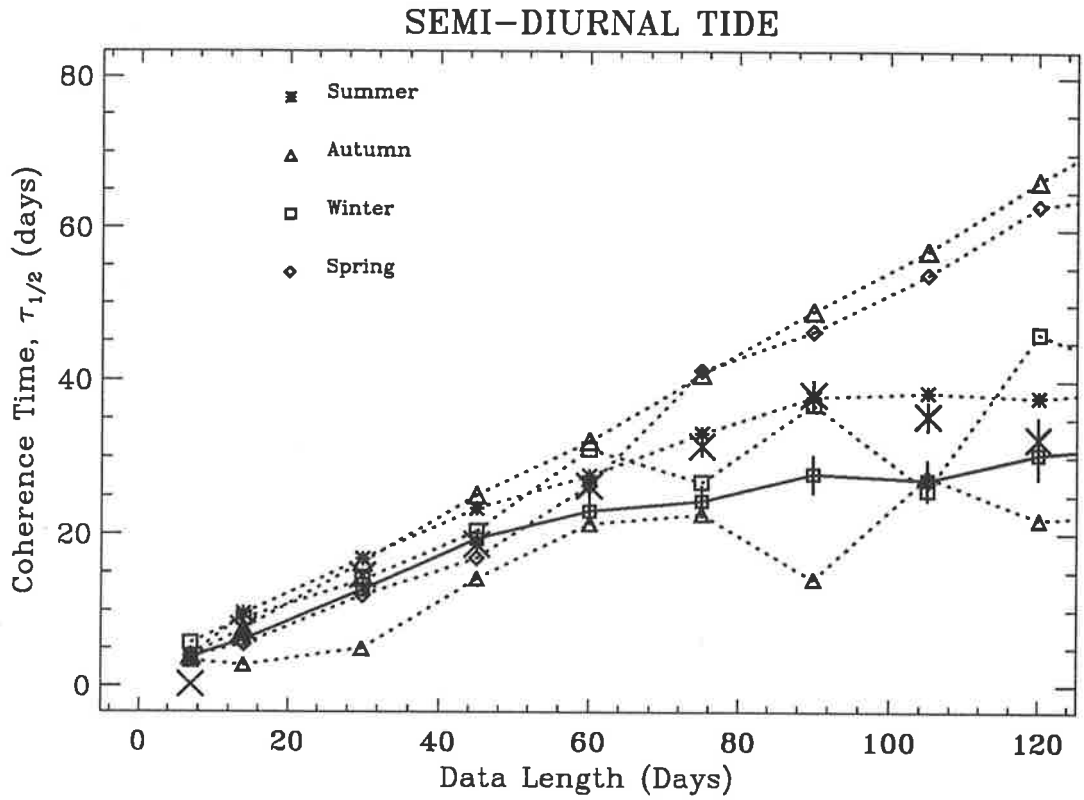

Figure 5.22: The seasonal response times for the semi-diurnal solar tide. Otherwise as for Figure 5.14.

Unlike for the diurnal tide, the response times for autumn, winter and spring are significantly different from those for the overall mean. The response times for autumn are consistently less than those for winter, which are less than for spring. Also, like the diurnal tide, during summer the response times follow a different pattern, being approximately the same as the overall mean. The response times during spring closely follow those of the simulated data. This indicates that the semi-diurnal tidal peak is very narrow during that season. Taking a simple view, the conclusion from this diagram is that on the average there are seasonal differences in the response time of the semi-diurnal tide. Specifically, the tide appears to have a longer response time during the equinoxes than during the other seasons. As other contributing factors may be involved during spring (see later), this interpretation must be viewed with some skepticism. The semi-diurnal tide also appears to have shorter response times during autumn and longer times during winter. This roughly follows the spread seen in Figure 5.1.

Displaying the response times as a histogram as before (Figures 5.23, 5.24, and 5.25), it can be seen that for longer data lengths ($\geq$ 180 days) the often bimodal distribution of the spectral width estimates have caused the average of the spectral-widths to be more unreliable than for

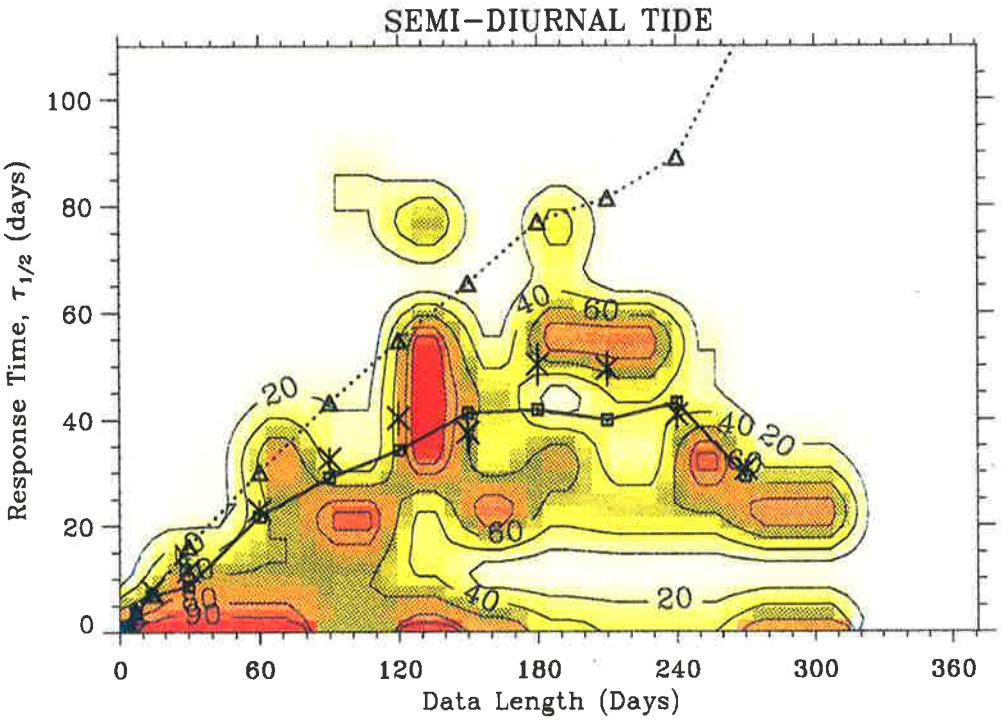

Figure 5.23: The distribution of response times for the semi-diurnal solar tide at 78 km. Otherwise as for Figure 5.15.

the diurnal tide. For shorter data lengths the average spectral width and the width of the mean spectra are in good agreement. At 86 km (Figure 5.16) the width of the mean spectra tracks the 90% contour region well. As discussed in the previous section, the width of the mean spectra should give the most reliable estimate of the tidal response time.

As before, a minimal response time is sought. The semi-diurnal tide exhibits two distinct sub-regions of linear response within Region-3 of Figure 5.9b. The response time for data lengths less than 180 days gives a minimal response time estimate tabulated in Table 5.2 as $\tau_{\frac{1}{2}}(1)$. At longer data lengths ($\geq$ 180 days) the response time remains nearly constant with increasing data length. These values have been tabulated as $\tau_{\frac{1}{2}}(2)$.

5.4 Discussion and Interpretation of Results

The response times, $\tau_{\frac{1}{2}}$, presented in Tables 5.1 and 5.2, represent the effective response time of the real atmospheric tides, which includes the effects of multi-mode interference. Therefore comparisons with the more theoretical values of *Bernard* [1981] and *Vial et al.* [1991] must not be viewed as definitive.

With this in mind it is surprising that the respective response time estimates agree so well. For example, for the diurnal tide near 78 km (Table 5.1) the value for the (1,1) mode from

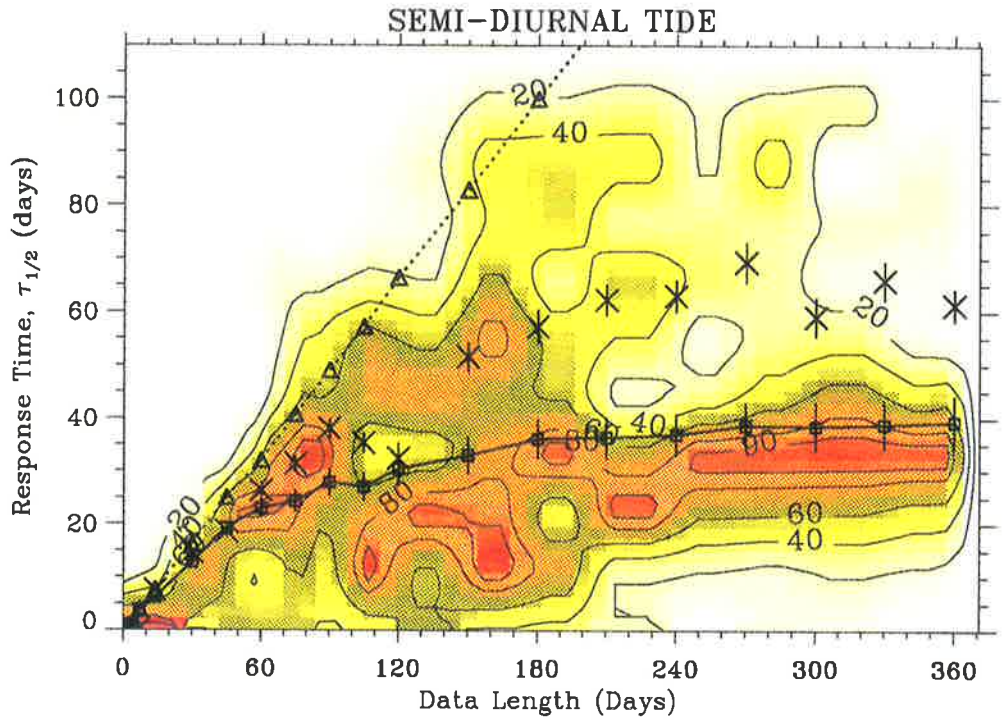

Figure 5.24: The distribution of response times for the semi-diurnal solar tide at 86 km. Otherwise as for Figure 5.16.

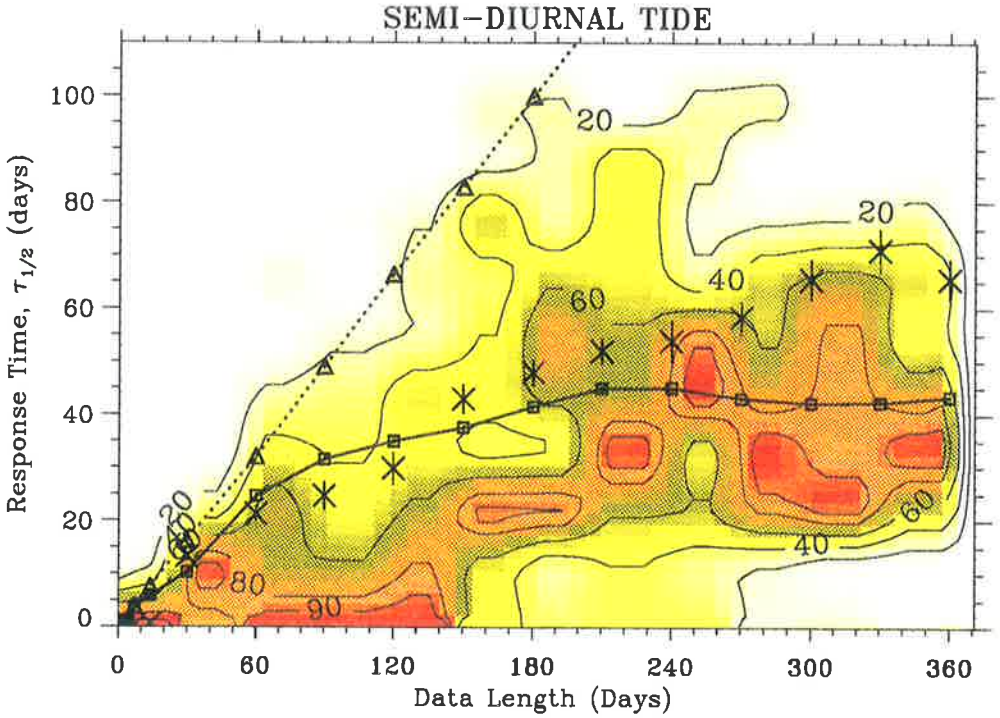

Figure 5.25: The distribution of response times for the semi-diurnal solar tide at 94 km. Otherwise as for Figure 5.17.

			78 km	86 km	94 km
$\tau_{\frac{1}{2}}(1)$	(all modes)		15 ± 3	20 ± 1	30 ± 2
$\tau_{\frac{1}{2}}(2)$	(all modes)		40 ± 1	35 ± 2	45 ± 1
τ_b	$(2,2)$	[*Bernard*, 1981]	2.5	2.5	2.5
τ_b	$(2,3)$	[*Bernard*, 1981]	4.2	4.2	4.2
τ_b	$(2,4)$	[*Bernard*, 1981]	6.1	6.1	6.1
τ_b	$(2,5)$	[*Bernard*, 1981]	8.0	8.0	8.0
τ_b	$(2,6)$	[*Bernard*, 1981]	10.1	10.1	10.1
τ_b	$(2,7)$	[*Bernard*, 1981]	12.2	12.2	12.2
τ_b	$(2,8)$	[*Bernard*, 1981]	14.5	14.5	14.5
τ_e	$(2,2)$	[*Vial et al.*, 1991]	24		
τ_c	$(2,2)$	[*Vial et al.*, 1991]	14		
$\tau_s(1)$	$(2,2)$	[*Vial et al.*, 1991]	40		
$\tau_s(2)$	$(2,2)$	[*Vial et al.*, 1991]	40		

Table 5.2: Response times (in days) for the various modes of the semi-diurnal tide. The definition of the different estimates are as explained in the text.

Bernard [1981] and the settling times, τ_s, from *Vial et al.* [1991] are in very good agreement with the minimal response time estimated here. So too are the $\tau_{\frac{1}{2}}(1)$ values for the semi-diurnal tide, the $(2,7)$ and $(2,8)$ modes from *Bernard* [1981] and the critical forcing time, τ_c, of the $(2,2)$ mode from *Vial et al.* [1991] (Table 5.2). Comparison with the estimates of *Bernard* [1981] suggest that most of the variability, if solely ascribed to multi-mode mixing, comes from higher-order modes such as the $(2,7)$ and $(2,8)$. Smaller response times may exist for the solar tides (as suggested by the estimates of *Bernard* [1981] for the lower order modes of the semi-diurnal tide). Values of the order of 10 days or less cannot be resolved using the current analysis technique as the frequency resolution becomes poorer with decreasing data window lengths.

The response time of the diurnal and semi-diurnal tide appears to increase with altitude. Comparison with the estimates of *Bernard* [1981] for the diurnal tide suggest that this increase is due to the greater influence of the $(1,3)$ mode at the higher altitude. This mode, though, has a short vertical wavelength in the real atmosphere (~ 15 km), so it should suffer very strong dissipation, hence is most unlikely to reach mesospheric altitudes. It is therefore unlikely to be of importance.

The increased response time with altitude is in contrast to the expectations of *Vial et al.* [1991] who state that both the τ_c and τ_s estimates should decrease with increasing altitude due to increased damping by dissipative processes. τ_e should also decrease with increasing altitude until it reaches the limit of the e-folding time for the dissipative processes — which should happen around the mesopause !. The current results suggest that the additional variability caused by

greater mixing of *in situ* and higher-order tidal modes may counteract the increased damping with increaed altitude.

At longer data lengths Figures 5.23, 5.24, and 5.25 appear to follow the expected behaviour for a single broadening mechanism (*c.f.* Figure 5.7) having a response time of ~ 40 days ($\tau_{\frac{1}{2}}(2)$ in Table 5.2). Closer investigation of this suggests that the dominant broadening at the longer data lengths is due to the rapid phase changes of this tide around the equinoxes. The semi-diurnal tide appears to be dominated by short vertical wavelength (~ 50–$80\,\mathrm{km}$) higher order modes in winter and longer vertical wavelength ($\geq 100\,\mathrm{km}$) lower order modes in summer [*Manson et al.*, 1989; *Vincent et al.*, 1989]. The transition between these two states causes a rapid phase variation during the equinoctial months. This is illustrated in Figure 5.26 which shows the amplitude and phase of the solar tides during 1985. Rapid phase transitions through 180° can be seen in the semi-diurnal tide during the equinoxes and in late summer (indicated in Figure 5.26 by solid arrows). The phase change is most rapid near day 250 (September) when it appears to jump by more than 1/3 of a cycle between the 4-hourly measurements.

The expected result of taking the Fourier transform of a sinusoidal time series which encompasses a 180° phase "flip" is shown in Figure 5.27. The energy in frequencies surrounding that of the sinusoids are enhanced while that at the sinusoidal frequency is severely diminished. The process is akin to the suppression of the amplitude of the carrier frequency in some broadcast communications (*e.g.* the double-sideband suppressed carrier waveform).

The spectra in Figures 5.19 and 5.21 show the minima at the tidal frequency predicted from such a phase flip. Under these conditions the model of the spectral response shown in Figure 5.2 is not valid. The smearing of the spectral line due to the phase variation dominates all other broadening mechanisms for the data windows ≥ 200 days, when each time series must encompass one of the equinoxes, hence a rapid phase transition.

5.5 Further Results

5.5.1 Mean Solar Tidal Powers

The noise-corrected version of the cumulative spectrum (as explained on page 202) was used to obtain an estimate of the total tidal signal variance. The analysis was performed on the average seasonal and total spectra so that the total tidal signal variances are in a sense incoherent averages in that the mean powers have been found. The individual spectra represent coherent averages. Thus as the data window length increases, and the number of individual spectra

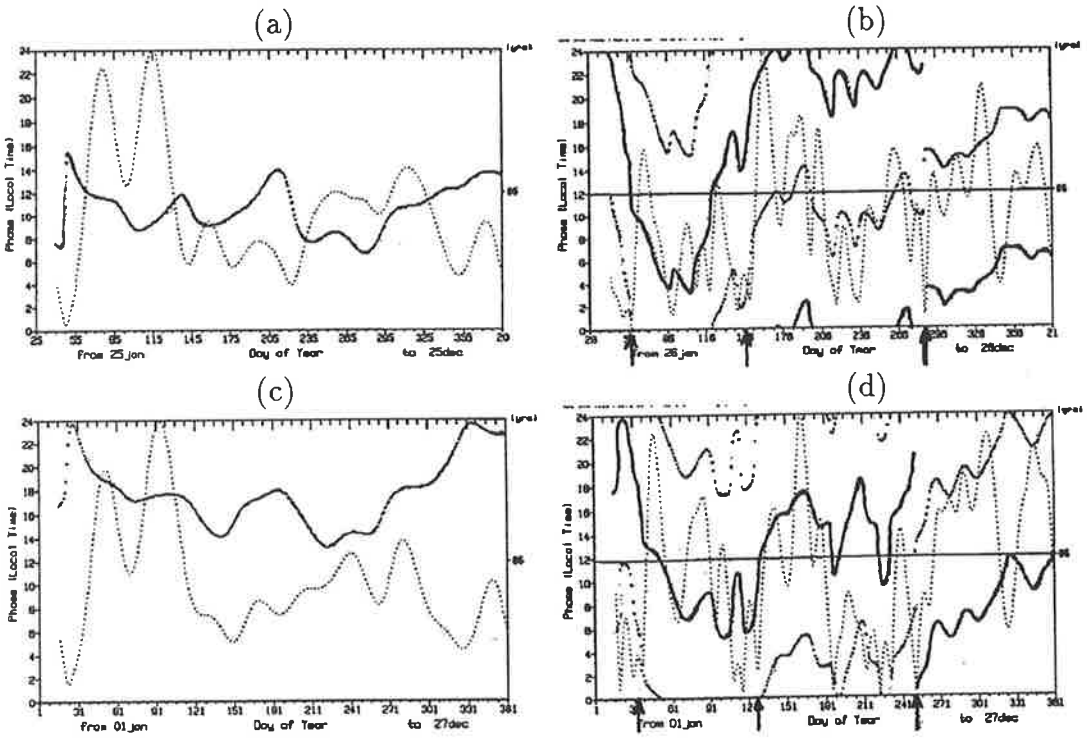

Figure 5.26: Amplitudes (thin dotted line) and phases (solid or thick dotted lines) of the solar tides at 86 km during 1985 for the (a) diurnal zonal component, (b) semi-diurnal zonal component,(c) diurnal meridional component,(d) semi-diurnal meridional component. The rapid phase transitions for the semi-diurnal tide are indicated by solid arrows.

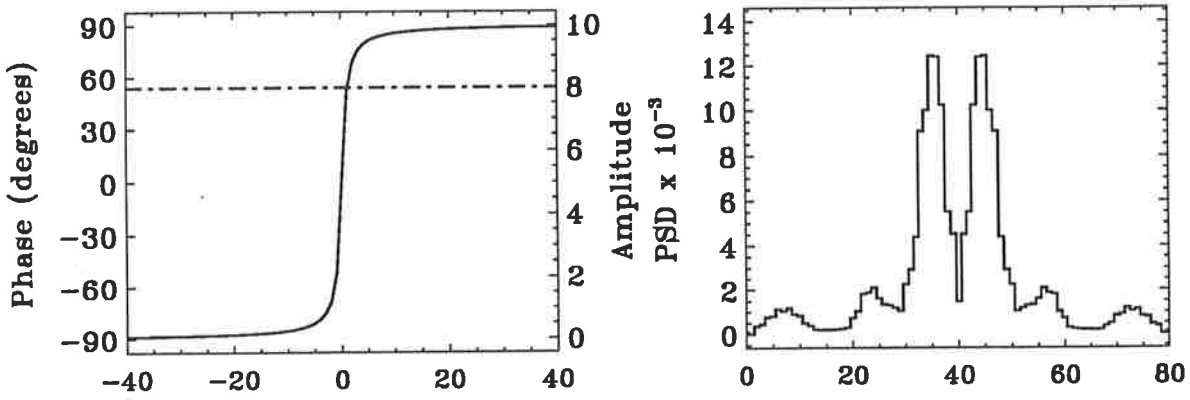

Figure 5.27: The effect on the power spectrum of a phase flip in the time series. The phase a sinusoidal time series is shown by a solid line and the constant amplitude by a dot-dashed line. The frequency of the sinusoid was 40 cycles per unit.

consequently decreases, the total tidal signal variances consist of more and more a coherent average. This could cause the estimated tidal signal variances to decrease with increasing data length as the coherent average of random fluctuations is smaller than the incoherent average (*c.f.* short proof later on regarding the mean of squares versus the square of the means).

The seasonal spectra, up to a data window length of 120 days, and the total spectrum are shown in Figure 5.28 as a function of the data window length. The square-root of these values gives an estimate of the average rms tidal wind speeds. These are shown in Figure 5.29. The estimated wind speeds are largest in autumn by a significant amount for the diurnal tide — by an extra third of the mean value — and are smallest for summer. In contrast, the semi-diurnal tide has its largest wind speeds in summer, with minimum speeds during winter. This is consistent with the behaviour of the rms wind speeds shown in Figure 4.76, on page 187. Comparison of the mean values for these two figures requires a better understanding of the differences in the processing. The current rms values reflect the power in the mean spectra whereas the dashed lines in Figure 4.76 reflect the mean of the rms winds. This is the difference between the mean of the squares and the square of the means, thus the current rms wind speeds would be expected to be the larger of the two. This can easily be shown if the mean of the rms winds in Figure 4.76 is denoted by $\overline{a}$, and each rms wind estimate by $a_j = \overline{a} + a'_j$. Then the variance of the tidal winds becomes a_j^2, and the mean variances shown in Figure 5.28 are $\sum_{j=1}^{n} a_j^2/n$, where there are n spectra in the average. Then,

$$\begin{aligned} \text{mean variance} &= \frac{1}{n}\sum_{j=1}^{n} a_j^2 \\ &= \overline{a}^2 + \frac{1}{n}\sum_{j=1}^{n} a_j'^2 \\ &> \overline{a}^2 \end{aligned} \tag{5.6}$$

Comparing the two means it is found that the opposite is true. This can be accounted for when it is realised that the noise floor has been removed for the estimates in Figure 5.28 but not for Figure 4.76, which also has used a wider bandpass. To estimate the contribution of the noise floor to the rms wind estimates of Figure 4.76 the lower decile values for the 9.6 hr wind component (which does not appear to have a strong wind oscillation at mid-latitudes) can be looked at. These values give an estimate of the noise of $\sim 5\,\mathrm{ms}^{-1}$. This could account for the $\sim 7\,\mathrm{ms}^{-1}$ discrepancy in the tidal estimates in Figures 4.76 and 5.28. Thus the mean rms wind speeds shown in these two figures are consistent, when the differences in the techniques are taken into account. The values in Figure 5.28 are the better estimate of the mean tidal wind speeds.

Finally, as predicted earlier, the estimated tidal signal variances, hence rms wind speeds,

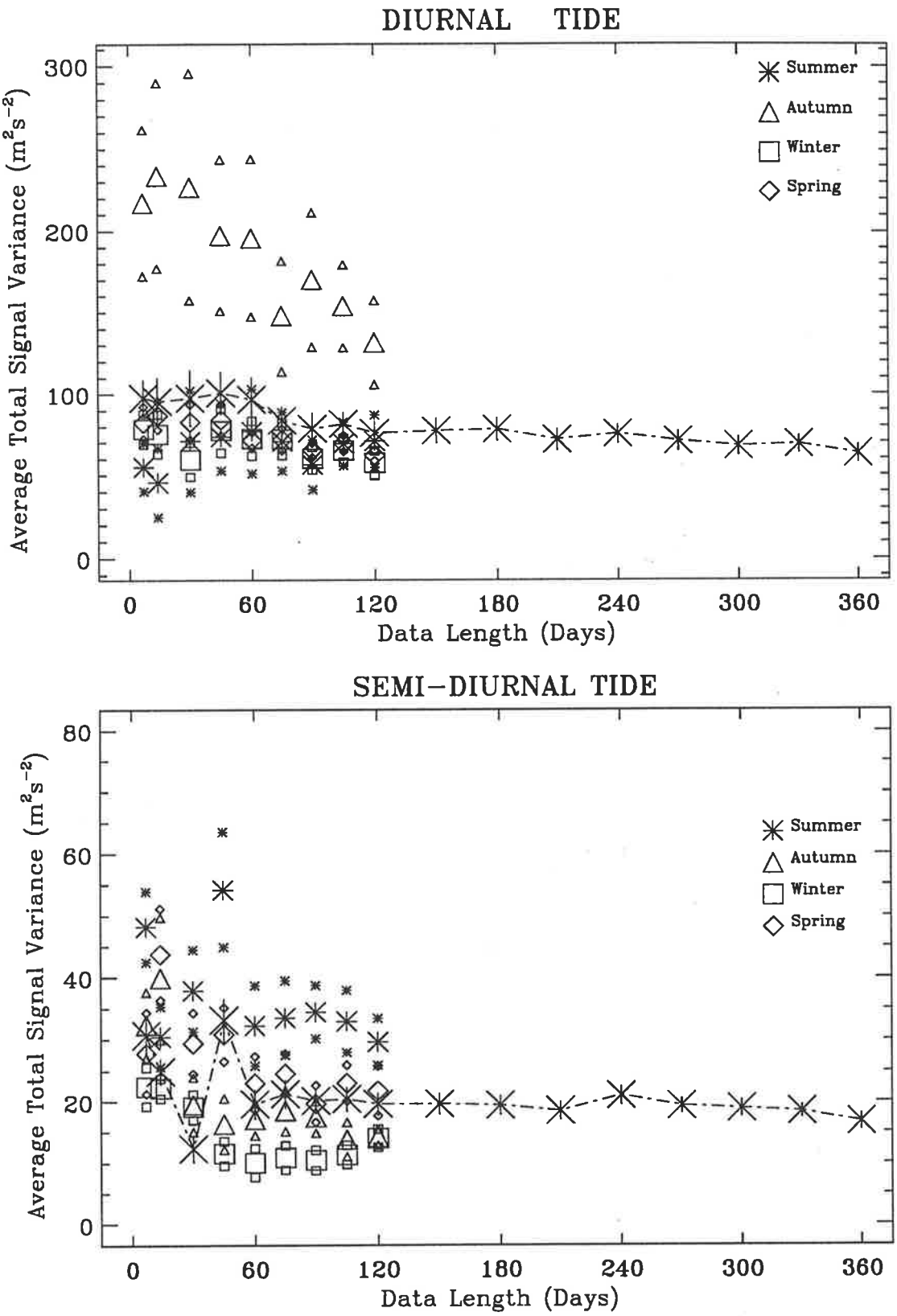

Figure 5.28: Average spectral variances for the meridional component of the solar diurnal and semi-diurnal tides at 86 km, corrected for spectral noise. The seasonal variances are shown out to data lengths of 120 days. One standard deviation errors are indicated by the smaller symbols for the seasonal data and by an error bar for the mean (the large X). The noise-corrected cumulation of the average spectrum has been used in each case.

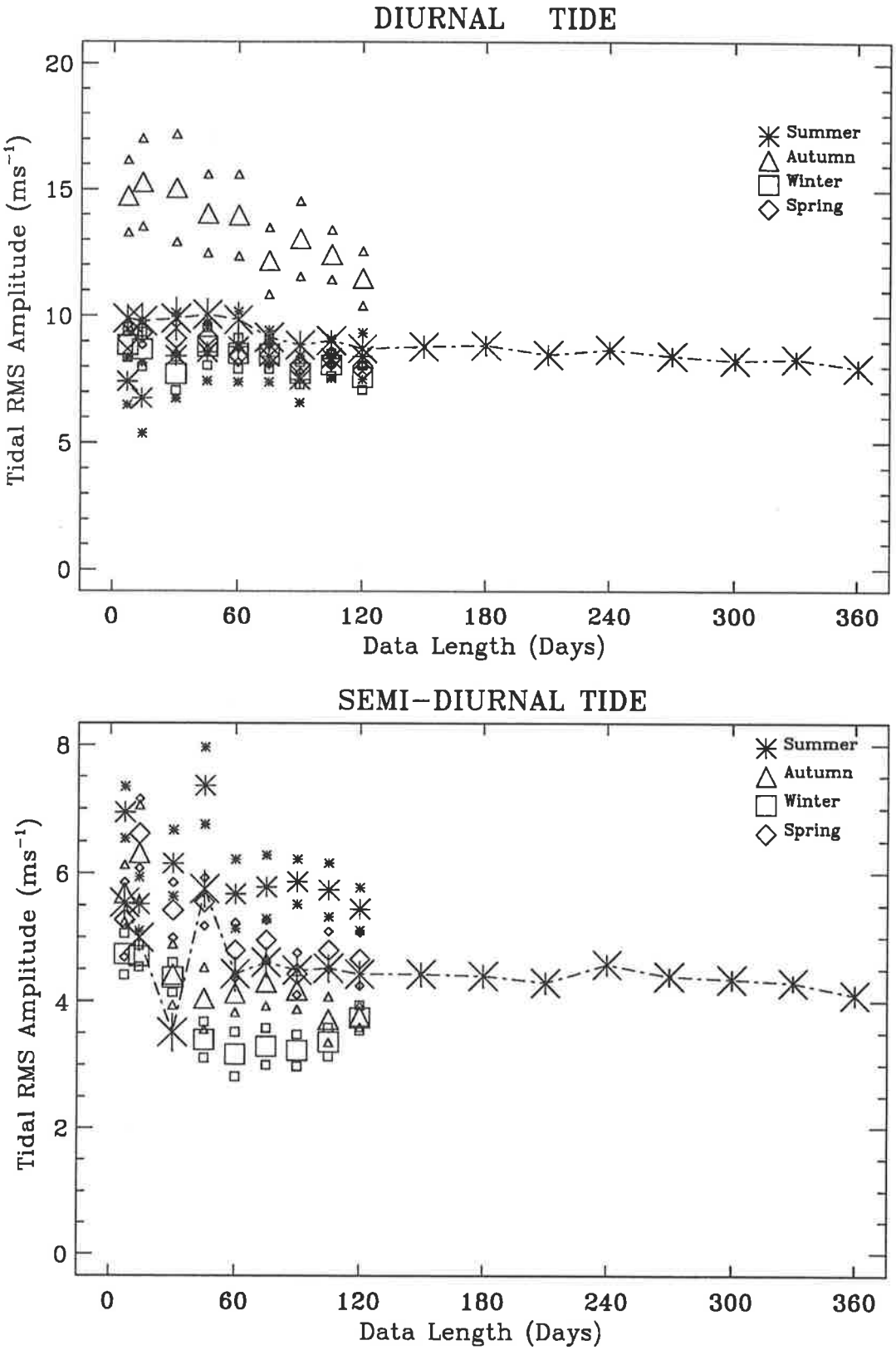

Figure 5.29: Average rms winds for the meridional component of the solar diurnal and semi-diurnal tides at 86 km, corrected for spectral noise. This is simply the square-root of the values in Figure 5.28. The labelling is the same as in that figure.

decrease with increasing data length. This is expected, as too is the convergence of the seasonal estimates to the mean for increasing data lengths, as the distinction between seasons becomes more and more meaningless.

5.5.2 In Search of the Lunar Tides

Because the lunar tides in the atmosphere are purely driven by the gravitational effects of the moon, their forcing mechanism is well understood. For this reason the study of the lunar tides allows easier interpretations in terms of the variability of the atmosphere. In practice, though, it is difficult to discern the lunar tidal lines as they are usually buried in the noise floor.

The two strongest lines of the lunar tide, the M2 and O1, are located at 12.4 and 24.8 hr, which are both near the much stronger solar tidal periods. Besides these pure lunar lines interference between the lunar and solar tides could produce observable energy at the sum and the difference frequencies [*Rush et al.*, 1970, for example]. Therefore the interaction between the solar diurnal tide and the lunar semi-diurnal M2 line (denoted as L_{21}^{-} and L_{21}^{+}) should produce spectral lines at $1.935 - 1.000 = 0.935$ and $1.935 + 1.000 = 2.935$ cpd, which is at ~ 25.7 and ~ 8.2 hr. Further lines such as the L_{11}^{+}, L_{12}^{-}, L_{13}^{-}, L_{23}^{-} at 1.968, 1.032, 2.032, and 1.065 cpd are close to O1 and M2 lines and may be observable. The O1 and M2 lines themselves have a fine structure [*Chapman & Malin*, 1970] due to lunar seasonal variations. For example the M2 line could be expected to have peaks at frequencies of 1.927, 1.930, 1.932, 1.935 and 1.937, whose relative strengths at sea-level are 1, 1, 5, 1, and 1 respectively.

All the lunar tidal lines mentioned above may be buried in the "skirts" of the solar lines. In order to increase the signal-to-noise ratio for the lunar lines long time series have to be used — remembering that the signal power will increase as the square of the length of the time series whereas the noise spectral density will only increase in a linear fashion, so the longer the time series the better the signal-to-noise ratio. Longer time series also allow for better frequency resolution, allowing better separation of the solar and lunar lines.

Two main ways of analysing the lunar tides have traditionally been used. The first is by the "fixed-lunar-age" method whereby the data is first grouped according to lunar age for each solar day. The solar variations are obtained by averaging over all lunar ages, and the lunar tide by Fourier analysis of the variations with lunar age. The second method is the "fixed-solar-hour", where the data is grouped according to solar hour and the lunar variations for each solar hour is determined by Fourier analysis with respect to lunar age. Both methods are theoretically equivalent; essentially forming the data into a two-dimensional array arranged by solar hour

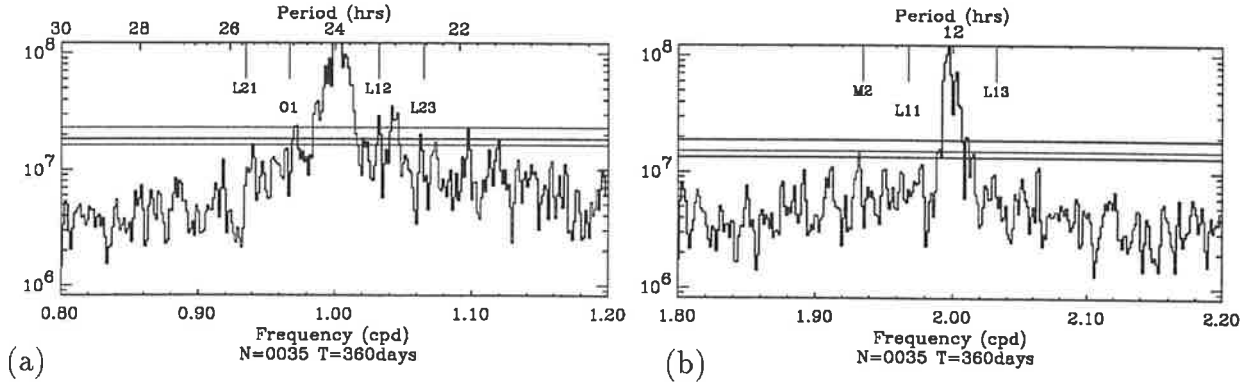

Figure 5.30: Portions of an average power spectrum around where (a) the O1 and (b) the M2 lunar tidal peaks are expected (Power is in units of $m^2s^{-2}Hz^{-1}$). The spectra have been derived from the average of 35 power spectra each from 360 day time series covering the 8 year period described previously. The absolute power has been clipped at $10^8\,m^2s^{-2}Hz^{-1}$ in order to show the lunar lines. The expected positions of the lunar lines and main interaction terms are marked by a vertical line on the top axis. The three horizontal lines denote the 90, 95 and 99% significance levels.

and lunar age. *Schlapp & Harris* [1993] (*c.f.* Appendix J) give a more detailed account of the different analyses and discuss some results from Adelaide using data from the 6 years of 1985–1990. Here only the observations of the spectral region around the lunar tidal lines will be presented using the long data set from Adelaide used throughout this chapter.

Figure 5.30 shows portions of a spectrum, which is the average of 35 high resolution power spectra, around where the O1 and M2 tidal peaks are expected. The three horizontal lines approximately denote the 90, 95 and 99% significance levels[2], derived as outlined in *Scargle* [1982]. That is, the chances that any peaks from a spectrum of white noise could be found above these lines are 10, 5 and 1% respectively. It can be seen that a significant peak (at the 99% level) appears near where the O1 lunar tidal line is expected (0.97 cpd), and is tentatively associated with the O1 line (Figure 5.30a). Also evident are peaks near 0.93 (at 90%), 1.03 (>99%) and 1.06 cpd (at 95%) which may be tentatively associated with the L_{21}^-, L_{12}^- and L_{23}^- lunar-solar lines respectively. The highly significant broad peak near 1.04 cpd presents a puzzle, and its cause has not been identified yet. There are some other "significant" peaks near 1.10 cpd whose cause have also not been identified. Another significant peak (at the 95% level) appears at a frequency near 1.94 cpd (see Figure 5.30b). This peak is tentatively associated with the M2 line. A non-significant peak is observed near 2.03 cpd which is where the L_{13}^- lunar-solar line is expected. Similarly a non-significant peak can be seen near 1.97 cpd, where the L_{11}^+ lunar-solar

[2]The significance levels are only approximate as the individual spectra are not independent. For the average of overlapping spectra the variance for each spectral estimate is actually less than for non-overlapping. A 50% overlap is optimal. Dependent on rejected segments, the current overlaps could range from 0–88%

line is expected. These may be fortuitous as there significance level is poor.

5.6 Conclusion

It has been found that there are many processes on different time scales contributing to the broadening of the solar tidal spectral lines. As the length of a time series increased it captured an increasing set of spectral broadening mechanisms. This necessitates a careful interpretation of the spectral-width information.

A minimal response time, $\tau_{\frac{1}{2}}$, was defined and interpretted as the time after which tidal variations due to transients responses had averaged out, leaving the steady state tidal characteristics. This was then critically compared to tidal response time estimates from the theoretical modelling work of *Bernard* [1981] and *Vial et al.* [1991] (see Tables 5.1 and 5.2 on pages 216 and 5.2 respectively). It was found that some estimates agreed well while other did not. This is not surprising as the model responses were for single tidal modes whereas the current results reflect the combined effects of all tidal modes present within the observed region of the atmosphere. The model results also do not necessarily agree with each other as the most appropriate definition of a tidal response time has not yet been resolved.

Tidal response times were found to increase with altitude in conflict with the predictions of *Vial et al.* [1991]. Again, the combined effects of all the propagating and *in situ* tidal modes may be the cause of this discrepancy.

Analysis of the semi-diurnal tide was hampered by the rapid phase change during the equinoxes, which gave rise to a response time of ~ 40 days once data lengths were greater than 200 days. Otherwise the response times for the diurnal and semi-diurnal tides were found to be very similar at ~ 20 days, and had the same variation with altitude. This requires further investigation.

A close look at Figure 5.13c reveals what appears to be two "skirt" regions, one wide the other narrow. This suggests two dominant spectral broadening processes on different time scales. Such a spectral shape may make the current form of analysis invalid when the data lengths are long enough to resolve it. A dual Gaussian fit may be required.

Using the long data set from Adelaide it was possible to resolve the lunar tidal lines. The strongest lines, the diurnal O1 and semi-diurnal M2 lines, were tentatively observed, along with some of the expected lunar-solar tidal interactions lines. Some peaks at greater significance levels were observed near the diurnal tides but could not be identified with any lunar-solar interactions.

Chapter 6

Summary

This thesis has been concerned with large-scale dynamics of the upper mesosphere and lower thermosphere. Specifically, the dynamics of a large amplitude planetary scale wave known as the 2-day wave, and the variability of the solar tides at mid-latitudes. In the process, a variety of data analysis techniques were introduced and their use and limitations considered.

The effects of different implementations of full correlation analysis were investigated in Chapter 3. It was shown that the individual wind speed estimates from different algorithms could differ by more than 20% on occasion but the mean differences were more of the order of 5%. Individual estimates from full correlation analysis were shown to be sensitive to the precise fitting and interpolating algorithms employed. Mean values (over an hour), on the otherhand, were more robust. The errors or uncertainty in the estimated wind speed, associated with the use of different implementations of FCA, were found to be of the same order as the statistical uncertainty[1], *i.e.* 10–15 ms^{-1} .

The first major research topic involved the investigation of the 2-day wave. This was introduced in Chapter 4.

Using 12 years of data from Adelaide, average properties at mid-latitudes in the southern hemisphere were determined. It was found that the zonal amplitudes of the 2-day wave at Adelaide are less than $20-30\,\mathrm{ms}^{-1}$ for 90 % of the time during summer, and exhibit little variation with altitude or from year to year. The meridional amplitudes were larger than the zonal, maximising between 86 – 90 km with wind speeds greater than $40-50\,\mathrm{ms}^{-1}$ for 10 % of the summer. Strong inter-annual variation was found for the meridional component, with some years having wind speeds less than $20\,\mathrm{ms}^{-1}$ for 90 % of the summer. A phase locking was also found when the wave amplitudes were large. The vector mean phases over all altitudes and

[1] due to the sampling over a small area of a temporally and spatially varying large scale diffraction pattern

the 12 summers from 1980–91 were found to be 13 ± 3 hr and 14.4 ± 0.8 hr LT for the zonal and meridional components respectively. No phase locking was apparent for small wave amplitudes in both components. The mean vector phase over all altitudes for time intervals of large wave amplitude, combining data from the summers of 1961, 1966–75, and 1980–91, was found to be 1340 hr LT, and a most probable error ellipse was found to lie mostly in the afternoon quadrant. The zonal wind component was found to lead the meridional by 0–15 hr. This is from 0–0.3 cycles, so that the 2-day wave components generally varied from being in-phase to in phase-quadrature. The vertical wavelength was determined as > 90 km, being smaller (≈ 40 km) when the maximum wave amplitude is small ($\approx 20\,\mathrm{ms}^{-1}$). The vertical wavelength derived from the 12 year mean phase was > 150 km. The mean period over the 12 summers and all altitudes was found to be 48.0 ± 0.4 hr for the zonal and 48.7 ± 0.5 hr for the meridional component. Altitude variations were of the order of ± 1 hr. Yearly median periods ranged from 46 up to 51 hr but gave a one standard deviation spread of the order of only ± 0.5 hr from their mean.

Differences in the wave properties of the 2-day wave during its period of maximum amplitude in each hemisphere were investigated using observations at the equatorial site of Christmas Island. During February, 1991, when the 2-day wave maximises in the southern-hemisphere, it was found that the period was 48 ± 0.5 hr and the vertical wavelength was 70 km. The zonal and meridional components were in anti-phase. During August, 1991, when the 2-day wave maximises in the northern-hemisphere, it was found that the period was 50 ± 1 hr and the vertical wavelength was also 70 km. The meridional component was found to lead the zonal by 3 – 9 hr, which is between being in-phase and phase-quadrature. The upper decile wave amplitudes for each of these intervals were $\sim 40\,\mathrm{ms}^{-1}$.

A 16-hr wind component, with similar time and height structure as the 2-day wave, was observed at Christmas Island. The upper decile wave amplitudes during February, 1991, were of the order of $25\,\mathrm{ms}^{-1}$, with median values of $12.5\,\mathrm{ms}^{-1}$. The vertical wavelength was found to be >150 km and the period was 16 ± 0.5 hr.

The presence of this wave, the 2^{nd} harmonic of the 2-day wave, suggested some non-linearity in the 2-day wave during times of large wave amplitude. Bispectral analysis suggested that the 16-hr wave was not due to non-linear interactions between the 2-day wave and either of the diurnal or semi-diurnal solar tides. Rather, it arose from the breaking of the 2-day wave due to its large amplitude. Interactions between the 2-day wave and the mean flow, the diurnal tide, and itself were also indicated. A non-linear interaction with the 24-hr wind component is not unexpected as this is the 1^{st} harmonic of the 2-day wave. It is suggested that destructive

interference between this harmonic and the diurnal tide may cause the observed decrease in tidal amplitude around the times of peak 2-day wave activity.

The interaction between the 2-day wave and the zonal mean flow was subsequently investigated. This took the form of a study of the impact of the 2-day wave on the angular momentum budget. It was found that the horizontal flux of horizontal momentum due to the 2-day wave was twice that due to the solar tides during local summer at mid-latitudes. This gave peak accelerations of the zonal mean flow of $\sim -16\,\mathrm{ms}^{-1}\mathrm{d}^{-1}$, which, though not insignificant, is not enough to counter-balance the strong Coriolis contribution at mid-latitudes. The balance is thought to be maintained by the large fluxes due to gravity waves propagating into the mesosphere from lower altitudes. At near Equatorial latitudes the Coriolis contribution is small. Thus the local zonal accelerations associated with the 2-day wave become more significant. Different forms of estimation of the gradient term at 2° N indicated that the zonal flow was accelerated by the action of the 2-day horizontal momentum flux. The total acceleration of the zonal flow was determined as being in the region from $+5.9$–$12.1\,\mathrm{ms}^{-1}\mathrm{d}^{-1}$.

Estimation of the acceleration of the zonal flow were shown to be critically dependent on the latitudinal gradient of the horizontal momentum flux. Due to the lack of suitable observations, this is a poorly determined quantity, and more observations at mid- to low-latitudes need to be encouraged.

The zonal wavenumber of the the 2-day wave was estimated by cross-spectral analysis of wind data from Adelaide (34.5° S, 138.5° E) and Grahamstown (33.3° S, 26.5° E). The results for several years of data and at several altitudes were close to the expected values of 3. The overall average zonal wavenumber was estimated as being 2.80 ± 0.09.

The observations of the 2-day wave at Christmas Island provide impotant new information on both the temporal variability and vertical structure of the wave, while the long-term study at Adelaide quantifies its variability at mid-latitudes (where the amplitude maximises). It is suggested that the 2-day wave is a manifestation of the $(3,0)$, mixed Rossby-gravity wave, atmospheric normal mode (first proposed by *Salby* [1981a]). Further, it is suggested that it may gain significant energy from half-yearly impulsive forcing due to the baroclinic instability of the summer stratospheric westward jet [*Plumb*, 1983; *Pfister*, 1985]. This view is supported by the findings of *Randel* [1993].

The second research topic covered in this thesis involved a preliminary study of the variability of the solar diurnal and semi-diurnal tides. This was introduced in Chapter 5.

A minimal response time, $\tau_{\frac{1}{2}}$, was defined and interpretted as the time after which tidal

variations due to transients responses had averaged out, leaving the steady state tidal characteristics. This was then critically compared to tidal response time estimates from the theoretical modelling work of *Bernard* [1981] and *Vial et al.* [1991]. It was found that some estimates agreed well while other did not. This is not surprising as the model responses were for single tidal modes whereas the current results reflected the combined effects of all tidal modes present within the observed region of the atmosphere. The model results also do not necessarily agree with each other as the most appropriate definition of a tidal response time has not yet been resolved. The results of this thesis contribute to this debate.

Finally, tidal response times were found to increase with altitude in conflict with the predictions of *Vial et al.* [1991]. The combined effects of all the propagating and *in situ* tidal modes present are suggested as the likely cause, showing their important role in the observed variablity of the solar tides.

Appendix A

Actual, Percentage and Vector Differences

In order to compare the different algorithms (and their differing versions) in Chapter 3, a number of decisions had to be made. Firstly, a qualitative comparison can be made using a scatter plot for each of the parameters derived from the FCA. A number of quantitative comparisons were considered. Each had its merit, but was usually best suited for the comparison of one single parameter from the analysis. Therefore a number of quantitative measures have been used. The theory behind each will now be described.

Consider the typical scatter plot in figure 2.15, where a quantity $\mathcal{X}$ is being compared to another quantity $\mathcal{Y}$. Ideally, if $\mathcal{X}$ and $\mathcal{Y}$ are good measures of the same quantity, the points should all lie on the dashed line of unity slope. Therefore it is desirable to measure how different the relationship is from 1:1. If a straight line is fit to the data using a least-squares criterion, the slope would give an indication of the trend of the difference and the intercept an estimate of the bias of one quantity compared to the other. The error in the fit is a measure of the spread of the scatter, which can be interpreted as an estimate of the error in the FCA determination of the quantity. From the discussion in Section 2.10 a total regression is the most appropriate fit to use for most situations considered in these studies.

In order to obtain statistics on the deviations from a 1:1 relationship, the differences, $\mathcal{X}-\mathcal{Y}$, were found and their distribution determined. The mean difference and the standard deviation are a measure of the bias and spread respectively. Alternatively, the distribution of $|\mathcal{X}-\mathcal{Y}|$ can be used to find the 90 percentile difference, which is another measure of the spread.

Taking the differences in this manner ignores any relationship that the differences may have with the actual value — there may be a constant percentage difference for example. The

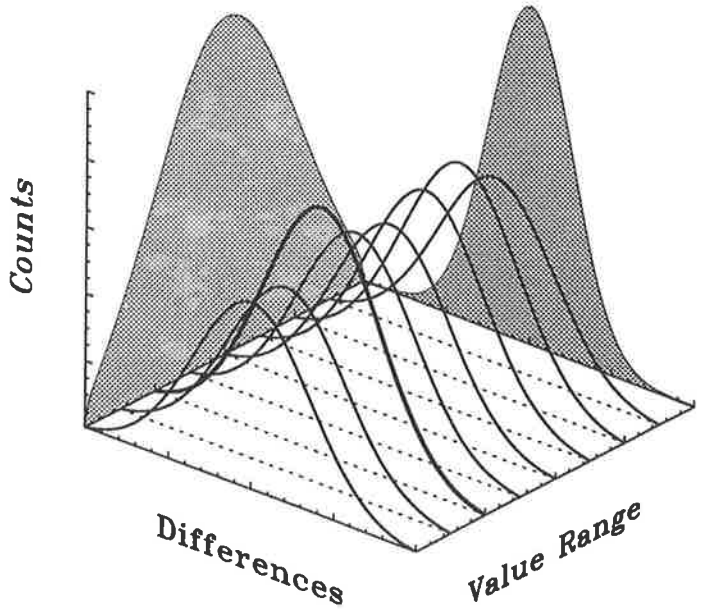

Figure A.1: Relation of value-range, total value-difference and individual difference distributions. Each value range has a distribution of differences (shown as Gaussian lines), but the total number of counts may vary. The value range differences may be totalled to give the full distribution of differences (shaded at the rear on the right-hand side), while the total counts per value range may be put into the value-range distribution (shaded on the left-hand side).

difference, $|\mathcal{X} - \mathcal{Y}|$, can be considered as the deviation from the average value,

$$\frac{\mathcal{X} + \mathcal{Y}}{2} \pm \frac{|\mathcal{X} - \mathcal{Y}|}{2}.$$

Hence a percentage difference can be defined as,

$$\% \text{ difference} = \frac{\mathcal{X} - \mathcal{Y}}{\mathcal{X} + \mathcal{Y}} \times 100\% \tag{A.1}$$

The distribution of the percentage difference can be formed and the bias and measures of spread found as for the actual differences.

If the differences are a non-uniform function of value then a further complication arises. Due to the prevalent wind conditions and the rejection criteria imposed by the FCA, the different values of wind speed, for example, can have a different number of points. A distribution of counts per value range can be formed as shown in figure A.1. The distribution obtained when all the differences are used (regardless of the value-range that they came from) gives greater weighting to those value-ranges with the largest number of observations. This does not present a problem if the actual or percentage difference is near constant, as then each value-range is an independent measure of the same difference. If, on the other hand, the differences are a more complicated function of the value then the full difference distribution must be corrected for the

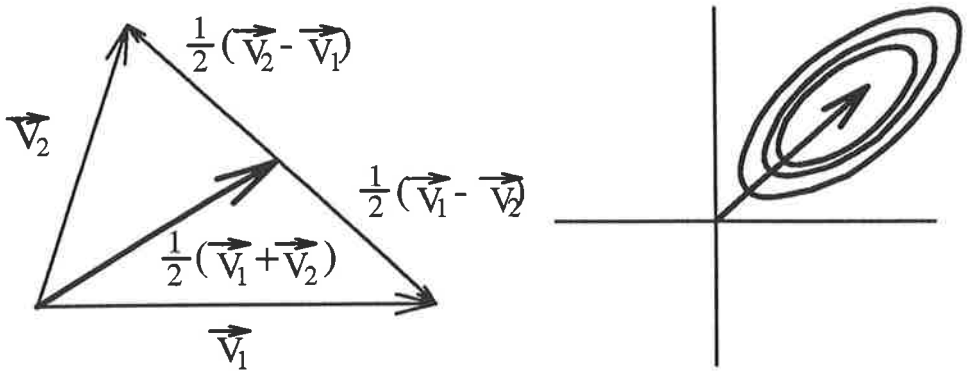

(a) (b)

Figure A.2: Representation of a vector difference

value-range distribution in order to obtain a proper estimate of the mean and spread. This can be accomplished by normalising the difference distributions by the total number of counts for each value range prior to summing, *i.e.* perform a weighted sum.

As some of the quantities derived are vectors (in particular the velocity) should the differences be considered as vectors ? This would seem a reasonable thing to do. If each term in equation A.1 is considered as a vector then a vector representation of the differences can be found as shown in figure A.2a. The error ellipse formed by the differences on the Cartesian plane (figure A.2b) can then be measured. An alternative to determining the parameters of the error ellipse is to measure the magnitude and angular spread caused by the scattered points. It is the latter procedure which has been adopted here. Some form of normalisation is required so that the vector differences can be considered to have been derived from the same population. The magnitude of the difference vectors were normalised by the instantaneous mean vector magnitudes to give percentage differences, while the angular differences were taken as the deviation of the difference vectors from that of the means. The magnitude and angular spread, $\%\Delta|\mathbf{V}|$ and $\Delta\theta$, were therefore found from each vector pair, $\mathbf{V}_1 = (u_1, v_1)$ and $\mathbf{V}_2 = (u_2, v_2)$, by first finding the difference vector,

$$\Delta\mathbf{V} = \frac{1}{2}(\mathbf{V}_2 - \mathbf{V}_1)\,, \tag{A.2}$$

whose direction is denoted by ϑ, and the mean vector,

$$\overline{\mathbf{V}} = \frac{1}{2}(\mathbf{V}_2 + \mathbf{V}_1)\,, \tag{A.3}$$

whose direction is denoted by $\overline{\vartheta}$. The angular deviation of the difference vector from that of the

mean is then given by $\overline{\vartheta} - \vartheta$, and

$$\%\Delta|\mathbf{V}| = \frac{|\Delta\mathbf{V}|\cos(\overline{\vartheta} - \vartheta)}{|\overline{\mathbf{V}}|} \times 100\%\,, \tag{A.4}$$

$$\Delta\theta \approx \tan^{-1}\left(\frac{|\Delta\mathbf{V}|\sin(\overline{\vartheta} - \vartheta)}{|\overline{\mathbf{V}}|}\right). \tag{A.5}$$

Vector differencing allows for the interdependence of the magnitude and the direction of the wind estimates.

The preceding discussion leads to 13 different (but related) ways of considering the differences in the FCA parameter estimates —

1. Scatter plots of the quantity, with least-squares regression fits, giving estimates of the trend and bias between the two algorithms, and an estimate of the error that could be expected in the determination of the quantity.

2. The distribution of *actual differences* in the quantities (assumed Gaussian), giving a weighted sample mean and standard deviation.

3. The distribution of the *absolute values of the actual differences* in the quantities. This is used to give weighted sample deciles.

4. The distribution of *percentage differences* in the quantities (assumed Gaussian) giving a weighted sample mean and standard deviation.

5. The distribution of the *absolute values of the percentage differences* in the quantities. Again, giving weighted sample deciles.

6. The distribution of *value-range normalised actual differences* in the quantities (assumed Gaussian). This is used to give a normalised sample mean and standard deviation.

7. The distribution of the *absolute values of the value-range normalised actual differences* in the quantities giving normalised sample deciles.

8. The distribution of *value-range normalised percentage differences* in the quantities (assumed Gaussian). This is used to give a normalised sample mean and standard deviation.

9. The distribution of the *absolute values of the value-range normalised percentage differences* in the quantities. Used to give normalised sample deciles.

10. The variation of the *actual difference* with the value of the quantity. This can be used to decide whether a constant actual difference is a realistic interpretation for the quantity.

11. The variation of the *percentage difference* with the value of the quantity. Likewise, this can be used to decide whether a constant percentage difference is a realistic interpretation for the quantity.

12. The value-range histogram, indicating the weighting of the samples due to the analysis rejection criteria and the data quality. This gives an idea of how important the normalised sample estimates are.

13. The vector differences can also be found for those quantity pairs which are more naturally represented as vectors. This gives an estimate of the spread in magnitude and direction of the quantity.

All these forms were considered and used to some extent in Chapter 3.

Appendix B

FCA Comparison Scatter and Distribution Plots

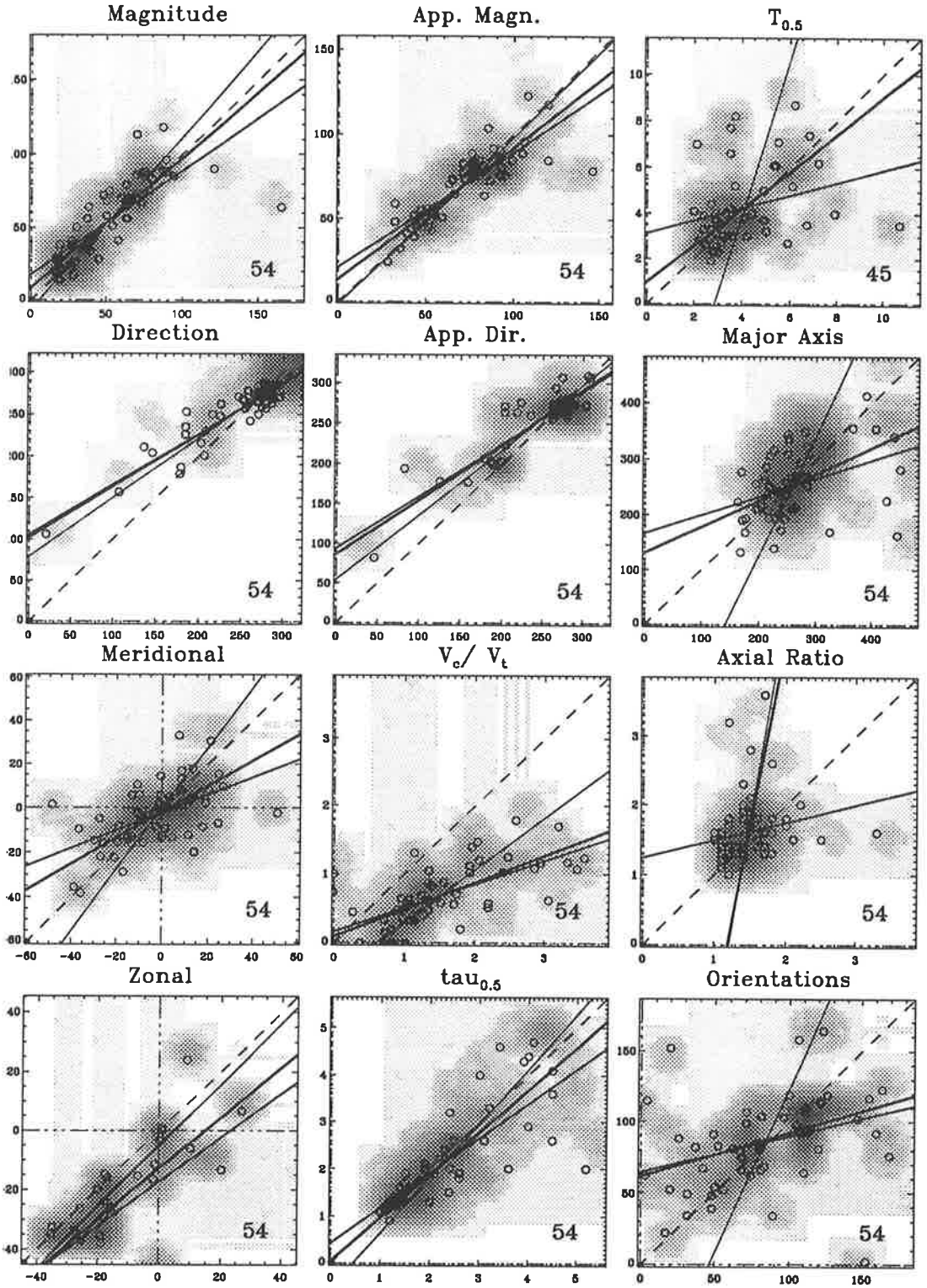

Figure B.1: Scatter plots of some of the FCA parameters for FCA3 trials t16 against t44. The dashed line shows the expected 1:1 relationship. The solid lines are a linear least-squares regression for y on x (medium) and x on y (thin). The thick solid line is a total-least-squares regression. The shading indicates the density of the distribution of scattered points (overlayed as small symbols), with the number of points used shown in the bottom right-hand corner

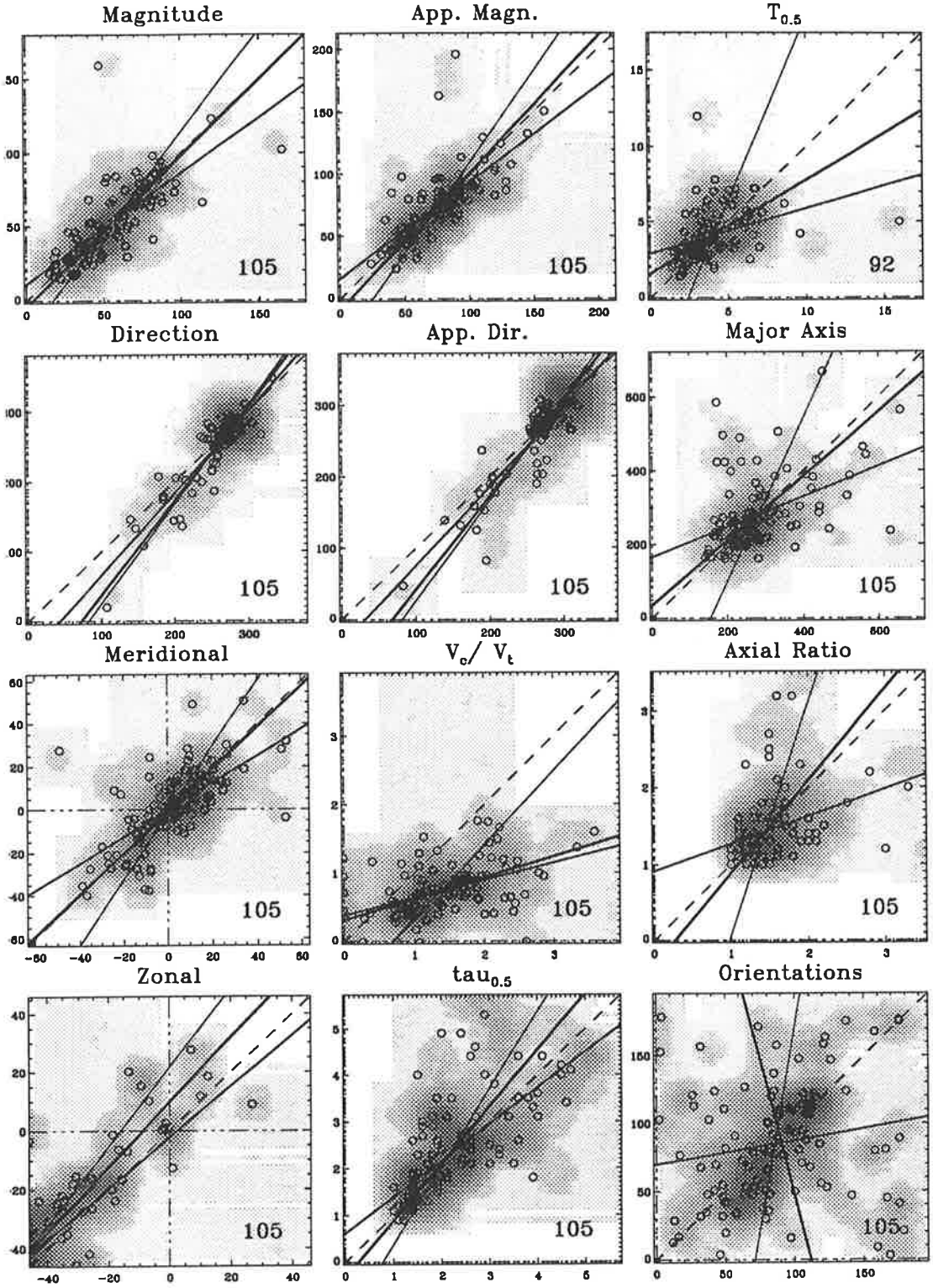

Figure B.2: Scatter plots of some of the FCA parameters for FCA3 trials t22 against t44, otherwise as for Figure B.1

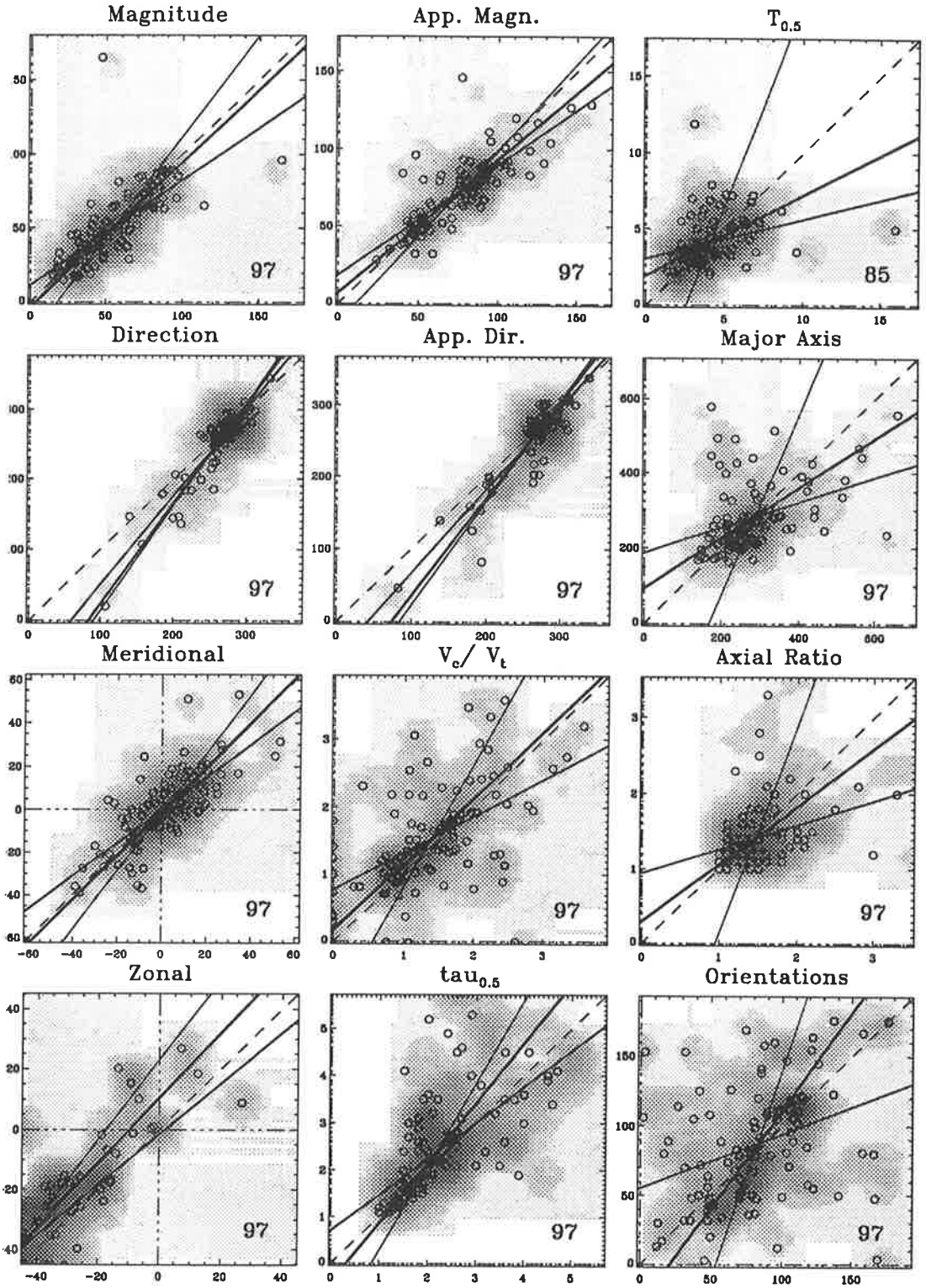

Figure B.3: Scatter plots of some of the FCA parameters for FCA3 trials t42 against t44, otherwise as for Figure B.1

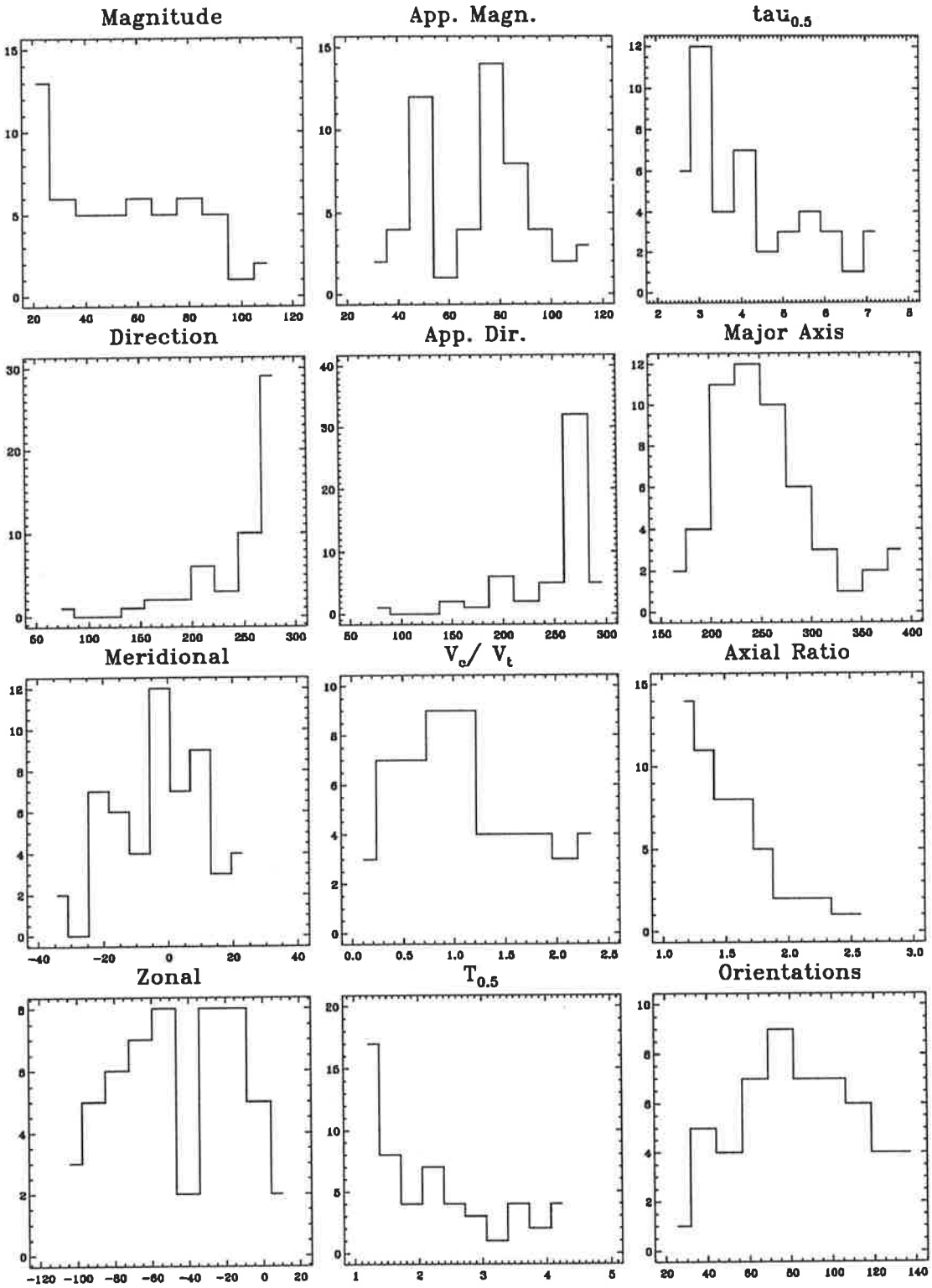

Figure B.4: Value-range histograms for test FCA3 16 vs 44

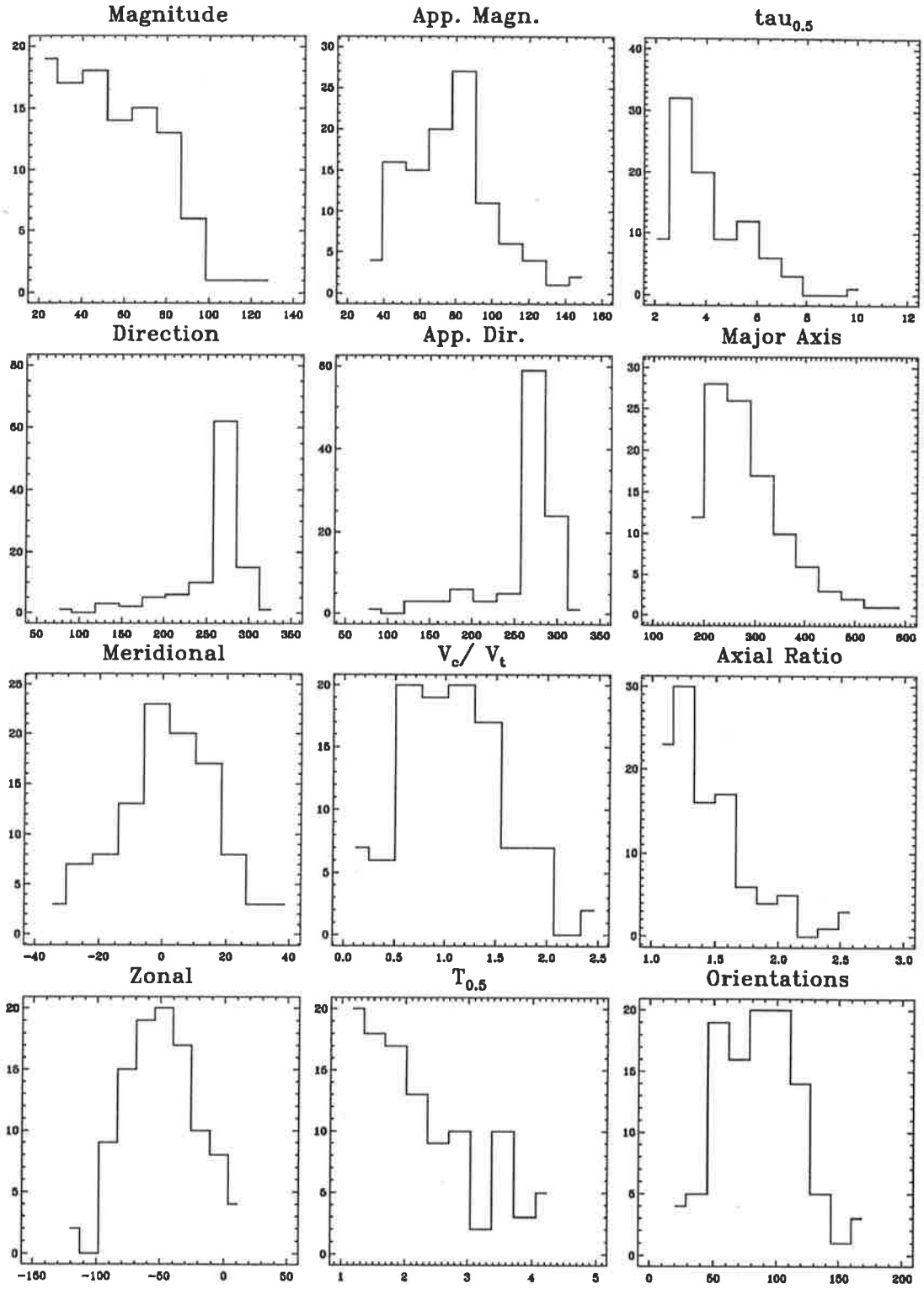

Figure B.5: Value-range histograms for FCA3 test 22 vs 44

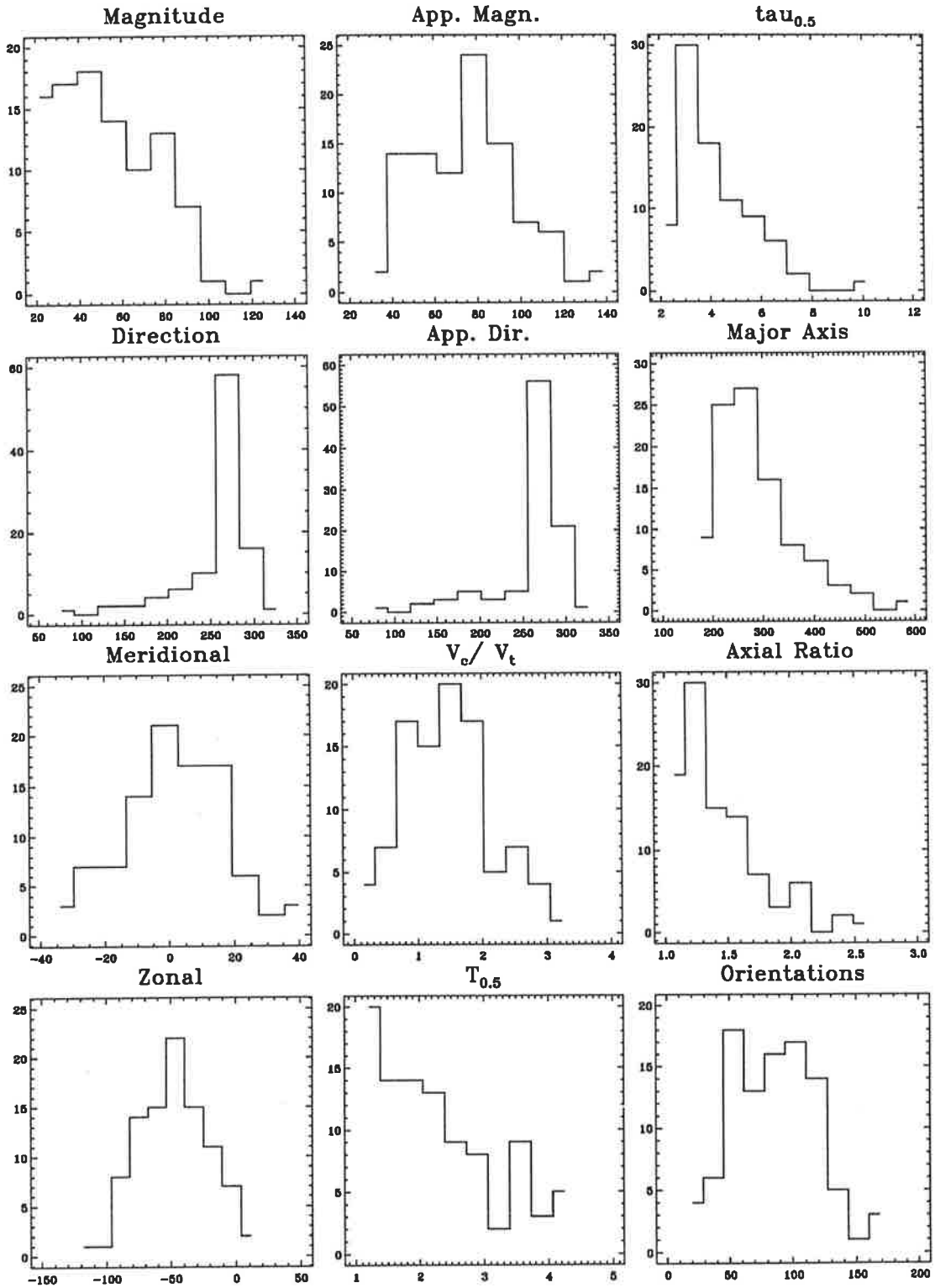

Figure B.6: Value-range histograms for FCA3 test 42 vs 44

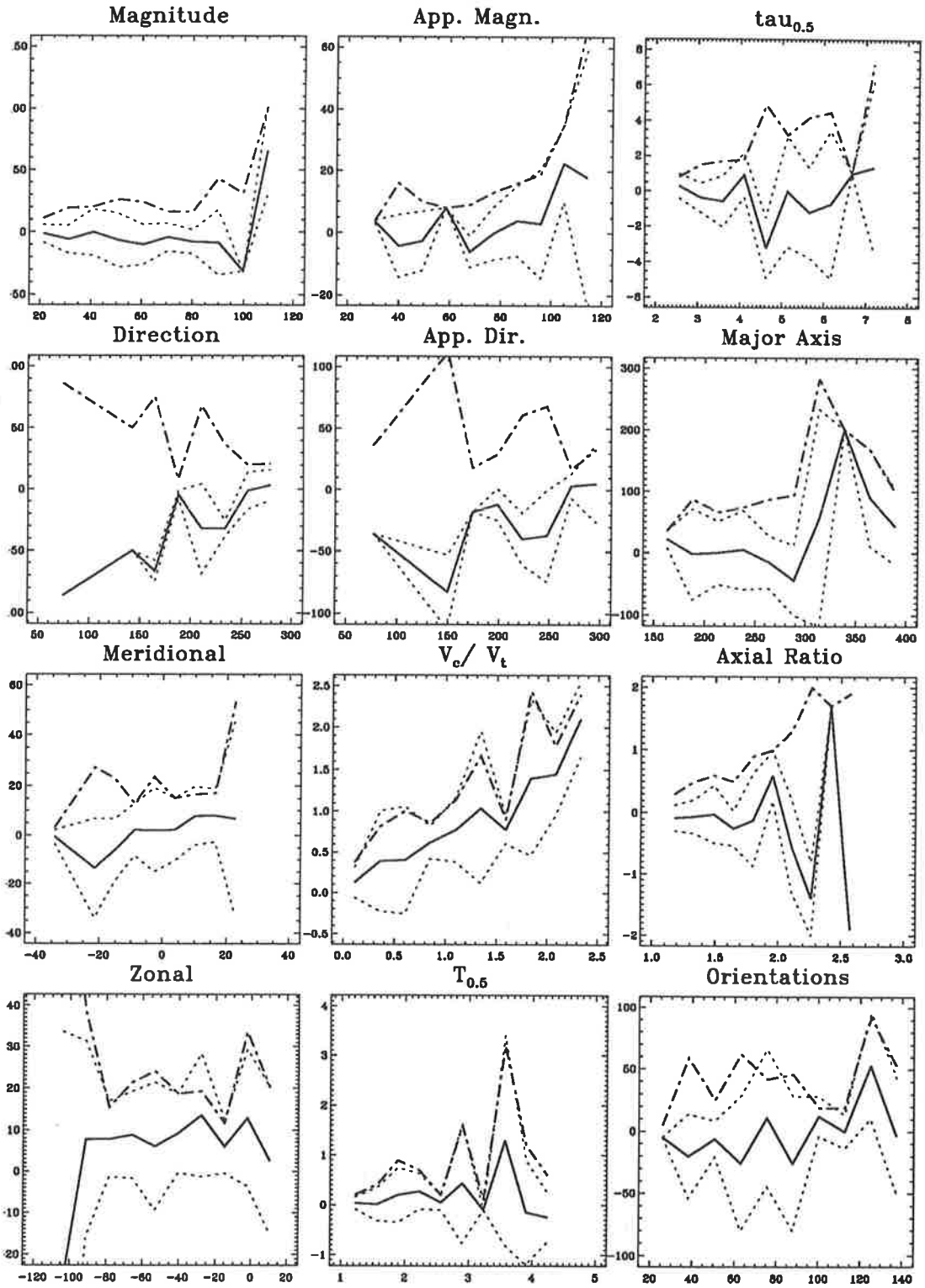

Figure B.7: Statistics of the value differences for FCA3 test 16 vs 44. The mean difference is shown as a solid line, with the standard deviations as dotted lines. The 90 percentile difference level is shown as a dot-dashed line.

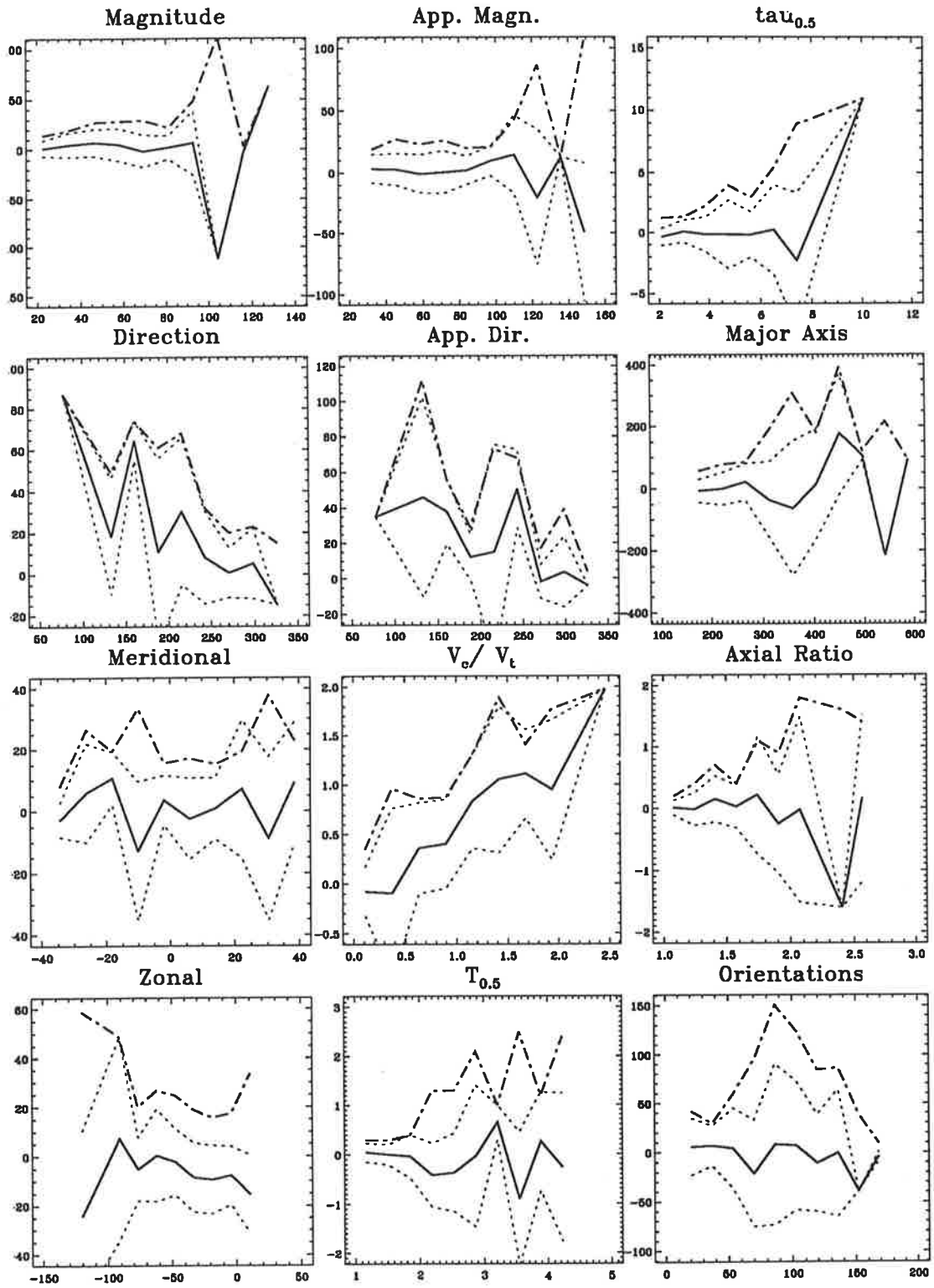

Figure B.8: Statistics of the value differences for FCA3 test 22 vs 44.

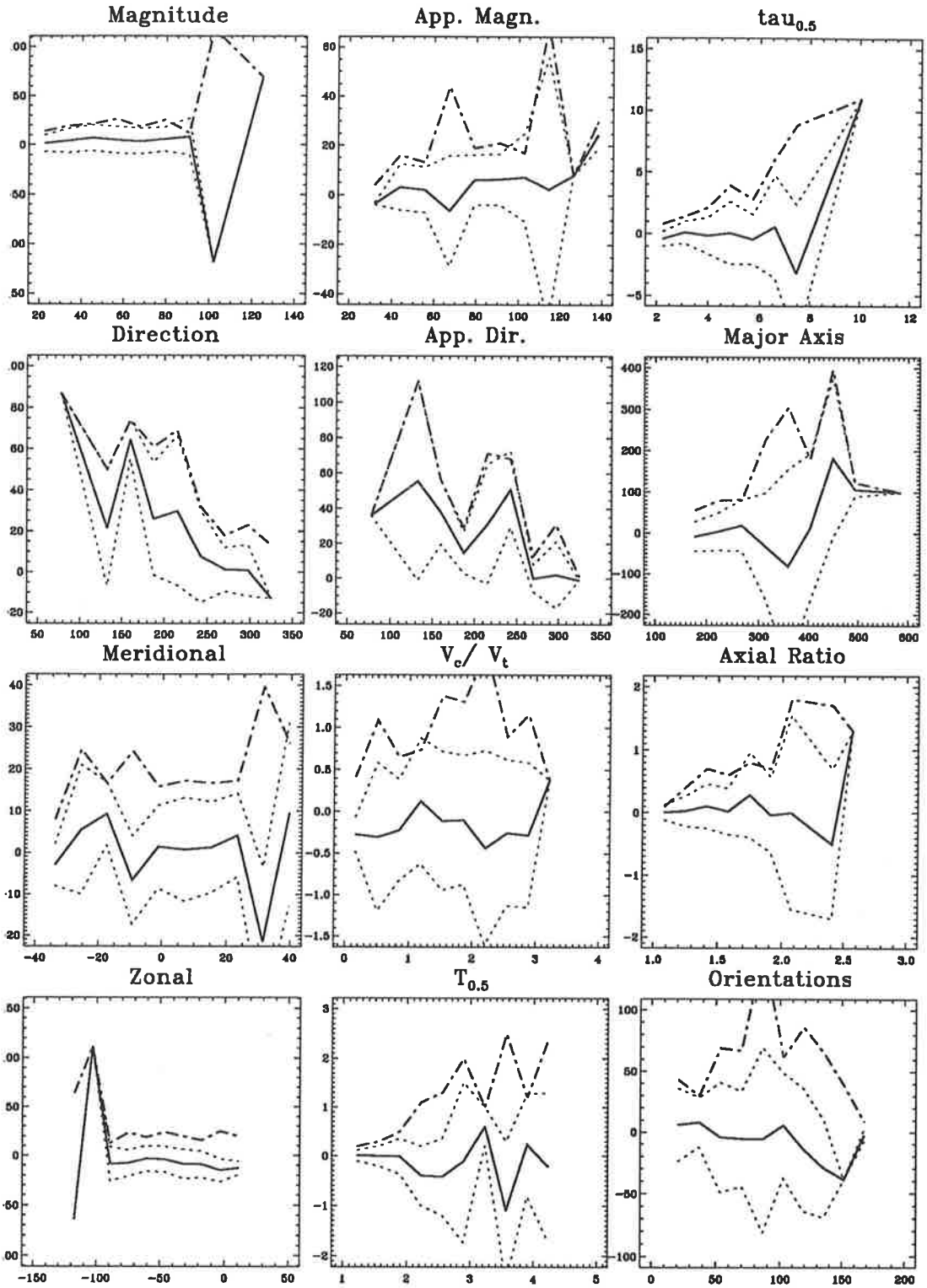

Figure B.9: Statistics of the value differences for FCA3 test 42 vs 44.

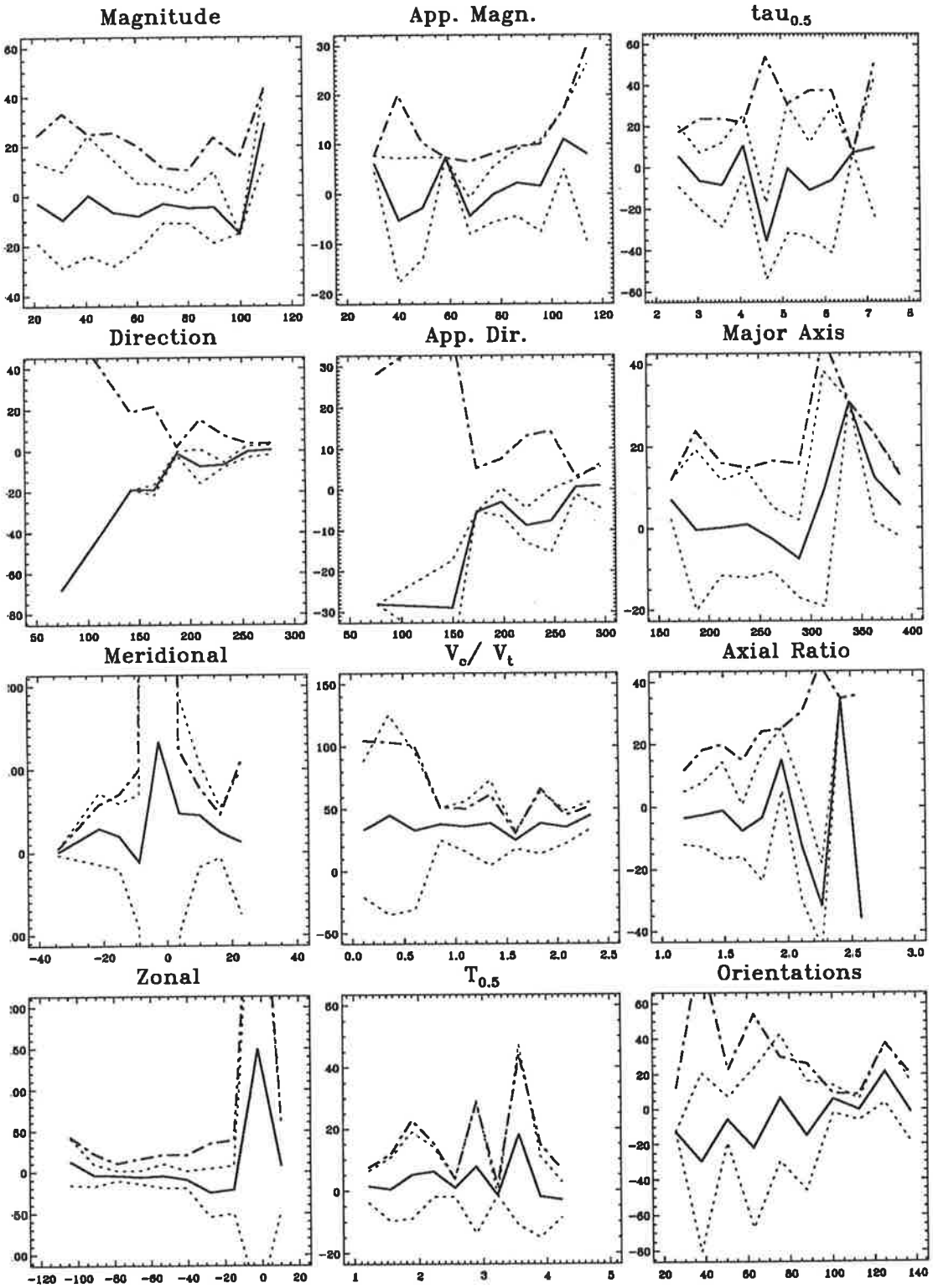

Figure B.10: Statistics of the percentage value differences for FCA3 test 16 vs 44. The mean difference is shown as a solid line, with the standard deviations as dotted lines. The 90 percentile difference level is shown as a dot-dashed line.

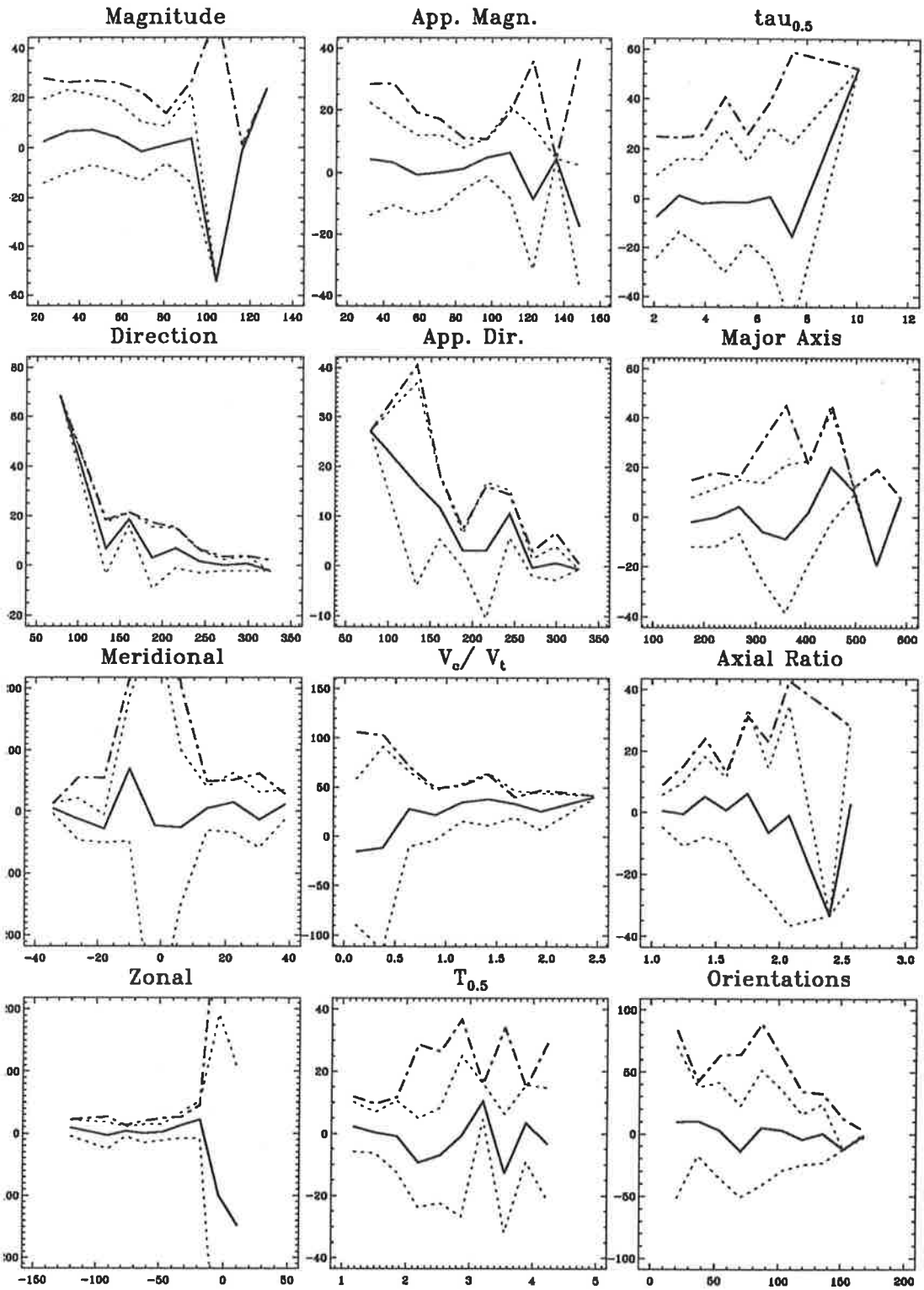

Figure B.11: Statistics of the percentage value differences for FCA3 test 22 vs 44.

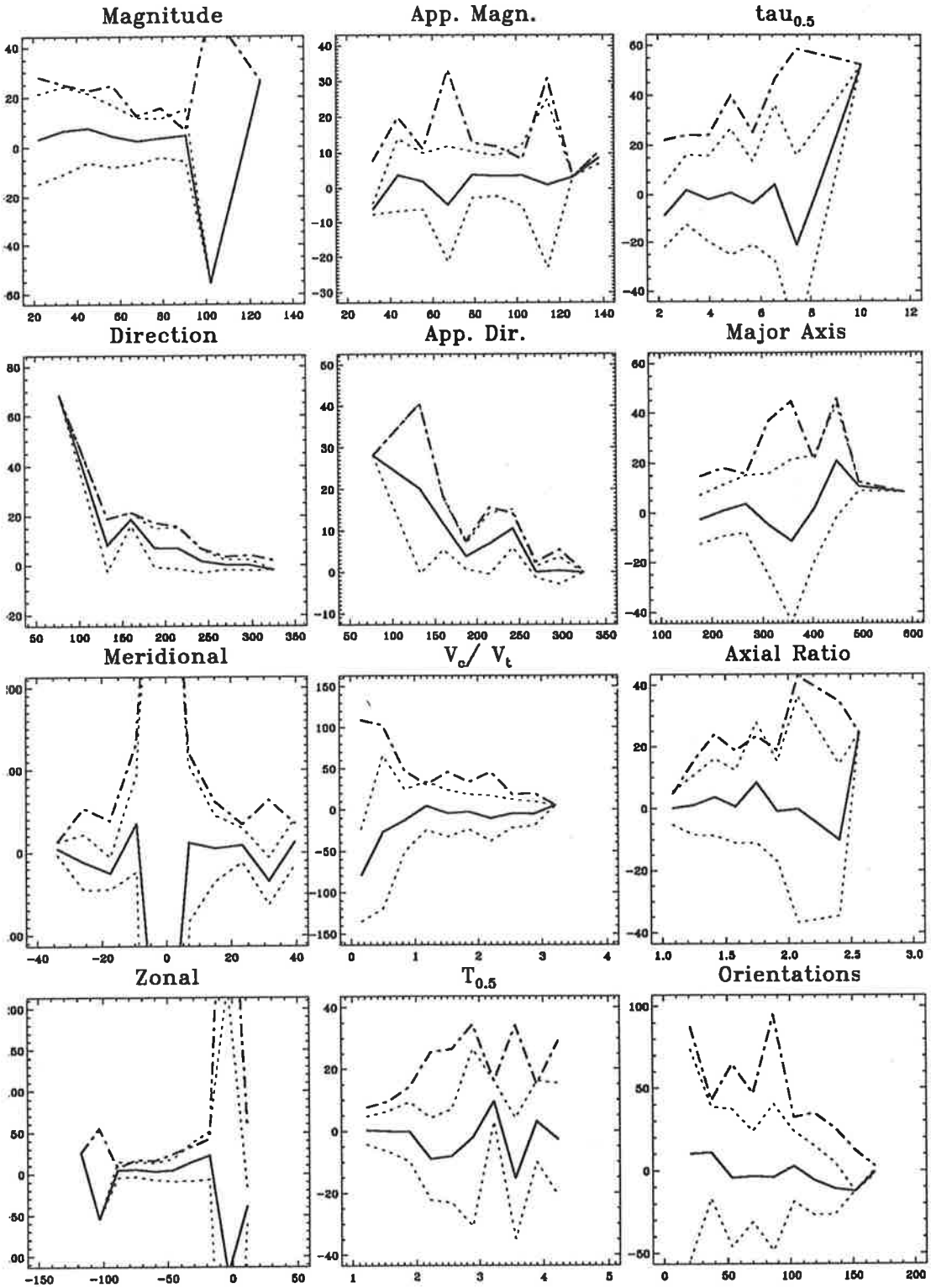

Figure B.12: Statistics of the percentage value differences for FCA3 test 42 vs 44.

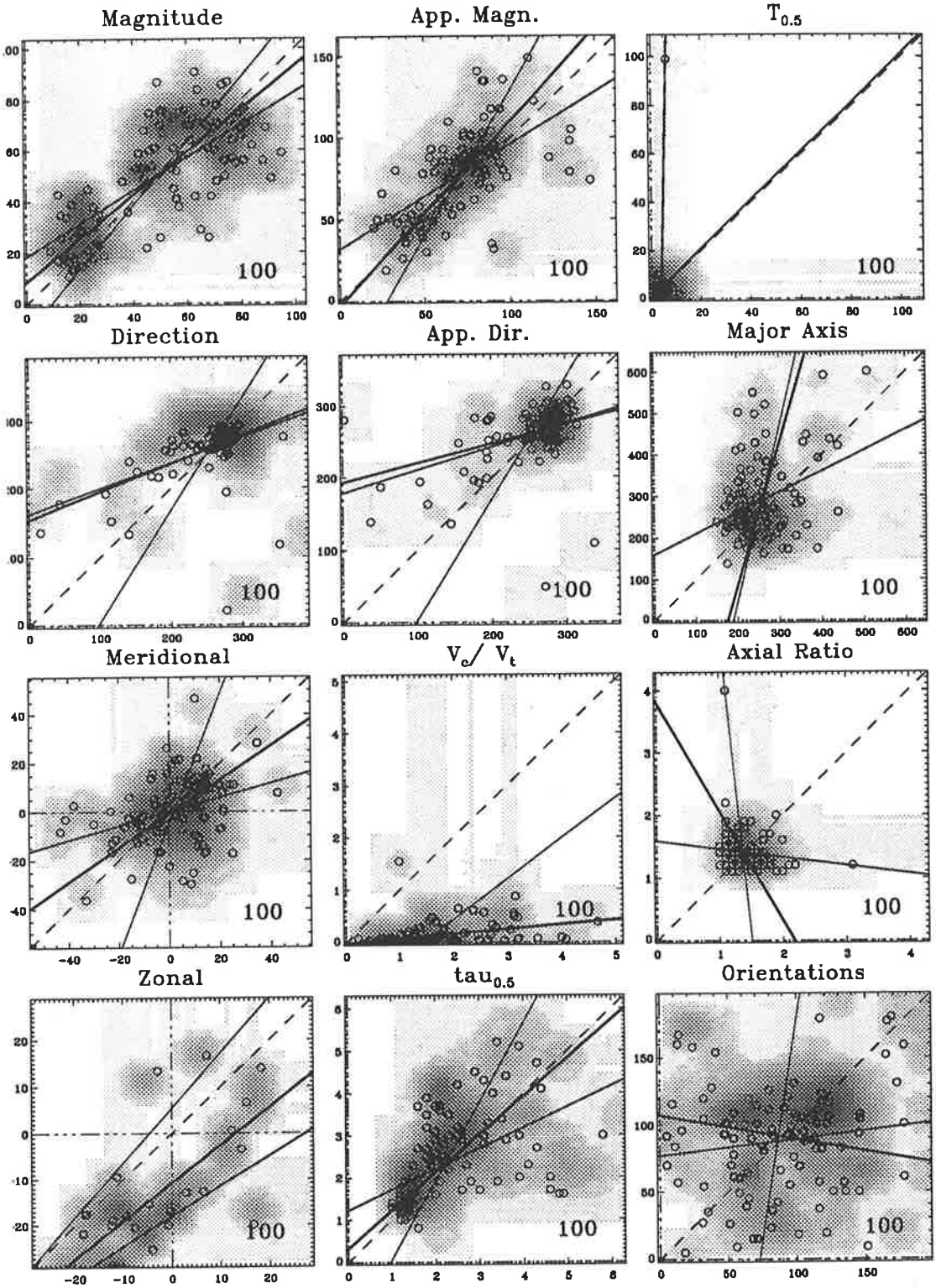

Figure B.14: Scatter plots of some of the FCA parameters for FCA2 trials r2 against r9. Otherwise as for Figure B.1

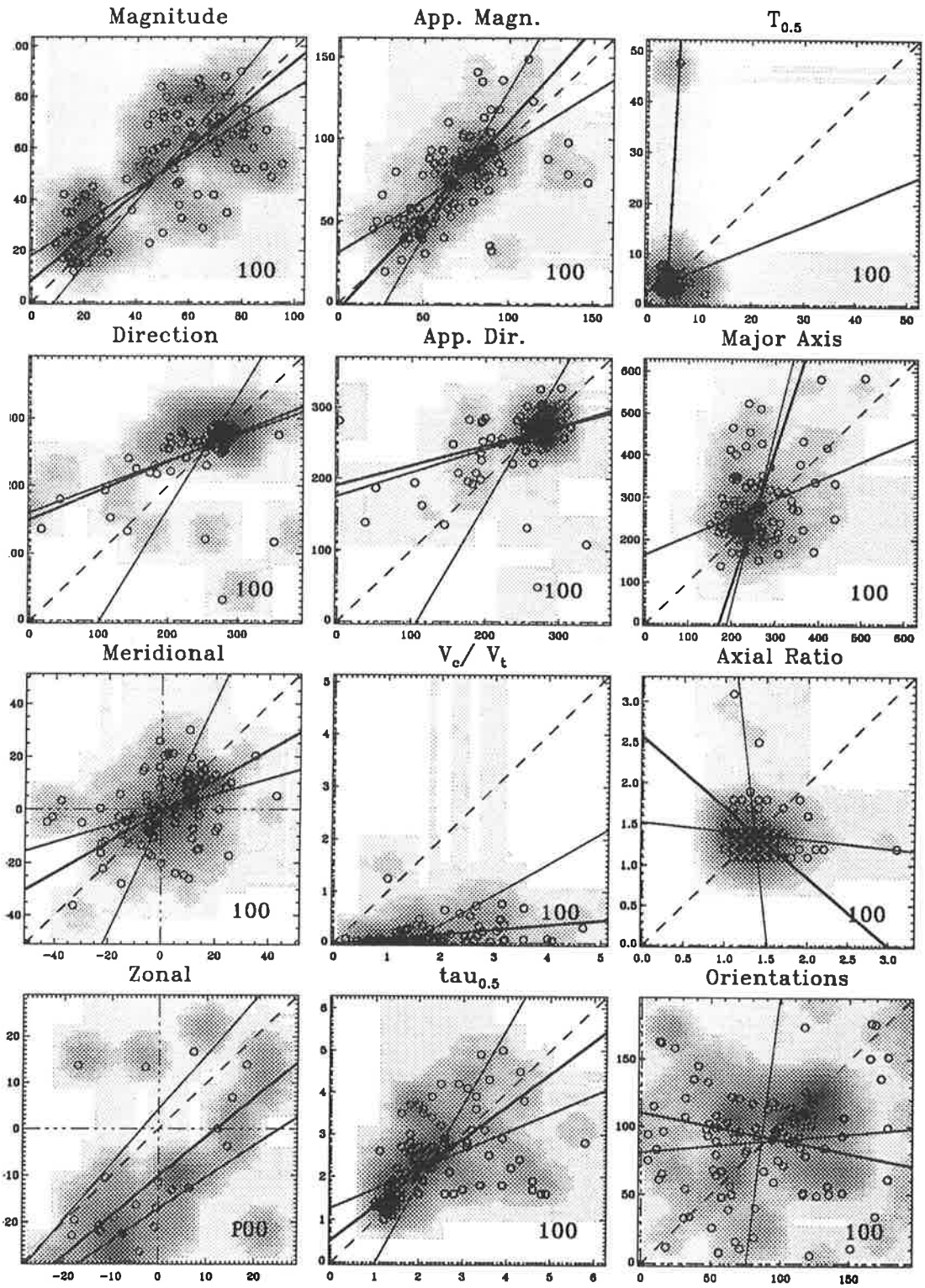

Figure B.15: Scatter plots of some of the FCA parameters for FCA2 trials r5 against r9. Otherwise as for Figure B.1

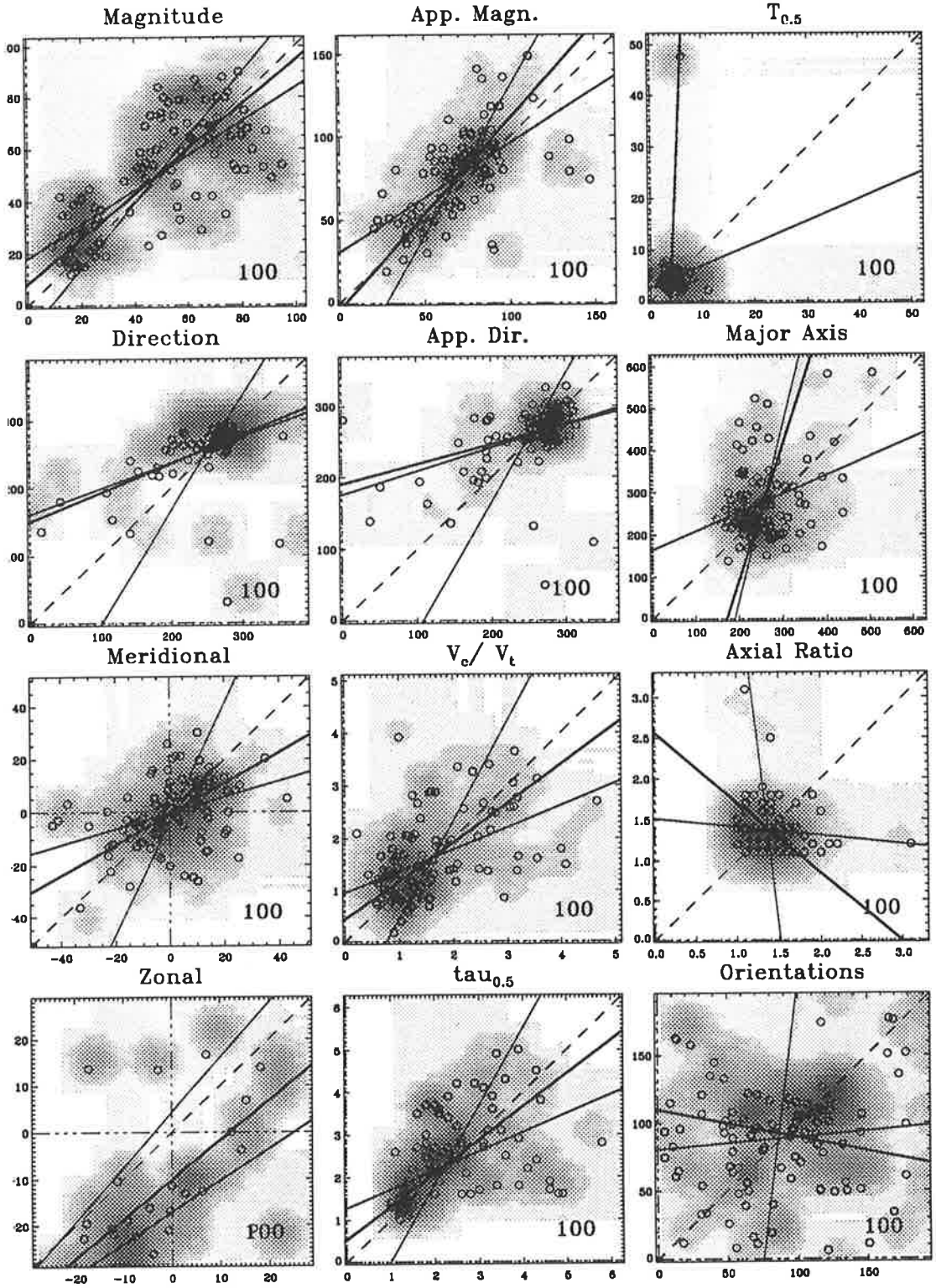

Figure B.16: Scatter plots of some of the FCA parameters for FCA2 trials r6 against r9. Otherwise as for Figure B.1

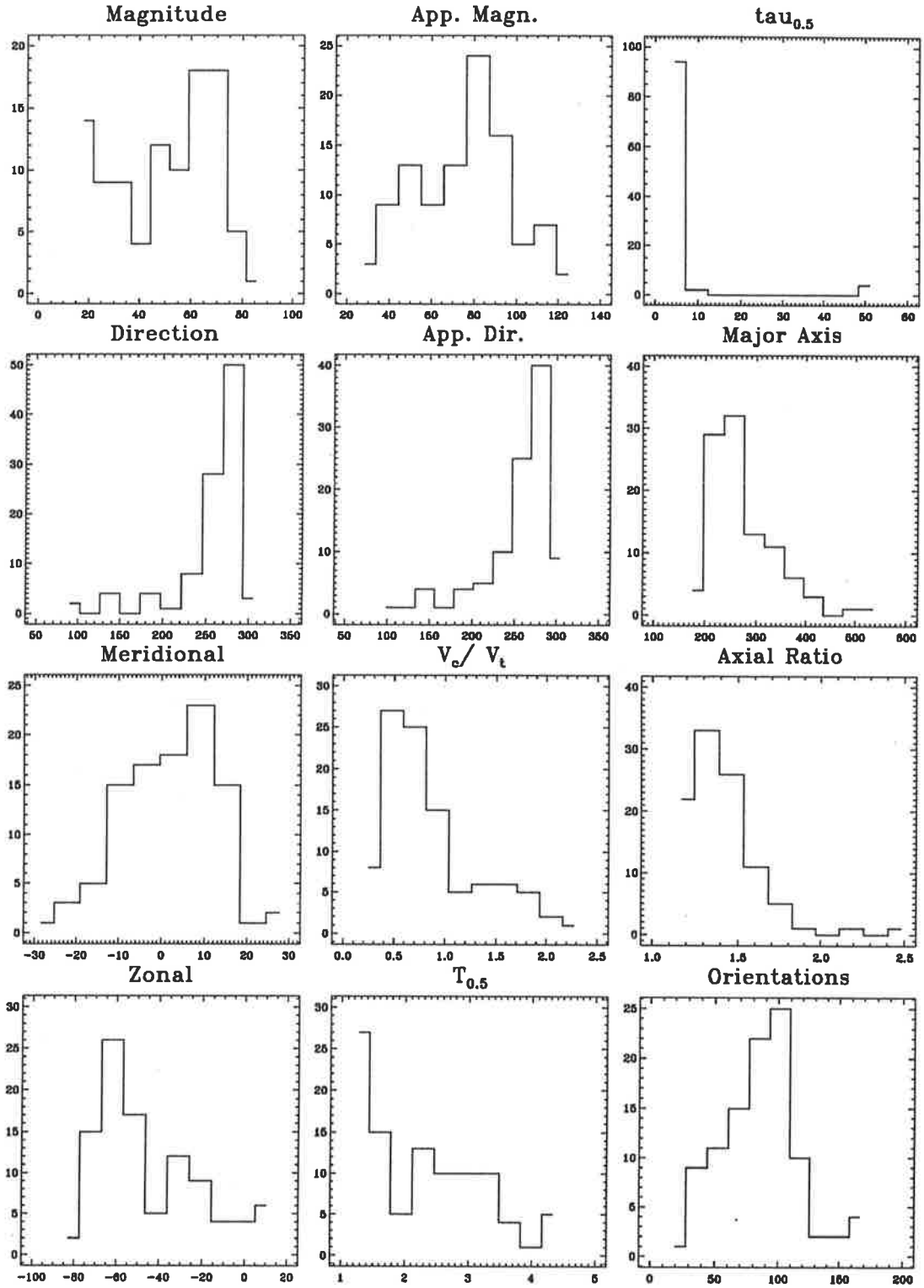

Figure B.17: Value-range histograms for test FCA2 1 vs 9

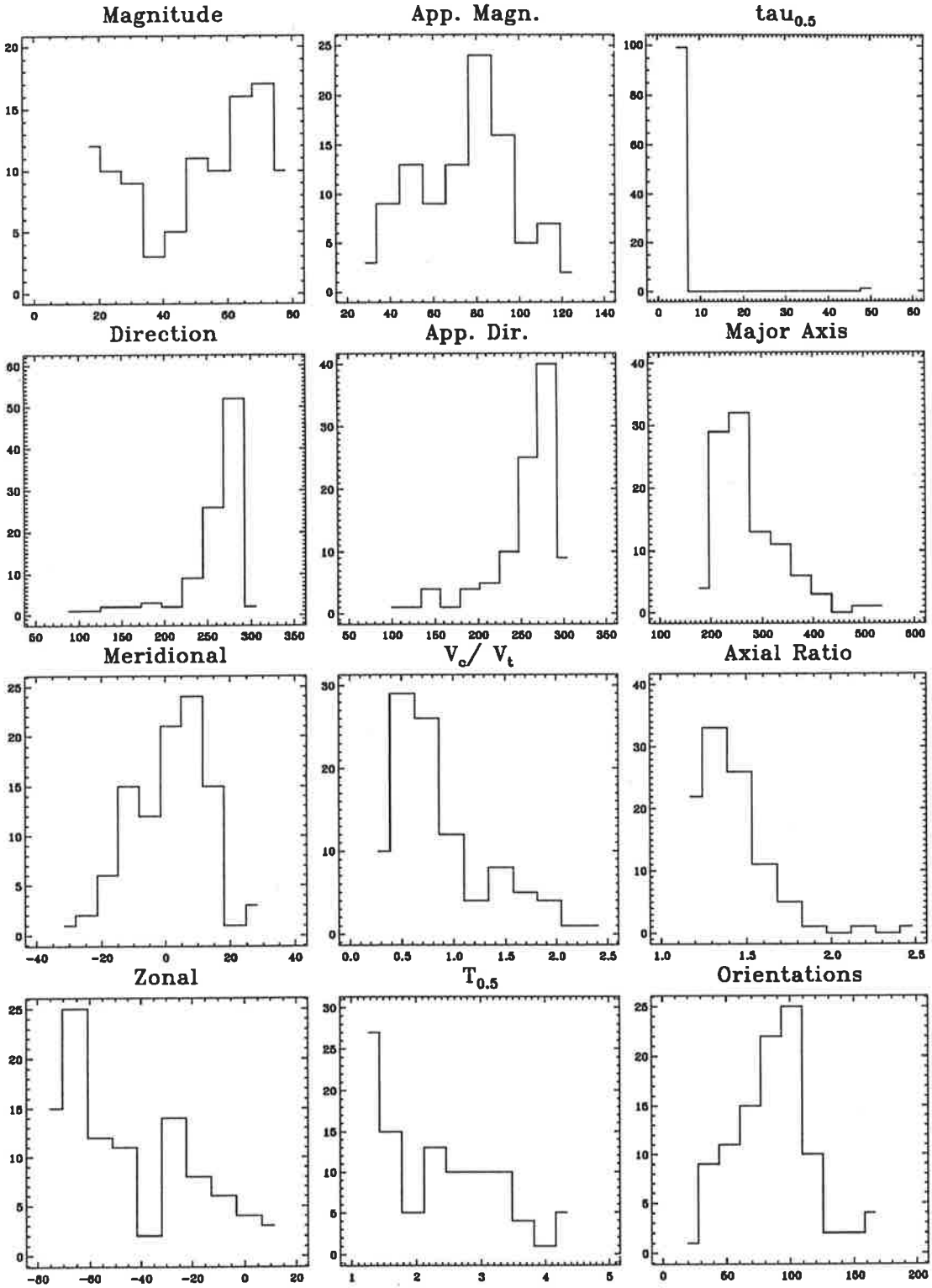

Figure B.18: Value-range histograms for test FCA2 2 vs 9

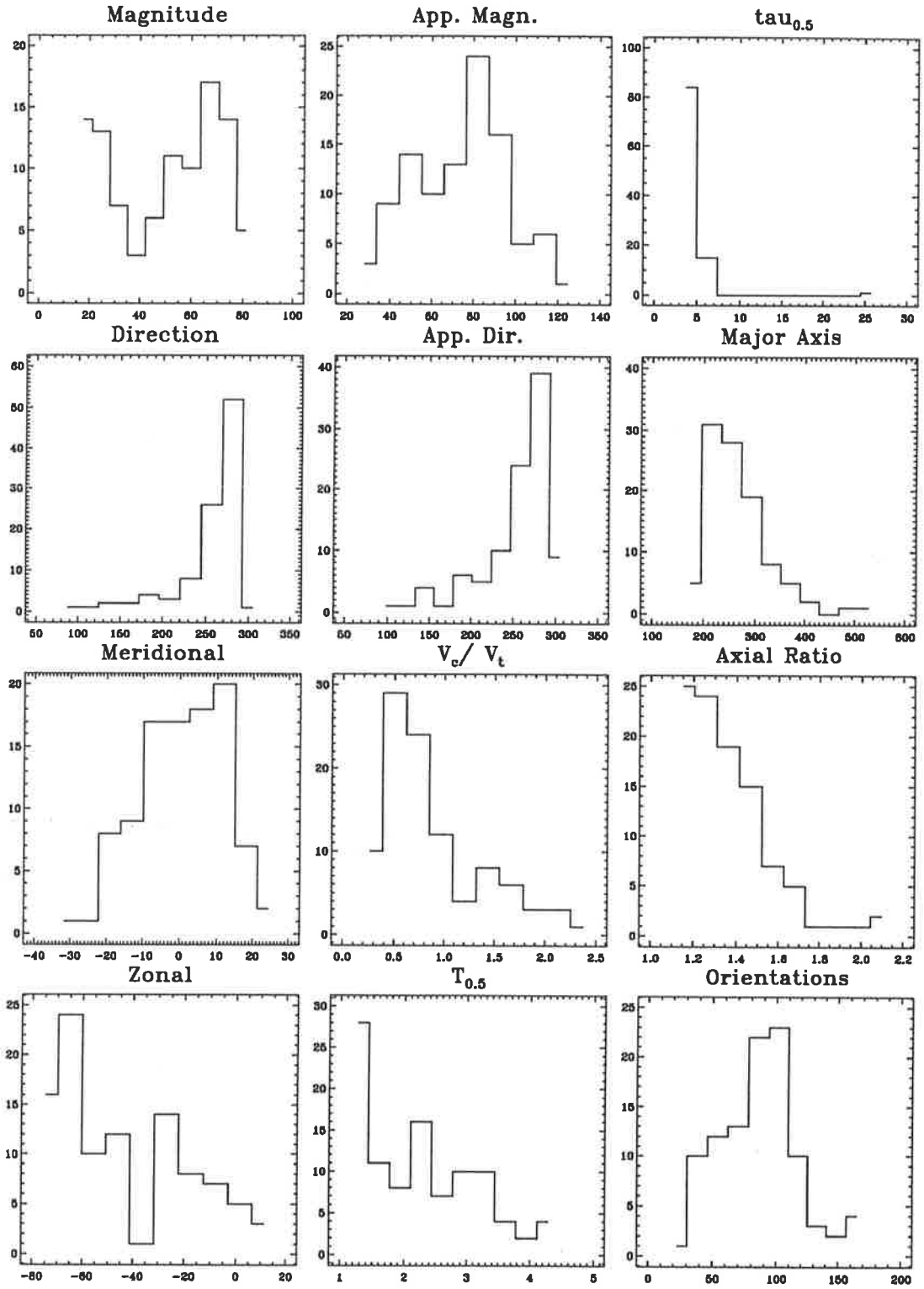

Figure B.19: Value-range histograms for test FCA2 5 vs 9

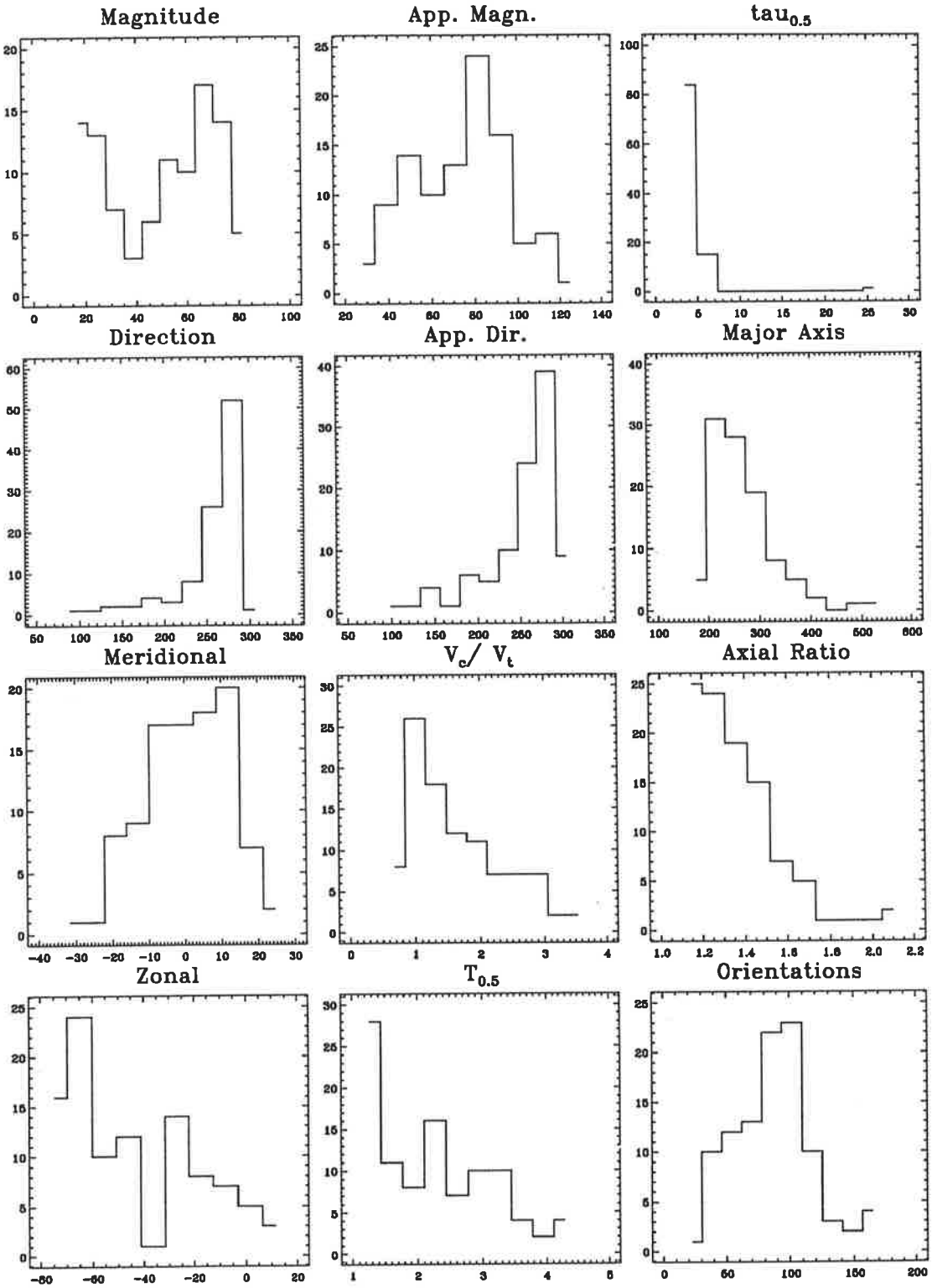

Figure B.20: Value-range histograms for test FCA2 6 vs 9

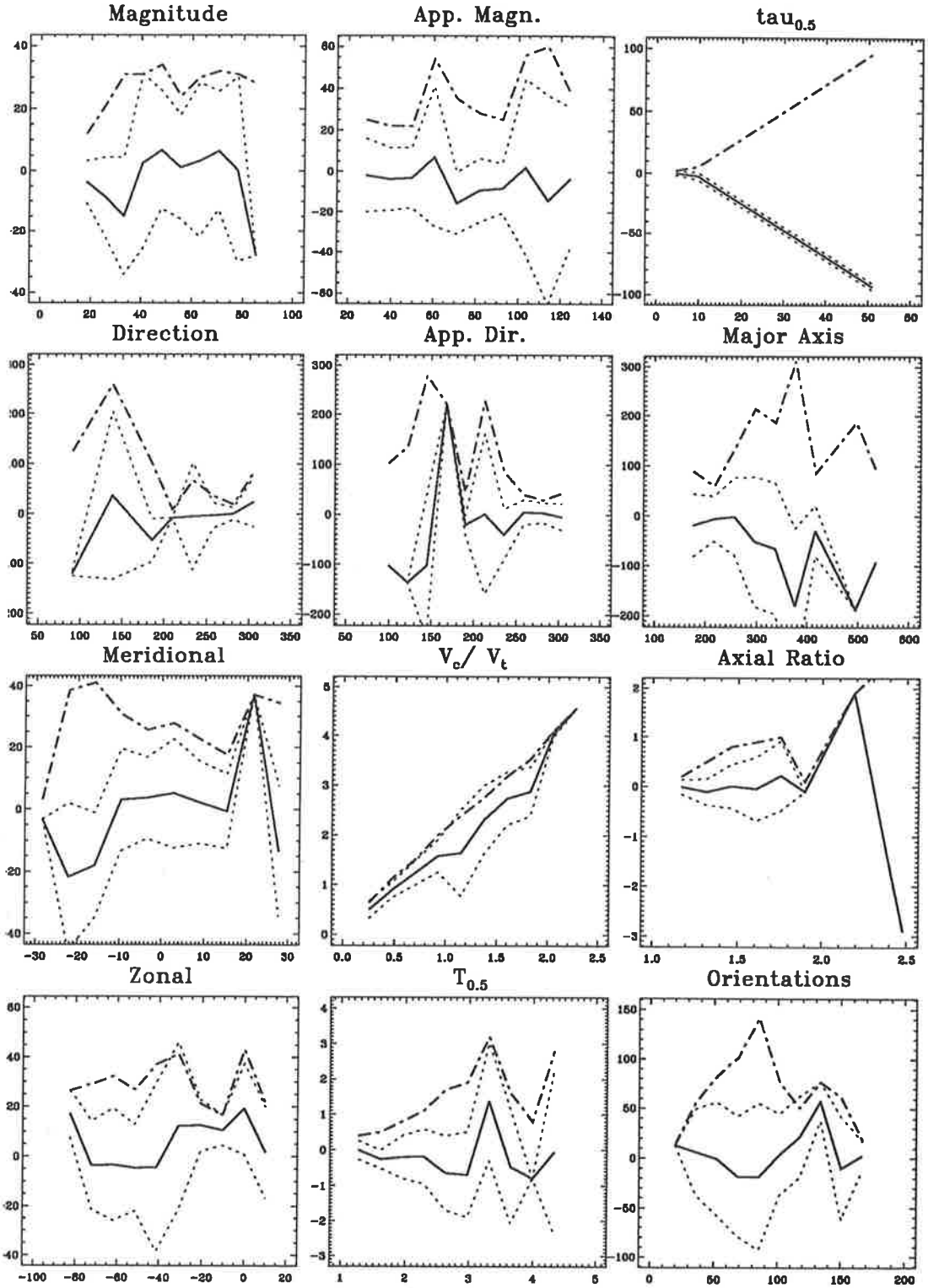

Figure B.21: Statistics of the value differences for FCA2 test 1 vs 9.

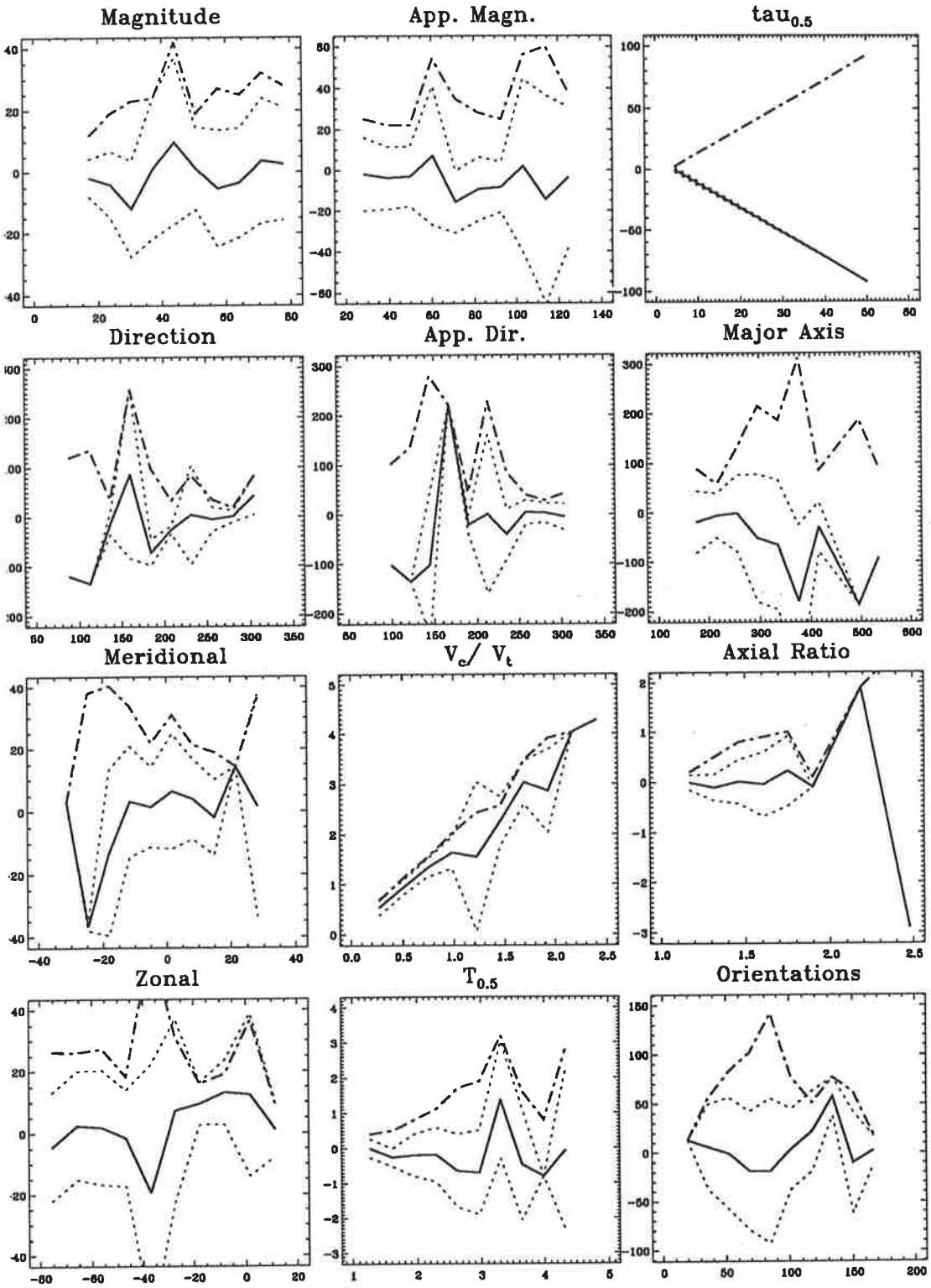

Figure B.22: Statistics of the value differences for FCA2 test 1 vs 9.

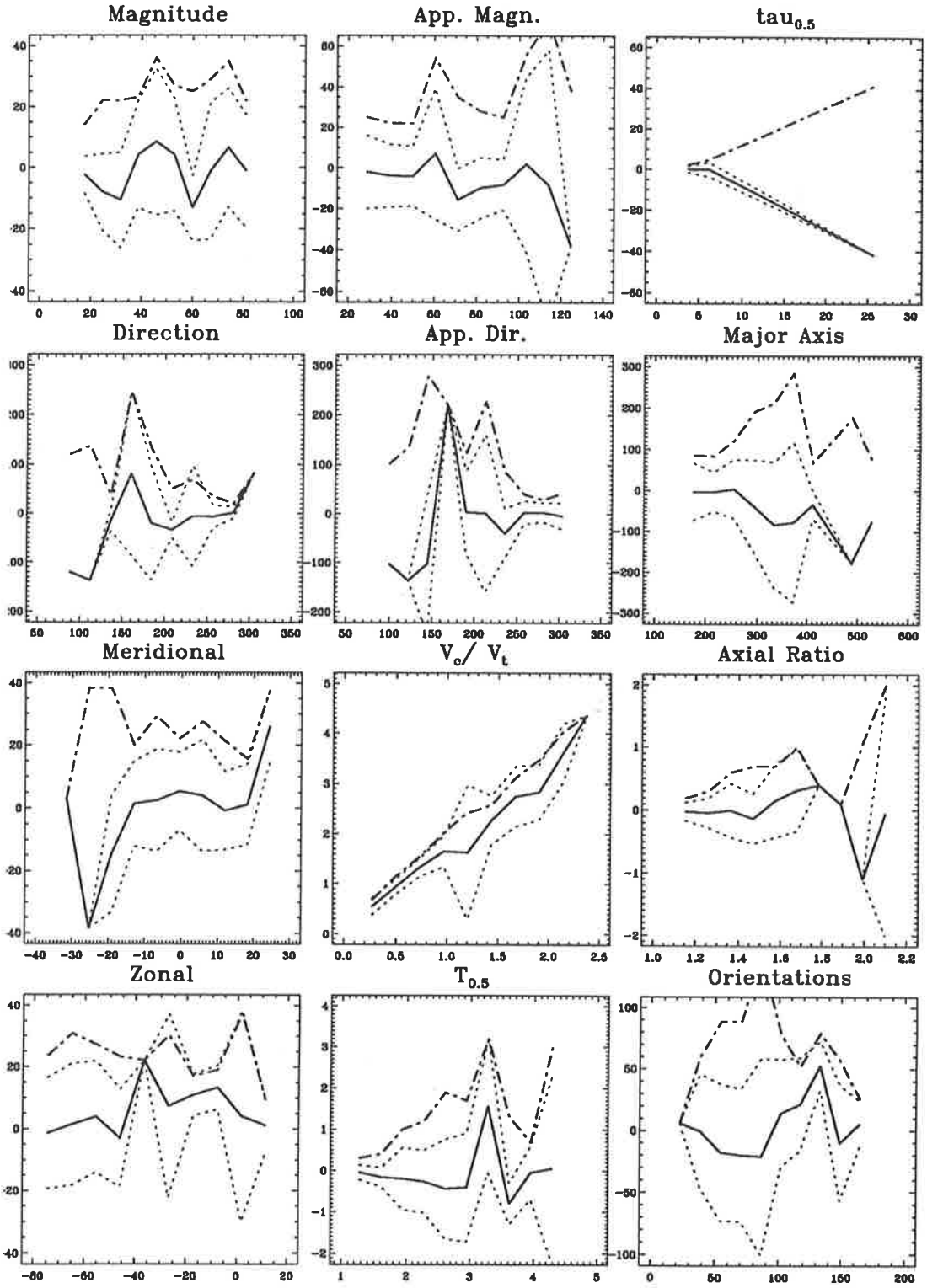

Figure B.23: Statistics of the value differences for FCA2 test 5 vs 9.

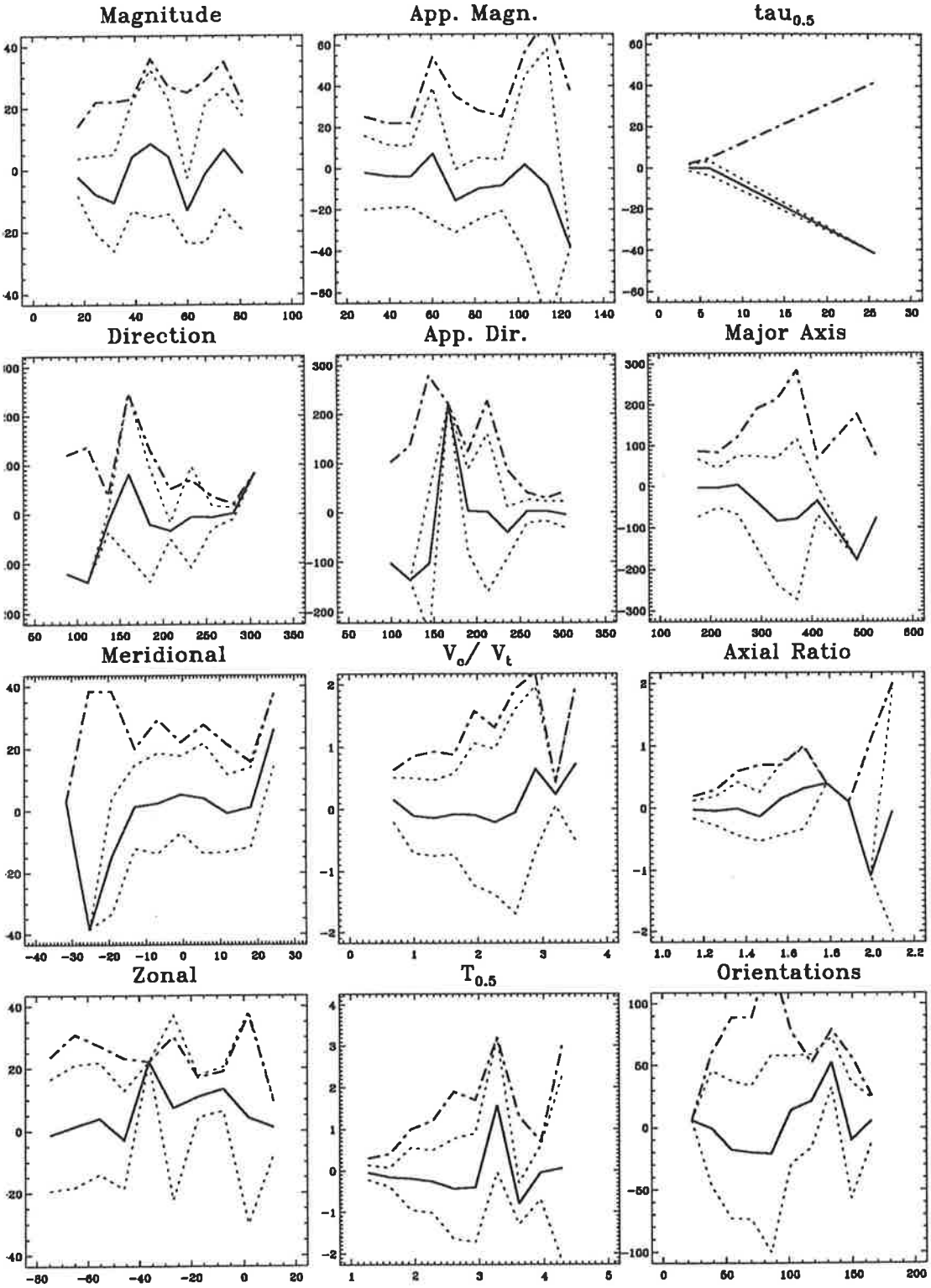

Figure B.24: Statistics of the value differences for FCA2 test 6 vs 9.

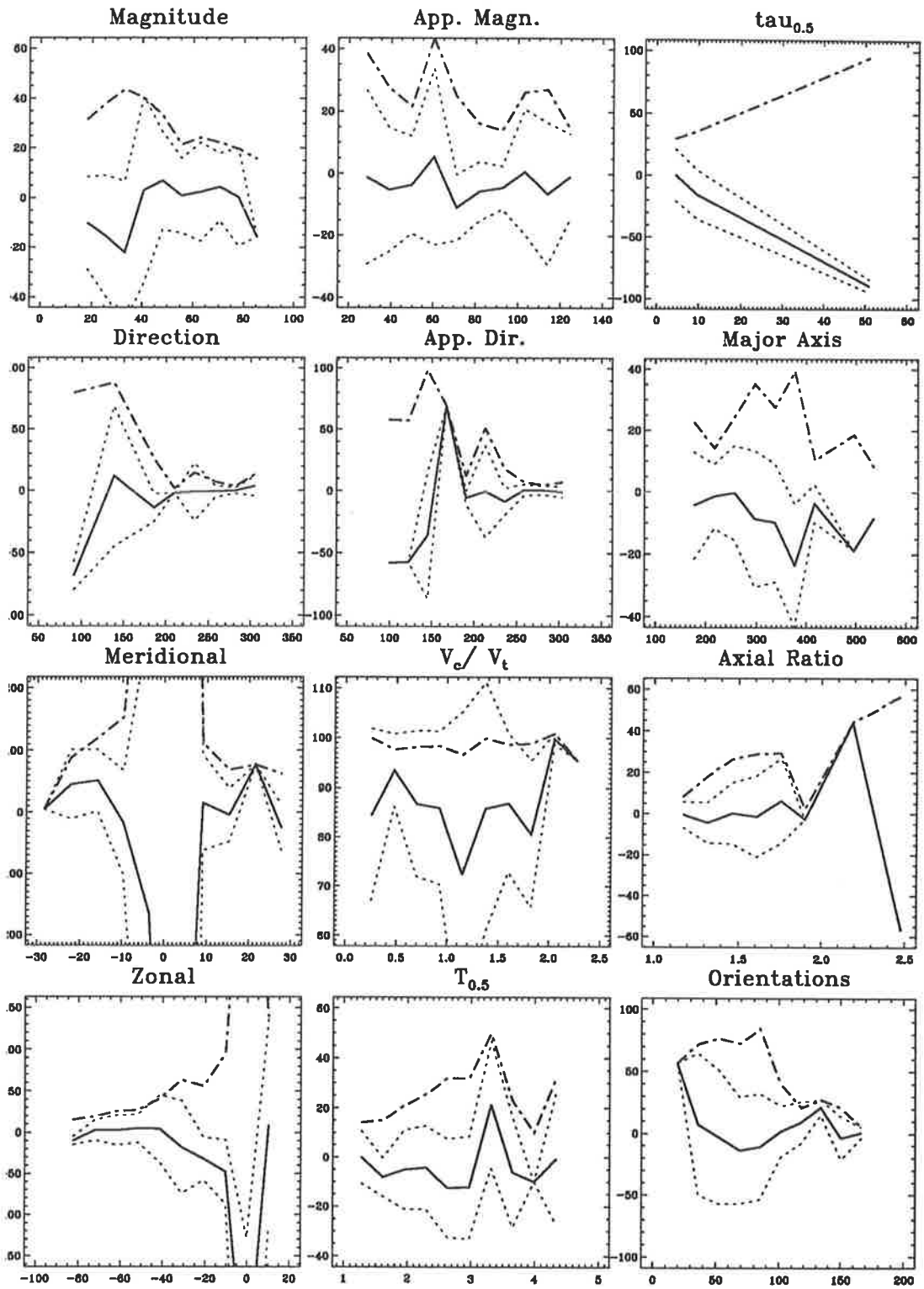

Figure B.25: Statistics of the percentage value differences for FCA2 test 1 vs 9.

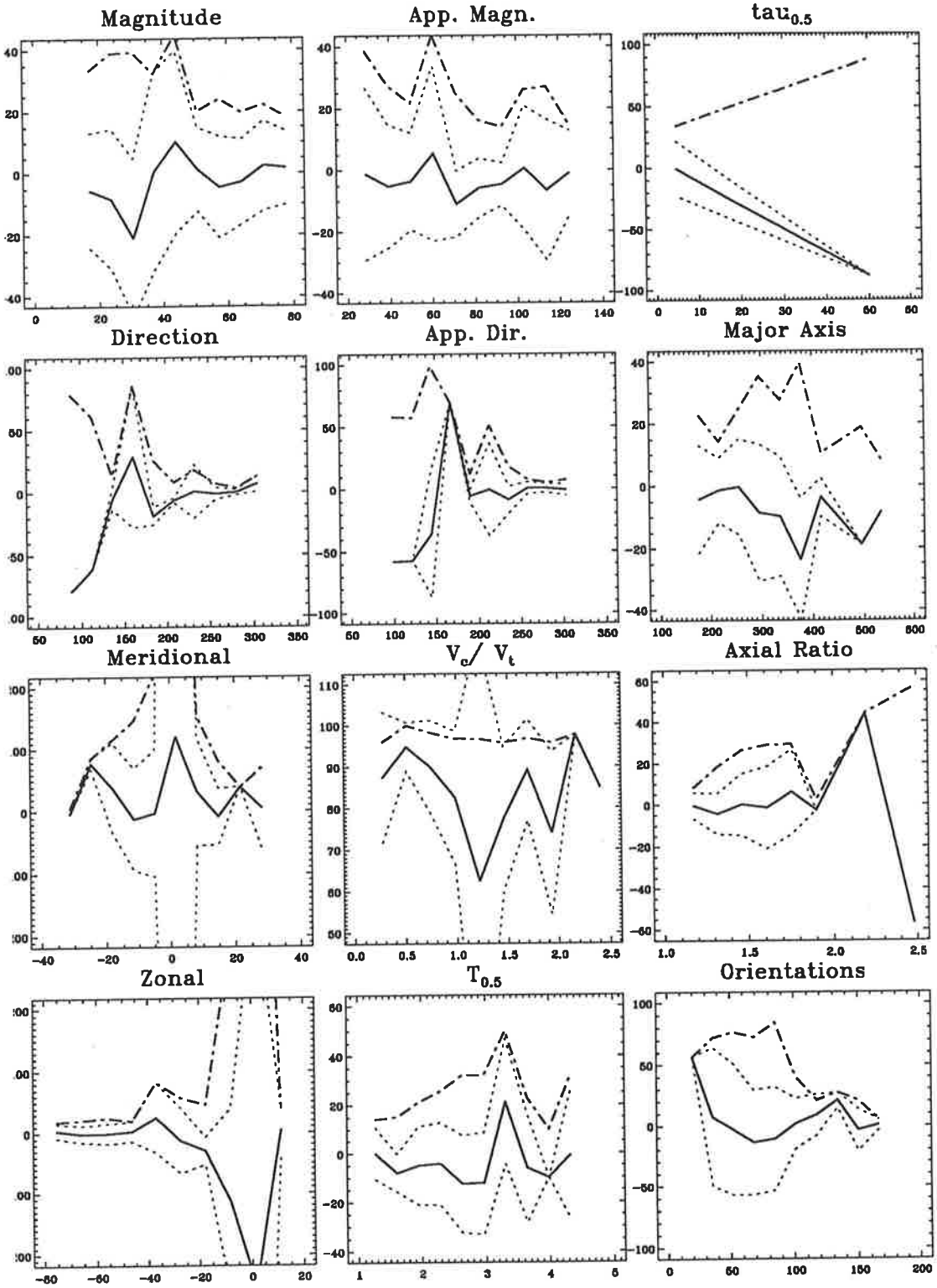

Figure B.26: Statistics of the percentage value differences for FCA2 test 2 vs 9.

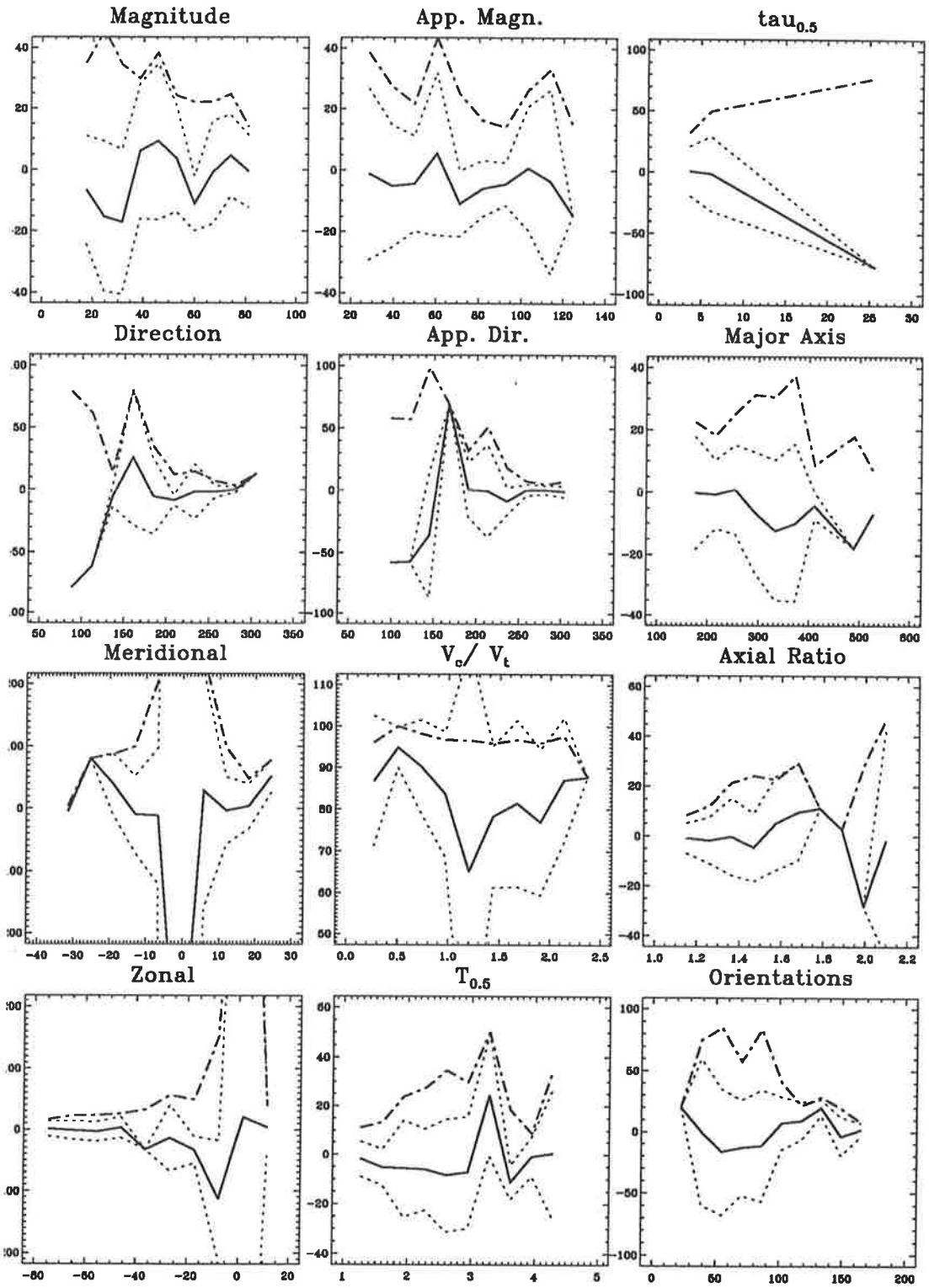

Figure B.27: Statistics of the percentage value differences for FCA2 test 5 vs 9.

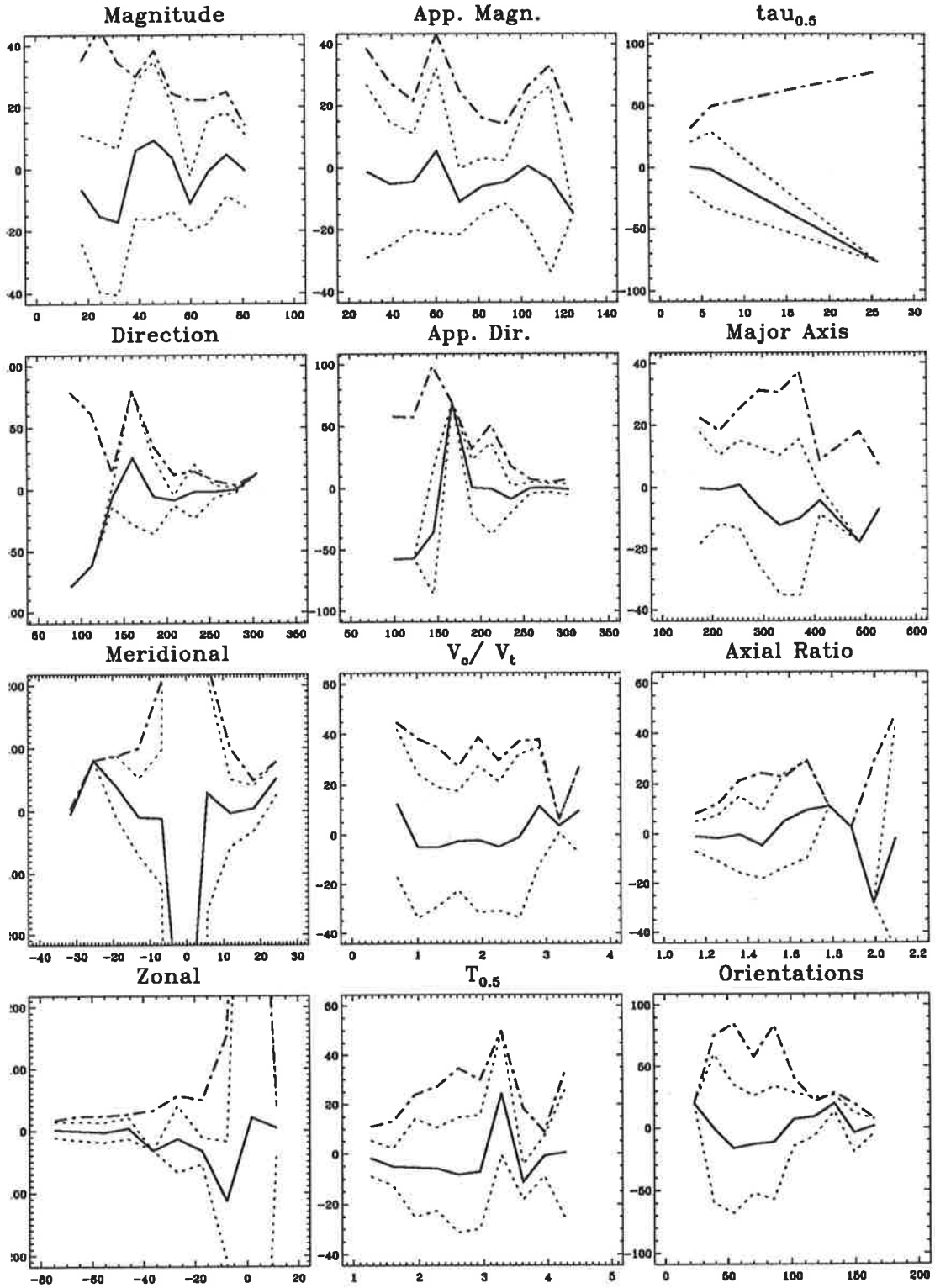

Figure B.28: Statistics of the percentage value differences for FCA2 test 6 vs 9.

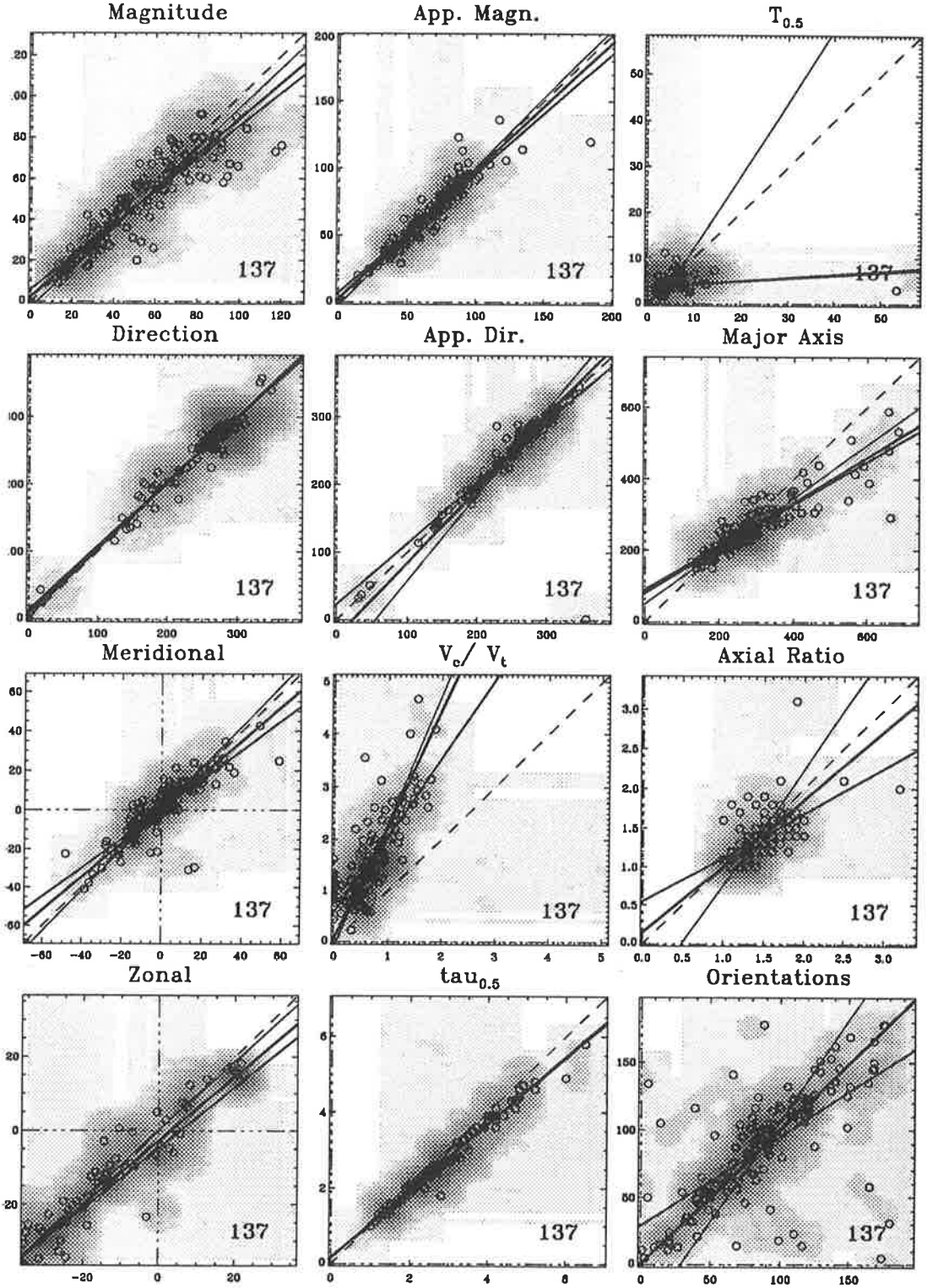

Figure B.29: Scatter plots of some of the FCA parameters for FCA1 against FCA2. Otherwise as for Figure B.1

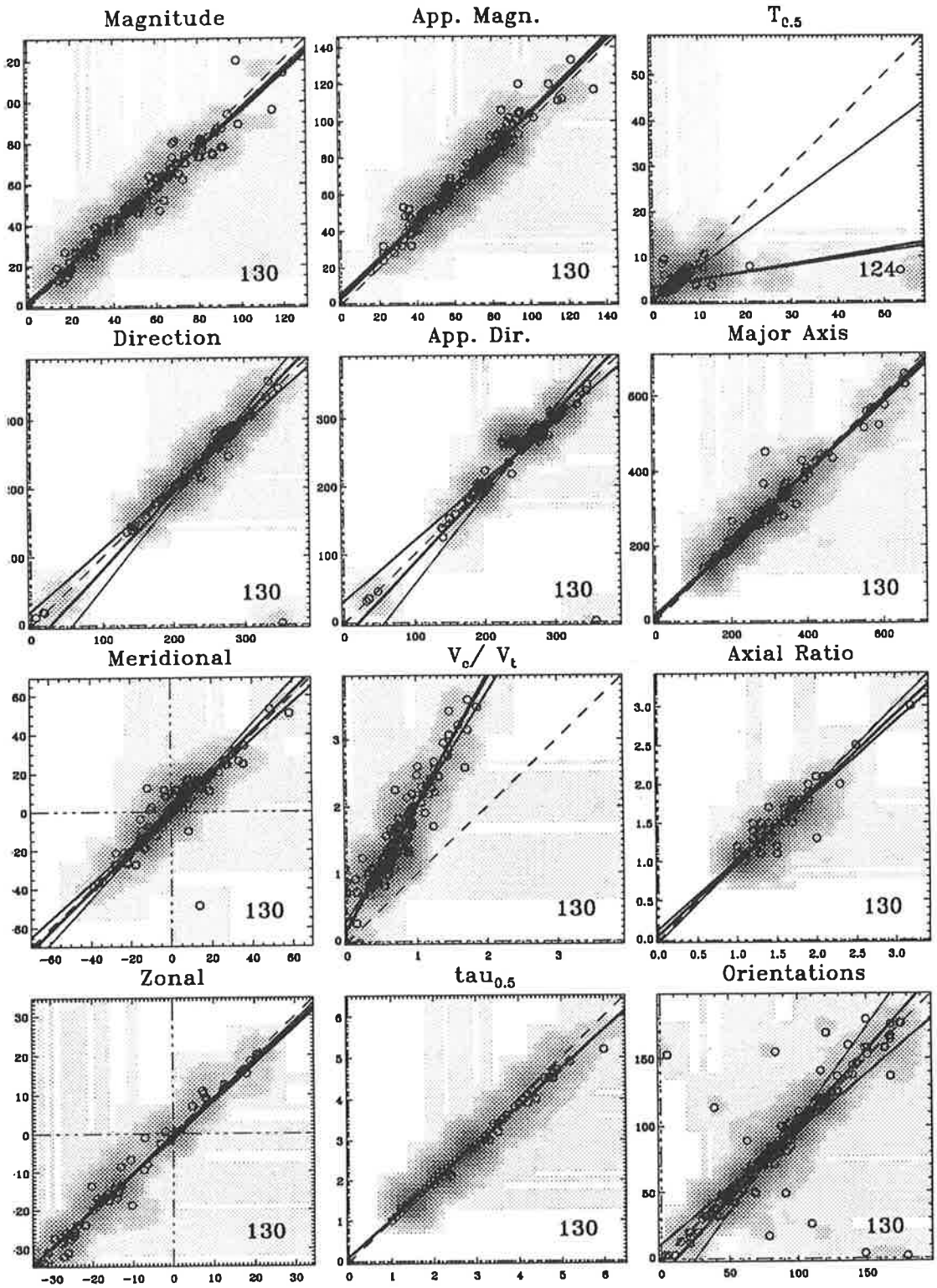

Figure B.30: Scatter plots of some of the FCA parameters for FCA1 against FCA3. Otherwise as for Figure B.1

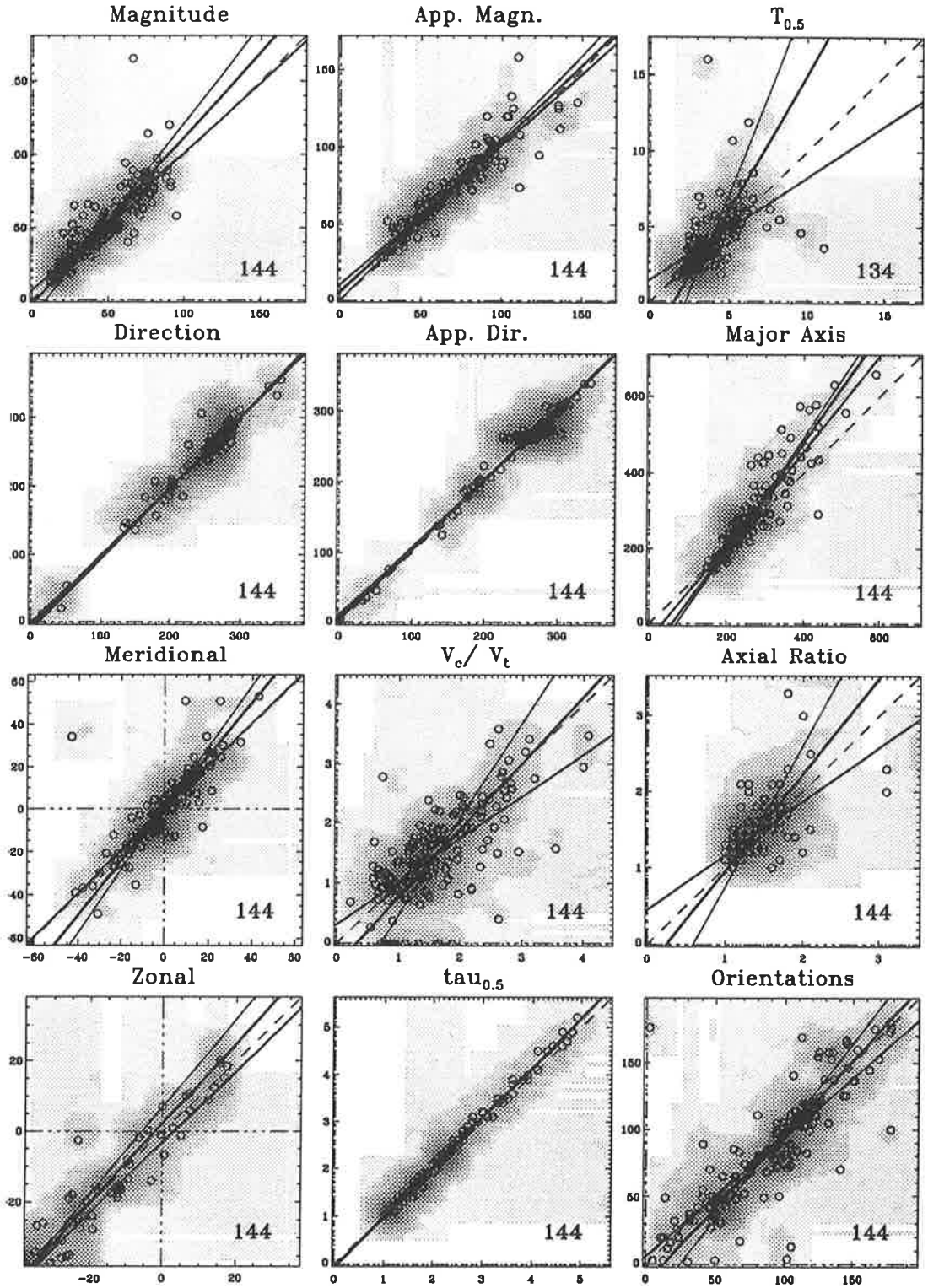

Figure B.31: Scatter plots of some of the FCA parameters for FCA2 against FCA3. Otherwise as for Figure B.1

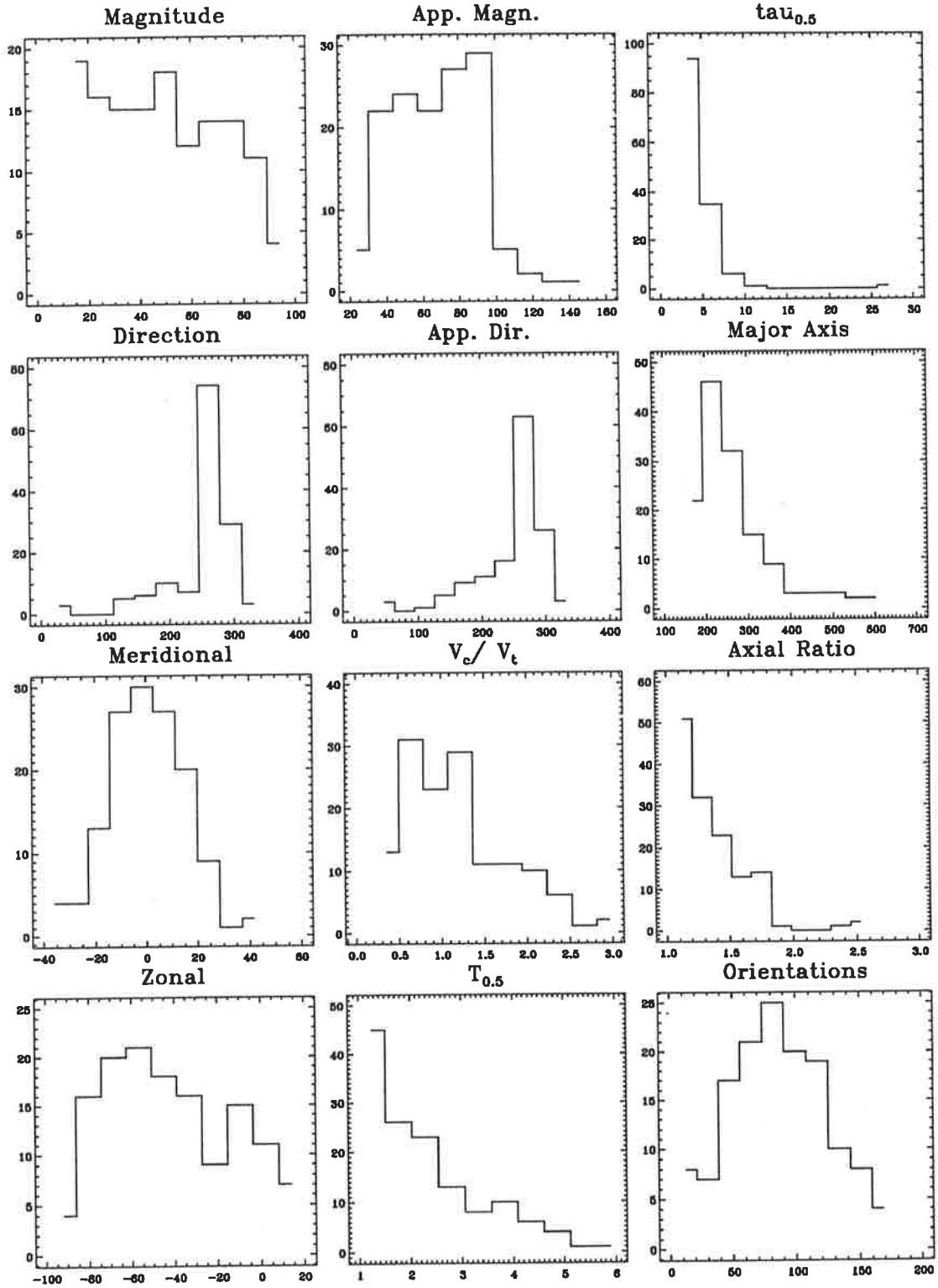

Figure B.32: Value-range histograms for FCA1 vs FCA2

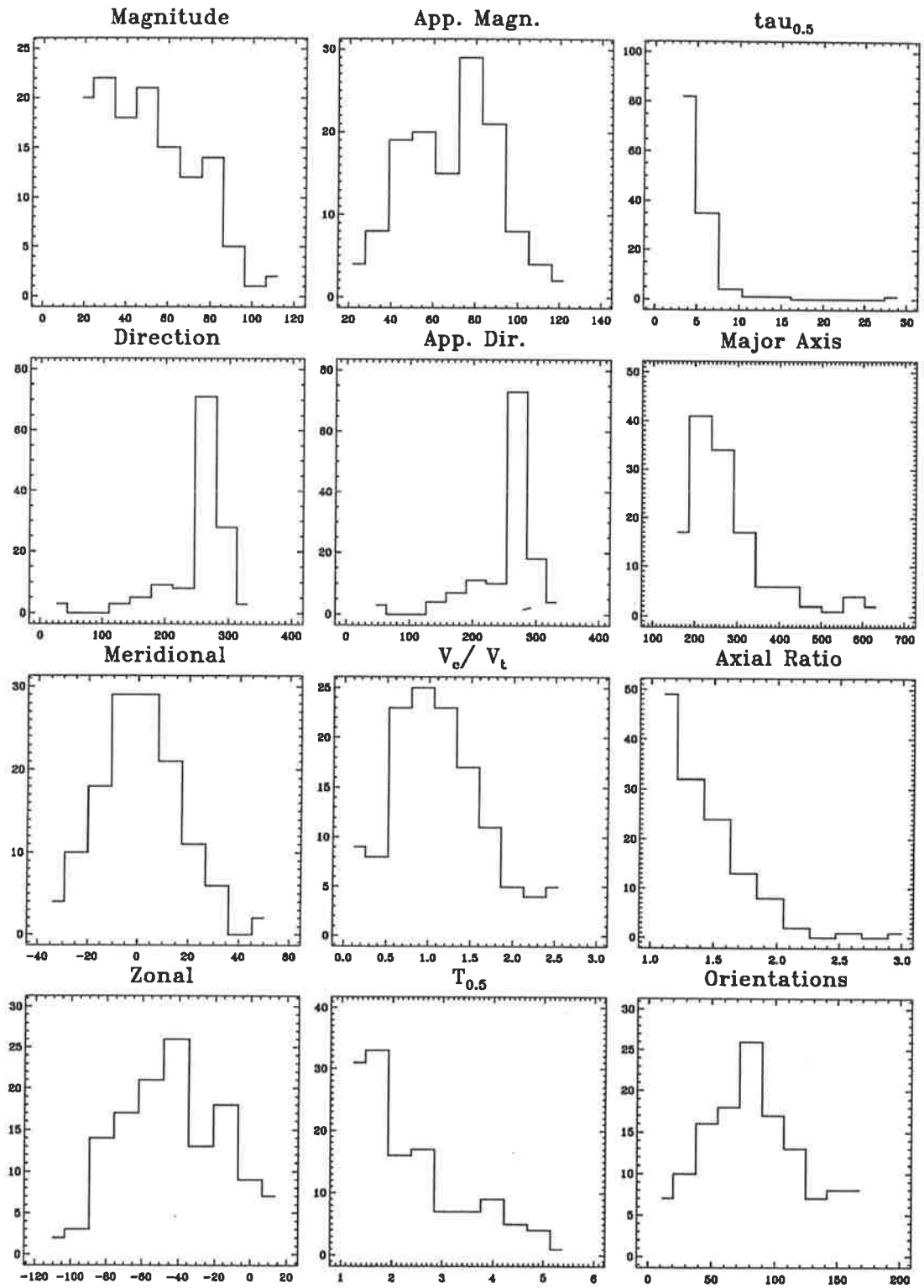

Figure B.33: Value-range histograms for FCA1 vs FCA3

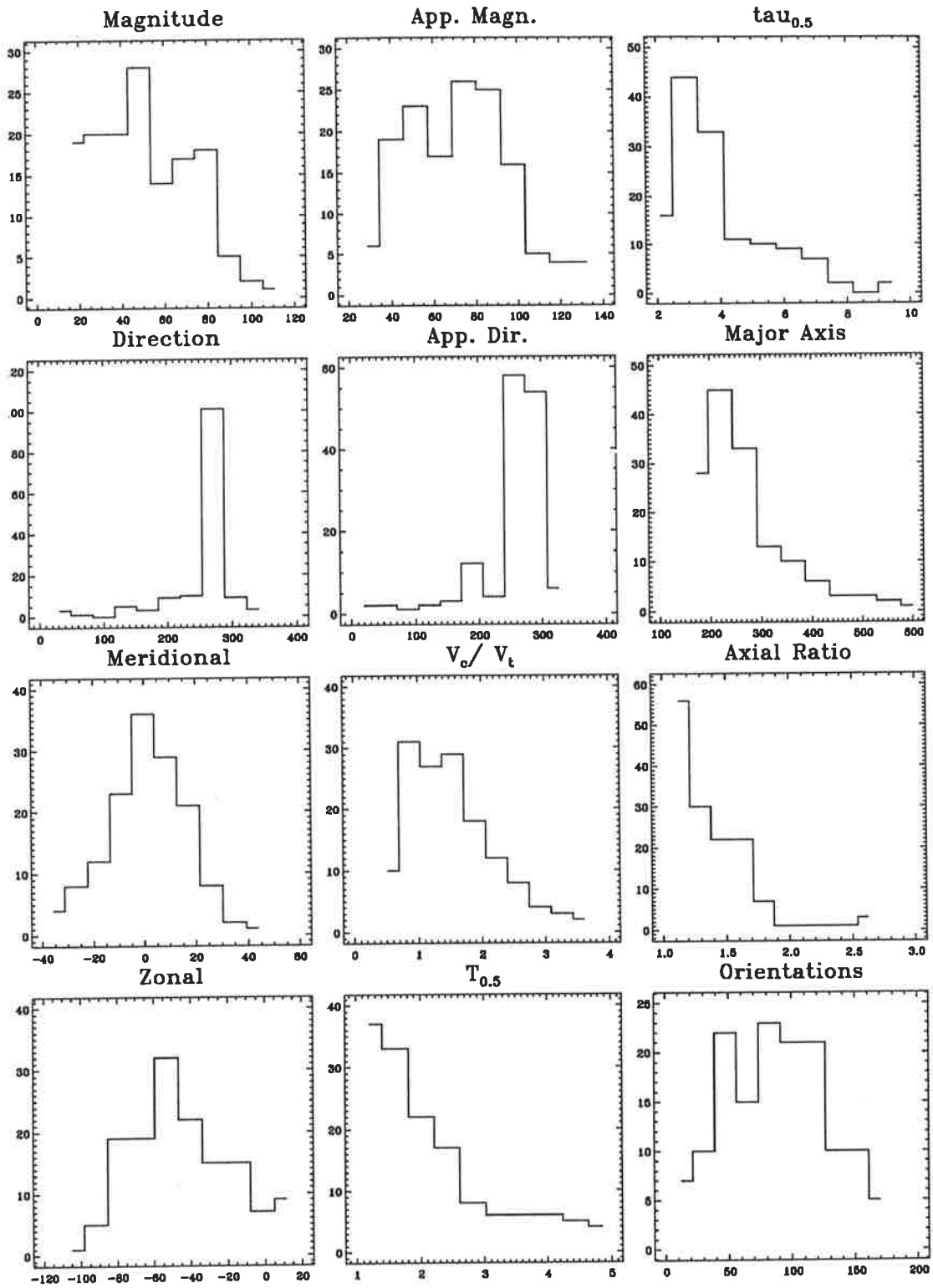

Figure B.34: Value-range histograms for FCA2 vs FCA3

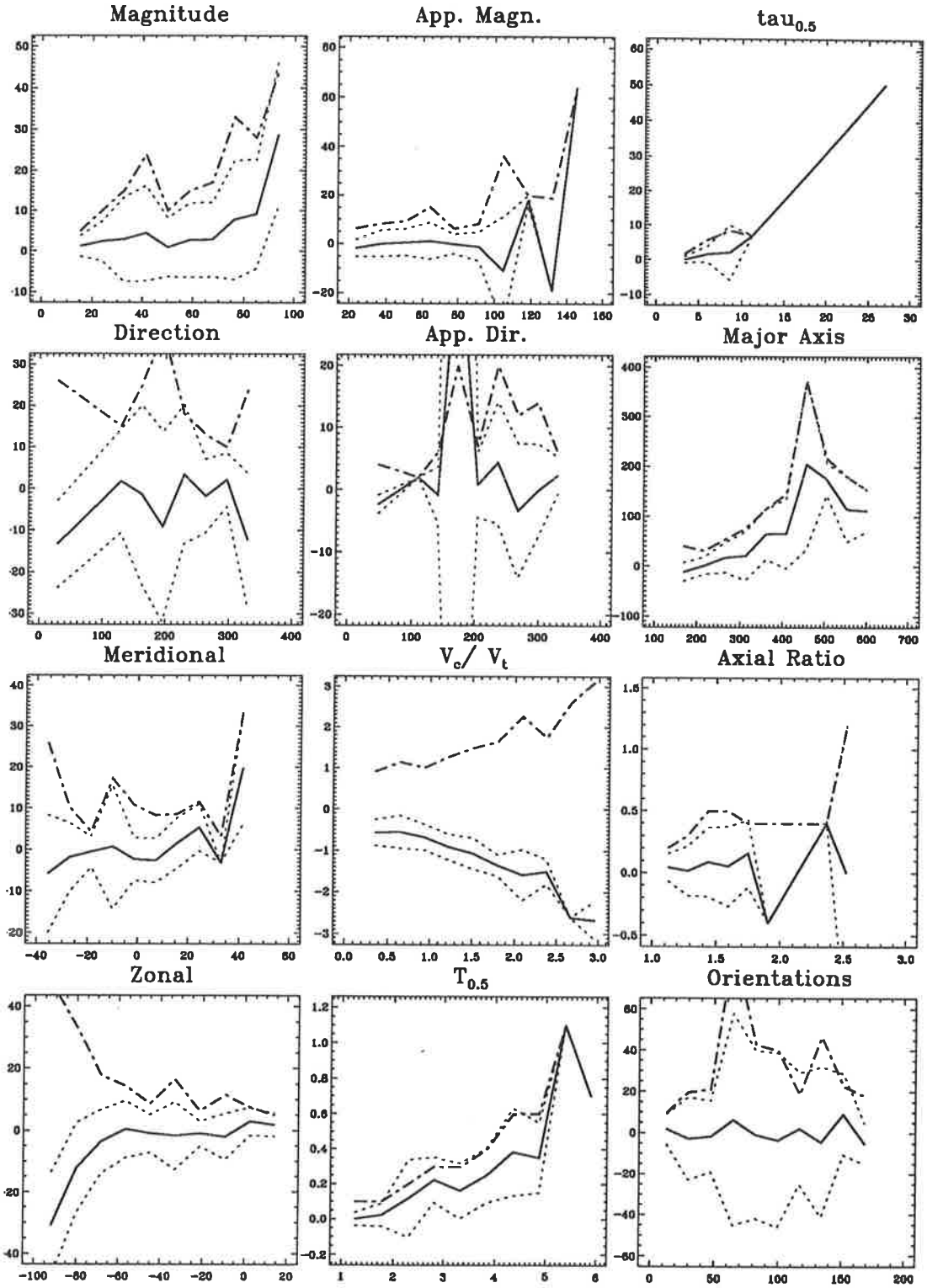

Figure B.35: Statistics of the value differences for FCA1 vs FCA2.

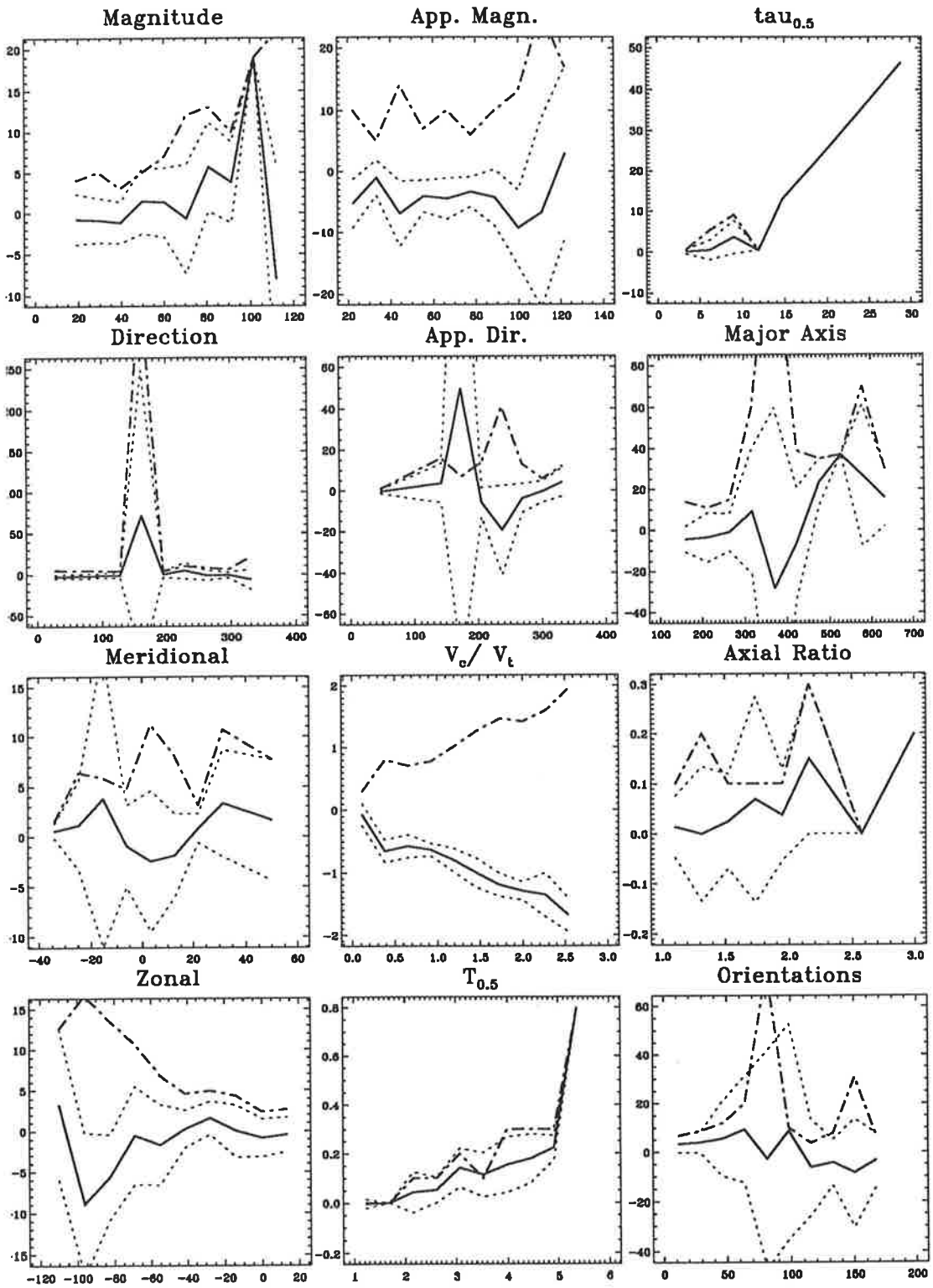

Figure B.36: Statistics of the value differences for FCA1 vs FCA3.

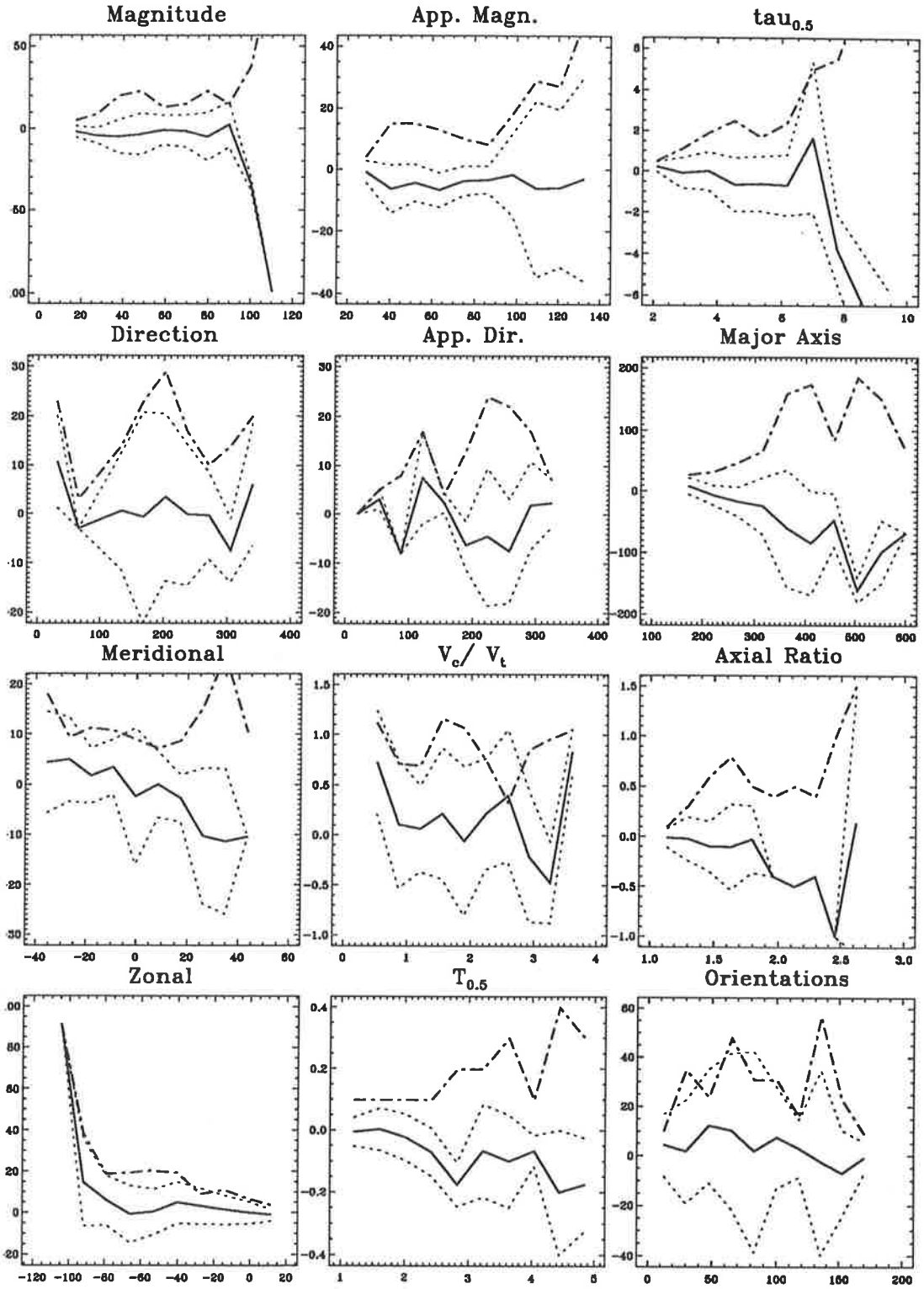

Figure B.37: Statistics of the value differences for FCA2 vs FCA3 .

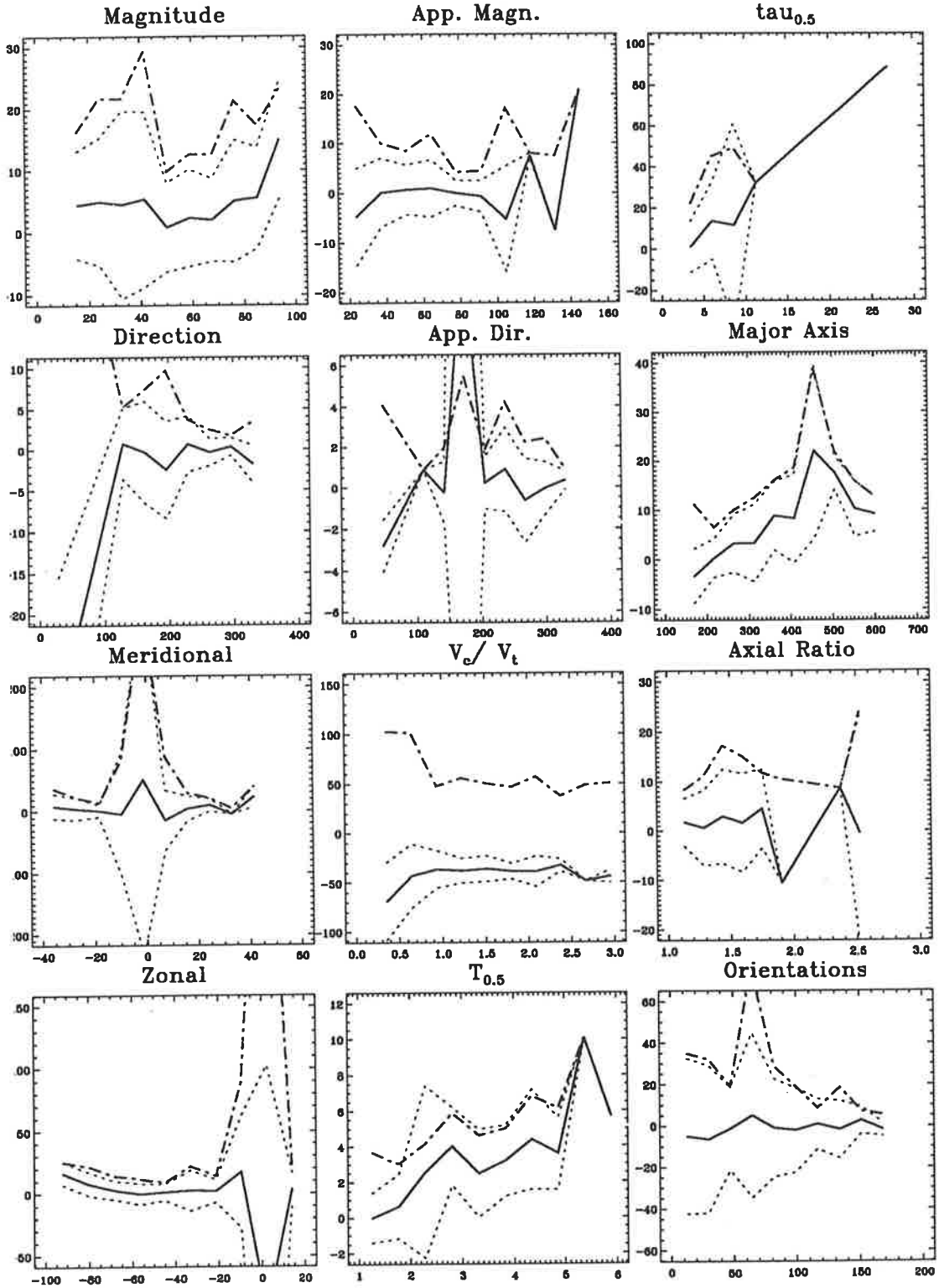

Figure B.38: Statistics of the percentage value differences for FCA1 vs FCA2.

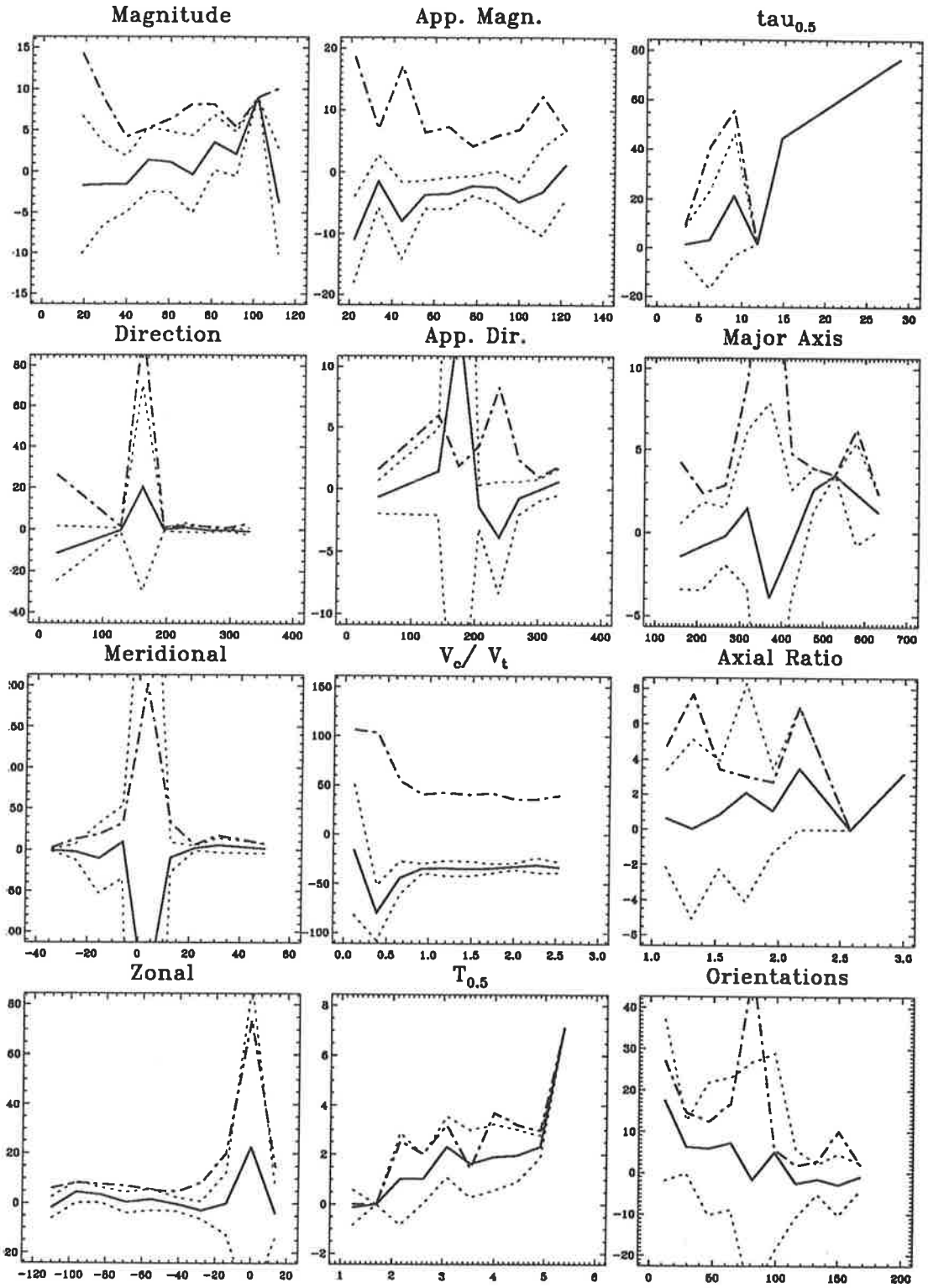

Figure B.39: Statistics of the percentage value differences for FCA1 vs FCA3.

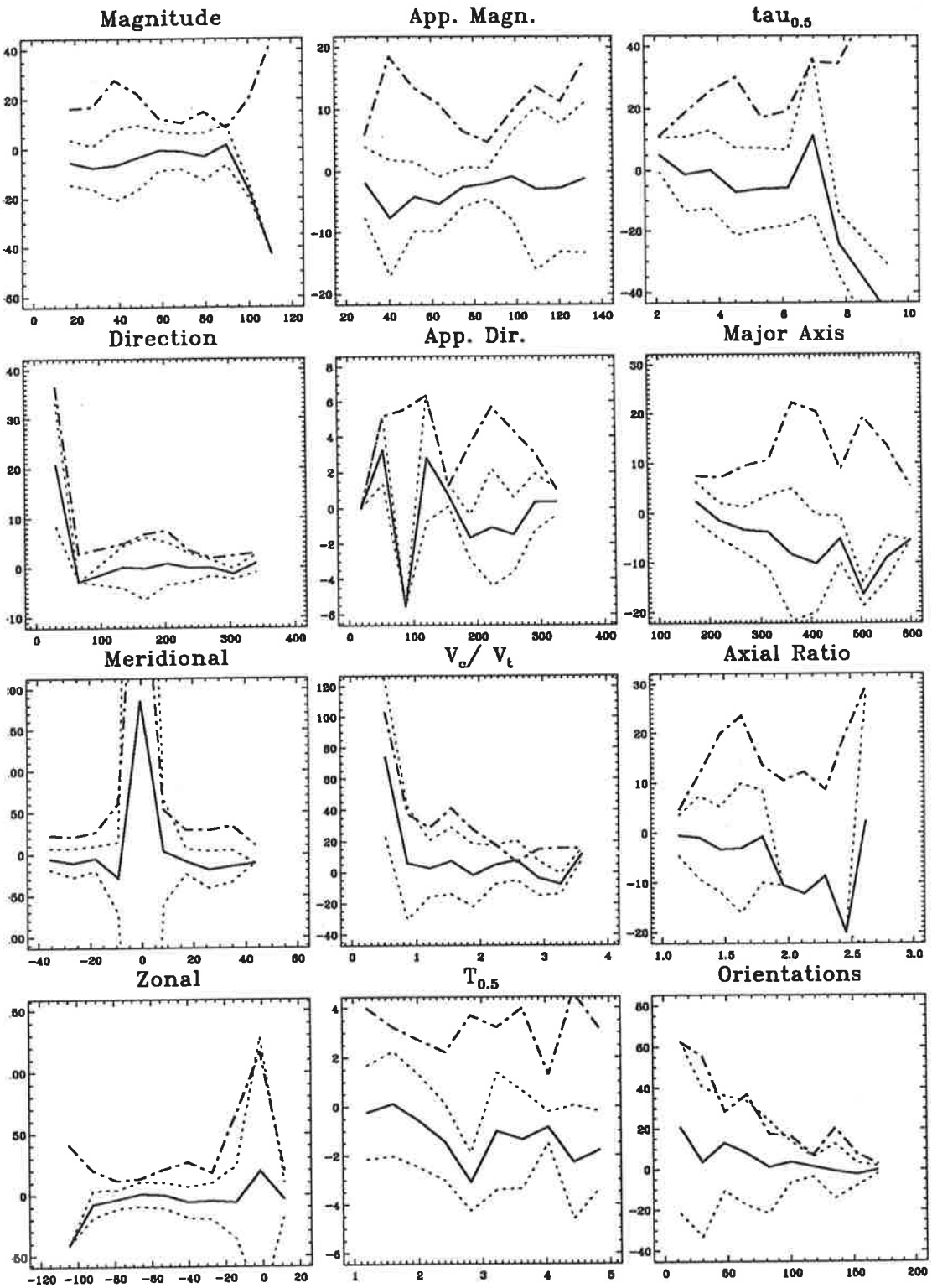

Figure B.40: Statistics of the percentage value differences for FCA2 vs FCA3 .

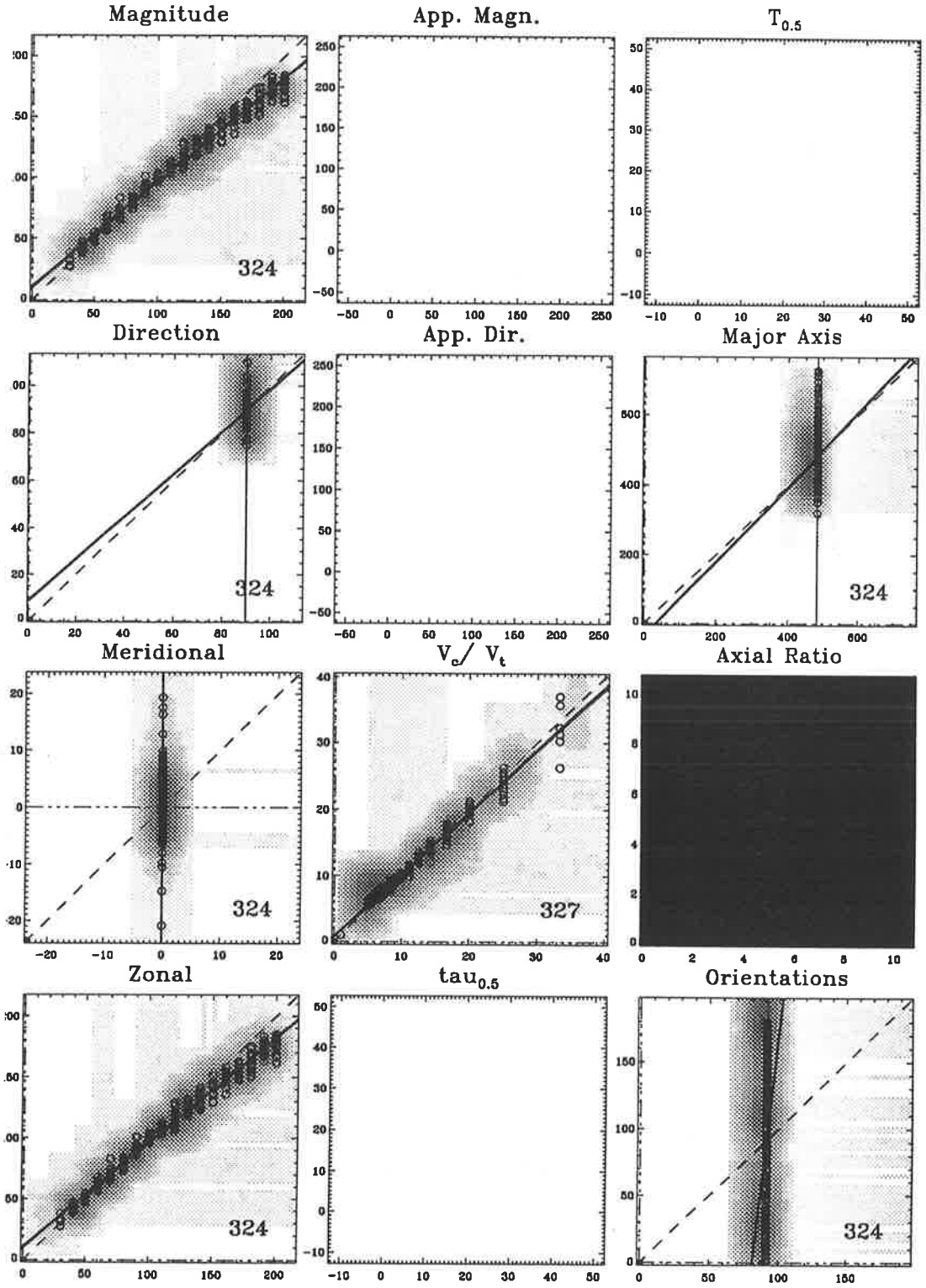

Figure B.41: Scatter plots of some of the FCA parameters for simulated data against FCA2. Otherwise as for Figure B.1

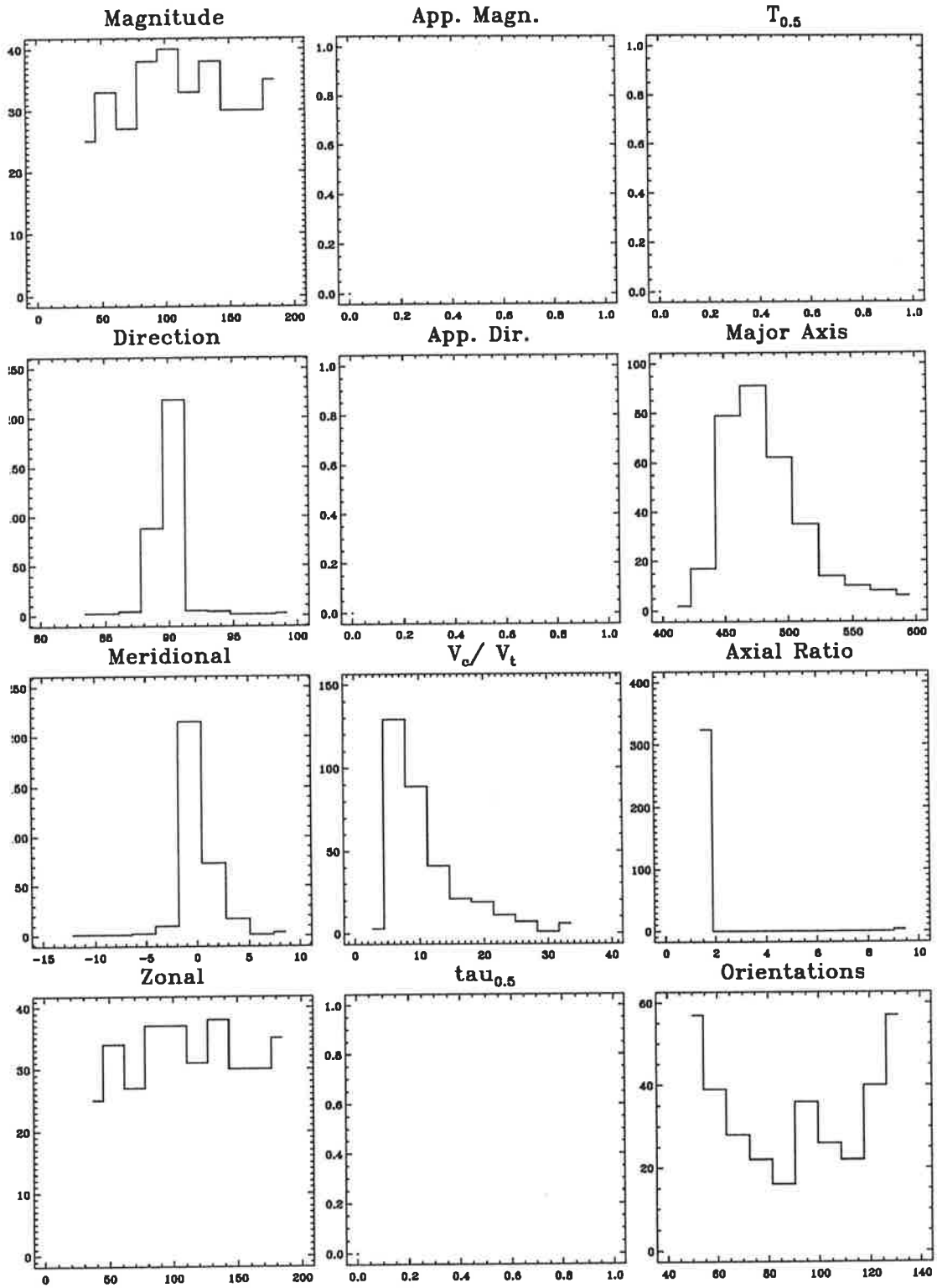

Figure B.42: Value-range histograms of FCA3 for the comparison against simulated data

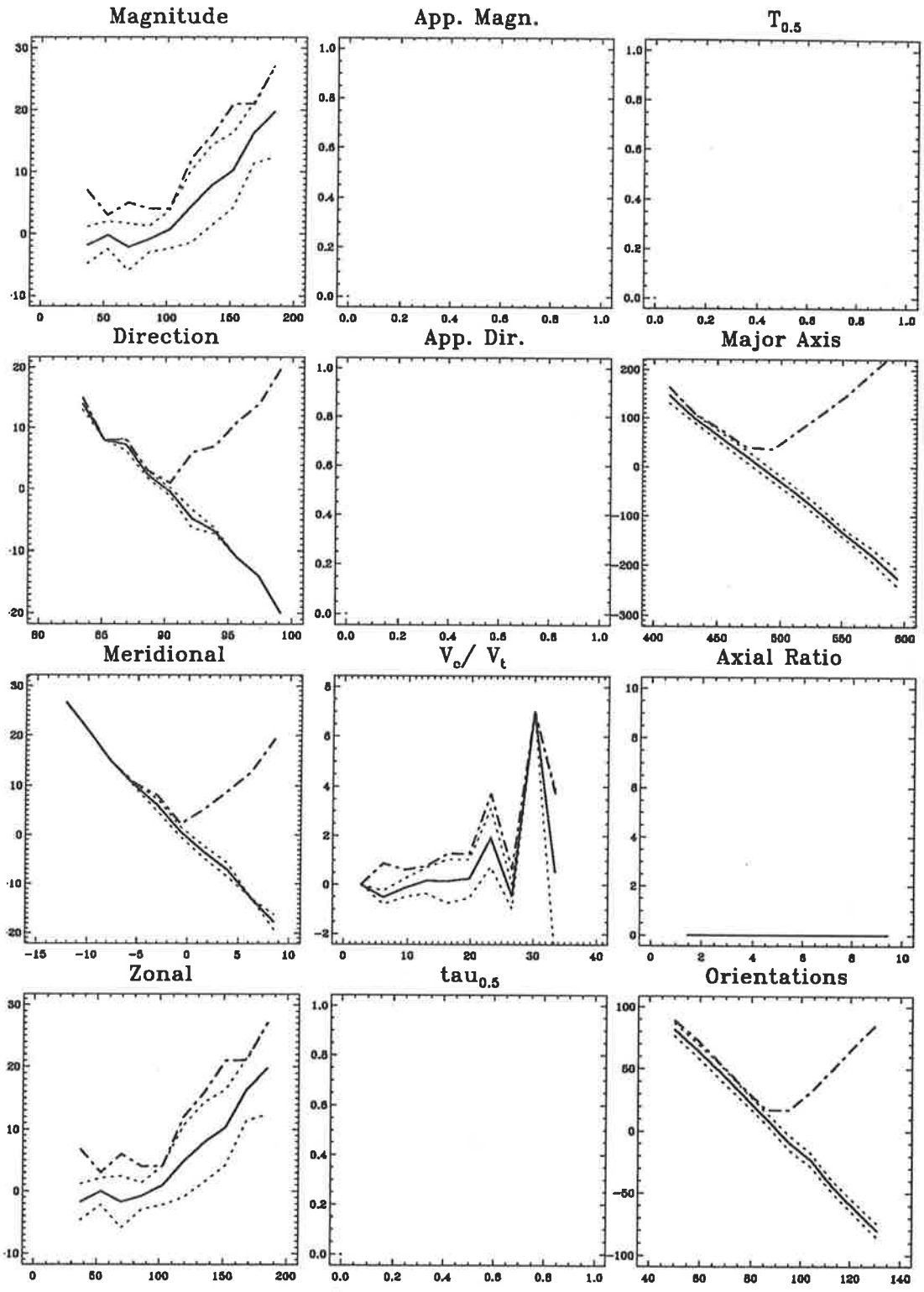

Figure B.43: Statistics of the value differences for simulated data vs FCA3.

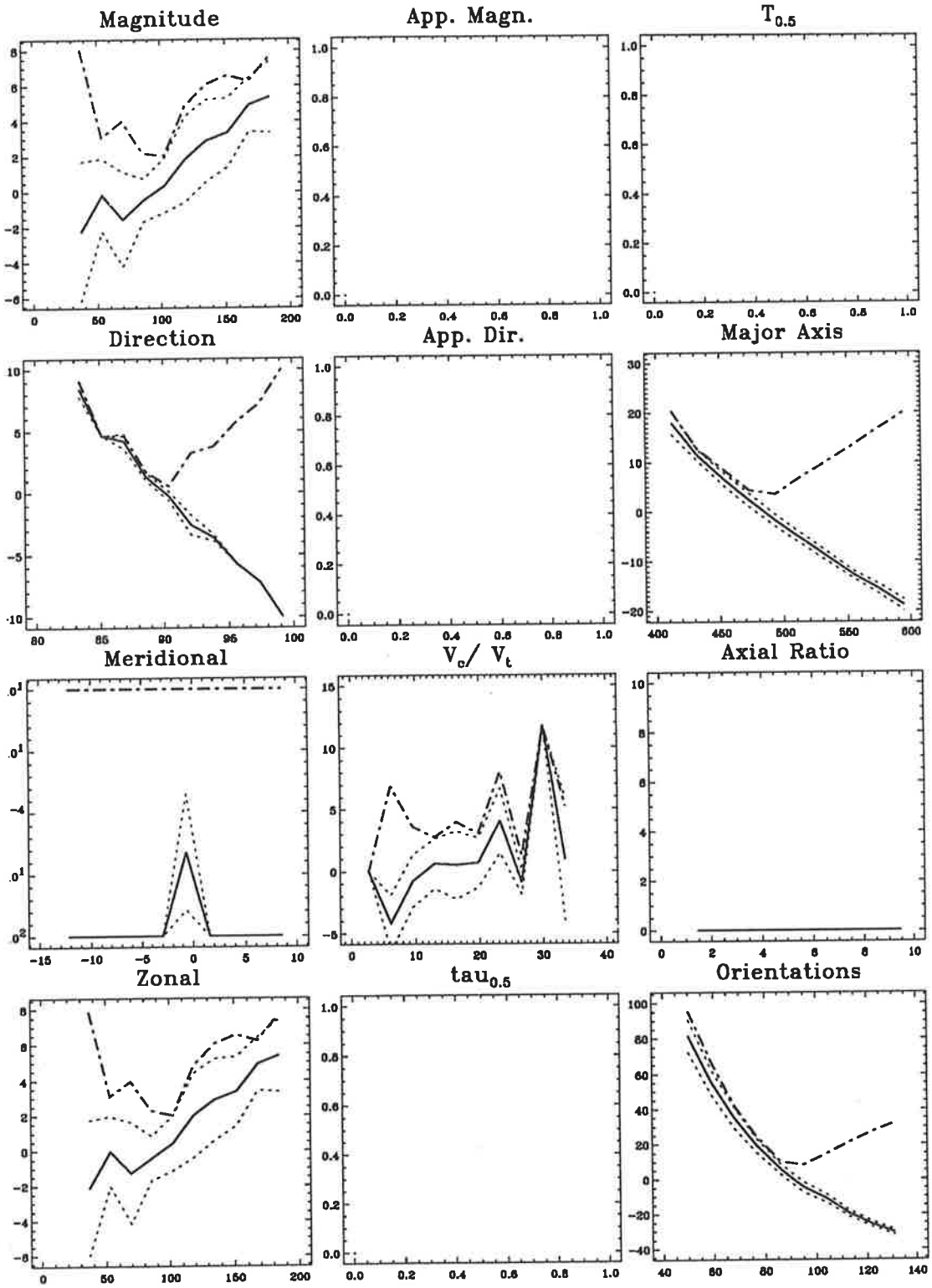

Figure B.44: Statistics of the percentage value differences for simulated data vs FCA3 .

Appendix C

Moments of the Power Spectra

from Woodman and Guillen, "Moments of the Power Spectra", J atmos. sci., **31**, *493-505, 1974*

The i^{th} moment, m_i, for the power spectrum, $F(\omega)$, is given by,

$$m_i = \int \omega^i F(\omega)\, d\omega \tag{C.1}$$

The total power, P, mean frequency shift, Ω, and spectral width, σ, are related to the moments by,

$$P = m_0 \tag{C.2}$$

$$\Omega = \frac{m_1}{m_0} \tag{C.3}$$

$$\sigma^2 = \frac{m_2}{m_0} - (\frac{m_1}{m_0})^2 \tag{C.4}$$

The auto-correlation function, $C(\tau)$, is the Fourier transform of $F(\omega)$,

$$C(\tau) = \int F(\omega) e^{i\omega\tau}\, d\omega \tag{C.5}$$

hence it can be easily shown that,

$$C(0) = m_0 \qquad \frac{dC(0)}{d\tau} = im_1 \qquad \frac{d^2C(0)}{d\tau^2} = -m_2 \tag{C.6}$$

It can also be shown that $C(\tau)$ has Hermitean symmetry ($i.e. C(\tau) = C^*(\tau)$). Using an amplitude-phase representation of $C(\tau)$, where

$$C(\tau) = A(\tau) e^{i\phi(\tau)} \tag{C.7}$$

means that A is an even function, and ϕ an odd function of τ. Using equation C.7,

$$C(0) = A(0) \tag{C.8}$$

$$\frac{dC(0)}{d\tau} = i\frac{d\phi(0)}{d\tau} A(0) \tag{C.9}$$

$$\frac{d^2C(0)}{d\tau^2} = \frac{d^2A(0)}{d\tau^2} - (\frac{d\phi(0)}{d\tau})^2 A(0) \tag{C.10}$$

hence

$$P = A(0) \tag{C.11}$$

$$\Omega = \frac{d\,\phi(0)}{d\tau} \tag{C.12}$$

$$\sigma^2 = \frac{-1}{A(0)} \frac{d^2\,A(0)}{d\tau^2} \tag{C.13}$$

For small lags, by Taylor expansion,

$$\phi(\tau) \simeq \frac{d\,\phi(0)}{d\tau}\tau \tag{C.14}$$

$$\frac{d\,A(\tau)}{d\tau} \simeq A(0) + \frac{1}{2}\frac{d^2\,A(0)}{d\tau^2}\tau^2 \tag{C.15}$$

with errors of the order of τ^3 and τ^4 respectively. Equations C.14 and C.15 combined with C.12 and C.13 give,

$$\Omega = \frac{\phi(\tau_1)}{\tau_1} \tag{C.16}$$

$$\sigma^2 = \frac{2[1 - \frac{A\tau_1}{A(0)}]}{\tau_1^2} \tag{C.17}$$

Thus the frequency Doppler-shift can be measured from the slope of the phase of the auto-correlation function, and the spectral width by a simple function of the slope of the amplitude.

Appendix D

The Ferraz-Mello Orthogonal Fourier Transform

from *Ferraz-Mello, Estimation of periods from unequally spaced observations, The Astronomical Journal,* **86**, *619, 1981*

The idea of this method is to ensure that we use an orthonormal basis set to expand on. The usual $\sin(x)$ and $\cos(x)$ are only orthogonal if the x are evenly spaced or continuous. The data spacing comes in through the inner product. This method becomes a normal discrete Fourier transform, or DFT, when the sample spacing is constant.

In his paper, Ferraz-Mello calls this method a "data compensated discrete Fourier transform", but I shall call it by the more general name of the "Ferraz-Mello orthogonal Fourier transform", or FMOFT.

Defining the inner product, (A, B), as

$$(A, B) = \sum_j A(t_j)B(t_j) \tag{D.1}$$

and the basis function, H, as

$$H_0(t) = 1 \tag{D.2}$$

$$H_1(t) = \sin(\omega t) \tag{D.3}$$

$$H_2(t) = \cos(\omega t) \tag{D.4}$$

the DFT, $F(\omega)$, of the N point time-series, $f(t_j)$, can then be defined as,

$$F(\omega) = (f, H_1 + iH_2) \tag{D.5}$$

To ensure that we still use an orthonormal basis function to expand on when the data spacing is non-uniform, the Gram-Schmidt orthogonalisation process is applied to H. Thus we set,

$$h_0 = a_0 H_0 \tag{D.6}$$

$$h_1 = a_1 H_1 - a_0 h_0 (h_0, H_1) \tag{D.7}$$

$$h_2 = a_2 H_2 - a_2 h_0 (h_0, H_2) - a_2 h_1 (h_1, H_2) \tag{D.8}$$

and insist that $(h_0, h0) = (h_1, h1) = (h_2, h2) = 1$. Hence,

$$a_0^{-2} = N \tag{D.9}$$

$$a_1^{-2} = (H_1, H_1) - a_0^2 (H_0, H_1)^2 \tag{D.10}$$

$$\begin{aligned} a_2^{-2} = {} & (H_2, H_2) - a_0^2 (H_0, H_2)^2 \\ & - a_1^2 (H_1, H_2)^2 - a_0^4 a_1^2 (H_0, H_1)^2 (H_0, H_2)^2 \\ & + 2 a_0^2 a_1^2 (H_0, H_1)(H_0, H_2)(H_1, H_2) \end{aligned} \tag{D.11}$$

Thus, the FMOFT, $F(\omega)$, of the N point time-series, $f(t_j)$, is

$$F(\omega) = \frac{1}{a_0 \sqrt{2}} (f, h_1 + i h_2) \tag{D.12}$$

Note that the FMOFT is equivalent to performing a maximum likelihood sinusoidal regression of the form,

$$f(t) = \sum_{\omega} [(f, h_0) H_0 + (f, h_1) H_1 + (f, h_2) H_2] \tag{D.13}$$

With mean corrected data, the first term is zero, and the intensity of the power spectrum, $I(\omega)$, then becomes,

$$I(\omega) = 2 a_0^2 ||F(\omega)|| = (f, h_1)(f, h_1) + (f, h_2)(f, h_2) \tag{D.14}$$

For evenly spaced and equally weighted data (a normal DFT), the inner products for the cross terms in H approach zero, *i.e.*

$$(H_0, H_1) \approx (H_0, H_2) \approx (H_1, H_2) \approx 0 \tag{D.15}$$

and the diagonal terms give,

$$(H_1, H_1) \approx (H_2, H_2) \approx \frac{1}{2} a_0^{-2} = \frac{N}{2} \tag{D.16}$$

hence $a_1 = a_2 = \sqrt{2} a_0$ from equation D.11 and the intensity of power spectrum from the FMOFT in equation D.14 becomes the familiar Fourier transform relation,

$$I(\omega) = 2 a_0^2 ||F(\omega)|| = 2 a_0^2 [(f, H_1)(f, H_1) + (f, H_2)(f, H_2)] \tag{D.17}$$

The approximations in equation D.15 approach equalitites as the data length, N, increases.

The definition of the inner product, (A, B), can be extended to cater for different precision in the data by adding a weighting function, $W(t_j)$. So equation D.1 becomes,

$$(A, B) = \sum_j W(t_j)A(t_j)B(t_j) \tag{D.18}$$

D.1 Coefficient of Spectral Correlation

Ferraz-Mello defines a statistic, the "coefficient of spectral correlation", $S(\omega)$,

$$S(\omega) = \frac{I(\omega)}{\sigma^2} \tag{D.19}$$

where $\sigma^2 = (f, f)$ is a measure of the total variance of the time-series.

Since,

$$0 \leq I(\omega) \leq \sigma^2 , \tag{D.20}$$

this implies that,

$$0 \leq S(\omega) \leq 1 \qquad \forall \ \omega \tag{D.21}$$

If the time-series, $f(t)$, is a random normal variate, such as white noise, then the regression coefficients,$(f, h_1)(f, h_1)$ and $(f, h_2)(f, h_2)$, in equation D.14 are normally distributed and of the same variance, so

$$\frac{I(\omega)}{\sigma^2} \sim \chi_2^2 \tag{D.22}$$

$(N-1)S(\omega)$ can be considered as a test variate, so that the probability of obtaining a result, $S(\omega) \geq R$, from white noise is equal to the probability that $\chi_2^2 \leq (N-1)R$. Or more formally,

$$\mathcal{P}(S(\omega) \geq R) = \mathcal{P}(\chi_2^2 \leq (N-1)R) \tag{D.23}$$

In this way the significance of the peaks can be tested.

Appendix E

COSPAR International Reference Atmosphere, 1986

On the following pages are shown the zonal mean zonal winds from the CIRA86 reference atmosphere, both as a function of season at mid- and low-latitudes, and as a function of latitude for the central months of each solstice and equinox.

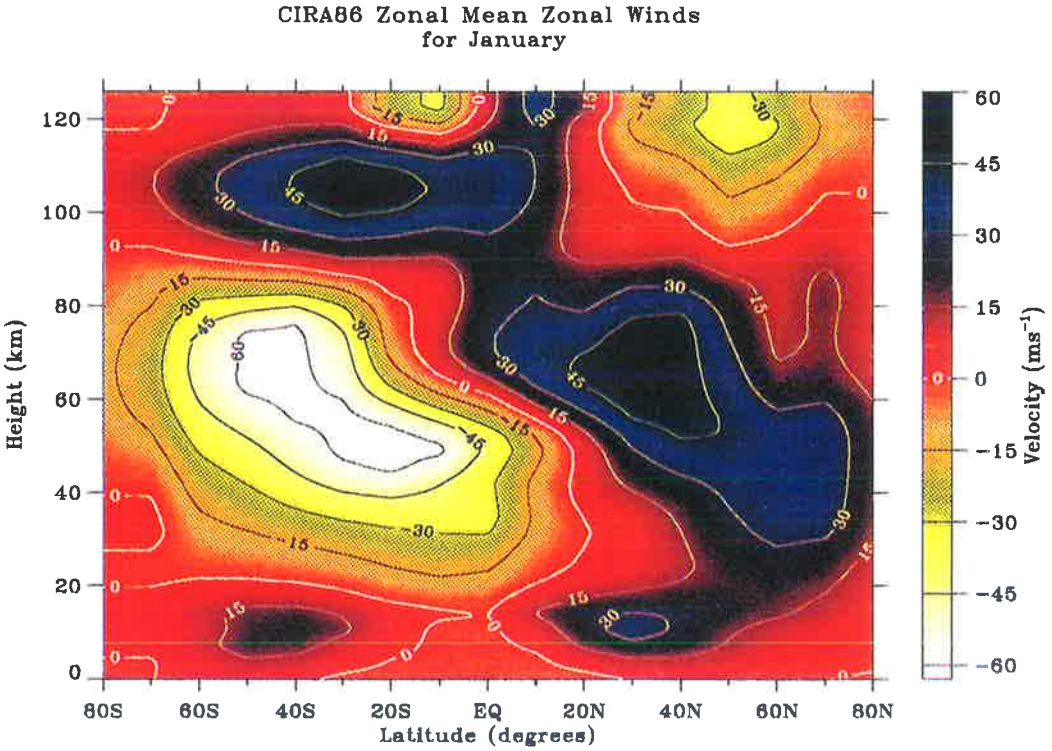

Figure E.1: CIRA86 zonal mean zonal winds as function of latitude for January

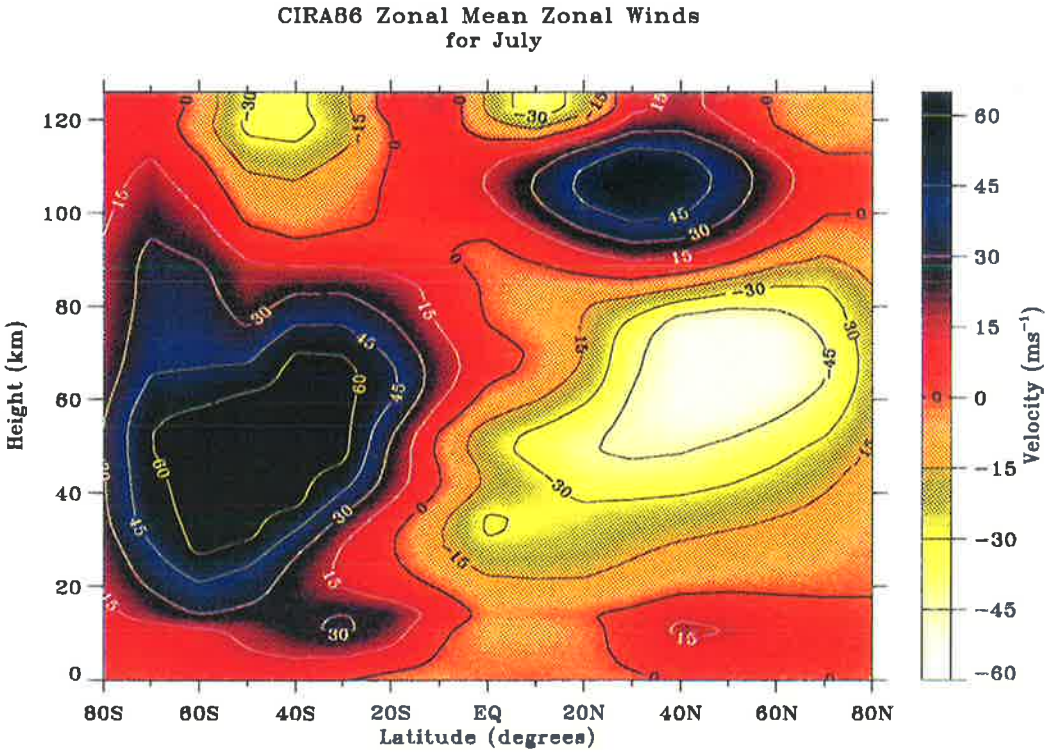

Figure E.2: CIRA86 zonal mean zonal winds as function of latitude for July

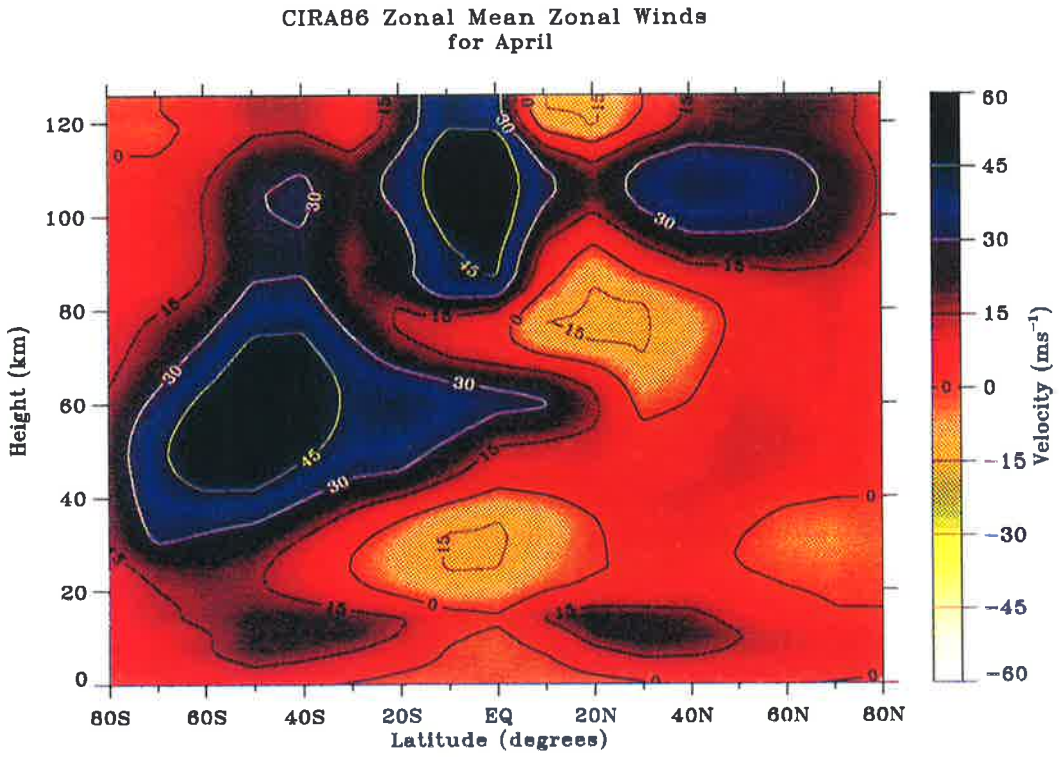

Figure E.3: CIRA86 zonal mean zonal winds as function of latitude for April

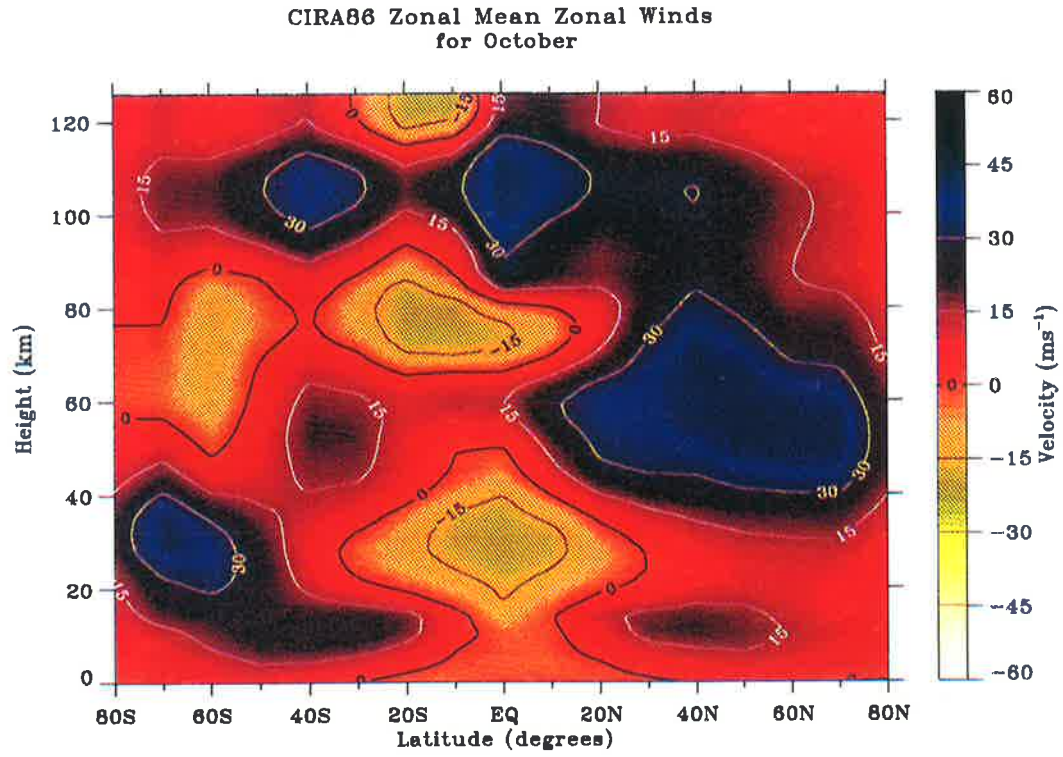

Figure E.4: CIRA86 zonal mean zonal winds as function of latitude for October

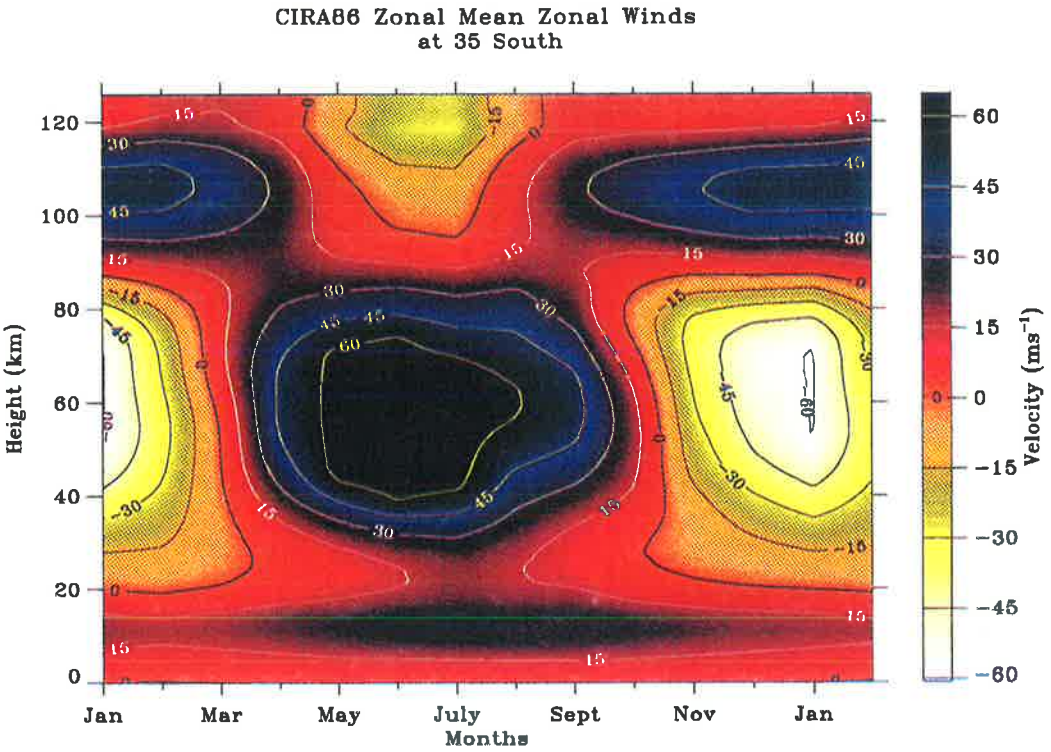

Figure E.5: CIRA86 zonal mean zonal winds over a year at 35° South

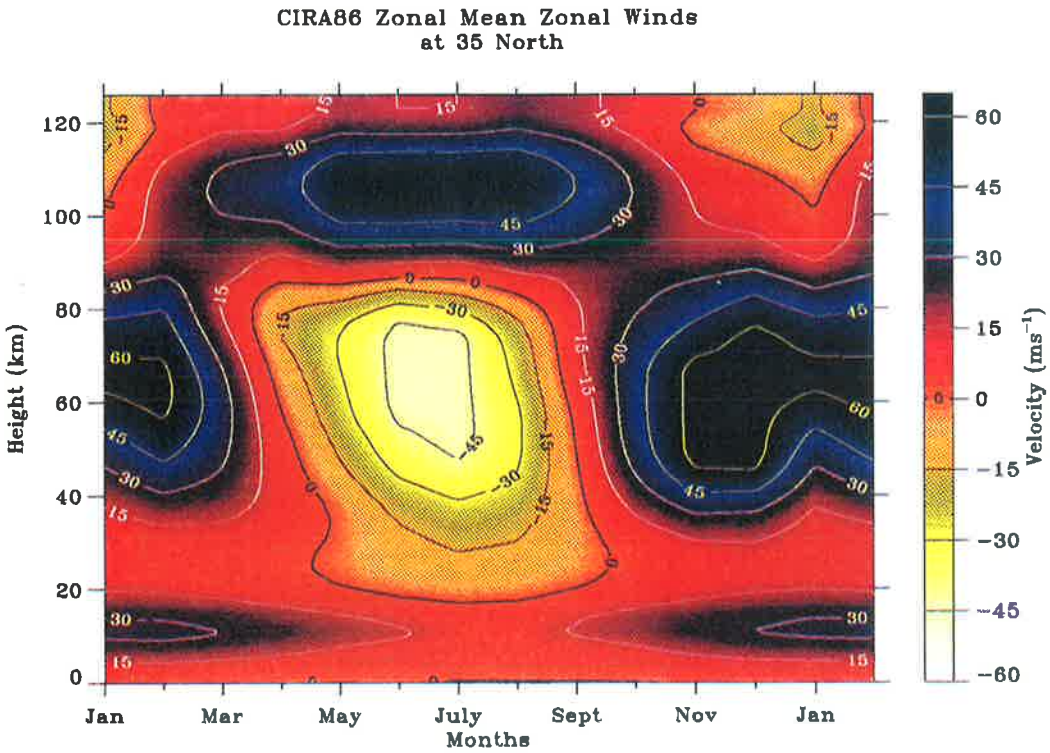

Figure E.6: CIRA86 zonal mean zonal winds over a year at 35° North

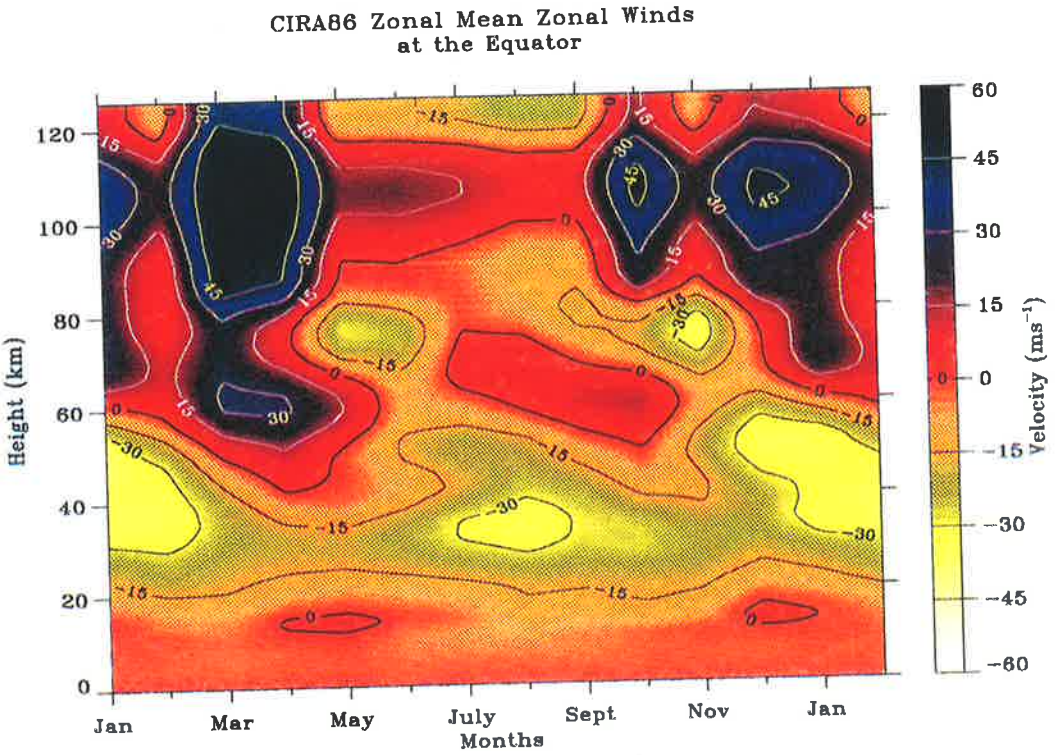

Figure E.7: CIRA86 zonal mean zonal winds over a year at the equator

Appendix F

Raw Winds at 86 km over Adelaide, 1984 – 1991

On the following pages are shown the winds at 86 km derived from spaced-antenna and FCA for Adelaide (34.5° S, 138.5° E). These are part of the unaveraged full wind records used within this thesis.

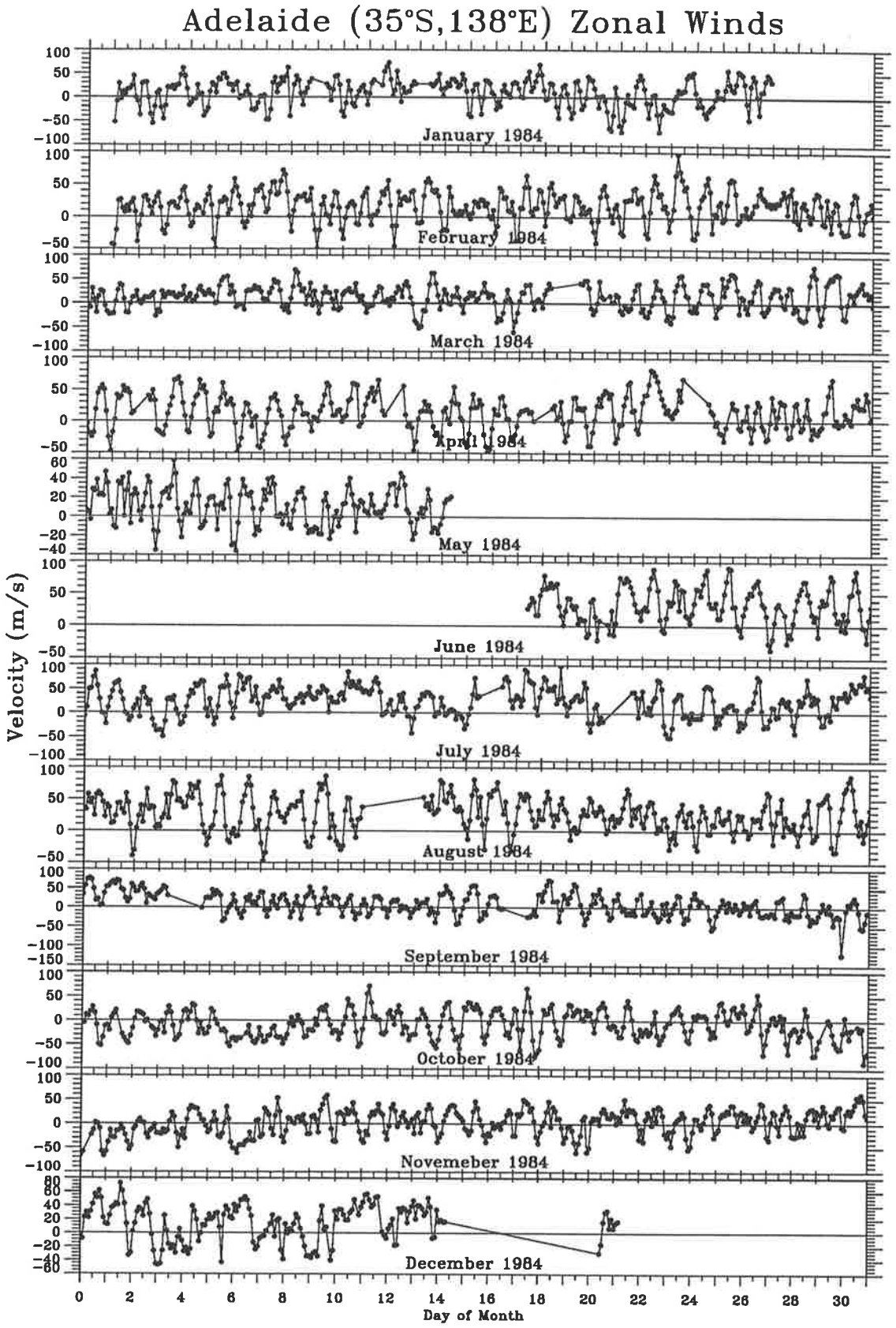

Figure F.1: Raw zonal winds at 86 km for 1984

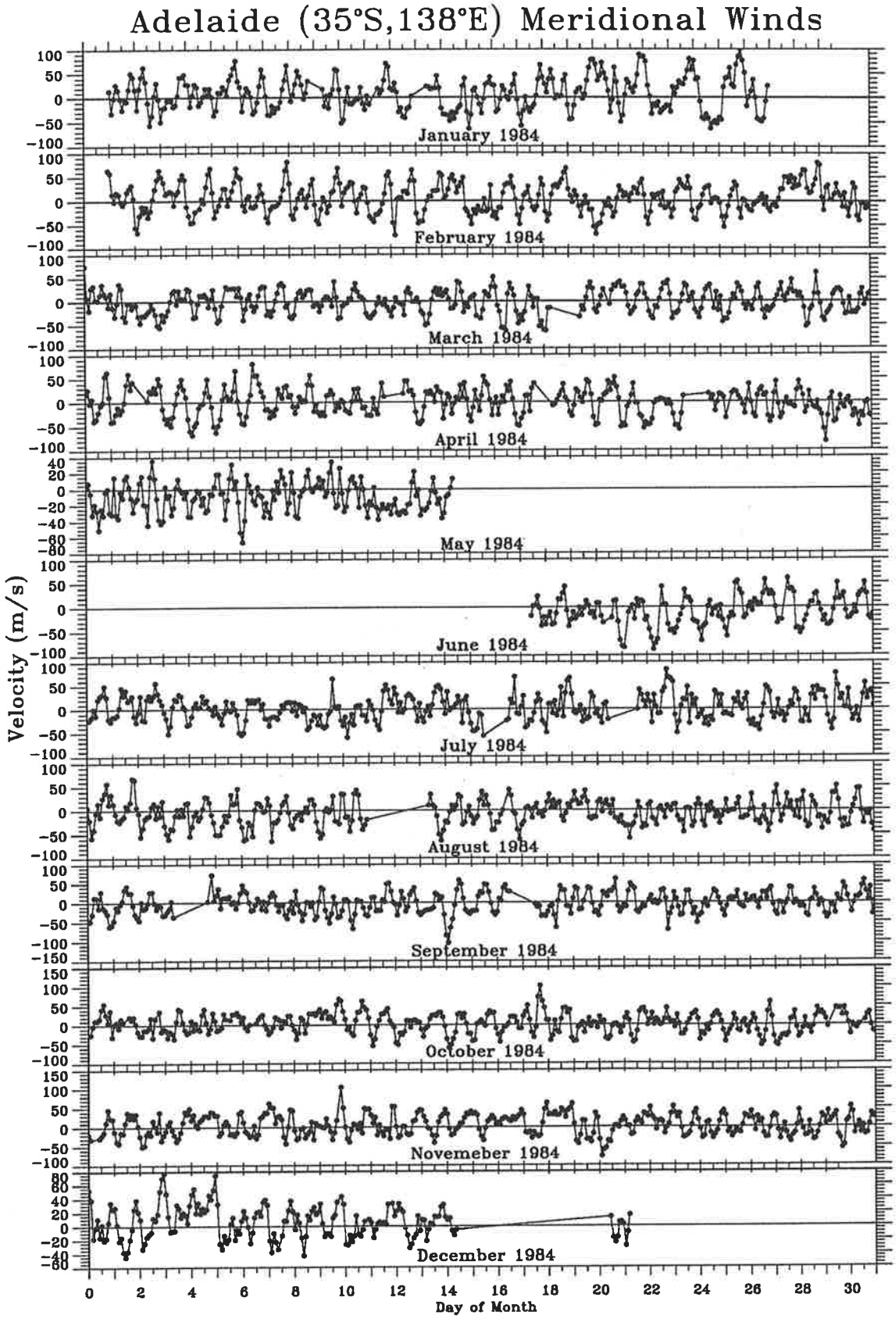

Figure F.2: Raw meridional winds at 86 km for 1984

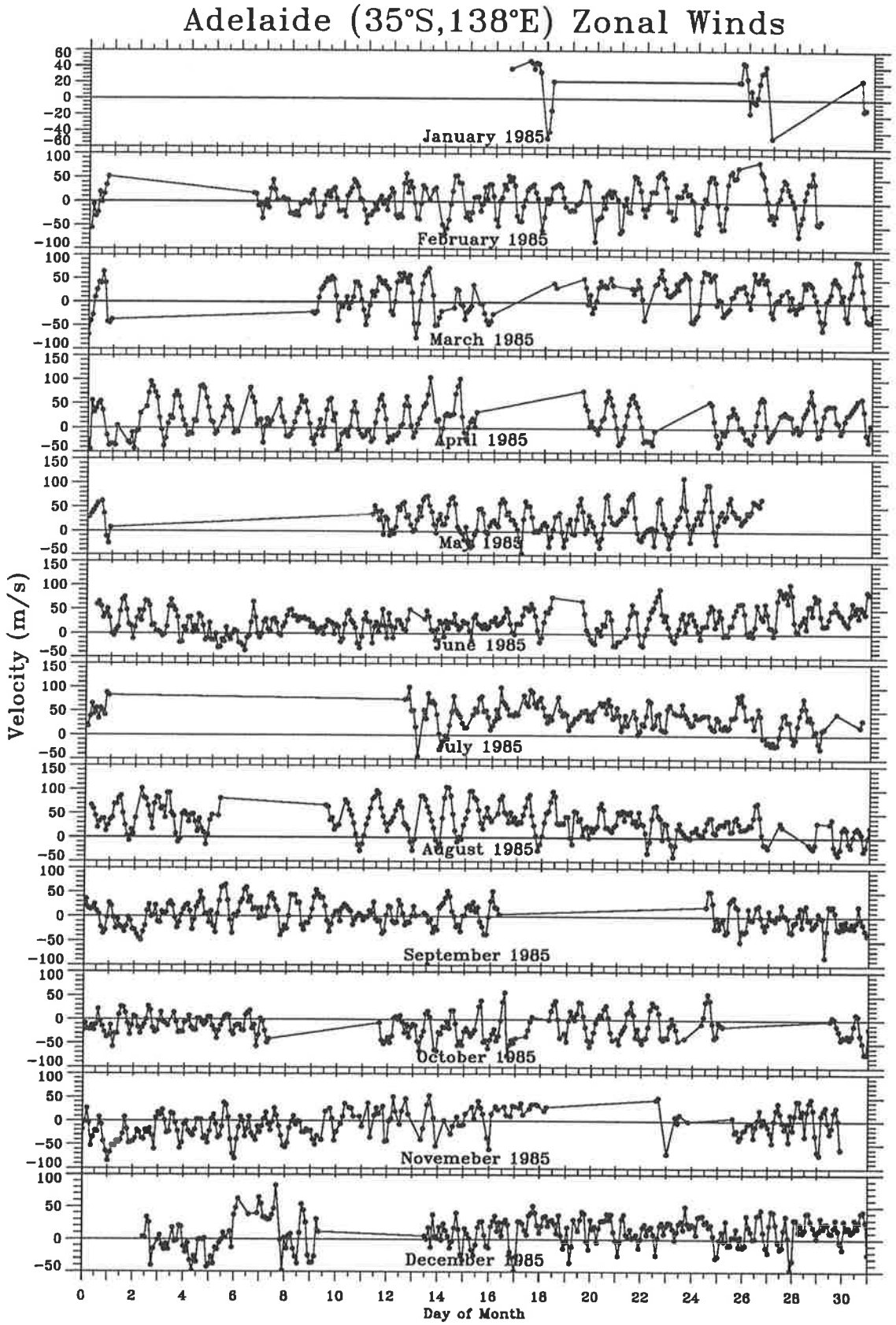

Figure F.3: Raw zonal winds at 86 km for 1985

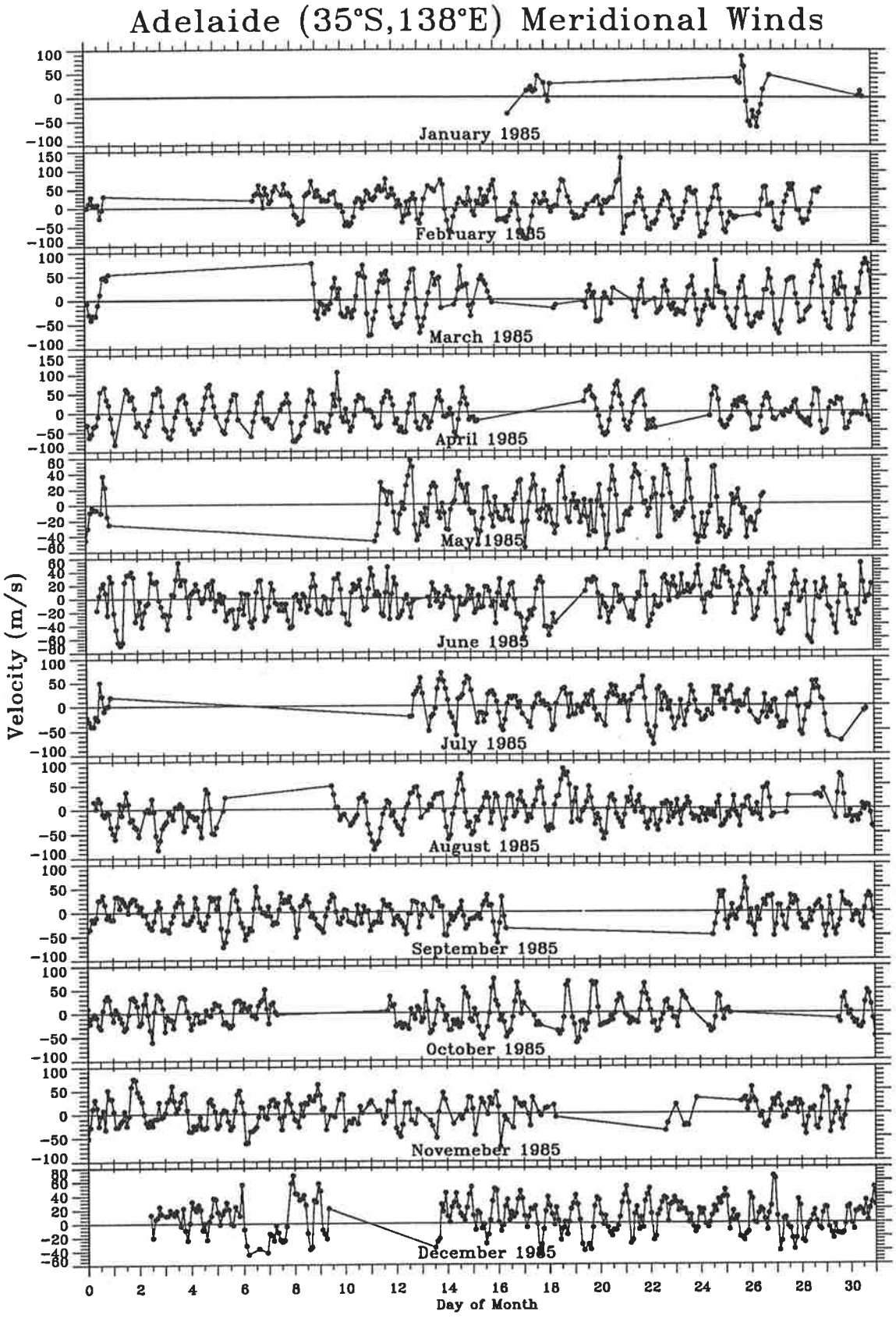

Figure F.4: Raw meridional winds at 86 km for 1985

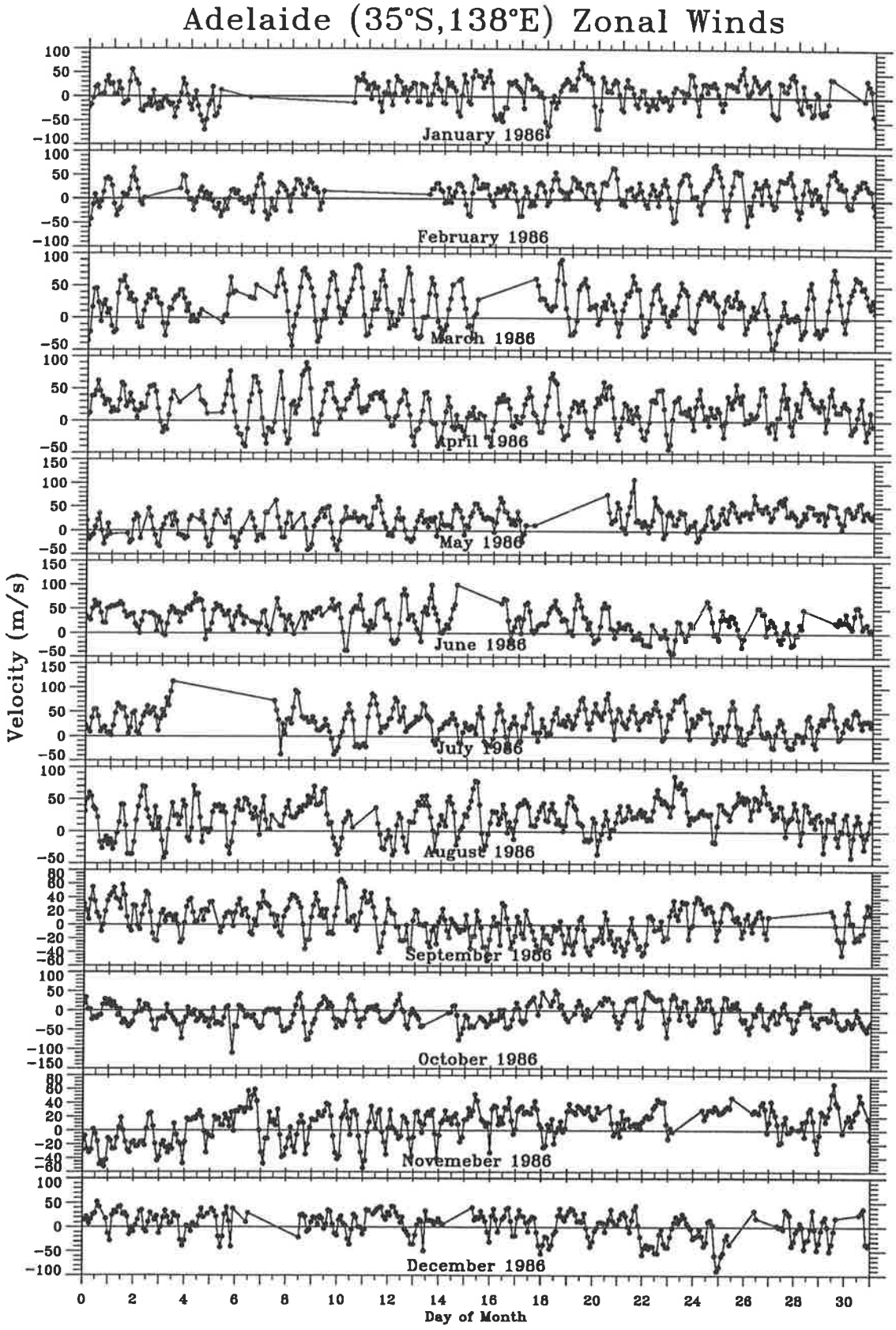

Figure F.5: Raw zonal winds at 86 km for 1986

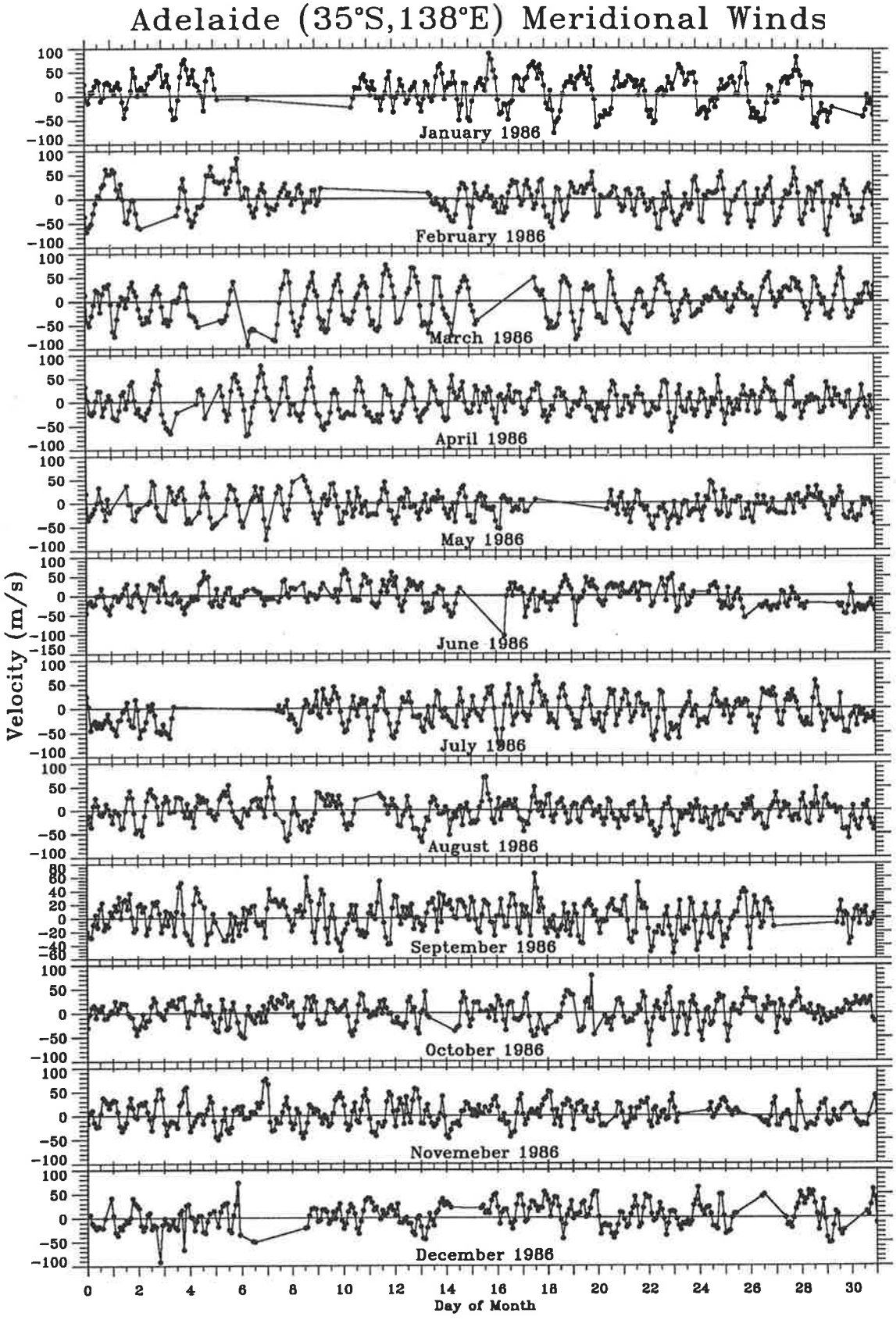

Figure F.6: Raw meridional winds at 86 km for 1986

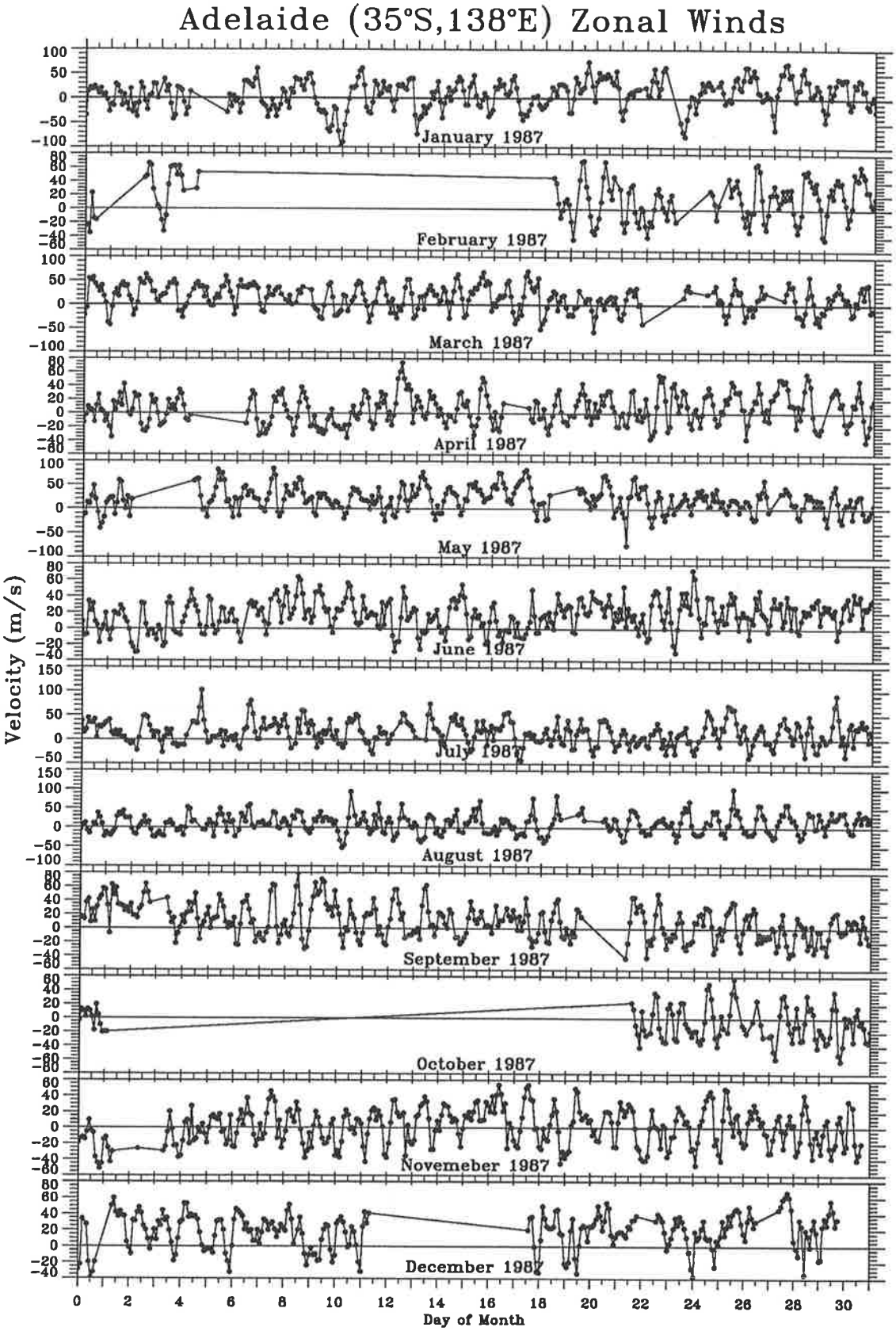

Figure F.7: Raw zonal winds at 86 km for 1987

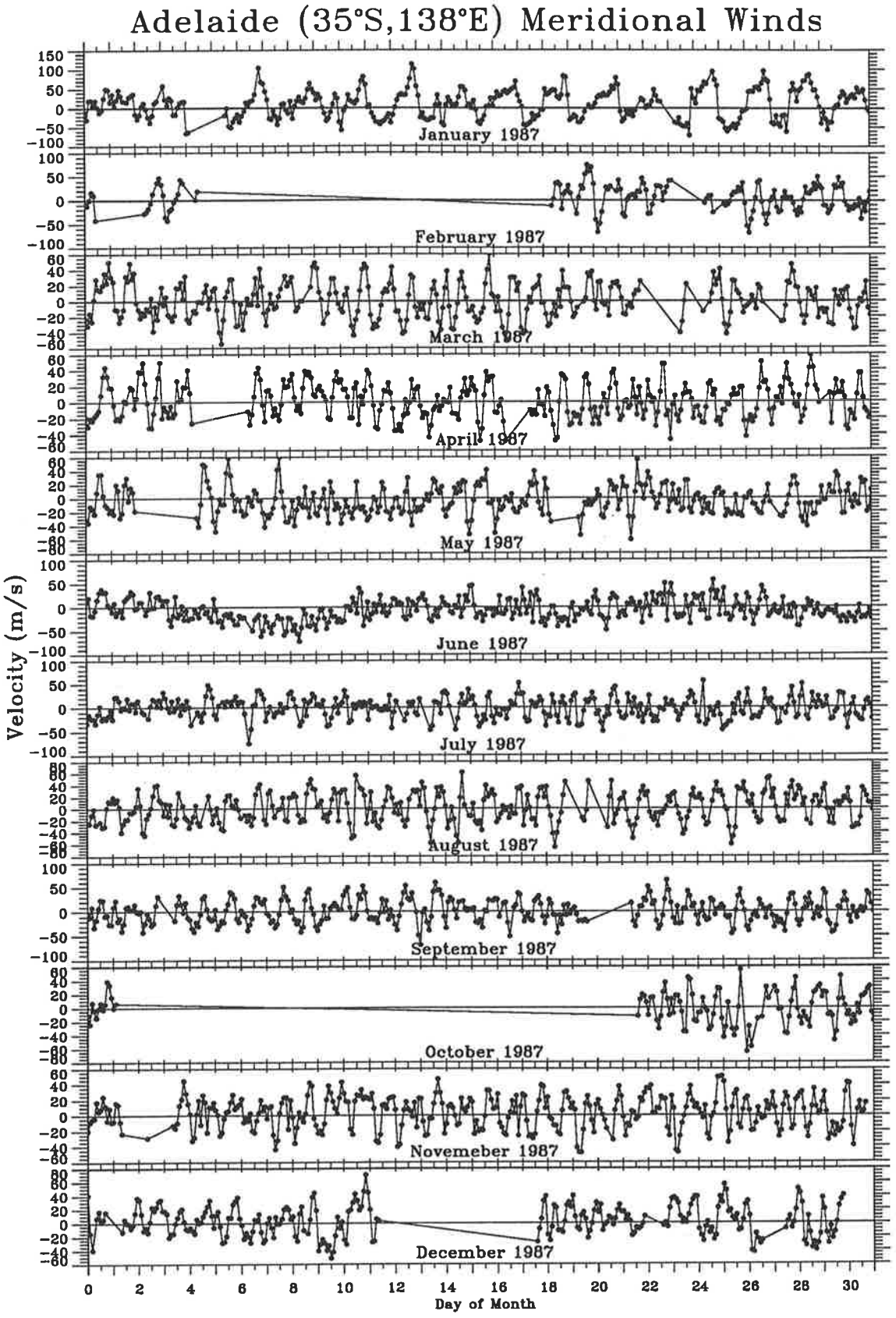

Figure F.8: Raw meridional winds at 86 km for 1987

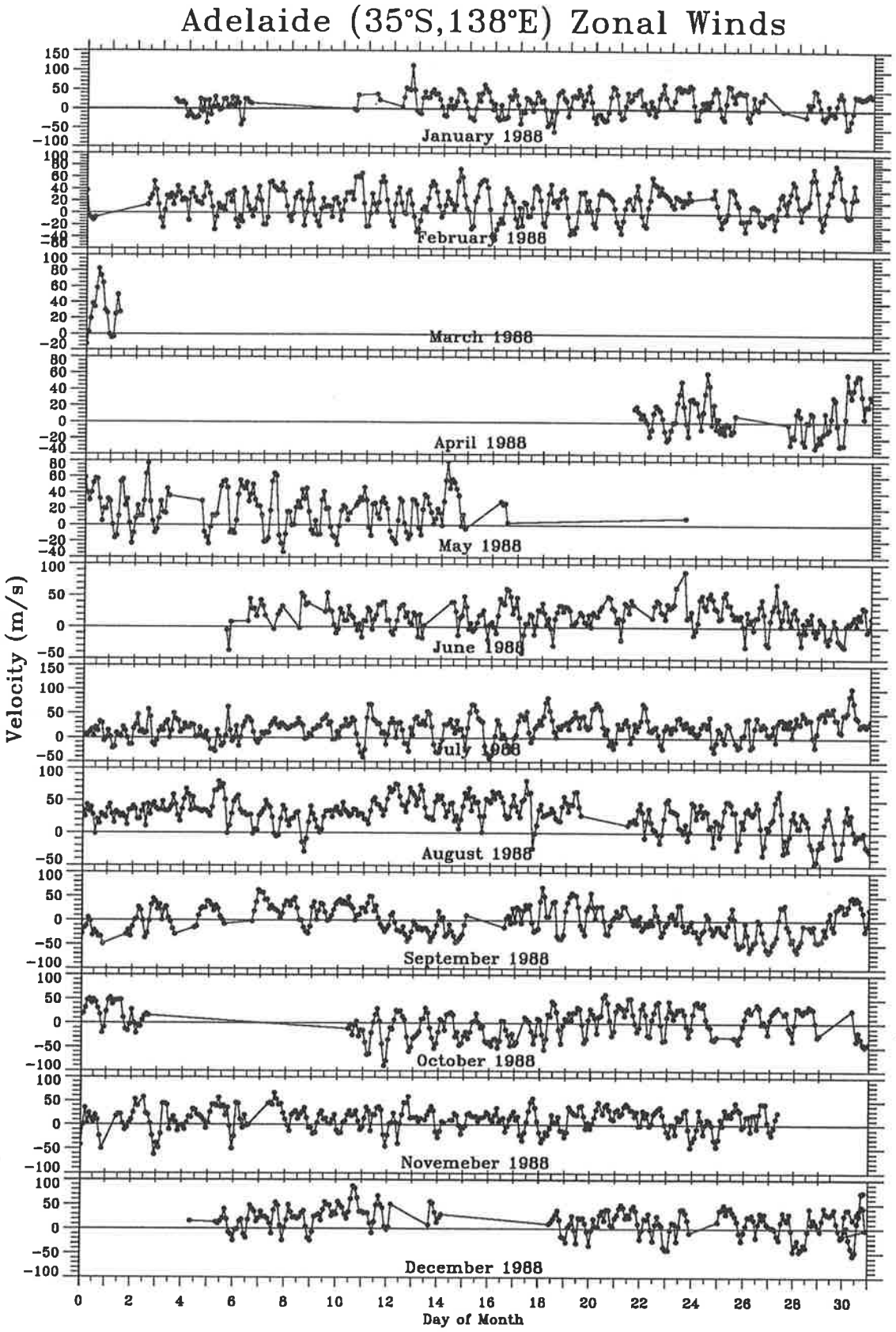

Figure F.9: Raw zonal winds at 86 km for 1988

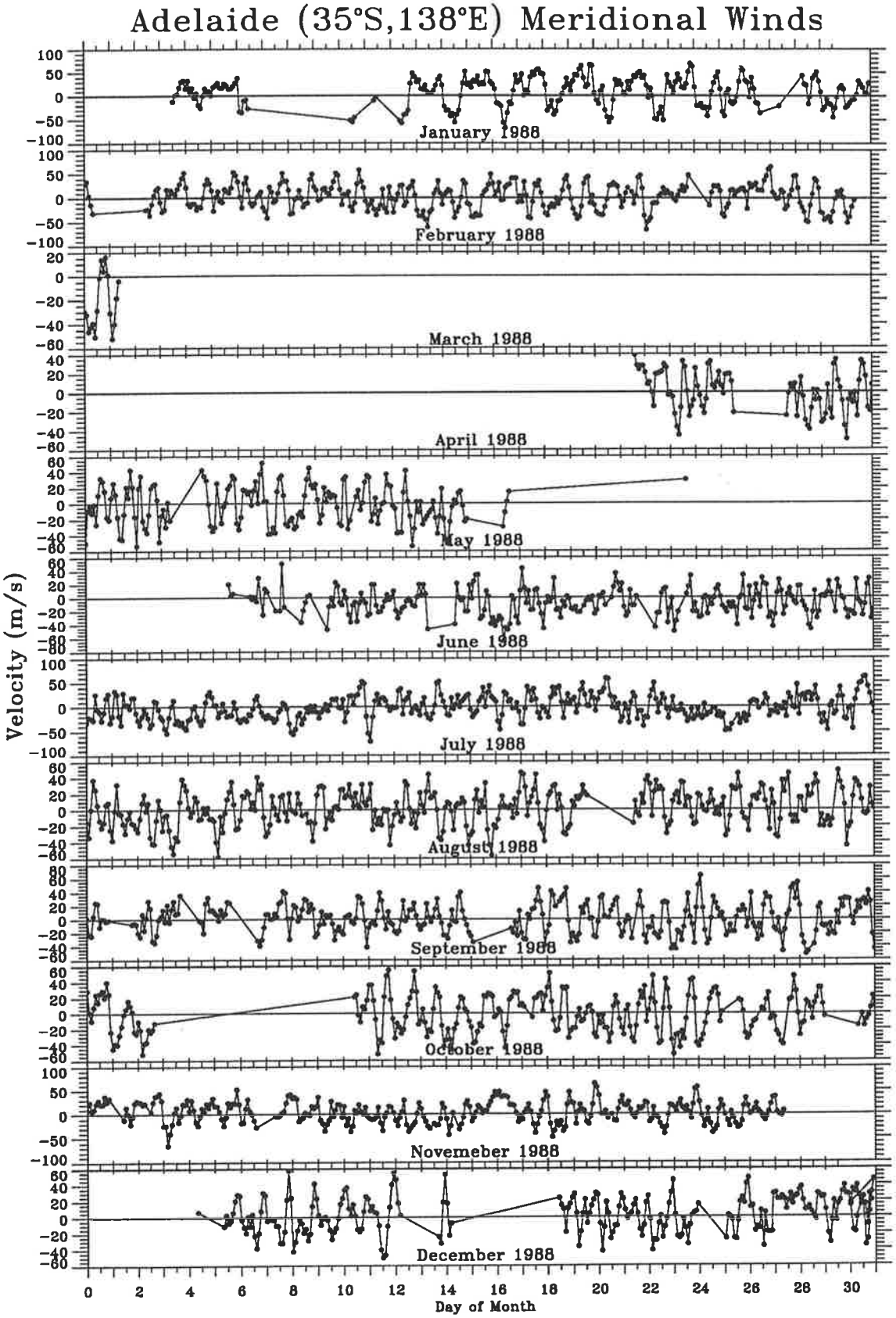

Figure F.10: Raw meridional winds at 86 km for 1988

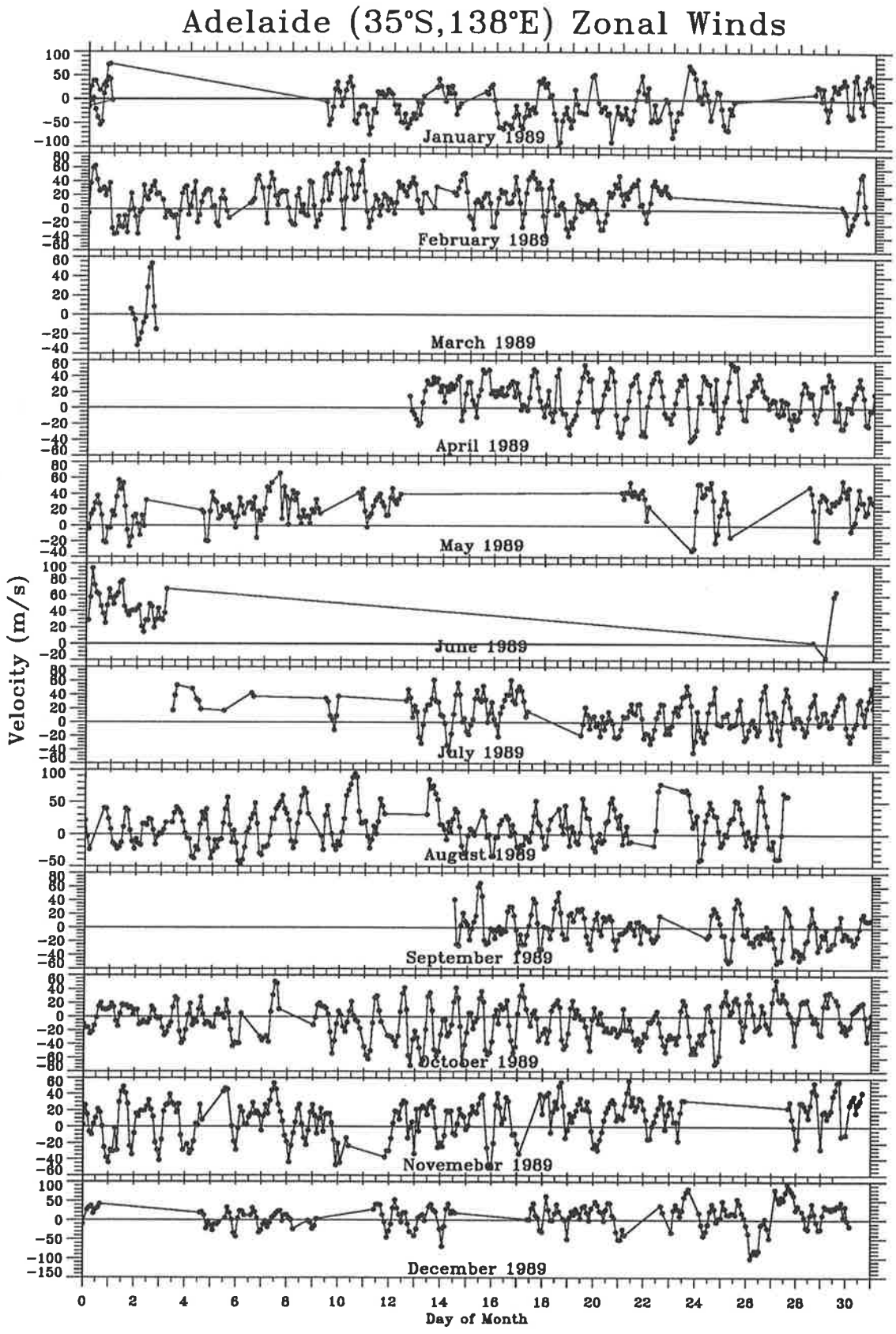

Figure F.11: Raw zonal winds at 86 km for 1989

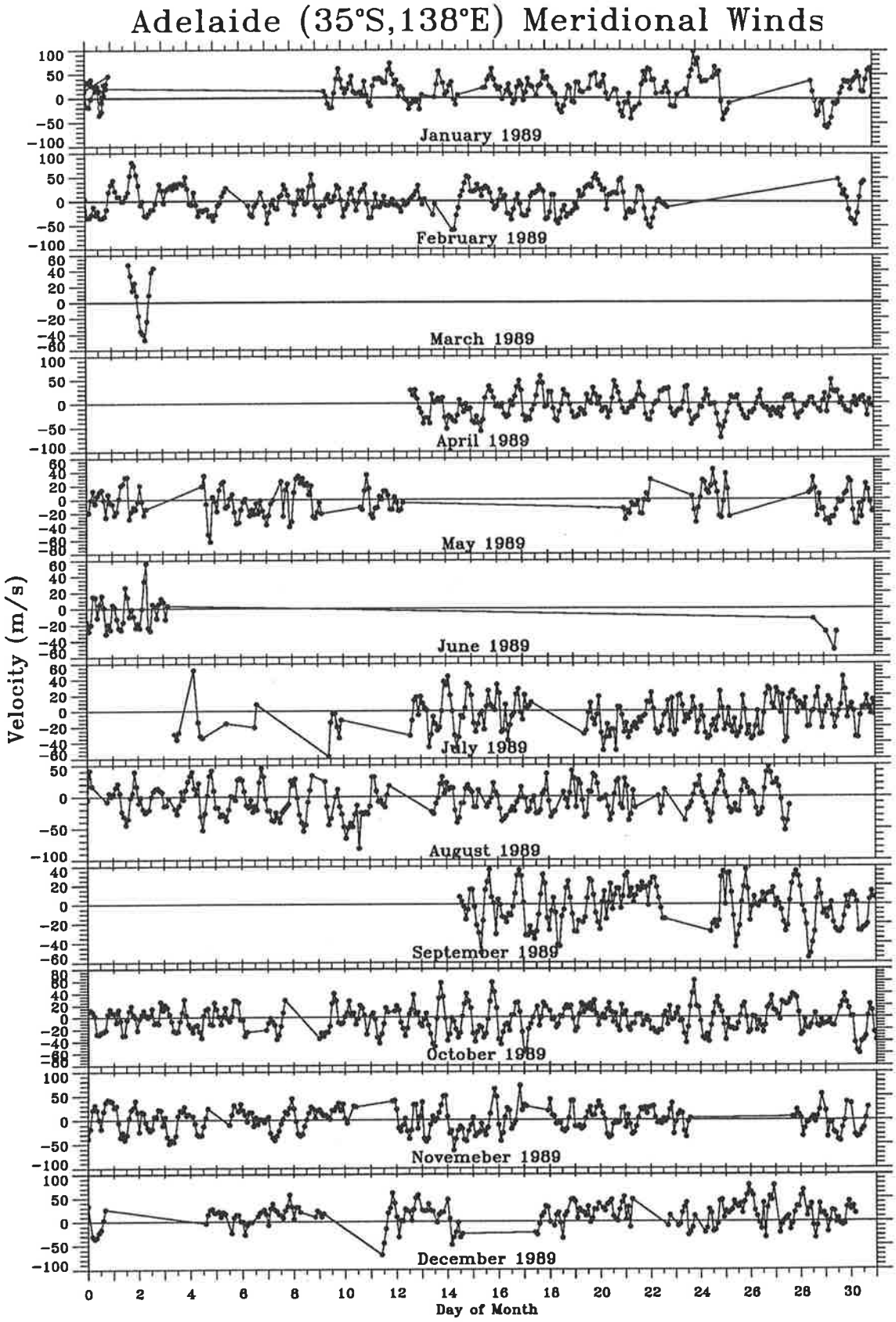

Figure F.12: Raw meridional winds at 86 km for 1989

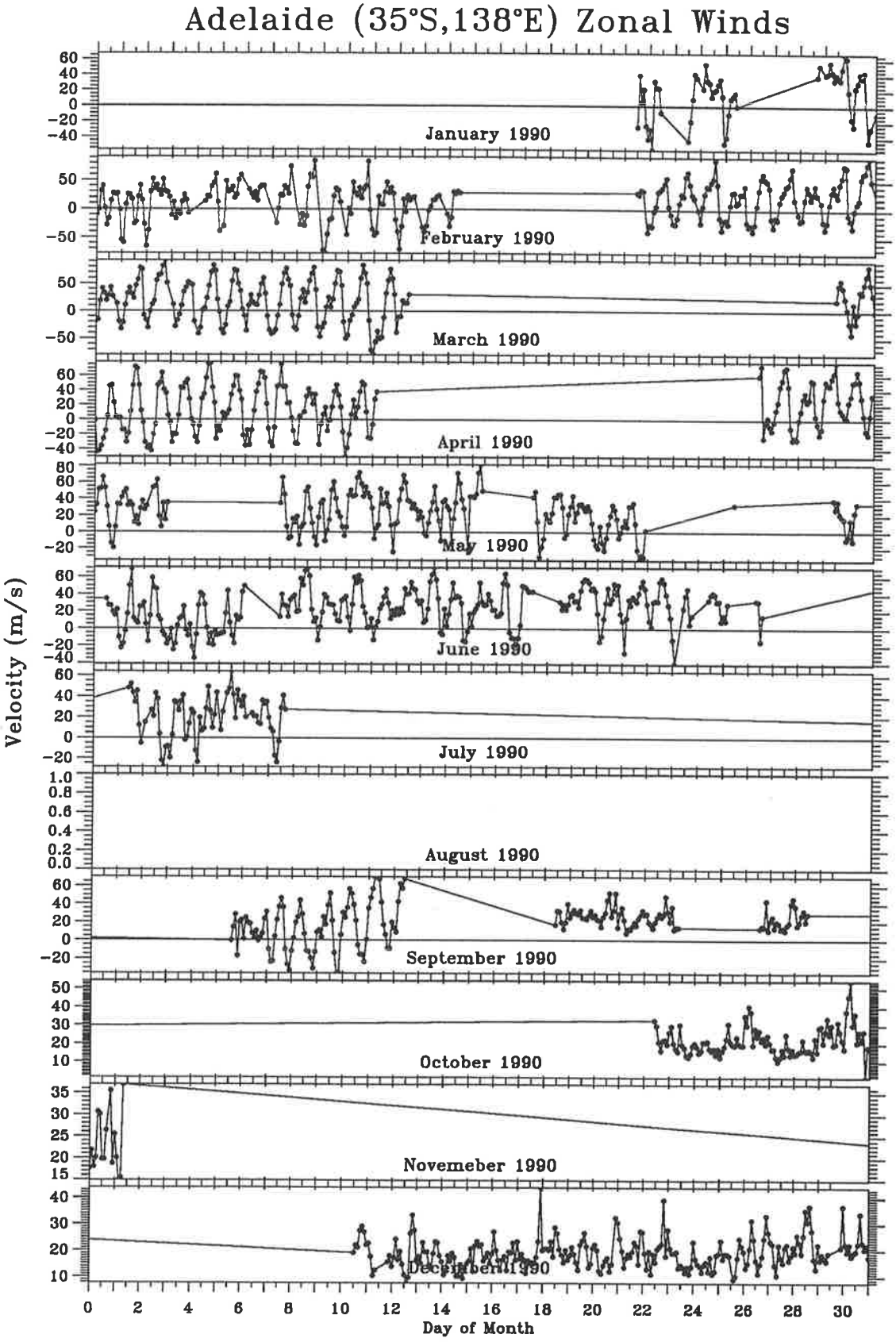

Figure F.13: Raw zonal winds at 86 km for 1990

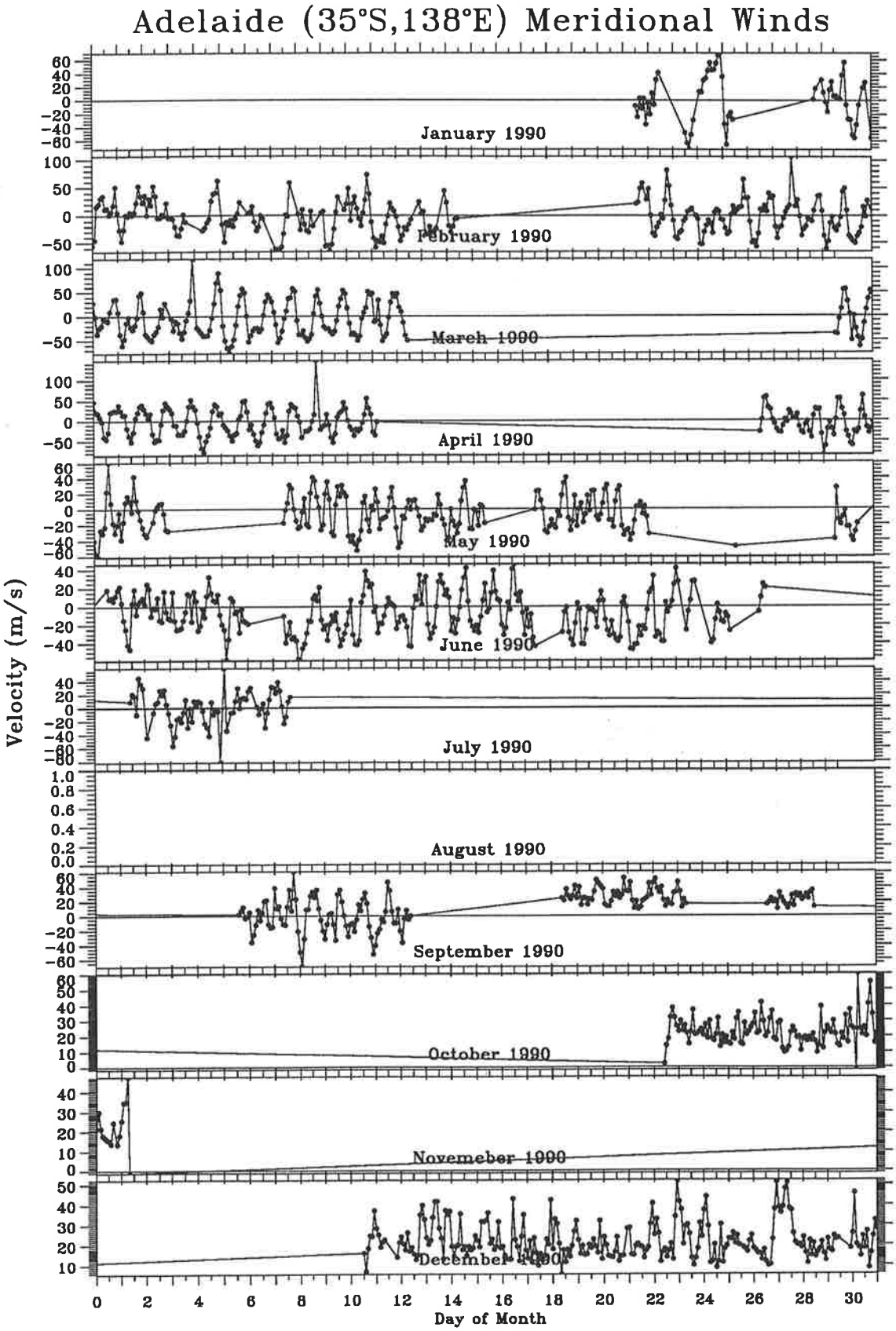

Figure F.14: Raw meridional winds at 86 km for 1990

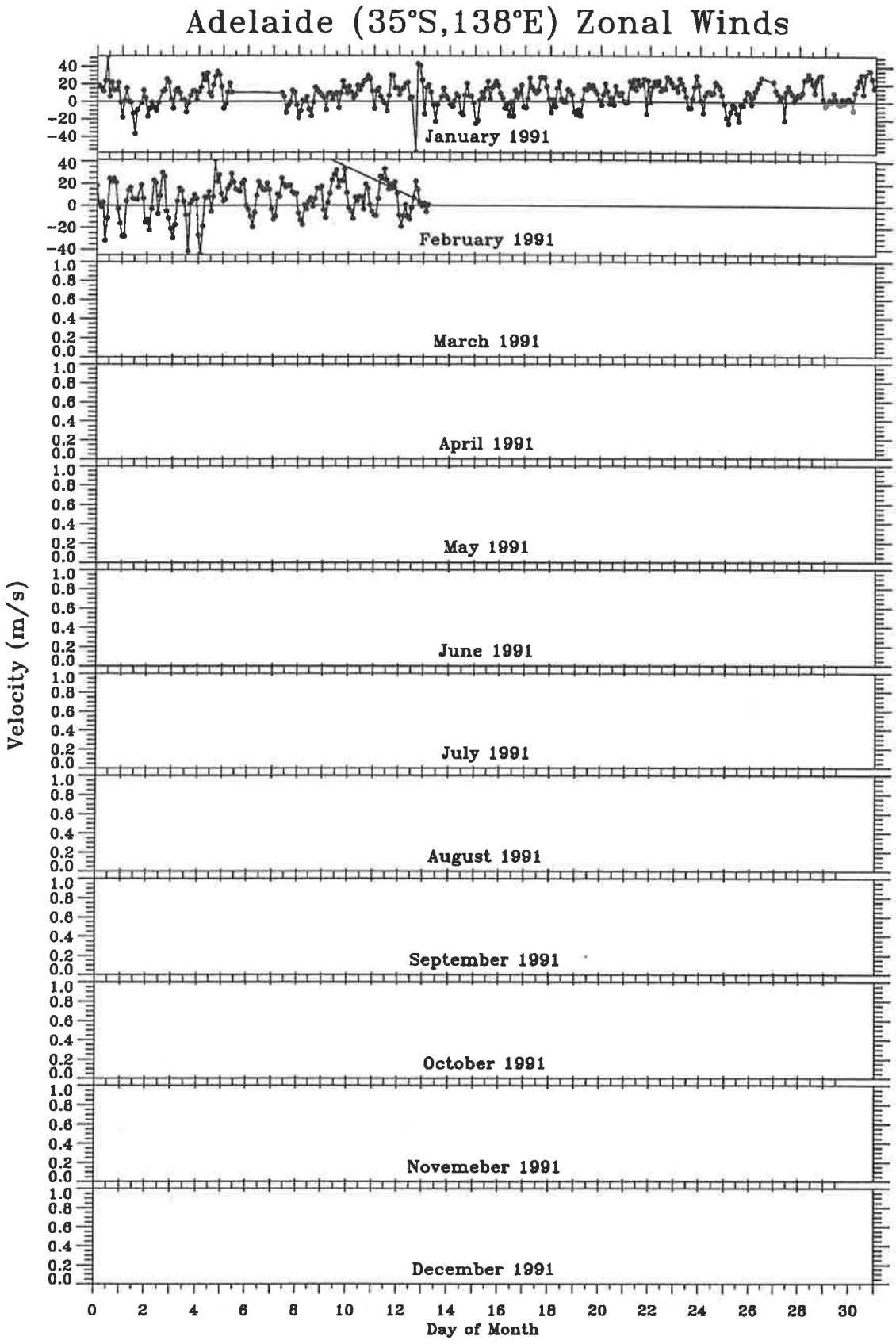

Figure F.15: Raw zonal winds at 86 km for 1991

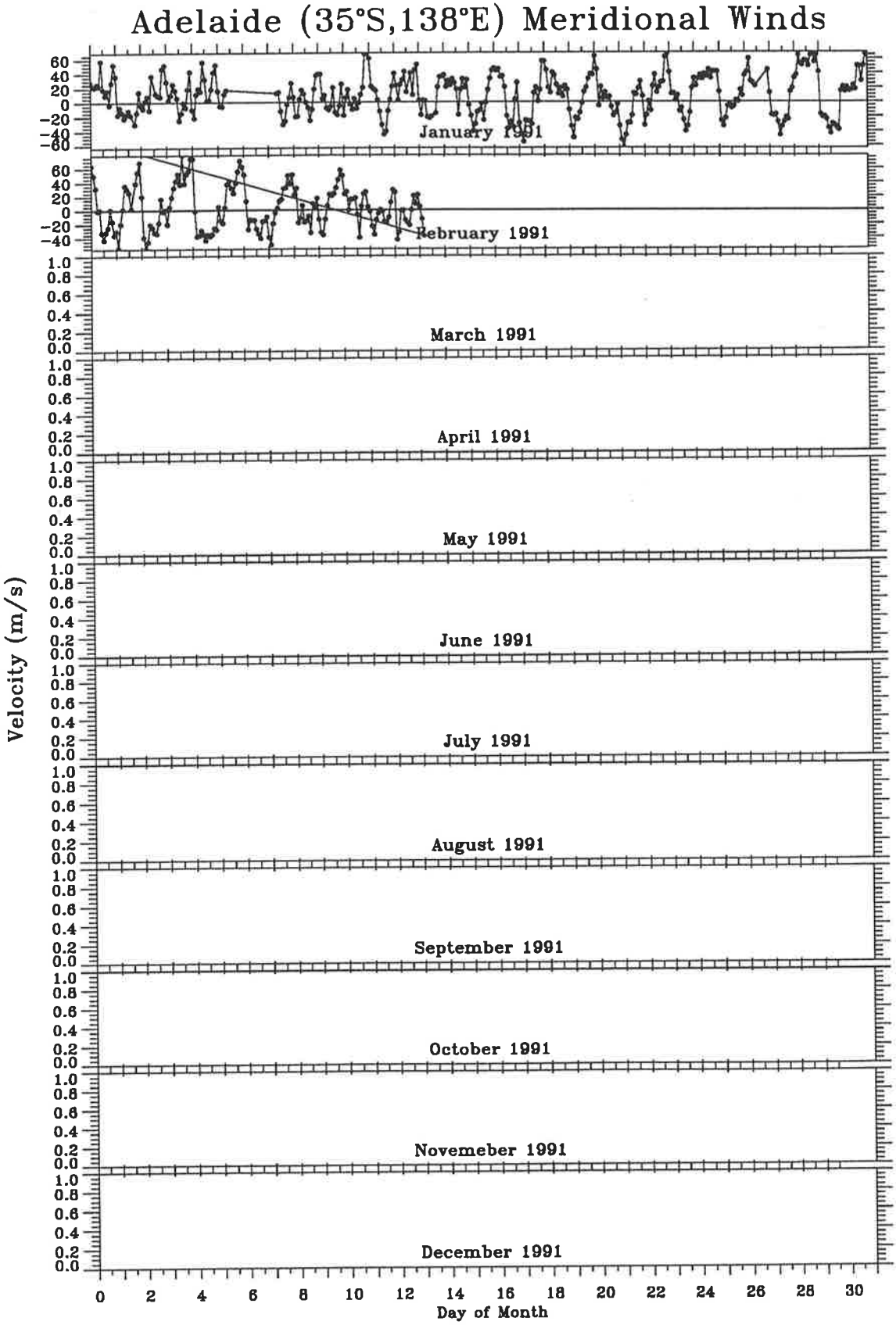

Figure F.16: Raw meridional winds at 86 km for 1991

Appendix G

Raw Winds at 86 km over Christmas Is., 1990 – 1992

On the following pages are shown the winds at 86 km derived from spaced-antenna and FCA for Christmas Island (2° N, 157° W). These are part of the unaveraged full wind records used within this thesis.

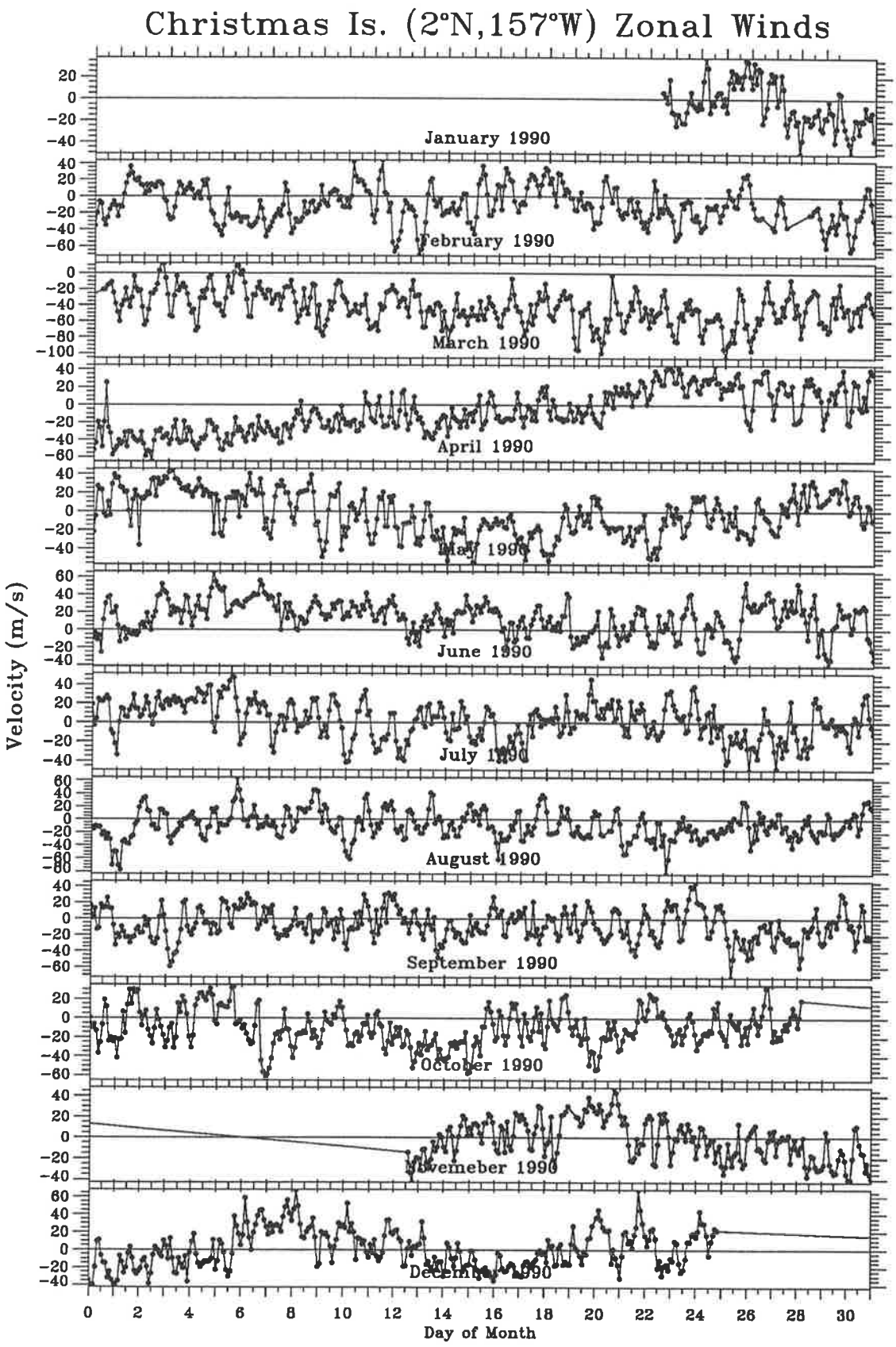

Figure G.1: Raw zonal winds at 86 km for 1990

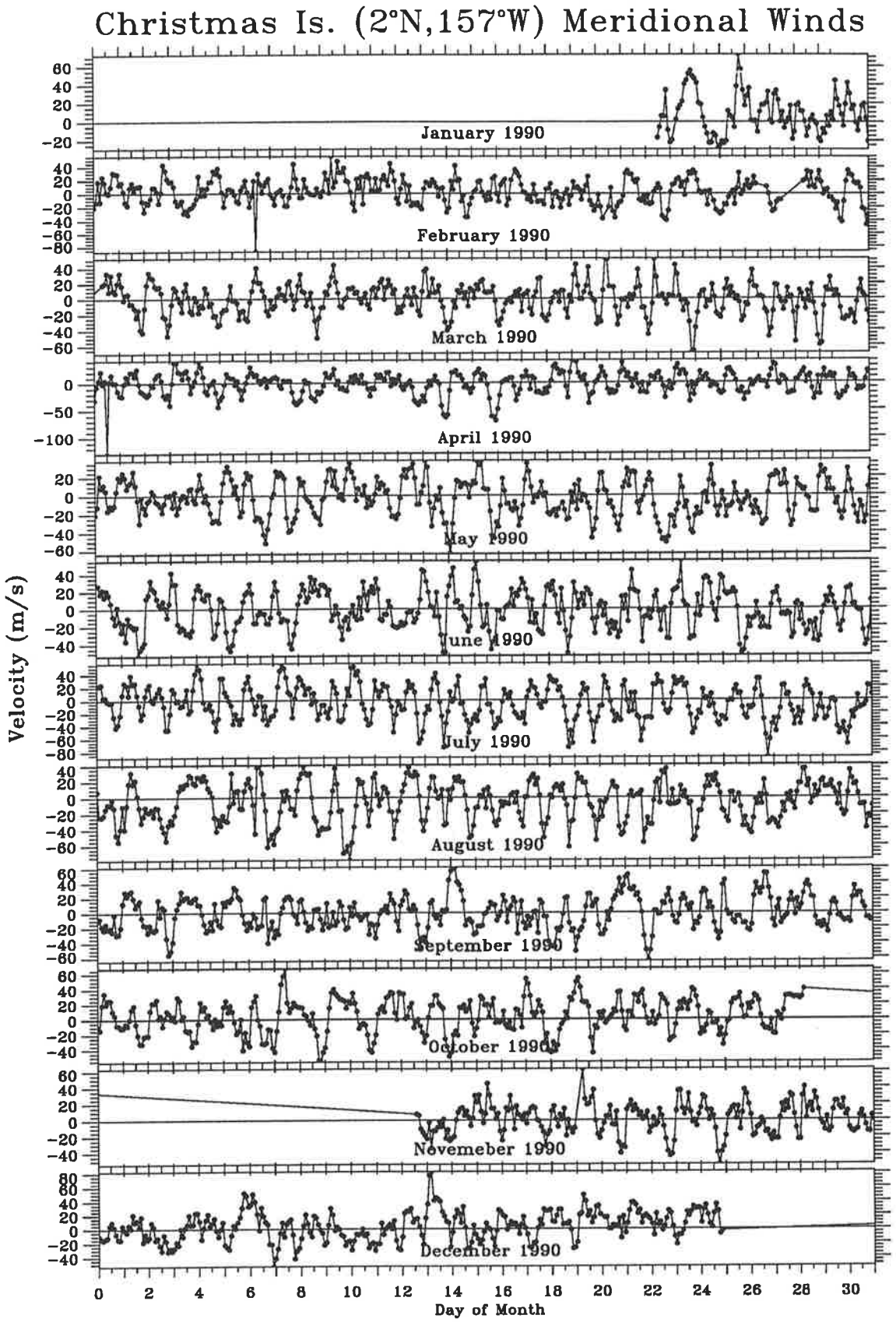

Figure G.2: Raw meridional winds at 86 km for 1990

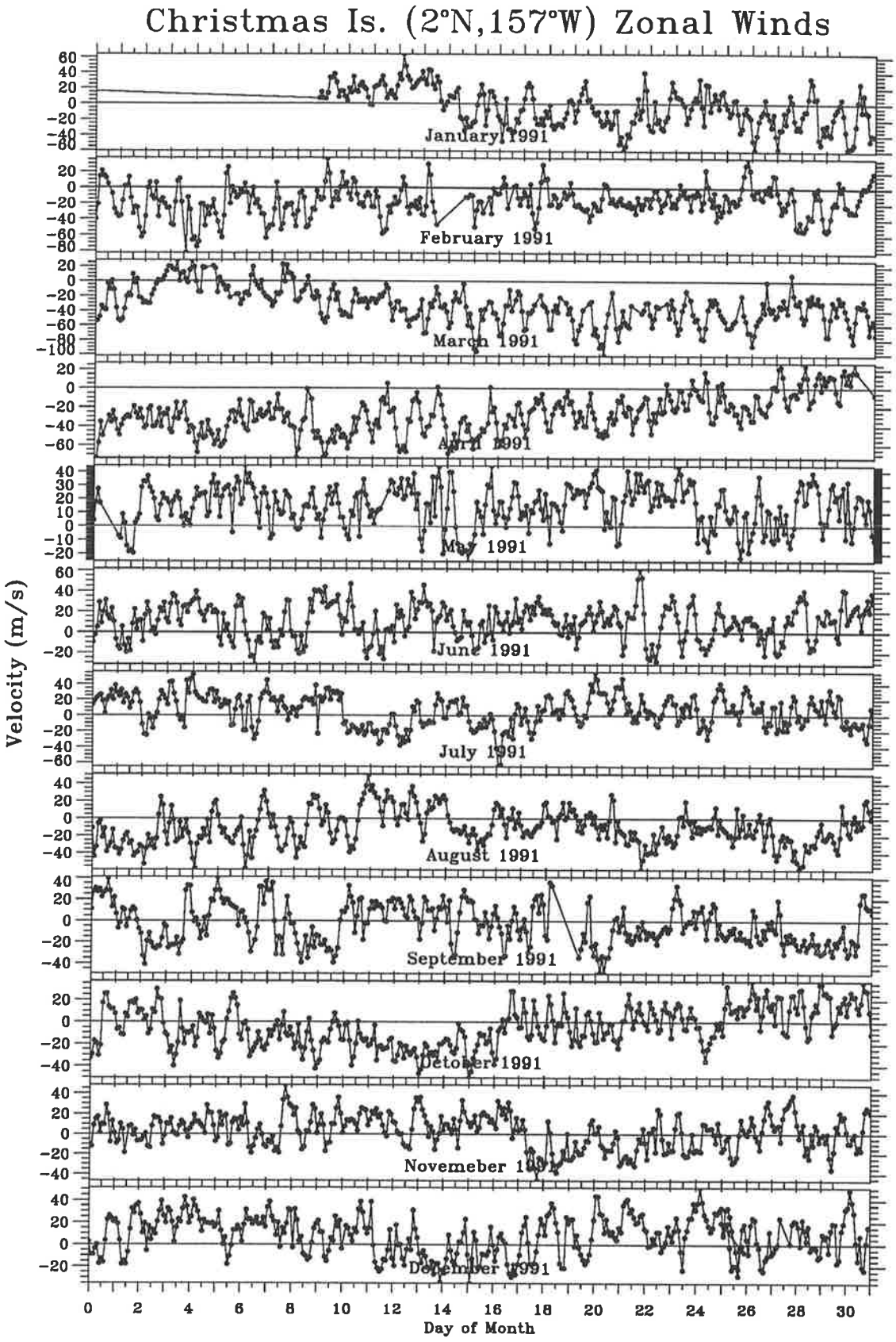

Figure G.3: Raw zonal winds at 86 km for 1991

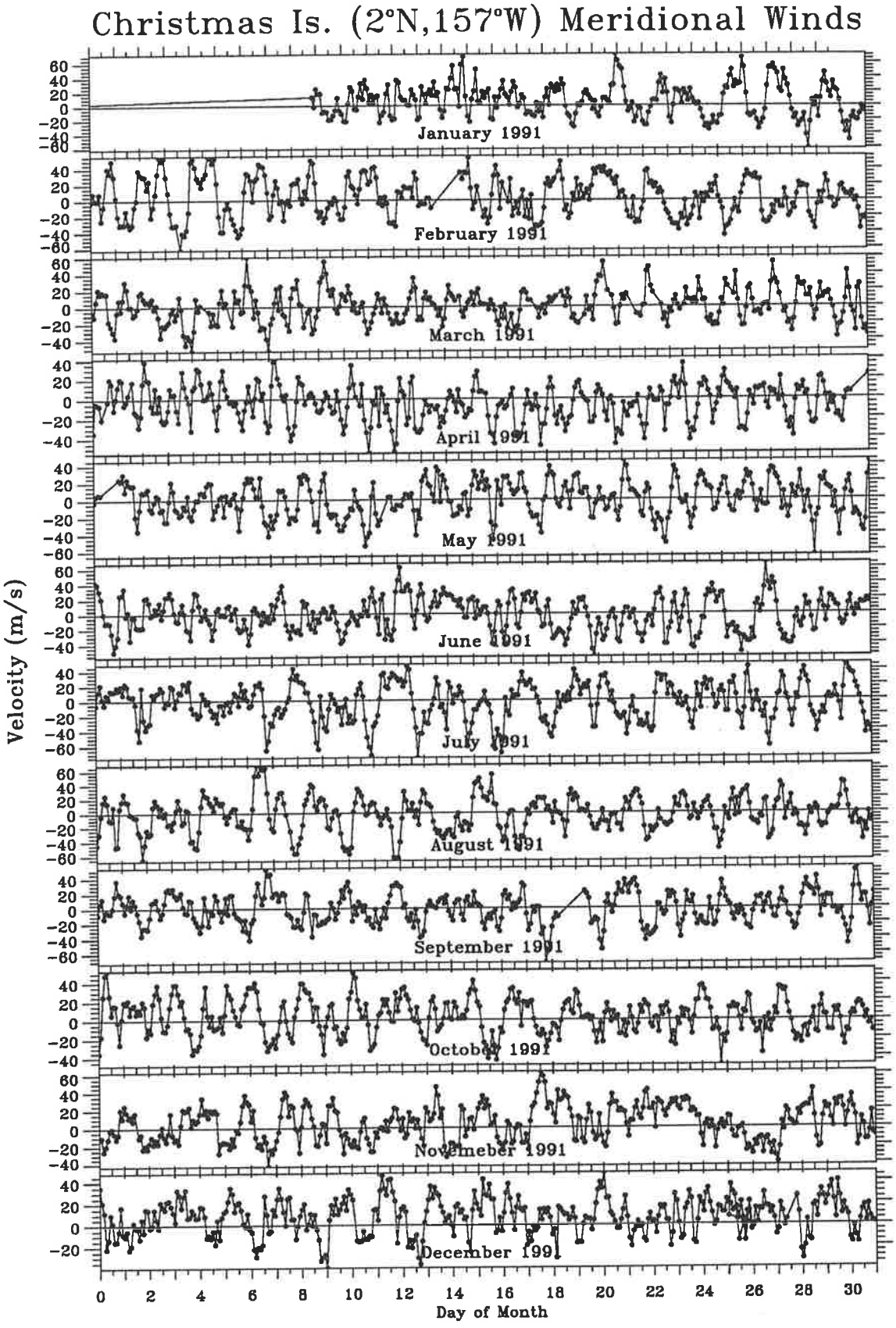

Figure G.4: Raw meridional winds at 86 km for 1991

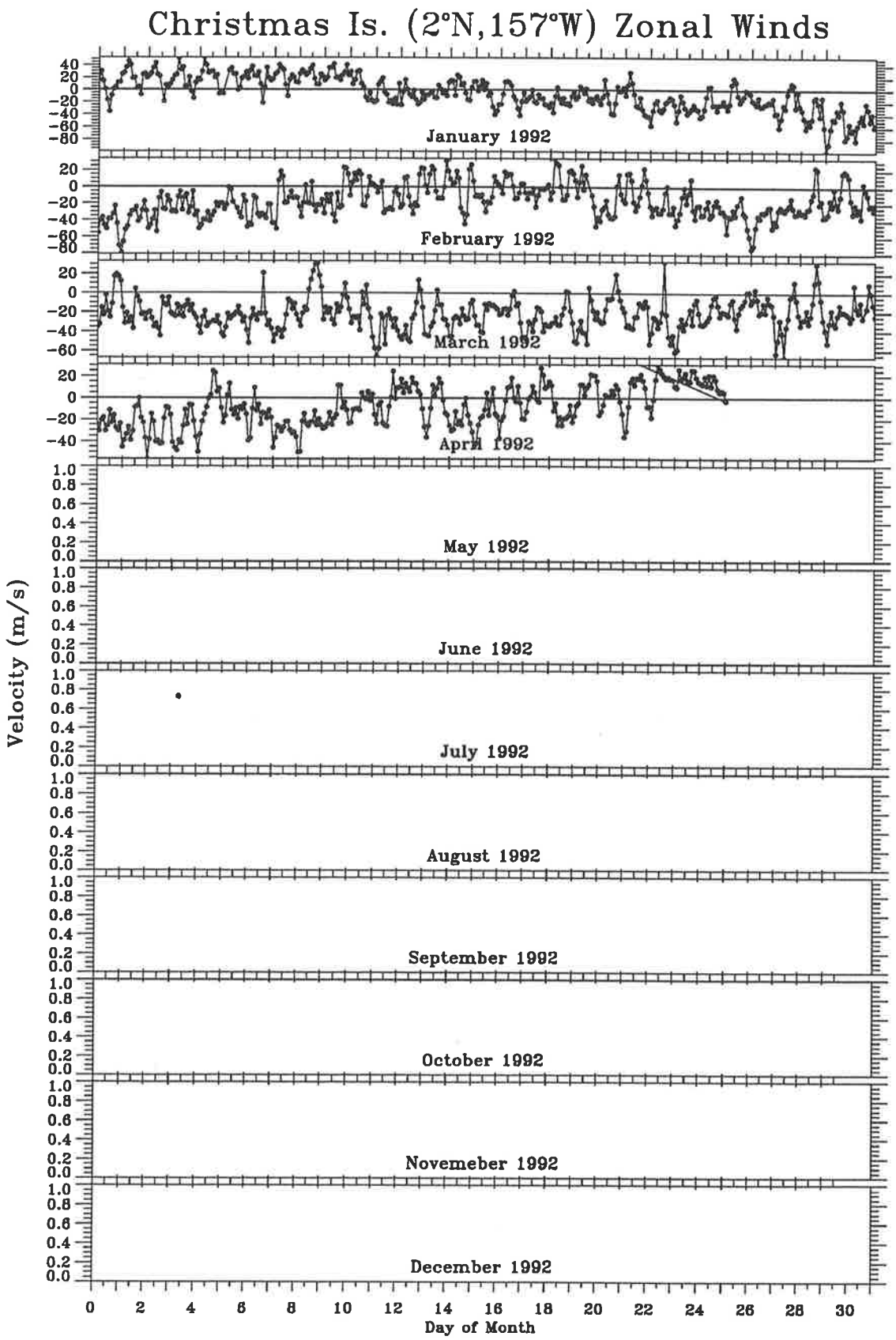

Figure G.5: Raw zonal winds at 86 km for 1992

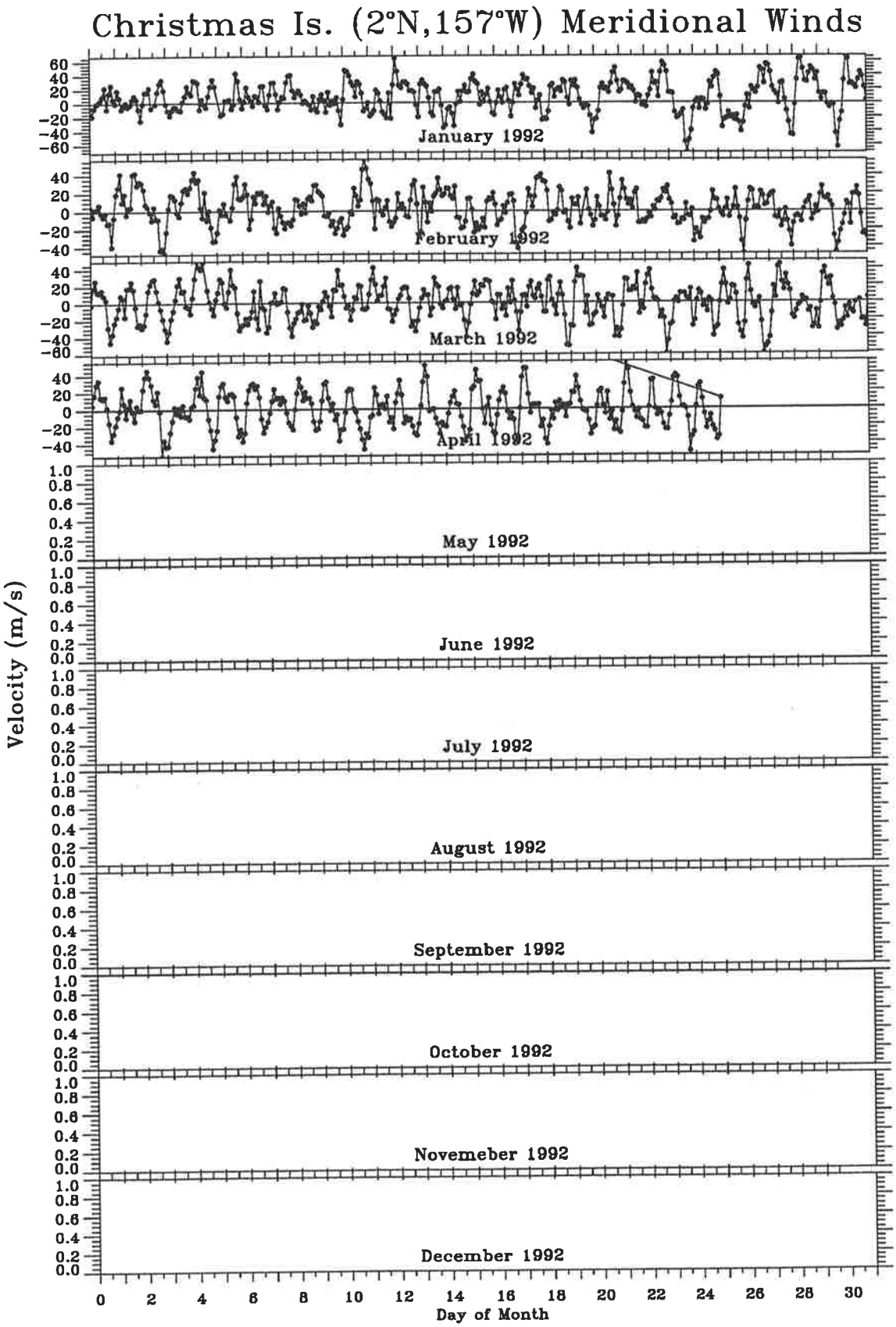

Figure G.6: Raw meridional winds at 86 km for 1992

Appendix H

A Long-Term Study of the Quasi-Two-Day Wave in the Middle Atmosphere

This is a reprint of the paper,

Harris, T. J. (1993), 'A long-term study of the quasi-two-day wave in the middle atmosphere', *Journal of Atmospheric and Terrestrial Physics.* (In Press).

Harris, T.J. (1993) A long-term study of the quasi-two-day wave in the middle atmosphere.
Journal of Atmospheric and Terrestrial Physics, v. 56(5), pp. 569-579

Appendix I

The Quasi-Two-Day Wave Observed in the Equatorial Middle Atmosphere

This is a reprint of the paper,

Harris, T. J. & Vincent, R. A. (1993), 'The quasi-two-day wave observed in the equatorial middle atmosphere', *Journal of Geophysical Research* **98**, 10481–10490.

JOURNAL OF GEOPHYSICAL RESEARCH, VOL. 98, NO. D6, PAGES 10,481–10,490, JUNE 20, 1993

The Quasi-Two-Day Wave Observed in the Equatorial Middle Atmosphere

T.J. HARRIS AND R.A. VINCENT

Department of Physics and Mathematical Physics, University of Adelaide, Adelaide, Australia

An oscillation with a period near 2 days is found in radar wind measurements made in the upper mesosphere and lower thermosphere at Christmas Island (2° N, 157° W) in the central Pacific. The oscillation is particularly strong in the meridional wind component, and seems to be present almost continuously in the 80-100 km height region, although some intermittency is evident. Wave amplitudes are especially large about one month after the solstices, in July/August and in January/February, at times coincident with large 2-day wave events in the summer mesosphere at extratropical latitudes. Power spectral and complex demodulation techniques are used to study the amplitude and frequency variations of the oscillation as a function of height and time. Downward phase propagation is found, consistent with upward energy propagation, and with a vertical wavelength of about 70 km. An unusual feature is a shift in wave period from near 50 hours in July/August to 48 hours in January/February, when the largest amplitudes (up to 45 m s^{-1}) are observed. A 16-hour oscillation is also found at times when the 2-day wave amplitudes are largest. The observations are consistent with the 2-day wave being a manifestation of the (3, 0) Rossby-gravity normal mode. Another, weaker oscillation, is also found in the meridional wind field at a period near 44 hours. This oscillation may be due to the (2, 0) normal mode.

INTRODUCTION

Long-period waves have been observed in the middle atmosphere over many years. Of particular interest to the present study are observations of a quasi-two-day wave in the upper middle atmosphere. Early observations of this feature were made with meteor wind radars located in both the mid-latitude southern [*Craig and Elford,* 1981] and northern hemispheres [*Muller and Nelson,* 1978]. Numerous studies from single sites have been made in more recent times using both meteor and MF radars [*Clark,* 1989; *Manson and Meek,* 1990; *Poole,* 1990]. Observations of the quasi-two-day wave were also extended to high-latitudes [*Phillips,* 1989]. Satellite measurements have also been reported [*Rodgers and Prata,* 1981].

From these studies it is known that the quasi-two-day wave (hereinafter referred to as the 2-day wave) at mid- to high-latitudes reaches its peak about one month after the solstice in the summer hemisphere. The satellite observations and longitudinally spaced radar comparisons suggest that the wave is westward propagating, and has a zonal wavenumber of three [e.g., *Rodgers and Prata,* 1981]. Hemispheric differences are also apparent. Amplitudes are larger in the southern hemisphere, being up to a factor of two larger than those found in the northern hemisphere. The amplitudes can be large enough on occasion at Adelaide (35° S, 138° E) that the wave appears to have a significant impact on the prevailing circulation at the southern hemisphere mesopause [*Plumb et al.,* 1987]. Another hemispheric difference that has been noticed is a tendency for the wave period to have a value greater than 50 hours in the northern hemisphere, but a period which is often indistinguishable from 48 hours in the southern hemisphere [*Muller and Nelson,* 1978; *Craig and Elford,* 1981; *Tsuda et al.,* 1988; *Poole,* 1990]. In the southern hemisphere there are also suggestions of a locking of the phase with local time [*Craig and Elford,* 1981; *Poole,* 1990].

Further observations are required in order to resolve questions about the generating mechanism as well as to understand better the role of the wave in the middle atmosphere. Reviews of the phenomenon [*Walterscheid,* 1980; *Salby,* 1984; *Vincent,* 1984] have pointed to the need for further observations at equatorial latitudes, where the small number of previous observations have found evidence of the 2-day wave [*Coy,* 1979; *Kalchenko,* 1987]. Strong 2-day oscillations have been found in mesospheric winds measured with MF radars recently established at equatorial and tropical locations [*Vincent and Lesicar,* 1991; *Fritts and Isler,* 1992]. Here we present a study of the temporal and vertical structure of the 2-day wave observed at one of these sites, Christmas Island (2° N, 157° W), in the central Pacific.

OBSERVATIONS

Mesospheric wind observations made with an MF spaced antenna radar commenced on Christmas Island in January 1990 [*Vincent and Lesicar,* 1991]. The radar operates at 1.98 MHz and takes measurements every 2 min at 2 km height intervals, with both wind components being measured simultaneously. The height range from 60 to 98 km is covered during the day and from 70 to 98 km at night, although the lack of sufficient ionization restricts the lower height of useful measurements to ~78-80 km at night. The raw data are analysed in real time by a dedicated computer and the winds information is stored on disk for later off-line analysis.

Here we discuss winds measurements made from January 1990 to April 1992. In this interval the system ran continuously, although data were lost for two 14-day intervals (from October 28 to November 12, 1990, and from December 24, 1990 to January 8, 1991) when the storage disk accidentally overflowed. Because data are obtained for the full 24 hours at heights above 78 km we restrict our discussion to observations made above this height. Since we are here only interested in long-period phenomena we used data averaged over 2 hours in the following analysis. This gives time series of winds at every height from 80 to 98 km at 2 km intervals.

Power Spectra

A convenient way to summarize the frequency distribution of variance in the wind field is to use power spectra. Since we are also concerned with temporal variations, moving power spectra are used to explore the seasonal changes in energy distribution. A short time segment (or window) of data was taken and the power spectrum calculated using a discrete

Paper number 93JD00380
0148-0227/93/93JD-00380$05.00

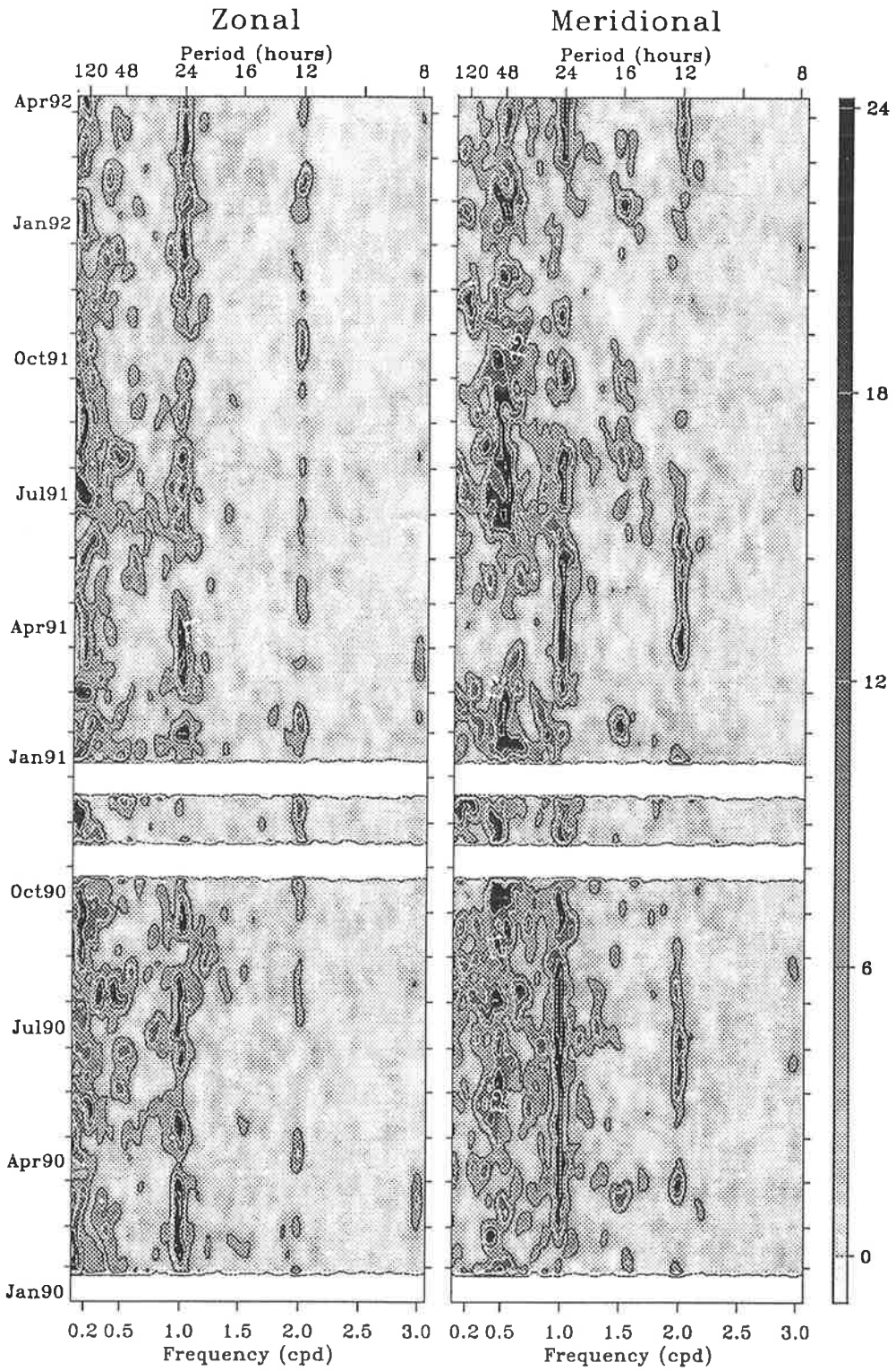

Fig. 1. Moving power spectra for the zonal (left) and meridional (right) winds measured at an altitude of 86 km over Chistmas Island (2° N,157° W). A discrete Fourier transform and a 14-day sliding window have been used. The tick marks on the time axis (vertical) mark the start of each month. The color scale indicated on the extreme right-hand-side shows the power spectral density in units of $10^6 m^2\ s^{-2}\ Hz^{-1}$.

Fourier transform. The window was then shifted by some time step and the power spectrum recalculated. By continuing this process we build-up a description of the spectral behavior with time. Using such a moving power spectrum on the long data sets from Christmas Island a number of features of the equatorial wind spectrum are evident. The results for both the zonal and meridional winds at an altitude of 86 km are shown in Figure 1, for periods from 120 hours (0.2 cpd) down to 8 hours (3 cpd). Similar features are found throughout the altitude range from 78 to 98 km, although the precise times of maximum power may vary. The power spectral densities have also been limited or "clipped" to be less than $2.4 \times 10^7 m^2\ s^{-2}\ Hz^{-1}$ in order to reduce the dynamic range for plotting purposes. The white

bands across all frequencies during October 1990, and December 1990, indicate missing data. A window size of 14 days and step size of 7 days were used. This means that the power is spread in time, and these plots are only indicative of the power variation. A more detailed description of temporal variations is given in later sections.

The variability of the solar diurnal and semidiurnal tides at frequencies of 1 and 2 cpd can clearly be seen and a terdiurnal tide at 3 cpd is also evident. A feature common to both plots is the temporal intermittency of the tidal winds, although some evidence of seasonal variations in tidal amplitudes are also apparent. For example, the semidiurnal amplitudes in the meridional component are largest near the June solstice. At periods longer than a few days there is appreciable energy in the zonal component. This is believed to be associated with Kelvin wave activity [*Vincent*, 1992].

Here we focus on the spectra at frequencies around 0.5 cpd or periods near 48 hours. In the zonal component (Figure 1) the power spectral amplitudes are small, and activity tends to blend in with the spectral features evident at longer periods. In the meridional component, however, power spectral amplitudes are large at periods near 0.5 cpd, and despite some intermittency, a clear feature can be seen over the whole 27 months of observation. It is this feature which we interpret as being due to the 2-day wave.

From previous observations [*Clark*, 1989; *Craig and Elford*, 1981; *Craig et al.*, 1983; *Muller and Nelson*, 1978; *Tsuda et al.*, 1988; *Vincent*, 1984] large enhancements in wave amplitude might be expected during the northern and southern hemisphere summers, as well as possible frequency shifts. To investigate these possibilities we repeated the spectral analysis with a finer frequency resolution, as shown in Figure 2 using the same moving power spectrum as in Figure 1, but with the window width increased to 40 days, to give an effective frequency resolution of 0.025 cpd. A step size of 20 days was used. We have also focussed on the frequency band of concern. Simulated data were used to test the analysis procedure in order to ensure that sidelobe effects due to the windowing are negligible. It should be noted that in Figure 2 the power spectral amplitudes are not truncated and that the scales are different. Hence, these plots give not only a more accurate measure of the relative strength of the oscillation in each wind component, but also a better representation of seasonal changes in wave energy. It is apparent that the meridional wind power spectral amplitudes are usually up to ten times those of the corresponding values for the zonal component.

The zonal wind component (Figure 2) has dominant peaks at periods near 53 hours in July and August of each year. Interestingly, for the December solstice the dominant periods are more like 52 hours in January 1991 and 53 hours in January 1992, which is very similar to the behavior in July, in contrast to the marked difference in the solstices in the meridional component. As well as the main spectral peaks near 52 hours there are also subsidary peaks near 44 hours.

From Figure 2 we can see that in the time interval from May to August 1990 the dominant period in the meridional wind component is approximately 50 hours (0.48 cpd). In September 1990 there are two peaks at periods near 56 and 44 hours. By the end of January 1991 the center period has shifted to 48 hours, but the spectral peak is broad, extending from about 52 to 45 hours. There is little activity during April and May 1991, as is the case in 1990. In July 1991 a strong peak near a period of 44 hours is evident. By August a peak around 50 hours is dominant. This is a stronger event than in 1990, but of shorter duration, and has almost disappeared into the background by the end of September. In January 1992 we see the return of the near 48-hour oscillation. The spectral peak is not as intense as in the previous year but is nearly as broad, extending from $\sim$50 hours down to 44 hours. In summary, there is evidence that amplitude and frequency changes coincident with the solstices are observed.

Coincident with the 2-day wave events in both February 1991 and 1992, there is also a strong peak in the meridional component at a period near 16 hours (see Figure 1). There is also significant activity around periods of 16 hours in August and September 1991, coincident with the August 2-day wave event. This feature will be discussed in more detail in section 2.5.

Amplitude and Frequency Variability

From the foregoing, it is clear that the character of the 2-day wave, as observed at Christmas Island, changes throughout the year. In order to better determine the nature of these changes as a function of height and time the method known as complex demodulation was used [*Bloomfield*, 1976]. This technique allows the amplitude and phase of an oscillation to be described as a function of time. The raw time series is multiplied by a complex sinusoid of prescribed frequency (the demodulation frequency) situated near the frequency of interest. The resultant complex time series is then low-pass filtered, thus demodulating the original time series; the process is akin to beating a Doppler-radar signal down to base-band. The amplitude of the resultant waveform is a measure of the amplitude of the components within a determined bandwidth in the original time series and is fairly robust to changes in the demodulation frequency. The rate of change of phase, on the other hand, is a direct measure of the difference between the demodulation frequency and the dominant frequency within the bandwidth of the original time series, and is consequently a sensitive measure of the dominant frequency. Using this method the frequency of the 2-day wave can be measured as a function of time.

Demodulating the meridional time series for all heights using a 0.5 cpd (48-hour period) sinusoid gives the amplitude of the near 48-hour wind components (Figure 3). The bandpass used was from 44.0 to 53.0 hours, giving 150 degrees of freedom. This allows amplitude variations on time scales greater than 10 days. Obvious features are the enhanced amplitudes during January/February at all heights, but which are especially pronounced from 84 to 96 km. There are also enhanced amplitudes from June to September 1990 and 1991 at the same altitudes. Similar amplitudes are obtained through both altitude and time if a 0.48 cpd (50-hour period) demodulation is used.

Using a 48-hour demodulation, the phase varies at a near constant negative rate during the interval from April to August 1990. This implies that the true frequency is lower than the demodulation frequency. During January and February 1991, when the amplitude of the 2-day wave is largest, the phase is almost constant, changing by less than 0.5 cycles in this 60-day interval. In Figure 4 the periods, calculated using the slope of the phase of the demodulated series and binned by season, are shown. We require that there be only one dominant frequency within the bandpass for each season so that the period determined corresponds to a single wave period. Thus, by reference to Figure 2, the two strong peaks in meridional component during the June 1991 solstice season need to be separated. For consistency with the

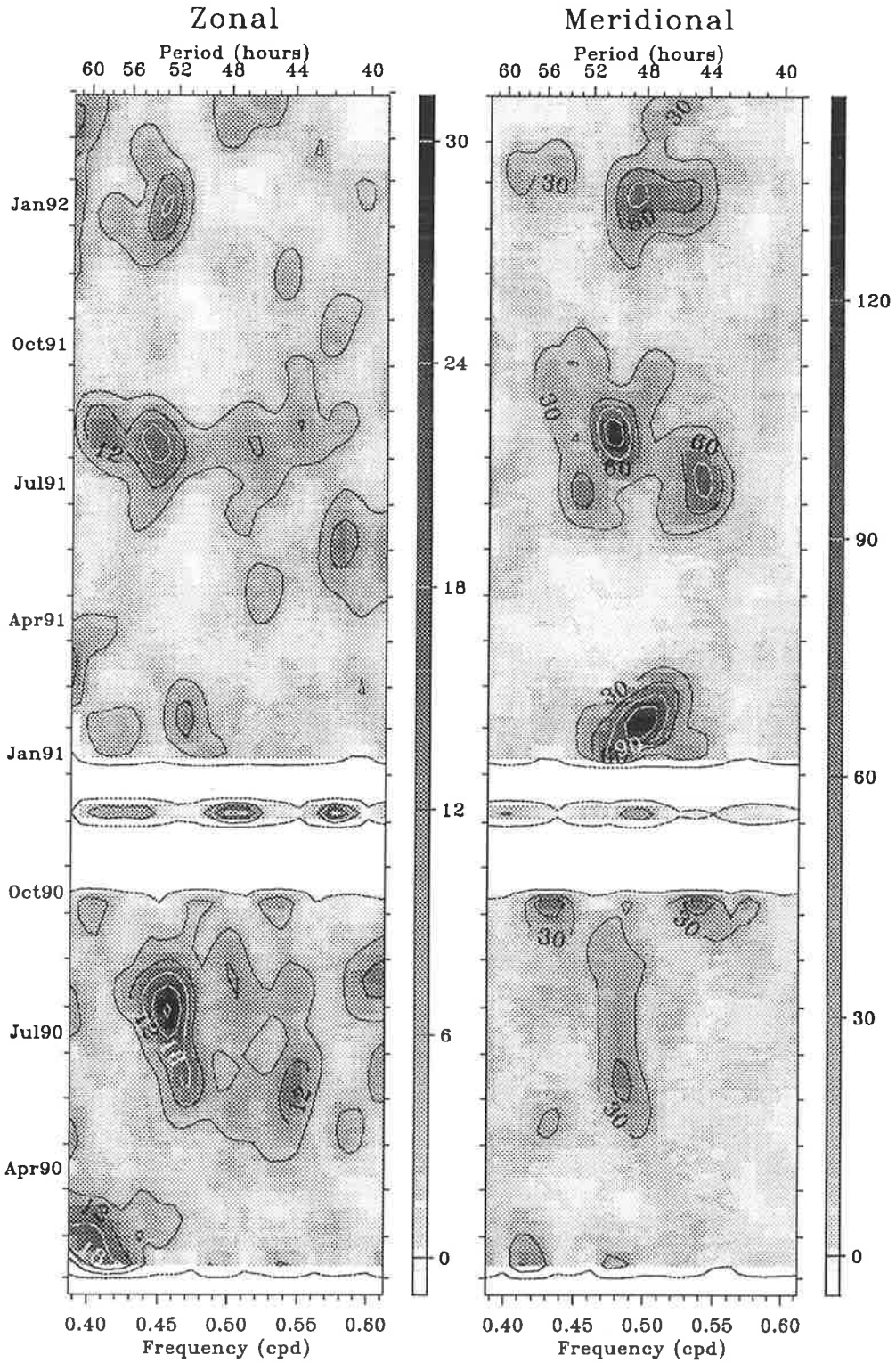

Fig. 2. Moving power spectra as in Figure 1 but using a 40 day sliding window giving an effective resolution of 0.012 cycles per day. Zonal winds are shown on the left and the meridional on the right, with the the color scale indicating the power spectral density in units of $10^6 m^2\ s^{-2}\ Hz^{-1}$. Note that the scale is different for the zonal and meridional winds.

June 1990 solstice season, a passband was chosen that eliminated the 44-hour peak while retaining the 50-hour peak and the 48-hour peaks of the December solstices. A demodulation period of 50 hours was used, with a bandpass from 46 to 54.8 hours. The extension of the passband out to 54.8 hours allows the same bandpass to be used for both the zonal and meridional winds (c.f. Figure 2), since the main peaks in the zonal component appear near a period of 53 hours for all solstices. Only data for times when the amplitudes were greater than 5 m s^{-1} have been used in the compilation of the period distributions in order to avoid any erroneous broadening due to noise. On average, around 4000 hours of data were used at each height, although at lower heights there were fewer points due to their lower mean amplitudes. The thick lines with the symbols (triangles for meridional, and squares for zonal components) show the median period

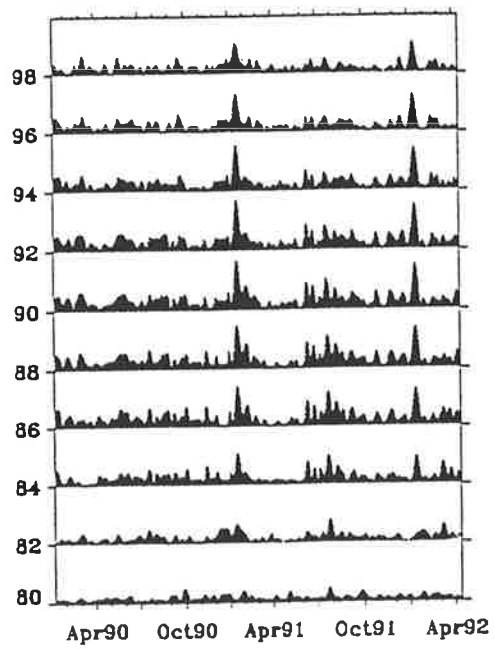

Fig. 3. Amplitude of the 48-hour meridional component as function of altitude. The effective bandpass is from 44.0 to 53.0 hours, giving 150 degrees of freedom. The vertical axis shows the altitude, with time along the horizontal (tick marks indicate the middle of each month). Each plot is displaced vertically by 50 m s^{-1}

as a function of altitude, with the upper and lower deciles shown as narrow lines. The meridional results are shown as solid lines while the zonal are dot-dashed lines.

For the meridional component it can be seen that during December to February the median period is 48 hours (for 84 km and above) with deciles spreading from 45 to near 51 hours. This is in agreement with the sliding spectral results presented earlier. From June to August the median period is just as firmly placed at 50 hours (for 86 km and above). The deciles range from 44 to 53 hours. For the zonal component, the median period ranges from 49 to 52 hours during both solstice periods. For both the zonal and meridional winds the amplitudes of the near 48-hour period components are small during the equinoctial months, so that the period determination has a larger uncertainty. Nevertheless, the March equinox shows a strong tendency to have a median period near 48 hours (for both the zonal and meridional winds) whereas the September equinox shows a tendency towards a 52-hour period.

Vertical Structure

The vertical structure of the 2-day wave as a function of season was obtained using a time series which had been passed through a broad-band filter. The bandpass used was from 30 to 80 hours. Again, two-hourly averaged data were used. A cosine function, $A\cos(2\pi f\tau + \phi)$, with $f = 0.5$ cpd, was fitted to the data for each day using a least squares method, and the amplitude, A, and phase, ϕ, determined. This gave equivalent results to simply choosing the local time of maximum positive amplitude of the bandpassed time series, but had computational advantages. The error in the daily phase estimate from fitting a sinusoid with a period of 48 hours to data with a dominant period of 52 hours is less than 1 hour. This reduces to 30 min for data with a dominant period of 50 hours. In both cases this error is less than the natural variation of the phase observed in the raw bandpassed time series.

For the two solstice conditions the meridional amplitudes increase to a maximum in the region of 86 to 90 km then slowly decrease with further increase of altitude. Amplitudes during each solstice season exceed 30 m s^{-1} for 10% of the time at these altitudes. Median values are around 15 m s^{-1} from 86 to 90 km and just over 5 m s^{-1} at 80 km for both solstices. There is good coherence with height. For equinoctial conditions the amplitudes show a more constant variation with altitude. The median increases from 5 m s^{-1} at 80 km to 10 m s^{-1} at 98 km for the March equinox, whereas during the September equinox the median amplitude increases from 7 m s^{-1} at 80 km to 15 m s^{-1} at 84 km, then decreases down to 10 m s^{-1} at 98 km. There is a large amplitude burst at 86 km in the September equinox which raises the upper decile to 25 m s^{-1}, otherwise this value would be between 7 and 10 m s^{-1} greater than the median for both equinoxes.

Figure 5 shows the mean vector phase for the meridional (solid line and triangles) and zonal (dotted line with squares) components of the 2-day wave. The bars shown indicate one standard deviation. The phase has been calculated assuming a wave period of 48 hours for all seasons except the June solstice where a 50-hour period has been used. Thus the values for the phase in Figure 5 can be taken as hours LT except for the June solstice where the phase is simply a relative measure with altitude. It can be seen that the phase tends to advance towards earlier times with increasing altitude, indicating descending phase and upward energy propagation. The main exception to this is during the period from March to May at altitudes of 82 to 88 km, where the phase is re-

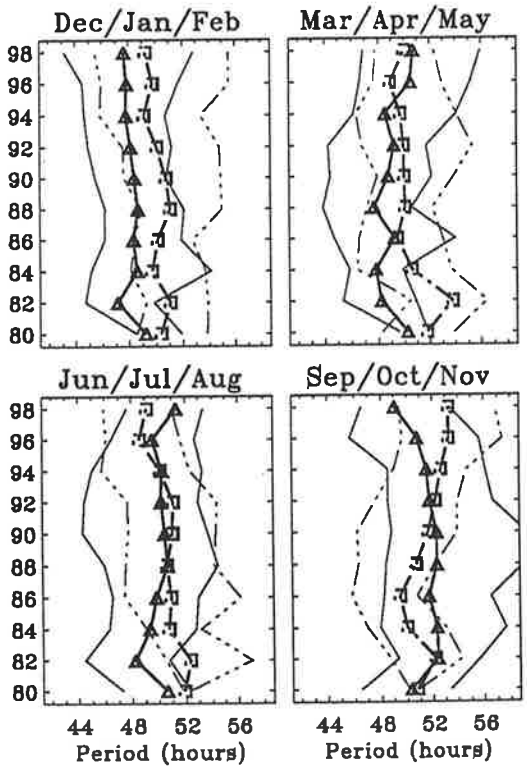

Fig. 4. The period of the near 48-hour zonal and meridional wind components for each season. The effective bandpass is from 46.0 to 56.0 hours, giving 150 degrees of freedom. The vertical axis shows the altitude in kilometers. The solid line with triangles and the dot-dashed lines with square symbols show the median period for the meridional and zonal components, respectively. Thin lines show the upper and lower deciles.

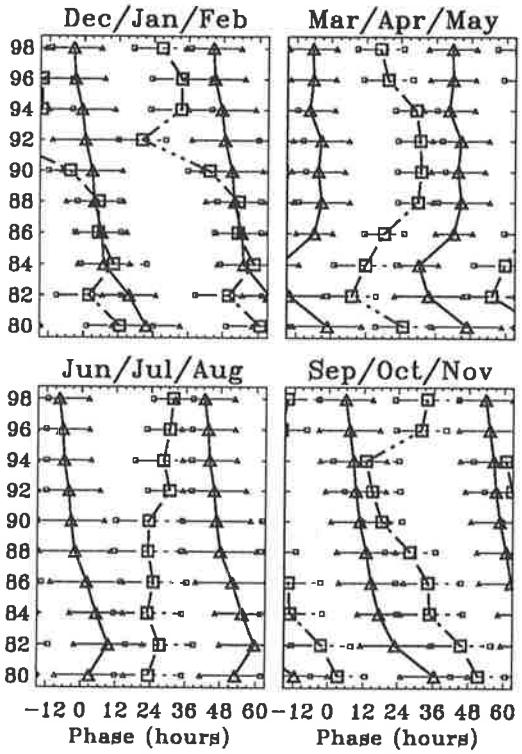

Fig. 5. The mean vector phase (hours LT) for the meridional (solid line and triangles) and zonal (dotted line with squares) components of the 2-day wave for each season as function of altitude. The bars indicate one vector standard deviation.

tarded with height. During this period the zonal leads the meridional component by approximately 15 hours at most heights, increasing to 24 hours at the lowest and highest heights. This is in contrast to the September equinox where the meridional component leads the zonal by about 18 hours at 86 km, decreasing to only 4 hours at 94 km, where the zonal winds show a large phase shift. The change in the phase with altitude suggests an average vertical wavelength greater than 150 km during the March equinox (above 86 km), and of the order of 55 km for the September equinox. The amplitude of the near 48-hour wind component (as previously mentioned) is small during the equinoctial months, so that the uncertainty in the phase is greater than for the solstices. However, the consistency with altitude and the consistent phase difference between the zonal and meridional components give us some confidence in these results. Note that the values for 80 and 82 km have the least confidence as the wave amplitudes are smallest at these altitudes.

During the December solstice the average zonal and meridional 2-day wave wind components are in-phase from 82 to 90 km, where the zonal winds show a large phase shift. Above 90 km the zonal leads the meridional winds by around 12 hours, i.e., the average wind components are in phase-quadrature. The vertical wavelength, obtained from the change in the phase with altitude, is of the order of 70 km. During the June solstice the average zonal phase appears to be constant with altitude suggesting an evanescent wave whereas the meridional has a definite phase retardation with increasing altitude, suggesting a propagating mode. The zonal and meridional wind components are approximately in phase-quadrature, especially at the lower heights. The average vertical wavelength was estimated to be 80 km above an altitude of 86 km, and 40 km below.

Case Studies

Since the 2-day wave can be quite intermittent, the seasonal averages may not describe the full behavior of the wave. To address this possibility the temporal behavior of the 2-day wave was examined during three short time intervals. Each interval, consisting of 2 weeks of data, represent each solstice and an interval in April 1990, when wave activity was small. Figure 6 shows the bandpassed meridional winds for these intervals. High temporal and spatial coherence is evident for those intervals of large amplitude. The coherence with altitude is apparent for all three intervals with a downward phase progression at both solstices, indicating upward energy transport. The change in phase with altitude for both the 2-week solstice intervals appears to indicate a similar wavelength to that estimated from the seasonal averages.

Table 1 summarizes the median and decile amplitudes as a function of altitude for the zonal and meridional 48-hour period wind components for the selected time intervals. The amplitudes were calculated in a similar manner as for the seasonal data, using 15 to 20 points in each estimate. We can see that the April period is indeed a time of low amplitude, with median values around 8-13 m s^{-1} for all heights in both components. The deciles are also fairly constant with altitude. The largest amplitudes are found in the meridional component during the February interval which coincides with the southern-hemisphere summer 2-day wave event. Figure 6 illustrates the impulsive nature of the 2-day wave with amplitudes attaining values of over 43 m s^{-1} for 10% of the time during February 1991, at altitudes of 88 km and greater than 15 m s^{-1} for 90% of the time from 84 to 98 km. At this time of the year the wave amplitudes are larger than the tidal amplitudes. The amplitude of the zonal component during this interval is half that of the meridional at most heights. The meridional component during the August time interval is also larger than the zonal amplitudes, but not to the same degree as in the February interval. The zonal median amplitudes are about two-thirds of the meridional median value for altitudes from 86 to 94 km.

Figure 7 shows the mean vector phase as a function of altitude for the 2-day wave for the selected solstice periods. The phases have been calculated in a similar manner as for the seasonal data with a cyclic period of 48 hours used for the January/February time interval and 50 hours for the interval in August. For the February time interval, the variation of the phase with altitude indicates a vertical wavelength around 70 km, with the zonal and meridional winds in near antiphase. In contrast, for the August time interval, the zonal and meridional winds are nearly in phase-quadrature, with the meridional leading by around 8-12 hours for most altitudes. The indicated vertical wavelength is also of the order of 70 km for this interval.

Other Wave Components

Using power spectra, such as those in Figure 1, allows us to explore the relationship between the two-day wave and other wind variations. An interesting phenomenon which is apparent in the meridional winds occurs just after the December solstices, when there is a strong spectral peak at a period near 16 hours (Figure 1). Similar peaks are also present after both June solstices, but with smaller amplitudes. Since a 16-hour component is the third harmonic of 48 hours this may be evidence of non-linearity in the 2-day wave oscillation. The structure of the 16-hour component was studied by bandpass filtering the raw wind data in a

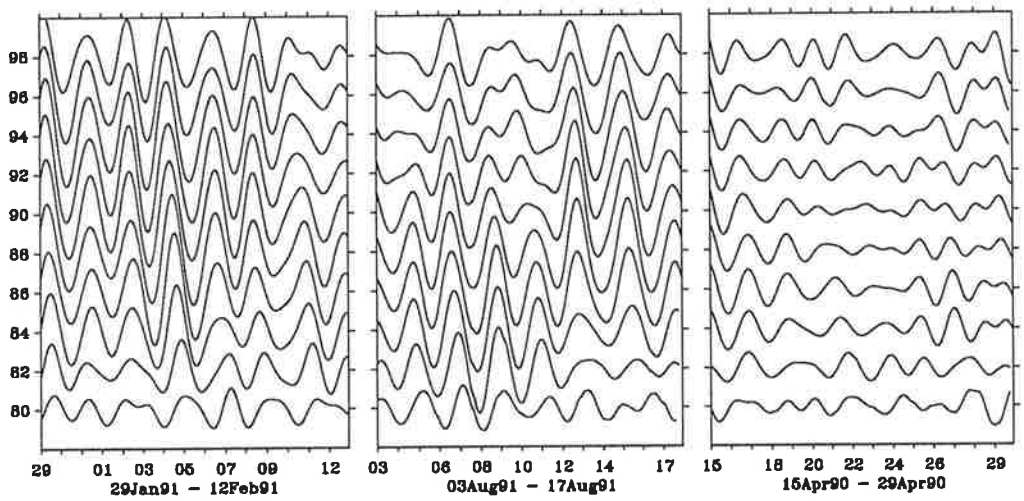

Fig. 6. Bandpass filtered meridional winds for the near 48-hour component during February 1991 (left), August 1991 (center), and April 1990 (right). A passband of 30 to 80 hours was used. The time axis tick marks indicate 1200 LT. The plots are displaced vertically by 30 m s^{-1}.

similar manner to that used for the 2-day wave, but with a bandpass extending from 15.0 to 17.1 hours. This bandpass allows amplitude variations with scales larger than 5 days to be discerned, compared with 10 days for the 48-hour component. The same time interval in January/February 1991 as for the 2-day wave was selected. The 16-hour meridional wind component was found to have amplitudes exceeding 25 m s^{-1} for 10% of this time interval at altitudes near 90 km (Figure 8). The median amplitude is near 12.5 m s^{-1} for altitudes from 86 to 98 km. The phase fronts are highly coherent with altitude and time and have a downward progression. The estimated vertical wavelength is in excess of 150 km. If we compare the temporal and vertical structure of the 16-hour component to that of the 2-day wave we find that the times and heights of peak amplitudes agree well.

The period of the near 16-hour component was determined more precisely at each height by complex demodulation for data taken in the February time interval, when the 48-hour component was largest. The effective bandpass used was 15.0 to 17.1 hours. In the altitude region from 84 to 92 km during the interval February 2–7, 1991, when the amplitude of the 16-hour component is large, the period is indistinguishable from 16 hours. This result is independent of the demodulation period and exact bandpass, indicating that there is a dominant 16-hour period wave present. Closer inspection shows that the amplitude peak in the 16-hour component during February 1991 occurs just after the peak in the 48-hour component. The sharp rise in the amplitude

TABLE 1. Amplitudes (m s^{-1}) of the 2-Day Wave for 2-Week Intervals in February 1991, April 1990 and August 1991.

Height, km	February Median	February Upper Decile	April Median	April Upper Decile	August Median	August Upper Decile
			Meridional			
98	25	32	9	12	16	27
96	29	32	7	15	25	32
94	30	38	7	13	25	37
92	34	40	7	8	26	38
90	33	39	5	6	28	38
88	28	43	5	11	30	35
86	23	40	7	12	27	32
84	19	30	6	14	22	31
82	12	20	7	10	21	30
80	10	15	5	8	12	17
			Zonal			
98	18	23	8	11	5	11
96	17	20	10	19	7	12
94	16	29	13	18	9	13
92	15	22	13	19	10	13
90	14	20	13	15	15	15
88	9	17	11	18	18	19
86	10	11	8	13	19	23
84	10	13	6	8	16	24
82	5	12	5	9	12	19
80	7	11	8	12	7	11

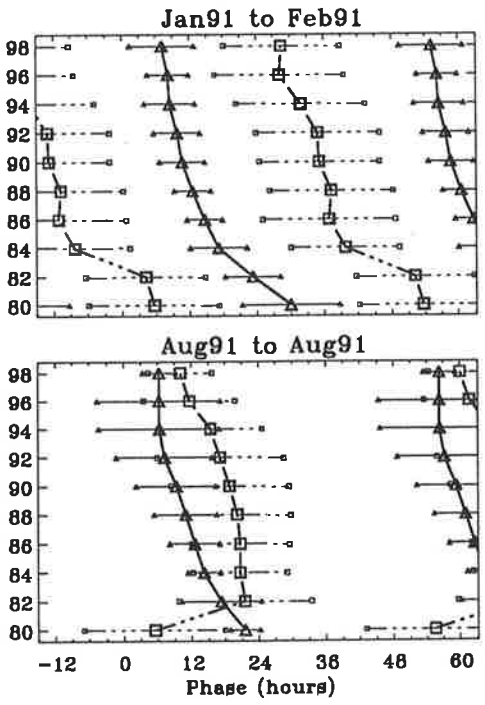

Fig. 7. The mean vector phase (hours LT) for the meridional and zonal components (as for Figure 5) for (top) February, and (bottom) August 1991, as a function of altitude.

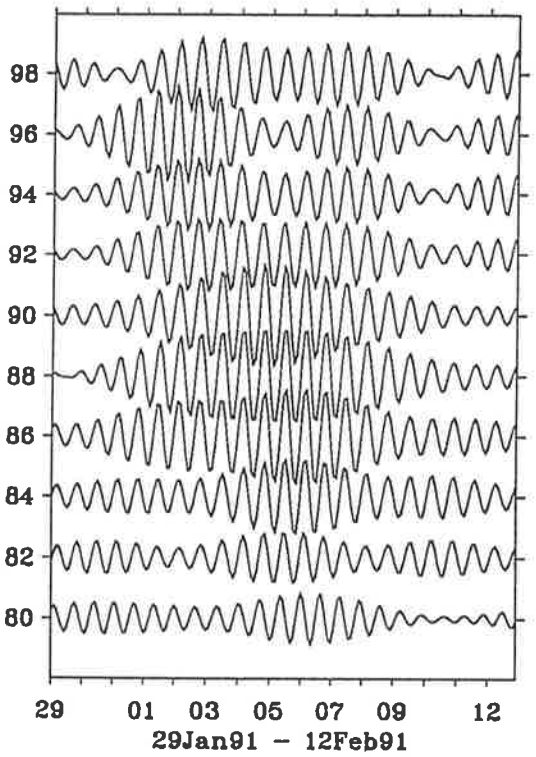

Fig. 8. Bandpass filtered meridional winds for the near 16-hour component during February 1991. A passband of 15.0 to 17.1 hours was used. Axes are the same as in Figure 6.

of the 16-hour component starts near the time of the maximum in the 48-hour component for all altitudes from 84 to 98 km.

Figure 9 places the temporal behavior of the 2-day wave and the 16-hour and 9.6-hour components in context with the variations of the prevailing zonal wind and the solar tides at an altitude of 92 km. Each plot is displaced vertically by a distance equivalent to 30 m s^{-1}, except for the the mean zonal wind which extends through ± 50 m s^{-1} (eastward shown positive), and the 2-day wave, which extends from 0 to 45 m s^{-1}. The low levels near October and December 1990 indicate missing data. As a reference against which the amplitudes of the various wave components can be compared, we also show the amplitude of the spectrum around a center period of 14 hours. The effective bandpass is 13.5 to 14.5 hours, giving 126 degrees of freedom and so has an equivalent width to the other frequency intervals. The amplitude in this period range rarely exceeds 10 m s^{-1} at all altitudes and there is little coherence with altitude. This contrasts with the coherent height and time structures apparent for the 48- and 16-hour components.

With regard to the solar tides, an interesting, and potentially important, feature is that the amplitude of the diurnal solar tide is reduced during the time of greatest amplitude of the 2-day wave in February 1991 and 1992. This effect is not obvious at the time of the other period of enhanced 2-day wave activity in July. In contrast, the semidiurnal solar tidal amplitude does not appear to change significantly during these intervals compared with its behavior during the rest of the year.

DISCUSSION

The results from Christmas Island (2° N, 157° W) discussed above show that the 2-day wave is a prominent feature of the dynamics of the equatorial middle atmosphere, especially in the meridional wind component. As such, our observations support the findings of *Kalchenko and Bulgakov* [1973], *Kascheev* [1987] and *Kalchenko* [1987], who discussed mesospheric wind observations made with a meteor radar located at Mogadishu (2° N, 45° E) from 1968 to 1970. Most of the Mogadishu measurements were made at a single height near 94 km. Our measurements, however, provide important new information on both the temporal variability and the vertical structure of the wave.

The wave is found to be present most of the time in the mesosphere, although its amplitude varies with season. Largest amplitudes are attained about 1 month after the solstices, and the smallest amplitudes observed in April. The period of the wave is also found to change. For much of the year the period is near 50 hours, but at the time of the largest amplitudes, in January/February, the period is close to 48 hours. It is a propagating mode in the equatorial mesosphere during the solstices, with a vertical wavelength of the order of 70 km. This compares with values of ~ 50 km found at Townsville (19° S, 147° E) [*Craig et al.*, 1980] and 20 km at Trivandrum (8.5° N, 76.9° E) [*Reddi et al.*, 1988]. Vertical wavelengths of ~ 100 km or more are typical of mid-latitudes [*Craig et al.*, 1980; *Craig and Elford*, 1981]. Recently, *Harris* [1993] summarized mesospheric wind measurements made at Adelaide between 1980 and 1991. He found a mean vertical wavelength of greater than 150 km, and a tendency for the 2-day wave to be locked in local time with the time of maximum northward wind occuring between 1200 and 1600 LT every year.

Observations at Christmas Island allow the 2-day wave to be studied during both solstices at one location. Our measurements are in accord with previous findings for mid- and high-latitude observations, in that the amplitudes are greatest at the solstices with the amplitude coinciding with the

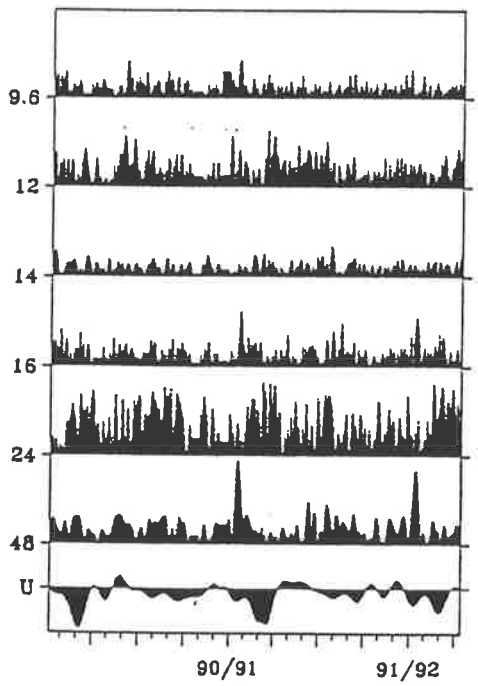

Fig. 9. Amplitudes of the meridional wind component at 92 km from late January 1990, to the end April 1992. The major tick marks along the horizontal axis are for the middle of January, April, July, and October. The scale of the mean zonal wind (U) is from ± 50 m s^{-1} (eastward positive). The range of the 48-hour component is 45 m s^{-1}. Each subsequent plot is separated by a distance equivalent to 30 m s^{-1}.

southern hemisphere summer larger than for the northern summer. The period changes are also in basic accord with previous observations [*Vincent*, 1984]. Our observations differ, however, in that the wave seems to be present for much of the year, albeit showing intermittent behavior. Another feature that has not been reported before is that two frequency components seem to be present, one with a period near 50 hours and the other with a period near 44 hours. The component near 50-hour period is dominant and is the one that we have focussed on here as it seems to have all the characteristics of what is usually referred to as the 2-day wave.

The mechanism by which the wave is generated is not yet resolved. *Salby* [1981*a*] proposed that it is a manifestation of the (3, 0) atmospheric normal mode driven by "noise" at lower levels. The (3, 0) mode has a period of about 50 hours (depending on what equivalent depth is used) in an atmosphere at rest. *Salby* [1981*b*,*c*] discussed how the mode structure changed in an atmosphere with realistic background winds and temperatures. In particular, he showed that the wave becomes locally propagating in the summer mesosphere where the prevailing wind is slightly eastward relative to the wave, and where there is an equatorward temperature gradient. In this region wave energy has exponential growth with height. An alternative generating mechanism was proposed by *Plumb* [1983] and *Pfister* [1985], who suggested that the wave could be due to baroclinic instability of the westward jet in the summer stratosphere and lower mesosphere. Stability analyses show peaks of unstable wave growth at zonal wavenumbers 2-4 with periods of 1.5-3 days.

The fact that the wave is present for most of the time in the meridional wind component at Christmas Island supports the proposal of *Salby* [1981*a*,*c*] that it is a manifestation of the (3, 0) Rossby-gravity normal mode, randomly forced in the lower atmosphere. The (3,0) mode is an asymmetric mode, and would therefore produce oscillations only in the meridional wind component at the equator. The nearly year-round presence of the wave precludes the baroclinic instability hypothesis which could occur only for limited times of the year when the summer stratospheric jet has its greatest curvature. To confirm this would require measurements of the horizontal structure which are of course not possible at a single site. However, most previous investigations have found a wavenumber 3 westward propagating wave [*Muller and Nelson*, 1978; *Craig et al.*, 1980; *Rodgers and Prata*, 1981].

While it seems plausible to identify the near 50-hour component with the (3, 0) normal mode this leaves open the question of the nature of the 44-hour component. It seems probable that it is a manifestation of the (2, 0) Rossby-gravity normal mode. This is an antisymmetric westward propagating zonal wavenumber 2 wave with a period of 1.6 days (38 hours) in an atmosphere at rest [*Kasahara*, 1976], but a peak near 1.8 days (43 hours) and an enhanced response in the range 1.6 to 1.9 days (38-46 hours) in an atmosphere with realistic wind and temperature [*Salby*, 1981*b*,*c*]. The larger amplitudes in the meridional component compared with the zonal (see Figure 2) are consistent with an antisymmetric mode. This mode has been tentatively noted in surface pressure data by *Hamilton and Garcia* [1986].

The Christmas Island observations, together with the Mogadishu measurements [e.g., *Kascheev*, 1987], show the ubiquitous nature of the 2-day wave at the equator, especially in the meridional wind component. Our results suggest that the (3, 0) normal mode is always present in the atmosphere, but at levels which are not detectable at mid-latitudes except in the summer middle atmosphere where the wave enounters a critical level. As noted, *Salby* [1981*c*] showed that the (3, 0) mode becomes locally propagating with wave growth, in regions where the background zonal flow is westward and the wave is Doppler shifted down in frequency. A westward flow prevails for much of the year in the equatorial mesosphere [*Vincent*, 1992]. This could account for the relatively large year round amplitudes in the equatorial mesosphere. It would also appear that the (2, 0) mode is also present, but with smaller amplitudes than the (3, 0) mode. One reason could be that it has a phase speed of 130 m s^{-1} compared with 75 m s^{-1} for the (3, 0) mode at the equator, and hence will suffer less Doppler shifting. According to *Salby* [1981*c*] the (2, 0) mode too should encounter a critical level in the summer middle atmosphere, but at a higher latitude than the (3, 0) wave and so will also show enhanced amplitudes in this season. Such enhancements are observed in Figure 2 near the solstices.

Another interesting result of the present study is the presence of a 16-hour component in the meridional winds when the two-day wave is at its strongest in July/August and January/February. There is a suggestion that a 9.6-hour component is also present at these times. One possibility is that the 16-hour wave is itself a normal mode. However, the only normal mode that has a period of 16 hours is a Kelvin wave [e.g., *Kasahara*, 1976; *Hamilton and Garcia*, 1986] which would produce oscillations in only the zonal wind component. Rather, the similarity between the instantaneous amplitude and height variations of the 16-hour component and the two-day wave suggests that they are dynamically linked in some manner. The presence of a 16-hour oscillation at the time of a large two-day wave has been noted before [e.g., *Manson and Meek*, 1990]. One suggested mechanism is that the 16-hour and the 9.6-hour components are generated by nonlinear interactions between the two-day wave and the semidiurnal tide [e.g., *Manson and Meek*, 1990; *Teitelbaum and Vial*, 1991].

An alternative hypothesis is that the 16- and 9.6-hour components are simply harmonic components associated with wave steepening during large amplitude two-day wave events. Large meridional velocities would produce large north-south parcel displacements. In a detailed analysis of one two-day wave event at Adelaide (where peak meridional velocities of greater than 50 m s^{-1} are not uncommon), *Plumb et al.* [1987] estimated horizontal parcel displacements of at least 3000 km, that is peak-to-peak latitudinal displacements of 60°. They concluded that wave overturning in the horizontal plane was possible. In such circumstances the presence of high-order harmonic components would be observed in the wind field.

One way to test whether the 2-day wave interacts with the solar tides to produce the 16-hour wave, or whether it is a harmonic of a large amplitude 2-day wave, is to perform higher order spectral analyses which would enable the nonlinear wave interactions to be investigated [e.g., *Kim and Powers*, 1979]. We are now conducting such a study, which will be reported elsewhere.

Higher order spectral analysis may also help resolve another interesting and puzzling feature of the 2-day wave, that is, its tendency to often have a frequency indistinguishable from 48 hours and to be locked in local time during the January/February events. The solar diurnal tide has a low amplitude during the enhanced 2-day wave interval at this

time, as can be seen in Figure 9. Close inspection of the meridional component in Figure 2 shows that at the beginning of January 1991 the 2-day wave has a period near 50 hours. As time progresses the peak shifts to 48 hours and the amplitude increases, as if the 50-hour wave has been "pulled" into some resonance condition whose natural period is 48 hours. It is at this time that the 16-hour peak occurs. In January 1992, however, the spectral peak maximises near a period of 49 hours, but extends across a broad period range to 44 hours. The shift in period observed for the previous year is not as apparent, although the 16-hour wave is still present. As previously noted, *Craig et al.* [1980], *Craig and Elford* [1981] and *Poole* [1990] reported a locking of the phase with local time in the southern hemisphere.

Finally, it is clear that the 2-day wave makes a significant contribution to the dynamics of the equatorial middle atmosphere. Especially at times of large amplitude, transient, events it may make an impact on the circulation and transport of the mesopause region in a manner similar to that discussed by *Plumb et al.* [1987]. A limitation of the present, single station, observations is that the horizontal structure of the wave, and especially the zonal wavenumber, cannot be studied. It is highly desirable that further radar observations be made at other longitudes in the equatorial region in order to investigate the zonal structure of the wave. Comparison of simultaneous mesospheric wind measurements made at stations with longitudinal separations of, say 60°, are essential for an unambiguous determination of the wavenumber, as well as for distinguishing the relative contributions of the (3, 0), (2, 0) and any other normal modes which may be important in the middle atmosphere. Longitudinally spaced measurements would also help to determine the role played by other planetary-scale motions, such as Kelvin waves, in the dynamics of the equatorial mesosphere.

Acknowledgments. We thank B. H. Briggs and R. L. Walterscheid for their many helpful comments. T.J. Harris is supported by a Defence Science and Technology Organisation Cadetship. This work was supported by a grant from the Australian Research Council.

REFERENCES

Bloomfield, P., *Fourier Analysis of Time series: An Introduction,* John Wiley, New York, 1976.

Clark, R. R., The quasi 2-day wave at Durham (43° N) ; solar and magnetic effects, *J. Atmos. Terr. Phys., 51,* 617-622, 1989.

Coy, L., A possible 2-day oscillation near the tropical stratospause, *J. Atmos. Sci., 36,* 1615-1618, 1979.

Craig, R. L., and W. G. Elford, Observations of the quasi 2-day wave near 90 km altitude at Adelaide (35° S), *J. Atmos. Terr. Phys., 43,* 1051-1056, 1981.

Craig, R. L., R. A. Vincent, G. J. Fraser, and M. J. Smith, The quasi 2-day wave in the Southern Hemisphere mesosphere, *Nature, 287,* 319-320, 1980.

Craig, R. L., R. A. Vincent, S. P. Kingsley, and H. G. Muller, Simultaneous observations of the quasi 2-day wave in the northern and southern hemispheres, *J. Atmos. Terr. Phys., 45,* 539-541, 1983.

Fritts, D. C., and J. R., Isler, First observations of mesospheric dynamics with a partial reflection radar in Hawaii (22° N, 160° W), *Geophys. Res. Lett., 19,* 409-412, 1992.

Hamilton, K., and R. R. Garcia, Theory and observations of the short-period normal mode oscillations of the atmosphere, *J. Geophys. Res., 91,* 11867-11875, 1986.

Harris, T. J., A long-term study of the quasi-two-day wave in the middle atmosphere, *J. Atmos. Terr. Phys.,* in press, 1993.

Kalchenko, B. V., Characteristics of atmospheric disturbances with a quasi two day period, in *Handbook for the Middle Atmosphere Program,* vol. 25, edited by R. G. Roper, SCOSTEP Secretariat, University of Illinois, Urbana, 1987.

Kalchenko, B. V., and S. V. Bulgakov, Study of periodic components of wind velcoty in the lower thermosphere above the equator, *Geomagn. Aeron., 13,* 955-956, 1973.

Kasahara, A., Normal modes of ultralong waves in the atmosphere, *Mon. Weather Rev., 104,* 669-690, 1976.

Kascheev, B. L., Atmospheric dynamics in the equatorial meteor zone, in *Handbook for the Middle Atmosphere Program,* vol. 25, edited by R. G. Roper, SCOSTEP Secretariat, University of Illinois, Urbana, 1987.

Kim, Y. C. and Powers E. J., Digital bispectral analysis and its applications to nonlinear wave interactions, *IEEE Trans. Plasma Sci., PS-7,* 120-131, 1979.

Manson, A. H., and C. E. Meek, Long period (~ 8-20 h) wind oscillations in the upper middle atmosphere at Saskatoon (52° N); evidence for non-linear tidal effects, *Planet. Space Sci., 38,* 1431-1441, 1990.

Muller, H. G., and L. Nelson, A travelling quasi 2-day wave in the meteor region, *J. Atmos. Terr. Phys., 40,* 761-766, 1978.

Pfister, L., Baroclinic instability of easterly jets with applications to the summer mesosphere, *J. Atmos. Sci., 42,* 313-330, 1985.

Phillips, A., Simultaneous observations of the quasi 2-day wave at Mawson, Antartica, and Adelaide, South Australia, *J. Atmos. Terr. Phys., 51,* 119-124, 1989.

Plumb, R. A., Baroclinic instability of the summer mesosphere: A mechanism for the 2-day wave?, *J. Atmos. Sci., 40,* 262-270, 1983.

Plumb, R. A., R. A. Vincent, and C. L. Craig, The quasi-two-day wave event of January 1984 and its impact on the mean mesospheric circulation, *J. Atmos. Sci., 44,* 3030-3036, 1987.

Poole, L. M. G., The characteristics of the mesospheric two-day wave as observed at Grahamstown (33.3° S, 26.5° E), *J. Atmos. Terr. Phys., 52,* 259-268, 1990.

Reddi, C. R., A. Geetha, and K. R. Lekshmi, Quasi 2-day wave in the middle atmosphere over Trivandrum, *Ann. Geophys., 6,* 231-238, 1988.

Rodgers, C. D., and A. Prata, Evidence for a travelling 2-day wave in the middle atmosphere, *J. Geophys. Res., 86,* 9661-9664, 1981.

Salby, M. L., The 2-day wave in the middle atmosphere; observations and theory, *J. Geophys. Res., 86,* 9654-9660, 1981*a*.

Salby, M. L., Rossby normal modes in nonuniform background configurations, Part 1, Simple fields, *J. Atmos. Sci., 38,* 1803-1826, 1981*b*.

Salby, M. L., Rossby normal modes in nonuniform background configurations, Part II, Equinox and solstice conditions, *J. Atmos. Sci., 38,* 1827-1840, 1981*c*.

Salby, M. L., Survey of planetary-scale traveling waves; The state of theory and observations, *Rev. Geophys., 22,* 209-236, 1984.

Teitelbaum, H., and F. Vial, On tidal variability induced by nonlinear interaction with planetary waves, *J. Geophys. Res., 96,* 14,169-14,178, 1991.

Tsuda, T., S. Kato, and R. A. Vincent, Long period wind oscillations observed by the Kyoto meteor radar and comparisons of the quasi-2-day wave with Adelaide HF radar, *J. Atmos. Terr. Phys., 50,* 225-230, 1988.

Vincent, R. A., MF/HF radar measurements of the dynamics of the mesopause region - A review, *J. Atmos. Terr. Phys., 46,* 961-974, 1984.

Vincent, R. A., Long period motions in the equatorial mesosphere, *J. Atmos. Terr. Phys.,* in press, 1993.

Vincent, R. A. and D. Lesicar, Dynamics of the equatorial mesosphere; first results with a new generation partial reflection radar, *Geophys. Res. Lett., 18,* 825-828, 1991.

Walterscheid, R. L., Traveling planetary waves in the stratosphere, *Pure Appl. Geophys., 118,* 240-265, 1980.

T. J. Harris and R. A. Vincent, Department of Physics and Mathematical Physics, University of Adelaide, GPO Box 498, Adelaide 5001, Australia.

(Received August 21, 1992;
revised February 8, 1993;
accepted February 8, 1993.)

Appendix J

Lunar Tidal Analysis of 6 yr of Mesospheric Wind Data at Adelaide

This is a reprint of the paper,

Schlapp, D. M. & Harris, T. J. (1993), 'Lunar tidal analysis of 6 yr of mesospheric wind data at Adelaide', *Journal of Atmospheric and Terrestrial Physics* **55**(13), 1629–1635.

Schlapp, D.M. & Harris, T.J. (1993) Lunar tidal analysis of 6 yr of mesospheric wind data at Adelaide.

Journal of Atmospheric and Terrestrial Physics,v.55(13), pp.1629-

References

Akima, H. (1970), 'A new method of interpolation and smooth curve fitting based on local procedures', *Journal of the ACM* **17**, 589–602.

Anderson, S. J., Mahoney, A. R. & Zollo, A. O. (1992), Applications of higher-order statistical signal processing to radar, A paper presented at the "International Conference on Higher-Order Statistical Signal Processing with Application to Nonlinear, NonGaussian, Nonstationary Signals and Systems", Gold Coast, Australia, 20–21 August, 1992.

Aso, T. (1993), 'Time-dependent numerical modelling of tides', *Journal of Geomagnetism and Geoelectricity* **45**, 41–63.

Bartlett, M. S. (1956), *An introduction to stochastic processes*, Cambridge University Press, New York.

Bath, M. (1974), *Spectral Analysis in Geophysics*, Vol. 7 of *Developments in Solid Earth Geophysics*, Elsevier Scientific Publishing Company, Amsterdam.

Bernard, R. (1981), 'Variability of the semi-diurnal tide in the upper mesosphere', *Journal of Atmospheric and Terrestrial Physics* **43**, 663–674.

Blackman, R. B. & Tukey, J. W. (1959), *The measurement of power spectra from the point of view of communications engineering*, Dover, New York.

Bloomfield, P. (1976), *Fourier analysis of time series: an introduction*, Wiley & Sons, New York.

Bracewell, R. N. (1978), *The Fourier transform and its applications*, McGraw-Hill Kogakusha.

Briggs, B. H. (1968), 'On the analysis of moving patterns in geophysics, Part I, Correlation Analysis', *Journal of Atmospheric and Terrestrial Physics* **30**, 1777–1788.

Briggs, B. H. (1980), 'Radar observations of atmospheric winds and turbulence: a comparison of techniques', *Journal of Atmospheric and Terrestrial Physics* **42**, 823–833.

Briggs, B. H. (1984), 'The analysis of spaced sensor records by correlation techniques', *Handbook for the Middle Atmosphere Program* **13**, 166–186. SCOSTEP Secretariat, University of Illinois, Urbana, IL.

Briggs, B. H. & Spencer, M. (1954), The variability of time shifts in measurements of ionospheric movements, *in* 'Report of the Physical Society Conference on "The Physics of the Ionosphere"', The Physical Society, London, pp. 123–201. Held at the Cavendish Laboratory, Cambridge.

Briggs, B. H. & Vincent, R. A. (1992), 'Spaced-antenna analysis in the frequency domain', *Radio Science* **27**(2), 117–129.

Briggs, B. H., Elford, W. G., Felgate, D. G., Golley, M. G., Rossiter, D. E. & Smith, J. W. (1969), 'Buckland Park aerial array', *Nature (London)* **223**, 1321–1325.

Briggs, B. H., Phillips, G. J. & Shinn, D. H. (1950), 'The analysis of observations on spaced recievers of the fading of radio signals', *Proceedings of the Physical Society. (London)* **B63**, 106.

Brillinger, D. R. (1975), *Time Series: data analysis and theory*, International series in decision processes, Holt, Rhinehart and Winston, Inc, New York.

Brillinger, D. R. & Krishnaiah, P. R., eds (1983), *Time Series in the Frequency Domain*, Vol. 3 of *Handbook of statistics*, Elsevier Science Publishers B.V., Amsterdam.

Brownlie, G. D., Dryburgh, L. G. & Whitehead, J. D. (1973), 'Measurement of the velocity of waves in the ionosphere: A comparison of the ray theory approach and diffraction theory', *Journal of Atmospheric and Terrestrial Physics* **35**, 2147–2162.

Butler, S. T. & Small, K. A. (1963), 'The excitation of atmospheric oscillations', *Proceedings of the Royal Society. (London)* **274**, 91–121.

Campbell, L. (1992), Stellar Scintillation and its use in Atmospheric measurements, PhD thesis, University of Adelaide, Adelaide, Australia.

Campbell, L. & Elford, W. G. (1990), 'measurement of atmospheric isoplanetism using stellar scintillation', *Journal of Atmospheric and Terrestrial Physics* **52**, 313–320.

Capon, J. (1969), 'High-resolution frequency-wavenumber spectrum analysis', *Proceedings of the IEEE* **57**, 1408–1418.

Chandra, H. & Briggs, B. H. (1978), 'The effect of filtering on ionospheric drift parameters determined by the full correlation analysis', *Journal of Atmospheric and Terrestrial Physics* **40**, 541–548.

Chapman, S. & Bartels, J. (1940), *Geomagnetism, Vol II*, The International Series of Monographs on Physics, Oxford University Press, London.

Chapman, S. & Lindzen, R. S. (1970), *Atmospheric tides*, Reidel, Dordrecht, Netherlands.

Chapman, S. & Malin, S. R. C. (1970), 'Atmospheric tides, thermal and gravitational: Nomenclature, notation and new results', *Journal of the Atmospheric Sciences* **27**(5), 707–710.

Charney, J. G. & Drazin, P. G. (1961), 'Propagation of planetary-scale disturbances from the lower into the upper atmosphere', *Journal of Geophysical Research* **66**, 83–109.

Chen, P.-R. (1992), 'Two day oscillations of the equatorial ionization anomaly', *Journal of Geophysical Research* **97**(A5), 6343–6357.

CIRA86 (1990), 'Cospar International Reference Atmosphere: 1986, Part II: Middle Atmosphere Models', *Advances in Space Research.* (COSPAR is the Committee on Space Research, a scientific committee of the International Council of Scientific Unions, ICSU).

Clark, R. R. (1989), 'The quasi 2-day wave at durham (43° n); solar and magnetic effects', *Journal of Atmospheric and Terrestrial Physics* **51**(7/8), 617–622. Special issue: Atmospheric Tides.

Cooley, J. W. & Tukey, J. W. (1965), 'An algorithm for the machine calculation of complex Fourier series', *Mathematics of Computation* **19**, 297–301.

Coy, L. (1979), 'A possible 2-day oscillation near the tropical stratopause', *Journal of the Atmospheric Sciences* **36**, 1615–1618.

Craig, R. A. (1965), *The upper atmosphere*, Vol. 8 of *International Geophysics Series*, Academic Press, New York.

Craig, R. L. & Elford, W. G. (1981), 'Observations of the quasi 2-day wave near 90 km altitude at adelaide (35° s)', *Journal of Atmospheric and Terrestrial Physics* **43**, 1051–1056.

Craig, R. L., Vincent, R. A., Fraser, G. J. & Smith, M. J. (1980), 'The quasi 2-day wave in the Southern Hemisphere mesosphere', *Nature (London)* **287**, 319–320.

Craig, R. L., Vincent, R. A., Kingsley, S. P. & Muller, H. G. (1983), 'Simultaneous observations of the quasi 2-day wave in the northern and southern hemispheres', *Journal of Atmospheric and Terrestrial Physics* **45**, 539–541.

Doyle, E. M. (1968), Wind Measurements in the Upper Atmosphere, PhD thesis, University of Adelaide, Adelaide, Australia.

Ebel, A. (1974), 'Heat and momentum sources of mean circulation at an altitude of 70 to 100 km', *Tellus* **26**, 325.

Elford, G. (1979), 'momentum transport due to atmospheric tides', *Journal of Geophysical Research* **84**(A8), 4432.

Felgate, D. G. (1970), 'On the point source effect in the measurement of ionospheric drifts', *Journal of Atmospheric and Terrestrial Physics* **32**, 241.

Felgate, D. G. & Golley, M. G. (1971), 'Ionospheric irregularities and movements observed with a large aerial array', *Journal of Atmospheric and Terrestrial Physics* **33**, 1353–1369.

Ferraz-Mello, S. (1981), 'Estimation of periods from unequally spaced observations', *The Astronomical Journal* **86**, 619–624.

Fleagle, R. G. & Businger, J. A. (1980), *An introduction to Atmospheric Physics*, Vol. 25 of *International Geophysics Series*, second edn, Academic Press, New York.

Fooks, G. F. (1965), 'Ionospheric drift measurements using correlation analysis; methods of computation and interpretation of results', *Journal of Atmospheric and Terrestrial Physics* **27**, 979–989.

Forbes, A. M. G. (1988), 'Fourier transform filtering: a cautionary note', *Journal of Geophysical Research* **93**, 6958–6962.

Forbes, J. M. (1982*a*), 'Atmospheric tides 1. Model description and results for the solar diurnal component', *Journal of Geophysical Research* **87**(A7), 5222–5240.

Forbes, J. M. (1982*b*), 'Atmospheric tides 2. The solar and lunar semi-diurnal component', *Journal of Geophysical Research* **87**(A7), 5241–5252.

Forbes, J. M. (1984), 'Middle atmosphere tides', *Journal of Atmospheric and Terrestrial Physics* **46**(11), 1049–1067.

Forbes, J. M. (1985), 'ATMAP report', *Handbook for the Middle Atmosphere Program* **17**, 6–81. SCOSTEP Secretariat, University of Illinois, Urbana, IL.

Forbes, J. M. (1986a), 'ATMAP report', *Handbook for the Middle Atmosphere Program* **21**, 12–55. SCOSTEP Secretariat, University of Illinois, Urbana, IL.

Forbes, J. M. (1986b), 'ATMAP report', *Handbook for the Middle Atmosphere Program* **21**, 56–64. SCOSTEP Secretariat, University of Illinois, Urbana, IL.

Forbes, J. M. & Garrett, H. B. (1976), 'Solar diiurnal tide in the thermosphere', *Journal of the Atmospheric Sciences* **33**, 2226–2241.

Forbes, J. M. & Garrett, H. B. (1978), 'Seasonal-latitudinal structure of the diurnal thermospheric tide', *Journal of the Atmospheric Sciences* **35**, 148–159.

Forbes, J. M. & Garrett, H. B. (1979), 'Theoretical studies of atmospheric tides', *Reviews of Geophysics and Space Physics* **17**(8), 1951–1981.

Forbes, J. M. & Salah, J. E. (1991), 'Mesosphere-thermosphere tidal coupling during the September 21–25, 1987, LTCS 1 campaign', *Journal of Geophysical Research* **96**(A2), 1135–1146. Special issue: Lower Thermosphere Coupling Study (LTCS).

Forbes, J. M. & Vial, F. (1989), 'Monthly simulations of the solar semidiurnal tide in the mesosphere and lower thermosphere', *Journal of Atmospheric and Terrestrial Physics* **51**(7/8), 649–662. Special issue: Atmospheric Tides.

Forbes, J. M. & Vial, F. (1991), 'Semidiurnal tidal climatology of the E-region', *Journal of Geophysical Research* **96**(A2), 1147–1158. Special issue: Lower Thermosphere Coupling Study (LTCS).

Fraser, G. J., Vincent, R. A., Manson, A. H., Meek, C. E. & Clark, R. R. (1989), 'Interannual variability of tides in the mesosphere and lower thermosphere', *Journal of Atmospheric and Terrestrial Physics* **51**(7/8), 555–568. Special issue: Atmospheric Tides.

Fritts, D. C. (1984), 'Gravity wave saturation in the middle atmosphere: A review of theory and observations', *Reviews of Geophysics and Space Physics* **22**, 275–308.

Fritts, D. C. & Isler, J. R. (1992), 'First observations of mesospheric dynamics with a partial reflection radar in Hawai (22° n, 160° w)', *Geophysical Research Letters* **19**, 409–412.

Fritts, D. C. & Vincent, R. A. (1987), 'Mesospheric momentum flux studies at Adelaide, Australia: Observations and a gravity wave-tidal interaction model', *Journal of the Atmospheric Sciences* 44(3), 605–619.

Gage, K. S. & Balsley, B. B. (1980), 'On the scattering and reflection mechanisms contributing to clear air radar echoes from the troposphere, stratosphere and mesopshere', *Radio Science* **15**, 243–258.

Golley, M. G. & Rossiter, D. E. (1970), 'Some tests of methods of analysis of ionospheric drift records using an array of 89 aerials', *Journal of Atmospheric and Terrestrial Physics* **32**, 1215.

Golub, G. H. & Van Loan, C. F. (1980), 'An analysis of the total least squares problem', *SIAM Journal of Numerical Analysis* **17**(6), 883–893.

Golub, G. H. & Van Loan, C. F. (1983), *Matrix Computations*, John Hopkins University Press, Baltimore, MD.

Gossard, E. E. & Hooke, W. H. (1975), *Waves in the atmosphere*, Vol. 2 of *Developments in Atmospheric Science*, Elsevier scientific publishing company, Amsterdam.

Groves, G. V. (1969), 'Wind models from 60 to 130 km altitude for different months and latitudes', *Journal of the British Interplanetary Society* **22**, 285.

Groves, G. V. (1971), Atmospheric structure and its variation in the region from 25 to 120 km, Technical Report 368, Air Force Cambridge Research Lab., Cambridge, Massachusetts, U.S.A.

Hamilton, K. & Garcia, R. R. (1986), 'Theory and observations of short-period normal mode oscillations of the atmosphere', *Journal of Geophysical Research* **91**, 11867–11875.

Harris, T. J. (1993), 'A long-term study of the quasi-two-day wave in the middle atmosphere', *Journal of Atmospheric and Terrestrial Physics.* (In Press).

Harris, T. J. & Vincent, R. A. (1993), 'The quasi-two-day wave observed in the equatorial middle atmosphere', *Journal of Geophysical Research* **98**, 10481–10490.

Hines, C. O. (1960), 'Internal atmospheric gravity waves at ionospheric heights', *Canadian Journal of Physics* **38**, 1441–1481.

Hines, C. O. (1972), 'Momentum deposition by atmospheric waves, and its effects on thermospheric circulation', *Space Research* **12**, 1157–1161.

Hines, C. O. (1974), *The upper atmosphere in motion*, Vol. 18 of *Geophysical Monograph Series*, American Geophysical Union, Washington, D.C. A selection of papers with annotation.

Hines, C. O. & Reddy, C. A. (1967), 'On the propagation of atmospheric gravity waves through regions of wind shear', *Journal of Geophysical Research* **72**, 1015–1034.

Hines, C. O., Paghis, I., Hartz, T. R. & Fejer, J. A., eds (1965), *Physics of the Earth's upper atmosphere*, Prentice-Hall, Inc, Englewood Cliffs, N.J.

Hocking, W. K., May, P. & Röttger, J. (1989), 'Interpretation, reliability and accuracies of parameters deduced by the spaced antenna method in middle atmosphere applications', *Pure and Applied Geophysics* **130**(2/3), 571–604.

Holton, J. R. (1979), *An introduction to dynamic meteorology*, Vol. 23 of *International Geophysics Series*, second edn, Academic Press, New York.

Horne, J. H. & Baliunas, S. L. (1986), 'A prescription for period analysis of unevenly sampled time series', *The Astrophysical Journal* **302**, 757–763.

Hough, S. S. (1898), 'The application of harmonic analysis to the dynamical theory of tides, Part II. On the general integration of Laplace's dynamical equations', *Philosophical Transactions of the Royal Society. (London)* **A191**, 139–185.

IMSL Inc (1987), *IMSL, Inc: Math/Library*, first edn, IMSL, Houston, Texas, USA.

Irvine, L. D., Marin, S. P. & Smith, P. W. (1986), Constrained interpolation and smoothing, *in* 'Constructive Approximation', Vol. 2, Unknown, pp. 129–151.

Kalchenko, B. V. (1987), 'Characteristics of atmospheric disturbances with a quasi two day period', *Handbook for the Middle Atmosphere Program* **25**, 112–118. SCOSTEP Secretariat, University of Illinois, Urbana, IL.

Kalchenko, B. V. & Bulgakov, S. V. (1973), 'Study of periodic components of wind velocity in the lower thermosphere above the equator', *Geomagnetism and Aeronomy* **13**, 955–956.

Kasahara, A. (1976), 'Normal modes of ultralong waves in the atmosphere', *Monthly Weather Review* **104**, 669–690.

Kascheev, B. L. (1987), 'Atmospheric dynamics in the equatorial meteor zone', *Handbook for the Middle Atmosphere Program*. SCOSTEP Secretariat, University of Illinois, Urbana, IL.

Kato, S. (1980), *Dynamics of the upper atmosphere*, Vol. 1 of *Developments in Earth and Plantary Sciences*, Center for Academic Publications Japan, Tokyo; D. Reidel Publishing Company, Dordrecht.

Kaydalov, O. & Portnyagin, Y. (1981), *Geomagnetism and Aeronomy* **21**, 647.

Kelley, M. C. (1989), *The Earth's ionosphere, plasma physics and electrodynamics*, Vol. 43 of *International Geophysics Series*, Academic Press.

Kim, Y. C. & Powers, E. J. (1979), 'Digital bispectral analysis and its applications to non-linear wave interactions', *IEEE Transactions on Plasma Science* **PS-7**, 120–131.

Lacoss, R. T. (1971), 'Data adaptive spectral analysis methods', *Geophysics* **36**(4), 661–675.

Lesicar, D. (1993), Study of the structure of partial reflection radar scatterers and their application in atmospheric measurements., PhD thesis, University of Adelaide, Adelaide, Australia.

Lindzen, R. S. (1967), 'Thermally driven diurnal tide in the atmosphere', *Quarterly Journal of the Royal Meteorological Society* **93**, 18.

Lindzen, R. S. (1974), Tides and internal gravity waves in the atmosphere, *in* F. Verniani, ed., 'Structure and Dynamics of the Upper Atmosphere', Vol. 1 of *Developments in Atmospheric Science*, Elsevier Scientific Publishing Company, Amsterdam, pp. 21–87. Proceedings of the 2nd Course of the International School of Atmospheric Physics, "Ettore Majoran" Centre for Scientific Culture, held in Erice (Italy), 13–27 June, 1971.

Lindzen, R. S. (1981), 'Turbulence and stress owing to gravity wave and tidal breakdown', *Journal of Geophysical Research* **86**, 9707–9714.

Liu, C. H., ed. (1989), *Experimental techniques*, Vol. 2 of *World Ionosphere/Thermosphere Study (WITS) Handbook*, ICSU Scientific Committee on Solar-Terrestrial Physics, SCOSTEP Secretariat, University of Illinois, Urbana, IL.

Longuet-Higgins, M. S. (1968), 'The eigenfunctions of Laplace's tidal equations over a sphere', *Philosophical Transactions of the Royal Society. (London)* **A262**, 511–607.

Manson, A. H. & Meek, C. E. (1987), 'Small-scale features in the middle atmosphere windfield at Saskatoon, Canada (52° N, 107° W): An analysis of MF radar data with rocket comparisons', *Journal of the Atmospheric Sciences* **44**, 3661–3672.

Manson, A. H. & Meek, C. E. (1990), 'Long period (8–20h) wind oscillations in the upper middle atmosphere at Saskatoon (52° N); evidence for non-linear tidal effects', *Planetary and Space Science* **38**, 1431–1441.

Manson, A. H., Meek, C. E., Teitelbaum, H., Vial, F., Schminder, R., Kürschner, D., Smith, M. J., Fraser, G. J. & Clark, R. R. (1989), 'Climatologies of semi-diurnal and diurnal tides in the middle atmosphere (70–110 km) at middle latitudes (40–55°)', *Journal of Atmospheric and Terrestrial Physics* **51**(7/8), 579–594. Special issue: Atmospheric Tides.

May, P. T. (1988), 'Statistical errors in the determination of wind velocities by the spaced antenna technique', *Journal of Atmospheric and Terrestrial Physics* **50**(1), 21–32.

May, P. T., Strauch, R. G. & Moran, K. P. (1988), 'The altitude coverage of temperature measurements using RASS with wind profilers', *Geophysical Research Letters* **15**(12), 1381–1384.

McIntyre, M. E. (1989), 'On the Antarctic ozone hole', *Journal of Atmospheric and Terrestrial Physics* **51**(1), 29–43.

Mendel, J. (1991), 'Tutorial om higher-order statistics (spectra) in signal processing and system theory: Theoretical results and some applications', *Proceedings of the IEEE* **79**(3), 278–304.

Micchelli, C. A., Smith, P. W. & Ward, J. D. (1985), Constrained L_p approximation, *in* 'Constructive Approximation', Vol. 1, Unknown, pp. 93–102.

Miyahara, S., Portnyagen, Y. I., Forbes, J. M. & Solovjeva, T. V. (1991), 'Mean zonal acceleration and heating of the 70- to 100-km region', *Journal of Geophysical Research* **96**(A2), 1225–1238.

Moore, Thomson & Shirtcliff (1988), 'Spectral analysis of ocean profiles from unequally spaced data', *Journal of Geophysical Research* **93**, 655–664.

Muller, H. & Nelson, L. (1978), 'A travelling quasi 2-day wave in the meteor region', *Journal of Atmospheric and Terrestrial Physics* **40**, 761–766.

Muller, H. G. (1974), Winds and turbulence in the meteor zone, *in* F. Verniani, ed., 'Structure and Dynamics of the Upper Atmosphere', Vol. 1 of *Developments in Atmospheric Science*, Elsevier Scientific Publishing Company, Amsterdam, pp. 347–388. Proceedings of the 2nd Course of the International School of Atmospheric Physics, "Ettore Majoran" Centre for Scientific Culture, held in Erice (Italy), 13–27 June, 1971.

Murphy, D. J. (1990), Measurements of Energy and Momentum in the Mesosphere, PhD thesis, University of Adelaide, Adelaide, Australia.

Nakamura, T. (1991), Mesosphere and Lower Thermosphere Dynamics reveaked by radar observations, PhD thesis, Radio Atmospheric Science Center, Kyoto University, Uji, Kyoto 611, Japan.

Palmen, E. & Newton, C. W. (1969), *Atmospheric circulation systems – their structure and physical interpretation*, Vol. 13 of *International Geophysics Series*, Academic Press, New York.

Parzen, E. (1969), Multiple time series modeling, *in* P. R. Krishnaiah, ed., 'Multivariate Analysis', Vol. II, Academic Press, New York.

Pawsey, J. L. (1935), 'Further investigations of the amplitude variations of downcoming wireless waves', *Proceedings of the Cambridge Philosophical Society* **31**, 125.

Pfister, L. (1985), 'Baroclinic instability of easterly jets with applications to the summer mesosphere', *Journal of the Atmospheric Sciences* **42**, 313–330.

Phillips, A. (1989), 'Simultaneous observations of the quasi 2-day wave at Mawson, Antarctica, and Adelaide, South Australia', *Journal of Atmospheric and Terrestrial Physics* **51**(2), 119–124.

Phillips, A. & Briggs, B. H. (1990), 'The day-to-day variability of upper-atmosphere tidal winds and dynamo currents', *Journal of Atmospheric and Terrestrial Physics* **53**, 39.

Phillips, G. J. & Spencer, M. (1955), 'The effects of anisometric amplitude patterns in the measurement of ionospheric drifts', *Proceedings of the Physical Society. (London)* **B68**, 481.

Plumb, R. A. (1983), 'Baroclinic instability of the summer mesosphere: A mechanism for the 2-day wave?', *Journal of the Atmospheric Sciences* **40**, 262–270.

Plumb, R. A., Vincent, R. A. & Craig, C. L. (1987), 'The quasi-two-day wave event of January 1984 and its impact on the mean mesospheric circulation', *Journal of the Atmospheric Sciences* **44**, 3030–3036.

Poole, L. M. G. (1988), *Journal of Atmospheric and Terrestrial Physics* **50**, 585.

Poole, L. M. G. (1990), 'The characteristics of the mesospheric two-day wave as observed at grahamstown (33.3° s, 26.5° e)', *Journal of Atmospheric and Terrestrial Physics* **52**, 259–268.

Prata, A. J. (1989), 'Observation of the 5-day wave in the stratosphere and mesosphere', *Journal of the Atmospheric Sciences* **46**(15), 2473–2477.

Press, W. H. & Rybicki, G. B. (1989), 'Fast algorithm for spectral analysis of unevenly sampled data', *The Astrophysical Journal* **338**, 277–280.

Press, W. H. & Teukolsky, S. A. (1988), 'Search algorithm for weak periodic signals in unevenly spaced data', *Computers in Physics* **Nov/Dec**, 77–82.

Press, W. H., Flannery, B. P., Teukolsky, S. A. & Vetterling, W. T. (1986), *Numerical Recipes*, Cambridge University Press.

Randel, W. J. (1993), 'Observations of the 2-day wave in NMC stratospheric analyses', *Journal of the Atmospheric Sciences*. (In Press).

Reddi, C. R., A. G. & Lekshmi, K. R. (1988), 'Quasi 2-day wave in the middle atmosphere over Trivandrum', *Annales Geophysica* **6**, 231–238.

Reid, I. M. (1986), 'Gravity wave motions in the upper middle atmosphere (60–110 km)', *Journal of Atmospheric and Terrestrial Physics* **48**(5), 1057–1072.

Reid, I. M. (1988), 'MF Doppler and spaced antenna radar measurements of upper middle atmosphere winds', *Journal of Atmospheric and Terrestrial Physics* **50**(2), 117–134.

Reid, I. M. & Vincent, R. A. (1987), 'Measurements of mesospheric gravity wave momentum fluxes and mean flow accelerations at Adelaide, Australia.', *Journal of Atmospheric and Terrestrial Physics* **49**(5), 443–460.

Richmond, A. D. (1971), 'Tidal winds at ionospheric heights', *Radio Science* **6**(2), 175–189.

Rishbeth, H. (1974), Structure of the F region and global thermospheric winds, *in* F. Verniani, ed., 'Structure and Dynamics of the Upper Atmosphere', Vol. 1 of *Developments in Atmospheric Science*, Elsevier Scientific Publishing Company, Amsterdam, pp. 435–479. Proceedings of the 2nd Course of the International School of Atmospheric Physics, "Ettore Majoran" Centre for Scientific Culture, held in Erice (Italy), 13–27 June, 1971.

Rishbeth, H. & Garriott, O. K. (1969), *Introduction to ionospheric physics*, Vol. 14 of *International Geophysics Series*, Academic Press, New York.

Rodgers, C. D. & Prata, A. (1981), 'Evidence for a travelling 2-day wave in the middle atmosphere', *Journal of Geophysical Research* **86**, 9661–9664.

Rosenlof, K. H. & Thomas, R. J. (1990), 'Five-day mesospheric waves observed in solar mesosphere explorer ozone', *Journal of Geophysical Research* **95**(D1), 895–899.

Ross, M. N. & Walterscheid, R. L. (1991), 'Changes in the solar forced tides caused by stratospheric ozone depletion', *Geophysical Research Letters* **18**(3), 420–423.

Rossiter, D. E. (1970), 'On the coupling between aerials used for measuring ionospheric drifts', *Nature (London)* **228**, 1299.

Röttger, J. (1981), 'Investigations of lower and middle atmosphere dynamics with spaced antenna drifts radars', *Journal of Atmospheric and Terrestrial Physics* **43**(4), 277–292.

Röttger, J. (1984), 'The MST radar technique', *Handbook for the Middle Atmosphere Program* **13**, 187–232. SCOSTEP Secretariat, University of Illinois, Urbana, IL.

Röttger, J. & Vincent, R. A. (1978), 'VHF radar studies of tropspheric velocities and irregularities using the spaced-antenna technique', *Geophysical Research Letters* **5**, 917–920.

Rush, C. M., St. John, D. E. & Venkateswaran, S. V. (1970), 'A unified description of the tidal effects in $f_o f_2$', *Radio Science* **5**(12), 1413–1428.

Salby, M. L. (1981a), 'The 2-day wave in the middle atmosphere; observations and theory', *Journal of Geophysical Research* **86**, 9654–9660.

Salby, M. L. (1981b), 'Rossby normal modes in nonuniform background configurations. Part I:Simple fields', *Journal of the Atmospheric Sciences* **38**, 1803–1826.

Salby, M. L. (1981c), 'Rossby normal modes in nonuniform background configurations. Part II: Equinox and solstice conditions', *Journal of the Atmospheric Sciences* **38**, 1827–1840.

Salby, M. L. (1984), 'Survey of planetary-scale travelling waves; The state of theory and observations', *Review Geophysics and Space Physics* **22**, 209–236.

Scargle, J. D. (1982), 'Studies in astronomical time series analysis. II. Statistical aspects of spectral analysis of unevenly spaced data', *The Astrophysical Journal* **263**, 835–853.

Schlapp, D. M. & Harris, T. J. (1993), 'Lunar tidal analysis of 6 yr of mesospheric wind data at Adelaide', *Journal of Atmospheric and Terrestrial Physics* **55**(13), 1629–1635.

Singleton, R. C. (1969), 'An algorithm for computing the mixed radix fast Fourier transform', *IEEE Transactions on Audio and Electroacoustics* **AU-17**(2), 93–103.

Stening, R. J., Meek, C. E., Manson, A. H. & Stephenson, D. G. (1978), 'Winds and wave motions to 110 km at midlatitudes. VI. Tidal, gravity and planetary waves, 1976', *Journal of the Atmospheric Sciences* **35**, 2194–2204.

Teitelbaum, H. & Vial, F. (1991), 'On tidal variability induced by nonlinear interaction with planetary waves', *Journal of Geophysical Research* **96**, 14169–14178.

Tsuda, T., Kato, S. & Vincent, R. (1988), 'Long period wind oscillations observed by the Kyoto meteor radar and comparisons of the quasi-2-day wave with Adelaide HF radar', *Journal of Atmospheric and Terrestrial Physics* **50**, 225–230.

Tukey, J. (1965), 'Data analysis and frontiers of geophysics', *Science* **148**(3675), 1283–1289.

Vial, F. & Forbes, J. M. (1989), 'Recent progress in tidal modelling', *Journal of Atmospheric and Terrestrial Physics* **51**(7/8), 663–672. Special issue: Atmospheric Tides.

Vial, F., Forbes, J. M. & Miyahara, S. (1991), 'Some transient aspects of tidal propagation', *Journal of Geophysical Research* **96**(A2), 1215–1224.

Vincent, R. A. (1984a), 'Gravity-wave motions in the mesosphere', *Journal of Atmospheric and Terrestrial Physics* **46**(2), 119–128.

Vincent, R. A. (1987), 'Planetary and gravity waves in the mesosphere and lower thermosphere', *Advances in Space Research* **7**(10), 10163–10169.

Vincent, R. A. (1993), 'Long period motions in the equatorial mesosphere', *Journal of Atmospheric and Terrestrial Physics* **55**(7), 1067–1080.

Vincent, R. A. & Ball, S. (1977), 'Tides and gravity waves in the mesosphere at mid- and low-altitudes', *Journal of Atmospheric and Terrestrial Physics* **39**, 965–970.

Vincent, R. A. & Lesicar, D. (1991), 'Dynamics of the equatorial mesosphere; first results from a new generation partial reflection radar', *Geophysical Research Letters* **18**, 825–828.

Vincent, R. A. & Röttger, J. (1980), 'Spaced antenna VHF radar observations of tropospheric velocities and irregularities', *Radio Science* **15**, 319–335.

Vincent, R. A., ed. (1984b), *Ground-based techniques*, Vol. 13 of *Handbook for the Middle Atmosphere Program*, ICSU Scientific Committee on Solar-Terrestrial Physics, SCOSTEP Secretariat, University of Illinois, Urbana, IL.

Vincent, R. A., Tsuda, T. & Kato, S. (1989), 'Asymmetries in mesospheric tidal structure', *Journal of Atmospheric and Terrestrial Physics* **51**(7/8), 609–616. Special issue: Atmospheric Tides.

Walterscheid, R. L. (1980), 'Travelling planetary waves in the stratosphere', *Pure and Applied Geophysics* **118**, 240–265.

Walterscheid, R. L., Sivjee, V. V., Schubert, G. & Hamway, R. M. (1986), *Nature (London)* **324**, 347.

Whitehead, J. D., From, W. R., Jones, K. L. & Monro, P. E. (1983), 'Measurement of movements in the ionosphere using radio reflections', *Journal of Atmospheric and Terrestrial Physics* **45**(5), 345–351.

Woodman, R. F. & Guillen, A. (1974), 'Radar observations of winds and turbulence in the stratosphere and mesosphere', *Journal of the Atmospheric Sciences* **31**, 493–505.